Theory of microrheology in complex fluids

Dissertation submitted for the degree of Doctor of Natural Sciences (Dr.rer.nat.)

by
Markus Gruber

at the

Universität Konstanz

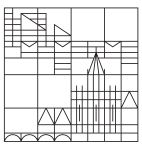

Mathematisch-Naturwissenschaftliche Sektion

Fachbereich Physik

Konstanz, 2019

Date of the oral examination: July 15, 2019
First referee: Prof. Dr. Matthias Fuchs
Second referee: Prof. Dr. Thomas Voigtmann

Abstract

The investigation of local viscoelastic properties of biological samples is of interest for both fundamental research on mechanical rigidity of cells [SSV+10] as well as the understanding of cancer [SVF+16; BNA09]. One method for these investigations is microrheology, where one puts the rheometer into the sample rather than the sample into the rheometer as in classical rheology. The measurement device for microrheology is a set of microscopic beads, which are immersed in the sample. The measurement itself consists of the observation of these probe particles under thermal motion only (passive microrheology) or under additional external fields like magnets or optical tweezers (active microrheology). There are, however, still open questions on how to relate the motion of the probe to the viscoelastic properties in complex liquids [Zia18], which consist of a simple liquid, the solvent, with suspended particles or polymers.

In this thesis a theoretical description of active microrheology in two model systems for complex fluids is studied: a colloidal glass and a dilute suspension of active, self-propelled particles. For the colloidal glass, mode-coupling theory (MCT) is employed to describe constant-force microrheology [GAPF16] and the resulting equations of motion are solved numerically. This allows the investigation of the delocalization transition, which separates the regime of an elastic response of the probe from the regime with a viscous response above a critical force. The critical behavior is studied analytically and numerically, supported by the analysis of schematic models and simulations. A comparison with an experiment reveals dynamic heterogeneities in the motion of the probe, which can be connected to a bimodal structure of the van Hove function. For the dilute suspension of active particles, an expansion of the pair correlation function is used to describe constant velocity active microrheology with a spheroidal probe. In this case, an increase of the friction coefficient of the probe is found for oblate spheroids at large activities, while for prolate spheroids the friction coefficient is reduced beyond the value in a pure solvent.

Zusammenfassung

Die Untersuchung von viskoelastischen Eigenschaften von biologischen Proben ist sowohl für die Grundlagenforschung zur mechanischen Festigkeit von Zellen [SSV+10], als auch bei der Krebsforschung [SVF+16; BNA09] von Interesse. Eine Methode für diese Untersuchungen ist Mikrorheologie, wo das Rheometer in die Probe, statt die Probe ins Rheometer gebracht wird. Als Messgerät für Mikrorheologie dienen mikroskopisch große Kügelchen (sog. Probenteilchen), die in die zu untersuchende Probe gegeben werden. Die Messung besteht darin, die Bewegung der Probenteilchen ohne (passive Mikrorheologie) oder mit externen Feldern wie Magnetfeldern oder optischen Pinzetten (aktive Mikrorheologie) zu beobachten. Allerdings ist die Frage, wie Bewegung der Teilchen mit den viskoelastischen Eigenschaften von komplexen Flüssigkeiten in Verbindung gebracht werden können noch nicht vollständig geklärt [Zia18]. Eine komplexe Flüssigkeit besteht aus einer einfachen Flüssigkeit, dem Lösungsmittel, in dem weitere Teilchen oder Polymere gelöst oder suspendiert sind.

In dieser Arbeit wird die theoretische Beschreibung von aktiver Mikrorheologie in zwei Modellsystemen für komplexe Flüssigkeiten untersucht: einem kolloidalen Glas und einer verdünnten Suspension von aktiven Teilchen. Für das kolloidale Glas wird Modenkopplungstheorie (MCT) verwendet, um Mikrorheologie mit konstanter Kraft zu beschreiben. Die zugehörigen Bewegungsgleichungen werden numerisch gelöst. Dies erlaubt die Analyse des Delokalisationsübergangs, der den Bereich eines elastischen Verhaltens des Probenteilchens von dem Bereich eines viskosen Verhaltens oberhalb einer kritischen Kraft trennt. Das kritische Verhalten wird analytisch und numerisch untersucht, unterstützt durch die Analyse von schematischen Modellen und Simulationen. Der Vergleich mit einem Experiment zeigt dynamische Heterogenitäten in der Bewegung des Probenteilchens, die mit einer bimodalen Struktur der van Hove Funktion in Verbindung gebracht werden können. Für die verdünnte Suspension aktiver Teilchen wird eine Entwicklung der Paarkorrelationsfunktion verwendet, um aktive Mikrorheologie mit konstanter Geschwindigkeit und einem Ellipsoid als Probenteilchens zu beschreiben. In diesem Fall erhöht sich der Reibungskoeffizient eines oblaten Probenteilchens für große Aktivität, während er sich für prolate Probenteilchen reduziert. Dieser Wert kann sogar unterhalb des Wertes liegen, den die Probe im reinen Lösungsmittel hätte.

Eine ausführliche deutsche Zusammenfassung findet sich in Kapitel 10.

Acknowledgements

I enjoyed the time of my PhD very much. It is therefore now the time, to thank everyone, who contributed to this wonderful period in manyfold ways. In particular, I want to thank

- Matthias Fuchs for providing the topic and the PhD position as well as for always having an open door for my questions and a suggestion how to solve them. I appreciate that he allowed me to extend my horizon about the different facets of rheology, soft matter and glasses in many conferences and for the research semester in the US,
- Gustavo Abade for the implementation of the numerical solution for the dynamic MCT equations and for the close collaboration during his stay,
- Antonio Puertas, Frank Scheffold and Nesrin Senbil for the fruitful collaborations,
- John Brady for hosting me at Caltech and teaching me about active matter,
- the German-American Fulbright Commission and University of Konstanz for financial support of my research stay at Caltech
- Aleena Laganapan, Johannes Häring, Lukas Schrack, Manuel Maier, Robin Kopp, Sebastian Fritschi and Tadeus Ras for proofreading parts of my thesis
- Stefan Gerlach for providing help and fixing all computer related problems
- the count- and nameless people sharing their ideas and skills by providing open source software
- Marianne Griesser for keeping the bureaucratic workload low
- my friends from P9 for introducing me to climbing, which provided times of sunshine during the period of writing, and for the other joint activities
- and my parents for their continuous support and their patience with the SEK, which took extraordinarily long to appear ;-)

Contents

List of symbols

$\langle A, B\rangle_{\text{eq}} = \langle A, B\rangle$ ..... equilibrium weighted inner product, 26
$\langle A\rangle$ ..... mean of variable A, 10, 13, 25
$\langle A\rangle_{\text{eq}} = \langle A\rangle$ ..... equilibrium average of variable A, 26
$\langle \Delta A^2\rangle = \langle (A - \langle A\rangle)^2\rangle$ ..... variance of variable A, 10, 13
$\langle \Delta x^2\rangle(t)$ ..... variance in x-direction, 47
$\langle \Delta z^2\rangle(t)$ ..... variance in z-direction, 47
$\langle x^2\rangle(t)$ ..... mean square displacement in x-direction, 47
$\langle z^2\rangle(t)$ ..... mean square displacement in z-direction, 47
$\langle z\rangle(t)$ ..... mean displacement in z-direction, 47
$\tilde{f}(s)$ (tilde over function) ..... Laplace transform of $f(t)$, 36, 146
$\hat{f}(s)$ (hat over function) ..... S-transform of $f(t)$, 146

$\hat{a}$ ..... ellipsoid aspect ratio, 59
$\boldsymbol{A}$ (bold uppercase symbol, not $\boldsymbol{F}$) ..... matrix or vector of vectors, 10
$\boldsymbol{a}$ (bold lowercase symbol) ..... vector, 10

c ..... contraction factor, 78
c_k ..... direct correlation function, 28
c^r ..... reduced contraction factor, 78, 104
c_k^s ..... probe-bath direct correlation function, 29

d ..... bath particle diameter, 23
D_0^s ..... probe particle diffusion short time diffusion coefficient, 23
$\mathrm{d}^d\boldsymbol{r} = \mathrm{d}\boldsymbol{r}$ ..... d-dimensional integration element, 25, 265
$\boldsymbol{\partial}_{\boldsymbol{r}}$ ..... nabla, multivariate derivative with respect to $\boldsymbol{r}$, 11
$\boldsymbol{\partial}_{\hat{\boldsymbol{q}}}^R = \hat{\boldsymbol{q}} \times \boldsymbol{\partial}_{\hat{\boldsymbol{q}}}$ ..... Rotational gradient operator, 18
$\delta(\boldsymbol{r})$ ..... Dirac-delta distribution, 12
D^R ..... rotational diffusion coefficient, 56, 251
$\partial\mathcal{V}^{\text{exc}}$ ..... excluded volume surface, 57
$\mathrm{d}X_j$ ..... moment for decimation algorithm, 81

$\mathcal{F}[f]$ ..... Fourier transform of f, 265
$f_{\boldsymbol{k}}$ ..... nonergodicity parameter of the bath correlation function, 44
F_{ex} ..... external force value, 24
$\boldsymbol{F}_{\text{ex}}$ ..... external force vector, 24
$f_{\boldsymbol{k}}^s$ ..... nonergodicity parameter of the probe correlation function, 44

$g(r)$ ..... pair correlation function, 28
γ ..... friction coefficient, 10, 251
$\Gamma_{\boldsymbol{k}^*}$ ..... short time decay rate, 42
$g(p,t)$ ..... memory kernel weight or helper function, 43, 76

$G^s(\boldsymbol{r},t)$ ..... self part of the van Hove function, 27
$G^{s\parallel}(z,t)$ ..... parallel part of the self part of the van Hove function, 44
$G^{s\perp}(x,t)$ ..... perpendicular part of the self part of the van Hove function, 44

i, $\mathrm{i}^2=-1$ ..... imaginary unit, 6

$\mathcal{J}(t)$ ..... creep compliance, 5, 55

$\boldsymbol{k}$ ..... wave vector, 27
k_B ..... Boltzmann's constant, 8

L ..... arc length, 247
ℓ ..... run length for active particles, 60

$\mathcal{M}_\alpha^{(1)}$ ..... first moment in direction α, 47
$\mathcal{M}_\alpha^{(2)}$ ..... second moment in direction α, 47
$m_{\boldsymbol{k}}^{\alpha\beta}$ ..... primitive memory function, 38, 41
MCT ..... mode-coupling theory, 22
$M_{\boldsymbol{k}^*}^{(i)}$ ..... effective memory function, 42, 43
$\boldsymbol{m}(\boldsymbol{r},t)$ ..... polar order field, 64
MSD ..... Mean square displacement, 13

n ..... particle number density, 28
$n(\boldsymbol{r},t)$ ..... average bath particle density, 64
$\boldsymbol{n}$ ..... surface normal vector, 22, 56
$\boldsymbol{n}_{ij}$ ..... surface normal vector of the excluded volume by particles i and j, 22, 56

Ω ..... Smoluchowski operator, 11, 14, 17–21

Pe^act ..... Péclet number for activity, 60
Pe^ext ..... Péclet number for external driving, 60
φ ..... packing fraction, 23
$\boldsymbol{\phi}(t)=(\phi_{q_1}(t),\phi^s_{q_2}(t),\ldots)$ ..... vector of all bath particle correlation functions, 43
$\phi_{\boldsymbol{k}}(t)$ ..... bath density correlation function, 29
$\boldsymbol{\phi}^s(t)=(\phi^s_{\boldsymbol{q}_1}(t),\phi^s_{\boldsymbol{q}_2}(t),\ldots)$ ..... vector of all probe particle correlation functions, 43
$\phi^s_{\boldsymbol{k}}(t)$ ..... probe density correlation function, 29
$\phi^{s\parallel}_q(t)$ ..... probe-correlation function parallel to external force, 43
$\phi^{s\perp}_q(t)$ ..... probe-correlation function perpendicular to external force, 43
Ψ ..... general phase space probability density, 11

$\boldsymbol{q}$ ..... wave vector, 27
q_d ..... difference wave vector grid, 77
$\boldsymbol{Q}(\boldsymbol{r},t)$ ..... nematic order field, 64

$\mathcal{R}$ ..... rotation matrix, 38
$\rho^b_{\boldsymbol{k}}=\rho_{\boldsymbol{k}}$ ..... Fourier transformed bath particle density, 27, 32
$\rho(\boldsymbol{r})$ ..... bath particle density, 27
$\rho^s_{\boldsymbol{k}}$ ..... Fourier transformed probe particle density, 27
$\rho^s(\boldsymbol{r})$ ..... probe particle density, 27

$\hat{S}$ ..... surface of unit sphere, 18, 56
s (as argument) ..... Laplace frequency, 36
s ..... probe/bath diameter ratio, 59
S_k ..... static structure factor, 28
S^c ..... stability matrix, 193
S_k^s ..... probe-bath static structure factor, 29

$\tau = d^2/D_0^s$ ..... probe particle diffusion time scale, 23

$\partial\mathcal{V}^{\text{exc}}$ ..... excluded volume surface, 21, 56, 59
$\mathcal{V}_i$ ..... excluded volume of particle i, 21
V^{int} ..... interaction potential, 21

1. Introduction

πάντα ῥεῖ (panta rhei) – everything flows

(Heraclitus of Ephesus)

What is the difference between water and honey? What do ice cream and beaten egg whites have in common? In physics, we are interested in the behavior of these materials, for example, how they deform if a force is applied. Water and honey both flow when their container is tilted, but they flow with different speeds, because the viscosity of honey is much higher than that of water. In contrast, ice cream and beaten egg whites remain in their container even if it is turned upside down. When they are slightly deformed, they go back to their original shape if the force is released. This is called an elastic behavior. Investigation of viscoelastic properties is the subject of rheology[1].

This field is not only relevant in the kitchen, but also for industrial processing of plastics [DW13], ceramics [RS05; Lag15], computer technology [Kar96] and resource industry [Bog09]. Moreover, it is also important for biology. Even though we consist of about 60 % of water[WWB80], we walk or swim, but we do not flow away. The rigidity of cells, but also the transport processes within them are still subject to recent investigations [TKW02; WMT06; dVKvD+07]. These studies use microrheological techniques for their investigations. Microrheology can be characterized as rheology on the micrometer scale, which allows to study living cells and their components without destroying them [dVKvD+07]. The rheometer suitable for investigations within a cell is just a number of small beads, whose motion can be tracked. If their motion is purely driven by thermal fluctuations, linear viscoelastic properties can be measured [TKW02]. This is called passive microrheology. It is also possible to manipulate these probe particles with external magnetic fields, optical tweezers or molecular motors, which allows to direct the motion of the probes, to examine nonlinear behavior or obtain better signal to noise ratios [dVKvD+07; WMT06]. Then, this technique is called *active microrheology*. It allows for example to measure whether a blood-cell under test is dead or alive [BLJS09]. Other researchers use this technique to identify cancer cells [SVF+16; BNA09]. Despite their widespread use, evaluation of these experiments is not always straightforward. Typically the probes should "be bigger than the structural length scale [...] of the complex material in order to treat the medium as continuum around the embedded probes" [SSV+10, Sec. 1.2, p. 21]. The reason for this restriction is that a complete theory for smaller sizes is not yet available. To obtain a better understanding of these processes, some theories and simulations have been worked out. In the conclusions of a review of those by R. Zia [Zia18], she states that "[t]heoretical modeling of microstructural evolution in networked and nonergodic complex fluids is an important future challenge" [Zia18, p. 400].

This challenge will be addressed in this thesis by analyzing a theoretical model for active microrheology in a colloidal glass. The other complex fluid investigated theoretically in this thesis is also inspired by the physics of life [Pop16]: a dilute suspension of active particles,

[1] from Greek ῥέω (rhéō), engl. "flow" and -λογία, (-logia), engl. "study of"

which can propel themselves by consuming energy, like the motor protein kinesin in biological systems, or by using other types of chemical or physical gradients in artificial model systems. This is physics far from thermal equilibrium, which can lead to surprising effects.

The thesis is organized as follows: In Chapter 2 we[2] introduce the important concepts for soft matter and its characterization by rheology. In particular, we give a short introduction into the experimental techniques of passive and active microrheology. The theoretical description for microrheology is based on the Smoluchowski equation, a partial differential equation for the probability distribution of the probe and bath particles. It is used to derive equations of motion in the mode-coupling theory (MCT) framework for active microrheology in dense suspensions. The main idea of MCT is the reduction of the many body problem to a set of equations for relevant variables, typically density correlation functions. The last section in this chapter is dedicated to a derivation of equations of motion for active microrheology in dilute suspension of active particles via the pair correlation function.

To solve the mode-coupling equations we are required to address several different numerical problems, which are discussed one by one in Chapter 3. The final section contains numerical tests and discussions of the convergence order, stability and consistency of the algorithm.

Based on the numerical solutions, we can investigate the behavior of the probe particle for small and large forces. We are specifically interested in the behavior in a colloidal glass, which exhibits a solid-like behavior with a liquid-like structure. This causes the probe particle to remain localized for small forces. For forces larger than a threshold force, called the critical force, the probe is able to break free. In Chapter 4 we characterize this critical force with different methods. This allows us to construct a phase diagram and to correlate the critical force with the yield stress and quiescent mean square displacements. Furthermore, we have a closer look on moments, transport coefficients, correlation functions and van Hove functions close, but not too close to the critical force.

The analysis of the critical laws in the proximity of the critical force is the topic of Chapter 5. This qualitative change from localized to delocalized behavior is also called the delocalization transition, which is studied using numerical and analytical approaches. This includes scaling laws for the long time limit as function of the force as well as critical dynamics.

A simplified version of the MCT equations is studied in Chapter 6 considering a schematic model invented by Gustavo Abade. This allows us to obtain some analytic and rigorous results for the critical laws, which are also tested numerically for their range of validity.

Chapter 7 crowns the analysis of our theory, by comparing it to an experiment in an emulsion glass. We will describe how to map our theory to the experiment and find interesting dynamics both in theory and experiment.

The project of active microrheology in active suspensions, which was carried out during a research semester with John F. Brady at the California Institute of Technology is presented in Chapter 8. The numerical solutions provide unintuitive insights into the motion of a spheroidal probe in a suspension of active Brownian particles.

We will summarize our conclusions in Chapter 9, which is followed by the German summary of this thesis. Additional calculations and information can be found in the Appendix.

[2] 'We' refers to me, the author, and you, the reader. Together we will discover the miracles and pitfalls of active microrheology in complex fluids.

2. Theoretical framework

> The whole of science is nothing more
> than the refinement of every day thinking.
>
> *(Albert Einstein [Ein36, p. 349])*

In this chapter we will provide an introduction into the field of soft matter, rheological phenomena (Sec. 2.1) and their characterization using a technique called microrheology (Sec. 2.2). Then we lay the foundations for the theoretical description of complex fluids based on the Smoluchowski equation (Sec. 2.3). We derive equations of motion for the probe particle in active microrheology in a dense colloidal suspension within the framework of mode-coupling theory (Sec. 2.4) and in a dilute suspension of active particles using a density expansion of the pair correlation function (Sec. 2.5).

2.1. Rheology and soft matter

The physics of soft matter characterizes the behavior of materials, which can be deformed rather easily. These materials are ubiquitous in everyday life: honey, mayonnaise, soap, saliva, toothpaste, paint and rubber, just to mention a few. These materials are typically composed of microscopic elements, like oil droplets in mayonnaise or polymers in saliva and rubber. Their interaction energy is typically of the order of thermal energy so that they play an essential role for life. Both ingredients, the large size of the microstructure compared to molecules and the small thermal energy compared to molecular binding energies, cause these materials to deform easily [GDR03, p. 12]. This justifies to classify them as *soft matter*. Their behavior from simple to complex is briefly discussed in the following.

2.1.1. Ideal solids and simple liquids

Let us start with the simplest cases, the response of ideal liquids and ideal solids to external forces. When deforming solids, the force is proportional to the deformation, which was published for the first time by Robert Hooke: “ut tensio, sic vis” (as the extension, so the force) [Hoo78, p. 1]. Initially, this law was proposed for springs, which have only a single degree of freedom, the extension. A solid on the other hand has many degrees of freedom, but we can think of it as being composed of many infinitesimally small units, each one having only few degrees of freedom. In this continuum theory the forces and deformations of the complete solid are split among these infinitesimal volumes, which leads to the *stress* $\sigma = F/(\mathrm{d}x\,\mathrm{d}y)$, the force per unit area and the *strain* $\gamma = \Delta x/\mathrm{d}y$, the deformation per unit length, as sketched in the left panel of Figure 2.1. Then, Hooke’s law is given by

$$\sigma = G\gamma, \tag{2.1}$$

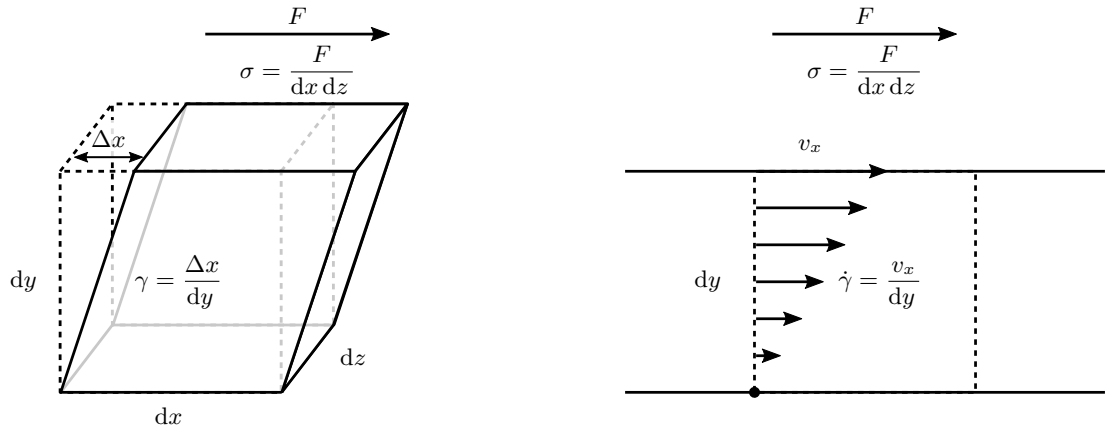

Figure 2.1.: Shearing a solid (left) and a liquid (right). The force F is applied in x-direction on the top surface, which leads to a stress $\sigma = F/(\mathrm{d}x\,\mathrm{d}y)$. The solid reacts with a shear deformation Δx, which leads to the strain $\gamma = \Delta x/\mathrm{d}y$. The top layer of the liquid moves with velocity v_x, while the bottom layer is still, which leads to a velocity gradient or shear rate $\dot{\gamma} = v_x/\mathrm{d}y$.

where G is the elastic modulus or elastic constant, a material property for the corresponding deformation. The stress is given in units of Pascal ($\mathrm{Pa} = \mathrm{kg}/(\mathrm{m\,s}^2)$) and since the strain is dimensionless, this is also the unit of the modulus [Osw09, Chap. 1.1.1, p. 3]. Since a solid is typically three-dimensional, forces can deform the material in many different ways. Therefore, a more elaborate description in terms of tensors is necessary for a full description, as introduced for example in [LLS+10; Fre14]. Nevertheless, any complicated deformation can be decomposed into two contributions, *hydrostatic compression* (or extension) and *pure shear* [LL70, p. 10, Eq. (4.2)]. Hydrostatic compression changes the volume of the body, but not its shape, while the pure shear changes the shape keeping the volume constant. The latter is sketched in Figure 2.1.

While the same description and deformations can be applied to fluids as well, they differ in their response to stresses. When shearing a fluid, as sketched in the right panel of Figure 2.1, the stress is proportional to the shear rate $\dot{\gamma} = v_x/\mathrm{d}y$ (or velocity gradient)

$$\sigma = \eta\dot{\gamma}, \tag{2.2}$$

where η is the dynamic shear viscosity, which is given in units of $\mathrm{Pa\,s}$ [Osw09, Sec. 1.1.2, p. 4]. The first conveyed systematic experiments on this relation were performed by Newton [New72; New86, Vol. II, Sec. VII., §61]. In his honor, fluids fulfilling (2.2) are called *Newtonian fluids*. As we have seen above, the behavior of soft materials is richer than these two ideal cases. This includes non-Newtonian fluids as well as viscoelastic solids and fluids which we will discuss in the following section.

2.1.2. Viscoelasticity

Ideal solids and fluids respond instantaneously to applied stress, because neither Hooke's law (2.1) nor Newton's law (2.2) include a time scale. It was first introduced by Maxwell that their response can be time dependent, governed by a timescale τ, a "time of relaxation" [Max67,

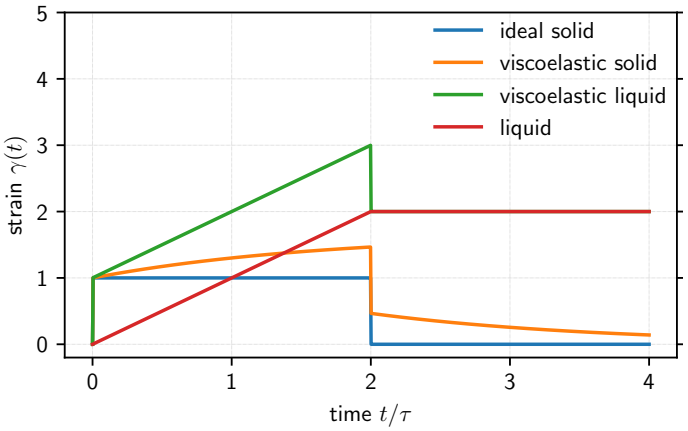

Figure 2.2.: Response of different viscoelastic materials to a sudden constant stress applied for $t/\tau \in [0, 2]$ and released for $t/\tau > 2$.

p. 52f], which determines whether a material reacts like a solid or a liquid as we will see in the following. Based on their behavior for long times, these materials are called viscoelastic solids, if they behave like solids for long times, or viscoelastic liquids, if they behave like liquids for long times. Their constitutive equation in modern notation is given by [Fre14, p. 211, Eq. (7.1)]

$$\sigma(t) = \int_0^t G(t - t')\dot{\gamma}(t')\mathrm{d}t' \,, \tag{2.3}$$

with a *relaxation modulus* $G(t)$. This function encodes the full time-dependent response of the material. Linear viscoelastic materials can be modeled by

$$G(t) = \mu_\infty + (\mu_0 - \mu_\infty)G'(t), \tag{2.4}$$

where μ_∞ and μ_0 ($\mu_0 > \mu_\infty$) are coefficients describing the long and short time elastic behavior, while $G'(t) \in [0, 1]$ is called the *relaxation kernel* [Fre14, p. 210f, Eq. (7.2),(7.3)]. This description can be traced back to Boltzmann [Bol68, p. 622, Eq. (4)], who used this concept to describe the torsion of wires. For Maxwell's model, the relaxation kernel is given by $G'(t) = \exp(-t/\tau)$[1].

When applying a constant stress σ at time t, we can find the strain as function of time for Maxwell's model with the help of the Laplace transform calculus (see Appendix B)

$$\gamma(t) = \frac{\sigma}{\mu_0} \begin{cases} \left(\mathrm{e}^{-\frac{\mu_\infty}{\mu_0}\frac{t}{\tau}} + \frac{\mu_0}{\mu_\infty}\left(1 - \mathrm{e}^{-\frac{\mu_\infty}{\mu_0}\frac{t}{\tau}}\right)\right), & \mu_\infty > 0, \\ 1 + \frac{t}{\tau}, & \mu_\infty = 0. \end{cases} \tag{2.5}$$

For $t/\tau \gg 1$ we recover Hooke's law $\sigma = \mu_\infty\gamma$ for $\mu_\infty > 0$ and Newton's law $\sigma = \tau\mu_0\dot{\gamma}$ for $\mu_\infty = 0$. Hence, the parameter μ_∞ determines whether the Maxwell model behaves for long times like a solid or a liquid. For short times $t/\tau \ll 1$ we find an elastic response with modulus μ_0 in both cases. The resulting strains for different models are shown in Figure 2.2. The strain response (2.5) to a step stress of unit amplitude is also called *creep compliance* $\mathcal{J}(t) = \gamma(t)/\sigma$ [FS17, p. 18]. This quantity is important, because it can be connected to microrheological measurements, which we will discuss below [FS17, p. 106, Eq. (3.99)].

[1] Strictly speaking Maxwell's model applies to the case $\mu_\infty = 0$ [FS17, Sec. 3.7.4, p. 113], while the limit $\tau \to 0$ with $\mu_0\tau = \mu_\infty\tau'$ describes the Kelvin-Voigt model with relaxation time τ' [FS17, Sec. 3.7.3, p. 112]

Considering an experiment, where a stress σ is applied at time $t = 0$ and removed at time $t = T$, as sketched in Figure 2.2, we find that solids relax back to their initial state, while liquids find a new equilibrium position. The solids remember their initial configuration, which is expressed by a non-vanishing long time limit of the relaxation modulus $G(t)$. Contrarily, viscoelastic liquids relax partially and ideal liquids have no memory at all.

Experimentally, the relaxation modulus can be probed by oscillatory shear. For example, a sinusoidal strain with frequency ω and amplitude γ_0 is imposed and the corresponding stress is measured. If the strain is small enough, the stress will be sinusoidal as well with an amplitude σ_0 and a phase lag δ. Representing the sinusoidal signals as complex exponential function, we can define the complex shear modulus [FS17, p. 14, Eq. (1.13)]

$$G^*(\omega) = \frac{\sigma(t)}{\gamma(t)} = \frac{\sigma_0 \mathrm{e}^{\mathrm{i}\delta}}{\gamma_0} = G'(\omega) + \mathrm{i}G''(\omega), \tag{2.6}$$

which is often split into the real part $G'(\omega)$ and the imaginary part $G''(\omega)$. i is the imaginary unit with $\mathrm{i}^2 = -1$. Since the response for a purely elastic material is always proportional to the strain and therefore in-phase, G' is also called the elastic or storage modulus. Similarly, the response of a purely viscous material is proportional to the strain rate so that G'' is called the viscous or loss modulus. $G^*(\omega)$ is therefore the frequency dependent generalization of the shear modulus. Using Fourier transformations (see Appendix A), the complex shear modulus can be related to the relaxation modulus via [FS17, p. 16, Eq. (1.28)][2]

$$\mathcal{F}\left[t \mapsto G(t)\right](\omega) = \frac{G^*(\omega)}{\mathrm{i}\omega}. \tag{2.7}$$

Note that G and G^* are not direct Fourier transforms, even though the notation might suggest it. Nevertheless, these are the common symbols. The complex modulus as well as the creep compliance for a broad variety of different model materials can be found in [FS17, Chap. 3.7, p. 110-118]. More details on the modeling of complex fluids are given in [Spa15, Chap. 1].

2.1.3. Complex fluids

Even though the response in the previous section was time-dependent, this is still linear rheology, because the coefficients are independent of the values of stress, the strain or the shear rate. Many phenomena however have their origins in non-linear behavior. Ketchup spilling over the table after shaking the bottle is just one. In physical terms this behavior is called *shear thinning*. Another application of non-linear effects can be found in paints. When painting, we would like to distribute it as homogeneously as possible on the wall, but when we are done the paint should not flow down before drying. The trick is to use a material which has a *yield stress*. It behaves like a solid if the stress is below the yield stress and like a liquid when it is larger. This prevents the paint from flowing down from the brush and the wall.

The origin for these nonlinear behaviors can be found in the microstructure and the microscopic interactions in complex liquids. The term complex refers not only to the complex behavior of those fluids, but also to their composition: They consist of at least two components, typically a solvent and other particles, fluids or polymers. Tuning their properties to achieve a

[2] If our definition of the Fourier transform is used, multiply the right hand side by -1.

desired behavior is a challenging task for rheologists in fields as diverse as food [Far90; TB05], plastics [DW13], ceramics [RS05], computer technology [Kar96] and resource industry (minerals, coal, sand, oil) [Bog00; Bog09], where it is not only necessary to extract and process the desired materials, but also to treat the waste.

In this work we will focus on the fundamental understanding of a recent measurement technique. Therefore, we investigate the simplest complex fluid possible: a colloidal suspension or dispersion of hard spheres. The IUPAC defines a colloidal dispersion as a "a system in which particles of colloidal size of any nature (e.g. solid, liquid or gas) are dispersed in a continuous phase of a different composition (or state)", where colloidal size refers to "at least in one direction a dimension roughly between 1 nm and 1 µm" [Eve72, Sec. 1.3, p. 605]. Characteristic of these systems is that the particles of this size are "evidently in motion; their motion consisting [...] of a change of place in the fluid" [Bro28, p. 466]. With careful experiments, Brown concluded that this motion is independent of the nature of the particles, being pollen, charcoal or even a fragment of the Sphinx [Bro28, p. 472], but is instead only connected to their size. In his honor this phenomenon is called *Brownian motion*. It took, however, until the beginning of the next century to explain this behavior with the existence of solvent molecules by Einstein [Ein05; Ein06], Langevin [Lan08], Perrin [PD10], Smoluchowski [vSmo06] and Sutherland [Sut05]. Their ideas for the microscopic motion will be discussed in the next sections. A good contemporary reference for the modelling of colloidal suspensions is [Dho96].

Despite their simple structure, colloidal hard sphere suspensions show already a rich phenomenology like shear thinning, shear thickening and yielding [WB09]. The latter occurs at high concentrations of particles. They hinder their motion so strongly that the material behaves like a solid. This state with a fluid-like structure (no long-range order), but solid like behavior is called a *glass* [LR15]. The crossover from fluid to solid behavior is the *glass transition* [Wee16]. For hard colloids, the concentration is the only parameter to obtain a glass, but for other systems – including the familiar glass for windows and bottles – also rapid cooling of the melt leads to a glass [CT59]. In any case, glasses are characterized by a very high viscosity (more than 10^{15} times that of water) and very long relaxation times, which makes equilibration difficult to impossible on experimental time scales [Wee16, p. 27]. Glasses can therefore be considered as non-equilibrium systems. This makes a theoretical description at the same time challenging and interesting.

Another non-equilibrium system can be obtained if the particles can move on their own, as for example bacteria. These so called *active matter systems* "consist of a large collection of individual agents, such as particles or macromolecules, that convert some form of energy (typically chemical) into mechanical work. This work, in turn, leads to microstructural changes in the system" [Spa15, p. 319]. The activity drives the system out of equilibrium and can lead to self-organization and collective behavior of the whole system [VZ12]. When applied to transport and transformation of proteins, this allows – on the macroscopic level – the most complex non-equilibrium process: life. For a fundamental understanding of these systems, of course much simpler models are studied as the mentioned bacterial suspensions [EWG15; SAJ+16] or artificial swimmers [HVCS10; EH10]. Their modeling will be discussed in Section 2.3.4.

2.2. Microrheology

To characterize and model the processes of life in a cell, we need some knowledge about the viscoelastic properties of the cell plasma. Since cells are small, we also need a very small rheometer. When shrinking a rheometer to the size of a cell or even smaller, we ultimately place the rheometer in the sample rather than the sample in a rheometer. Our micro-rheometer is then nothing else than a single probe particle, typically a sphere. But how do we then measure or apply strain and stress? The microscopic equivalent of strain is the displacement of the probe particle, which can be measured by video microscopy or scattering techniques. The stress is applied by nature itself: The solvent molecules kick the probe randomly causing it to perform a random walk, the Brownian motion. Additionally, external forces can be applied e.g. via magnetic or optical tweezers to study non-linear properties. What remains is to find a relation between the motion and the properties of the material.

Once such a relation is found, microrheology experiments have many advantages, as discussed in [FS17, Sec. 1.1.1, p. 4f]. We will only quote a few: The small sample volumes allow characterization of scarce or expensive materials and speed up screening of different samples under different conditions due to fast heat and mass exchange. The small dimensions also imply fast time-scales, which allow short acquisition times and an extended range of frequencies as compared to conventional rheology. Furthermore, this method is more sensitive to fluids with low viscosity and solids with small elastic moduli. Finally, it allows local measurements in heterogeneous samples, which is not possible by conventional rheology at all.

2.2.1. Passive microrheology

When Perrin proved experimentally the existence of atoms by measuring Avogadro's constant in many different ways, he also established the Stokes-Einstein-Sutherland relation, which connects the diffusion of the probe to the viscosity of the solvent [PD10, §§29f, p. 75-81], in particular

$$D = \frac{k_\mathrm{B} T}{3\pi\eta d} \tag{2.8}$$

(cf. [Spa15, p. 119, Eq. (3.2)]), where D is the diffusion coefficient, k_B Boltzmann's constant[3], T the temperature, d the diameter of the probe particle and η the viscosity of the solvent. While at that time, this experiment was performed in a well known solvent to measure essentially Boltzmann's constant, we can use it nowadays to determine the viscosity of an unknown sample measuring the other quantities.

The initial formulation of passive microrheology relies crucially on the assumptions for the Stokes-Einstein-Sutherland relation (2.8): "a rigid particle in a Newtonian solvent [which is] a rather narrow class of simple fluids" [Spa15, p. 120]. In particular Einsteins derivation of the effective viscosity of a dilute suspension already shows that this simple relation is not always true [Spa15, p. 120, Eq. (3.4)].

Due to these limitations of this theory, it was not until Mason and Weitz in 1995 [MW95] to study single particle dynamics to infer rheological properties. They derived a generalized

[3] From May 20, 2019 on it is defined to be exactly $1.380\,649 \cdot 10^{-23}$ J/K [BIPM18], similar to the definition of the speed of light

version of the Stokes-Einstein-Sutherland relation for viscoelastic materials [MW95, p. 1251, Eq. (4)], which allowed them to measure frequency dependent linear viscoelastic moduli using diffusing wave spectroscopy. Gittes *et al.* [GSO+97] followed with measuring the position fluctuations of a single particle to deduce the viscoelastic moduli of F-actin biopolymer solutions and polyacrylamide gels. With the development of digital cameras it became also possible to do video microscopy, where the particles are tracked and evaluated by computers [BP03]. This generalization however treats the probed material as continuum and requires therefore the probe to be much larger than the microscopic structures of the material [Spa15, p. 129]. For probes with sizes comparable to the structures a complete theory does still not exist. Probing length scales larger than a probe can be achieved with at least two approaches: *two-point microrheology* evaluating correlations between two probes in a certain distance and *active microrheology*, where a probe is driven through the sample by external forces [Spa15, p. 130].

2.2.2. Active microrheology

The idea of active microrheology, pulling a probe through a material to determine its viscoelastic properties, is in fact as old as the foundations for the passive microrheology. The first experiment employing active microrheology was reported already in 1912 by Heilbronn [Hei12]. He studied the properties of the cell plasma of stratocytes. Stratocytes are cells in plants which are responsible to detect gravity. This allows the plants to grow the roots downwards into the soil and the sprout up towards the sun. For this porpose these cells contain starch grains, statoliths, which have a higher density than the surrounding cell plasma so that they sink to the lower part of the cell. Heilbronn designed a microscopic setup, where he could turn the cells upside down to measure the motion of the statoliths, when they will move again to the lower part of the cell. He reported an increase of the stratolith speeds for repeated experiments. However, due to a lack of theory and calibration of the forces, his conclusions about the cell plasma were only qualitative.

The next step was the use of micron-sized nickle particles in a magnetic field to study gels by Freundlich and Seifritz [FS23] and the elasticity of the protoplasm by Seifritz [Sei24]. All those measurements were mainly qualitative, because the control of the probes and the magnetic force was limited. Due to the lack of theories, they could only get a rough idea of the viscosity by comparing the motion to that in different glycerine solutions.

A first theoretical description for active microrheology with magnetic particles has been developed by Crick in 1950 [CH50; Cri50]. But in the following decades this field was quite quiet until passive microrheology was established. Then, magnetic tweezers were used to study viscoelastic response in actin networks [AMY+96]. In 2004 the first active microrheology experiment in a colloid close to the glass transition has been carried out with magnetic particles by Habdas *et al.* [HSLW04]. For dilute suspensions a theory for suspensions has been developed by Zia and Brady [ZB12]. For crowded environments such as dense colloidal suspensions close to and above the glass transition, a complete theoretical description is not yet available. First steps in this direction have been done by my predecessors Gazuz [Gaz08; GPVF09; GF13] and Harrer [HPVF12; Har13]. Since their theory became unphysical for large forces, we will evaluate the features of a modified theory, which I started to analyze in my Master's thesis [Gru14].

To summarize, microrheology is a measurement technique to characterize the local viscoelastic

properties of a (small) sample by observing the motion of some probe particle(s). It can be passive, probing the linear response of the material with the help of thermal fluctuations or active, where non-linear effects can be probed. It can be used to complement conventional rheological measurements [FS17, p. 6, Fig. 1.2], but also to investigate local properties in heterogeneous samples, which are not accessible to conventional rheological measurements at all.

2.3. Smoluchowski equation

From this section on we start modeling the systems using a first principles approach on the level of the constituents of the complex fluids. Those complex fluids consist of two components: the solvent, which consists of small molecules, and much larger objects like macromolecules (polymers) or particles (colloids) [HK83, §1, p. 174]. Due to the separation of length scales between the solvent and the immersed objects, we can coarse grain the effects of the solvent molecules on the large objects into hydrodynamic and stochastic forces acting on them.

Before going into the details, let us fix some conventions first. Bold lowercase symbols denote vectors of arbitrary dimension. $\boldsymbol{r} \in \mathbb{R}^3$ for example typically describes the particle position. Bold uppercase symbols usually denote matrices or vectors of vectors. As an example $\boldsymbol{R} \in \mathbb{R}^{3N}$ is used to describe the positions of N particles, while $\mathcal{R} \in \mathbb{R}^{3\times 3}$ will describe a rotation matrix in three dimensions. The major exception of this rule is $\boldsymbol{F} \in \mathbb{R}^3$, which is used to describe the forces on the particles.

Hence, we can describe the motion of spheres of diameter d and mass m in a solvent of viscosity η with the following Langevin equation (cf. [Ris96, Sec. 3.1.2, p. 36], originally [Lan08, p. 531, Eq. (3)])

$$m\ddot{\boldsymbol{r}}(t) = \gamma\dot{\boldsymbol{r}} + \boldsymbol{F}^{\mathrm{rand}}(t), \tag{2.9}$$

with the Stokes friction coefficient $\gamma = 3\pi\eta d$ [Sto51, §42, p. 51, Eq. (126)]. The random force $\boldsymbol{F}^{\mathrm{rand}}(t)$ arises from the interactions with the solvent molecules and has the following properties: It vanishes on average[4]

$$\left\langle F_i^{\mathrm{rand}}(t)\right\rangle = 0 \qquad (i \in \{x,y,z\}, t \in \mathbb{R}) \tag{2.10a}$$

and is delta correlated, i.e. noise for different directions or different times is stochastically independent

$$\left\langle F_i^{\mathrm{rand}}(t)F_j^{\mathrm{rand}}(t')\right\rangle = 2\gamma k_{\mathrm{B}}T\delta_{ij}\delta(t-t') \qquad (i,j \in \{x,y,z\}, t,t' \in \mathbb{R}) \tag{2.10b}$$

(cf. [Ris96, p. 36, Eq. (3.22)][5]). The strength of the fluctuations (2.10b) is determined by the equipartition theorem [WB51; WBS92], assigning to each degree of freedom the average energy $k_{\mathrm{B}}T/2$, where k_{B} is Boltzmann's constant. On average, the particle remains at its initial position, but calculating the mean square displacement (cf. [Ris96, Chap. 3.1]) leads to

$$\left\langle (\boldsymbol{r}(t) - \boldsymbol{r}(0))^2\right\rangle = 6Dt, \tag{2.11}$$

[4] We usually consider an ensemble average, which is obtained by repeating the (Gedanken-)experiment several times with the same macroscopic initial conditions.

[5] The friction coefficient there is given by $\gamma' = \gamma/m$

with a diffusion coefficient D. This implies that the particles spread out from their initial position. The diffusion coefficient D is connected to the friction coefficient via the Einstein-Sutherland relation

$$\gamma D = k_\mathrm{B} T \tag{2.12}$$

(cf. [Ein05, p. 555], [Sut05, p. 782, Eq. (3)], [Ein06, p. 303]). The description using the Langevin equation (2.9) is a standard approach for simulations [Ris96, Sec. 3.6, p. 60].

Instead of looking at the averages of the stochastic trajectories obtained as solutions of the Langevin equation, we can equivalently ask for the probability $\Psi(\boldsymbol{r}, t)\mathrm{d}\boldsymbol{r}$ to find a particle at time t in the infinitesimal volume $[\boldsymbol{r}, \boldsymbol{r} + \mathrm{d}\boldsymbol{r}]$. Ψ incorporates all relevant degrees of freedom and is therefore often referred to as *phase space probability density* (cf. [HK83, §2, p. 185] and [Maz02, Chap. 10, p. 131]). The moments of this probability distribution then correspond to the averages obtained from the stochastic trajectories. In fact, there is a mathematical correspondence between the Langevin equation for the stochastic trajectories and the so called *Fokker-Planck equation*, which describes the evolution of the probability distribution of the particle velocities and displacement. The algorithm to determine the coefficients for the partial differential Fokker-Planck equation is the Kramers-Moyal expansion [Ris96, Chap. 4, p. 63].

A mathematically rigorous treatment of stochastic differential equation of the Langevin type (2.9) and the relation to the Fokker-Planck equation can be found in [Pav14, Chap. 6]. In their formalism, there is a generator which characterizes the underlying Markov process and can be used to obtain the Fokker-Planck equation, see [Pav14, Chap. 2.3, p. 38f], as well as the corresponding stochastic differential equation. The example for the diffusion process is discussed in [Pav14, Chap. 3.4, Eq. (3.47) and Eq. (3.48), p. 66f].

In the case of the overdamped Langevin equation, the corresponding Fokker-Planck equation is also called *Smoluchowski equation* [vSmo06]. This approximation is valid if we are looking at time scales, which are much larger than $m/\eta d$, the *Brownian, Diffusive or Smoluchowski time scale*, on which the velocities have relaxed to their equilibrium distribution and on which the mean square displacement increases diffusively, i.e. proportional to the time [Dho96, p. 76]. For micrometer sized particles in water this time scale is about $\tau_B = 10^{-6}\,\mathrm{s}$ (see [Dho96, p. 77f, exercise 2.3] for details), which is also a typical lower limit for particle tracking based experimental methods [FS17, p. 129]. An extensive justification for this approximation can be found in [HK83, §12, p. 266].

The general *Smoluchowski equation* is given in the following form

$$\partial_t \Psi(\boldsymbol{r}, t) = \Omega \Psi(\boldsymbol{r}, t), \tag{2.13}$$

where the *Smoluchowski operator* Ω describes the dynamics of the system. For a single freely diffusing particle with diffusion coefficient $D = k_\mathrm{B} T/\gamma$ it reads

$$\Omega_\mathrm{free} = D \boldsymbol{\partial}_{\boldsymbol{r}} \cdot \boldsymbol{\partial}_{\boldsymbol{r}}, \tag{2.14}$$

where $\boldsymbol{\partial}_{\boldsymbol{r}} = (\partial_{r_x}, \partial_{r_y}, \partial_{r_z})$ is a vector valued version of the partial derivatives (also known as *nabla* ∇). Since we will deal with more particles in the long run, a bare nabla is not specific enough to describe the derivatives with respect to the different particles and degrees of freedom. We therefore introduce the notation $\boldsymbol{\partial}_{\boldsymbol{a}}$, which refers to the derivatives with respect to the

components of $\boldsymbol{a}$.[6]

Before solving this equation and extending it to more complex situations, we want to introduce natural units for this problem in order to non-dimensionalize it. We need to specify a time scale τ and a length scale ℓ, i.e. a time t is given by $t = \bar{t}\tau$, a length is given by $x = \bar{x}\ell$. This leads to $\partial_t = \partial_{\bar{t}}/\tau$, $\partial_{\boldsymbol{r}} = \partial_{\bar{\boldsymbol{r}}}/\ell$, $\Psi(\boldsymbol{r}, t) = \overline{\Psi}(\boldsymbol{r}/\ell, t/\tau)/\ell^3$ and in consequence to

$$\partial_{\bar{t}}\overline{\Psi}(\bar{\boldsymbol{r}}, \bar{t}) = \frac{\tau}{\ell^2} D \boldsymbol{\partial}_{\bar{\boldsymbol{r}}} \cdot \boldsymbol{\partial}_{\bar{\boldsymbol{r}}}\overline{\Psi}(\bar{\boldsymbol{r}}, \bar{t}). \tag{2.15}$$

Choosing $\tau = \ell^2/D$, we find an equation, which does not depend on the system properties any more

$$\partial_{\bar{t}}\overline{\Psi}(\bar{\boldsymbol{r}}, \bar{t}) = \boldsymbol{\partial}_{\bar{\boldsymbol{r}}} \cdot \boldsymbol{\partial}_{\bar{\boldsymbol{r}}}\overline{\Psi}(\bar{\boldsymbol{r}}, \bar{t}), \tag{2.16}$$

since all relevant properties of the system only change the length or time scales. In particular, the temperature T and the viscosity η of the solvent only enter via the diffusion coefficient $D = k_\mathrm{B}T/3\pi\eta d$ for a sphere of diameter d. A typical choice for the length scale is the particle diameter $\ell = d$. In this case the time scale $\tau = d^2/D$ measures the time it takes the particle to diffuse about one diameter, as we will see in the following.

For a unique solution, we still need initial and boundary conditions. In the following, we will always assume that the particle position $\bar{\boldsymbol{r}}_0$ is known exactly at the beginning of the experiment at $\bar{t} = 0$. This translates into the initial condition

$$\overline{\Psi}(\bar{\boldsymbol{r}}, \bar{t} = 0) = \delta(\bar{\boldsymbol{r}} - \bar{\boldsymbol{r}}_0), \tag{2.17}$$

where δ is the Dirac-delta distribution. Since we do not want to care about boundary effects, we let the particle explore the whole space $\mathbb{R}^3$ and impose only that the probability to find the particle somewhere is equal to 1 for all times, i.e.

$$\int_{\mathbb{R}^3} \overline{\Psi}(\bar{\boldsymbol{r}}, \bar{t}) \mathrm{d}\bar{\boldsymbol{r}} = 1. \tag{2.18}$$

Note that the long time limit in an infinite system may violate this condition, since the homogeneous probability to find a particle in a volume V is V^{-1}, which vanishes in the limit of infinite systems. We would therefore loose the particle. Hence, care has to be taken when analyzing the long time limit of this distribution.

In the following we will discuss different versions of the Smoluchowski equation exploring different strategies to solve this partial differential equation.

2.3.1. ... for a single diffusive particle

Let us start with the simplest case: the single, freely diffusing particle. As a reminder, we have to solve the following partial differential equation

$$\partial_{\bar{t}}\overline{\Psi}(\bar{\boldsymbol{r}}, \bar{t}) = \boldsymbol{\partial}_{\bar{\boldsymbol{r}}} \cdot \boldsymbol{\partial}_{\bar{\boldsymbol{r}}}\overline{\Psi}(\bar{\boldsymbol{r}}, \bar{t}), \tag{2.19a}$$

$$\overline{\Psi}(\bar{\boldsymbol{r}}, \bar{t} = 0) = \delta(\bar{\boldsymbol{r}} - \bar{\boldsymbol{r}}_0), \tag{2.19b}$$

[6] $\boldsymbol{a}$ can represent the spatial coordinates $\boldsymbol{r}$ as well as the orientational degrees of freedom $\boldsymbol{q}$, which will be introduced later.

$$1 = \int_{\mathbb{R}^3} \overline{\Psi}(\overline{\boldsymbol{r}}, \overline{t}) \mathrm{d}\overline{\boldsymbol{r}}\,. \tag{2.19c}$$

A common technique to solve this type of equation is to use the Fourier transform in the spatial variables $\boldsymbol{r}$. This converts the derivatives into a multiplication with the Fourier variable $\overline{\boldsymbol{k}}$ (see Appendix A for the rules and the convention for the Fourier transform) and we obtain an ordinary differential equation. In particular,

$$\partial_{\overline{t}} \overline{\phi}(\overline{\boldsymbol{k}}, \overline{t}) = -\overline{\boldsymbol{k}} \cdot \overline{\boldsymbol{k}} \overline{\phi}(\overline{\boldsymbol{k}}, \overline{t}), \tag{2.20a}$$

$$\overline{\phi}(\overline{\boldsymbol{k}}, \overline{t} = 0) = \mathrm{e}^{\mathrm{i}\overline{\boldsymbol{r}}_0 \overline{\boldsymbol{k}}}, \tag{2.20b}$$

$$\overline{\phi}(\overline{\boldsymbol{k}} = 0, \overline{t}) = 1, \tag{2.20c}$$

where $\overline{\phi}(\overline{\boldsymbol{k}}, \overline{t}) = \mathcal{F}\left[\overline{\boldsymbol{r}} \mapsto \overline{\Psi}(\overline{\boldsymbol{r}}, \overline{t})\right](\overline{\boldsymbol{k}})$ is the Fourier transform in $\overline{\boldsymbol{r}}$ of $\overline{\Psi}(\overline{\boldsymbol{r}}, \overline{t})$ and $\overline{\boldsymbol{k}} = \boldsymbol{k}d$ the non-dimensional wave vector. In later sections, in particular when using mode-coupling theory (see Section 2.4) we will also use the notation $\overline{\phi}_{\overline{\boldsymbol{k}}}(\overline{t}) = \overline{\phi}(\overline{\boldsymbol{k}}, \overline{t})$ for the Fourier transform.

A solution of the ordinary linear differential equation (2.20a) with initial condition (2.20b) is given by

$$\overline{\phi}(\overline{\boldsymbol{k}}, \overline{t}) = \exp\left(\mathrm{i}\overline{\boldsymbol{r}}_0 \overline{\boldsymbol{k}}\right) \exp\left(-\overline{\boldsymbol{k}} \cdot \overline{\boldsymbol{k}} \overline{t}\right). \tag{2.21}$$

Setting $\overline{\boldsymbol{k}} = 0$, we see that the normalization condition (2.20c) is fulfilled for all $t \geq 0$. However, the limits $\boldsymbol{k} \to 0$ and $t \to \infty$ are not interchangeable, because

$$\lim_{\overline{t} \to \infty} \lim_{\overline{\boldsymbol{k}} \to 0} \overline{\phi}(\overline{\boldsymbol{k}}, \overline{t}) = 1 \neq 0 = \lim_{\overline{\boldsymbol{k}} \to 0} \lim_{\overline{t} \to \infty} \overline{\phi}(\overline{\boldsymbol{k}}, \overline{t}). \tag{2.22}$$

This is due to the fact that the particle can spread over an infinitely large space in infinite time, which makes normalization of the probability distribution impossible.

Application of the inverse Fourier transform (using the shift rule (A.7a)) yields

$$\overline{\Psi}(\overline{\boldsymbol{r}}, \overline{t}) = \frac{1}{(4\pi\overline{t})^{3/2}} \exp\left(-\frac{(\overline{\boldsymbol{r}} - \overline{\boldsymbol{r}}_0) \cdot (\overline{\boldsymbol{r}} - \overline{\boldsymbol{r}}_0)}{4\overline{t}}\right). \tag{2.23}$$

This is a Gaussian distribution with mean

$$\langle \overline{\boldsymbol{r}} \rangle (\overline{t}) = \int \overline{\boldsymbol{r}} \overline{\Psi}(\overline{\boldsymbol{r}}, \overline{t}) \mathrm{d}\overline{\boldsymbol{r}} \; = \overline{\boldsymbol{r}}_0 \tag{2.24a}$$

and variances

$$\left\langle \Delta \overline{r}_\alpha^2 \right\rangle (\overline{t}) = \left\langle (\overline{r}_\alpha - \langle \overline{r}_\alpha \rangle)^2 \right\rangle (\overline{t}) = 2\overline{t}, \qquad (\alpha = x, y, z). \tag{2.24b}$$

In this context, the variances are often referred to as *mean square displacements* (MSD). A linear increase of the MSD with time is characteristic for diffusion [Ein05, p. 559]. With this result, we can rationalize our choice of the length and time scale. After a time $\overline{t} = 1$ the particle has diffused a distance of $\sqrt{\langle \Delta r_\alpha^2 \rangle (1)}\ell = \sqrt{2}\ell = \sqrt{2}d$ in each direction, which is of the order of the particle diameter d.

If we resubstitute the dimensional variables, we find

$$\phi(\boldsymbol{k},t) = \exp\left(-\mathrm{i}\boldsymbol{r}_0\cdot\boldsymbol{k}\right)\exp\left(-D\boldsymbol{k}\cdot\boldsymbol{k}t\right), \tag{2.25a}$$

$$\Psi(\boldsymbol{r},t) = \frac{\overline{\Psi}(\boldsymbol{r}/\ell,t/\tau)}{\ell^3} = \frac{1}{(4\pi Dt)^{3/2}}\exp\left(-\frac{(\boldsymbol{r}-\boldsymbol{r}_0)\cdot(\boldsymbol{r}-\boldsymbol{r}_0)}{4Dt}\right), \tag{2.25b}$$

which results in the well known expression for the three-dimensional MSD [Dho96, p. 325, Eq. (6.22)]

$$\left\langle\Delta\boldsymbol{r}^2\right\rangle = \left\langle\Delta r_x^2\right\rangle + \left\langle\Delta r_y^2\right\rangle + \left\langle\Delta r_z^2\right\rangle = 6Dt. \tag{2.26}$$

This result can also be inferred directly from the dimensionless result (2.24b) by substituting $\overline{t} = tD/d^2$ for the time and $\overline{r}_\alpha = r_\alpha/d$ ($\alpha = x,y,z$) for the lengths. This concludes this introductory section about the conversion to and from natural units (aka non-dimensionalization). From now on, we will mainly use the equations and their solutions in their non-dimensional form if not otherwise specified, but for the sake of clarity of the notation, we will omit the bars.

2.3.2. . . . for a single harmonically bound particle

In this section, we want to discuss a one-dimensional Brownian particle, which is trapped in a harmonic potential and demonstrate another analytical approach to solve this equation of motion. The harmonic potential is characterized by its stiffness κ and centered around the origin

$$V(x) = \frac{\kappa}{2}x^2. \tag{2.27}$$

The corresponding Smoluchowski operator is given by

$$\Omega_{\text{harmonic}} = D\partial_x^2 - \frac{D}{k_\mathrm{B}T}\partial_x(-\partial_x V(x)) = D\partial_x^2 + \frac{D\kappa}{k_\mathrm{B}T}\partial_x x. \tag{2.28}$$

Note that the derivative in front of the potential $\partial_x V(x)$ is acting only on the potential, while the derivative to the left of it is finally acting on the product $(-\partial_x V(x))\Psi(x,t)$. Introducing the length scale ℓ and the time scale $\tau = \ell^2/D$, we obtain

$$\overline{\Omega}_{\text{harmonic}} = \partial_{\overline{x}}^2 + \overline{\kappa}\partial_{\overline{x}}\overline{x} \tag{2.29}$$

with the non-dimensional trap-stiffness $\overline{\kappa} = \kappa\ell^2/k_\mathrm{B}T$. To solve this, we again Fourier transform the Smoluchowski equation to obtain

$$\partial_t\phi(k,t) = -k^2\phi(k,t) - \overline{\kappa}k\partial_k\phi(k,t), \tag{2.30a}$$

$$\phi(k,t=0) = \mathrm{e}^{\mathrm{i}\overline{x}_0 k}, \tag{2.30b}$$

$$\phi(k=0,t) = 1. \tag{2.30c}$$

As before $\phi(k,t)$ is the Fourier transform in $\overline{x}$ of $\overline{\Psi}(\overline{x},\overline{t})$ and for the sake of simplicity, we omit the bars associated with the non-dimensional quantities. The Fourier transform of the sequence $\partial_{\overline{x}}\overline{x}f(\overline{x})$ is given by $-k\partial_k\tilde{f}(k)$ as shown in (A.10). As opposed to the previous case, we still have a partial differential equation so that we have to use a different approach for the solution. Nevertheless, doing the Fourier transform is convenient, because the partial

differential equations reduces from second order to first order and the initial condition can be represented by a regular function.

We will use the *method of characteristics* to find a solution for this problem. The main idea of this method is to reduce the partial differential equation to a system of ordinary differential equations. To do so, we substitute the variables t and k by functions $t(\lambda)$ and $k(\lambda)$, which depend on the parameter λ and fulfill the initial conditions $t(\lambda = 0) = 0$, $k(\lambda = 0) = \xi$. Then, $\phi(k(\lambda), t(\lambda))$ is a function of λ only as well and we find for its derivative

$$\frac{\mathrm{d}}{\mathrm{d}\lambda}\phi(k(\lambda), t(\lambda)) = \partial_t \phi(k(\lambda), t(\lambda))\frac{\mathrm{d}t}{\mathrm{d}\lambda} + \partial_k \phi(k(\lambda), t(\lambda))\frac{\mathrm{d}k}{\mathrm{d}\lambda} = -k^2\phi(k(\lambda), t(\lambda)). \tag{2.31a}$$

The last equality is only true if we make use of (2.30a) and identify

$$\frac{\mathrm{d}t(\lambda)}{\mathrm{d}\lambda} = 1, \tag{2.31b}$$

$$\frac{\mathrm{d}k(\lambda)}{\mathrm{d}\lambda} = \overline{\kappa}k(\lambda). \tag{2.31c}$$

Hence, we have three ordinary differential equations (2.31) in λ with initial conditions

$$t(\lambda = 0) = 0, \tag{2.32a}$$

$$k(\lambda = 0) = \xi, \tag{2.32b}$$

$$\phi(\lambda = 0) = \phi(t = 0, k = \xi) = \mathrm{e}^{\mathrm{i}\overline{x}_0\xi}. \tag{2.32c}$$

ξ is only a helper variable, which will disappear in the end result. Since (2.31b) and (2.31c) are two (decoupled) ordinary differential equations, we find their solutions with the corresponding initial conditions to be

$$t(\lambda) = \lambda, \tag{2.33a}$$

$$k(\lambda) = \xi\exp(\overline{\kappa}\lambda). \tag{2.33b}$$

This allows us to substitute and eliminate the k dependency in (2.31a) to find

$$\frac{\mathrm{d}\phi(\lambda)}{\mathrm{d}\lambda} = -\xi^2\mathrm{e}^{2\overline{\kappa}\lambda}\phi(\lambda). \tag{2.34}$$

This can be solved using *separation of variables*, which results in

$$\phi(\lambda) = \mathrm{e}^{\mathrm{i}\overline{x}_0\xi}\exp\left(-\frac{\xi^2}{2\overline{\kappa}}\left(\mathrm{e}^{2\overline{\kappa}\lambda} - 1\right)\right). \tag{2.35}$$

Now, we can invert (2.33) to find

$$\lambda(t) = t, \tag{2.36a}$$

$$\xi(k, t) = k\exp(-\overline{\kappa}t). \tag{2.36b}$$

This allows us to express the complete solution in k and t as

$$\phi(k, t) = \mathrm{e}^{\mathrm{i}\overline{x}_0 k\mathrm{e}^{-\overline{\kappa}t}}\exp\left(-\frac{k^2}{2\overline{\kappa}}\left(1 - \mathrm{e}^{-2\overline{\kappa}t}\right)\right). \tag{2.37}$$

If we check $\phi(k = 0, t)$, we find that the normalization condition is again fulfilled for all times $t \geq 0$. In this particular case even the limits $t \to \infty$ and $k \to 0$ can be interchanged, because

$\phi(k, t \to \infty) \neq 0$ for all k and $\overline{\kappa} > 0$. This is the prototype for non-ergodic behavior, where correlations do not decay even for infinite time. Therefore, time averaging and ensemble averaging can be different in this system.

The transformation back to real space yields

$$\overline{\Psi}(\overline{x}, \overline{t}) = \frac{1}{\sqrt{2\pi(1 - \mathrm{e}^{-2\overline{\kappa}\overline{t}})/\overline{\kappa}}} \exp\left(-\frac{\overline{\kappa}\left(\overline{x} - \overline{x}_0 \mathrm{e}^{-\overline{\kappa}\overline{t}}\right)^2}{2(1 - \mathrm{e}^{-2\overline{\kappa}\overline{t}})} \right), \tag{2.38}$$

where we reintroduced the bars indicating non-dimensional quantities to avoid confusion. The long time limit is given by

$$\lim_{\overline{t}\to\infty} \overline{\Psi}(\overline{x}, \overline{t}) = \frac{1}{\sqrt{2\pi/\overline{\kappa}}} \exp\left(-\frac{\overline{\kappa}\overline{x}^2}{2} \right), \tag{2.39a}$$

or, in dimensional units,

$$\lim_{t\to\infty} \Psi(x, t) = \frac{1}{\sqrt{2\pi k_\mathrm{B} T/\kappa}} \exp\left(-\frac{\kappa x^2}{2k_\mathrm{B} T} \right), \tag{2.39b}$$

which is the well known Boltzmann factor [Dho96, p. 36, Eq. (1.50)], stating $\Psi_\mathrm{eq}(x) \propto \exp(V(x)/k_\mathrm{B} T)$. The relaxation time scale τ_relax on which the memory of the initial configuration is lost and on which the long time limit is reached is given by

$$\tau_\mathrm{relax} = \frac{k_\mathrm{B} T}{\kappa D} = \frac{\gamma}{\kappa}, \tag{2.40}$$

i.e. the lower the friction γ and the stiffer the trap κ, the faster equilibrium will be reached. For $t \ll \tau_\mathrm{relax}$ (or equivalently $\overline{\kappa}\overline{t} \ll 1$), we recover the free diffusion from (2.23) or (2.25b).

If we apply an external force F_ex to the particle in the harmonic trap, the potential will change to

$$V(x) = \frac{\kappa}{2}x^2 - F_\mathrm{ex} x = \frac{\kappa}{2}\left(x - \frac{F_\mathrm{ex}}{\kappa} \right)^2 - \frac{F_\mathrm{ex}^2}{2\kappa}. \tag{2.41}$$

Completing the square after the second equality leaves us with a harmonic potential centered around $x_c = F_\mathrm{ex}/\kappa$. The additional constant does not play a role, because only the derivative of the potential enters the calculation. The non-dimensional force is given by $\overline{F_\mathrm{ex}} = F_\mathrm{ex}\ell/k_\mathrm{B} T$ and consequently the non-dimensional displacement $\overline{x}_c = x_c/\ell = \overline{F_\mathrm{ex}}/\overline{\kappa}$. Substituting $\overline{x}' = \overline{x} - \overline{x}_c$, the new Smoluchowski equation reduces to the old one with the initial condition $\overline{x}'_0 = \overline{x}_0 - \overline{x}_c$. This allows us to use the former solution to find the new solution to be

$$\overline{\phi}(\overline{k}, \overline{t}) = \exp\left(\mathrm{i}\left(\frac{\overline{F_\mathrm{ex}}}{\overline{\kappa}} + \left(\overline{x}_0 - \frac{\overline{F_\mathrm{ex}}}{\overline{\kappa}} \right) \mathrm{e}^{-\overline{\kappa}\overline{t}} \right) \overline{k} \right) \exp\left(-\frac{\overline{k}^2}{2\overline{\kappa}} \left(1 - \mathrm{e}^{-2\overline{\kappa}\overline{t}} \right) \right), \tag{2.42a}$$

$$\overline{\Psi}(\overline{x}, \overline{t}) = \frac{1}{\sqrt{2\pi(1 - \mathrm{e}^{-2\overline{\kappa}\overline{t}})/\overline{\kappa}}} \exp\left(-\frac{\overline{\kappa}\left(\overline{x} - \frac{\overline{F_\mathrm{ex}}}{\overline{\kappa}} - (\overline{x}_0 - \frac{\overline{F_\mathrm{ex}}}{\overline{\kappa}}) \mathrm{e}^{-\overline{\kappa}\overline{t}} \right)^2}{2(1 - \mathrm{e}^{-2\overline{\kappa}\overline{t}})} \right), \tag{2.42b}$$

and the long time limits read

$$\lim_{\bar{t}\to\infty} \overline{\phi}(\bar{k},\bar{t}) = \exp\left(\mathrm{i}\bar{k}\frac{\overline{F_{\mathrm{ex}}}}{\overline{\kappa}} - \frac{\bar{k}^2}{2\overline{\kappa}}\right), \tag{2.43a}$$

$$\lim_{\bar{t}\to\infty} \overline{\Psi}(\bar{x},\bar{t}) = \frac{1}{\sqrt{2\pi/\overline{\kappa}}} \exp\left(-\frac{\overline{\kappa}}{2}\left(\bar{x} - \frac{\overline{F_{\mathrm{ex}}}}{\overline{\kappa}}\right)^2\right). \tag{2.43b}$$

Since $\overline{\Psi}(\bar{x},\bar{t})$ is a Gaussian, we can directly read off the mean displacement and the variance

$$\langle \bar{x} \rangle (\bar{t}) = \frac{\overline{F_{\mathrm{ex}}}}{\overline{\kappa}} + \left(\bar{x}_0 - \frac{\overline{F_{\mathrm{ex}}}}{\overline{\kappa}}\right) \mathrm{e}^{-\overline{\kappa}\bar{t}}, \tag{2.44a}$$

$$\left\langle \bar{x}^2 \right\rangle = \frac{1}{\overline{\kappa}} \left(1 - \mathrm{e}^{-2\overline{\kappa}\bar{t}}\right). \tag{2.44b}$$

2.3.3. . . . for a single Brownian particle in a moving harmonic trap

We extend the previous model by moving the trap with a constant velocity v, i.e. the potential is given by

$$V(x,t) = \frac{\kappa}{2}(x - vt)^2. \tag{2.45}$$

This modifies the previous Smoluchowski operator in the following way

$$\overline{\Omega}_{\substack{\text{moving}\\ \text{harmonic}}} = \partial_{\bar{x}}^2 + \overline{\kappa}\partial_{\bar{x}}(\bar{x} - \overline{v}\bar{t}), \tag{2.46}$$

with $\overline{v} = v/(\ell/\tau) = (v\ell)/D$. This non-dimensional number is often called *Péclet* number [FS17, p. 296] and describes the strength of advection compared to diffusion. For $\overline{v} \ll 1$ diffusion dominates, while for $\overline{v} \gg 1$ advection effects are prevailing. The length and time scales for the definition of a Péclet number depend on the problem (see e.g. [Dho96, p. 331] or [FS17, p. 296]), but the concept of weighting advection against diffusion remains the same.

In order to solve this equation with the same initial conditions as before, we will do a substitution and reduce it to the previous equation. To do so, we define

$$x' = \bar{x} - (\overline{v}\bar{t} + c), \tag{2.47}$$

where we subtract the motion of the trap and allow for a (yet unknown) average displacement c of the probe with respect to the center of the trap. Deriving the identity $\overline{\Psi}(\bar{x},\bar{t}) = \Psi'(x'(\bar{x},\bar{t}),\bar{t})$ with respect to time and substituting the equations of motion for $\overline{\Psi}$, we obtain the following equation of motion for Ψ'

$$\partial_{\bar{t}}\Psi'(x',\bar{t}) = \partial_{x'}^2\Psi'(x',\bar{t}) + \overline{\kappa}\partial_{x'}\left(\frac{\overline{v}}{\overline{\kappa}} + c + x'\right)\Psi'(x',\bar{t}). \tag{2.48}$$

Setting $c = -\overline{v}/\overline{\kappa}$, this equation reduces with definition (2.29) to $\partial_{\bar{t}}\Psi' = \overline{\Omega}_{\mathrm{harmonic}}\Psi'$ with initial condition $x_0' = \bar{x}_0 + \overline{v}/\overline{\kappa}$. Since this equation was solved in the previous section, we can come back to this solution and insert our new variables. A shift by $\overline{v}\bar{t} - \overline{v}/\overline{\kappa}$ leads to a prefactor of $\exp(\mathrm{i}(\overline{v}\bar{t} - \overline{v}/\overline{\kappa})k)$ in Fourier space. With that we find

$$\phi(\bar{k},\bar{t}) = \exp\left(\mathrm{i}\left(\left(\overline{v}\bar{t} - \frac{\overline{v}}{\overline{\kappa}}\right) + \left(\bar{x}_0 + \frac{\overline{v}}{\overline{\kappa}}\right)\mathrm{e}^{-\overline{\kappa}\bar{t}}\right)\bar{k}\right) \exp\left(-\frac{\bar{k}^2}{2\overline{\kappa}}\left(1 - \mathrm{e}^{-2\overline{\kappa}\bar{t}}\right)\right) \tag{2.49}$$

in Fourier space and

$$\overline{\Psi}(\overline{x},\overline{t}) = \frac{1}{\sqrt{2\pi(1-\mathrm{e}^{-2\overline{\kappa}\overline{t}})/\overline{\kappa}}} \exp\left(-\frac{\overline{\kappa}\left(\overline{x}-\overline{v}\overline{t}+\frac{\overline{v}}{\overline{\kappa}}-\left(\overline{x}_0+\frac{\overline{v}}{\overline{\kappa}}\right)\mathrm{e}^{-\overline{\kappa}\overline{t}}\right)^2}{2(1-\mathrm{e}^{-2\overline{\kappa}\overline{t}})}\right) \tag{2.50}$$

in real space. From that we can compute the mean displacement (the first moment of $\overline{\Psi}(\overline{x},\overline{t})$ for given time $\overline{t}$)

$$\langle\overline{x}\rangle(\overline{t}) = \overline{v}\overline{t} - \frac{\overline{v}}{\overline{\kappa}} + \left(\overline{x}_0+\frac{\overline{v}}{\overline{\kappa}}\right)\mathrm{e}^{-\overline{\kappa}\overline{t}}, \tag{2.51}$$

i.e. the particle is moving with the same velocity as the trap for long times, but lagging behind a distance $\ell\overline{v}/\overline{\kappa} = vk_\mathrm{B}T/D$.

Analyzing (2.49) for the long time limit, we see that this limit does not exist for $k \neq 0$ because of the oscillating term $\mathrm{e}^{\mathrm{i}\overline{v}\overline{t}}$ and the nonzero limit of the remaining terms. Hence, the limits $k \to 0$ and $\overline{t} \to \infty$ cannot be exchanged either. However, in the frame of reference of the trap $x' = \overline{x} - \overline{v}\overline{t}$ a stationary limit $\Psi(x')$ does exist. Once again, care must be taken when analyzing the limit $\overline{t} \to \infty$. While there is no stationary solution in the generic coordinate frame, there might be a suitable frame of reference, where such a solution does exist.

In the limit $\overline{\kappa} \to 0$, we recover the case of a driven diffusing Brownian particle,

$$\phi(\overline{k},\overline{t}) = \exp\left(\mathrm{i}\left(\overline{v}\overline{t}+\overline{x}_0\right)\overline{k}\right)\exp\left(-\overline{k}^2 t\right), \tag{2.52}$$

where one needs $\lim_{x\to 0}(1-\exp(-ax))/x = a$ by l'Hospital [BMMS08, Sec. 2.4.1.8.1, p. 56].

2.3.4. ... for a single active particle

Instead of pulling the particles externally, we can also let the particles propel themselves. This description aims to model biological swimmers such as bacteria, algae and sperms [EWG15; SAJ+16] as well as artificial particles using a variety of chemical and physical effects to perform directed motion [HVCS10; EH10]. This directed motion implies that we have to introduce another degree of freedom, the orientation or direction of swimming $\hat{\boldsymbol{q}}$. The vector $\hat{\boldsymbol{q}}$, which describes the direction of swimming, is normalized (as indicated by the hat) and can be described as point on the surface of a sphere with radius 1, in short $\hat{\boldsymbol{q}} \in \hat{S}$. Assuming otherwise isotropic properties of the swimmer, we obtain the following Smoluchowski operator for a particle with orientation

$$\Omega_\mathrm{orientable} = \boldsymbol{\partial_r}\cdot\boldsymbol{D}\cdot\boldsymbol{\partial_r} + \boldsymbol{\partial}^R_{\hat{\boldsymbol{q}}}\cdot\boldsymbol{D}^R\cdot\boldsymbol{\partial}^R_{\hat{\boldsymbol{q}}} \tag{2.53}$$

with the orientational gradient operator $\boldsymbol{\partial}^R_{\hat{\boldsymbol{q}}} = (\hat{\boldsymbol{q}}\times\boldsymbol{\partial}_{\hat{\boldsymbol{q}}})$, the translational diffusion tensor $\boldsymbol{D} = D\mathbb{1}$ and rotational diffusion tensor $\boldsymbol{D}^R = D^R\mathbb{1}$ (cf. [Dho96, p. 216, Eq.(4.149)]). The symbol $\cdot$ in connection with vectors and matrices always indicates matrix-vector multiplication, $\boldsymbol{a}\cdot\boldsymbol{D}\cdot\boldsymbol{b} = \boldsymbol{a}^T\boldsymbol{D}\boldsymbol{b} = \sum_{i,j} a_i D_{ij} b_j$ and the symbol $\times$ indicates the cross product, which appears naturally because $\hat{\boldsymbol{q}}$ must only change perpendicular to its direction. This particle shows Brownian motion for the position $\boldsymbol{r}$ as well as for the orientation $\hat{\boldsymbol{q}}$. In this simple case both motions decouple.

A coupling between motion and orientation arises if the particle is not spherically symmetric anymore (which will be discussed in the next section) or when we account for the swimming. Active particles, which swim with a fixed speed u_0 along swimming direction $\hat{\boldsymbol{q}}$, are modeled by

$$\Omega_{\text{active}} = \boldsymbol{\partial}_{\boldsymbol{r}} \cdot (-u_0 \hat{\boldsymbol{q}} + D \boldsymbol{\partial}_{\boldsymbol{r}}) + D^R \boldsymbol{\partial}^R_{\hat{\boldsymbol{q}}} \cdot \boldsymbol{\partial}^R_{\hat{\boldsymbol{q}}} \tag{2.54}$$

(cf. [YB15a, Eq. (2.1)]). Analytical solutions in Fourier space for the corresponding intermediate scattering function $\phi(k,t)$ in terms of generalized spheroidal wave functions have been worked out by Kurzthaler *et al.* for 3D [KLF16, Eq. (13)] and 2D [KF17, Eq. (18)].

On the other hand, the effect of these active particles on boundaries [YB15a] and other tracer particles [BB17] has been studied and described using the concept of a swim pressure [TYB14]. In this context, it is helpful to interpret the Smoluchowski equation as a continuity equation

$$0 = \partial_t \Psi(\boldsymbol{r}, \hat{\boldsymbol{q}}, t) + \boldsymbol{\partial}_{\boldsymbol{r}} \cdot \boldsymbol{j}^T + \boldsymbol{\partial}^R_{\hat{\boldsymbol{q}}} \cdot \boldsymbol{j}^R, \tag{2.55a}$$

$$\boldsymbol{j}^T = u_0 \hat{\boldsymbol{q}} \Psi(\boldsymbol{r}, \hat{\boldsymbol{q}}, t) - D \boldsymbol{\partial}_{\boldsymbol{r}} \Psi(\boldsymbol{r}, \hat{\boldsymbol{q}}, t), \tag{2.55b}$$

$$\boldsymbol{j}^R = -D^R \boldsymbol{\partial}^R_{\hat{\boldsymbol{q}}} \Psi(\boldsymbol{r}, \hat{\boldsymbol{q}}, t) \tag{2.55c}$$

with the translational flux $\boldsymbol{j}^T$ and the rotational flux $\boldsymbol{j}^R$. This is an elegant way to express the conservation of probability. It also allows to specify and interpret the boundary conditions of this partial differential equation, which will become important when considering many interacting particles. The flux describes the probability per unit time for a particle to cross the unit area perpendicular to its direction (or other directions $\boldsymbol{n}$ via $\boldsymbol{n} \cdot \boldsymbol{j}$). It has units of one over time and area, in the nondimensional units $(\tau \ell^2)^{-1}$.

2.3.5. . . . for many interacting particles

We now consider the most general problem of N interacting particles with orientations. This will be the starting point for all calculations. Due to the many degrees of freedom, a full solution of this problem is even numerically inaccessible. Therefore, different techniques have been developed to find approximate solutions under certain conditions. We will present two of them. A density expansion for dilute suspensions in Section 2.5 and the mode-coupling theory for very dense suspensions in Section 2.4.

For the modeling, we use the following conventions: Particle i is at position $\boldsymbol{r}_i$ and has an orientation vector $\hat{\boldsymbol{q}}_i$. To keep the notation concise, we introduce $\boldsymbol{R} = (\boldsymbol{r}_1, \ldots, \boldsymbol{r}_N)$ and $\boldsymbol{Q} = (\hat{\boldsymbol{q}}_1, \ldots, \hat{\boldsymbol{q}}_n)$, i.e. the probability density for a configuration ($\boldsymbol{R}$, $\boldsymbol{Q}$) at a time t is given by $\Psi(\boldsymbol{R}, \boldsymbol{Q}, t)$. The full Smoluchowski operator is then given by

$$\begin{aligned}\Omega^N_{\text{HI}} = \sum_{i,j=1}^{N} &\boldsymbol{\partial}_i \cdot \boldsymbol{D}^{TT}_{ij} \cdot \left(\boldsymbol{\partial}_j + \frac{\boldsymbol{\partial}_j V(\boldsymbol{R}, \boldsymbol{Q})}{k_{\text{B}} T} \right) + \boldsymbol{\partial}_i \cdot \boldsymbol{D}^{TR}_{ij} \cdot \left(\boldsymbol{\partial}^R_j + \frac{\boldsymbol{\partial}^R_j V(\boldsymbol{R}, \boldsymbol{Q})}{k_{\text{B}} T} \right) \\ &+ \boldsymbol{\partial}^R_i \cdot \boldsymbol{D}^{RT}_{ij} \cdot \left(\boldsymbol{\partial}_j + \frac{\boldsymbol{\partial}_j V(\boldsymbol{R}, \boldsymbol{Q})}{k_{\text{B}} T} \right) + \boldsymbol{\partial}^R_i \cdot \boldsymbol{D}^{RR}_{ij} \cdot \left(\boldsymbol{\partial}^R_j + \frac{\boldsymbol{\partial}^R_j V(\boldsymbol{R}, \boldsymbol{Q})}{k_{\text{B}} T} \right),\end{aligned} \tag{2.56}$$

where $\boldsymbol{\partial}_i = \boldsymbol{\partial}_{\boldsymbol{r}_i}$ and $\boldsymbol{\partial}^R_i = \boldsymbol{\partial}^R_{\hat{\boldsymbol{q}}_i} = (\hat{\boldsymbol{q}}_i \times \boldsymbol{\partial}_{\hat{\boldsymbol{q}}_i})$. $\boldsymbol{D}^{\alpha\beta}_{ij}$ are 3×3 sub-matrices of the total diffusion

matrix

$$\boldsymbol{\mathcal{D}} = \begin{pmatrix} \boldsymbol{D}_{ij}^{TT} & \boldsymbol{D}_{ij}^{TR} \\ \boldsymbol{D}_{ij}^{RT} & \boldsymbol{D}_{ij}^{RR} \end{pmatrix}_{i,j=1,\ldots,N} \tag{2.57}$$

(cf. [Dho96, p. 211, Eq. (4.132)]), which describes in general all hydrodynamic interactions between translational (superscript T) and rotational (superscript R) motion of particles i and j. An extensive discussion of hydrodynamic interactions can be found in [FS17, Sec. 2.6, p. 67-79]. For a pair of spheres this is summarized in [HK83, Sec. 1.4, p. 181-184]. For more than two particles, these interactions become very complex and can usually only be determined approximately [CS91]. However, if hydrodynamic interactions are ignored, the diffusion matrix reduces to a diagonal form, i.e. $\boldsymbol{D}_{ij}^{\alpha\beta} = 0$ for $i \neq j$, and translational and rotational motions decouple as well, i.e. $\boldsymbol{D}_{ii}^{RT} = \boldsymbol{D}_{ii}^{TR} = 0$. Even though hydrodynamic interactions may play an important role [Rei06] and have subtle effects for high frequency viscosities [MW12, Sec. 3.5.2, p. 102], the simplification of vanishing hydrodynamic interactions is reasonable for very dilute systems as well as very dense systems, where the hydrodynamic interactions affect mostly the time scales [Göt09, p. 324, p. 332]. Hence, the Smoluchowski operator simplifies to

$$\Omega_{\text{no HI}}^{N} = \Omega_{\text{translation}}^{N} + \Omega_{\text{rotation}}^{N}, \tag{2.58a}$$

with

$$\Omega_{\text{translation}}^{N} = \sum_{i=1}^{N} \boldsymbol{\partial}_i \cdot \boldsymbol{D}_i \cdot \left(\boldsymbol{\partial}_i + \frac{\boldsymbol{\partial}_i V(\boldsymbol{R}, \boldsymbol{Q})}{k_{\mathrm{B}} T} \right), \tag{2.58b}$$

$$\Omega_{\text{rotation}}^{N} = \sum_{i=1}^{N} \boldsymbol{\partial}_i^R \cdot \boldsymbol{D}_i^R \cdot \left(\boldsymbol{\partial}_i^R + \frac{\boldsymbol{\partial}_i^R V(\boldsymbol{R}, \boldsymbol{Q})}{k_{\mathrm{B}} T} \right). \tag{2.58c}$$

This operator further simplifies when we specialize the shape of the particles; in particular their symmetries. For axisymmetric particles we have

$$\boldsymbol{D}_i = D_i^{\parallel} \hat{\boldsymbol{q}}_i \hat{\boldsymbol{q}}_i + D_i^{\perp} (\mathbb{1} - \hat{\boldsymbol{q}}_i \hat{\boldsymbol{q}}_i), \tag{2.59a}$$

$$\boldsymbol{D}_i^R = D_i^R \mathbb{1}, \tag{2.59b}$$

where $\hat{\boldsymbol{q}}_i \hat{\boldsymbol{q}}_i$ is the dyadic product, i.e. the matrix $(\hat{\boldsymbol{q}}_i^{\alpha} \hat{\boldsymbol{q}}_i^{\beta})_{\alpha\beta}$. $D_i^{\parallel}$ and $D_i^{\perp}$ are the translational diffusion coefficients parallel and perpendicular to the symmetry axis of particle i and D_i^R is the rotational diffusion coefficient (cf. [Dho96, p. 211, Eq. (4.133), Eq. (4.134)]). These diffusion coefficients can be calculated for simple axisymmetric shapes of the particles via the Stokes-Einstein relation from their friction coefficients [Bre74]. Since the translational diffusion coefficient depends on the orientation $\hat{\boldsymbol{q}}_i$ of the particle, there is a coupling between the rotational and translational motion.

In order to easily separate the contributions arising from anisotropic features of the particles, it is convenient to introduce an average translational diffusion coefficient $\overline{D}$ and a difference ΔD via

$$\overline{D}_i = \frac{1}{3} \left(D_i^{\parallel} + 2 D_i^{\perp} \right), \tag{2.60a}$$

$$\Delta D_i = D_i^{\parallel} - D_i^{\perp}. \tag{2.60b}$$

It can be seen that for isotropic particles with $D^{\parallel} = D^{\perp} = D$ we have $\overline{D} = D$ and $\Delta D = 0$.

Separating the Smoluchowski operator into these two contributions results in

$$\Omega^N_{\text{translation}} = \Omega^N_{\text{isotropic}} + \Omega^N_{\text{anisotropic}}, \tag{2.61a}$$

with

$$\Omega^N_{\text{isotropic}} = \sum_{i=1}^{N} \overline{D}_i \boldsymbol{\partial}_i \cdot \left(\boldsymbol{\partial}_i + \frac{\boldsymbol{\partial}_i V(\boldsymbol{R}, \boldsymbol{Q})}{k_{\mathrm{B}} T} \right), \tag{2.61b}$$

$$\Omega^N_{\text{anisotropic}} = \sum_{i=1}^{N} \Delta D_i \boldsymbol{\partial}_i \cdot \left(\hat{\boldsymbol{q}}_i \hat{\boldsymbol{q}}_i - \frac{1}{3} \mathbb{1} \right) \cdot \left(\boldsymbol{\partial}_i + \frac{\boldsymbol{\partial}_i V(\boldsymbol{R}, \boldsymbol{Q})}{k_{\mathrm{B}} T} \right). \tag{2.61c}$$

Finally, we will split the potential

$$V(\boldsymbol{R}, \boldsymbol{Q}) = V^{\text{ext}}(\boldsymbol{R}, \boldsymbol{Q}) + V^{\text{int}}(\boldsymbol{R}, \boldsymbol{Q}) \tag{2.62}$$

into internal contributions V^{int}, which arise from interactions between particles and external contributions V^{ext} such as imposed forces and torques.

For the external potential, we will focus on two special cases, which correspond to the two operation modes for microrheology: *constant force or torque* and *constant translational or angular velocity*. In the first case, we simply get a constant contribution

$$\boldsymbol{\partial}_i V^{\text{ext}} = -\boldsymbol{F}_i^{\text{ext}}, \tag{2.63a}$$

$$\boldsymbol{\partial}_i^R V^{\text{ext}} = -\boldsymbol{T}_i^{\text{ext}}. \tag{2.63b}$$

Complementary to imposing forces and torques, one can also impose translational velocities $\boldsymbol{u}_i$ and angular velocities $\boldsymbol{\omega}_i$ by identifying

$$-\frac{\boldsymbol{D}_i}{k_{\mathrm{B}} T} \boldsymbol{\partial}_i V^{\text{ext}}(\boldsymbol{R}, \boldsymbol{Q}) = \boldsymbol{u}_i, \tag{2.64a}$$

$$-\frac{\boldsymbol{D}_i^R}{k_{\mathrm{B}} T} \boldsymbol{\partial}_i^R V^{\text{ext}}(\boldsymbol{R}, \boldsymbol{Q}) = \boldsymbol{\omega}_i, \tag{2.64b}$$

in (2.58), because forces and torques $-\boldsymbol{\partial} V^{\text{ext}}$ are related to the corresponding velocities via a friction matrix $\boldsymbol{\Gamma} = k_{\mathrm{B}} T \boldsymbol{\mathcal{D}}^{-1}$, which is essentially the inverse of the diffusion matrix $\boldsymbol{\mathcal{D}}$ (see (2.57)) up to a factor $k_{\mathrm{B}} T$ (see Eq. (4.128) and Eq. (4.132) of [Dho96, p.209ff]). Hence, we just add the terms $\boldsymbol{\partial}_i \boldsymbol{u}_i$ or $\boldsymbol{\partial}_i^R \boldsymbol{\omega}_i$ for the corresponding particle to the Smoluchowski operator.

For hard objects without additional interactions (like charge), the interaction potential is given by

$$V^{\text{int}}(\boldsymbol{R}, \boldsymbol{Q}, t) = \begin{cases} 0 & \text{if } \mathcal{V}_i(\boldsymbol{r}_i, \hat{\boldsymbol{q}}_i) \cap \mathcal{V}_j(\boldsymbol{r}_j, \hat{\boldsymbol{q}}_j) = \emptyset \\ & \text{for all } i, j \in \{1, \ldots, N\}, i \neq j, \\ \infty & \text{else,} \end{cases} \tag{2.65}$$

where $\mathcal{V}_i(\boldsymbol{r}_i, \hat{\boldsymbol{q}}_i)$ is the volume occupied by particle i at position $\boldsymbol{r}_i$ with orientation $\hat{\boldsymbol{q}}_i$, which is the statement, that particles must not overlap. As there are no interactions when the particles are separated by a finite distance, this translates to boundary conditions for $\Psi(\boldsymbol{R}, \boldsymbol{Q}, t)$: The flux into the excluded volume of two particles has to vanish. Mathematically,

$$\boldsymbol{n}_{ij}(\boldsymbol{r}_i, \boldsymbol{r}_j, \hat{\boldsymbol{q}}_i, \hat{\boldsymbol{q}}_j) \cdot \boldsymbol{j}_i(\boldsymbol{R}, \boldsymbol{Q}, t) = 0 \tag{2.66}$$

for $i \neq j$, $\boldsymbol{Q} \in \hat{S}^N$, $\boldsymbol{R} \in \mathbb{R}^{3N}$ with $(\boldsymbol{r}_j - \boldsymbol{r}_i) \in \partial \mathcal{V}_{ij}^{\text{exc}}(\hat{\boldsymbol{q}}_i, \hat{\boldsymbol{q}}_j)$, where $\partial \mathcal{V}_{ij}^{\text{exc}}(\hat{\boldsymbol{q}}_i, \hat{\boldsymbol{q}}_j)$ specifies

the boundary of the excluded volume of particles i and j with orientations $\hat{\boldsymbol{q}}_i$ and $\hat{\boldsymbol{q}}_j$ and $\boldsymbol{n}_{ij}(\boldsymbol{r}_i, \boldsymbol{r}_j, \hat{\boldsymbol{q}}_i, \hat{\boldsymbol{q}}_j)$ is the surface normal of the excluded volume caused by particle j, i.e. which is inaccessible to particle i. Since it depends for anisotropic particles on the orientation of both particles, we assign the indices of both particles to it.

To summarize, the equation of motion for the probability density distribution $\Psi(\boldsymbol{R}, \boldsymbol{Q}, t)$ of N axially symmetric particles with positions $\boldsymbol{R}$ and orientations $\boldsymbol{Q}$, interacting via the potential V^{int}, but neglecting hydrodynamic interactions, and subject to the external potential V^{ext} is given by

$$\partial_t \Psi(\boldsymbol{R}, \boldsymbol{Q}, t) = \left(\Omega^N_{\text{isotropic}} + \Omega^N_{\text{anisotropic}} + \Omega^N_{\text{rotation}}\right) \Psi(\boldsymbol{R}, \boldsymbol{Q}, t) \tag{2.67}$$

or in form of a continuity equation

$$0 = \partial_t \Psi(\boldsymbol{R}, \boldsymbol{Q}, t) + \sum_{i=1}^{N} \left(\boldsymbol{\partial}_i \boldsymbol{j}_i^T + \boldsymbol{\partial}_i^R \boldsymbol{j}_i^R\right) \tag{2.68a}$$

$$\boldsymbol{j}_i^T = \left(\overline{D}_i \left(\boldsymbol{\partial}_i + \frac{\boldsymbol{\partial}_i V^{\text{int}} + \boldsymbol{\partial}_i V^{\text{ext}}}{k_{\text{B}} T}\right) + \Delta D_i \left(\hat{\boldsymbol{q}}_i \hat{\boldsymbol{q}}_i - \frac{1}{3}\mathbb{1}\right) \left(\boldsymbol{\partial}_i + \frac{\boldsymbol{\partial}_i V^{\text{int}} + \boldsymbol{\partial}_i V^{\text{ext}}}{k_{\text{B}} T}\right)\right) \Psi(\boldsymbol{R}, \boldsymbol{Q}, t) \tag{2.68b}$$

$$\boldsymbol{j}_i^R = D_i^R \left(\boldsymbol{\partial}_i^R + \frac{\boldsymbol{\partial}_i^R V^{\text{int}} + \boldsymbol{\partial}_i^R V^{\text{ext}}}{k_{\text{B}} T}\right) \Psi(\boldsymbol{R}, \boldsymbol{Q}, t), \tag{2.68c}$$

where imposed velocities $\boldsymbol{u}_i$ or angular velocities can be described by adding $-\boldsymbol{u}_i \Psi(\boldsymbol{R}, \boldsymbol{Q}, t)$ or $-\boldsymbol{\omega}_i \Psi(\boldsymbol{R}, \boldsymbol{Q}, t)$ to the translational or rotational fluxes, respectively.

2.4. Mode-coupling theory for dense systems

Now, we consider a dense system of colloidal particles. In this case we have to account for the interactions between all particles, because they will hinder each other. Therefore, a different method has to be applied to find coarse grained equations for the dynamics of the system. We will use the so called *mode-coupling theory* (MCT) introduced by Götze and Sjögren [GS92], which was developed to describe the dynamics of dense systems, in particular glasses and supercooled liquids.

Specifically, we will discuss a suspension of N spherical particles with diameter d_b in a volume $\mathcal{V}$ as sketched in Figure 2.3. The position of particle i is given by $\boldsymbol{r}_i$. Furthermore, we consider a special spherical probe particle with diameter d with position $\boldsymbol{r}_s$, which can be observed specifically and will be subject to an external force. To simplify the notation, we introduce the vector $\boldsymbol{R} = (\boldsymbol{r}_s, \boldsymbol{r}_1, \ldots, \boldsymbol{r}_N)$ which combines the positions of all particles. Since we consider an overdamped system, the positions are sufficient to characterize the system completely. The interaction between the particles is given by potential $V(\boldsymbol{R})$. Later, we will use the interaction potential of hard sphere, but for now, we only assume that it is isotropic, i.e. $V(\mathcal{R}\boldsymbol{R}) = V(\boldsymbol{R})$ with $\mathcal{R}\boldsymbol{R} = (\mathcal{R}\boldsymbol{r}_s, \mathcal{R}\boldsymbol{r}_1, \ldots, \mathcal{R}\boldsymbol{r}_N)$ for all rotation matrices $\mathcal{R}$ compatible with the symmetry of the system[7]. Since the colloids are subject to Brownian motion, they have a bare diffusion coefficient D_0 and the probe particle has a diffusion coefficient D_0^s. This diffusion coefficient

[7]This relation is fulfilled for potentials, which can be decomposed into a sum of isotropic pair potentials

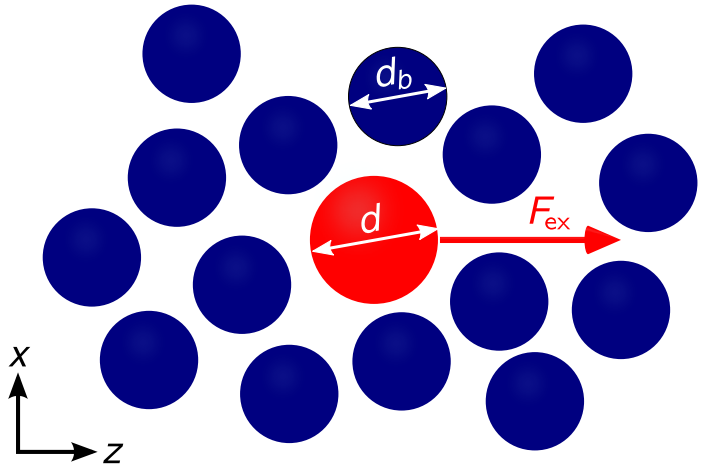

Figure 2.3.: Model system for active microrheology in dense systems. It consists of a bath of hard spheres with diameter d_b (blue) and a probe particle (red) which is a hard sphere with diameter d and which is subject to an external force $\boldsymbol{F}_{\mathrm{ex}} = F_{\mathrm{ex}}\hat{\boldsymbol{z}}$.

characterizes the short time behavior, where steric interactions between particles do not play a role. Since this theory does not include hydrodynamic interactions, one way to account for those is the use of a density dependent short time diffusion coefficient as will be demonstrated in Section 7.2. A detailed comparison to experimental data will follow in Chapter 7.

The Smoluchowski operator Ω_{AMR} for this system[8] is based on the one for many interacting particles (2.58) without hydrodynamic interactions and without rotational degrees of freedom

$$\Omega_{\mathrm{AMR}} = \sum_{i=1}^{N} D_0 \boldsymbol{\partial}_i \cdot \left(\boldsymbol{\partial}_i + \frac{\boldsymbol{\partial}_i V(\boldsymbol{R})}{k_{\mathrm{B}}T} \right) + D_0^s \boldsymbol{\partial}_s \cdot \left(\boldsymbol{\partial}_s + \frac{\boldsymbol{\partial}_s V(\boldsymbol{R})}{k_{\mathrm{B}}T} \right). \tag{2.69}$$

To nondimensionalize the equations, we use the diameter d of the bath particle as length scale[9] ($\overline{x} = x/d$) as this is the predominant length scale in the system. Since we are mostly interested in the motion of the probe particle, we choose its short time diffusion coefficient D_0^s to set the timescale via d^2/D_0^s ($\overline{t} = t/(d^2/D_0^s)$). The relative bath particle diffusion coefficient is then given by $\overline{D} = D_0/D_0^s$. The energy scale is given by the thermal energy $k_{\mathrm{B}}T$, i.e. the nondimensional potential is given by $\overline{V} = V/k_{\mathrm{B}}T$ and forces are therefore given in units of $k_{\mathrm{B}}T/d$ ($\overline{F} = F/(k_{\mathrm{B}}T/d)$). The density of the system is characterized by the packing fraction, which tells what fraction of the volume is occupied by the colloids. It is given by

$$\varphi = \frac{N}{\mathcal{V}} \frac{4\pi r^3}{3} = n \frac{\pi d^3}{6} \tag{2.70}$$

with the particle number density n. For hard sphere colloids this is the only control parameter for a phase transition. Experimentally, the sample starts to partially crystallize for $\varphi \approx 0.49$, fully crystallizes for $\varphi \approx 0.54$ and undergoes a glass transition at $\varphi \approx 0.58$ [PvM86; PZV+09]. The packing fraction has an upper limit of $\varphi_{\mathrm{fcc}} = \pi/\sqrt{18} \approx 0.7405$ for a closely packed face-centered cubic lattice [TTD00] and of $\varphi_{\mathrm{RCP}} \approx 0.64$ for random close packing[10] [SK69].

$V(\boldsymbol{R}) = \sum_{\substack{i,j \\ i \neq j}} V(|\boldsymbol{r}_i - \boldsymbol{r}_j|)$

[8] AMR = active microrheology

[9] For soft particles one could use their characteristic size based on their potential.

[10] More precise values depend on the details how to define *random close packing* (see [TTD00]).

Alltogether, the nondimensional Smoluchowski operator reads

$$\overline{\Omega}_{\mathrm{AMR}} = \overline{D}\sum_{i=1}^{N} \boldsymbol{\partial}_i \cdot \left(\boldsymbol{\partial}_i + \boldsymbol{\partial}_i \overline{V}(\boldsymbol{R})\right) + \boldsymbol{\partial}_s \cdot \left(\boldsymbol{\partial}_s + \boldsymbol{\partial}_s \overline{V}(\boldsymbol{R})\right). \tag{2.71}$$

This is our starting point. For the further calculation, we are interested in the response of the equilibrium system on the external force. Hence, we will obtain equilibrium weighted averages (see below) and it therefore proves to be helpful to separate the equilibrium contributions from the external ones. Hence, we split

$$\overline{\Omega}_{\mathrm{AMR}} = \overline{\Omega}_{\mathrm{eq}} + \overline{\Omega}_{\mathrm{ext}}, \tag{2.72a}$$

$$\overline{\Omega}_{\mathrm{eq}} = \overline{D}\sum_{i=1}^{N} \boldsymbol{\partial}_i \cdot \left(\boldsymbol{\partial}_i + \left(\boldsymbol{\partial}_i \overline{V}^{\mathrm{int}}(\boldsymbol{R})\right)\right) + \boldsymbol{\partial}_s \cdot \left(\boldsymbol{\partial}_s + \left(\boldsymbol{\partial}_s \overline{V}^{\mathrm{int}}(\boldsymbol{R})\right)\right), \tag{2.72b}$$

$$\overline{\Omega}_{\mathrm{ext}} = \boldsymbol{\partial}_s \cdot (\boldsymbol{\partial}_s \overline{V}^{\mathrm{ext}}(\boldsymbol{r}_s)), \tag{2.72c}$$

where the potential $\overline{V}^{\mathrm{int}}(\boldsymbol{R})$ describes the interactions between all $N+1$ particles, which are always present. The external potential $\overline{V}^{\mathrm{ext}}(\boldsymbol{r}_s)$ provides the force on the probe particle. We can consider three different cases: a spatially homogeneous force

$$\overline{V}^{\mathrm{ext}}_{\mathrm{homogeneous}}(\boldsymbol{r}_s) = -\overline{F_{\mathrm{ex}}} r_{s,z}, \tag{2.73a}$$

a constant force in $\hat{\boldsymbol{z}}$ direction with a harmonically restoring force in the perpendicular directions, which is used in experiments (see Chapter 7)

$$\overline{V}^{\mathrm{ext}}_{\mathrm{linetrap}}(\boldsymbol{r}_s) = -\overline{F_{\mathrm{ex}}} r_{s,z} + \frac{\overline{\kappa}}{2}\left(r_{s,x}^2 + r_{s,y}^2\right), \tag{2.73b}$$

and a spatially homogeneous, but temporally oscillating force

$$\overline{V}^{\mathrm{ext}}_{\mathrm{periodic}}(\boldsymbol{r}_s, \overline{t}) = -\overline{F_{\mathrm{ex}}} \sin(\overline{\omega}\overline{t}) r_{s,z}. \tag{2.73c}$$

Since the rest of this chapter will include many manipulations of the equations above, we will omit the bars of the nondimensional quantities to keep the notation simple. Implementing the homogeneous force is the easiest, because it conserves the translational invariance of the system, which is broken in two directions by the line trap. For the homogeneous periodic force one has to check the compatibility with the Laplace transforms for the MCT approximations.

2.4.1. Dynamical variables

We have now established the dynamics of the full system. This is a second order partial differential equation in $3(N+1)+1$ variables. Apart from the problem that this can hardly be solved even numerically for typical systems, it is also a challenge to visualize and interpret this high-dimensional solution. Therefore, one has to do some averaging or projections of these data so that they fit into our two and three-dimensional world. Since we are only interested in those coarse grained data, we will circumvent the problem of solving the full problem by deriving and solving equations of motion for the quantities of interest.

As an example consider an ideal gas in a box. It is macroscopically characterized by temperature, pressure and particle density (which are not even independent in equilibrium). Microscopically one has to characterize the probabilities of all possible configurations of gas atoms with about 10^{23} positions and velocities. Experimentally these configurations can neither be accessed nor controlled. It is however one of the great achievements of statistical mechanics to link the microscopic quantities to the macroscopic ones. In particular, we can use the average microscopic kinetic energy of the gas atoms to calculate the temperature. Averaging means in this case that one has to calculate the kinetic energy of the system for every configuration of positions and velocities and then weight it with the probability of this configuration with respect to the macroscopic control parameters.

In our case, we will follow a similar path. Let Γ characterize the configuration of the system (e.g. vector of positions, velocities, orientations) and let $\Psi(\Gamma, t)$ be the (time-dependent) probability distribution for this configuration. Our variable of interest is a function $A(\Gamma)$ of the configuration of the system. Then the (implicitly time-dependent) average of this quantity is given by

$$\langle A \rangle (t) = \int \mathrm{d}\Gamma \, A(\Gamma) \Psi(\Gamma, t). \tag{2.74}$$

The evolution of $\Psi(\Gamma, t)$ is of course given by the Smoluchowski equation (2.13) and the initial condition $\Psi_0(\Gamma)$ (here repeated for convenience)

$$\partial_t \Psi(\Gamma, t) = \Omega \Psi(\Gamma, t), \tag{2.75a}$$
$$\Psi(\Gamma, t = 0) = \Psi_0(\Gamma). \tag{2.75b}$$

This equation looks very similar to the Schrödinger equation in quantum mechanics, where the Hamiltonian is replaced by the Smoluchowski operator[11]. An important difference is that our time evolution is real valued in contrast to the imaginary unit as prefactor for quantum mechanics. This leads to the complex valued quantum mechanical wave functions. More importantly, this missing imaginary unit in statistical mechanics makes the time evolution operator non-unitary and destroys the time reversal symmetry found in quantum mechanics [Den12, Chap. 2, p. 18ff]. The analogy can be exploited to use techniques from quantum mechanics, such as path integrals, for statistical mechanics as well [Maz02, p. 79], but not all results can be directly translated as already seen for the time reversal symmetry [Maz02, p. 131].

Similarly to quantum mechanics, a formal solution of this linear partial differential equation can be written as

$$\Psi(\Gamma, t) = \mathrm{e}^{\Omega t} \Psi_0(\Gamma). \tag{2.76}$$

The definition for this operator exponential is either given by the exponential power series $\exp(\Omega t) = \sum_{k=0}^{\infty} (\Omega t)^k / k!$ or – more formally – by interpreting it in the context of semigroup theory for partial differential equations. This formal solution can now be used to transfer the time dependence from the probability distribution to the variable via

$$\langle A \rangle (t) = \int \mathrm{d}\Gamma \, \left(\mathrm{e}^{\Omega t} \Psi_0(\Gamma) \right) A(\Gamma) = \int \mathrm{d}\Gamma \, \Psi_0(\Gamma) \mathrm{e}^{\Omega^\dagger t} A(\Gamma) = \int \mathrm{d}\Gamma \, \Psi_0(\Gamma) A(\Gamma(t)) = \langle A(t) \rangle_0 \,, \tag{2.77}$$

[11] and $\hbar$ by $k_\mathrm{B} T$ in the dimensional form

where $\Omega^\dagger$ is the adjoint operator of Ω with respect to the unweighted inner product $\langle A, B\rangle = \int \mathrm{d}\Gamma\, A^*(\Gamma)B(\Gamma)$. $\Gamma(t)$ is the configuration of the system, which evolved from Γ at $t = 0$. Hence, we can also say that the variable A evolves according to

$$\partial_t A(t) = \Omega^\dagger A(t), \tag{2.78}$$

while the probability distribution is stationary. This transformation corresponds to the change from the Schrödinger to the Heisenberg picture in quantum mechanics.

This picture can be interpreted as the following experimental procedure: The system is prepared in an initial state. Then the system is changed such that the Smoluchowski operator Ω describes the evolution of the system (e.g. a force is applied to a probe particle). From this time on, the evolution of the variable $A(t)$ is recorded (e.g. the trajectory of this particle is recorded). This procedure is repeated and the variable is averaged over these different realizations of this experiment.

There remains the question, how to prepare the system in the initial state. Usually one just waits until the system settles into an equilibrium configuration, which is formally defined via

$$\Omega_{\mathrm{eq}}\Psi_{\mathrm{eq}}(\Gamma) = 0, \tag{2.79}$$

i.e. this configuration is stationary with respect to the equilibrium Smoluchowski operator. It turns out that the equilibrium state for Ω_{eq} as defined above in (2.72b) is given by

$$\Psi_{\mathrm{eq}}(\Gamma) = \frac{1}{Z}\mathrm{e}^{-V(\Gamma)}, \tag{2.80}$$

where Z is the normalization constant $Z = \int \mathrm{d}\Gamma\, \mathrm{e}^{-V(\Gamma)}$ for arbitrary interaction potentials. Note that in homogeneous systems (systems with translational symmetry) any point can serve equally well as origin of our frame of reference. We will choose it such, that the probe particle is placed at the origin $\boldsymbol{r}^s = 0$ at $t = 0$, i.e. all other positions are relative to the position of the probe particle at $t = 0$.

This allows us to introduce an equilibrium average

$$\langle A(t)\rangle_{\mathrm{eq}} := \int \mathrm{d}\Gamma\, \Psi_{\mathrm{eq}}(\Gamma)A(\Gamma, t) \tag{2.81}$$

and an equilibrium weighted inner product[12] via

$$\langle A, B\rangle_{\mathrm{eq}} := \langle A^* B\rangle_{\mathrm{eq}} := \int \mathrm{d}\Gamma\, \Psi_{\mathrm{eq}}(\Gamma)A^*(\Gamma)B(\Gamma). \tag{2.82}$$

Since basically all following averages and inner products will be based on these definitions, we will omit the subscript eq in the following and reestablish it only when necessary to avoid confusion.

With this definitions in mind, we can define a *dynamical variable* more precisely. The set of dynamical variables are all functions $A : \Gamma \to \mathbb{C}$, such that they form a Hilbert space with the inner product (2.82). The proof that this set is not empty is left to the mathematicians.

[12] This is indeed an inner product, because $\Psi_{\mathrm{eq}}(\Gamma)$ is a probability distribution. Use $\Psi_{\mathrm{eq}}(\Gamma) \geq 0$ and $\int \mathrm{d}\Gamma\, \Psi_{\mathrm{eq}}(\Gamma) = 1$ to prove this.

We will assume that every physical quantity derived from a configuration will be a dynamical variable.

Typical dynamical variables for our system are the all-particle or bath particle density [Göt09, p. 132, Eq. (3.57)] in real space (argument $\boldsymbol{r}$) and Fourier space (argument $\boldsymbol{k}$ or also $\boldsymbol{q}$, see Appendix A for the definition of the Fourier transform):

$$\rho(\boldsymbol{r}) := \sum_{i=1}^{N} \delta(\boldsymbol{r} - \boldsymbol{r}_i), \tag{2.83a}$$

$$\rho_{\boldsymbol{k}} := \sum_{i=1}^{N} \mathrm{e}^{\mathrm{i}\boldsymbol{k}\cdot\boldsymbol{r}_i}, \tag{2.83b}$$

and the probe particle density at position $\boldsymbol{r}$ (or wave vector $\boldsymbol{k}$) labeled by superscript s [Göt09, p. 100ff, Eq. (3.7), Eq. (3.10)]

$$\rho^s(\boldsymbol{r}) := \delta(\boldsymbol{r} - \boldsymbol{r}_s), \tag{2.84a}$$

$$\rho^s_{\boldsymbol{k}} := \mathrm{e}^{\mathrm{i}\boldsymbol{k}\cdot\boldsymbol{r}_s}. \tag{2.84b}$$

Note that we set the Fourier space argument as a subscript, which will be convenient for the following calculations. The bath particle density $\rho(\boldsymbol{r})$ gives the probability to find any bath particle in the volume $[\boldsymbol{r}, \boldsymbol{r} + \mathrm{d}\boldsymbol{r}\,]$ and it is also worth to note that each position $\boldsymbol{r}$ is its own dynamical variable. Similarly, $\rho^s(\boldsymbol{r})$ describes the probability of finding the probe particle in this volume. The densities with index $\boldsymbol{k}$ are obtained by a Fourier transformation in the spatial coordinates. One advantage is that they are regular functions in contrast to the distributions necessary to define $\rho(\boldsymbol{r})$ and $\rho^s(\boldsymbol{r})$. We will also see that the correlation functions obtained from these dynamical variables have more convenient properties for the following MCT formalism.

In order to obtain physically accessible quantities, we have to perform the average of these dynamical variables. For the probe particle density we obtain

$$\begin{aligned} \langle \rho^s(\boldsymbol{r}) \rangle\,(t) &= \int \mathrm{d}\Gamma\, \Psi(\Gamma, t)\delta(\boldsymbol{r} - \boldsymbol{r}_s) = \int \mathrm{d}\boldsymbol{r}_1 \cdots \mathrm{d}\boldsymbol{r}_N\, \Psi(\boldsymbol{r}, \boldsymbol{r}_1, \ldots, \boldsymbol{r}_N, t) \\ &= p^s(\boldsymbol{r}, t|\boldsymbol{r}_s = 0, t = 0) =: G^s(\boldsymbol{r}, t) \end{aligned} \tag{2.85}$$

where the conditional probability enters through our choice of the frame of reference, in which the probe particle is located at the origin at $t = 0$. In other words, $\langle \rho^s(\boldsymbol{r}) \rangle$ describes the probability to find the probe particle at time t displaced by the vector $\boldsymbol{r}$ from its initial position. $G^s(\boldsymbol{r}, t)$ is also called the *self part of the van Hove function* or the *van Hove self space-time-correlation function* [FS17, p. 155, Eq. (4.18)] in honor of Léon van Hove [Van54].

In the dynamical picture, where the variables evolve in time instead of the probability density, we can express the van Hove function as follows

$$G^s(\boldsymbol{r}, t) = \int \mathrm{d}\Gamma\, \Psi_{\mathrm{eq}}(\Gamma)\delta(\boldsymbol{r} - \boldsymbol{r}^s(t))\delta(0 - \boldsymbol{r}^s) = \int \mathrm{d}\Gamma\, \rho^s(\boldsymbol{r}, t)^* \rho^s(0, 0) = \langle \rho^s(\boldsymbol{r}, t), \rho^s(0, 0) \rangle\,. \tag{2.86}$$

In words: from all configurations and their evolutions, we take those in which the probe particle starts at $\boldsymbol{r}^s = 0$ and ends at $\boldsymbol{r}^s = \boldsymbol{r}$ at time t and average them according to their equilibrium probability. The inner product on the right hand side provides a measure for the similarity (or *overlap* [Göt09, p. 57]) between the dynamical variables $\rho^s(\boldsymbol{r}, t)$ and $\rho^s(0, 0)$.

This leads to the important concept of *correlation functions*, where the similarity between a

variable $A(t)$ at time t and a variable $B(0)$ at time $t = 0$ is measured:

$$\phi_{AB}(t) = \langle A(t), B(0)\rangle = \langle A(t)^* B(0)\rangle \,. \tag{2.87}$$

An important class of correlation functions are those with $B = A$, the so called *autocorrelators*. It can be shown that they are bounded by their initial values, i.e.

$$|\phi_{A,A}(t)| \leq \phi_{A,A}(0), \tag{2.88}$$

see [Göt09, p. 62, Eq. (2.20b)]. An extensive discussion of their properties is done in [Göt09, Chap. 2, p. 51-78].

In this thesis, we will mostly work with density auto-correlation functions. The reason for this is that in homogeneous systems the correlations between different wave vectors for any wave vector dependent dynamical variables $X_{\boldsymbol{k}}$ and $Y_{\boldsymbol{p}}$ have to vanish [Göt09, p. 103, Eq. (3.11b)]

$$\langle X_{\boldsymbol{k}}(t), Y_{\boldsymbol{p}}\rangle = \delta_{\boldsymbol{kp}} \langle X_{\boldsymbol{k}}(t), Y_{\boldsymbol{k}}\rangle \,. \tag{2.89}$$

If the system is only homogeneous along a particular direction, this statement holds true for wave vectors parallel to this direction (following the lines of the proof [Göt09, p. 603]). This causes problems for an harmonic potential and the line trap, since the homogeneity is broken perpendicular to the line force. More properties of correlation functions (auto-correlators) can be found in [Göt09, Chapter 2].

In the following we will present the most important correlation functions for this work and their properties or physical interpretations. We start with the structure factor S_k [Göt09, p. 133, Eq. (3.58c)]. It is a static equilibrium quantity given by

$$S_k = \frac{1}{N} \langle \rho_{\boldsymbol{k}}, \rho_{\boldsymbol{k}}\rangle \,. \tag{2.90}$$

Due to the isotropy, it does only depend on the modulus $k = |\boldsymbol{k}|$. It can be shown that $S_k \to 1$ in the limit $k \to \infty$ [Göt09, p. 134, Eq. (3.60d)] and for $k \to 0$ we recover the isothermal compressibility κ of the system [Göt09, p. 134, Eq. (3.62)]

$$\lim_{k\to 0} S_k = n k_{\mathrm{B}} T \kappa. \tag{2.91}$$

n is the number density of the particles in the system. Some theories for these structural correlations are based on the *direct correlation function* c_k instead of the static structure factor. It is related via the *Ornstein-Zernike relation* [Göt09, p. 134, Eq. (3.61)]

$$S_k = \frac{1}{1 - n c_k}. \tag{2.92}$$

A Fourier transform connects the structure factor to a function $g(r)$ by [Göt09, p. 133, Eq. (3.59)]

$$S_k = 1 + n \int \mathrm{d}\boldsymbol{r}\, \mathrm{e}^{\mathrm{i}\boldsymbol{k}\cdot\boldsymbol{r}} g(r), \tag{2.93}$$

which is called *pair correlation function* or *radial distribution function* and defined as [Göt09,

p. 133, Eq. (3.59c)]

$$g(r) = \frac{1}{nN} \sum_{i \neq j} \langle \delta(r - |\boldsymbol{r}_i - \boldsymbol{r}_j|) \rangle \,. \tag{2.94}$$

$ng(r)$ is the average density of finding another particle at a distance r from the considered particle (at distance 0)[13]. For $r < d$ we have $g(r) = 0$ for hard spheres, because they cannot penetrate each other. For $r \to \infty$ we find $g(r) \to 1$. This leads to δ-functions in the Fourier transform so that one usually uses the relation $(S_k - 1) = n \int \mathrm{d}\boldsymbol{r}\, \mathrm{e}^{\mathrm{i}\boldsymbol{k}\cdot\boldsymbol{r}} (g(r) - 1)$ [Göt09, p. 134, Eq. (3.60)]. In between there are (for larger packing fractions) peaks for the different shells of next neighbors, which decrease in amplitude for increasing distance.

A similar quantity arises when considering the correlations between the probe particle and the bath: the probe-bath static structure factor [GF13, Eq. (73)]

$$S_k^s = \langle \rho_{\boldsymbol{k}}^s, \rho_{\boldsymbol{k}} \rangle \,, \tag{2.95}$$

which is connected to the probability to find a bath particle at a distance r from the tracer particle $g^s(r)$ in the same way as the static structure factor S_k to the pair correlation function. Furthermore, another direct correlation function c_k^s can be used to connect these structure factors via [Göt09, p. 322, Eq. (5.23d)]

$$S_k^s = n c_k^s S_k. \tag{2.96}$$

These structural quantities which describe the equilibrium structure will enter as input for our theory. We will mostly use the Percus-Yevick-approximation for hard spheres (see [PY58] and [HM07, Sec. 4.4, p. 90-95]), but the input of structure factors from simulations or other theories is also possible, see [VPF04, Sec. III, p. 5], [IB13, Sec. C, p. 3], [VW72], [HR04]. However, we are more interested in describing the dynamics of the system. This will be described in terms of time dependent correlation functions. In particular, the bath density correlation function [Göt09, p. 135, Eq. (3.63)]

$$\phi_{\boldsymbol{k}}(t) = \frac{1}{NS_k} \langle \rho_{\boldsymbol{k}}(t), \rho_{\boldsymbol{k}}(0) \rangle = \frac{1}{NS_k} \langle \rho_{\boldsymbol{k}}(t)^* \rho_{\boldsymbol{k}}(0) \rangle \,, \tag{2.97}$$

and the probe density correlation function [Göt09, p. 108, Eq.(3.25a)]

$$\phi_{\boldsymbol{k}}^s(t) = \langle \rho_{\boldsymbol{k}}^s(t), \rho_{\boldsymbol{k}}^s(0) \rangle = \langle \rho_{\boldsymbol{k}}^s(t)^* \rho_{\boldsymbol{k}}^s(0) \rangle \,. \tag{2.98}$$

Mixed correlation function like $\langle \rho_{\boldsymbol{k}}(t), \rho_{\boldsymbol{k}}^s(0) \rangle$ or $\langle \rho_{\boldsymbol{k}}^s(t), \rho_{\boldsymbol{k}}(0) \rangle$ can appear as well. They can be used to study higher order correlation functions such as the tracer-probe pair correlation function

$$g^s(t, \boldsymbol{r}) = \sum_i \langle \delta(\boldsymbol{r} - (\boldsymbol{r}_i(t) - \boldsymbol{r}_s(t))) \rangle \,. \tag{2.99}$$

[13] For systems with broken isotropy (e.g. crystals), one can also define $g(\boldsymbol{r})$ fully space dependent by summing over $\langle \delta(\boldsymbol{r} - (\boldsymbol{r}_i - \boldsymbol{r}_j)) \rangle$.

A Fourier transform leads to

$$\begin{aligned} g^s_{\boldsymbol{k}}(t) &= \mathcal{F}\left[g^s(t,\cdot)\right](\boldsymbol{k}) = \sum_i \left\langle \mathrm{e}^{\mathrm{i}\boldsymbol{k}\cdot(\boldsymbol{r}_i(t)-\boldsymbol{r}_s(t))}\right\rangle = \left\langle \mathrm{e}^{\mathrm{i}\boldsymbol{k}\cdot(\boldsymbol{r}_s(t)-\boldsymbol{r}_s(0))}\right\rangle \sum_i \left\langle \mathrm{e}^{\mathrm{i}\boldsymbol{k}\cdot(\boldsymbol{r}_i(t)-\boldsymbol{r}_s(0))}\right\rangle \\ &= \phi^s_{\boldsymbol{k}}(t)\left\langle \rho_{\boldsymbol{k}}(t), \rho^s_{\boldsymbol{k}}(0)\right\rangle, \end{aligned} \tag{2.100}$$

which expresses the Fourier transformed tracer-probe pair correlation function in terms of the probe density correlation function and the mixed bath-probe correlation function. This expression will not be used within this thesis, but can be used to extend the theory to analyze the structure of the bath particles around the probe.

2.4.2. Zwanzig-Mori formalism

The Zwanzig-Mori formalism is a scheme to obtain mathematically equivalent equations of motion for a reduced set of variables. It is based on projections available in a Hilbert space and was introduced by Hazime Mori [Mor65] and Robert Zwanzig [Zwa61], who also wrote a book from which the discussion here is mainly taken [Zwa01, p. 149-160].

Starting point is the evolution equation for a dynamical variable A (cf. (2.78))

$$\partial_t A(t) = LA(t), \tag{2.101}$$

where L is the operator describing the evolution of A.[14]

Now we choose a selection $\boldsymbol{A} = (A_i)_i$ of dynamical variables (a vector of dynamical variables, for example the bath particle densities), which we consider important and call them *relevant variables*. Unfortunately, there is no method known, telling us beforehand which are the really relevant variables. To quote Zwanzig: "If we choose well, the results may be useful; if we choose badly, the results (while still formally correct) will probably be useless" [Zwa01, p. 146].

The projection on the relevant variables $\boldsymbol{A}$ can be described by the following projection operator

$$\mathcal{P} = \sum_{j,k} \langle A_j, \cdot\rangle \left(\langle \boldsymbol{A}, \boldsymbol{A}\rangle\right)^{-1}_{jk} A_k, \tag{2.102}$$

where $(\langle \boldsymbol{A}, \boldsymbol{A}\rangle)^{-1}$ is the inverse matrix of the matrix $(\langle \boldsymbol{A}, \boldsymbol{A}\rangle)_{ij} = \langle A_i, A_j\rangle$, which consists of all combinations of overlaps between the relevant dynamical variables. If they are orthonormalized, this matrix reduces to the identity matrix [Zwa01, p. 148, Eq. (8.19)]. The projection operator, which projects onto the orthogonal complement of these variables is given by $\mathcal{Q} = \mathbb{1} - \mathcal{P}$. With some formal manipulations involving an elaborate operator identity[15] one finds the following equations of motion for the correlation functions of the relevant variables $(\phi_{\boldsymbol{A},\boldsymbol{A}}(t))_{ij} := \langle A_i(t), A_j(0)\rangle$

$$\partial_t \phi_{\boldsymbol{A},\boldsymbol{A}}(t) + \boldsymbol{\Gamma}\phi_{\boldsymbol{A},\boldsymbol{A}}(t) + \int_0^t \boldsymbol{M}(t-t')\phi_{\boldsymbol{A},\boldsymbol{A}}(t')\mathrm{d}t' = 0 \tag{2.103a}$$

[14] Zwanzig calls L *Liouville operator* and the corresponding equation *Liouville equation*, but it only matters that L is a linear differential operator

[15] Details on the calculation can be found in [Zwa01, Sec. 8.2] or [Gru14, Sec. 2.3] adapted to the notation used here.

or in components

$$\partial_t \langle A_i(t), A_j(0)\rangle + \sum_k (\boldsymbol{\Gamma})_{ik} \langle A_k(t), A_j(0)\rangle + \int_0^t \sum_k (\boldsymbol{M}(t-t'))_{ik} \langle A_k(t'), A_j(0)\rangle \,\mathrm{d}t' = 0, \quad (2.103b)$$

where

$$(\boldsymbol{\Gamma})_{ik} := -\sum_j \langle A_j, LA_i\rangle \left(\langle \boldsymbol{A}, \boldsymbol{A}\rangle^{-1}\right)_{jk}, \quad (2.104a)$$

$$(\boldsymbol{M}(t))_{ik} := -\sum_j \left\langle A_j, L\mathrm{e}^{\mathcal{Q}Lt}\mathcal{Q}LA_i\right\rangle \left(\langle \boldsymbol{A}, \boldsymbol{A}\rangle^{-1}\right)_{jk}. \quad (2.104b)$$

The matrix $\boldsymbol{\Gamma}$ is often called *frequency matrix*, because it describes the initial decay of the correlation functions and can be used to determine dispersion relations of crystals with defects [Ras17] or so called *Cluster crystals* [HWSF15]. The irrelevant variables do not show up in this equation anymore. Instead we find an integral, which couples the evolution of the correlation functions to their history. The matrix valued function $\boldsymbol{M}(t)$ is therefore called *memory kernel*. So far, this is an exact transformation [Zwa01, p. 158]. An instructive example can be found in [Zwa01, p. 147, Eqs. (8.12)-(8.14)].

We have achieved equations of motion which are expressed in terms of the relevant variables only. However, this was traded in by the memory integral, which is tricky in two ways: First, the memory kernel is difficult to evaluate due to the projections on the irrelevant variables. Second, integrodifferential equations are not easy to solve and in contrast to ordinary or partial differential equations only little is known about methods to solve them. For the first problem, the *mode coupling approximation* was invented. And over the last years different methods have been developed to solve integrodifferential equations numerically in similar contexts [BGS84; FGHL91]. Even though this is a complicated problem, we should also appreciate its advantages: this approach leads us from a microscopic starting point to the desired macroscopic variables, without much space for fitting parameters.

2.4.3. Derivation of MCT equations

Now we want to apply the Zwanzig-Mori-formalism in order to find equations of motion for the density correlation functions $\phi_{\boldsymbol{k}}$ and $\phi^s_{\boldsymbol{k}}$ as introduced in Eqs. (2.97) and (2.98). It is already known that this choice is a good set of relevant variables, which give reasonable results [GL76; GS91]. While it is possible to include time-dependent forces like (2.73c) as done by Brader *et al.* [BSB+10], we circumvent the complications of the additional Fourier series in time by looking only at time independent forces.

First, we need the adjoint operator of (2.72) with respect to the unweighted inner product $\langle A, B\rangle = \int \mathrm{d}\Gamma\, A^*(\Gamma)B(\Gamma)$. This is a straightforward calculation using integration by parts to swap the derivatives. The result is

$$\Omega^\dagger_{\mathrm{eq}} = D\sum_{i=1}^{N} (\boldsymbol{\partial}_i - \boldsymbol{\partial}_i V(\boldsymbol{R}))\cdot\boldsymbol{\partial}_i + (\boldsymbol{\partial}_s - \boldsymbol{\partial}_s V(\boldsymbol{R}))\cdot\boldsymbol{\partial}_s, \quad (2.105a)$$

$$\Omega^\dagger_{\mathrm{ext}} = -\boldsymbol{\partial}_s V^{\mathrm{ext}}(\boldsymbol{r}_s)\cdot\boldsymbol{\partial}_s \quad (2.105b)$$

(cf. [Gru14, p. 16] and [GF13, Eq. (15)]). This result is — with this order of forces and derivatives — independent of the choice of the potentials $V(\boldsymbol{R})$ and $V^{\mathrm{ext}}(\boldsymbol{r}_s)$.

Choosing the Fourier transforms of the bath density $\rho_{\boldsymbol{k}}$ (2.83) and the probe density $\rho^s_{\boldsymbol{k}}$ (2.84) as relevant variables, we obtain the following correlation functions

$$\phi^{\mu\nu}_{\boldsymbol{kp}}(t) := \left\langle \rho^{\mu}_{\boldsymbol{k}}(t), \rho^{\nu}_{\boldsymbol{p}}(0) \right\rangle, \tag{2.106}$$

with $\mu, \nu \in \{b, s\}$ where we renamed the bath density $\rho^b_{\boldsymbol{k}} := \rho_{\boldsymbol{k}}$ to simplify the equations. In homogeneous systems, correlations between different wave vectors vanish due to (2.89). This condition however is violated for the case of the line trap potential (2.73b). There, homogeneity is only given in force direction, which implies

$$\langle X_{\boldsymbol{k}}(t), Y_{\boldsymbol{p}}(0) \rangle = \delta_{k_z p_z} \left\langle X_{k_x,k_y,k_z}(t), Y_{p_x,p_y,k_z}(0) \right\rangle. \tag{2.107}$$

For the Zwanzig-Mori scheme (2.103b) we use the (two times infinitely many) relevant variables $\boldsymbol{A} = (\rho^b_{\boldsymbol{k}_1}, \rho^s_{\boldsymbol{k}_1}, \rho^b_{\boldsymbol{k}_2}, \rho^s_{\boldsymbol{k}_2}, \ldots)$ This leads to the projector

$$\mathcal{P} = \sum_{\substack{\mu\nu \\ \boldsymbol{pq}}} \left\langle \rho^{\mu}_{\boldsymbol{p}}, \cdot \right\rangle \left(\langle \boldsymbol{A}, \boldsymbol{A} \rangle^{-1} \right)^{\mu\nu}_{\boldsymbol{pq}} \rho^{\nu}_{\boldsymbol{q}} \tag{2.108}$$

with $\mu, \nu \in \{b, s\}$ and $\mathcal{Q} = \mathbb{1} - \mathcal{P}$. With these definitions, we find

$$\partial_t \phi^{\mu\nu}_{\boldsymbol{kp}}(t) + \sum_{\boldsymbol{q},\lambda} (\boldsymbol{\Gamma})^{\mu\lambda}_{\boldsymbol{kq}} \phi^{\lambda\nu}_{\boldsymbol{qp}}(t) + \int_0^t \sum_{\boldsymbol{q},\lambda} (\boldsymbol{M}(t-t'))^{\mu\lambda}_{\boldsymbol{kq}} \phi^{\lambda\nu}_{\boldsymbol{qp}}(t') \mathrm{d}t' = 0, \tag{2.109}$$

where $\lambda, \mu, \nu \in \{b, s\}$ and

$$(\boldsymbol{\Gamma})^{\mu\nu}_{\boldsymbol{kq}} := -\sum_{\boldsymbol{p},\lambda} \left\langle \rho^{\lambda}_{\boldsymbol{p}}, \Omega^{\dagger} \rho^{\mu}_{\boldsymbol{k}} \right\rangle \left(\langle \boldsymbol{A}, \boldsymbol{A} \rangle^{-1} \right)^{\lambda\nu}_{\boldsymbol{pq}}, \tag{2.110a}$$

$$(\boldsymbol{M}(t))^{\mu\nu}_{\boldsymbol{kq}} := -\sum_{\boldsymbol{p},\lambda} \left\langle \rho^{\lambda}_{\boldsymbol{p}}, \Omega^{\dagger} \mathrm{e}^{\mathcal{Q}\Omega^{\dagger} t} \mathcal{Q}\Omega^{\dagger} \rho^{\mu}_{\boldsymbol{k}} \right\rangle \left(\langle \boldsymbol{A}, \boldsymbol{A} \rangle^{-1} \right)^{\lambda\nu}_{\boldsymbol{pq}}. \tag{2.110b}$$

The matrix $(\langle \boldsymbol{A}, \boldsymbol{A} \rangle)^{-1}$ is block-diagonal in $\boldsymbol{q}$ (because the equilibrium system is homogeneous) with the blocks given by (using definitions (2.90) and (2.95))

$$(\langle \boldsymbol{A}, \boldsymbol{A} \rangle)^{-1}_{\boldsymbol{pq}} = \delta_{\boldsymbol{pq}} \begin{pmatrix} \left\langle \rho^b_{\boldsymbol{q}}, \rho^b_{\boldsymbol{q}} \right\rangle & \left\langle \rho^b_{\boldsymbol{q}}, \rho^s_{\boldsymbol{q}} \right\rangle \\ \left\langle \rho^s_{\boldsymbol{q}}, \rho^b_{\boldsymbol{q}} \right\rangle & \left\langle \rho^s_{\boldsymbol{q}}, \rho^s_{\boldsymbol{q}} \right\rangle \end{pmatrix}^{-1} = \delta_{\boldsymbol{qp}} \frac{1}{N S_q - (S^s_q)^2} \begin{pmatrix} 1 & -S^s_q \\ -S^s_q & N S_q \end{pmatrix}. \tag{2.111}$$

The matrix elements of the frequency matrix (2.110a) can be calculated directly, while we have to do some approximations for the memory kernel matrix (2.110b). The following identity will prove useful for the direct calculations: Let A be an arbitrary dynamical variable. Then

we obtain for its average weighted by the internal (equilibrium) forces

$$\begin{aligned}\langle(\boldsymbol{\partial}_i V)A\rangle &= \int \mathrm{d}\Gamma\, \Psi_{\mathrm{eq}}(\Gamma)(\boldsymbol{\partial}_i V(\Gamma))A(\Gamma) = \int \mathrm{d}\Gamma\, \frac{1}{Z}\mathrm{e}^{-V(\Gamma)}(\boldsymbol{\partial}_i V(\Gamma))A(\Gamma) \\ &= -\int \mathrm{d}\Gamma\, \left(\boldsymbol{\partial}_i \frac{1}{Z}\mathrm{e}^{-V(\Gamma)}\right) A(\Gamma) = \int \mathrm{d}\Gamma\, \frac{1}{Z}\mathrm{e}^{-V(\Gamma)}\boldsymbol{\partial}_i A(\Gamma) \\ &= \langle \boldsymbol{\partial}_i A\rangle\,,\end{aligned} \tag{2.112}$$

where we used the explicit representation of the equilibrium probability distribution (2.80) and integration by parts in the second line. Since A can be any dynamical variable, this yields as well a relation for inner products

$$\langle B, (\boldsymbol{\partial}_i V)A\rangle = \langle (\boldsymbol{\partial}_i V)B^* A\rangle = \langle \boldsymbol{\partial}_i B^* A\rangle\,. \tag{2.113}$$

With this, we find from (2.105) (see Appendix C.1 for the detailed calculations)

$$\left\langle \rho_{\boldsymbol{p}}, \Omega^\dagger \rho_{\boldsymbol{k}} \right\rangle = -\delta_{\boldsymbol{pk}} N D k^2, \tag{2.114a}$$

$$\left\langle \rho^s_{\boldsymbol{p}}, \Omega^\dagger \rho_{\boldsymbol{k}} \right\rangle = 0, \tag{2.114b}$$

$$\left\langle \rho_{\boldsymbol{p}}, \Omega^\dagger \rho^s_{\boldsymbol{k}} \right\rangle = -\delta_{\boldsymbol{pk}} S^s_k \mathrm{i}\boldsymbol{k}\cdot\boldsymbol{\partial}_s V^{\mathrm{ext}}, \tag{2.114c}$$

$$\left\langle \rho^s_{\boldsymbol{p}}, \Omega^\dagger \rho^s_{\boldsymbol{k}} \right\rangle = -\delta_{\boldsymbol{pk}}(k^2 + \mathrm{i}\boldsymbol{k}\cdot\boldsymbol{\partial}_s V^{\mathrm{ext}}). \tag{2.114d}$$

If the external force varies spatially, one has to take the value $\boldsymbol{\partial}_s V^{\mathrm{ext}}(\boldsymbol{r}_s = 0)$, because we chose our frame of reference such that $\boldsymbol{r}_s = 0$ for $t = 0$. With this information, we can calculate the frequency matrix, which reads in the thermodynamic limit ($N \to \infty$)

$$\boldsymbol{\Gamma}_{\boldsymbol{kq}} = \delta_{\boldsymbol{kq}} \begin{pmatrix} \frac{Dk^2}{S_k} & -\frac{S^s_k}{S_k} Dk^2 \\ 0 & k^2 + \mathrm{i}\boldsymbol{k}\cdot(\boldsymbol{\partial}_s V^{\mathrm{ext}}) \end{pmatrix}. \tag{2.115}$$

To make some progress for the memory kernel (2.110b), we first rewrite it in a more symmetric form using that $(\langle \boldsymbol{A}, \boldsymbol{A}\rangle)^{-1}$ is block diagonal (2.111) and that $\mathcal{Q}$ is a projection operator[16]

$$(\boldsymbol{M}(t))^{\mu\nu}_{\boldsymbol{kq}} := -\sum_\lambda \left\langle \mathcal{Q}\Omega^{\mathrm{adj}}\rho^\lambda_{\boldsymbol{q}}, \mathrm{e}^{\mathcal{Q}\Omega^\dagger t}\mathcal{Q}\Omega^\dagger \rho^\mu_{\boldsymbol{k}} \right\rangle \left(\langle \boldsymbol{A}, \boldsymbol{A}\rangle^{-1}\right)^{\lambda\nu}_{\boldsymbol{qq}}. \tag{2.116}$$

The operator Ω^{adj} is the adjoint operator of $\Omega^\dagger$ (2.72) with respect to the equilibrium inner product. Even though the equilibrium operator $\Omega^\dagger_{\mathrm{eq}}$ is Hermitian with respect to this inner product [Gaz08, p. 89, Eq. (B.1)], the complete operator is not. For homogeneous forces, this calculation was done by Gazuz [GF13, Eq. (17)], [Gaz08, p. 90, Eq. (B.10)] and for general external potentials $V^{\mathrm{ext}}(\boldsymbol{r}_s)$, we obtain

$$\Omega^{\mathrm{adj}} = \Omega^\dagger_{\mathrm{eq}} - (\boldsymbol{\partial}_s V^{\mathrm{ext}})\cdot(\boldsymbol{\partial}_s V - \boldsymbol{\partial}_s) + \boldsymbol{\partial}_s \cdot \boldsymbol{\partial}_s V^{\mathrm{ext}}. \tag{2.117}$$

Operating on $\rho_{\boldsymbol{k}}$ and $\rho^s_{\boldsymbol{k}}$ and projecting by $\mathcal{Q}$, we obtain (see Appendix C for details)

$$\mathcal{Q}\Omega^{\mathrm{adj}}\rho_{\boldsymbol{k}} = -\mathrm{i}D\boldsymbol{k}\sum_i \mathcal{Q}(\boldsymbol{\partial}_i V)\mathrm{e}^{\mathrm{i}\boldsymbol{k}\boldsymbol{r}_i} \tag{2.118a}$$

[16] Projection operators are hermitian $\langle f, \mathcal{Q}g\rangle = \langle \mathcal{Q}f, g\rangle$ and idempotent $\mathcal{Q}^2 = \mathcal{Q}$. The second property gives the identity $\mathrm{e}^{t\mathcal{Q}L}\mathcal{Q} = \mathcal{Q}\mathrm{e}^{t\mathcal{Q}L}\mathcal{Q}$ (using for example the series definition of the operator exponential).

$$\mathcal{Q}\Omega^{\mathrm{adj}}\rho^s_{\boldsymbol{k}} = \left(-\mathrm{i}\boldsymbol{k} + (\boldsymbol{\partial}_s V^{\mathrm{ext}})\right)\cdot \mathcal{Q}(\boldsymbol{\partial}_s V)\mathrm{e}^{\mathrm{i}\boldsymbol{k}\boldsymbol{r}_s} + \left[\mathcal{Q}, (\boldsymbol{\partial}_s V^{\mathrm{ext}})\right]\cdot(\boldsymbol{\partial}_s V)\mathrm{e}^{\mathrm{i}\boldsymbol{k}\boldsymbol{r}_s} \tag{2.118b}$$

For a spatially homogeneous potential V^{ext} the commutator $\left[\mathcal{Q}, (\boldsymbol{\partial}_s V^{\mathrm{ext}})\right]$ vanishes. This is in general not true for inhomogeneous potentials. Even though it is possible to calculate the commutator, it does not have a form suitable for the following calculations. We will therefore ignore this term for the time being and continue with the spatially homogeneous forces, as this the main focus of this work.

Combining those results, we find

$$\left\langle \mathcal{Q}\Omega^{\mathrm{adj}}\rho^b_{\boldsymbol{q}}, \mathrm{e}^{\mathcal{Q}\Omega^\dagger t}\mathcal{Q}\Omega^\dagger\rho^b_{\boldsymbol{k}}\right\rangle = D^2\sum_{i,j}\left\langle \boldsymbol{q}\cdot\mathcal{Q}(\boldsymbol{\partial}_i V)\mathrm{e}^{\mathrm{i}\boldsymbol{q}\boldsymbol{r}_i}, \mathrm{e}^{\mathcal{Q}\Omega^\dagger\mathcal{Q}t}\boldsymbol{k}\cdot\mathcal{Q}(\boldsymbol{\partial}_j V)\mathrm{e}^{\mathrm{i}\boldsymbol{k}\boldsymbol{r}_j}\right\rangle \tag{2.119a}$$

$$\left\langle \mathcal{Q}\Omega^{\mathrm{adj}}\rho^s_{\boldsymbol{q}}, \mathrm{e}^{\mathcal{Q}\Omega^\dagger t}\mathcal{Q}\Omega^\dagger\rho^s_{\boldsymbol{k}}\right\rangle = \sum_{\alpha,\beta\in\{x,y,z\}} k^\beta\left\langle (q^\alpha - \mathrm{i}(\partial_{s,\alpha}V^{\mathrm{ext}}))\mathcal{Q}(\partial_{s,\alpha}V)\mathrm{e}^{\mathrm{i}\boldsymbol{q}\boldsymbol{r}_s}, \mathrm{e}^{\mathcal{Q}\Omega^\dagger\mathcal{Q}t}\mathcal{Q}(\partial_{s,\beta}V)\mathrm{e}^{\mathrm{i}\boldsymbol{k}\boldsymbol{r}_s}\right\rangle \tag{2.119b}$$

Note that the indices $\alpha, \beta, \gamma \in \{x, y, z\}$ label the dimensions rather than the correlator species. The mixed terms with $\left\langle \ldots\rho^b_{\boldsymbol{k}}, \ldots\rho^s_{\boldsymbol{p}}\right\rangle$ will not contribute in the thermodynamic limit and are therefore not calculated explicitly. This also implies that there is again no coupling from the probe correlator to the bath correlator. We can therefore keep the assumption of homogeneity for the bath and eliminate the couplings between different wave vectors. Hence, we find

$$(\boldsymbol{M}(t))^{bb}_{\boldsymbol{k}\boldsymbol{q}} = -\delta_{\boldsymbol{k}\boldsymbol{q}}\frac{D}{S_k}\frac{D}{N}\left\langle\sum_{i,\alpha}\mathcal{Q}k^\alpha\cdot(\partial_{i,\alpha}V)\mathrm{e}^{\mathrm{i}\boldsymbol{k}\boldsymbol{r}_i}, \mathrm{e}^{\mathcal{Q}\Omega^\dagger\mathcal{Q}t}\sum_j\mathcal{Q}k^\beta(\partial_{j,\beta}V)\mathrm{e}^{\mathrm{i}\boldsymbol{k}\boldsymbol{r}_j}\right\rangle \tag{2.120a}$$

If we want to bring the memory function of the probe correlator into the same form, we have to assume that the force $\boldsymbol{\partial}V^{\mathrm{ext}}$ is constant. From this point on we cannot proceed the same way with an inhomogeneous force. This requires new ideas, maybe similar to confinement [LBO+10]. Therefore, we will assume a spatially homogeneous force from here. Thus, we know again that there is no coupling between different wave vectors. In total

$$(\boldsymbol{M}(t))^{ss}_{\boldsymbol{k}\boldsymbol{q}} = -\delta_{\boldsymbol{k}\boldsymbol{q}}\sum_{\alpha,\beta}(k^\alpha + \mathrm{i}(\partial_{s,\alpha}V^{\mathrm{ext}}))k^\beta\left\langle\mathcal{Q}(\partial_{s,\alpha}V)\mathrm{e}^{\mathrm{i}\boldsymbol{k}\boldsymbol{r}_s}, \mathrm{e}^{\mathcal{Q}\Omega^\dagger\mathcal{Q}t}\mathcal{Q}(\partial_{s,\beta}V)\mathrm{e}^{\mathrm{i}\boldsymbol{k}\boldsymbol{r}_s}\right\rangle. \tag{2.120b}$$

It was shown by Cichocki and Hess [CH87] that it is better to perform approximations on the so called *irreducible* operators and memory functions. This arises from the fact that we are considering here the overdamped Smoluchowski equation instead of the full Fokker-Planck equation. This procedure was already carried out in [Gru14, Sec. 3.3, p. 19f] and is repeated in Appendix C.2. Using the definitions

$$m^{\mu\alpha,\nu\beta}(t) := \left\langle F^{\mu\alpha}_{\boldsymbol{k}}, \mathrm{e}^{\mathcal{Q}\Omega^\dagger\mathcal{Q}t}F^{\nu\beta}_{\boldsymbol{k}}\right\rangle, \tag{2.121a}$$

$$m^{\mu\alpha,\nu\beta}_{\mathrm{irr}}(t) := \left\langle F^{\mu\alpha}_{\boldsymbol{k}}, \mathrm{e}^{\Omega^\dagger_{\mathrm{irr}}t}F^{\nu\beta}_{\boldsymbol{k}}\right\rangle, \tag{2.121b}$$

with $\mu, \nu \in \{b, s\}$ and

$$F^{b\alpha}_{\boldsymbol{k}} := \sum_i\sqrt{\frac{D}{N}}\mathcal{Q}(\boldsymbol{\partial}_{i,\alpha}V)\mathrm{e}^{\mathrm{i}\boldsymbol{k}\boldsymbol{r}_i}, \tag{2.121c}$$

$$F_{\boldsymbol{k}}^{s\alpha} := \mathcal{Q}(\boldsymbol{\partial}_{s,\alpha} V) \mathrm{e}^{\mathrm{i}\boldsymbol{k}\boldsymbol{r}_s}, \tag{2.121d}$$

we find the following relation between the reducible and the irreducible primitive memory functions (cf. (C.16))

$$m^{\mu\alpha,\nu\beta}(t) = m_{\mathrm{irr}}^{\mu\alpha,\nu\beta}(t) - \sum_{\lambda,\gamma} \int_0^t \mathrm{d}t'\, m_{\mathrm{irr}}^{\mu\alpha,\lambda\gamma}(t-t') m^{\lambda\gamma,\nu\beta}(t'). \tag{2.122}$$

This convolution equation will be later solved by a Laplace transform.

For now, we will focus on expressing the irreducible memory kernels in terms of the correlation functions. This follows the procedure which is generic in any mode-coupling theory approach. We start by projecting the forces $F_{\boldsymbol{k}}^{\alpha}$ in the irreducible memory functions onto higher order correlation functions, which are not projected out by $\mathcal{Q}$. In our case this is the bath-bath and tracer-bath density modes $\rho_{\boldsymbol{k}}\rho_{\boldsymbol{p}}$ and $\rho_{\boldsymbol{k}}^s\rho_{\boldsymbol{p}}$. The corresponding projector is given by[17] [Göt09, p. 180, Eq. (4.2) with g^{-1} on p. 183 and p. 322]

$$\mathcal{P} = \sum_{\boldsymbol{p}<\boldsymbol{q}} \frac{1}{N^2 S_p S_q} \rho_{\boldsymbol{p}}\rho_{\boldsymbol{q}} \langle \rho_{\boldsymbol{p}}\rho_{\boldsymbol{q}}, \cdot \rangle + \sum_{\boldsymbol{p},\boldsymbol{q}} \frac{1}{N S_q} \rho_{\boldsymbol{p}}^s \rho_{\boldsymbol{q}} \left\langle \rho_{\boldsymbol{p}}^s \rho_{\boldsymbol{q}}, \cdot \right\rangle. \tag{2.123}$$

The notation $\boldsymbol{p} < \boldsymbol{q}$ indicates that we do not count pair correlations with $\boldsymbol{p}$ and $\boldsymbol{q}$ interchanged (which are the same). This leads to the following approximation

$$\begin{aligned} m_{\mathrm{irr}}^{\mu\alpha,\nu\beta}(t) &\approx \left\langle \mathcal{P} F_{\boldsymbol{k}}^{\mu\alpha}, \mathrm{e}^{\Omega_{\mathrm{irr}}^\dagger t} \mathcal{P} F_{\boldsymbol{k}}^{\nu\beta} \right\rangle \\ &= \sum_{\substack{\boldsymbol{p}<\boldsymbol{q},\\ \boldsymbol{p}'<\boldsymbol{q}'}} \frac{1}{N^4 S_p S_q S_{p'} S_{q'}} \langle F_{\boldsymbol{k}}^{\mu\alpha}, \rho_{\boldsymbol{p}}\rho_{\boldsymbol{q}} \rangle \left\langle \rho_{\boldsymbol{p}}\rho_{\boldsymbol{q}}, \mathrm{e}^{\Omega_{\mathrm{irr}}^\dagger t} \rho_{\boldsymbol{p}'}\rho_{\boldsymbol{q}'} \right\rangle \left\langle \rho_{\boldsymbol{p}'}\rho_{\boldsymbol{q}'}, F_{\boldsymbol{k}}^{\nu\beta} \right\rangle \\ &\quad + \sum_{\substack{\boldsymbol{p},\boldsymbol{q},\\ \boldsymbol{p}',\boldsymbol{q}'}} \frac{1}{N^2 S_q S_{q'}} \left\langle F_{\boldsymbol{k}}^{\mu\alpha}, \rho_{\boldsymbol{p}}^s \rho_{\boldsymbol{q}} \right\rangle \left\langle \rho_{\boldsymbol{p}}^s \rho_{\boldsymbol{q}}, \mathrm{e}^{\Omega_{\mathrm{irr}}^\dagger} \rho_{\boldsymbol{p}'}^s \rho_{\boldsymbol{q}'} \right\rangle \left\langle \rho_{\boldsymbol{p}'}^s \rho_{\boldsymbol{q}'}, F_{\boldsymbol{k}}^{\nu\beta} \right\rangle. \end{aligned} \tag{2.124}$$

The next step is the *factorization ansatz* [Göt09, p. 182, Eq. (4.7a) and p. 322]

$$\left\langle \rho_{\boldsymbol{q}}^\lambda \rho_{\boldsymbol{k}}^\mu, \mathrm{e}^{\Omega_{\mathrm{irr}}^\dagger t} \rho_{\boldsymbol{q}'}^\lambda \rho_{\boldsymbol{k}'}^\mu \right\rangle \approx \left\langle \rho_{\boldsymbol{k}}^\lambda, \mathrm{e}^{\Omega^\dagger t} \rho_{\boldsymbol{k}'}^\lambda \right\rangle \left\langle \rho_{\boldsymbol{q}}^\mu, \mathrm{e}^{\Omega^\dagger t} \rho_{\boldsymbol{q}'}^\mu \right\rangle = \phi_{\boldsymbol{k}\boldsymbol{k}'}^{\lambda\lambda}(t) \phi_{\boldsymbol{q}\boldsymbol{q}'}^{\mu\mu}(t), \tag{2.125}$$

where as a further approximation the irreducible operator $\Omega_{\mathrm{irr}}^\dagger$ was replaced again by the original one $\Omega^\dagger$. In this step we recover the correlation functions, which we introduced in the beginning of this section. Rewriting them in terms of the bath- and probe-bath correlation functions (2.97) and (2.98) we find (again invoking homogeneity)

$$\begin{aligned} m_{\mathrm{irr}}^{\mu\alpha,\nu\beta}(t) = &\sum_{\boldsymbol{p}<\boldsymbol{q}} \frac{1}{N^2 S_p S_q} \langle F_{\boldsymbol{k}}^{\mu\alpha}, \rho_{\boldsymbol{p}}\rho_{\boldsymbol{q}} \rangle \left\langle \rho_{\boldsymbol{p}}\rho_{\boldsymbol{q}}, F_{\boldsymbol{k}}^{\nu\beta} \right\rangle \phi_{\boldsymbol{p}}(t)\phi_{\boldsymbol{q}}(t) \\ &+ \sum_{\boldsymbol{p},\boldsymbol{q}} \frac{1}{N S_q} \left\langle F_{\boldsymbol{k}}^{\mu\alpha}, \rho_{\boldsymbol{p}}^s \rho_{\boldsymbol{q}} \right\rangle \left\langle \rho_{\boldsymbol{p}}^s \rho_{\boldsymbol{q}}, F_{\boldsymbol{k}}^{\nu\beta} \right\rangle \phi_{\boldsymbol{p}}^s(t)\phi_{\boldsymbol{q}}(t) \end{aligned}. \tag{2.126}$$

[17] This representation already includes the thermodynamic limit as well as the factorization ansatz as discussed in [Göt09, p. 182].

To close these equations we finally need to calculate only four more inner products (assuming that $\mathcal{Q}\rho_{\boldsymbol{k}}\rho_{\boldsymbol{q}} = \rho_{\boldsymbol{k}}\rho_{\boldsymbol{q}}$ and $\mathcal{Q}\rho^s_{\boldsymbol{k}}\rho_{\boldsymbol{q}} = \rho^s_{\boldsymbol{k}}\rho_{\boldsymbol{q}}$)

$$\begin{aligned}\sqrt{\frac{N}{D}}\left\langle F^{b\alpha}_{\boldsymbol{k}}, \rho_{\boldsymbol{p}}\rho_{\boldsymbol{q}}\right\rangle =& \mathrm{i}(p^\alpha + q^\alpha - k^\alpha)\left\langle \rho_{\boldsymbol{k}-\boldsymbol{p}-\boldsymbol{q}}\right\rangle + \mathrm{i}(p^\alpha - k^\alpha)\delta_{\boldsymbol{k}-\boldsymbol{p},\boldsymbol{q}} N S_q \\ &+ \mathrm{i}(q^\alpha - k^\alpha)\delta_{\boldsymbol{k}-\boldsymbol{q},\boldsymbol{p}} N S_p - \mathrm{i}k^\alpha\left\langle \rho_{\boldsymbol{k}}, \rho_{\boldsymbol{p}}\rho_{\boldsymbol{q}}\right\rangle, \end{aligned} \tag{2.127a}$$

$$\sqrt{\frac{N}{D}}\left\langle F^{b\alpha}_{\boldsymbol{k}}, \rho^s_{\boldsymbol{p}}\rho_{\boldsymbol{q}}\right\rangle = -\mathrm{i}k^\alpha\left\langle \rho_{\boldsymbol{k}}, \rho^s_{\boldsymbol{p}}\rho_{\boldsymbol{q}}\right\rangle + \mathrm{i}q^\alpha\delta_{\boldsymbol{k}-\boldsymbol{q}}S^s_{\boldsymbol{p}}, \tag{2.127b}$$

$$\left\langle F^{s\alpha}_{\boldsymbol{k}}, \rho_{\boldsymbol{p}}\rho_{\boldsymbol{q}}\right\rangle = -\mathrm{i}k^\alpha\left\langle \rho^s_{\boldsymbol{k}}, \rho_{\boldsymbol{p}}\rho_{\boldsymbol{q}}\right\rangle, \tag{2.127c}$$

$$\left\langle F^{s\alpha}_{\boldsymbol{k}}, \rho^s_{\boldsymbol{p}}\rho_{\boldsymbol{q}}\right\rangle = -\mathrm{i}(k^\alpha - p^\alpha)\delta_{\boldsymbol{k}-\boldsymbol{p},\boldsymbol{q}}S^s_q. \tag{2.127d}$$

In the thermodynamic limit ($N \to \infty$) the couplings between the bath memory kernels and the probe memory kernels vanish and we obtain

$$\begin{aligned}m^{b\alpha,b\beta}_{\mathrm{irr}}(t) = \frac{1}{2}\sum_{\boldsymbol{p}\boldsymbol{q}}\frac{D}{NS_pS_q}\delta_{\boldsymbol{k},\boldsymbol{q}+\boldsymbol{k}}\left(q^\alpha S_p + p^\alpha S_q - k^\alpha S_pS_q(1+\rho^2 c_3(k,p,q))\right) \\ \cdot\left(q^\beta S_p + p^\beta S_q - k^\beta S_pS_q(1+\rho^2 c_3(k,p,q))\right)\phi_{\boldsymbol{p}}(t)\phi_{\boldsymbol{q}}(t),\end{aligned} \tag{2.128a}$$

where the triple-density average $\langle \rho_{\boldsymbol{k}}, \rho_{\boldsymbol{p}}\rho_{\boldsymbol{q}}\rangle$ is expressed through a triple-correlation function $c_3(k,p,q)$ (cf. [Göt09, p. 182, Eq. (4.6)]). The factor 1/2 comes from allowing the sum over all combinations of wave vectors. For the probe memory kernels we find

$$m^{s\alpha,s\beta}_{\mathrm{irr}}(t) = \sum_{\boldsymbol{p}\boldsymbol{q}}\frac{1}{NS_q}\left(q^\alpha S^s_q\delta_{\boldsymbol{k}-\boldsymbol{p},\boldsymbol{q}}\right)\left(q^\beta S^s_q\delta_{\boldsymbol{k}-\boldsymbol{p},\boldsymbol{q}}\right)\phi^s_{\boldsymbol{p}}(t)\phi_{\boldsymbol{q}}(t). \tag{2.128b}$$

The next step is now to rewrite the reducible memory kernels (2.120) in terms of the irreducible ones above. We note that

$$M^{bb}_{\boldsymbol{k}\boldsymbol{q}}(t) = -\delta_{\boldsymbol{k}\boldsymbol{q}}\frac{D}{S_k}\sum_{\alpha\beta}k^\alpha k^\beta m^{b\alpha,b\beta}(t), \tag{2.129a}$$

$$M^{ss}_{\boldsymbol{k}\boldsymbol{q}}(t) = -\delta_{\boldsymbol{k}\boldsymbol{q}}\sum_{\alpha\beta}(k^\alpha + \mathrm{i}(\boldsymbol{\partial}_{s,\alpha}V^{\mathrm{ext}}))k^\beta m^{s\alpha,s\beta}(t). \tag{2.129b}$$

Hence, it remains to solve the relation (2.122) for the reducible memory function. We use the Laplace transform (see Appendix B for details) on this equation to find

$$\tilde{m}^{\mu\alpha,\nu\beta}(s) = \tilde{m}^{\mu\alpha,\nu\beta}_{\mathrm{irr}}(s) - \sum_{\lambda,\gamma}\tilde{m}^{\mu\alpha,\lambda\gamma}_{\mathrm{irr}}(s)\tilde{m}^{\lambda\gamma,\nu\beta}(s), \tag{2.130}$$

where the tilde indicates the Laplace transform of the corresponding symbols. The thermodynamic limit decouples also in this case bath from probe memory kernels such that only memory kernels with $\mu = \nu$ appear. These equations can be interpreted as matrix equations with $(\tilde{\boldsymbol{m}}^\mu(s))_{\alpha,\beta} = \tilde{m}^{\mu\alpha,\mu\beta}(s)$ and correspondingly for the irreducible memory function and

solved formally via

$$(\tilde{\boldsymbol{m}}^{\mu}(s)) = (\mathbb{1} + \tilde{\boldsymbol{m}}^{\mu}_{\mathrm{irr}}(s))^{-1}(\tilde{\boldsymbol{m}}^{\mu}_{\mathrm{irr}}(s)) = \mathbb{1} - (\mathbb{1} + \tilde{\boldsymbol{m}}^{\mu}_{\mathrm{irr}}(s))^{-1}. \tag{2.131}$$

Assuming isotropy for the bath correlator dynamics[18], i.e. a dependence on $k := |\boldsymbol{k}|$ rather than $\boldsymbol{k}$, the following sum reduces to

$$\sum_{\alpha\beta} k^{\alpha}k^{\beta}\tilde{m}^{\mu\alpha,\mu\beta}(s) = \sum_{\alpha\beta} k^{\alpha}k^{\beta}(\delta_{\alpha\beta} - (\mathbb{1} - \tilde{\boldsymbol{m}}^{\mu}_{\mathrm{irr}}(s))_{\alpha\beta}) = k^2 \frac{\tilde{m}^{\mu}_{\mathrm{irr},k}(s)}{1 + \tilde{m}^{\mu}_{\mathrm{irr},k}(s)} \tag{2.132}$$

(cf. [Gru14, p. 26]), where $\tilde{m}^{\mu}_{\mathrm{irr},k}$ is the isotropic irreducible memory function (for example $\tilde{m}^{\mu z,\mu z}_{\mathrm{irr}}(s)$ for the choice $\boldsymbol{k} = k\hat{\boldsymbol{z}}$). Therefore,

$$\left(\tilde{\boldsymbol{M}}\right)^{bb}_{\boldsymbol{kq}}(s) = -\delta_{\boldsymbol{kq}} \frac{D}{S_k} k^2 \frac{\tilde{m}^{\mu}_{\mathrm{irr},k}(s)}{1 + \tilde{m}^{\mu}_{\mathrm{irr},k}(s)}. \tag{2.133}$$

For the probe memory this simplification is only possible in the quiescent case without external forces. In any other case we need the full inverse (2.131).

The results for the memory kernels cannot be plugged into our initial equations of motion (2.109) yet, because they need the memory kernels in time space. Instead, we apply the Laplace transform to these equations as well and obtain

$$s\tilde{\phi}^{\alpha\beta}_{\boldsymbol{kp}}(s) - 1 + \sum_{\boldsymbol{q},\gamma} (\boldsymbol{\Gamma})^{\alpha\gamma}_{\boldsymbol{kq}} \tilde{\phi}^{\gamma\beta}_{\boldsymbol{qp}}(s) + \sum_{\boldsymbol{q},\gamma} (\tilde{\boldsymbol{M}}(s))^{\alpha\gamma}_{\boldsymbol{kq}} \tilde{\phi}^{\gamma\beta}_{\boldsymbol{qp}}(s) = 0. \tag{2.134}$$

Combining all results we find

$$0 = s\tilde{\phi}_k(s) - 1 + \frac{Dk^2}{S_k}\tilde{\phi}_k(s) + \tilde{m}_k(s)(s\tilde{\phi}_k(s) - 1), \tag{2.135a}$$

$$m_k(t) = \sum_{\boldsymbol{p}+\boldsymbol{q}=\boldsymbol{k}} \frac{Dk^2}{S_k}\frac{n^2}{2N} S_p S_q \frac{1}{k^4} \left(\boldsymbol{k}\cdot(\boldsymbol{p}c_p + \boldsymbol{q}c_q) + k^2\rho c_3(k,p,q)\right)^2 \phi_p(t)\phi_q(t), \tag{2.135b}$$

where the Ornstein-Zernike relation (2.92) was used to express S_k in terms of the direct correlation function c_k (2.93). In the following, we will use the *convolution approximation* [Göt09, p. 182], [JF62], i.e. we will neglect three particle correlations $c_3 = 0$. This is the well known result for the bath correlation functions (see for example [GF13, Eq. (82)], [Göt09, p. 186, Eq. (4.11c,d)]).

For the probe correlation function we find

$$0 = (s\tilde{\phi}^{s}_{\boldsymbol{k}}(s) - 1) + \tilde{\phi}^{s}_{\boldsymbol{k}}(s)\sum_{\alpha\beta}(k^{\alpha} + \mathrm{i}\partial_{s,\alpha}V^{\mathrm{ext}})(\mathbb{1} + \tilde{\boldsymbol{m}}^{s}_{\boldsymbol{k}}(s))^{-1}_{\alpha\beta}k^{\beta}, \tag{2.136a}$$

$$(\boldsymbol{m}^{s}_{\boldsymbol{k}}(t))_{\alpha\beta} = m^{s\alpha,s\beta}_{\mathrm{irr}}(t) = \sum_{\boldsymbol{p}+\boldsymbol{q}=\boldsymbol{k}} \frac{(S^{s}_q)^2}{NS_q} q^{\alpha}q^{\beta}\phi^{s}_{\boldsymbol{p}}(t)\phi_{\boldsymbol{q}}(t) \tag{2.136b}$$

(see also [GAPF16, Eq. (52)]). This result has to be revisited if considering a sinusoidal force with frequency ω. In this case we obtain Laplace transforms of $\tilde{\phi}^{s}_{\boldsymbol{k}}$ and $\tilde{\boldsymbol{m}}^{s}_{\boldsymbol{k}}$ evaluated at $s \pm \mathrm{i}\omega$

[18] If isotropy applies for the reducible dynamics it should as well apply for irreducible dynamics.

in different combinations (see property (B.7) of the Laplace transform). One might hope that this does not alter the structure of the equations such that we could recover the sinusoidal force after doing the inverse Laplace transform at the end of the calculations. This is not the main interest of this thesis and may be addressed in future work.

Finally, we also have to apply the thermodynamic limit to the memory functions. The calculations above implicitly assumed that the N particles are contained in a volume V, which leads to the number particle density $n = N/V$. Letting $N \to \infty$ keeping n constant, we also have to increase V, which allows more wave vectors in the system. Götze shows in [Göt09, p. 102] that in this case the sum over wave vectors

$$\frac{1}{V}\sum_{\boldsymbol{k}} = \frac{1}{(2\pi)^3}\int \mathrm{d}\boldsymbol{k} \tag{2.137}$$

can be replaced by an integral and Kronecker deltas

$$V\delta_{\boldsymbol{kp}} = (2\pi)^3\delta(\boldsymbol{k}-\boldsymbol{p}) \tag{2.138}$$

transform into Dirac δ-distributions. This yields in the thermodynamic limit

$$m_k(t) = \frac{1}{16\pi^3}\frac{D}{S_k k^2}\int \mathrm{d}\boldsymbol{q}\, nS_{|\boldsymbol{k}-\boldsymbol{q}|}S_q\left(\boldsymbol{k}\cdot((\boldsymbol{k}-\boldsymbol{q})c_{|\boldsymbol{k}-\boldsymbol{q}|}+\boldsymbol{q}c_q)\right)^2\phi_{|\boldsymbol{k}-\boldsymbol{q}|}(t)\phi_q(t), \tag{2.139a}$$

$$m_{\boldsymbol{k}}^{\alpha\beta}(t) := (\boldsymbol{m}_{\boldsymbol{k}}^s(t))_{\alpha\beta} = \frac{1}{(2\pi)^3}\int \mathrm{d}\boldsymbol{p}\,\frac{(S^s_{|\boldsymbol{k}-\boldsymbol{p}|})^2}{NS_{|\boldsymbol{k}-\boldsymbol{p}|}}(k^\alpha-p^\alpha)(k^\beta-p^\beta)\phi^s_{\boldsymbol{p}}(t)\phi_{|\boldsymbol{k}-\boldsymbol{p}|}(t). \tag{2.139b}$$

The memory kernels $m_{\boldsymbol{k}}^{\alpha\beta}$ will be called *primitive memory kernels*, because the full memory kernel is a combination of these primitive memory kernels.

2.4.4. Cylindrical symmetry

In this section we want to simplify the expression for the memory kernel using the cylindrical symmetry of the problem. For the ease of notation, we assume that the symmetry axis of the system is aligned with the $\hat{\boldsymbol{z}}$-axis. Cylindrical symmetry can then be expressed as follows. Let $\mathcal{R}$ be a rotation matrix around the $\hat{\boldsymbol{z}}$ axis, i.e.

$$\mathcal{R}\mathcal{R}^T = \mathbb{1} = \mathcal{R}^T\mathcal{R} \quad \text{and} \quad \mathcal{R}\hat{\boldsymbol{z}} = \hat{\boldsymbol{z}}. \tag{2.140}$$

Then, a scalar quantity $f(\boldsymbol{k})$ has cylindrical symmetry if and only if

$$f(\mathcal{R}\boldsymbol{k}) = f(\boldsymbol{k}) \tag{2.141}$$

holds for all $\mathcal{R}$ fulfilling (2.140) and all arguments $\boldsymbol{k} \in \mathbb{R}^3$.

Using the equations of motion (2.136) for the probe correlation function, we find that to show cylindrical symmetry for the probe correlator is equivalent (cf. [Gru14, Sec. 4.1.2, p. 34], Section C.2.1) to showing that

$$\tilde{\boldsymbol{m}}^s_{\mathcal{R}\boldsymbol{k}}(s) = \mathcal{R}\tilde{\boldsymbol{m}}^s_{\boldsymbol{k}}(s)\mathcal{R}^T. \tag{2.142a}$$

This relation in turn is equivalent to showing the same relation for the time dependent memory functions, because the rotation matrix does not depend on time.

To do so, we start with the very definition of $\boldsymbol{m}_{\boldsymbol{k}}^{s}(t)$ in (2.121b). It is given by

$$\begin{aligned}(\boldsymbol{m}_{\boldsymbol{k}}^{s}(t))_{\alpha\beta} &= \left\langle \mathcal{Q}(\partial_{s,\alpha}V)\mathrm{e}^{\mathrm{i}\boldsymbol{k}\boldsymbol{r}_s}, \mathrm{e}^{\Omega_{\mathrm{irr}}^{\dagger}t}\mathcal{Q}(\partial_{s,\beta}V)\mathrm{e}^{\mathrm{i}\boldsymbol{k}\boldsymbol{r}_s}\right\rangle \\ &= \int \mathrm{d}\boldsymbol{r}_s \int \mathrm{d}\Gamma\, \Psi_{\mathrm{eq}}(\boldsymbol{r}_s,\Gamma)\mathrm{e}^{\mathrm{i}\boldsymbol{k}\boldsymbol{r}_s}(\partial_{s,\alpha}V(\boldsymbol{r}_s,\Gamma))\mathcal{Q}\mathrm{e}^{\Omega_{\mathrm{irr}}^{\dagger}(\boldsymbol{r}_s,\Gamma)t}\mathcal{Q}(\partial_{s,\beta}V(\boldsymbol{r}_s,\Gamma))\mathrm{e}^{\mathrm{i}\boldsymbol{k}\boldsymbol{r}_s}.\end{aligned} \tag{2.143}$$

Γ represents the coordinates of all bath particles $\Gamma := (\boldsymbol{r}_1,\dots,\boldsymbol{r}_N)$. Evaluating this memory function at $\boldsymbol{k}' = \mathcal{R}\boldsymbol{k}$, we find $\mathcal{R}\boldsymbol{k}\cdot\boldsymbol{r}_s$ in the exponents with the rest of the expression remaining the same. Since $\mathcal{R}\boldsymbol{k}\cdot\boldsymbol{r}_s = \boldsymbol{k}\cdot\mathcal{R}^T\boldsymbol{r}_s$, the idea is to do a substitution $\boldsymbol{r}_s' := \mathcal{R}^T\boldsymbol{r}_s$ and $\Gamma' := \mathcal{R}^T\Gamma := (\mathcal{R}^T\boldsymbol{r}_1,\dots,\mathcal{R}^T\boldsymbol{r}_N)$ to recover the memory function $\boldsymbol{m}_{\boldsymbol{k}}^{s}(t)$. Therefore, we need to discuss how the different objects in this integral will transform under this substitution.

We have

$$\mathcal{Q} = \mathbb{1} - \sum_{\boldsymbol{p}} \mathrm{e}^{\mathrm{i}\boldsymbol{k}\cdot\mathcal{R}\boldsymbol{r}_s}\left\langle \mathrm{e}^{\mathrm{i}\boldsymbol{k}\mathcal{R}\boldsymbol{r}_s}, \cdot\right\rangle = \mathbb{1} - \sum_{\boldsymbol{k}} \mathrm{e}^{\mathrm{i}\mathcal{R}^T\boldsymbol{k}\cdot\boldsymbol{r}_s}\left\langle \mathrm{e}^{\mathrm{i}\mathcal{R}^T\boldsymbol{k}\cdot\boldsymbol{r}_s}, \cdot\right\rangle = \mathcal{Q}, \tag{2.144a}$$

since we sum over all $\boldsymbol{p}$ (for every $\mathcal{R}^T\boldsymbol{k}$ there is also $\boldsymbol{k}$ in the sum). Furthermore, we already applied the thermodynamic limit as before (which removes the projections on the bath density correlators).

The chain rule for differentiation implies

$$\boldsymbol{\partial}_i = \mathcal{R}\boldsymbol{\partial}_i' \qquad \text{and} \qquad (\boldsymbol{\partial}_i\cdot\boldsymbol{\partial}_i) = (\mathcal{R}\boldsymbol{\partial}_i')\cdot(\mathcal{R}\boldsymbol{\partial}_i') = (\boldsymbol{\partial}_i')\cdot(\boldsymbol{\partial}_i'), \tag{2.144b}$$

since $\mathcal{R}$ is an isometry. Similarly, we obtain

$$(\boldsymbol{\partial}_i V(\boldsymbol{r}_s,\Gamma))\cdot\boldsymbol{\partial}_i = (\boldsymbol{\partial}_i' V(\mathcal{R}\boldsymbol{r}_s',\mathcal{R}\Gamma'))\cdot\boldsymbol{\partial}_i' \tag{2.144c}$$

for $i\in\{s,1,\dots,N\}$ and for a single component

$$\partial_{i,\alpha}V(\boldsymbol{r}_s,\Gamma) = \sum_{\gamma} Q^{\alpha\gamma}\partial_{i,\gamma}V(\mathcal{R}\boldsymbol{r}_s',\mathcal{R}\Gamma'). \tag{2.144d}$$

Since we required the external potential to have cylindrical symmetry, we have

$$\mathcal{R}(\boldsymbol{\partial}_s V^{\mathrm{ext}}(\boldsymbol{r}_s,\Gamma)) = \boldsymbol{\partial}_s V^{\mathrm{ext}}(\mathcal{R}\boldsymbol{r}_s',\mathcal{R}\Gamma') \tag{2.144e}$$

and therefore (collecting all previous results)

$$\Omega^{\dagger}(\boldsymbol{r}_s,\Gamma) = \Omega^{\dagger}(\mathcal{R}\boldsymbol{r}_s',\mathcal{R}\Gamma'). \tag{2.144f}$$

An explicit calculation (see Appendix C.2.1) shows that this invariance translates also to the irreducible operator

$$\Omega_{\mathrm{irr}}^{\dagger}(\boldsymbol{r}_s,\Gamma) = \Omega_{\mathrm{irr}}^{\dagger}(\mathcal{R}\boldsymbol{r}_s',\mathcal{R}\Gamma'), \tag{2.144g}$$

and via the series representation of the exponential to

$$\exp(\Omega^\dagger_{\mathrm{irr}}(\boldsymbol{r}_s,\Gamma)t) = \exp(\Omega^\dagger_{\mathrm{irr}}(\mathcal{R}\boldsymbol{r}'_s,\mathcal{R}\Gamma')t). \tag{2.144h}$$

As $\mathcal{R}$ is unitary, we have $|\det\mathcal{R}| = 1$ so that we obtain after the substitution

$$\begin{aligned}(\boldsymbol{m}^s_{\mathcal{R}\boldsymbol{k}}(t))_{\alpha\beta} = \int \mathrm{d}\boldsymbol{r}'_s \int \mathrm{d}\Gamma\, \Psi_{\mathrm{eq}}(\mathcal{R}\boldsymbol{r}'_s,\mathcal{R}\Gamma')\mathrm{e}^{\mathrm{i}\boldsymbol{k}\boldsymbol{r}'_s}\sum_\gamma \mathcal{R}^{\alpha\gamma}(\partial'_{s,\gamma}V(\mathcal{R}\boldsymbol{r}'_s,\mathcal{R}\Gamma'))\cdot \\ \cdot\mathcal{Q}\mathrm{e}^{\Omega^\dagger_{\mathrm{irr}}(\mathcal{R}\boldsymbol{r}'_s,\mathcal{R}\Gamma')t}\mathcal{Q}\sum_\delta \mathcal{R}^{\beta\delta}(\partial'_{s,\delta}V(\mathcal{R}\boldsymbol{r}'_s,\mathcal{R}\Gamma'))\mathrm{e}^{\mathrm{i}\boldsymbol{k}\boldsymbol{r}'_s}.\end{aligned} \tag{2.145}$$

In the case of isotropic interactions, i.e. the potential V depends only on $|\boldsymbol{r}_i - \boldsymbol{r}_j| = |\mathcal{R}\boldsymbol{r}_i - \mathcal{R}\boldsymbol{r}_j|$, we may replace the remaining $\mathcal{R}\boldsymbol{r}'_s \to \boldsymbol{r}'_s$ and $\mathcal{R}\gamma \to \Gamma$. Then we can identify the memory kernel elements $(\boldsymbol{m}^s_{\boldsymbol{k}}(t))_{\gamma\delta}$ to find

$$(\boldsymbol{m}^s_{\mathcal{R}\boldsymbol{k}}(t))_{\alpha\beta} = \sum_{\gamma\delta}\mathcal{R}^{\alpha\gamma}(\boldsymbol{m}^s_{\boldsymbol{k}}(t))_{\gamma\delta}\mathcal{R}^{\beta\delta} = (\mathcal{R}\boldsymbol{m}^s_{\boldsymbol{k}}(t)\mathcal{R}^T)_{\alpha\beta}. \tag{2.146}$$

This was the relation to prove. Therefore,

$$\phi^s_{\mathcal{R}\boldsymbol{k}}(t) = \phi^s_{\boldsymbol{k}}(t) \tag{2.147}$$

and without loss of generality, we can therefore choose $\boldsymbol{k}^* = (k_x, 0, k_z)$. The correlation function for any other $\boldsymbol{k}$ is then given by $\phi^s_{\boldsymbol{k}^*}$ evaluated at $\boldsymbol{k}^* = (\sqrt{(k'_x)^2 + (k'_y)^2}, 0, k_z)$.

This special choice of $\boldsymbol{k}^*$ allows us to simplify the inversion of the memory matrix. First, we will show that $(\boldsymbol{m}^s_{\boldsymbol{k}^*}(t))_{y\alpha} = 0$ for $\alpha \in \{x, z\}$. Consider the transformation $y_i \mapsto -y_i$ (for $i \in \{s, 1, \ldots, N\}$. Then

$$\mathrm{e}^{\mathrm{i}\boldsymbol{k}^*\boldsymbol{r}_s} \mapsto \mathrm{e}^{\mathrm{i}\boldsymbol{k}^*\boldsymbol{r}_s}, \tag{2.148a}$$

because $\boldsymbol{k}^*\boldsymbol{r}_s = k_x x_s + k_z z_s$ does not depend on y_s. For the derivatives we find

$$\partial_{s,y} \mapsto -\partial_{s,y}, \qquad \partial_{s,x/z} \mapsto \partial_{s,x/z} \tag{2.148b}$$

and the forces transform similarly

$$\partial_{s,y}V \mapsto -\partial_{s,y}V, \qquad \partial_{s,x/z}V \mapsto \partial_{s,x/z}V. \tag{2.148c}$$

Note that using the simultaneous substitution $y_i \mapsto -y_i$, the potential remains the same due to $|y_i - y_j| = |-y_i - (-y_j)|$. This allows us to have the same arguments before and after the substitution. As above we obtain

$$\mathcal{Q} \mapsto \mathcal{Q}, \tag{2.148d}$$

because for every $\boldsymbol{p}$ in the sum there is also $-\boldsymbol{p}$ in the sum. Combining all these results, there is

$$\Omega^\dagger \mapsto \Omega^\dagger, \qquad \Omega^\dagger_{\mathrm{irr}} \mapsto \Omega^\dagger_{\mathrm{irr}}, \tag{2.148e}$$

which also translates to the exponentials of these operators (via series expansion). The equilibrium probability density Ψ_{eq} is isotropic and therefore also invariant under this substitution.

Hence, we find

$$\begin{aligned}&\Psi_{\mathrm{eq}}(\boldsymbol{r}_s,\Gamma)\mathrm{e}^{\mathrm{i}\boldsymbol{k}^*\boldsymbol{r}_s}(\partial_{s,y}V(\boldsymbol{r}_s,\Gamma))\mathcal{Q}\mathrm{e}^{\Omega^\dagger_{\mathrm{irr}}(\boldsymbol{r}_s,\Gamma)t}\mathcal{Q}(\partial_{s,\alpha}V(\boldsymbol{r}_s,\Gamma))\mathrm{e}^{\mathrm{i}\boldsymbol{k}^*\boldsymbol{r}_s}\\ \mapsto&-\Psi_{\mathrm{eq}}(\boldsymbol{r}_s,\Gamma)\mathrm{e}^{\mathrm{i}\boldsymbol{k}^*\boldsymbol{r}_s}(\partial_{s,y}V(\boldsymbol{r}_s,\Gamma))\mathcal{Q}\mathrm{e}^{\Omega^\dagger_{\mathrm{irr}}(\boldsymbol{r}_s,\Gamma)t}\mathcal{Q}(\partial_{s,\alpha}V(\boldsymbol{r}_s,\Gamma))\mathrm{e}^{\mathrm{i}\boldsymbol{k}^*\boldsymbol{r}_s}.\end{aligned} \tag{2.148f}$$

This implies

$$(\boldsymbol{m}^s_{\boldsymbol{k}^*}(t))_{y\alpha}=-(\boldsymbol{m}^s_{\boldsymbol{k}^*}(t))_{y\alpha} \tag{2.149}$$

and therefore $(\boldsymbol{m}^s_{\boldsymbol{k}^*}(t))_{y\alpha}=0$ for $\alpha\in\{x,z\}$.

Consequently, the memory matrix has the following structure

$$\boldsymbol{m}^s_{\boldsymbol{k}^*}(t)=\begin{pmatrix}m^{xx}_{\boldsymbol{k}^*}(t) & 0 & m^{xz}_{\boldsymbol{k}^*}(t)\\ 0 & m^{yy}_{\boldsymbol{k}^*}(t) & 0\\ m^{xz}_{\boldsymbol{k}^*}(t) & 0 & m^{zz}_{\boldsymbol{k}^*}(t)\end{pmatrix} \tag{2.150}$$

with the matrix elements $m^{\alpha\beta}_{\boldsymbol{k}^*}$ as defined by (2.139b). The inverse of $(\mathbb{1}+\tilde{\boldsymbol{m}}^s_{\boldsymbol{k}^*}(s))$ has the same structure of zero- and nonzero entries and we obtain

$$\begin{aligned}&\sum_{\alpha\beta}(k^*_\alpha-\mathrm{i}F_{\mathrm{ex}})(\mathbb{1}+\tilde{\boldsymbol{m}}_{\boldsymbol{k}^*}(s))^{-1}_{\alpha\beta}k^*_\beta\\ =&\frac{(k^*_x)^2\left(\tilde{m}^{zz}_{\boldsymbol{k}^*}(s)+1\right)+k^*_z(k^*_z-\mathrm{i}F_{\mathrm{ex}})\left(\tilde{m}^{xx}_{\boldsymbol{k}^*}(s)+1\right)-(2k^*_xk^*_z-\mathrm{i}k^*_xF_{\mathrm{ex}})\tilde{m}^{xz}_{\boldsymbol{k}^*}(s)}{\left(\tilde{m}^{xx}_{\boldsymbol{k}^*}(s)+1\right)\left(\tilde{m}^{zz}_{\boldsymbol{k}^*}(s)+1\right)-\left(\tilde{m}^{xz}_{\boldsymbol{k}^*}(s)\right)^2}.\end{aligned} \tag{2.151}$$

A more direct calculation of these symmetry properties based on the particular form of the memory functions can be found in [Gru14, Sec. 3.6, p. 23-26 and Sec. 4.1 and 4.2, p. 29-36].

2.4.5. MCT equations

To summarize, we have to solve the following equations for the bath correlation function (see Eq. (2.135a) and (2.139a))

$$0=s\tilde{\phi}_k(s)-1+\frac{Dk^2}{S_k}\tilde{\phi}_k(s)+\tilde{m}_k(s)(s\tilde{\phi}_k(s)-1), \tag{2.152a}$$

$$m_k(t)=\frac{1}{16\pi^3}\frac{D}{S_kk^2}\int\mathrm{d}\boldsymbol{q}\,nS_{|\boldsymbol{k}-\boldsymbol{q}|}S_q\left(\boldsymbol{k}\cdot((\boldsymbol{k}-\boldsymbol{q})c_{|\boldsymbol{k}-\boldsymbol{q}|}+\boldsymbol{q}c_q)\right)^2\phi_{|\boldsymbol{k}-\boldsymbol{q}|}(t)\phi_q(t) \tag{2.152b}$$

This equation of motion translates to an integro-differential equation

$$\partial_t\phi_k(t)+\frac{Dk^2}{S_k}\phi_k(t)+\int_0^t\mathrm{d}t'\,m_k(t-t')\partial_{t'}\phi_k(t')=0 \tag{2.153}$$

in the time domain with initial condition $\phi_k(t=0)=1$. This can be considered an integral equation (in $\partial_t\phi_{\boldsymbol{k}}$) of the Volterra type of the second kind [VW59, p. 42, Eq. (3')]. The input parameters are the dimensionless diffusion coefficient D and the static structure factor S_k or equivalently, the direct correlation function c_k. In the thermodynamic limit there is no coupling of the probe dynamics to the bath so that the solution of this equation can be reused for any

other calculation of the probe dynamics at the same packing fraction.

For the probe correlation function we obtain (see Eq. (2.136a), (2.139b), (2.151))

$$0 = (s\tilde{\phi}^s_{\boldsymbol{k}^*}(s) - 1) + \tilde{\phi}^s_{\boldsymbol{k}^*}(s)\tilde{\mathcal{M}}_{\boldsymbol{k}^*}(s), \tag{2.154a}$$

$$\tilde{\mathcal{M}}_{\boldsymbol{k}^*}(s) = \frac{\Gamma^x_{\boldsymbol{k}^*}\left(\tilde{m}^{zz}_{\boldsymbol{k}^*}(s)+1\right) + \Gamma^z_{\boldsymbol{k}^*}\left(\tilde{m}^{xx}_{\boldsymbol{k}^*}(s)+1\right) - \Gamma^{xz}_{\boldsymbol{k}^*}\tilde{m}^{xz}_{\boldsymbol{k}^*}(s)}{\left(\tilde{m}^{xx}_{\boldsymbol{k}^*}(s)+1\right)\left(\tilde{m}^{zz}_{\boldsymbol{k}^*}(s)+1\right) - \left(\tilde{m}^{xz}_{\boldsymbol{k}^*}(s)\right)^2}, \tag{2.154b}$$

$$m^{\alpha\beta}_{\boldsymbol{k}}(t) = \frac{1}{(2\pi)^3}\int \mathrm{d}\boldsymbol{q}\, \frac{\left(S^s_{|\boldsymbol{k}-\boldsymbol{q}|}\right)^2}{NS_{|\boldsymbol{k}-\boldsymbol{q}|}}(k^\alpha - q^\alpha)(k^\beta - q^\beta)\phi_{|\boldsymbol{k}-\boldsymbol{q}|}(t)\phi^s_{\boldsymbol{q}}(t) \tag{2.154c}$$

with the definitions

$$\Gamma^x_{\boldsymbol{k}^*} = (k^*_x)^2, \tag{2.155a}$$

$$\Gamma^z_{\boldsymbol{k}^*} = k^*_z(k^*_z - \mathrm{i}F_{\mathrm{ex}}), \tag{2.155b}$$

$$\Gamma^{xz}_{\boldsymbol{k}^*} = k^*_x(2k^*_z - \mathrm{i}F_{\mathrm{ex}}). \tag{2.155c}$$

and the initial condition $\phi^s_{\boldsymbol{k}}(t=0) = 1$. A direct transformation into the time domain leads to double convolutions because of the triple-products

$$0 = \partial_t\phi^s_{\boldsymbol{k}^*}(t) + \Gamma_{\boldsymbol{k}^*} + \int_0^t M^{(1)}_{\boldsymbol{k}^*}(t-t')\partial_{t'}\phi^s_{\boldsymbol{k}^*}(t')\mathrm{d}t' + \int_0^t M^{(2)}_{\boldsymbol{k}^*}(t-t')\phi^s_{\boldsymbol{k}^*}(t')\mathrm{d}t', \tag{2.156a}$$

with the definitions

$$\Gamma_{\boldsymbol{k}^*} = \Gamma^x_{\boldsymbol{k}^*} + \Gamma^z_{\boldsymbol{k}^*} = (k^*_x)^2 + (k^*_z)^2 - \mathrm{i}k^*_z F_{\mathrm{ex}}, \tag{2.156b}$$

$$M^{(1)}_{\boldsymbol{k}^*}(t) = m^{xx}_{\boldsymbol{k}^*}(t) + m^{zz}_{\boldsymbol{k}^*}(t-t') + \int_0^t \left(m^{xx}_{\boldsymbol{k}^*}(t-t')m^{zz}_{\boldsymbol{k}^*}(t') + m^{xz}_{\boldsymbol{k}^*}(t-t')m^{xz}_{\boldsymbol{k}^*}(t')\right)\mathrm{d}t', \tag{2.156c}$$

$$M^{(2)}_{\boldsymbol{k}^*}(t) = \Gamma^x_{\boldsymbol{k}^*}m^{zz}_{\boldsymbol{k}^*}(t) + \Gamma^z_{\boldsymbol{k}^*}m^{xx}_{\boldsymbol{k}^*}(t) - \Gamma^{xz}_{\boldsymbol{k}^*}m^{xz}_{\boldsymbol{k}^*}(t). \tag{2.156d}$$

Since most numerical schemes for these equations are derived for single convolution integrals, we will try to reformulate them in terms of single convolutions (see Chapter 3) by introducing an effective memory kernel via

$$\tilde{m}^{\mathrm{eff}}_{\boldsymbol{k}}(s) = \frac{\Gamma_{\boldsymbol{k}^*}}{\tilde{\mathcal{M}}_{\boldsymbol{k}^*}(s)} - 1 \quad \text{or equivalently} \quad \frac{\Gamma_{\boldsymbol{k}^*}}{1 + \tilde{m}^{\mathrm{eff}}_{\boldsymbol{k}^*}(s)} = \tilde{\mathcal{M}}_{\boldsymbol{k}^*}(s), \tag{2.157}$$

which transforms the equation of motion for the correlator to

$$0 = \left(s\tilde{\phi}^s_{\boldsymbol{k}^*}(s) - 1\right) + \Gamma_{\boldsymbol{k}^*}\tilde{\phi}^s_{\boldsymbol{k}^*}(s) + \left(s\tilde{\phi}^s_{\boldsymbol{k}^*}(s) - 1\right)\tilde{m}^{\mathrm{eff}}_{\boldsymbol{k}^*}(s). \tag{2.158}$$

This equation has the same form as the equation of motion for the bath correlator (2.152a). Of course, all the complications are now shifted to the determination of the effective memory kernel (2.157), but we can still apply the numerical methods which were developed to solve equations of the form (2.152) (as e.g. in [FGHL91, Sec. 3.4, p. 5060ff], see Chapter 3).

In time space, we obtain the following equations of motion for the correlation function and

the effective memory kernel

$$0 = \partial_t \phi^s_{\boldsymbol{k}^*}(t) + \Gamma_{\boldsymbol{k}^*} \phi^s_{\boldsymbol{k}^*}(t) + \int_0^t m^{\text{eff}}_{\boldsymbol{k}^*}(t-t') \partial_{t'} \phi^s_{\boldsymbol{k}^*}(t') \mathrm{d}t' \,, \tag{2.159a}$$

$$M^{(3)}_{\boldsymbol{k}^*}(t) = m^{\text{eff}}_{\boldsymbol{k}^*}(t) + \int_0^t \frac{1}{\Gamma_{\boldsymbol{k}^*}} M^{(2)}_{\boldsymbol{k}^*}(t-t') m^{\text{eff}}_{\boldsymbol{k}^*}(t') \mathrm{d}t' \,, \tag{2.159b}$$

$$\begin{aligned} M^{(3)}_{\boldsymbol{k}^*}(t) = {} & \frac{1}{\Gamma_{\boldsymbol{k}^*}} \left(\Gamma^x_{\boldsymbol{k}^*} m^{xx}_{\boldsymbol{k}^*}(t) + \Gamma^z_{\boldsymbol{k}^*} m^{zz}_{\boldsymbol{k}^*}(t) + \Gamma^{xz}_{\boldsymbol{k}^*} m^{xz}_{\boldsymbol{k}^*}(t) \right) \\ & + \int_0^t \left(m^{xx}_{\boldsymbol{k}^*}(t-t') m^{zz}_{\boldsymbol{k}^*}(t') - m^{xz}_{\boldsymbol{k}^*}(t-t') m^{xz}_{\boldsymbol{k}^*}(t') \right) \mathrm{d}t' \,. \end{aligned} \tag{2.159c}$$

This is an integral equation of the Volterra type of the second kind.

The primitive memory kernels (2.154c) are linear functionals in the bath correlation function $\boldsymbol{\phi}(t)$ and the probe correlation function $\boldsymbol{\phi}^s(t)$ (with respect to the wave vector dependency), which can be expressed formally as

$$m^{\alpha\beta}_{\boldsymbol{k}}[\boldsymbol{\phi}(t), \boldsymbol{\phi}^s(t)] = \frac{1}{(2\pi)^3} \int \mathrm{d}\boldsymbol{q}\, p_\alpha p_\beta \frac{(S^s_p)^2}{n S_p} \phi_p(t) \phi^s_{\boldsymbol{q}}(t) \tag{2.160}$$

with the abbreviation $\boldsymbol{p} = \boldsymbol{k} - \boldsymbol{q}$. The bold symbols include all wave vectors. Since $\phi_p(t)$ (and S_p, S^s_p) only enter as input, we introduce the helper function

$$g(p,t) = \frac{1}{(2\pi)^3} \frac{(S^s_p)^2}{n S_p} \phi_p(t) \tag{2.161}$$

to facilitate the discussion of the properties of the memory functionals.

Note that this complicated equation of motion reduces to the well known result for tagged particles dynamics [Göt09, p. 323, Eq. (5.25) and (5.27)] in the case of a vanishing external force [Gru14, Sec. 3.6, p. 23-26].

Since we will often discuss features of correlation functions parallel or perpendicular to the external force, we introduce the following shorthands:

$$\phi^{s\parallel}_q(t) := \phi^s_{(0,0,q)}(t), \tag{2.162a}$$

$$\phi^{s\perp}_q(t) := \phi^s_{(q,0,0)}(t). \tag{2.162b}$$

In the same spirit we introduce the parallel and perpendicular marginal van Hove functions (see (2.85))

$$G^{s\parallel}(z,t) := \int \mathrm{d}x\, \mathrm{d}y\, G^s(\boldsymbol{r},t) = \frac{1}{2\pi} \int \mathrm{d}q\, e^{-iqz} \phi^{s\parallel}_q(t), \tag{2.163a}$$

$$G^{s\perp}(x,t) := \int \mathrm{d}y\, \mathrm{d}z\, G^s(\boldsymbol{r},t) = \frac{1}{2\pi} \int \mathrm{d}q\, e^{-iqx} \phi^{s\perp}_q(t). \tag{2.163b}$$

For the last equalities see Appendix A.3. For the perpendicular marginal van Hove function,

one could also define a radial van Hove function for the variable $r = \sqrt{x^2 + y^2} \in [0, \infty)$. However, one does not gain any further insight from that, because the moments can be directly transformed into each other (see Appendix A.4). Calculating the moments is easier for $G^{s\perp}(x,t)$ as defined above, because we can directly apply a one dimensional fast Fourier transform, while the other definition requires the evaluation of the full twodimensional Fourier transform and the integration along z.

Congratulations! You have passed the toughest theory part in this thesis. With this section we conclude the derivation of the mode-coupling equations. In the following sections, we will use these equations to derive equations for the long-time limits, transport coefficients and moments.

The equations of motion above and consequently the derived results in the next sections are based on the assumption that the force is constant in space and time. The case of a line trap leads to complications already in the calculation of the projections as we cannot use orthogonality anymore. A force varying sinusoidally in time leads to a coupling of different (and complex valued) Laplace frequencies and is therefore not pursued further. Both cases require a more detailed analysis of the derivation and are therefore beyond the scope of this work. Another route for possible improvements could be a change of the reference frame co-moving with the mean displacement as we will find numerical problems for large displacements. This might be achieved by deriving equations of motion for

$$\phi^{s'}_{\boldsymbol{k}}(t) = \mathrm{e}^{-\mathrm{i}\langle z\rangle(t)k_z}\phi^s_{\boldsymbol{k}}(t), \tag{2.164}$$

where $\langle z\rangle(t)$ could be determined self-consistently through $\langle z\rangle(t) = -\mathrm{i}\partial_z\, \phi^s_{\boldsymbol{k}}(t)|_{\boldsymbol{k}=0}$ (see Section 2.4.9).

2.4.6. Long time limit

In ideal glasses, the dynamics is slowed down so much that the correlation functions decay to a nonzero plateau value. Hence the long-time limit of these correlation functions is nontrivial and often called *nonergodicity parameter*. In our case, it can be obtained without solving the full dynamics using the limit theorem of the Laplace transform (B.3)

$$f_{\boldsymbol{k}} := \lim_{t\to\infty}\phi_{\boldsymbol{k}}(t) = \lim_{s\to 0} s\phi_{\boldsymbol{k}}(s), \tag{2.165a}$$

$$f^s_{\boldsymbol{k}} := \lim_{t\to\infty}\phi^s_{\boldsymbol{k}}(t) = \lim_{s\to 0} s\phi^s_{\boldsymbol{k}}(s). \tag{2.165b}$$

The primitive memory functionals (2.160) then convert into linear functionals of the nonergodicity parameters via

$$\mu^{\alpha\beta}_{\boldsymbol{k}} := \lim_{t\to\infty} m^{\alpha\beta}_{\boldsymbol{k}}(t) = \frac{1}{(2\pi)^3}\int \mathrm{d}\boldsymbol{q}\, p_\alpha p_\beta \frac{(S^s_p)^2}{nS_p} f^s_{\boldsymbol{q}} f_p = m^{\alpha\beta}_{\boldsymbol{k}}[\boldsymbol{f}, \boldsymbol{f}^s] \tag{2.166}$$

(with $\boldsymbol{p} = \boldsymbol{k} - \boldsymbol{q}$) and the equation of motion (2.154) leads in the limit $s \to 0$ to

$$f^s_{\boldsymbol{k}^*} = \left(1 + \frac{\Gamma^x_{\boldsymbol{k}^*}\mu^{zz}_{\boldsymbol{k}^*} + \Gamma^z_{\boldsymbol{k}^*}\mu^{xx}_{\boldsymbol{k}^*} - \Gamma^{xz}_{\boldsymbol{k}^*}\mu^{xz}_{\boldsymbol{k}^*}}{\mu^{xx}_{\boldsymbol{k}^*}\mu^{zz}_{\boldsymbol{k}^*} - (\mu^{xz}_{\boldsymbol{k}^*})^2}\right)^{-1}. \tag{2.167}$$

This is an implicit (because the primitive memory kernels depend on $\boldsymbol{f}^s$) nonlinear integral equation for $\boldsymbol{f}^s$, which can be solved by a fixed point iteration as discussed in Section 3.3. The prefactors $\Gamma^\alpha_{\boldsymbol{k}^*}$ are given in (2.155).

2.4.7. Constant bath approximation

Even though the equation of motion (2.154a) is formulated in Laplace space, it is not possible to solve it directly in Laplace space. The problem is that the memory kernel depends on the product of two time dependent correlation functions. The Laplace transform of such a product cannot be expressed in terms of the Laplace transforms of the factors. In order to get some insights about the long time behavior, we can approximate the bath correlation function by its long time limit

$$\phi_k(t) \approx f_k. \tag{2.168}$$

This approximation ignores the short time behavior introduced by the bath but remains useful on timescales when the bath correlation function has relaxed to its long time limit. Of course, this approximation is only useful in the glass, when a nontrivial long time limit $\boldsymbol{f} \neq 0$ exists. Then, we can interchange the Laplace transform and the memory kernel integration and obtain

$$\tilde{m}^{\alpha\beta}_{\boldsymbol{k}}(s) \approx m^{\alpha\beta}_{\boldsymbol{k}}\left[\boldsymbol{f}, \tilde{\boldsymbol{\phi}}^s(s)\right]. \tag{2.169}$$

Together with the equation of motion (2.154) we obtain the following nonlinear implicit equation for the probe correlation function in Laplace space $\tilde{\phi}^s_{\boldsymbol{k}^*}(s)$

$$\tilde{\phi}^s_{\boldsymbol{k}^*}(s) = \left(s + \frac{\Gamma^x_{\boldsymbol{k}^*}\left(\tilde{m}^{zz}_{\boldsymbol{k}^*}\left[\tilde{\boldsymbol{\phi}}^s(s)\right]+1\right) + \Gamma^z_{\boldsymbol{k}^*}\left(\tilde{m}^{xx}_{\boldsymbol{k}^*}\left[\tilde{\boldsymbol{\phi}}^s(s)\right]+1\right) - \Gamma^{xz}_{\boldsymbol{k}^*}\tilde{m}^{xz}_{\boldsymbol{k}^*}\left[\tilde{\boldsymbol{\phi}}^s(s)\right]}{\left(\tilde{m}^{xx}_{\boldsymbol{k}^*}\left[\tilde{\boldsymbol{\phi}}^s(s)\right]+1\right)\left(\tilde{m}^{zz}_{\boldsymbol{k}^*}\left[\tilde{\boldsymbol{\phi}}^s(s)\right]+1\right) - \left(\tilde{m}^{xz}_{\boldsymbol{k}^*}\left[\tilde{\boldsymbol{\phi}}^s(s)\right]\right)^2} \right)^{-1}, \tag{2.170}$$

where we omitted the argument $\boldsymbol{f}$ of the memory functionals for brevity. After multiplication by s this equation reduces to (2.167) in the limit $s \to 0$. Furthermore, this equation has the virtue that it can be solved for any s independently. Therefore, s is just a parameter and we can apply basically the same solution scheme as for the long time limit (see Sec. 3.4).

2.4.8. Transport coefficients

The counterpart to the nonergodicity parameters in the delocalized state are the transport coefficients defined via

$$D_{\boldsymbol{k}} := \int_0^\infty \phi_{\boldsymbol{k}}(t')\mathrm{d}t' = \lim_{s\to 0}\phi_{\boldsymbol{k}}(s), \tag{2.171a}$$

$$D^s_{\boldsymbol{k}} := \int_0^\infty \phi^s_{\boldsymbol{k}}(t')\mathrm{d}t' = \lim_{s\to 0}\phi^s_{\boldsymbol{k}}(s), \tag{2.171b}$$

using the property (B.6) of the Laplace transform for the integral. In the constant bath approximation from the previous section, we can again provide an implicit equation for them

$$D^s_{\boldsymbol{k}^*} = \frac{\left(m^{xx}_{\boldsymbol{k}^*}\left[\boldsymbol{D}^s\right]+1\right)\left(m^{zz}_{\boldsymbol{k}^*}\left[\boldsymbol{D}^s\right]+1\right) - \left(m^{xz}_{\boldsymbol{k}^*}\left[\boldsymbol{D}^s\right]\right)^2}{\Gamma^x_{\boldsymbol{k}^*}\left(m^{zz}_{\boldsymbol{k}^*}\left[\boldsymbol{D}^s\right]+1\right) + \Gamma^z_{\boldsymbol{k}^*}\left(m^{xx}_{\boldsymbol{k}^*}\left[\boldsymbol{D}^s\right]+1\right) - \Gamma^{xz}_{\boldsymbol{k}^*}m^{xz}_{\boldsymbol{k}^*}\left[\boldsymbol{D}^s\right]}, \tag{2.172}$$

where again the effect of the short time dynamics of the bath is ignored. Hence, the numerical values of these coefficients are probably off, but the limiting behavior for long times can be reproduced if the separation of timescales between the bath dynamics and the probe dynamics is large enough (in particular in a glass, where the bath dynamics becomes arrested). Despite their restricted physical meaning, these coefficients can also be used to determine the delocalization transition, which is discussed in Chapter 4. The short version: In a glassy host, the correlation functions of the probe particle remain finite at long times and small forces. Above a threshold force, the correlation functions do decay to zero. Since the transport coefficients are finite if the correlations decay, but diverge if the correlations remain finite at long times, we have a strong numerical signal to detect (see Section 4.1.1).

The name *transport coefficient* refers to the fact that time integrals of certain correlation functions lead to viscosity [EM14, p. 93, Eq. (4.56)] or thermal conductivity [EM14, p. 94, Eq. (4.68)], which describe the transport of fluid elements or heat. This general relationship between the time integral of a correlation function and a corresponding transport coefficient has been found by Green [Gre54] and Kubo [Kub57] and is therefore called Green-Kubo relation. One important use of these relations is the calculation of transport coefficients in computer simulations. There, one can use the time integral of the velocity auto-correlation function to obtain the diffusion coefficient [EM14, p. 120, Table 6.1]. Generalizations of these relations lead to frequency dependent transport coefficients, which are essentially the Laplace transforms of the correlation functions [Zwa65b; Zwa65a].

A physical meaning of the transport coefficients (2.171) introduced above is not directly obvious. In a crude way they encode how fast the correlation functions decay. since all auto-correlation functions start at 1, the transport coefficient is smaller, the faster the decay of the corresponding correlation function. Nevertheless they prove to be very useful in characterizing the critical force (see Chapter 4).

2.4.9. Moments of the van Hove function

An important concept in statistics is the use of moments like mean or variance to characterize probability distributions, which we have already used when discussing the solutions of the Smoluchowski equation in Section 2.3. The moment of order $|\boldsymbol{\alpha}| := \sum_{i=1}^{3} \alpha_i$ of a probability distribution $p(\boldsymbol{r})$ is defined by

$$\langle \boldsymbol{r}^{\boldsymbol{\alpha}} \rangle_p := \left\langle \prod_{i=1}^{3} r_i^{\alpha_i} \right\rangle_p = \int \prod_{i=1}^{3} r_i^{\alpha_i} p(\boldsymbol{r}) \mathrm{d}\boldsymbol{r} \,. \tag{2.173}$$

In our case, we want to apply this concept to the van Hove function. These moments can be expressed through the intermediate scattering functions $\phi^s_{\boldsymbol{k}}(t)$ via

$$\langle \boldsymbol{r}^{\boldsymbol{\alpha}} \rangle (t) = (-\mathrm{i})^{|\boldsymbol{\alpha}|} \, \boldsymbol{\partial}^{\boldsymbol{\alpha}} \phi^s_{\boldsymbol{k}}(t)|_{\boldsymbol{k}=0} \tag{2.174}$$

(see Appendix A). For the first and second moments we introduce the following notations

$$\mathcal{M}^{(1)}_\alpha := \langle r_\alpha \rangle \,, \tag{2.175a}$$

$$\mathcal{M}^{(2)}_\alpha := \left\langle (r_\alpha)^2 \right\rangle . \tag{2.175b}$$

Of interest is also the second central moment, which is defined as

$$\left\langle \Delta r_\alpha^2 \right\rangle := \left\langle (r_\alpha - \langle r_\alpha \rangle)^2 \right\rangle = \left\langle r_\alpha^2 \right\rangle - (\langle r_\alpha \rangle)^2. \tag{2.176}$$

To introduce a nomenclature, we call $\langle z \rangle (t) = \mathcal{M}_z^{(1)}(t)$ the mean displacement, $\langle x^2 \rangle = \mathcal{M}_x^{(2)}(t)$ and $\langle z^2 \rangle := \mathcal{M}_z^{(2)}(t)$ the mean square displacements and $\langle \Delta z^2 \rangle$ the second central moment or variance. In the following we will show $\langle x \rangle (t) = 0$ and therefore $\langle \Delta x^2 \rangle = \langle x^2 \rangle$.

We can use the equations of motion for the correlation function (2.154a) to determine equations of motion for the moments as well. Since these calculations lead to a lot of terms, we will use the abbreviations as defined below. We will also make use of the fact that the choice $\boldsymbol{k} = \boldsymbol{k}^*$ (i.e. $k_y = 0$) leads to a matrix representation of the memory kernel with two dimensions only via

$$L_{\boldsymbol{k}^*} = \begin{pmatrix} k_x \\ k_z - iF_{\mathrm{ex}} \end{pmatrix}, \qquad R_{\boldsymbol{k}^*} = \begin{pmatrix} k_x \\ k_z \end{pmatrix}, \tag{2.177a}$$

$$M_{\boldsymbol{k}^*}(s) = \left((1 + m_{\boldsymbol{k}^*}^{xx}(s))(1 + m_{\boldsymbol{k}^*}^{zz}(s)) + (m_{\boldsymbol{k}^*}^{xz}(s))^2 \right)^{-1} \begin{pmatrix} 1 + m_{\boldsymbol{k}^*}^{zz}(s) & -m_{\boldsymbol{k}^*}^{xz}(s) \\ -m_{\boldsymbol{k}^*}^{xz}(s) & 1 + m_{\boldsymbol{k}^*(s)}^{xx} \end{pmatrix}. \tag{2.177b}$$

Then the equation of motion (2.154a) reads in Laplace space

$$\phi_{\boldsymbol{k}^*}^s(s) = \left(s + L_{\boldsymbol{k}^*}^T M_{\boldsymbol{k}^*}(s) R_{\boldsymbol{k}^*} \right)^{-1}. \tag{2.178}$$

Since writing out all dependencies makes the notation quite long and crowded, we will omit the Laplace frequency in the following calculations and put the wavevector dependency only where necessary to avoid confusion. Keep in mind, that $L_{\boldsymbol{k}^*}, R_{\boldsymbol{k}^*}$ and $M_{\boldsymbol{k}^*}$ are wave vector dependent and therefore subject to the derivatives even if we just write L, R or M.

The following discussion is focused on the first moments (mean displacement) and second moments (mean square displacements and variance). According to (2.174) this requires calculating first and second order partial derivatives of $\phi_{\boldsymbol{k}^*}^s(s)$. Since the Laplace frequency s or the time t enter these calculations only as a parameter, we will do the calculation in Laplace space, because we can use here a more compact notation. It would be equivalently possible to do the calculation in time space, but the intermediate results get quite lengthy due to the convolution integrals.

We start by calculating the partial derivatives of the correlation function and obtain for $\alpha \in \{x, z\}$

$$\frac{\partial}{\partial k_\alpha} \phi_{\boldsymbol{k}^*}^s = -\frac{1}{(s + L^T M R)^2} \frac{\partial}{\partial k_\alpha} \left(L^T M R \right), \tag{2.179a}$$

$$\frac{\partial^2}{\partial {k_\alpha}^2} \phi_{\boldsymbol{k}^*}^s = \frac{2}{(s + L^T M R)^3} \left(\frac{\partial}{\partial k_\alpha} \left(L^T M R \right) \right)^2 - \frac{1}{(s + L^T M R)^2} \frac{\partial^2}{\partial {k_\alpha}^2} \left(L^T M R \right). \tag{2.179b}$$

To continu,e we need the partial derivatives of $L^T M R$, which are given by

$$\frac{\partial}{\partial k_\alpha} (L^T M R) = \boldsymbol{e}_\alpha^T M \boldsymbol{k}^* + (\boldsymbol{k} - \mathrm{i} F_{\mathrm{ex}} \boldsymbol{e}_z)^T \left(\frac{\partial}{\partial k_\alpha} M \right) \boldsymbol{k}^* + (\boldsymbol{k}^* - \mathrm{i} F_{\mathrm{ex}} \boldsymbol{e}_z)^T M \boldsymbol{e}_\alpha, \tag{2.180a}$$

$$\frac{\partial^2}{\partial {k_\alpha}^2}(L^T M R) = 2\boldsymbol{e}_\alpha^T M \boldsymbol{e}_\alpha + 2\boldsymbol{e}_\alpha^T \left(\frac{\partial}{\partial k_\alpha} M\right) \boldsymbol{k}^* + 2(\boldsymbol{k}^* - \mathrm{i}F_{\mathrm{ex}}\boldsymbol{e}_z)^T \left(\frac{\partial}{\partial k_\alpha} M\right) \boldsymbol{e}_\alpha \tag{2.180b}$$

$$+ (\boldsymbol{k}^* - \mathrm{i}F_{\mathrm{ex}}\boldsymbol{e}_z)^T \left(\frac{\partial^2}{\partial {k_\alpha}^2} M\right) \boldsymbol{k}^*, \tag{2.180c}$$

where $\boldsymbol{k}^*$ has to be interpreted as 2-dimensional vector $(k_x, k_z)^T$ and the unit vectors are given by $\boldsymbol{e}_x = (1,0)^T$ and $\boldsymbol{e}_z = (0,1)^T$, respectively. In appendix C.3 we show that all elements $\partial_\alpha^n M_{\beta\gamma}$ (including $n = 0$) remain finite in the limit $k \to 0$. As we are only interested in the derivatives for $\boldsymbol{k} = 0$, we can neglect all terms which are multiplied by $\boldsymbol{k}$. Hence, we obtain

$$\left.\frac{\partial}{\partial k_\alpha}\phi^s_{\boldsymbol{k}^*}(s)\right|_{\boldsymbol{k}=0} = -\frac{1}{s^2}\left(-\mathrm{i}F_{\mathrm{ex}} M_0^{z\alpha}\right), \tag{2.181a}$$

$$\left.\frac{\partial^2}{\partial {k_\alpha}^2}\phi^s_{\boldsymbol{k}^*}(s)\right|_{\boldsymbol{k}=0} = -\frac{2}{s^3}F_{\mathrm{ex}}^2 \left(M_0^{z\alpha}\right)^2 - \frac{2}{s^2}\left(M_0^{\alpha\alpha} - \mathrm{i}F_{\mathrm{ex}}\frac{\partial}{\partial k_\alpha} M_0^{z\alpha}\right), \tag{2.181b}$$

with $M_0^{\alpha\beta}$ denoting the $k \to 0$ limit of $M^{\alpha\beta}_{\boldsymbol{k}^*}$. This leads to the following equations for the moments

$$\mathcal{M}_\alpha^{(1)}(s) = \frac{1}{s^2} F_{\mathrm{ex}} M_0^{z\alpha}(s), \tag{2.182a}$$

$$\mathcal{M}_\alpha^{(2)}(s) = \frac{2}{s^3}F_{\mathrm{ex}}^2 \left(M_0^{z\alpha}(s)\right)^2 + \frac{2}{s^2}\left(M_0^{\alpha\alpha}(s) - \mathrm{i}F_{\mathrm{ex}}\frac{\partial}{\partial k_\alpha} M_0^{z\alpha}(s)\right) \tag{2.182b}$$

Expressing M_0 through the primitive memory functions results in

$$\mathcal{M}_x^{(1)}(s) = 0, \tag{2.183a}$$

$$\mathcal{M}_z^{(1)}(s) = \frac{1}{s^2} F_{\mathrm{ex}} \frac{1}{1 + m_0^{zz}(s)} \tag{2.183b}$$

for the first moments, where we used that $m_0^{xz}(s) = 0$ due to symmetry (see Appendix C.3). For the second moments we obtain

$$\mathcal{M}_x^{(2)}(s) = \frac{2}{s^2}\frac{1}{1 + m_0^{xx}(s)} + \frac{2\mathrm{i}F_{\mathrm{ex}}}{s^2}\frac{1}{(1 + m_0^{xx})(1 + m_0^{zz})}\frac{\partial m_0^{xz}}{\partial k_x}, \tag{2.184a}$$

$$\mathcal{M}_z^{(2)}(s) = \frac{2}{s^3}F_{\mathrm{ex}}^2 \frac{1}{(1 + m_0^{zz}(s))^2} + \frac{2}{s^2}\left(\frac{1}{1 + m_0^{zz}(s)} + \frac{\mathrm{i}F_{\mathrm{ex}}}{(1 + m_0^{zz})^2}\frac{\partial m_0^{zz}}{\partial k_z}\right). \tag{2.184b}$$

These equations of motion can be transformed into the time domain and read

$$\mathcal{M}_x^{(1)}(t) = 0, \tag{2.185a}$$

$$\partial_t \mathcal{M}_z^{(1)}(t) + \int_0^t \mathrm{d}t'\, m_0^{zz}(t - t')\partial_{t'}\mathcal{M}_z^{(1)}(t') = F_{\mathrm{ex}}, \tag{2.185b}$$

$$\partial_t \mathcal{M}_x^{(2)}(t) + \int_0^t \mathrm{d}t'\, m_0^{\perp}(t - t')\partial_{t'}\mathcal{M}_x^{(2)}(t') = 2, \tag{2.185c}$$

$$\partial_t \mathcal{M}_z^{(2)}(t) + \int_0^t m_0^{\parallel}(t-t')\partial_{t'}\mathcal{M}_z^{(2)}(t') = F_{\mathrm{ex}}^2 t + 2 + \int_0^t \mathrm{d}t' \left(m^{zz}(t') + \mathrm{i}F_{\mathrm{ex}} \frac{\partial m_0^{zz}}{\partial k_z}(t') \right), \quad (2.185\mathrm{d})$$

with the initial conditions $\mathcal{M}_x^{(1)}(0) = \mathcal{M}_z^{(1)}(0) = \mathcal{M}_x^{(2)}(0) = \mathcal{M}_z^{(2)}(0) = 0$. For the defining equations of $m_0^{\perp}$ and $m_0^{\parallel}$ see below. The transformation into time space is not unique. We can also identify the first moment according to (2.183b). Then we obtain

$$\partial_t \mathcal{M}_z^{(2)}(t) + \int_0^t \mathrm{d}t'\, m_0^{zz}(t-t')\partial t' \mathcal{M}_z^{(2)}(t') = 2F_{\mathrm{ex}}\mathcal{M}_z^{(1)}(t) + 2 + 2\int_0^t \mathrm{d}t'\, \mathrm{i}\frac{\partial m_0^{zz}}{\partial k_z}(t-t')\partial_{t'}\mathcal{M}_z^{(1)}(t'). \quad (2.185\mathrm{e})$$

When we are interested in the variance rather than the second moment, we can transform the last equation using the identity (omitting the time arguments on the right hand side)

$$\partial_t \left\langle \Delta z^2 \right\rangle (t) = \partial_t \left\langle (z - \langle z \rangle)^2 \right\rangle = \partial_t \left(\left\langle z^2 \right\rangle - (\langle z \rangle)^2 \right) = \partial_t \mathcal{M}_z^{(2)} - 2\mathcal{M}_z^{(1)} \partial_t \mathcal{M}_z^{(1)}, \quad (2.185\mathrm{f})$$

to get

$$\begin{aligned} \partial_t \left\langle \Delta z^2 \right\rangle (t) + \int_0^t \mathrm{d}t'\, m_0^{zz}(t-t')\partial_{t'} \left\langle \Delta z^2 \right\rangle (t') = 2 - 2\mathcal{M}_z^{(1)}(t) \int_0^t \mathrm{d}t'\, m_0^{zz}(t-t')\partial_{t'}\mathcal{M}_z^{(1)}(t') \\ + 2\int_0^t \mathrm{d}t'\, \mathrm{i}\frac{\partial m_0^{zz}}{\partial k_z}(t-t')\partial_{t'}\mathcal{M}_z^{(1)}(t') \\ - \int_0^t \mathrm{d}t'\, m_0^{zz}(t-t')\partial_{t'} \left(\mathcal{M}_z^{(1)}(t') \right)^2. \end{aligned} \quad (2.185\mathrm{g})$$

The corresponding effective memory kernels have to fulfill the following integral equations

$$\begin{aligned} m_0^{\perp}(t) + \int_0^t \mathrm{d}t'\, m_0^{\perp}(t-t') \left(m_0^{zz}(t') + \mathrm{i}F_{\mathrm{ex}} \frac{\partial m_0^{xz}}{\partial k_x}(t') \right) \\ = m_0^{xx}(t) - \mathrm{i}F_{\mathrm{ex}} \frac{\partial m_0^{xz}}{\partial k_x}(t) + \int_0^t \mathrm{d}t'\, m_0^{xx}(t-t') m_0^{zz}(t') \end{aligned} \quad (2.186\mathrm{a})$$

and

$$m_0^{\parallel}(t) = 2m_0^{zz}(t) + \int_0^t \mathrm{d}t'\, m_0^{zz}(t-t') m_0^{zz}(t'). \quad (2.186\mathrm{b})$$

These equations are structurally similar to the equations of motion for the correlation functions. At first sight, one may attempt to solve these equations independently, without solving for the correlation functions. However, the primitive memory functions depend directly on the correlation functions. Therefore, it is not possible to find a solution for the moments without solving the full equations. Nevertheless these equations are useful, because they give more

accurate solutions than the numerical derivative of the correlation functions.

These results coincide with those obtained by Gustavo Abade using a cumulant expansion [Aba17]. In his notes there is the following correspondence $\mathscr{m}^R_{0,\parallel} = \mathrm{Re}\, m_0^{zz}$, $\mathscr{m}^I_{0,\parallel} = \mathrm{Im}\, \partial_{k_z} m_0^{zz}$, $\hat{m}_0^{xz} = \partial_{k_x} m_0^{xz}$ and $\hat{m}_0^{zz} = \partial_{k_z} m_0^{zz}$. Finally we note that $m_0^{\alpha\beta}$ is real valued (based on the symmetry of $\phi^s_{\boldsymbol{k}}$) and correspondingly $\partial_{k_\gamma} m_0^{\alpha\beta}$ is purely imaginary. Therefore $\mathrm{i}\partial_{k_\gamma} m_0^{\alpha\beta} = -\mathrm{Im}\, \partial_{k_\gamma} m_0^{\alpha\beta}$. This ensures that the equations of motion for the moments are real valued. Explicit expressions for $m_0^{\alpha\beta}(t)$ and their derivatives can be found in Appendix C.3, Eq. (C.20).

Similarly to the long time limit of the full MCT equations in Section 2.4.6, we can also consider the long time limits of the moment equations. This may allow us to obtain more accurate values for the moments than by pure numerical differentiation. Remember that these long time limits are finite if and only if the nonergodicity parameter is nonzero. Under this assumption we find

$$\lim_{t\to\infty} \mathcal{M}_x^{(1)}(t) = 0, \tag{2.187a}$$

$$\lim_{t\to\infty} \mathcal{M}_z^{(1)}(t) = \frac{F_{\mathrm{ex}}}{\mu_0^{zz}}, \tag{2.187b}$$

$$\lim_{t\to\infty} \mathcal{M}_x^{(2)}(t) = \frac{2}{\mu_0^{xx}} + \frac{2\mathrm{i}F_{\mathrm{ex}}}{\mu_0^{xx}\mu_0^{zz}} \frac{\partial \mu_0^{xz}}{\partial k_x}, \tag{2.187c}$$

$$\lim_{t\to\infty} \mathcal{M}_z^{(2)}(t) = \frac{2}{\mu_0^{zz}} + \frac{2}{(\mu_0^{zz})^2} \left(F_{\mathrm{ex}}^2 + \mathrm{i}F_{\mathrm{ex}} \frac{\partial \mu_0^{zz}}{\partial k_z} \right), \tag{2.187d}$$

with the definition $\mu_0^{\alpha\beta} = \lim_{t\to\infty} m_0^{\alpha\beta}(t) = \lim_{s\to 0} s m_0^{\alpha\beta}(s)$. Those results have the same structure as the ones for the previous theory [Har13, p. 63, Eq. (5.33)-(5.35)]. While the memory functions for the moments parallel to the force direction are the same, the memory function for the perpendicular direction is different μ_0^{xx} (see (2.166)) in our case but $\hat{m}^s_\perp$ (see [Har13, p. 57, Eq. (5.9)]) for the previous theory.

These equations can also be used to determine the steady state velocity and long time diffusion coefficient. The steady state velocity is defined via

$$v_{\mathrm{steady}} := \lim_{t\to\infty} \partial_t \langle z \rangle (t). \tag{2.188}$$

Using the limit value theorem (B.3) and the differentiation rule (B.4) we find

$$v_{\mathrm{st}} = \lim_{s\to 0} s^2 \mathcal{M}_z^{(1)}(s) = \frac{F_{\mathrm{ex}}}{1 + \int_0^\infty m_0^{zz}(t')\mathrm{d}t'}, \tag{2.189}$$

where the last equality was obtained using (2.183b) and $\mathcal{L}[f](0) = \int_0^\infty f(t)\mathrm{d}t$. Note that the memory function remains finite in a nonergodic state so that the integral diverges. This leads to a vanishing v_{st} as expected. From this steady state velocity, we can obtain the friction coefficient ξ via

$$\xi = \frac{F_{\mathrm{ex}}}{v_{\mathrm{st}}} = 1 + \int_0^\infty m_0^{zz}(t')\mathrm{d}t'. \tag{2.190}$$

This result has also been found by Gazuz with the previous approach [GF13, p. 3f, Eq. (28)-(30)] and [Gaz08, Sec. 2.4, p. 25ff].

The long time diffusion coefficient is given by

$$D_\alpha = \frac{1}{2} \lim_{t\to\infty} \partial_t \left\langle \Delta r_\alpha^2 \right\rangle (t) \tag{2.191}$$

and with a similar calculation we find

$$D_x = \frac{1}{1 + \int_0^\infty m_0^{xx}(t')\mathrm{d}t'} + \frac{F_\mathrm{ex} \int_0^\infty \mathrm{i}\frac{\partial m_0^{xz}(t')}{\partial k_x}\mathrm{d}t'}{(1 + \int_0^\infty m_0^{xx}(t')\mathrm{d}t')\,(1 + \int_0^\infty m_0^{zz}(t')\mathrm{d}t')}. \tag{2.192}$$

This result differs from the previous theory [Har13, p. 63, Eq. (5.37)]. There, the memory function for the first term is different and the second term does not exist.

For the direction parallel to the force there is unfortunately no such simple equation, because there is no general relation for the Laplace transform of the square of a function. In particular, we cannot represent $\mathcal{L}\left[(\langle z\rangle)^2\right]$ in terms of Laplace transforms of the moments. We can only do an asymptotic expansion around $s = 0$ or $t = \infty$ for ergodic states. In this case, we assume that the $s \to 0$ limit of the memory functions is finite and can be expanded in a power series[19]. Then $m_0^{\alpha\beta}(s) \approx m_0^{\alpha\beta}(0) + s\partial_s m_0^{\alpha\beta}(0) + \mathcal{O}(s^2)$ and consequently the Laurent series for the first moment is given by

$$\mathcal{M}_z^{(1)}(s) \approx \frac{1}{s^2}\frac{F_\mathrm{ex}}{1 + m_0^{zz}(0)} - \frac{1}{s}\frac{F_\mathrm{ex}\partial_s m_0^{zz}(0)}{(1 + m_0^{zz}(0))^2} + \mathcal{O}(s^0). \tag{2.193}$$

This implies

$$\langle z\rangle (t) \approx \frac{F_\mathrm{ex}}{1 + \int_0^\infty m_0^{zz}(t')\mathrm{d}t'}t + \frac{F_\mathrm{ex}\int_0^\infty t' m_0^{zz}(t')\mathrm{d}t'}{(1 + \int_0^\infty m_0^{zz}(t')\mathrm{d}t')^2} + \mathcal{O}(t^{-1}) \tag{2.194}$$

so that we find

$$\mathcal{L}\left[(\langle z\rangle)^2\right](s) \approx \left(\frac{F_\mathrm{ex}}{1 + m_0^{zz}(0)}\right)^2 \frac{2}{s^3} - \frac{2(F_\mathrm{ex})^2\partial_s m_0^{zz}(0)}{(1 + m_0^{zz}(0))^3}\frac{1}{s^2} + \mathcal{O}(s^{-1}). \tag{2.195}$$

The first term cancels exactly the first term in (2.184b) in the limit $s \to 0$. Hence, the diffusion coefficient is approximately given by

$$D_z \approx \frac{1}{1 + \int_0^\infty m_0^{zz}(t')\mathrm{d}t'} + \frac{F_\mathrm{ex}\int_0^\infty \mathrm{i}\frac{\partial m_0^{zz}(t')}{\partial k_z}\mathrm{d}t'}{(1 + \int_0^\infty m_0^{zz}(t')\mathrm{d}t')^2} + \frac{(F_\mathrm{ex})^2\int_0^\infty t' m_0^{zz}(t')\mathrm{d}t'}{(1 + \int_0^\infty m_0^{zz}(t')\mathrm{d}t')^3}. \tag{2.196}$$

This corresponds to the result obtained by Harrer for the previous theory [Har13, p. 64, Eq. (5.40)]. Again we notice that for nonergodic systems the diffusion coefficients vanish due to the diverging memory integrals. On the other hand, this equation is only valid and meaningful if the long time behavior of $\langle \Delta z^2\rangle (t)$ is linear in time. If it increases faster, the diffusion coefficient will diverge. Based on the expansion (2.196), this can happen if the integral $\int_0^\infty \mathrm{d}t'\, t' m_0^{zz}(t')$ diverges. Tracing back its origin, we have to check whether the first moment

[19] This excludes all cases with diverging derivative for $s \to 0$, such as $m(s) = m_0 + s^\alpha$ with $\alpha < 1$.

allows a power series expansion as performed in (2.193). If we find that the memory function can only be described by $m_0^{zz}(s) \approx m_0^{zz}(0) + cs^\alpha$ with $0 < \alpha < 1$ and $c \in \mathbb{R}$, the variance will scale like $\langle \Delta z^2 \rangle (t) \propto t^{2-\alpha}$ to leading order. For $0 < \alpha < 1$ this grows faster than linear so that we could call it *superdiffusive* [MM80; BGK+90].

2.4.10. Linear response

Linear response describes the reaction of a system on a small perturbation. This response is generically expressed by equilibrium correlation functions. Therefore, one can either measure the equilibrium correlation functions by measuring the response or one can predict the response based on the correlation functions.

To introduce this concept, we consider a Smoluchowski operator $\Omega = \Omega_{\text{eq}} + F(t)\Omega_{\text{ext}}$ with an external perturbation described by Ω_{ext} while $F(t)$ models its time dependency. Let Ψ_{eq} be the stationary solution to Ω_{eq}, i.e. $\Omega_{\text{eq}}\Psi_{\text{eq}} = 0$ and let A be the observable, whose response shall be measured. Then its deviation from its stationary value $\langle A \rangle$ is given by

$$\langle \Delta A \rangle (t) = \langle A(t) \rangle - \langle A \rangle = \int_{-\infty}^{\infty} R_{A,\Omega}(t - t') F(t') \mathrm{d}t' \tag{2.197a}$$

(cf. [Ris96, p. 165, Eq. (7.9)]) with the response function $R_{A,\Omega}(t)$ defined as

$$R_{A,\Omega}(t) = \begin{cases} \int \mathrm{d}\Gamma\, A(\Gamma) e^{\Omega_0 t} \Omega_{\text{ext}} \Psi_{\text{eq}}(\Gamma), & t \geq 0, \\ 0, & t < 0, \end{cases} \tag{2.197b}$$

(cf. [Ris96, p. 165, Eq. (7.10)]). This response function can be identified as the correlation function $\phi_{A,B}(t) = \langle A(t)B(0) \rangle$ between the variables A and

$$B(\Gamma) = (\Psi_{\text{eq}}(\Gamma))^{-1} \Omega_{\text{ext}} \Psi_{\text{eq}}(\Gamma) \tag{2.198}$$

(cf. [Ris96, p. 167, Eq. (7.14)]). Therefore we can express the response of A to a step perturbation[20] $F(t) = \Theta(t)$ as follows

$$\langle \Delta A \rangle (t) = \int_0^t \phi_{A,B}(t') \mathrm{d}t' \tag{2.199}$$

(cf. [Ris96, p. 166, Eq. (7.11b)]).

To get a feeling of how this works, we have a look at a single particle in a harmonic potential as discussed in Section 2.3.2. The equilibrium Smoluchowski operator is given in nondimensional form by $\Omega_0 = \partial_x^2 + \partial_x V'(x)$ from (2.29) with $V(x) = \kappa x^2/2$ and we will apply an external force as perturbation $\Omega_{\text{ext}} = -F_{\text{ex}}\partial_x$. We are interested in the response of the mean position of the particle, i.e. $A = x$. The stationary solution is given by $\Psi_{\text{eq}}(x) = Z^{-1}\mathrm{e}^{-V(x)}$ with Z being the normalization constant. Hence, the variable for our correlation function is given via

$$B = \mathrm{e}^{V(x)} \Omega_{\text{ext}} \mathrm{e}^{-V(x)} = -F_{\text{ex}} \mathrm{e}^{V(x)} \partial_x \mathrm{e}^{-V(x)} = F_{\text{ex}} V'(x) = F_{\text{ex}} \kappa x \tag{2.200}$$

[20] The perturbation is switched on at time $t = 0$ and then kept constant.

and the correlation function can be identified to be

$$\phi_{A,B}(t) = F_{\mathrm{ex}}\kappa \left\langle x(t)x(0)\right\rangle = F_{\mathrm{ex}}\kappa \int \mathrm{d}x \int \mathrm{d}x_0\, x\Psi_0(x,t|x_0,0)x_0\Psi_{\mathrm{eq}}(x_0) = F_{\mathrm{ex}}\mathrm{e}^{-\kappa t}. \tag{2.201}$$

$\Psi_0(x,t|x_0,0)$ is the probability to find a particle at position x at time t provided it was at position x_0 at time 0 for the equilibrium system. It is given by (2.38). Consequently, we find

$$\left\langle \Delta x\right\rangle (t) = \int_0^t \phi_{A,B}(t')\mathrm{d}t' = \frac{F_{\mathrm{ex}}}{\kappa}(1-\mathrm{e}^{-\kappa t}), \tag{2.202}$$

which is exactly the result we obtained from the full calculation (2.42), when starting from the equilibrium position $x_0 = 0$.

To summarize, linear response theory can predict the response of a system to an external perturbation based on an appropriate equilibrium correlation function. In fact, this relation is also used in the opposite direction to measure equilibrium correlation functions by perturbing the system and measuring its response [Göt09, Sec. 2.5, p. 82-89].

In our case of the active microrheology in a glass, the procedure is not so straightforward. While the correlation function turns into a position-force correlation

$$\phi_{A,B}(t) = F_{\mathrm{ex}} \left\langle \boldsymbol{r}_{s,z}(t)F_z^s(0)\right\rangle, \tag{2.203}$$

where $F_z^s(0)$ is the z-component of the sum of all forces applied to the probe particle. However, neither the equilibrium probability distribution $\Psi_{\mathrm{eq}}(\boldsymbol{x})$ nor the conditional probability distribution $\Psi_0(\boldsymbol{x},t|\boldsymbol{x}_0,0)$ are known analytically. We therefore search for a different strategy to relate the mean displacement to some equilibrium correlation functions.

We start by looking at the equations of motion for the moments (2.185) in terms of the memory functionals. Those functionals are by definition (2.143) correlation functions of the forces on the probe with respect to the dynamics of the irreducible Smoluchowski operator. When approximating this irreducible operator by the regular one, as it is also done for the derivation of the MCT equations, the memory functionals are equilibrium correlation functions similar to the one defined above.

In Section 2.4.9 we could derive equations of motion for the moments in terms of the memory functionals. For the mean square displacement in z-direction in equilibrium we find from (2.185g) (bars denote nondimensional quantities)

$$\partial_{\bar{t}} \left\langle \Delta\bar{z}^2\right\rangle_{\mathrm{eq}}(\bar{t}) + \int_0^{\bar{t}} \mathrm{d}\bar{t}'\, m_{0,\mathrm{eq}}^{zz}(\bar{t}-\bar{t}')\partial_{\bar{t}'} \left\langle \Delta\bar{z}^2\right\rangle_{\mathrm{eq}}(\bar{t}') = 2, \tag{2.204}$$

since the mean displacement vanishes identically due to isotropy in the quiescent case.

When applying an external force, the evolution is governed by (2.185b). In the case of small forces we can approximate its memory kernel, which depends implicitly on the force through

the correlation function, by its quiescent memory kernel $m^{zz}_{0,\mathrm{eq}}$. Then,

$$\partial_{\bar{t}} \langle \bar{z} \rangle(\bar{t}) + \int_0^{\bar{t}} m^{zz}_{0,\mathrm{eq}}(\bar{t} - \bar{t}') \partial_{\bar{t}'} \langle \bar{z} \rangle(\bar{t}') \mathrm{d}\bar{t}' = \overline{F_{\mathrm{ex}}}, \tag{2.205}$$

which is identical to (2.204) except for the right hand side. Since these integro-differential equations are linear, a solution of (2.204) will also solve (2.205) when scaled appropriately. In particular,

$$\langle \bar{z} \rangle(\bar{t}) = \frac{\overline{F_{\mathrm{ex}}}}{2} \left\langle \Delta \bar{z}^2 \right\rangle_{\mathrm{eq}}(\bar{t}). \tag{2.206a}$$

In dimensional form this equation reads

$$\langle z \rangle(t) = \frac{F_{\mathrm{ex}}}{2 k_{\mathrm{B}} T} \left\langle \Delta z^2 \right\rangle_{\mathrm{eq}}(t). \tag{2.206b}$$

This result does not describe linear response in the strict sense of (2.199), because $\left\langle \Delta z^2 \right\rangle_{\mathrm{eq}}$ is not a proper correlation function. Nevertheless, it provides a means to predict the response based on an equilibrium observable, which we will test in Section 7.3 theoretically and experimentally.

Concerning the universality of this relation we have to be careful. Its derivation is not based on first principles as in the original linear response formalism. Instead, we rely on the equations of motion for the moments obtained by the MCT approach. Even though the memory kernels are treated exactly by the Zwanzig-Mori approach, we used the mode coupling approximation to derive the closed equations of motion. For this reason, we can only expect this relation to work in systems where a MCT description works reasonably well.

It can be directly verified that relation (2.206) does not hold for the example of a harmonically bound particle, which has been derived in Section 2.3.2. In particular, the long time limit is off by a factor of 2. Surprisingly, we find that in the opposite limit $t\kappa \ll 1$ relation (2.206) is fulfilled. This can be a hint that a modeling of the cage by a static harmonic trap is adequate only for short times. On the other hand, it was shown by Kilx *et al.* [KEW+12, Supplementary Material] that in a nonergodic system the long time limit of the mean square displacement is twice the equal time variance of the displacements [KEW+12, Supplementary Material, Eq. (17)]. This is due to the different averages in nonergodic systems. As a consequence, Harrer finds for the $t \to \infty$ response in a glass

$$\langle z \rangle = \frac{\overline{F_{\mathrm{ex}}}}{2} \left\langle \Delta z^2 \right\rangle \tag{2.207}$$

by combining Eq. (4.9), Eq. (4.10) and Eq. (4.12) from [Har13, p. 46f] or Eq. (6) and Eq. (8) from [HPVF12] for the dimensional form. This is exactly the long time limit result of relation (2.206).

Finally, we found similar linear response calculations based on the constitutive equation (2.3) of the viscoelastic material, which connect the *creep compliance* $\mathcal{J}(t)$, the strain response of a viscoelastic material on a step stress of unit amplitude (see 2.1.2 and [FS17, p. 18f]) with the quiescent MSD

$$\mathcal{J}(t) = \frac{3\pi d}{2 k_{\mathrm{B}} T} \left\langle \Delta z^2 \right\rangle_{\mathrm{eq}}(t), \tag{2.208}$$

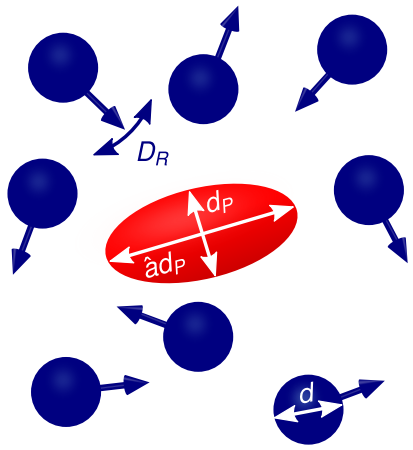

Figure 2.4.: Active microrheology in an active suspension. A spheroidal probe with aspect ratio $\hat{a}$ (red) is pulled through a dilute suspension of active particles (blue) with swim speed u_0 in a solution (not shown).

(cf. [FS17, p. 106, Eq. (3.99)]). In Chapter 8 of the same book, a creep response experiment in a material with the same constitutive equation is discussed, where the displacement of the probe is given by

$$z(t) = \frac{F_{\text{ex}}}{3\pi d}\mathcal{J}(t) \tag{2.209}$$

(cf [FS17, p. 325, Eq. (8.52)]). The usual average is omitted here, because they do not account for Brownian motion. Combining both equations (which they did not do), we find

$$z(t) = \frac{F_{\text{ex}}}{2k_{\text{B}}T}\left\langle \Delta z^2 \right\rangle_{\text{eq}}(t), \tag{2.210}$$

which is exactly (2.206b) (except for the average on the left hand side).

2.5. Dilute theory for active suspensions

In Chapter 8 we will analyze the microrheology in a suspension of active particles measured as depicted in Figure 2.4. The probe is a spheroid (ellipsoid of rotation) with length l_p (along the axis of symmetry) and diameter d_p. Let $\hat{a} = l_p/d_p$ be the aspect ratio (length-to-diameter-ratio) of the spheroid. As the spheroid is axisymmetric, we need its position $\boldsymbol{r} \in \mathbb{R}^3$ and its orientation $\hat{\boldsymbol{q}} \in \hat{S}$, a vector on the unit sphere, to characterize its motion. The bath consists of spherical active Brownian particles (ABP) as described in Section 2.3.4 with a swim speed u_0 and diameter d.

In the following we will derive a set of equations, which describe the friction experienced by a spheroidal probe in a dilute suspension of ABP. This can be related to the density of bath particles around the probe as shown in Section 2.5.4. This density in turn can be calculated from a moment expansion of the pair correlation function, which is performed in Section 2.5.2. The pair correlation function itself is derived from the Smoluchowski equation for active and anisotropic particles in Section 2.5.1. Furthermore, two technical aspects will be discussed. To simplify the boundary conditions, we need to transform to spheroidal coordinates, which is done in Section 2.5.3 and we will also need diffusion coefficients for spheroids, which are summarized in Section 2.5.5.

2.5.1. Equations of motion

This model system will be studied using a low density description following the approaches described in [KB08; ZB10; YB15a]. The main idea for low densities is that the problem can be reduced to only two particles, the probe and one bath particle [SB05, Appendix A, p. 15]. Let index $i = 1$ describe the ellipsoidal probe particle and let index $i = 2$ describe the active bath particle. As the bath particles are spherical there holds $\Delta D_2 = 0$. The Smoluchowski operator for the two particle probability distribution $\Psi_2(\boldsymbol{r}_1, \boldsymbol{r}_2, \hat{\boldsymbol{q}}_1, \hat{\boldsymbol{q}}_2)$ then reads

$$\Omega = \sum_{i=1}^{2} \overline{D}_i \boldsymbol{\partial}_i^2 + \Delta D_i \boldsymbol{\partial}_i \left(\hat{\boldsymbol{q}}_i \hat{\boldsymbol{q}}_i - \frac{1}{3}\mathbb{1} \right) \boldsymbol{\partial}_i + D_i^R \left(\boldsymbol{\partial}_i^R \right)^2 - \boldsymbol{\partial}_i \cdot \boldsymbol{u}_i, \tag{2.211}$$

with $\boldsymbol{u}_1 = \boldsymbol{u}^{\text{ext}}$ being the constant drag velocity of the probe and $\boldsymbol{u}_2 = u_0 \hat{\boldsymbol{q}}_2$ being the velocity of the ABP. The orientation vectors $\hat{\boldsymbol{q}}_i \in \hat{S}$ are described by points on the unit sphere, which is abbreviated as $\hat{S} := \{\boldsymbol{r} \in \mathbb{R}^3 : \|\boldsymbol{r}\| = 1\}$.

Since we are modeling hard particles, their interaction will only show up as boundary condition for the fluxes as introduced in Section 2.3.5. In this version, the equation of motion for the probability density Ψ_2 is given by

$$0 = \partial_t \Psi_2(\boldsymbol{r}_1, \boldsymbol{r}_2, \hat{\boldsymbol{q}}_1, \hat{\boldsymbol{q}}_2, t) + \sum_{i=1}^{N} \left(\boldsymbol{\partial}_i \cdot \boldsymbol{j}_i^T + \boldsymbol{\partial}_i^R \cdot \boldsymbol{j}_i^R \right), \tag{2.212a}$$

$$\boldsymbol{j}_i^T = \left(\overline{D}_i \boldsymbol{\partial}_i + \Delta D_i \left(\hat{\boldsymbol{q}}_i \hat{\boldsymbol{q}}_i - \frac{1}{3}\mathbb{1} \right) \boldsymbol{\partial}_i - \boldsymbol{u}_i \right) \Psi_2(\boldsymbol{r}_1, \boldsymbol{r}_2, \hat{\boldsymbol{q}}_1, \hat{\boldsymbol{q}}_2, t), \tag{2.212b}$$

$$\boldsymbol{j}_i^R = D_i^R \boldsymbol{\partial}_i^R \Psi_2(\boldsymbol{r}_1, \boldsymbol{r}_2, \hat{\boldsymbol{q}}_1, \hat{\boldsymbol{q}}_2, t). \tag{2.212c}$$

The boundary condition then reads

$$\boldsymbol{n}_{12}(\boldsymbol{r}_1, \boldsymbol{r}_2, \hat{\boldsymbol{q}}_1, \hat{\boldsymbol{q}}_2) \cdot \boldsymbol{j}_1(\boldsymbol{r}_1, \boldsymbol{r}_2, \hat{\boldsymbol{q}}_1, \hat{\boldsymbol{q}}_2) = 0 \tag{2.213a}$$

for $(\hat{\boldsymbol{q}}_1, \hat{\boldsymbol{q}}_2) \in (\hat{S})^2$, $(\boldsymbol{r}_1, \boldsymbol{r}_2) \in \mathbb{R}^6$ with $\boldsymbol{r}_2 - \boldsymbol{r}_1 \in \partial \mathcal{V}_{12}^{\text{exc}}(\hat{\boldsymbol{q}}_1, \hat{\boldsymbol{q}}_2)$ and

$$\boldsymbol{n}_{21}(\boldsymbol{r}_1, \boldsymbol{r}_2, \hat{\boldsymbol{q}}_1, \hat{\boldsymbol{q}}_2) \cdot \boldsymbol{j}_2(\boldsymbol{r}_1, \boldsymbol{r}_2, \hat{\boldsymbol{q}}_1, \hat{\boldsymbol{q}}_2) = 0 \tag{2.213b}$$

for $(\hat{\boldsymbol{q}}_1, \hat{\boldsymbol{q}}_2) \in (\hat{S})^2$, $(\boldsymbol{r}_1, \boldsymbol{r}_2) \in \mathbb{R}^6$ with $\boldsymbol{r}_1 - \boldsymbol{r}_2 \in \partial \mathcal{V}_{21}^{\text{exc}}(\hat{\boldsymbol{q}}_1, \hat{\boldsymbol{q}}_2)$.

Translational coordinate transformation

In the long run, we are looking for stationary solutions of this problem, where the probe is moving with a constant velocity. Therefore, it is convenient to describe the system in the frame of reference of the moving probe particle. This requires transformation of both the position as well as the orientation.

The position will be transformed via

$$\boldsymbol{r}_p = \boldsymbol{r}_1, \qquad \boldsymbol{r}_r = \boldsymbol{r}_2 - \boldsymbol{r}_1, \tag{2.214}$$

with the position of the probe particle $\boldsymbol{r}_p$ and the position of the bath particle relative to

the probe $\boldsymbol{r}_r$, while the orientations remain the same for the moment. This implies that the gradient operators transform like

$$\boldsymbol{\partial}_1 = \boldsymbol{\partial}_p - \boldsymbol{\partial}_r, \qquad \boldsymbol{\partial}_2 = \boldsymbol{\partial}_r, \tag{2.215}$$

which leads to the definition of new new fluxes with respect to the derivatives $\boldsymbol{\partial}_p$ and $\boldsymbol{\partial}_r$. They are related to the previous fluxes $\boldsymbol{j}_1$ and $\boldsymbol{j}_2$ via

$$\boldsymbol{j}_p = \boldsymbol{j}_1, \qquad \boldsymbol{j}_r = \boldsymbol{j}_2 - \boldsymbol{j}_1. \tag{2.216a}$$

With these identities, we find the new boundary conditions (with the abbreviations $\boldsymbol{R} = (\boldsymbol{r}_p, \boldsymbol{r}_r)$, $\boldsymbol{Q} = (\hat{\boldsymbol{q}}_1, \hat{\boldsymbol{q}}_2)$) to be

$$0 = \boldsymbol{n}_{12}(\boldsymbol{R}, \boldsymbol{Q}) \cdot \boldsymbol{j}_p(\boldsymbol{R}, \boldsymbol{Q}) \tag{2.217a}$$

for $\boldsymbol{Q} \in (\hat{S})^2$, $\boldsymbol{R} \in \mathbb{R}^6$ with $\boldsymbol{r}_s \in \partial V_{12}^{\text{ext}}(\hat{\boldsymbol{q}}_1, \hat{\boldsymbol{q}}_2)$ and

$$0 = \boldsymbol{n}_{21}(\boldsymbol{R}, \boldsymbol{Q}) \cdot (\boldsymbol{j}_p(\boldsymbol{R}, \boldsymbol{Q}) + \boldsymbol{j}_r(\boldsymbol{R}, \boldsymbol{Q})) \tag{2.217b}$$

for $\boldsymbol{Q} \in (\hat{S})^2$, $\boldsymbol{R} \in \mathbb{R}^6$ with $\boldsymbol{r}_s \in \partial V_{21}^{\text{ext}}(\hat{\boldsymbol{q}}_1, \hat{\boldsymbol{q}}_2)$. As the excluded volume is the same in both cases, we can rewrite the last condition into

$$0 = \boldsymbol{n}_{21}(\boldsymbol{R}, \boldsymbol{Q}) \cdot \boldsymbol{j}_r(\boldsymbol{R}, \boldsymbol{Q}). \tag{2.217c}$$

In explicit form, the fluxes read

$$\boldsymbol{j}_p = -\left(\overline{D}_1(\boldsymbol{\partial}_p - \boldsymbol{\partial}_r) + \Delta\boldsymbol{D}_p(\boldsymbol{\partial}_p - \boldsymbol{\partial}_r) - \boldsymbol{u}_1\right)\Psi_2(\boldsymbol{r}_p, \boldsymbol{r}_r, \hat{\boldsymbol{q}}_1, \hat{\boldsymbol{q}}_2), \tag{2.218a}$$

$$\boldsymbol{j}_r = -\left(-\left(\overline{D}_1 + \Delta\boldsymbol{D}_p\right)\boldsymbol{\partial}_p + \left(\overline{D}_r + \Delta\boldsymbol{D}_r\right)\boldsymbol{\partial}_r - \boldsymbol{u}_r\right)\Psi_2(\boldsymbol{r}_p, \boldsymbol{r}_j, \hat{\boldsymbol{q}}_1, \hat{\boldsymbol{q}}_2), \tag{2.218b}$$

with the abbreviations

$$\Delta\boldsymbol{D}_p = \Delta D_1\left(\hat{\boldsymbol{q}}_1\hat{\boldsymbol{q}}_1 - \frac{1}{3}\mathbb{1}\right), \tag{2.219a}$$

$$\Delta\boldsymbol{D}_r = \Delta\boldsymbol{D}_p + \Delta D_2\left(\hat{\boldsymbol{q}}_2\hat{\boldsymbol{q}}_2 - \frac{1}{3}\mathbb{1}\right), \tag{2.219b}$$

$$\overline{D}_r = \overline{D}_1 + \overline{D}_2, \tag{2.219c}$$

$$\boldsymbol{u}_r = u_0\hat{\boldsymbol{q}}_2 - \boldsymbol{u}^{\text{ext}}. \tag{2.219d}$$

Rotational coordinate transformation

In order to express the equations of motion in the frame of reference of the probe particle, we have to apply a rotation $\mathcal{R}$ on the relative position $\boldsymbol{r}_r$ and the orientation $\hat{\boldsymbol{q}}_2$. This rotation has to be such that the orientation of the probe after the rotation $\mathcal{R}\hat{\boldsymbol{q}}_1$ points into a specific direction. We choose this direction to be $\hat{\boldsymbol{z}}$. As the probe is axisymmetric, this rotation is not uniquely defined, since any additional rotation around the $\hat{\boldsymbol{z}}$-axis gives the same orientation of

$\mathcal{R}\hat{\boldsymbol{q}}_1$. This rotation matrix can be given by a rotation around $\hat{\boldsymbol{q}}_1 \times \hat{\boldsymbol{z}}$ and then looks like

$$\mathcal{R}(\hat{\boldsymbol{q}}_1) = \begin{pmatrix} \frac{q_{1,z}q_{1,y}^2+q_{1,x}^2}{q_{1,x}^2+q_{1,y}^2} & -\frac{q_{1,x}q_{1,y}(1-q_{1,z})}{q_{1,x}^2+q_{1,y}^2} & -q_{1,x} \\ -\frac{q_{1,x}q_{1,y}(1-q_{1,z})}{q_{1,x}^2+q_{1,y}^2} & \frac{q_{1,y}^2+q_{1,z}q_{1,x}^2}{q_{1,x}^2+q_{1,y}^2} & -q_{1,y} \\ q_{1,x} & q_{1,y} & q_{1,z} \end{pmatrix}. \tag{2.220}$$

The transformation into the frame of reference of the probe particle is then given by

$$\boldsymbol{r}_{p'} = \boldsymbol{r}_p, \qquad \boldsymbol{r}_{r'} = \mathcal{R}(\hat{\boldsymbol{q}}_1)\boldsymbol{r}_r, \tag{2.221}$$

$$\hat{\boldsymbol{q}}_{p'} = \hat{\boldsymbol{q}}_1, \qquad \hat{\boldsymbol{q}}_{r'} = \mathcal{R}(\hat{\boldsymbol{q}}_1)\hat{\boldsymbol{q}}_2. \tag{2.222}$$

This implies for the corresponding differential operators

$$\boldsymbol{\partial}_p = \boldsymbol{\partial}_{p'}, \tag{2.223a}$$

$$\boldsymbol{\partial}_r = \mathcal{R}(\hat{\boldsymbol{q}}_{p'})\boldsymbol{\partial}_{r'}, \tag{2.223b}$$

$$\boldsymbol{\partial}_{\hat{q}_1} = \boldsymbol{\partial}_{\hat{q}_{p'}} + R'(\hat{\boldsymbol{q}}_{p'}, \boldsymbol{r}_{r'})\boldsymbol{\partial}_{r'} + R'(\hat{\boldsymbol{q}}_{p'}, \hat{\boldsymbol{q}}_{r'})\boldsymbol{\partial}_{\hat{q}_{r'}}, \tag{2.223c}$$

$$\boldsymbol{\partial}_{\hat{q}_2} = \mathcal{R}(\hat{\boldsymbol{q}}_{p'})\boldsymbol{\partial}_{\hat{q}_{r'}}, \tag{2.223d}$$

where

$$R'(\hat{\boldsymbol{q}}_1, \boldsymbol{a}')_{ij} = \frac{\partial}{\partial \hat{\boldsymbol{q}}_{1,i}}(\mathcal{R}(\hat{\boldsymbol{q}}_1)\boldsymbol{a})_j\Big|_{\boldsymbol{a}=\mathcal{R}(\hat{\boldsymbol{q}}_1)^T\boldsymbol{a}'}. \tag{2.224}$$

This leads again to a new definition for the transformed fluxes

$$\boldsymbol{j}_{p'} = \boldsymbol{j}_p, \tag{2.225a}$$

$$\boldsymbol{j}_{r'} = \mathcal{R}^T(\hat{\boldsymbol{q}}_{p'})\boldsymbol{j}_r. \tag{2.225b}$$

The transformed boundary conditions with the abbreviations $\boldsymbol{R'} = (\boldsymbol{r}_{p'}, \mathcal{R}(\hat{\boldsymbol{q}}_{p'})^T\boldsymbol{r}_{r'})$ and $\boldsymbol{Q'} = (\hat{\boldsymbol{q}}_{p'}, \mathcal{R}(\hat{\boldsymbol{q}}_{p'})^T\hat{\boldsymbol{q}}_{r'})$ are given by the requirement

$$\boldsymbol{n}_{12}(\boldsymbol{R'}, \boldsymbol{Q'}) \cdot \boldsymbol{j}_{p'}(\boldsymbol{R'}, \boldsymbol{Q'}) = 0 \tag{2.226a}$$

for $\boldsymbol{Q'} \in (\hat{S})^2$, $\boldsymbol{R'} \in \mathbb{R}^6$ with $\boldsymbol{r}_{r'} \in \partial\mathcal{V}^{\text{exc}}(\hat{\boldsymbol{q}}_{p'}, \mathcal{R}(\hat{\boldsymbol{q}}_{p'})^T\hat{\boldsymbol{q}}_{r'})$. As the rotation is an isometry, which keeps the normals and the excluded volume constant, we can rewrite the condition as follows: for $\hat{\boldsymbol{q}}_{r'} \in \hat{S}$, $\boldsymbol{r}_{r'} \in \partial\mathcal{V}^{\text{exc}}(\hat{\boldsymbol{z}}, \hat{\boldsymbol{q}}_{r'})$. The same argument holds for the second boundary condition, which we find to be

$$\boldsymbol{n}_{21}(\boldsymbol{R'}, \boldsymbol{Q'}) \cdot \boldsymbol{j}_{r'}(\boldsymbol{R'}, \boldsymbol{Q'}) = 0 \tag{2.226b}$$

for $\hat{\boldsymbol{q}}_{r'} \in \hat{S}$, $\boldsymbol{r}_{r'} \in \partial\mathcal{V}^{\text{exc}}(\hat{\boldsymbol{z}}, \hat{\boldsymbol{q}}_{r'})$. In the case of the bath particles being spherical, we can even drop the $\hat{\boldsymbol{q}}_{r'}$ dependency of the excluded volume.

Simplification to motion along the symmetry axis

The full problem with all orientational degrees of freedom is difficult to analyze and solve. We therefore focus on the simpler model, where the orientation of the probe is fixed. In particular, we move the probe in direction of its symmetry axis, which we define to be $\hat{\boldsymbol{z}}$, i.e. $\boldsymbol{q}_{q'} = \hat{\boldsymbol{z}}$, $\boldsymbol{u}_{p'} = u^{\mathrm{ext}}\hat{\boldsymbol{z}}$. This implies $R(\boldsymbol{q}_{p'}) = \mathbb{1}$, which leaves all gradient operators untouched and $R'(\boldsymbol{q}_{q'}, \boldsymbol{r}_{r'}) = R'(\boldsymbol{q}_{q'}, \boldsymbol{q}_{r'}) = 0$, which makes $\boldsymbol{\partial}^R_{p'}$ vanish. In addition, we assume that the translational diffusion tensor of the active bath particles is isotropic, i.e. $\Delta D_2 = 0$. We then obtain the following continuity equation for the two particle probability density (with only one orientational degree of freedom and the primes removed from the labels for clarity)

$$0 = \partial_t \Psi_2(\boldsymbol{r}_p, \boldsymbol{r}_r, \hat{\boldsymbol{q}}_r, t) + \boldsymbol{\partial}_p \boldsymbol{j}^T_p + \boldsymbol{\partial}_r \boldsymbol{j}^T_r + \boldsymbol{\partial}^R_r \boldsymbol{j}^R_r, \tag{2.227a}$$

$$\boldsymbol{j}^T_p = -\left(\overline{D}_1(\boldsymbol{\partial}_p - \boldsymbol{\partial}_r) + \Delta\boldsymbol{D}_p(\boldsymbol{\partial}_p - \boldsymbol{\partial}_r) - u^{\mathrm{ext}}\hat{\boldsymbol{z}}\right)\Psi_2(\boldsymbol{r}_p, \boldsymbol{r}_r, \hat{\boldsymbol{q}}_r, t), \tag{2.227b}$$

$$\boldsymbol{j}^T_r = -\left(-\left(\overline{D}_1 + \Delta\boldsymbol{D}_p\right)\boldsymbol{\partial}_p + \left(\overline{D}_r + \Delta\boldsymbol{D}_p\right)\boldsymbol{\partial}_r - u_0\hat{\boldsymbol{q}}_r - u^{\mathrm{ext}}\hat{\boldsymbol{z}}\right)\Psi_2(\boldsymbol{r}_p, \boldsymbol{r}_r, \hat{\boldsymbol{q}}_r, t), \tag{2.227c}$$

$$\boldsymbol{j}^R_r = -D^R_2\boldsymbol{\partial}^R_r\Psi_2(\boldsymbol{r}_p, \boldsymbol{r}_r, \hat{\boldsymbol{q}}_r, t). \tag{2.227d}$$

with the boundary conditions

$$\boldsymbol{n}_{12}(\boldsymbol{r}_r)\cdot\boldsymbol{j}_i(\boldsymbol{r}_r) = 0 \tag{2.228}$$

for $i \in \{p, r\}$ and $\boldsymbol{r}_r \in \partial\mathcal{V}^{\mathrm{exc}}(\hat{\boldsymbol{z}})$. The corresponding Smoluchowski operator then reads

$$\begin{aligned}\Omega^{\mathrm{fix}} =& \overline{D}_1\boldsymbol{\partial}^2_p - u^{\mathrm{ext}}\partial_{p,z} + (\boldsymbol{\partial}_p - \boldsymbol{\partial}_r)\Delta\boldsymbol{D}_p(\boldsymbol{\partial}_p - \boldsymbol{\partial}_r) + \overline{D}_r\boldsymbol{\partial}^2_r - u_0\boldsymbol{\partial}_r\cdot\hat{\boldsymbol{q}}_r + u^{\mathrm{ext}}\partial_{r,z} \\ & - \overline{D}_1(\boldsymbol{\partial}_p\boldsymbol{\partial}_r + \boldsymbol{\partial}_r\boldsymbol{\partial}_p) + D^R_2(\hat{\boldsymbol{q}}_r\times\boldsymbol{\partial}_{\hat{\boldsymbol{q}}_r})^2.\end{aligned} \tag{2.229}$$

Nondimensionalization

In order to nondimensionalize the equations, we define that we measure length scales in terms of bath particle diameters d and time scales in terms of the self-diffusion time of bath particles d^2/D_b. Introducing the probe diameter to bath particle diameter ratio $s = d_p/d$ and the length to diameter ratio $\hat{a} = l_p/d_p$, the axes of the ellipsoid are given in nondimensional form by $s\hat{a}$ along the symmetry axis $\hat{\boldsymbol{z}}$ and by s perpendicular to it.

For the equations of motion this choice of length and time scales implies

$$r = \overline{r}d, \qquad\qquad t = \overline{t}\frac{d^2}{D_b}, \tag{2.230a}$$

and

$$\boldsymbol{\partial}_{r/p} = \frac{1}{d}\boldsymbol{\partial}_{\overline{r}/\overline{p}}, \qquad\qquad \partial_t = \frac{D_b}{d^2}\partial_{\overline{t}}, \tag{2.230b}$$

where bars denote the nondimensional variables. The equations of motion (2.227) then read

$$0 = \partial_{\overline{t}}\overline{\Psi}_2(\overline{\boldsymbol{r}}_p, \overline{\boldsymbol{r}}_r, \hat{\boldsymbol{q}}_r, \overline{t}) + \boldsymbol{\partial}_{\overline{p}}\overline{\boldsymbol{j}}^T_p + \boldsymbol{\partial}_{\overline{r}}\overline{\boldsymbol{j}}^T_r + \boldsymbol{\partial}^R_r\overline{\boldsymbol{j}}^R_r, \tag{2.231a}$$

$$\overline{\boldsymbol{j}}_p^T = -\left(\frac{\overline{D}_1}{D_b}(\boldsymbol{\partial}_{\overline{p}} - \boldsymbol{\partial}_{\overline{r}}) + \frac{\Delta \boldsymbol{D}_p}{D_b}(\boldsymbol{\partial}_{\overline{p}} - \boldsymbol{\partial}_{\overline{r}}) - \mathrm{Pe}^{\mathrm{ext}}\hat{\boldsymbol{z}}\right)\overline{\Psi}_2(\overline{\boldsymbol{r}}_p, \overline{\boldsymbol{r}}_r, \hat{\boldsymbol{q}}_r, \overline{t}), \tag{2.231b}$$

$$\overline{\boldsymbol{j}}_r^T = -\left(-\frac{\overline{D}_1 + \Delta \boldsymbol{D}_p}{D_b}\boldsymbol{\partial}_{\overline{p}} + \frac{\overline{D}_r + \Delta \boldsymbol{D}_p}{D_b}\boldsymbol{\partial}_{\overline{r}} - \mathrm{Pe}^{\mathrm{act}}\hat{\boldsymbol{q}}_r + \mathrm{Pe}^{\mathrm{ext}}\hat{\boldsymbol{z}}\right)\overline{\Psi}_2(\overline{\boldsymbol{r}}_p, \overline{\boldsymbol{r}}_r, \hat{\boldsymbol{q}}_r, \overline{t}), \tag{2.231c}$$

$$\overline{\boldsymbol{j}}_r^R = -\frac{d^2 D_2^R}{D_b}\boldsymbol{\partial}_r^R \overline{\Psi}_2(\overline{\boldsymbol{r}}_p, \overline{\boldsymbol{r}}_r, \hat{\boldsymbol{q}}_r, \overline{t}), \tag{2.231d}$$

where we already identified two *Péclet numbers*, one due to the externally forced motion

$$\mathrm{Pe}^{\mathrm{ext}} = \frac{u^{\mathrm{ext}} d}{D_b} \tag{2.232a}$$

and one due to the activity of the active swimmers

$$\mathrm{Pe}^{\mathrm{act}} = \frac{u_0 d}{D_b}. \tag{2.232b}$$

The Péclet numbers characterize the transport mechanism: For $\mathrm{Pe} \ll 1$ the motion is dominated by diffusion, while for $\mathrm{Pe} \gg 1$ advection dominates [FS17, p. 296].

Introducing the run length ℓ of the active particles defined by the distance travelled during the average reorientation time τ, which is given by the inverse rotational diffusion constant

$$\ell = u_0 \tau = \frac{u_0}{D_2^R}. \tag{2.233}$$

and its nondimensional form $\overline{\ell} = \ell/d$, we can express the prefactor of the nondimensional rotational flux as

$$\frac{d^2 D_2^R}{D_b} = \frac{D_2^R d}{u_0}\frac{u_0 d}{D_b} = \frac{\mathrm{Pe}^{\mathrm{act}}}{\overline{\ell}}. \tag{2.234}$$

In case of the purely thermal rotational diffusion of a sphere, this ratio is $\mathrm{Pe}^{\mathrm{act}}/\ell = 3$, but for bacteria or other biological swimmers this can be different. For the nondimensional diffusion coefficients, we note according to (2.219) with $D_b = D_2$

$$\frac{\Delta \boldsymbol{D}_p}{D_b} = \frac{\Delta D_1}{D_b}\left(\hat{\boldsymbol{z}}\hat{\boldsymbol{z}} - \frac{1}{3}\mathbb{1}\right), \tag{2.235a}$$

$$\frac{\overline{D_r}}{D_b} = \frac{\overline{D}_1 + D_2}{D_b} = 1 + \frac{\overline{D}_1}{D_b}. \tag{2.235b}$$

It remains to determine the nondimensional diffusion coefficients for the ellipsoidal particle, which are summarized in Section 2.5.5. Anticipating the results of Eq. (2.271) we obtain

$$\frac{\overline{D}_1}{D_b} = \frac{1}{3s}\left(k_\parallel^T(\hat{a}) + 2k_\perp^T(\hat{a})\right) =: \frac{\overline{D}(\hat{a})}{s}, \tag{2.236a}$$

$$\frac{\Delta D_1}{D_b} = \frac{1}{s}\left(k_\parallel^T(\hat{a}) - k_\perp^T(\hat{a})\right) =: \frac{\Delta D(\hat{a})}{s}, \tag{2.236b}$$

with some functions $k_\parallel^T(\hat{a})$ and $k_\perp^T(\hat{a})$, accounting for the geometry of the probe as defined in (2.272). $s := d_p/d$ is the probe diameter to bath particle diameter ratio and $\hat{a} := l_p/d_p$ the length to diameter ratio of the probe.

Combining these results, we find for the dimensionless fluxes (omitting the arguments of

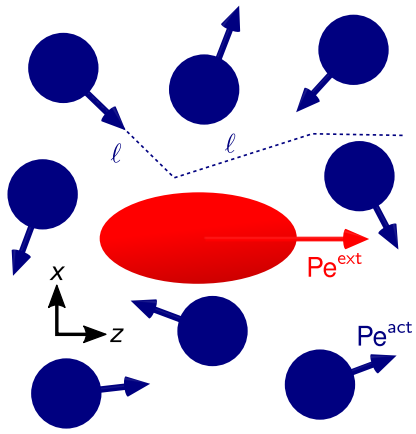

Figure 2.5.: Active microrheology in an active suspension. A spheroidal probe with (red) is pulled with fixed orientation and constant speed $\mathrm{Pe}^{\mathrm{ext}}\hat{\boldsymbol{z}}$ through a dilute suspension of active particles (blue) with swim speed $\mathrm{Pe}^{\mathrm{act}}$ and run length ℓ in a solution (not shown).

$\overline{\Psi}_2(\overline{\boldsymbol{r}}_p, \overline{\boldsymbol{r}}_r, \hat{\boldsymbol{q}}_r, \overline{t})$ for brevity)

$$\overline{\boldsymbol{j}}_p^T = -\left(\frac{\overline{D}(\hat{a})}{s}(\boldsymbol{\partial}_{\overline{p}} - \boldsymbol{\partial}_{\overline{r}}) + \frac{\Delta D(\hat{a})}{s}\left(\hat{\boldsymbol{z}}\hat{\boldsymbol{z}} - \frac{1}{3}\mathbb{1}\right)(\boldsymbol{\partial}_{\overline{p}} - \boldsymbol{\partial}_{\overline{r}}) - \mathrm{Pe}^{\mathrm{ext}}\hat{\boldsymbol{z}}\right)\overline{\Psi}_2, \tag{2.237a}$$

$$\overline{\boldsymbol{j}}_r^T = -\left(\boldsymbol{\partial}_{\overline{r}} + \frac{\overline{D}(\hat{a})}{s}(\boldsymbol{\partial}_{\overline{r}} - \boldsymbol{\partial}_{\overline{p}}) + \frac{\Delta D(\hat{a})}{s}\left(\hat{\boldsymbol{z}}\hat{\boldsymbol{z}} - \frac{1}{3}\mathbb{1}\right)(\boldsymbol{\partial}_{\overline{r}} - \boldsymbol{\partial}_{\overline{p}}) - \mathrm{Pe}^{\mathrm{act}}\hat{\boldsymbol{q}}_r + \mathrm{Pe}^{\mathrm{ext}}\hat{\boldsymbol{z}}\right)\overline{\Psi}_2, \tag{2.237b}$$

$$\overline{\boldsymbol{j}}_r^R = -\frac{\mathrm{Pe}^{\mathrm{act}}}{\overline{\ell}}(\hat{\boldsymbol{q}}_r \times \boldsymbol{\partial}_{\hat{\boldsymbol{q}}_r})\overline{\Psi}_2. \tag{2.237c}$$

The boundary condition (2.228) is not affected by the nondimensionalization, except for expressing the excluded volume in terms of the new lengthscale.

Since it is convenient for the next steps to work with the Smoluchowski equation of this model, we also give the corresponding nondimensional Smoluchowski operator

$$\begin{aligned}\overline{\Omega}^{\mathrm{fix}} =& \frac{\overline{D}(\hat{a})}{s}\left(\boldsymbol{\partial}_{\overline{p}}^2 + \boldsymbol{\partial}_{\overline{r}}^2 - \boldsymbol{\partial}_{\overline{p}}\boldsymbol{\partial}_{\overline{r}} - \boldsymbol{\partial}_{\overline{r}}\boldsymbol{\partial}_{\overline{p}}\right) + \boldsymbol{\partial}_{\overline{r}}^2 - \mathrm{Pe}^{\mathrm{ext}}\partial_{\overline{p},z} - \mathrm{Pe}^{\mathrm{act}}\boldsymbol{\partial}_{\overline{r}}\cdot\hat{\boldsymbol{q}}_r + \mathrm{Pe}^{\mathrm{ext}}\partial_{\overline{r},z} \\ &+ \frac{\Delta D(\hat{a})}{s}\left(\partial_{\overline{p},z}^2 + \partial_{\overline{r},z}^2 - \partial_{\overline{p},z}\partial_{\overline{r},z} - \partial_{\overline{r},z}\partial_{\overline{p},z} - \frac{1}{3}\left(\boldsymbol{\partial}_{\overline{p}}^2 + \boldsymbol{\partial}_{\overline{r}}^2 - \boldsymbol{\partial}_{\overline{p}}\boldsymbol{\partial}_{\overline{r}} - \boldsymbol{\partial}_{\overline{r}}\boldsymbol{\partial}_{\overline{p}}\right)\right) \\ &+ \frac{\mathrm{Pe}^{\mathrm{act}}}{\overline{\ell}}(\hat{\boldsymbol{q}}_r \times \boldsymbol{\partial}_{\hat{\boldsymbol{q}}_r})^2.\end{aligned} \tag{2.238}$$

As usual, we will omit the bars in the following sections and reintroduce them as necessary to avoid ambiguities.

2.5.2. Moment expansion for the bath-particle-distribution

In the following we will derive equations of motion for the bath particle density around the probe and their orientation. We assume that the probe particle is pulled with a constant velocity along its symmetry axis, which is defined to be the z-axis, see Figure 2.5. Furthermore, we assume that its orientation remains fixed as well. We only consider pairwise interactions of one bath particle with the probe. Both particles are modeled as hard particles, which translates

into no-flux boundary conditions on the excluded volume. These are the conditions under which we derived the Smoluchowski equation of the previous section.

Starting from the Smoluchowski equation (2.238), we will do a low density expansion for the bath-probe pair correlation function, following [SB05, Sec. IV], [KB05, Sec. II.A] or [KB06, Sec. 2]. After that, we will expand its dependency on the orientation of the bath particles in terms of orientational moments such as the average orientation, following [YB15b]. Closing this series of equations, we obtain a partial differential equation for the mean bath particle density n and the polar order field $\boldsymbol{m}$ (definitions see below).

We start with a Fourier transform in the variable $\boldsymbol{r}_p \to \boldsymbol{k}$. According to (A.8) this is done by replacing $\boldsymbol{\partial}_p$ with $-\mathrm{i}\boldsymbol{k}$ and we get

$$\partial_t \Psi_2(\boldsymbol{k}, \boldsymbol{r}_r, \hat{\boldsymbol{q}}_r, t) = \Omega_{\boldsymbol{k}}^{\mathrm{fix}} \Psi_2(\boldsymbol{k}, \boldsymbol{r}_r, \hat{\boldsymbol{q}}_r, t) \tag{2.239a}$$

with

$$\begin{aligned}\Omega_{\boldsymbol{k}}^{\mathrm{fix}} =& \frac{\overline{D}(\hat{a})}{s}\left(\boldsymbol{\partial}_r^2 - \boldsymbol{k}^2 + 2\mathrm{i}\boldsymbol{k}\cdot\boldsymbol{\partial}_r\right) + \boldsymbol{\partial}_r^2 + \mathrm{Pe}^{\mathrm{ext}}\mathrm{i}k_z - \mathrm{Pe}^{\mathrm{act}}\boldsymbol{\partial}_r\cdot\hat{\boldsymbol{q}}_r + \mathrm{Pe}^{\mathrm{ext}}\partial_{r,z} \\ &+ \frac{\Delta D(\hat{a})}{s}\left(\partial_{r,z}^2 - k_z^2 + 2\mathrm{i}k_z\partial_{r,z} - \frac{1}{3}\left(\boldsymbol{\partial}_r^2 - \boldsymbol{k}^2 + 2\mathrm{i}\boldsymbol{k}\boldsymbol{\partial}_r\right)\right) + \frac{\mathrm{Pe}^{\mathrm{act}}}{\overline{\ell}}(\hat{\boldsymbol{q}}_r \times \boldsymbol{\partial}_{\hat{\boldsymbol{q}}_r})^2.\end{aligned} \tag{2.239b}$$

Next, we derive equations of motion for the one-particle probability

$$\Psi_1(\boldsymbol{k}, t) = \int \mathrm{d}\boldsymbol{r}_r \oint \mathrm{d}\hat{\boldsymbol{q}}_r\, \Psi_2(\boldsymbol{k}, \boldsymbol{r}_r, \hat{\boldsymbol{q}}_r, t) \tag{2.240}$$

by integrating (2.239) over $\boldsymbol{r}_r \in \mathbb{R}^3 \setminus \mathcal{V}^{\mathrm{exc}}$ and $\hat{\boldsymbol{q}}_r \in \hat{S}$, which leads to

$$\begin{aligned}\partial_t \Psi_1(\boldsymbol{k}, t) =& \left(-\frac{\overline{D}(\hat{a})}{s}\boldsymbol{k}^2 + \frac{\Delta D(\hat{a})}{s}\left(-k_z^2 + \frac{1}{3}\boldsymbol{k}^2\right) + \mathrm{Pe}^{\mathrm{ext}}\mathrm{i}k_z\right)\Psi_1(\boldsymbol{k}, t) \\ &+ \int \mathrm{d}\boldsymbol{r}_r \oint \mathrm{d}\hat{\boldsymbol{q}}_r \left(\frac{\overline{D}(\hat{a})}{s}\mathrm{i}\boldsymbol{k} + \frac{\Delta D(\hat{a})}{s}\left(\mathrm{i}k_z\hat{\boldsymbol{z}} - \frac{\mathrm{i}\boldsymbol{k}}{3}\right)\right)\cdot\boldsymbol{\partial}_r \Psi_2(\boldsymbol{k}, \boldsymbol{r}_r, \hat{\boldsymbol{q}}_r, t).\end{aligned} \tag{2.241}$$

For this result, we used that the boundary condition $\boldsymbol{n}\cdot\boldsymbol{j}_r = 0$ eliminates all contributions from the flux $\boldsymbol{j}_r$ with the divergence theorem and by a version of Stokes' theorem (cf. [Dho96, Sec. 4.8.3, p. 218]) we have $\oint \mathrm{d}\hat{\boldsymbol{q}}_r\, \boldsymbol{\partial}_r^R(\ldots) = 0$. Unfortunately, there remains one term, which depends on the two particle density Ψ_2 so that we cannot solve this equation for the one particle density Ψ_1 on its own.

To overcome this problem, we make the ansatz

$$\Psi_2(\boldsymbol{k}, \boldsymbol{r}_r, \hat{\boldsymbol{q}}_r, t) = n_b g(\boldsymbol{k}, \boldsymbol{r}_r, \hat{\boldsymbol{q}}_r, t)\Psi_1(\boldsymbol{k}, t), \tag{2.242}$$

where $g(\boldsymbol{k}, \boldsymbol{r}_r, \hat{\boldsymbol{q}}_r, t)$ is a generalized (because it includes the orientation) pair distribution function and n_b is the bath particle density. The product rule for differentiation applied on (2.242) leads to the following identity

$$n_b \Psi_1(\boldsymbol{k}, t)\partial_t g(\boldsymbol{k}, \boldsymbol{r}_r, \hat{\boldsymbol{q}}_r, t) = \partial_t \Psi_2(\boldsymbol{k}, \boldsymbol{r}_r, \hat{\boldsymbol{q}}_r, t) - n_b g(\boldsymbol{k}, \boldsymbol{r}_r, \hat{\boldsymbol{q}}_r, t)\partial_t \Psi_1(\boldsymbol{k}, t). \tag{2.243}$$

Inserting the equations of motion for $\partial_t\Psi_2$ (2.239) and $\partial_t\Psi_1$ (2.241) and noticing that $\Psi_1(\boldsymbol{k}, t)$

can be interchanged with all operators, because there are only multiplications, we find the following result for the evolution of the pair distribution function $g(\boldsymbol{k}, \boldsymbol{r}_r, \hat{\boldsymbol{q}}_r, t)$

$$\begin{aligned}\partial_t g = &\left(\frac{\overline{D}(\hat{a})}{s} \left(\boldsymbol{\partial}_r^2 + 2\mathrm{i}\boldsymbol{k}\cdot\boldsymbol{\partial}_r \right) + \boldsymbol{\partial}_r^2 - \mathrm{Pe}^{\mathrm{act}} \boldsymbol{\partial}_r \cdot \hat{\boldsymbol{q}}_r + \mathrm{Pe}^{\mathrm{ext}} \partial_{r,z} + \frac{\mathrm{Pe}^{\mathrm{act}}}{\overline{\ell}} (\hat{\boldsymbol{q}}_r \times \boldsymbol{\partial}_{\hat{\boldsymbol{q}}_r})^2 \right. \\ &\left. + \frac{\Delta D(\hat{a})}{s} \left(\partial_{r,z}^2 + 2\mathrm{i}k_z \partial_{r,z} - \frac{1}{3} \left(\boldsymbol{\partial}_r^2 + 2\mathrm{i}\boldsymbol{k}\boldsymbol{\partial}_r \right) \right) \right) g(\boldsymbol{k}, \boldsymbol{r}_r, \hat{\boldsymbol{q}}_r, t) \\ &- n_b g(\boldsymbol{k}, \boldsymbol{r}_r, \hat{\boldsymbol{q}}_r, t) \int \mathrm{d}\boldsymbol{r}_r \oint \mathrm{d}\hat{\boldsymbol{q}}_r \left(\frac{\overline{D}(\hat{a})}{s} \mathrm{i}\boldsymbol{k} + \frac{\Delta D(\hat{a})}{s} \left(\mathrm{i}k_z \hat{\boldsymbol{z}} - \frac{\mathrm{i}\boldsymbol{k}}{3} \right) \right) \cdot \boldsymbol{\partial}_r g(\boldsymbol{k}, \boldsymbol{r}_r, \hat{\boldsymbol{q}}_r, t).\end{aligned} \tag{2.244}$$

The last line would make life complicated, but as it is proportional to n_b, we can neglect it in the dilute limit.

The next step is to expand $g(\boldsymbol{k}, \boldsymbol{r}_r, \hat{\boldsymbol{q}}, t)$ in powers of $\boldsymbol{k}$ via

$$g(\boldsymbol{k}, \boldsymbol{r}_r, \hat{\boldsymbol{q}}_r, t) = g_0(\boldsymbol{r}_r, \hat{\boldsymbol{q}}_r, t) + \mathrm{i}\boldsymbol{k} \cdot \boldsymbol{d}(\boldsymbol{r}_r, \hat{\boldsymbol{q}}_r, t) + \mathcal{O}(k^2). \tag{2.245}$$

The expansion coefficients g_0 and $\boldsymbol{d}$ are functions of the remaining variables and have to be determined such that (2.244) is solved up to the desired order in $\boldsymbol{k}$. $g_0(\boldsymbol{r}_r, \hat{\boldsymbol{q}}_r, t)$ describes the mean configuration of bath particles around the probe, while $\boldsymbol{d}(\boldsymbol{r}_r, \hat{\boldsymbol{q}}_r, t)$ is a "probability-weighted displacement, or fluctuation field, which gives the strength and direction of 'kicks' from probe-bath interactions" [HZ16, p. 747]. For the zeroth order in k we obtain

$$\partial_t g_0(\boldsymbol{r}_r, \hat{\boldsymbol{q}}_r, t) = \Omega_0 g_0(\boldsymbol{r}_r, \hat{\boldsymbol{q}}_r, t) \tag{2.246}$$

and for the first order in k the three equations[21] (to be read component-wise)

$$\partial_t \boldsymbol{d}(\boldsymbol{r}_r, \hat{\boldsymbol{q}}_r, t) = \Omega_0 \boldsymbol{d}(\boldsymbol{r}_r, \hat{\boldsymbol{q}}_r, t) + \boldsymbol{\Omega}_1 g_0(\boldsymbol{r}_r, \hat{\boldsymbol{q}}_r, t) \tag{2.247}$$

with the operators

$$\begin{aligned}\Omega_0 = &\left(1 + \frac{\overline{D}(\hat{a})}{s} \right) \boldsymbol{\partial}_r^2 + \frac{\Delta D(\hat{a})}{s} \left(\partial_{r,z}^2 - \frac{1}{3} \boldsymbol{\partial}_r^2 \right) + \mathrm{Pe}^{\mathrm{ext}} \partial_{r,z} \qquad (2.248a) \\ &- \mathrm{Pe}^{\mathrm{act}} \boldsymbol{\partial}_r \cdot \hat{\boldsymbol{q}}_r + \frac{\mathrm{Pe}^{\mathrm{act}}}{\overline{\ell}} (\hat{\boldsymbol{q}}_r \times \boldsymbol{\partial}_{\hat{\boldsymbol{q}}_r})^2, \\ \boldsymbol{\Omega}_1 = &\, 2 \left(\frac{\overline{D}(\hat{a})}{s} \boldsymbol{\partial}_r + \frac{\Delta D(\hat{a})}{s} \left(\hat{\boldsymbol{z}} \partial_{r,z} - \frac{1}{3} \boldsymbol{\partial}_r \right) \right), \qquad (2.248b)\end{aligned}$$

and the boundary conditions

$$0 = \boldsymbol{n} \cdot \left[\left(\left(\frac{\overline{D}(\hat{a})}{s} + \frac{\Delta D(\hat{a})}{s} \left(\hat{\boldsymbol{z}}\hat{\boldsymbol{z}} - \frac{1}{3}\mathbb{1} \right) \right) \boldsymbol{\partial}_r - \mathrm{Pe}^{\mathrm{ext}} \hat{\boldsymbol{z}} \right) g_0(\boldsymbol{r}_r, \hat{\boldsymbol{q}}_r, t) \right], \tag{2.249a}$$

$$0 = \boldsymbol{n} \cdot \left[\left(\boldsymbol{\partial}_r - \mathrm{Pe}^{\mathrm{act}} \hat{\boldsymbol{q}}_r + 2\mathrm{Pe}^{\mathrm{ext}} \hat{\boldsymbol{z}} \right) g_0(\boldsymbol{r}_r, \hat{\boldsymbol{q}}_r, t) \right], \tag{2.249b}$$

[21] Since (2.244) has to be solved for any choice of $\boldsymbol{k}$, we obtain three equations for the choices $\boldsymbol{k} = (k_x, 0, 0)$, $\boldsymbol{k} = (0, k_y, 0)$ and $\boldsymbol{k} = (0, 0, k_z)$.

for $g_0(\boldsymbol{r}_r, \hat{\boldsymbol{q}}_r, t)$ with $\boldsymbol{r}_r \in \partial\mathcal{V}^{\text{exc}}$ and $\hat{\boldsymbol{q}}_r \in \hat{S}$ and

$$0 = \boldsymbol{n} \cdot \left[\left(\frac{\overline{D}(\hat{a})}{s} + \frac{\Delta D(\hat{a})}{s} \left(\hat{\boldsymbol{z}}\hat{\boldsymbol{z}} - \frac{1}{3}\mathbb{1} \right) \right) \left(\boldsymbol{\partial}_r d_i(\boldsymbol{r}_r, \hat{\boldsymbol{q}}_r, t) + \hat{\boldsymbol{i}} g_0(\boldsymbol{r}_r, \hat{\boldsymbol{q}}_r, t) \right) - \mathrm{Pe}^{\text{ext}} \hat{\boldsymbol{z}} d_i(\boldsymbol{r}_r, \hat{\boldsymbol{q}}_r, t) \right], \tag{2.250a}$$

$$0 = \boldsymbol{n} \cdot \left[\left(\boldsymbol{\partial}_r - \mathrm{Pe}^{\text{act}} \hat{\boldsymbol{q}}_r + 2\mathrm{Pe}^{\text{ext}} \hat{\boldsymbol{z}} \right) d_i(\boldsymbol{r}_r, \hat{\boldsymbol{q}}_r, t) \right], \tag{2.250b}$$

for $\boldsymbol{r}_r \in \partial\mathcal{V}^{\text{exc}}$ and $\hat{\boldsymbol{q}}_r \in \hat{S}$. $\hat{\boldsymbol{i}}$ denotes the vector in direction i. Note that the second boundary conditions (derived from $\boldsymbol{n} \cdot \boldsymbol{j}_r^T$) have been simplified by subtracting the first ones (derived from $\boldsymbol{n} \cdot \boldsymbol{j}_p^T$). While the pair correlation function can be used to determine the friction coefficient (via the force, see Section 2.5.4) or the velocity (see [HZ16, p. 748, Eq. (3.7)]), the fluctuation field leads to diffusion coefficients (see [ZB10, p. 195, Eq. (2.12)] and [HZ16, p. 748, Eq. (3.8)]). In the following, we will focus on the the pair correlation function, even though this scheme can also be applied to the fluctuation field.

Finally, we average over all probe positions $\boldsymbol{r}_p$. The information about the orientational degree of freedom will be expanded in the corresponding moments of the probability distribution (see [SS15, p. 326, Eq. (9.6)]), namely the *average bath particle* density

$$n(\boldsymbol{r}_r, t) = \int \mathrm{d}\boldsymbol{r}_p \int \mathrm{d}\hat{\boldsymbol{q}}_r \, \Psi_2(\boldsymbol{r}_p, \boldsymbol{r}_r, \hat{\boldsymbol{q}}_r, t), \tag{2.251a}$$

the *polar order field*

$$\boldsymbol{m}(\boldsymbol{r}_r, t) = \int \mathrm{d}\boldsymbol{r}_p \int \mathrm{d}\hat{\boldsymbol{q}}_r \, \hat{\boldsymbol{q}}_r \Psi_2(\boldsymbol{r}_p, \boldsymbol{r}_r, \hat{\boldsymbol{q}}_r, t), \tag{2.251b}$$

and the *nematic order field*

$$\boldsymbol{Q}(\boldsymbol{r}_r, t) = \int \mathrm{d}\boldsymbol{r}_p \int \mathrm{d}\hat{\boldsymbol{q}}_r \left(\hat{\boldsymbol{q}}_r \hat{\boldsymbol{q}}_r - \frac{1}{3}\mathbb{1} \right) \Psi_2(\boldsymbol{r}_p, \boldsymbol{r}_r, \hat{\boldsymbol{q}}_r, t). \tag{2.251c}$$

These definitions can be reformulated using the Fourier transformed probability

$$\begin{aligned} n(\boldsymbol{r}_r, t) = &\int \mathrm{d}\boldsymbol{r}_p \int \mathrm{d}\hat{\boldsymbol{q}}_r \, \Psi_2(\boldsymbol{r}_p, \boldsymbol{r}_r, \hat{\boldsymbol{q}}_r, t) \exp(\mathrm{i}\boldsymbol{k} \cdot \boldsymbol{r}_r) \Big|_{\boldsymbol{k}=0} = \int \mathrm{d}\hat{\boldsymbol{q}}_r \, \Psi_2(\boldsymbol{k} = 0, \boldsymbol{r}_r, \hat{\boldsymbol{q}}_r, t) \\ = &n_b \int \mathrm{d}\hat{\boldsymbol{q}}_r \, g_0(\boldsymbol{r}_r, \hat{\boldsymbol{q}}_r, t), \end{aligned} \tag{2.252}$$

where we used that $\Psi_1(\boldsymbol{k} = 0, t) = 1$, due to the normalization. Similarly, we can replace $\int \mathrm{d}\boldsymbol{r}_p \, \Psi_2(\boldsymbol{r}_p, \boldsymbol{r}_r, \hat{\boldsymbol{q}}_r, t)$ by $n_b g_0(\boldsymbol{r}_r, \hat{\boldsymbol{q}}_r, t)$ in the other expressions. Hence, we can find a series of equations for the moments

$$\begin{aligned} \partial_t n(\boldsymbol{r}_r, t) = &\left(\left(1 + \frac{\overline{D}(\hat{a})}{s} \right) \boldsymbol{\partial}_r^2 + \frac{\Delta D(\hat{a})}{s} \left(\partial_{r,z}^2 - \frac{1}{3}\boldsymbol{\partial}_r^2 \right) + \mathrm{Pe}^{\text{ext}} \partial_{r,z} \right) n(\boldsymbol{r}_r, t) \\ &- \mathrm{Pe}^{\text{act}} \boldsymbol{\partial}_r \cdot \boldsymbol{m}(\boldsymbol{r}_r, t) \end{aligned} \tag{2.253a}$$

$$\partial_t \boldsymbol{m}(\boldsymbol{r}_r, t) = \left(\left(1 + \frac{\overline{D}(\hat{a})}{s} \right) \boldsymbol{\partial}_r^2 + \frac{\Delta D(\hat{a})}{s} \left(\partial_{r,z}^2 - \frac{1}{3}\boldsymbol{\partial}_r^2 \right) + \mathrm{Pe}^{\text{ext}} \partial_{r,z} - 2\frac{\mathrm{Pe}^{\text{act}}}{\overline{\ell}} \right) \boldsymbol{m}(\boldsymbol{r}_r, t)$$

$$- \mathrm{Pe}^{\mathrm{act}} \boldsymbol{\partial}_r \cdot \left(\boldsymbol{Q}(\boldsymbol{r}_r, t) + \frac{\mathbb{1}}{3} n(\boldsymbol{r}_r, t) \right) \tag{2.253b}$$

This kind of expansion can be done for a quite general class of Smoluchowski equations [SS15, p. 325, Eq. (9.3)] and also for higher moments [SS15, p. 327, Eqs. (9.8)-(9.10)]. As the last equation depends on $\boldsymbol{Q}$, we would need another equation to determine $\boldsymbol{Q}$, but for a first approach, we will close this set of equations by setting $\boldsymbol{Q} = 0$, which has been shown to be sufficient for systems like ours [YB15a, p. R1-3 and Appendix B].

For the boundary conditions of $n(\boldsymbol{r}_r, t)$ and the components of $\boldsymbol{m}(\boldsymbol{r}_r, t)$ do the same moment expansion, based on the boundary conditions (2.249). Since the variable $\boldsymbol{r}_p$ has been integrated out, we only need to consider the boundary condition derived for the flux $\boldsymbol{j}_r$, which can be obtained by adding both boundary conditions in (2.249). This boundary condition translates into a no-flux boundary condition for the fields $n(\boldsymbol{r}_r, t)$ and $\boldsymbol{m}(\boldsymbol{r}_R, t)$ on the excluded volume surface $\partial\mathcal{V}^{\mathrm{exc}}$

$$0 = \boldsymbol{n} \cdot \boldsymbol{j}_n(\boldsymbol{r}_r, t) \tag{2.254a}$$

$$0 = \boldsymbol{n} \cdot \boldsymbol{j}_{m,i}(\boldsymbol{r}_r, t) \tag{2.254b}$$

with the fluxes (omitting the argument $\hat{a}$ of the diffusion coefficients for brevity)

$$\boldsymbol{j}_n(\boldsymbol{r}_r, t) = - \left(\left(1 + \frac{\overline{D}}{s} \right) \boldsymbol{\partial}_r + \frac{\Delta D}{s} \left(\hat{\boldsymbol{z}} \partial_{r,z} - \frac{1}{3} \boldsymbol{\partial}_r \right) + \mathrm{Pe}^{\mathrm{ext}} \hat{\boldsymbol{z}} \right) n(\boldsymbol{r}_r, t) + \mathrm{Pe}^{\mathrm{act}} \boldsymbol{m}(\boldsymbol{r}_r, t), \tag{2.255a}$$

$$\boldsymbol{j}_{m,i}(\boldsymbol{r}_r, t) = - \left(\left(1 + \frac{\overline{D}}{s} \right) \boldsymbol{\partial}_r + \frac{\Delta D}{s} \left(\hat{\boldsymbol{z}} \partial_{r,z} - \frac{1}{3} \boldsymbol{\partial}_r \right) + \mathrm{Pe}^{\mathrm{ext}} \hat{\boldsymbol{z}} \right) m_i(\boldsymbol{r}_r, t) + \mathrm{Pe}^{\mathrm{act}} \frac{1}{3} \hat{\boldsymbol{i}} n(\boldsymbol{r}_r, t). \tag{2.255b}$$

These boundary conditions specify only the value of the derivative on the boundary and thus do not determine the values of n and $\boldsymbol{m}$ uniquely, since any multiple of $(n, \boldsymbol{m})$ will solve these equations and the boundary conditions, too. We therefore require additionally, that the bath particle density $n(\boldsymbol{r}, t)$ approaches the average value far from the probe, i.e. $n(\boldsymbol{r}, t) \to n_b$ for $|\boldsymbol{r}| \to \infty$.

The excluded volume of two spheres is a sphere with a diameter being the sum of the diameters of the two spheres. However, the shape of the excluded volume of a spheroid and a sphere is similar to a spheroid, but technically no spheroid anymore. Nevertheless we can approximate the excluded volume by a spheroid with semiaxes $(d_p + d)/2$ and $(l_p + d)/2$, which correspond to $(s + 1)/2$ and $(s\hat{a} + 1)/2$ in dimensionless units. A different point of view would be to assume the excluded volume to be an exact spheroid and treat the diffusion coefficients as approximations for the non-spheroidal probe. Both cases are visualized in Figure 2.6.

To summarize, we have found equations of motion for the average density of bath particles $n(\boldsymbol{r}, t)$ and their average orientation $\boldsymbol{m}(\boldsymbol{r}, t)$ at a given distance $\boldsymbol{r}$ from the center of the probe. These partial differential equations are given by

$$\partial_t n(\boldsymbol{r}, t) = \left(\left(1 + \frac{\overline{D}(\hat{a})}{s} \right) \boldsymbol{\partial}_r^2 + \frac{\Delta D(\hat{a})}{s} \left(\partial_{r,z}^2 - \frac{1}{3} \boldsymbol{\partial}_r^2 \right) + \mathrm{Pe}^{\mathrm{ext}} \partial_{r,z} \right) n(\boldsymbol{r}, t) \tag{2.256a}$$

$$
\begin{aligned}
&- \mathrm{Pe}^{\mathrm{act}} \sum_{i=1}^{3} \partial_{r,i} m_i(\boldsymbol{r},t) \\
\partial_t m_i(\boldsymbol{r},t) = &\left(\left(1 + \frac{\overline{D}(\hat{a})}{s} \right) \boldsymbol{\partial}_r^2 + \frac{\Delta D(\hat{a})}{s} \left(\partial_{r,z}^2 - \frac{1}{3} \boldsymbol{\partial}_r^2 \right) + \mathrm{Pe}^{\mathrm{ext}} \partial_{r,z} - 2 \frac{\mathrm{Pe}^{\mathrm{act}}}{\bar{\ell}} \right) \boldsymbol{m}(\boldsymbol{r},t) \\
&- \frac{\mathrm{Pe}^{\mathrm{act}}}{3} \partial_{r,i} n(\boldsymbol{r},t)
\end{aligned} \tag{2.256b}
$$

with no flux boundary conditions for the fluxes (2.255) on the surface of the excluded volume, which will be described by a spheroid of semiaxes $(s+1)/2$ (x and y direction) and $(s\hat{a}+1)/2$ (z-direction).

2.5.3. Transformation to spheroidal coordinates

For both, analytical and numerical solutions it is instructive to describe the problem in coordinates which reflect the symmetry of the problem. In this case we choose spheroidal coordinates, which simplify the boundary condition. The coordinate transform from Cartesian for prolate[22] spheroidal coordinates is given by [MS71, p. 28, Table 1.06][23].

$$
\begin{aligned}
x &= c \sinh\xi \sin\eta \cos\phi \\
y &= c \sinh\xi \sin\eta \sin\phi \\
z &= c \cosh\xi \cos\eta.
\end{aligned} \tag{2.257}
$$

with $0 \leq \xi < \infty$, $0 \leq \eta \leq \pi$, $0 \leq \phi < 2\pi$. The coordinate surface $\xi = \text{const}$ describes the surface of a spheroid with semiaxes $a_0 = c\sinh\xi$ and $b_0 = c\cosh\xi$ as shown in Figure 2.6. The condition that $\xi = \xi_0$ describes the surface of our excluded volume requires

$$
c = \frac{1}{2} \sqrt{s^2(\hat{a}^2 - 1) + 2s(\hat{a} - 1)} \tag{2.258a}
$$

[22] There is also oblate spheroidal coordinates for oblate spheroids. The conversion from one to the other can be found in Appendix D.5.

[23] Our notation is based on the convention used by [KB08; WeiPro]. The corresponding symbols for [MS71] are $c \hat{=} a$, $\xi \hat{=} \eta$, $\eta \hat{=} \theta$, $\phi \hat{=} \psi$. A third convention is used by [Fla57], who also gives an overview over the conventions used in different books.

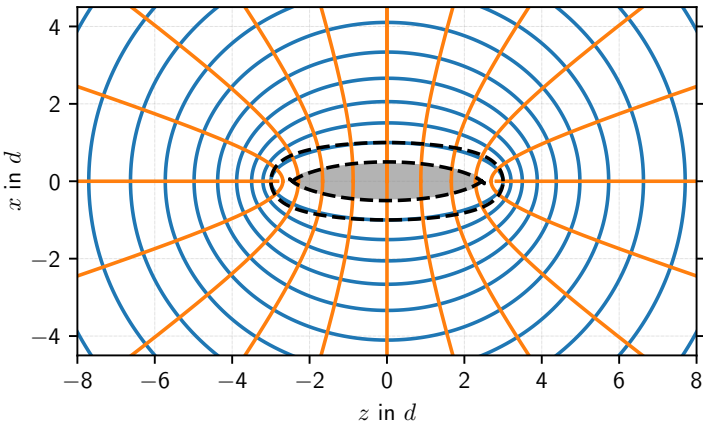

Figure 2.6.: Sketch of spheroidal coordinates. Blue lines show $\xi = \text{const}$, orange lines $\eta = \text{const}$. Not shown is the cylindrical symmetry around the z-axis (to the right). The spheroid with $\hat{a} = 5$ is shown in grey and the innermost blue line corresponds to a spheroid with semiaxes $s\hat{a}+1$ and $s+1$. The exact excluded volume surfaces are shown as dashed black lines.

$$\xi_0 = \frac{1}{2}\ln\left(\frac{s(\hat{a}+1)+2}{s(\hat{a}-1)}\right) \tag{2.258b}$$

Together with the coordinates, we have to transform the differential operators (as described in Section D.2), the vector components (as described in Section D.3) and their derivatives (as described in Section D.2). It turns out that the ϕ dependency can be separated. If the initial conditions do not depend on ϕ, this symmetry is conserved so that the fields depend on ξ, η and t only. Carrying out all calculations leads to

$$\begin{aligned}
\partial_t n(\xi,\eta,t) = &\left(1+\frac{\overline{D}(\hat{a})}{s}\right) C^2 \left(\frac{\cosh(\xi)}{\sinh(\xi)}\partial_\xi + \frac{\cos(\eta)}{\sin(\eta)}\partial_\eta + \partial_\xi^2 + \partial_\eta^2\right) n(\xi,\eta,t) \\
&+ \mathrm{Pe}^{\mathrm{ext}} c C^2 \left(\cos(\eta)\sinh(\xi)\partial_\xi - \sin(\eta)\cosh(\xi)\partial_\eta\right) n(\xi,\eta,t) \\
&- \mathrm{Pe}^{\mathrm{act}} \Big(C\left(\partial_\xi m_\xi(\xi,\eta,t) + \partial_\eta m_\eta(\xi,\eta,t)\right) \\
&\qquad + c^2 C^3 \left(\sin^2(\eta) + 2\sinh^2(\xi)\right) \frac{\cosh(\xi)}{\sinh(\xi)} m_\xi(\xi,\eta,t) \\
&\qquad + c^2 C^3 \left(2\sin^2(\eta) + \sinh^2(\xi)\right) \frac{\cos(\eta)}{\sin(\eta)} m_\eta(\xi,\eta,t)\Big) + \mathcal{O}\left(\frac{\Delta D(\hat{a})}{s}\right)
\end{aligned} \tag{2.259a}$$

with the abbreviation $C^{-1} = c(\sin^2(\eta) + \sinh^2(\xi))^{1/2}$, which is one of the metric coefficients in the system. We skip the terms related anisotropic part of the diffusion tensor as it is even longer than the equations presented above. For constant velocity microrheology, which we will analyze in the following, diffusion is suppressed anyway.

For the components of the polar order field $\boldsymbol{m}$ we find in spheroidal coordinates

$$\begin{aligned}
\partial_t m_\xi(\xi,\eta,t) = &\tilde{D} C^2 \left(\frac{\cosh(\xi)}{\sinh(\xi)}\partial_\xi + \frac{\cos(\eta)}{\sin(\eta)}\partial_\eta + \partial_\xi^2 + \partial_\eta^2\right) m_\xi(\xi,\eta,t) \\
&+ \tilde{D} C^2 \Bigg(- \left(\frac{\cosh(4\xi) - \cos(4\eta)}{8(\sin^2(\eta) + \sinh^2(\xi))^2} + \frac{\cosh^2(\xi)}{\sinh^2(\xi)}\right) m_\xi(\xi,\eta,t) \\
&\qquad - 2\frac{\cos(\eta)}{\sin(\eta)} \frac{\sinh(2\xi)}{\cosh(2\xi) - \cos(2\eta)} m_\eta(\xi,\eta,t)\Bigg) \\
&+ 2\tilde{D} C^2 \left(\frac{\sin(2\eta)\partial_\xi m_\eta(\xi,\eta,t) - \sinh(2\xi)\partial_\eta m_\eta(\xi,\eta,t)}{\cosh(2\xi) - \cos(2\eta)}\right) \\
&+ \mathrm{Pe}^{\mathrm{ext}} c C^2 \left(\cos(\eta)\sinh(\xi)\partial_\xi - \sin(\eta)\cosh(\xi)\partial_\eta\right) m_\xi(\xi,\eta,t) \\
&+ \mathrm{Pe}^{\mathrm{ext}} c C^2 \sinh(\xi)\sin(\eta) \frac{\cosh^2(\xi) + \cos^2(\eta)}{\cosh^2(\xi) - \cos^2(\eta)} m_\eta(\xi,\eta,t) \\
&- 2\frac{\mathrm{Pe}^{\mathrm{act}}}{\ell} m_\xi(\xi,\eta,t) - C\frac{\mathrm{Pe}^{\mathrm{act}}}{3}\partial_\xi n(\xi,\eta,t) + \mathcal{O}\left(\frac{\Delta D(\hat{a})}{s}\right),
\end{aligned} \tag{2.259b}$$

where we used the abbreviation $\tilde{D} = (1 + \overline{D}(\hat{a})/s)$ and

$$\begin{aligned}
\partial_t m_\eta(\xi,\eta,t) =& \tilde{D}C^2 \left(\frac{\cosh(\xi)}{\sinh(\xi)}\partial_\xi + \frac{\cos(\eta)}{\sin(\eta)}\partial_\eta + \partial_\xi^2 + \partial_\eta^2 \right) m_\eta(\xi,\eta,t) \\
&+ \tilde{D}C^2 \left(-2\frac{\cosh(\xi)}{\sinh(\xi)} \frac{\sin(2\eta)}{\cosh(2\xi) - \cos(2\eta)} m_\xi(\xi,\eta,t) \right. \\
&\qquad \left. - \left(\frac{\cosh(4\xi) - \cos(4\eta)}{8(\sin^2(\eta) + \sinh^2(\xi))^2} + \frac{\cos^2(\eta)}{\sin^2(\eta)} \right) m_\eta(\xi,\eta,t) \right) \\
&+ 2\tilde{D}C^2 \left(\frac{-\sin(2\eta)\partial_\xi m_\xi(\xi,\eta,t) + \sinh(2\xi)\partial_\eta m_\xi(\xi,\eta,t)}{\cosh(2\xi) - \cos(2\eta)} \right) \\
&+ \mathrm{Pe}^{\mathrm{ext}} cC^2 \left(\cos(\eta)\sinh(\xi)\partial_\xi - \sin(\eta)\cosh(\xi)\partial_\eta \right) m_\eta(\xi,\eta,t) \\
&- \mathrm{Pe}^{\mathrm{ext}} cC^2 \sinh(\xi)\sin(\eta) \frac{\cosh^2(\xi) + \cos^2(\eta)}{\cosh^2(\xi) - \cos^2(\eta)} m_\xi(\xi,\eta,t) \\
&- 2\frac{\mathrm{Pe}^{\mathrm{act}}}{\ell} m_\eta(\xi,\eta,t) - \frac{\mathrm{Pe}^{\mathrm{act}}}{3} C\partial_\eta n(\xi,\eta,t) + \mathcal{O}\left(\frac{\Delta D(\hat{a})}{s} \right).
\end{aligned} \tag{2.259c}$$

The reason for the extra terms for the polar order field components is the transformation of the components into the local coordinate frame. Since it depends on the position all derivatives act on the unit vectors as well (see Section D.3 for the details). The main reason for this coordinate transform is that the boundary condition simplifies significantly. Since $\xi = \xi_0$ describes the surface of the excluded volume and the new coordinates are orthogonal, the normal of the surface is given by $\hat{\boldsymbol{\xi}}$. Thus, the boundary conditions reduce to

$$0 = \hat{\boldsymbol{\xi}} \cdot \boldsymbol{j}_n = (\boldsymbol{j}_n)_\xi, \tag{2.260a}$$

$$0 = \hat{\boldsymbol{\xi}} \cdot \boldsymbol{j}_{m,i} = (\boldsymbol{j}_{m,i})_\xi, \tag{2.260b}$$

for $i \in \{x, y, z\}$, $\xi = \xi_0$. After a transformation into the prolate spheroidal components, we find

$$0 = \tilde{D}C\partial_\xi n(\xi_0,\eta,t) + \mathrm{Pe}^{\mathrm{ext}} cC \sinh(\xi_0)\cos(\eta) n(\xi_0,\eta,t) - \mathrm{Pe}^{\mathrm{act}} m_\xi(\xi_0,\eta,t) + \mathcal{O}(\Delta D) \tag{2.261a}$$

$$\begin{aligned}
0 =& \tilde{D}C \left(\frac{\sin(2\eta)}{\cosh(2\xi_0) - \cos(2\eta)} m_\eta(\xi_0,\eta,t) + \partial_\xi m_\xi(\xi_0,\eta,t) \right) \\
&+ \mathrm{Pe}^{\mathrm{ext}} cC \sinh(\xi_0)\cos(\eta) m_\xi(\xi_0,\eta,t) - \frac{\mathrm{Pe}^{\mathrm{act}}}{3} n(\xi_0,\eta,t) + \mathcal{O}(\Delta D)
\end{aligned} \tag{2.261b}$$

$$\begin{aligned}
0 =& \tilde{D}C \left(-\frac{\sin(2\eta)}{\cosh(2\xi_0) - \cos(2\eta)} m_\xi(\xi_0,\eta,t) + \partial_\xi m_\eta(\xi_0,\eta,t) \right) \\
&+ \mathrm{Pe}^{\mathrm{ext}} cC \sinh(\xi_0)\cos(\eta) m_\eta(\xi_0,\eta,t) + \mathcal{O}(\Delta D).
\end{aligned} \tag{2.261c}$$

Since these boundary conditions only determine the value for the derivative, we need another boundary condition to obtain a unique solution. We require that the bath particle density far away has its average value n_b and that the polar order field vanishes there, too. In mathematical terms

$$\lim_{\xi\to\infty} n(\xi,\eta) = n_b, \qquad \lim_{\xi\to\infty} m_\xi(\xi,\eta) = 0, \qquad \lim_{\xi\to\infty} m_\eta(\xi,\eta) = 0. \tag{2.262}$$

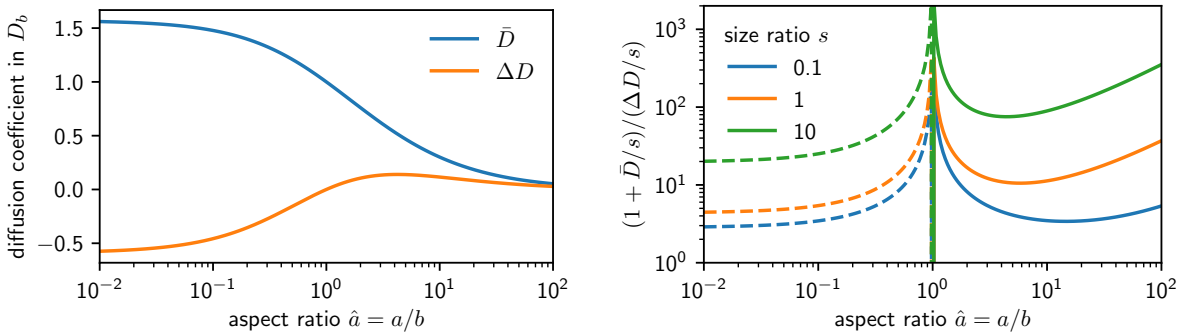

Figure 2.7.: Left: Dimensionless diffusion coefficients for spheroidal particles, see (2.272). Oblate spheroids can be found on the left, prolate ones on the right and all spheroids have the same diameter perpendicular to the symmetry axis. Right: Ratio of the isotropic and the anisotropic prefactors for different aspect ratios $\hat{a}$ and probe to bath particle size ratios s. Dashed lines indicate negative values of the ratio.

Finally, we require single-valuedness for the density field $n(\xi, 0) = n(\xi, 2\pi)$ and the components of the polar order field $m_\alpha(\xi, 0) = m_\alpha(\xi, 2\pi)$ for a continuous solution.

Since some complications arise from the fact that the derivatives associated with ΔD are not compatible with the spheroidal symmetry, we will have a look at the importance of this term. The corresponding values are shown in Figure 2.7 for different aspect ratios $\hat{a}$ and different size ratios s.

We note that the anisotropic part becomes less important when the sizes ratio increases. If the probe is very large compared to the bath particles we can neglect these terms. For oblate spheroids the signs of these two terms are different, but the same for prolate spheroids. In any case the modulus of the isotropic term is always larger than the modulus of the anisotropic one. For aspect ratios $0.5 \leq \hat{a} \leq 1.5$ the isotropic term is at least one order of magnitude larger than the anisotropic term. For very large aspect ratios we find that the anisotropic part becomes less and less important because both $\overline{D}$ and ΔD tend to zero. For small aspect ratios (oblate spheroids) the modulus of the ratio approaches a constant value, which is not very large compared to 1.

2.5.4. The microviscosity increment or the friction of the probe

In the previous section we derived equations of motion for the bath particle density distribution $n(\boldsymbol{r})$ around the probe. This density, or more precisely the values on the excluded volume surface can be used to calculate the average force on the probe as follows. According to [KB08, p. 171, Eq. (9)], the average force on a body pulled with velocity $\boldsymbol{u}$ through a complex fluid is given by

$$\langle \boldsymbol{F}_{\mathrm{ex}} \rangle = M^{-1}\boldsymbol{u} + k_{\mathrm{B}}T \oint_{\partial \mathcal{V}^{\mathrm{exc}}} \boldsymbol{n} n(\boldsymbol{r}) \mathrm{d}S\,,, \tag{2.263}$$

where M is the hydrodynamic mobility tensor proportional to the the diffusion matrix (2.57). In other words $M^{-1}\boldsymbol{u}$ is the hydrodynamic friction force experienced by the probe through the motion in the solvent. In addition to that we have to consider the resistance from the interaction with the particles from the complex fluid. This is essentially given by integrating

the forces on each surface element $\mathrm{d}S$, given by the surface normal $\boldsymbol{n}$ and the pressure of the particles $k_\mathrm{B}Tn\mathrm{d}S$. Summarizing both contributions into the microviscosity or friction tensor H via

$$\langle \boldsymbol{F}_\mathrm{ex} \rangle = H \langle \boldsymbol{u} \rangle , \tag{2.264}$$

we find

$$H = M^{-1} + k_\mathrm{B}T \oint_{\partial \mathcal{V}^\mathrm{exc}} \frac{\langle \boldsymbol{u} \rangle}{\langle u \rangle} \boldsymbol{n} n(\boldsymbol{r}) \mathrm{d}S . \tag{2.265}$$

When the probe is moving with constant velocity $\boldsymbol{u}^\mathrm{ext}$ along its axis of symmetry, there is only one nonvanishing force component. Let z be the direction of the motion, then the equation for the friction coefficient in this direction reads

$$\mu_\parallel = \frac{k_\parallel^T(\hat{a})}{3\pi\eta s d} + \frac{k_\mathrm{B}T}{u^\mathrm{ext}} \oint_{\partial \mathcal{V}^\mathrm{exc}} n_z n(\boldsymbol{r}) \mathrm{d}S , \tag{2.266}$$

where we inserted the mobility of the spheroidal probe as defined in (2.271). To make this quantity dimensionless, we scale by the free friction (without any other particles present) of the spheroidal probe

$$\overline{\mu}_\parallel = \mu_\parallel \frac{3\pi\eta d}{k_\parallel^T(\hat{a})} = 1 + \frac{k_\mathrm{B}T k_\parallel^T(\hat{a})}{u^\mathrm{ext}\eta 3\pi s d} \oint_{\partial \mathcal{V}^\mathrm{exc}} n_z n(\boldsymbol{r}) \mathrm{d}S . \tag{2.267}$$

Using the Péclet number Pe^ext from (2.232a) we find for the *microviscosity* or *friction increment*

$$\Delta\overline{\mu}_\parallel = \overline{\mu}_\parallel - 1 = \frac{k_\parallel^T(\hat{a}) d}{\mathrm{Pe}^\mathrm{ext} s} \oint_{\partial \mathcal{V}^\mathrm{exc}} n_z n(\boldsymbol{r}) \mathrm{d}S . \tag{2.268}$$

Furthermore, we can rewrite the bath particle density n in terms of the pair distribution function g via

$$n(\boldsymbol{r}) = n_b g(\boldsymbol{r}) = \frac{6\varphi}{\pi d^3} g(\boldsymbol{r}) \tag{2.269}$$

using the dimensionless packing fraction φ as parameter for the density.

For cylindrically symmetric $g(\boldsymbol{r})$, we can calculate the integral over ϕ and find

$$\Delta\overline{\mu}_\parallel = \frac{3\varphi k_\parallel^T(\hat{a})}{\mathrm{Pe}^\mathrm{ext}} \frac{(s+1)^2}{s} \int_0^\pi \frac{\sin(2\eta)}{2} g(\xi_0, \eta) \mathrm{d}\eta \tag{2.270}$$

for g given in prolate or oblate spheroidal coordinates, where $\xi = \xi_0$ describes the surface of the excluded volume. With this relation we can calculate the force on the probe, once we found the bath particle density around the probe.

A similar reasoning can be employed to calculate the average torque on the probe particle, which was done for active microrheology in a dilute colloidal suspension by Khair and Brady [KB08, Appendix C, p. 192, Eq. (C1)]. This also allows to characterize the stable modes for motion.

2.5.5. Diffusion coefficients for spheroids

Let us consider spheroids of length l (along the axis of symmetry) and diameter d. We define $\hat{a} = l/d$ to be the aspect ratio (length-to-diameter ratio). For $\hat{a} > 1$ we call the spheroid *prolate*, for $\hat{a} < 1$ *oblate*. The corresponding ellipsoid has semiaxes $a = b = d/2$ and $c = l/2$. In the following, we use the convention, that the index $\parallel$ indicates translation or rotation along an axis parallel to the axis of symmetry, while $\perp$ indicates translation or rotation along an axis perpendicular to the axis of symmetry.

We now quote the results for the diffusion coefficients of the spheroids described above from [Bre74, p. 209f][24]:

$$D_\perp^R = \frac{k_\mathrm{B}T}{\eta}\frac{1}{\pi d^3}k_\perp^R(\hat{a}), \tag{2.271a}$$

$$D_\perp^T = \frac{k_\mathrm{B}T}{\eta}\frac{1}{3\pi d}k_\perp^T(\hat{a}), \tag{2.271b}$$

$$D_\parallel^R = \frac{k_\mathrm{B}T}{\eta}\frac{1}{\pi d^3}k_\parallel^R(\hat{a}), \tag{2.271c}$$

$$D_\parallel^T = \frac{k_\mathrm{B}T}{\eta}\frac{1}{3\pi d}k_\parallel^T(\hat{a}), \tag{2.271d}$$

with

$$k_\perp^R(\hat{a}) = \frac{3}{2}\frac{2\beta\hat{a}^2 - \beta - \hat{a}}{\hat{a}^4 - 1}, \tag{2.272a}$$

$$k_\perp^T(\hat{a}) = \frac{3}{8}\frac{2\beta\hat{a}^2 - 3\beta + \hat{a}}{\hat{a}^2 - 1}, \tag{2.272b}$$

$$k_\parallel^R(\hat{a}) = \frac{3}{2}\frac{\hat{a} - \beta}{\hat{a}^2 - 1}, \tag{2.272c}$$

$$k_\parallel^T(\hat{a}) = \frac{3}{4}\frac{2\beta\hat{a}^2 - \beta - \hat{a}}{\hat{a}^2 - 1}, \tag{2.272d}$$

where

$$\beta = \begin{cases} \dfrac{\cosh^{-1}(\hat{a})}{(\hat{a}^2-1)^{1/2}}, & \hat{a} > 1 \quad \text{(prolate)} \\ \dfrac{\cos^{-1}(\hat{a})}{(1-\hat{a}^2)^{1/2}}, & \hat{a} < 1 \quad \text{(oblate).} \end{cases} \tag{2.272e}$$

The terms $k(\hat{a})$ accounting for the geometry of the particle are normalized in the sense that $k(\hat{a} = 1) = 1$. Thus, we recover the diffusion constants of a sphere by setting $k = 1$.

See also [HB65, p. 222-225] for a more detailed calculation of the translational friction coefficients.

[24] As we are only interested in these particular spheroids, we use a more compact notation.

3. Numerical implementation

> Numerical analysis is very much an experimental science.
>
> *(Peter Wynn, [Wyn64, p. 195])*

For a numerical solution we need to approximate the continuous functions $\phi^s_{\boldsymbol{q}}(t)$ in space and time by finite-dimensional vectors[1]. Furthermore, the memory integrals (2.139b) of the type

$$m_{\boldsymbol{q}}\left[\boldsymbol{\phi}^s(t)\right] = \int \mathrm{d}\boldsymbol{k}\, f(\boldsymbol{q},\boldsymbol{k})\phi^s_{\boldsymbol{k}}(t) \tag{3.1}$$

have to be approximated by finite sums and finally, we have to find numerical scheme to solve integral equations of Volterra type

$$X(t) + \int_0^t A(t-t')X(t')\mathrm{d}t' \;= B(t) \tag{3.2}$$

including versions with derivatives as well, which have to be approximated by finite differences. The details of how to do this properly will be worked out in this chapter.

In the following we will use the following nomenclature for the discretized versions of the variables. The wave vectors are given on a (non-uniform) grid with N_{q_x} elements perpendicular to the force direction and N_{q_z} elements parallel to the force direction:

$$q_x \mapsto q_x^m, \quad (0 \le m < N_{q_x}), \tag{3.3a}$$
$$q_z \mapsto q_z^n, \quad (0 \le n < N_{q_z}). \tag{3.3b}$$

As shown in Section 2.4.4, we can set $q_y = 0$ to simplify the calculations. The details for the choice of the grid will be discussed in Section 3.1. Based on this grid, we can define the discretized correlation functions and memory kernels

$$\phi^{\boldsymbol{s}}_{mn}(t) := \phi^{\boldsymbol{s}}_{(q_x^m,0,q_z^n)}(t), \tag{3.3c}$$
$$m^{\alpha\beta}_{mn}(t) := m^{\alpha\beta}_{(q_x^m,0,q_z^n)}(t). \tag{3.3d}$$

Their discretization is discussed in Section 3.2 and the time enters merely as a (continuous) parameter here. With this groundwork, we can define a numerical scheme to solve for the long time limit in Section 3.3 and extend it to find numerical solutions in Laplace space in Section 3.4. A different approach is needed to solve the integro-differential equation in time space. This is worked out in Section 3.5. First, general schemes for the solution of Volterra integral equations and integro-differential equations are introduced. Furthermore the so called

[1] To ensure compatibility with the codes, we use the letter $\boldsymbol{q}$ as generic index for the correlators, while the letter $\boldsymbol{k}$ appears in the memory integrals.

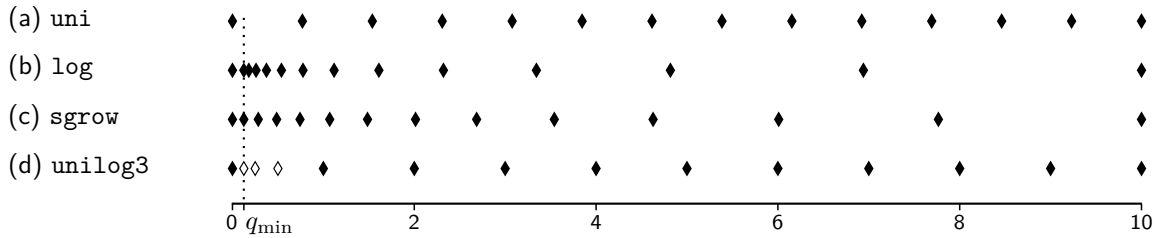

Figure 3.1.: Sketch of the different grids with $q_{\max} = 10$ and $N_q = 14$. All grids with a refinement for small numbers share the smallest non-zero grid point $q_{\min} = 0.125$. Note the coarse spacing of the logarithmic grid and the feature that the second point is much closer to the third one than to the first one. The open symbols for `unilog3` visualize the logarithmic part of this combined grid.

decimation scheme is described, which allows to solve the equations over several decades in time. Then all those parts are combined into the algorithm for the full model. The last section in this chapter is dedicated to the testing of the time evolution algorithm.

3.1. Wave vector discretization

Considering the symmetries of the correlation function, it is sufficient to discuss discretizations of the interval $[0, q_{\max}]$. From this interval we will choose N_q points, which will hopefully sample the shape of the correlation function adequately. We will briefly introduce four different types of grids: `uni`, `log`, `sgrow`, and `unilogX` (as they are labeled in the computer programs) and discuss their advantages and drawbacks. Sketches of the different grid types are shown in Figure 3.1.

`uni` – The *uniform grid* is the simplest choice. The interval is divided into N_q pieces of equal length $\Delta_q = q_{\max}/(N_q - 1)$ and the grid points are given by

$$q_m = m\Delta_q \quad (0 \leq m < N_q). \tag{3.4}$$

While this choice simplifies the integrations a lot, because the difference between grid points is always the same, it turned out that we need a high resolution at small wave vectors. Using a uniform grid would imply using a large N_q, because the lowest grid point is given by Δ_q, which makes the problem computationally more than demanding. In [Gru14, Fig. 4.11, p. 47] it was shown that the time per iteration scales like $N^{2.35\pm0.08}$, where $N = N_{q_x} N_{q_z}$ is the total number of grid points. For a two-dimensional uniform grid this implies that halving the step size Δ_q requires an increase of the computation time per iteration by a factor of 23 to 30. In order to finish the calculations for this PhD thesis in a lifetime, more sophisticated grids have to be used.

`log` – In order to cover several orders of magnitudes without too many points, we can use a uniform grid on a logarithmic axis, a *logarithmic grid*. Since 0 cannot be represented in this grid, we need to specify a minimal (non-zero) wave vector cutoff $q_{\min}$ as well. Then the grid is defined via

$$q_m = \begin{cases} 0, & m = 0, \\ q_{\min} \left(\frac{q_{\max}}{q_{\min}}\right)^{\frac{m-1}{N_q-2}}, & 0 < m < N_q. \end{cases} \tag{3.5}$$

The major drawback of this grid is that q_1 is much closer to q_2 than to 0 (for $(q_{\max}/q_{\min})^{\frac{1}{N_q-2}} < 2$), which looks like a gap in the grid for small wave vectors. If this quotient is chosen to be larger than 2, there will not be enough points for large wave vectors to reasonably sample the structure factor.

`sgrow` – To avoid this gap at small wave vectors, we can grow the intervals between the points exponentially instead of the points themselves. Again, we have to specify the minimal wave vector cutoff $q_{\min}$. The grid is then given by

$$q_m = q_{\min}\frac{\alpha^m - 1}{\alpha - 1} \quad (0 \leq m < N_q), \tag{3.6}$$

where α has to be determined numerically such that $(\alpha^{N_q-1} - 1)/(\alpha - 1) = q_{\max}/q_{\min}$. While having more evenly spaced points, this grid lacks the problem that changing cutoffs or number of grid points, will change the positions of all points in the grid. This behavior is not desirable, because the critical points of the fixed point iteration may depend sensitively on the grid. It is therefore better to distinguish the effects of extending the grid from those from changing the grid points themselves.

`unilogX` – Finally, we combine the uniform and the logarithmic grid. This grid consists of a uniform grid with N_{uni} points and stepsize $\Delta_q = q_{\max}/(N_{\text{uni}} - 1)$ for large wave vectors and a logarithmic grid of $X = N_{\log}$ points for small wave vectors. Hence, `unilog3` with $N_q = 14$ points consists of a uniform grid with $N_{\text{uni}} = 11$ points and $N_{\log} = 3$ points in the logarithmic part. To avoid the gap in the logarithmic grid as discussed for the `log` grid, we choose the following procedure: Take the interval $[0, \Delta_q]$ of the uniform grid and add a point at middle of this interval. Repeat this with the interval enclosed by 0 and the new point for $N_{\log}$ times. This effectively halves the step size every time and leads to the following definition

$$q_m = \begin{cases} 0, & m = 0, \\ \Delta_q 2^{m-1-N_{\log}}, & 0 < m \leq N_{\log}, \\ \Delta_q(m - N_{\log}), & N_{\log} < m < N_q, \end{cases} \tag{3.7}$$

hence $N_{\text{uni}} = N_q - N_{\log} = N_q - X$ and $\Delta_q = q_{\max}/(N_q - N_{\log} - 1)$. With this grid, we can reach quite small wave vectors $q_{\min} = 2^{-N_{\log}}\Delta_q$ while maintaining a moderate resolution Δ_q at large wave vectors. We can extend the grid in the logarithmic part or the uniform part separately and without changing the other points. Finally, this grid also allows a trick to speed up the Fourier transform as shown in Section A.5.1. For these reasons, this will be our main choice for the calculations.

3.2. Memory kernel discretization

In this section, we will show how to discretize our primitive memory functionals (2.160). First we will reduce the three dimensional integration to a two-dimensional one. Then, we will construct a discretized version of these integrals.

Using polar coordinates we can exploit the cylindrical symmetry of the correlator and express

the memory functionals in the following form

$$m^{\alpha\beta}_{q_x,0,q_z}\left[\boldsymbol{\phi}^s(t)\right] = \int_{-\infty}^{\infty} \mathrm{d}k_z \int_0^{\infty} \mathrm{d}\rho\, \phi^s_{\rho,0,k_z}(t)\rho J^{\alpha\beta}(q_x,\rho,q_z-k_z;t) \tag{3.8}$$

with

$$J^{xx}(q_x,k_x,\Delta;t) = \left(\frac{k_x^2}{2}+q_x^2\right)\overline{g}_0(q_x,k_x,\Delta;t) - 2q_xk_x\overline{g}_1(q_x,k_x,\Delta;t) + \frac{q_x^2}{2}\overline{g}_2(q_x,k_x,\Delta;t) \tag{3.9a}$$

$$J^{xz}(q_x,k_x,\Delta;t) = \Delta\Big(q_x\overline{g}_0(q_x,k_x,\Delta;t) - k_x\overline{g}_1(q_x,k_x,\Delta;t)\Big) \tag{3.9b}$$

$$J^{zz}(q_x,k_x,\Delta;t) = \Delta^2\overline{g}_0(q_x,k_x,\Delta;t) \tag{3.9c}$$

and

$$\overline{g}_i(q_x,k_x,\Delta;t) = \int_0^{2\pi} \mathrm{d}\theta\, \cos(i\theta) g\left(\sqrt{q_x^2+k_x^2+\Delta^2-2q_xk_x\cos(\theta)};t\right) \quad (i\in\{0,1,2\}), \tag{3.9d}$$

$$g(p;t) = \frac{1}{(2\pi)^3}\frac{(S_p^s)^2}{nS_p}\phi_p(t) \tag{3.9e}$$

(see [GAPF16, Eq. (B1)-(B7)] and [Gru14, Sec. 4.1, Sec. 4.2, p. 29-37] for a more detailed derivation). The functions $J^{\alpha\beta}$ and $\overline{g}_i$ depend on $\boldsymbol{\phi}(t)$ only and need to be calculated only once for every time (or for the infinite time limit). Their symmetries

$$\overline{g}_i(q_x,k_x,-\Delta;t) = \overline{g}_i(q_x,k_x,\Delta;t) = \overline{g}_i(k_x,q_x,-\Delta;t), \tag{3.10a}$$

$$J^{xx}(q_x,k_x,-\Delta;t) = J^{xx}(q_x,k_x,\Delta;t), \tag{3.10b}$$

$$J^{xz}(q_x,k_x,-\Delta;t) = -J^{xz}(q_x,k_x,\Delta;t), \tag{3.10c}$$

$$J^{zz}(q_x,k_x,-\Delta;t) = J^{zz}(q_x,k_x,\Delta;t), \tag{3.10d}$$

which can be found by inspection of the defining equations, can be exploited to reduce the memory requirements.

For the discretization of (3.8) the integral is replaced by the sum

$$m^{\alpha\beta}_{mn}[\boldsymbol{\phi}^s(t)] = \sum_{j=-N_{q_z}+1}^{N_{q_z}-1}\sum_{i=0}^{N_{q_x}-1} w_j^z w_i^x \phi^s_{ij}(t) k_i^x J^{\alpha\beta}(k_m^x,k_i^x,k_n^z-k_j^z;t), \tag{3.11a}$$

where the indices label the grid points as introduced above. A negative index corresponds to the negative grid point $q_{-i} = -q_i$. The variables w_i^α correspond to the weights of the quadrature rule used for the corresponding integration. The sum over j for the z-integration can be reduced to a sum from 0 to $N_{q_z}-1$ if the complex conjugate symmetry of $\phi^s_{-mn} = (\phi^s_{mn})^*$ is exploited.

Then

$$m_{mn}^{\alpha\beta} = \sum_{j=0}^{N_{qz}-1} \sum_{i=0}^{N_{qx}-1} w_j^z w_i^x k_i^x \left(\phi_{ij}^s(t) J^{\alpha\beta}(k_m^x, k_i^x, k_n^z - k_j^z; t) + (\phi_{ij}^s(t))^* J^{\alpha\beta}(k_m^x, k_i^x, k_n^z + k_j^z; t) \right). \tag{3.11b}$$

For the composite trapezoidal rule on a nonuniform grid the weights are given by

$$w_i^\alpha = \frac{1}{2} \begin{cases} q_{i+1}^\alpha - q_i^\alpha, & i = 0, \\ q_{i+1}^\alpha - q_{i-1}^\alpha, & 0 < i < N_q - 1, \\ q_i^\alpha - q_{i-1}^\alpha, & i = N_q - 1. \end{cases} \tag{3.11c}$$

The differences $k_n^z - k_j^z$ range from 0 to $2q_{\max}$ (using the symmetry in Δ), but they do not form a regular grid. Instead there is a lot of clusters of close points, because some wave vectors are quite small. Therefore, we decided to calculate $J^{\alpha\beta}(q_x, k_x, \Delta)$ in Δ on a uniform grid from 0 to $2q_{\max}$ with a step size which is somewhat smaller than for the correlators. Then the desired values are calculated via linear interpolation. This grid will be referred to as q_d-grid.

Finally, we need to find a numerical solution for the integrals (3.9d). The function $g(p;t)$ is interpolated in p, because $\phi_p(t)$ is only known numerically. In order to avoid the need for extrapolation, $\phi_p(t)$ has to be given for $p \in [0, 2\sqrt{((q_{\max}^x)^2 + (q_{\max}^z)^2)}]$. Then the integral is solved on a uniform grid with 100 points and the trapezoidal rule for the dynamics and spline interpolation for the long time limit.

3.3. Long time limit scheme

With the discretization of the memory kernels, we are already prepared to solve for the nonergodicity parameters. The relation (2.167) can be used for a fixed point iteration. Starting with $(\boldsymbol{f}^{s,(0)})_{ij} = 1$, we calculate the next iterate via

$$f_{mn}^{s,(i+1)} = \left(1 + \mu_{mn}\left[\boldsymbol{f}^{s,(i)}\right]\right)^{-1} \tag{3.12a}$$

$$\mu_{mn}\left[\boldsymbol{f}^{s,(i)}\right] = \frac{\Gamma_{mn}^x m_{mn}^{zz}\left[\boldsymbol{f}, \boldsymbol{f}^{s,(i)}\right] + \Gamma_{mn}^z m_{mn}^{xx}\left[\boldsymbol{f}, \boldsymbol{f}^{s,(i)}\right] - \Gamma_{mn}^{xz} m_{mn}^{xz}\left[\boldsymbol{f}, \boldsymbol{f}^{s,(i)}\right]}{m_{mn}^{xx}\left[\boldsymbol{f}, \boldsymbol{f}^{s,(i)}\right] m_{mn}^{zz}\left[\boldsymbol{f}, \boldsymbol{f}^{s,(i)}\right] - \left(m_{mn}^{xz}\left[\boldsymbol{f}, \boldsymbol{f}^{s,(i)}\right]\right)^2}, \tag{3.12b}$$

where $m_{mn}^{\alpha\beta}$ is the discretized primitive memory functional (3.11) and $\Gamma_{mn}^\alpha := \Gamma_{(k_m^x, 0, k_n^z)}^\alpha$ the discrete versions of (2.155). For the polynomial mode coupling functionals with real coefficients it can be shown that this procedure leads to a fixed point [Göt09, p. 219, Eq. (4.53)], in particular the maximum fixed point, which can be identified by the nonergodicity parameter [GS95, Sec. 4.1, p.823]. This proof does not apply to our problem, because it relies on the theorem that a sequence of monotonously falling and bounded sequence of real numbers converges. Since there is no ordering on complex numbers this cannot be translated easily to our problem. The numerical solution however suggests, that this algorithm works nevertheless.

Since we cannot iterate forever to find the fixed point, this iteration is stopped, when the difference between two iterations is small enough. We choose the maximum metric to

characterize this difference. The maximum norm is defined via

$$\|\boldsymbol{f}\|_\infty := \max_{mn} |f_{mn}| \tag{3.13}$$

and the error in the ith iteration ε_i is then given by

$$\varepsilon_i := \left\| \boldsymbol{f}^{s,(i+1)} - \boldsymbol{f}^{s,(i)} \right\|_\infty . \tag{3.14}$$

Other choices for the norm are possible, but this choice allows us to get a robust estimate on how accurate the results are. This reasoning is based on a corollary of the Banach fixed-point theorem [Ban22, p. 160, Théorème 6]. Even though we cannot prove that the mapping (3.12) is a contraction (with respect to the maximum metric)[2], we find that it behaves numerically like one: The error evolves like

$$\frac{\varepsilon_{i+1}}{\varepsilon_i} = c, \tag{3.15}$$

with a *contraction factor* $0 < c < 1$, which is basically constant when one has iterated long enough. This allows the following estimate for the error to the true fixed point [Gru14, p. 44, Eq. (4.7)]

$$\left\| \boldsymbol{f}^{s,(\infty)} - \boldsymbol{f}^{s,(i+1)} \right\|_\infty \leq \frac{c}{1-c} \varepsilon_i. \tag{3.16}$$

Due to the definition of $\|\cdot\|_\infty$, we know that the difference in every component from the true fixed point is smaller than $c(1-c)^{-1}e_i$. This is particularly useful, if the convergence is slow and one has to distinguish zero from nonzero values. It turns out that the bifurcations in this problem are connected with a slowing down of the convergence of this iteration. Therefore, we also define here the *reduced contraction factor* $c^r := 1 - c$.

The last quantity to characterize the iterations is the *evolution quotient*

$$e_i := \frac{1}{N_{q_x} N_{q_z}} \sum_{m,n} \left| \frac{f_{mn}^{s,(i+1)}}{f_{mn}^{s,(i)}} \right|, \tag{3.17}$$

which has the limit $\lim_{i\to\infty} e_i = 1$ for the nonergodic case $\boldsymbol{f}^{s,(\infty)} \neq 0$ and $\lim_{i\to\infty} e_i = c$ for the ergodic case $\boldsymbol{f}^{s,(\infty)} = 0$. Hence we can use this quantity to determine that an iteration leads to the nonergodic case if $e_i > (1+c)/2$ and to the ergodic otherwise [Gru14, Sec. (5.1.3), p. 51]. The main point here is to iterate long enough, so that the estimate for the contraction factor c is basically constant. The success of other methods to determine the bifurcation point has been investigated in [Gru14, Sec. 5.1.4, p. 53, Fig. 5.3].

3.4. Numerical solution in Laplace space

The equations of motion (2.170) for the probe correlator in Laplace space (in the constant bath approximation, see Sec. 2.4.7) have the same structure as the equations for the long time limit. Therefore, we can apply the same fixed-point method to this equation. The Laplace frequency s enters only as a parameter. The equations for different s can be solved independently. The

[2] In fact, we can prove that this mapping cannot always be a contraction, because $\boldsymbol{f}^s = 0$ is already a fixed point and the Banach fixed-point theorem guarantees that there is exactly one fixed point

fixed point iteration is given by

$$\tilde{\phi}_{mn}^{s,(i+1)}(s) = \left(s + \tilde{m}_{mn}\left[\tilde{\boldsymbol{\phi}}^{s,(i)}\right]\right)^{-1}, \tag{3.18a}$$

$$\tilde{m}_{mn}\left[\tilde{\boldsymbol{\phi}}^{s,(i)}\right] = \frac{\Gamma_{mn}^{x}\left(m_{mn}^{zz}\left[\tilde{\boldsymbol{\phi}}^{s,(i)}(s)\right]+1\right) + \Gamma_{mn}^{z}\left(m_{mn}^{xx}\left[\tilde{\boldsymbol{\phi}}^{s,(i)}(s)\right]+1\right) - \Gamma_{mn}^{xz} m_{mn}^{xz}\left[\tilde{\boldsymbol{\phi}}^{s,(i)}(s)\right]}{\left(m_{mn}^{xx}\left[\tilde{\boldsymbol{\phi}}^{s,(i)}(s)\right]+1\right)\left(m_{mn}^{zz}\left[\tilde{\boldsymbol{\phi}}^{s,(i)}(s)\right]+1\right) - \left(m_{mn}^{xz}\left[\tilde{\boldsymbol{\phi}}^{s,(i)}(s)\right]\right)^2}, \tag{3.18b}$$

with the $m_{mn}^{\alpha\beta}\left[\boldsymbol{f}, \tilde{\boldsymbol{\phi}}^{s}(s)\right]$ being discretized primitive memory functionals (3.11), where the argument $\boldsymbol{f}$ has been suppressed for brevity.

The initial values for this iteration are chosen to be $(\tilde{\boldsymbol{\phi}}^{s,(0)})_{mn} = 1$ for large s. There the iteration converges rather quickly[3] so that the initial values do not really matter. However, it proves to be beneficial to calculate the solutions for different s consecutively. When starting from large s and going to smaller s one can use the previous result as starting point for the next iteration.

In order to speed up the convergence of this iteration, we use the following empirical relation, which was already found in [Gru14, p. 43]. It is based on the observation that the difference between two iterations scales with a constant factor (the contraction factor of the iteration to be precise). Extrapolating this to infinitely many iterations results in a geometric series and therefore

$$\tilde{\phi}_{mn}^{s,(\infty)}(s) \approx \tilde{\phi}_{mn}^{s,(i)}(s) + \frac{1}{1-c}\left(\tilde{\phi}_{mn}^{s,(i)}(s) - \tilde{\phi}_{mn}^{s,(i-1)}(s)\right), \tag{3.19a}$$

where c is the contraction factor as defined in (3.15). Before this estimate can be applied, a sufficient number of iterations has to be performed such that the contraction factor does not change too much anymore. Therefore, we apply this estimate only if already more than 500 iterations have been performed. Furthermore, we average c over the last ten iterations to reduce numerical noise. After the extrapolation we again iterate the scheme (3.18) to check that we have a proper solution. After 100 iterations the extrapolation is applied again and we iterate until we have reached the desired accuracy.

In addition to the absolute maximum error, we also consider the absolute relative error defined via

$$\varepsilon_i^{\mathrm{rel}} := \left\| \frac{\tilde{\phi}^{s,(i+1)}(s) - \tilde{\phi}^{s,(i)}(s)}{\tilde{\phi}^{s,(i)}(s)} \right\|_{\infty}, \tag{3.20}$$

where the division has to be performed componentwise. This is necessary because the values of $\tilde{\phi}_{mn}^{s}(s)$ can get very large. A typical termination condition is $\varepsilon_i^{\mathrm{rel}} < 10^{-10}$.

This method allows us to speed up the iteration for the Laplace space solution significantly. Hence, one could also consider to apply this to the long time limit solution as well. When doing so, it works in some cases but not in others. When it does not work, the error is getting larger instead of smaller. A reason might be that the nonergodic solution is getting smaller and smaller and therefore closer and closer to the ergodic solution. Therefore, one cannot apply this method to the solution for the long time limit reliably.

[3] typically less than 20 iterations for $s > 10^2$

3.5. Numerical solution in time space

The numerical solution of the equation of motion in time space can be split into three tasks. We have to find a solution scheme for a Volterra integral equation, for a integro-differential equation and finally extend these algorithms so that we can cover several decades in time without requiring exponentially many resources. These algorithms have mainly been worked out by Gustavo Abade based on the ideas of Hofacker [FGHL91].

3.5.1. Discretization of Volterra integral equations

In this section, we want to derive two numerical schemes to solve Volterra integral equations of the type

$$X(t) + \int_0^t A(t-t')X(t')\mathrm{d}t' = B(t) \tag{3.21}$$

with some functions $A(t)$ and $B(t)$ on a uniform grid in time. Let N_t be the number of grid points and Δ_t the step size. Then, the discrete t_i times are defined as

$$t_i = i\Delta_t \quad (0 \leq i < N_t). \tag{3.22}$$

For convenience, we define

$$Y_i := Y(t_i), \tag{3.23}$$

where Y is a placeholder for A, B, X. The uniform grid has the advantage that $A(t_i - t_j) = A(\Delta_t(i-j)) = A_{i-j}$ falls on the same grid. This is especially useful if A itself is only known numerically. If A is known analytically or is independent of $X(t)$, other approaches for calculating a convolution integral are possible [Fre14, Appendix E, p. 329-339].

Explicit method

The integral is approximated by a quadrature method of your choice. We just require that its integration points lie on this grid. Hence,

$$\int_0^{t_i} A(t-t')X(t')\mathrm{d}t' \approx \sum_{j=0}^{i} w_{ij}A_{i-j}X_j, \tag{3.24}$$

with w_{ij} being the integration weights. For the composite trapezoidal rule, they read for $i > 0$ (for $i = 0$ the integral is zero)

$$w_{ij} = \frac{\Delta_t}{2}\begin{cases} 1, & j = 0, \\ 2, & 0 < j < i, \\ 1, & j = i, \end{cases} \tag{3.25}$$

cf. [SK11, p. 310, Eq. (7.13)]. The error of this composite trapezoidal rule scales like Δ_t^2 and is proportional to the length of the integration interval [SK11, p. 310, Eq. (7.15)].

With this approximation, we can solve (3.21) step by step. By definition we have

$$X_0 = X(0) = B(0) = B_0 \tag{3.26a}$$

and if X_j is known for $j < i$ we find

$$X_i = \frac{B_i - \sum_{j=0}^{i-1} w_{ij} A_{i-j} X_j}{1 + w_{ii} A_0} \tag{3.26b}$$

by solving the approximated integral equation for X_i.

Integral method with moments

Alternatively, one can make use of the symmetry of the integrand and separate short times from long times, based on [FGHL91, Sec. 3.4, p. 5060ff]. With a change of variables $t'' = t - t'$ we find for $0 < \bar{t} < t$

$$\int_0^t A(t-t')X(t')\mathrm{d}t' = \int_0^{\bar{t}} A(t-t')X(t')\mathrm{d}t' + \int_0^{t-\bar{t}} X(t-t'')A(t'')\mathrm{d}t'' . \tag{3.27}$$

These integrals are approximated in the following way for $\bar{t} = \Delta_t \bar{\imath}$

$$\int_0^{\bar{t}} \mathrm{d}t'\, A(t_i - t')X(t') = \sum_{j=1}^{\bar{\imath}} \int_{t_{j-1}}^{t_j} \mathrm{d}t'\, A(t-t')X(t') \approx \sum_{j=1}^{\bar{\imath}} \Delta_t \frac{A_{i-j} + A_{i-j+1}}{2} \mathrm{d}X_j \,, \tag{3.28a}$$

with the so called *moments*

$$\mathrm{d}X_j = \frac{1}{\Delta_t} \int_{t_{j-1}}^{t_j} X(t')\mathrm{d}t' . \tag{3.28b}$$

These moments will prove useful, when we want to extend this solution scheme to longer times on coarser time grids (see Sec. 3.5.3). Similarly, we find

$$\int_0^{t-\bar{t}} X(t_i - t')A(t')\mathrm{d}t' \approx \Delta_t \sum_{j=1}^{i-\bar{\imath}} \frac{X_{i-j} + X_{i-j+1}}{2} \mathrm{d}A_j \,, \tag{3.28c}$$

with

$$\mathrm{d}A_j = \frac{1}{\Delta_t} \int_{t_{j-1}}^{t_j} A(t')\mathrm{d}t' . \tag{3.28d}$$

We can plug these relations into our original equation and solve for X_i so that we find

$$X_i = \frac{B_i - \frac{\Delta_t}{2}\left(X_{i-1}\mathrm{d}A_1 + \sum_{j=1}^{\bar{\imath}} (A_{i-j} + A_{i-j+1})\mathrm{d}X_j + \sum_{j=2}^{i-\bar{\imath}} (X_{i-j} + X_{i-j+1})\mathrm{d}A_j \right)}{1 + \Delta_t \mathrm{d}A_1} . \tag{3.29}$$

In order to minimize memory consumption, we choose the time $\bar{t} = \bar{\imath}\Delta_t$ such that the sums have the same upper bound, which implies that we need the same amount of moments in both sums. This requires $\bar{\imath} = i - \bar{\imath}$ or equivalently $\bar{\imath} = i/2$. Since i can be odd, we define $\bar{\imath} := \lfloor i/2 \rfloor$, where this floor bracket indicates that the largest integer less or equal than the argument is chosen. Finally, to close these equations, we use the trapezoidal rule to calculate the moments

for $j \leq \bar{\imath}$

$$\mathrm{d}Y_j \approx \frac{Y_j + Y_{j-1}}{2}. \tag{3.30}$$

Note that the interval length Δ_t cancels in the moment calculation. Again, these equations can be solved step by step starting with $X_0 = B_0$.

Integro-differential method with moments

The third option is to convert the integral equation into an integro-differential method by deriving it. This yields

$$\dot{X}(t) + \frac{\mathrm{d}}{\mathrm{d}t} \int_0^t A(t-t')X(t')\mathrm{d}t' = \dot{B}(t). \tag{3.31}$$

In this case, we need to discretize both, the derivative and the integration. Since we want to apply the same moment scheme as in the algorithm above, we need to rewrite the integral expression. Differentiation using the Leibniz rule for the variable limit of integration leads to

$$\frac{\mathrm{d}}{\mathrm{d}t} \int_0^t A(t-t')X(t')\mathrm{d}t' = A(0)X(t) + \int_0^t \dot{A}(t-t')X(t')\mathrm{d}t'\,. \tag{3.32}$$

After splitting the integral on the right hand side in the same way as in (3.27), we can use integration by parts to move the time derivative from A to X and we obtain

$$\frac{\mathrm{d}}{\mathrm{d}t} \int_0^t A(t-t')X(t')\mathrm{d}t' = \int_0^{\bar{t}} \dot{A}(t-t')X(t')\mathrm{d}t' + \int_0^{t-\bar{t}} \dot{X}(t-t')A(t')\mathrm{d}t' + A(t-\bar{t})X(\bar{t}) \tag{3.33}$$

for $0 < \bar{t} < t$. Approximating the derivative by the secants

$$\dot{Y}(t) \approx \frac{Y(t_j) - Y(t_{j-1})}{\Delta_t} \tag{3.34}$$

for $t \in (t_{j-1}, t_j)$, we can discretize these integrals in the same way as above via (note the sign change due to the integration in direction $-t'$)

$$\int_0^{\bar{t}} \dot{A}(t-t')X(t')\mathrm{d}t' \approx -\sum_{j=1}^{\bar{\imath}} \left(A_{i-j} - A_{i-j+1}\right) \mathrm{d}X_j\,, \tag{3.35a}$$

$$\int_0^{t-\bar{t}} \dot{X}(t-t')A(t')\mathrm{d}t' \approx -\sum_{j=1}^{i-\bar{\imath}} \left(X_{i-j} - X_{i-j+1}\right) \mathrm{d}A_j\,, \tag{3.35b}$$

with the moments (cf. (3.28b) and (3.28d))

$$\mathrm{d}Y_j = \frac{1}{\Delta_t} \int_{t_{j-1}}^{t_j} Y(t')\mathrm{d}t'\,. \tag{3.36}$$

What remains is the numerical solution of the differential equation. In order to choose a suitable method from the huge toolbox for numerical solutions of ordinary differential equations,

we bring the integro-differential equation into the following form of a differential equation

$$\dot{X}(t) = f(t, X(t)) \tag{3.37a}$$

$$f(t, X(t)) = \dot{B}(t) - \frac{\mathrm{d}}{\mathrm{d}t}\int_0^t A(t-t')X(t')\mathrm{d}t' \,. \tag{3.37b}$$

Since f depends on the full history of X, we cannot use Runge-Kutta methods, because they need to evaluate f in between the steps. However, there are so called *linear multistep methods*, which make use of the past function values and *multiderivative methods*, which also include derivatives of X or f [But08, Sec. 223, p. 90] to improve the numerics. We will restrict ourselves to the linear multistep models, which are given by the following general form

$$X_i = \sum_{j=1}^{k} \alpha_j X_{n-j} + \Delta_t \sum_{j=0}^{k} \beta_j f(t_{n-j}, X_{n-j}) \tag{3.38}$$

using the input of the previous k steps [But08, p. 107, Eq. (242a)]. For $\alpha_1 = 1$ and $\alpha_k = 0$ ($k > 1$) these models are called Adams methods, which can furthermore be distinguished into the explicit *Adams-Bashforth* methods with $\beta_0 = 0$ and the implicit *Adams-Moulton* methods. Alternatively, one can choose $\beta_k = 0$ for $k > 1$ and consider the coefficients $\alpha_k \neq 0$. These methods are called *backward difference formulae* [But08, Sec. 412, p. 332]. For each of these methods the coefficients are chosen such that the consistency order of the method is maximized. A consistency order of p indicates that the error of the approximation scales with the step size Δ_t as $(\Delta_t)^p$. The coefficients for different orders are given in [But08, Tab. 244(I), p. 110] for the Adams-Bashforth methods, in [But08, Tab. 244(II), p. 110] for the Adams-Moulton methods and in [But08, Tab. 412(I), p. 333] for the backward difference methods.

Using the discretization (3.35) for the integral, we find for the discrete values

$$\begin{aligned} f(t_i, X_i) &= \dot{B}_i - A_{i-\bar{\imath}}X_{\bar{\imath}} + \sum_{j=1}^{\bar{\imath}}(A_{i-j} - A_{i-j+1})\mathrm{d}X_j \; + \sum_{j=1}^{i-\bar{\imath}}(X_{i-j} - X_{i-j+1})\mathrm{d}A_j \\ &=: -X_i \mathrm{d}A_1 \; + g_i, \end{aligned} \tag{3.39}$$

where we separated the dependency on X_i on the right hand side to simplify the following calculations. Plugging this into the general multistep model (3.38) and solving for X_i we find

$$X_i = \frac{\sum_{j=1}^{k} X_{i-j}(\alpha_j - \beta_j \Delta_t \mathrm{d}A_1\,) + \Delta_t \sum_{j=0}^{k} \beta_j g_{i-j}}{1 + \Delta_t \beta_0 \mathrm{d}A_1}, \tag{3.40a}$$

$$g_i = \dot{B}_i - A_{i-\bar{\imath}}X_{\bar{\imath}} + X_{i-1}\mathrm{d}A_1 \; + \sum_{j=1}^{\bar{\imath}}(A_{i-j} - A_{i-j+1})\mathrm{d}X_j \; + \sum_{j=2}^{i-\bar{\imath}}(X_{i-j} - X_{i-j+1})\mathrm{d}A_j \tag{3.40b}$$

Since the evaluation of the g_{i-j} is the computationally most expensive part in this algorithm, we stay with the backward difference formulate[4]. Our choice is the backward difference method

[4] This problem could be overcome by saving g_i after each time step, but this has not been implemented and tested.

of order 2 (and $k = 2$) with [But08, Tab. 412(I), p. 333]

$$\alpha_1 = \frac{4}{3}, \qquad \alpha_2 = -\frac{1}{3}, \qquad \beta_0 = \frac{2}{3}, \tag{3.41}$$

(all other coefficients being 0) which leads to

$$X_i = \frac{\frac{1}{3}\left(4X_{i-1} - X_{i-2}\right) + \Delta_t \frac{2}{3} g_i}{1 + \frac{2}{3}\Delta_t \mathrm{d}A_1} = \frac{\frac{1}{2\Delta_t}\left(4X_{i-1} - X_{i-2}\right) + g_i}{\frac{3}{2\Delta_t} + \mathrm{d}A_1} \tag{3.42}$$

(cf. [GAPF16, Eq. (D12)-(D16)]). What remains is the determination of the solutions for the first steps with $i < k$. It is possible to use a lower order scheme, but this nullifies the advantage of the higher order scheme at later times [But08, p. 112]. A Runge-Kutta method of the same order would be nice, but is not possible in our case. Another possibility is a forward-backward integration iteration for X_i with $-k < i < 0$ with the same method [But08, Sec. 246, p. 112f]. In our final algorithm we will circumvent this problem using the decimation algorithm (see Section 3.5.3) by starting with a very small step size.

3.5.2. Discretization of integro-differential equations

The equation of motion for our correlation function is of the type

$$\partial_t X(t) + \Gamma X(t) + \int_0^t A(t-t')\partial_{t'} X(t')\mathrm{d}t' = C(t), \tag{3.43}$$

which we will solve on the same uniform grid. This derivation basically follows the path of discretizing (3.31) using the moment scheme. With integration by parts and change of variables we find

$$\int_0^t A(t-t')\dot{X}(t')\mathrm{d}t' = A(t-\bar{t})X(\bar{t}) - A(t)X(0) + \int_0^{\bar{t}} \dot{A}(t-t')X(t')\mathrm{d}t' + \int_0^{t-\bar{t}} \dot{X}(t-t')A(t')\mathrm{d}t', \tag{3.44}$$

which can be approximated as in (3.35) with the moments as

$$\int_0^{t_i} A(t_i-t')\dot{X}(t')\mathrm{d}t' \approx A_{i-\bar{\imath}}X_{\bar{\imath}} - A_i X(0) + \sum_{j=1}^{\bar{\imath}}(A_{i-j+1} - A_{i-j})\mathrm{d}X_j + \sum_{j=1}^{i-\bar{\imath}}(X_{i-j+1} - X_{i-j})\mathrm{d}A_j\,. \tag{3.45}$$

For the differential part we use again the backward difference method of order 2 to find

$$X_i = \frac{\frac{1}{2\Delta_t}\left(4X_{i-1} - X_{i-2}\right) + (X_0 - \mathrm{d}X_1)A_i + g_i}{\frac{3}{2\Delta_t} + \Gamma + \mathrm{d}A_1} \tag{3.46a}$$

$$\begin{aligned} g_i = {} & C_i - A_{i-\bar{\imath}}X_{\bar{\imath}} + A_{i-1}\mathrm{d}X_1 + X_{i-1}\mathrm{d}A_1 \\ & + \sum_{j=2}^{\bar{\imath}}(A_{i-j} - A_{i-j+1})\mathrm{d}X_j + \sum_{j=2}^{i-\bar{\imath}}(X_{i-j} - X_{i-j+1})\mathrm{d}A_j \end{aligned} \tag{3.46b}$$

(cf. [GAPF16, Eq. (C5)-(C11)]).

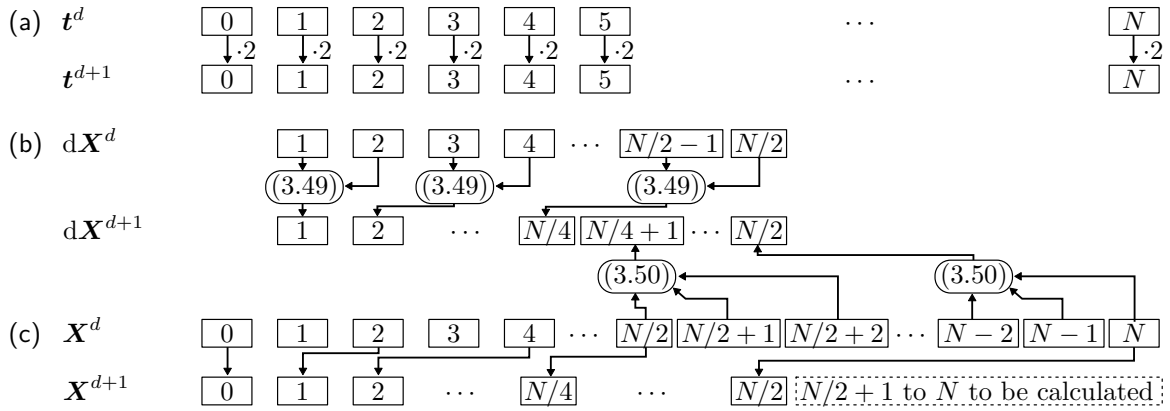

Figure 3.2.: A sketch of the decimation operation. Each line is an array of the variable indicated at the left hand side: the time (a), the moment of the variable $\mathrm{d}\boldsymbol{X}$ (b) and the variable $\boldsymbol{X}$ itself (c). Each rectangle corresponds to an array element with the given index. In the decimation step the new values are calculated according to the arrows. The rounded boxes reference the corresponding equations in the text. After the decimation the elements X_i^{d+1} for $i > N/2$ (in the dashed box) have to be calculated using the integral or integro-differential equation.

3.5.3. Decimation scheme

The algorithms presented so far are based on a uniform grid, i.e. the calculation effort for a given time resolution Δ_t scales at least linearly with the maximum time $t_{\max}$. While this does not sound too problematic at first sight, it implies that the calculation time increases by orders of magnitude if we want to cover the evolution over several orders of magnitude. Since glasses are characterized by their slow dynamics, this is a mandatory requirement for our numerics. Fortunately, this problem is already known for a long time [FGHL91, Sec. 3.4] and we can follow their lines to implement our version of this so called *decimation algorithm*.

The idea of this algorithm is as follows: First, we solve the problem on a uniform grid using the algorithms provided above. Then, we want to solve the integral equation on a grid whose time step is doubled. We can use the results on the finer grid to initialize the solution and the moments for the first half of this grid (see below). Then we continue to solve for the unknown values in the second half of the grid with the algorithms above. Repeating this procedure allows us to double the maximum time $t_{\max}$ in each step while the effort is restricted to calculating the new solution on the second half of the time grid. Hence, the effort scales linearly with the number of decimations and therefore logarithmically with the maximum time. A sketch of this procedure is shown in Figure 3.2 to visualize the procedure.

To formalize this idea, we start with $X_i^{(0)}$ being the numerical solution on the initial time grid at time $t_i := i\Delta_t$ $(0 \le i < N_t)$ and $X_i^{(d)}$ the solution after the dth decimation at time

$$t_i^{(d)} = i\Delta_t^{(d)} = i2\Delta_t^{(d-1)} = i2^d\Delta_t. \tag{3.47}$$

On every decimation level, the time grid consists of N_t points. What increases is only the step size $\Delta_t^{(d)}$. In general, $Y_i^{(d)} := Y(t_i^{(d)})$ is defined to be the (numerical) value of Y at time $t_i^{(d)}$ decimation level d.

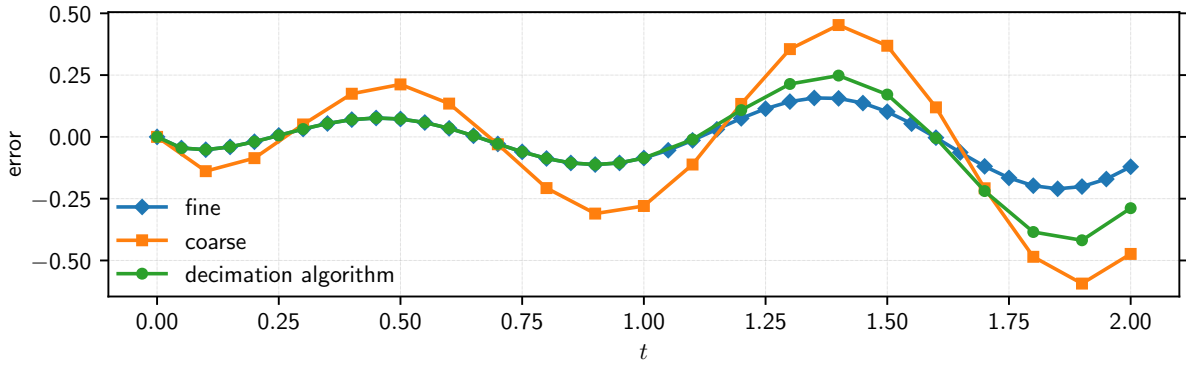

Figure 3.3.: Error of the decimation method as compared to the uniform time grids. The fine grid has the initial time step of the decimation scheme, while the coarse grid has the final time step of the decimation scheme. The first decimation step covers the interval $[0,1]$ at a step size of $\Delta_t = 0.05$. The second decimation step then consequently the interval $[0,2]$ with a step size of $\Delta_t = 0.1$. While maintaining the same number of grid points as for the coarse grid for the calculation we achieve smaller errors for longer times. A calculation on the full grid has of course even smaller errors but is also computationally more expensive.

It remains to find the relations between the values for consecutive decimation levels. For the times, we find the recursion $t_i^{(d)} = t_{2i}^{(d-1)}$ if $2i < N_t$. This allows us to write

$$Y_i^{(d)} = Y(t_i^{(d)}) = Y(2t_i^{(d-1)}) = Y(t_{2i}^{(d-1)}) = Y_{2i}^{(d-1)} \tag{3.48}$$

provided $2i < N_t$ (see Figure 3.2(c)). For the moments we find

$$\begin{aligned} \mathrm{d}Y_i^{(d)} =& \frac{1}{\Delta_t^{(d)}} \int_{t_{i-1}^{(d)}}^{t_i^{(d)}} Y(t')\mathrm{d}t' = \frac{1}{2\Delta_t^{(d-1)}} \left(\int_{t_{2i-2}^{(d-1)}}^{t_{2i-1}^{(d-1)}} Y(t')\mathrm{d}t' + \int_{t_{2i-1}^{(d-1)}}^{t_{2i}^{(d-1)}} Y(t')\mathrm{d}t' \right) \\ =& \frac{1}{2} \left(\mathrm{d}Y_{2i-1}^{(d-1)} + \mathrm{d}Y_{2i}^{(d-1)} \right), \end{aligned} \tag{3.49}$$

provided $2i \leq \bar{\imath}$, i.e. $i \leq N_t/4$. For $N_t/4 < i < N_t/2$ we can use the composite trapezoidal rule [SK11, p. 309, Eq. (7.10)]

$$\mathrm{d}Y_i^{(d)} \approx \frac{1}{4} \left(Y_{2i-2}^{(d-1)} + 2Y_{2i-1}^{(d-1)} + Y_{2i}^{(d-1)} \right) \tag{3.50a}$$

or the Simpson rule [SK11, p. 309, Eq. (7.11)] as used in [FGHL91, p. 5062, Eq. (36)]

$$\mathrm{d}Y_i^{(d)} \approx \frac{1}{6} \left(Y_{2i-2}^{(d-1)} + 4Y_{2i-1}^{(d-1)} + Y_{2i}^{(d-1)} \right), \tag{3.50b}$$

which has in theory better convergence properties [SK11, p. 310, Eq. (7.15), Eq. (7.16)]. The decimation of the moments is summarized in Figure 3.2(b).

With these definitions we can initialize our solution vector with any of the algorithms of the previous sections on the uniform grid for $i < N_t/2$. We can then continue with these algorithms to solve for $i \geq N_t/2$.

In Figure 3.3 we compare the error using a coarse grid, which has the same step size as the

▷ *Initialization*
for $0 \leq i \leq N_{\text{init}}$ **do**
  $\phi^s(k_x, k_z, 0, i) = 1 - \Gamma_{\boldsymbol{k}^*} \Delta_t i$
  Calculate $m^{\text{eff}}(k_x, k_z, 0, i)$ via (3.26)
  Initialize moments $\mathrm{d}Y_i$ via (3.30)
end for
▷ *Decimation steps*
for $0 \leq d < N_d$ **do**
  if $d = 0$ **then**
    $N_{\text{cont}} = N_{\text{init}} + 1$
  else
    $N_{\text{cont}} = N_t/2$
  end if
  for $N_{\text{cont}} \leq i \leq N_t$ **do**
    ▷ *Start with solution of previous time*
    $\phi^s(k_x, k_z, d, i) = \phi^s(k_x, k_z, d, i-1)$
    ▷ *Iteratively improve the solution*
    repeat
      Calculate $m^{\alpha\beta}(k_x, k_z) \left[\boldsymbol{\phi}(t_i^{(d)}), \boldsymbol{\phi}^s(t_i^{(d)})\right]$ via (3.11)
      Calculate $m^{\text{eff}}(k_x, k_z, d, i)$ via (3.29) (integral) or (3.42) (integro-differential)
      Calculate $\phi^s_{\text{new}}(k_x, k_z, d, i)$ via (3.46)
    until $\|\phi^s_{\text{new}}(\cdot, \cdot, d, i) - \phi^s(\cdot, \cdot, d, i)\|_\infty < \varepsilon$
  end for
  Save solutions for $i \leq N_t/2 < N_t$
  Decimate function values according to (3.48)
  Decimate existing moments ($0 \leq i < N_t/4$) according to (3.49)
  Calculate new moments ($N_t/4 \leq i \leq N_t/2$) according to (3.50a)
end for

Figure 3.4.: Pseudocode of the algorithm to solve the mode coupling equations

final stage of the decimation algorithm, a fine grid, which has the same step size as the initial stage of the decimation algorithm, and the decimation algorithm itself. As a test case we used the integral equation corresponding to (E.2) on a very coarse grid to highlight the differences between the methods. For a clear representation we only use one decimation step. The overall error is smallest for the fine grid, but the decimation method shows the best compromise between a small time grid and a small error.

3.5.4. The full algorithm

In total, we have to solve (2.159), which consists of an integro-differential equation for $\phi^s_{\boldsymbol{k}^*}(t)$ and an integral equation for the effective memory kernel with the memory functionals given by (2.160). Therefore, we combine all algorithms described in the sections before. This is schematically summarized in Figure 3.4 and described in words in the following.

We start with an equidistant grid in time (and a suitable grid for the wave vectors) with

step size Δ_t and N_t steps. The initial values $\phi^s_{\boldsymbol{k}^*}(t_i)$ for $i \leq N_{\text{init}}$ are determined by the short time solution (neglecting the memory contribution)

$$\phi^s_{\boldsymbol{k}^*}(t_i^{(0)}) = 1 - \Gamma_{\boldsymbol{k}^*} t_i^{(0)} \quad (0 \leq i < N_t/2). \tag{3.51}$$

The effective memory integral is initialized (on the same grids) using these values as input for the explicit method (3.26) for the integral equation (2.159b). The correlators and memory functions at the remaining times $i > N_{\text{init}}$ can be determined with the given method as described in the following. Choosing $N_{\text{init}} = N_t$, we start directly with the decimation in the next step. This has the drawback of introducing some errors when the end time $t^{(0)}_{N_t}$ is not short enough anymore. The choice $N_{\text{init}} = 1$ allows to use second order solution schemes from the very beginning.

Then, the integro-differential equation for $\phi^s_{\boldsymbol{k}^*}(t)$ (2.159a) is solved via (3.46) with $X := \phi^s_{\boldsymbol{k}^*}$, $\Gamma := \Gamma_{\boldsymbol{k}^*}$ and $A := m^{\text{eff}}_{\boldsymbol{k}^*}$ for each value $\boldsymbol{k}^*$ in the wave vector grid. To do so, we first need to solve for $m^{\text{eff}}_{\boldsymbol{k}^*}(t_i^{(0)})$ using the integral algorithm (3.29) or integro-differential algorithm (3.42) to discretize (2.159b) with $X := m^{\text{eff}}_{\boldsymbol{k}^*}$, $A := \Gamma^{-1}_{\boldsymbol{k}^*} M^{(2)}_{\boldsymbol{k}^*}$ and $B := M^{(3)}_{\boldsymbol{k}^*}$. Since $M^{(3)}_{\boldsymbol{k}^*}$ contains a convolution integral, we apply the procedure (3.33) to (3.36) to determine $\dot{B}$ for the integro-differential method and (3.27) to (3.28d) for the integral method.

As input for $M^{(2)}$ and $M^{(3)}$ we need the memory functionals (2.160), which are discretized by (3.11). Note that we need $\phi^s_{\boldsymbol{k}^*}(t_i^{(0)})$ at this point, which has not been calculated yet. Therefore, we do the same self-consistency iteration as in the long time limit. We start with $\phi^s(t_i^{(0)}) = \phi^s(t_{i-1}^{(0)})$ and follow the calculation described in this paragraph to find better values for $\phi^s_{\boldsymbol{k}^*}(t_i^{(0)})$. This can be used for new values of $m^{\alpha\beta}(t_i^{(0)})$, which can again be used to determine a new $\phi^s(t_i^{(0)})$. This is repeated until the maximum norm of the difference between subsequent iterates (cf. (3.14)) is small enough (typically $\varepsilon = 10^{-10}$).

Once $i = N_t$ is reached, we perform the decimation of all necessary function values (3.48) and all necessary moments from the already existing ones (3.49) and the new ones (3.50). Then we start calculating the new correlators again for $i = N_t/2$ on the next decimation level.

3.5.5. Solution for the moments

The simplest approach to determine the moments is to numerically differentiate the correlation functions $\phi^s_{\boldsymbol{k}}(t)$. This leads to

$$\langle z \rangle (t) = \frac{\operatorname{Im} \phi^s_{(0,0,q)}(t)}{q}, \tag{3.52a}$$

$$\left\langle x^2 \right\rangle (t) = 2\frac{1 - \operatorname{Re} \phi^s_{(q,0,0)}(t)}{q^2}, \tag{3.52b}$$

$$\left\langle z^2 \right\rangle (t) = 2\frac{1 - \operatorname{Re} \phi^s_{(0,0,q)}(t)}{q^2}, \tag{3.52c}$$

where q is the smallest nonzero wave-vector in the corresponding direction. While being simple, this method is also prone to numerical artifacts when the derivatives are very small (for example for small times) or very large.

A more stable approach can be used when the correlation function and the memory functions have been calculated. We can use this information to solve the equations of motion for the moments. The mean displacement has to fulfill (2.185b), the mean square displacements have to fulfill (2.185c), (2.185e) and the variance or second cumulant (2.185g). These equations are integro-differential equations of the type (3.43). We therefore apply the solution scheme (3.43) combined with the decimation as introduced in Sec. 3.5.3. For the convolution integrals on the right hand side of the equations of motion for the second moments we use the discretization (3.45) to express them in terms of the moments.

3.6. Tests

In this section, we evaluate the performance and consistency of our proposed algorithms using integral equations with analytically known solutions. Some useful test integral equations and their solutions are discussed in Appendix E. Two main topics of numerical analysis are convergence and stability, which we will only access numerically.

3.6.1. Convergence order on the uniform grid

A numerical algorithm has convergence order p if that the error between the exact and the numerical solution scales like $(\Delta_t)^p$. An order of 2 implies that the error decreases quadratically with the step size. It is desirable to have a large convergence order so that increasing the number of grid points reduces the error more significantly. To test this, we solve different integral-equations of the type

$$X(t) + \int_0^t A(t-t')X(t')\mathrm{d}t' = B(t) \tag{3.53}$$

on $[0, 10]$ using an increasing number of grid points for this interval. The functions A and B are chosen such that an analytic solution can be found (see Appendix E). If A depends on X as well, we call this integral equation *nonlinear*.

The numerical error is defined via

$$e_{\mathrm{num}} = \max_i |X_i - X(t_i)|\,, \tag{3.54}$$

where X_i is the numerical solution at time t_i and $X(t_i)$ the analytical one. This error is shown as a function of step size Δ_t in Figure 3.5 for our different algorithms from Section 3.5.1 on a uniform grid.

For the linear integral equations we find a quadratic convergence for the moment methods and a linear convergence for the explicit method, even though the explicit method shows a quadratic behavior for $A(t) = 1$ and $B(t) = 1$ or $B(t) = \exp(-t)$. In terms of the absolute error, the integral moment method is better by a factor of 2 to 12 (with the best agreement for kernels of type E.1.3, in particular $A(t) = 90\exp(-0.1t)$). For the nonlinear integral equations with $A(t) = X(t)$ we find only linear convergence for both the explicit method and the integral moment method. We find that the error is largest for the first point in the grid. This indicates

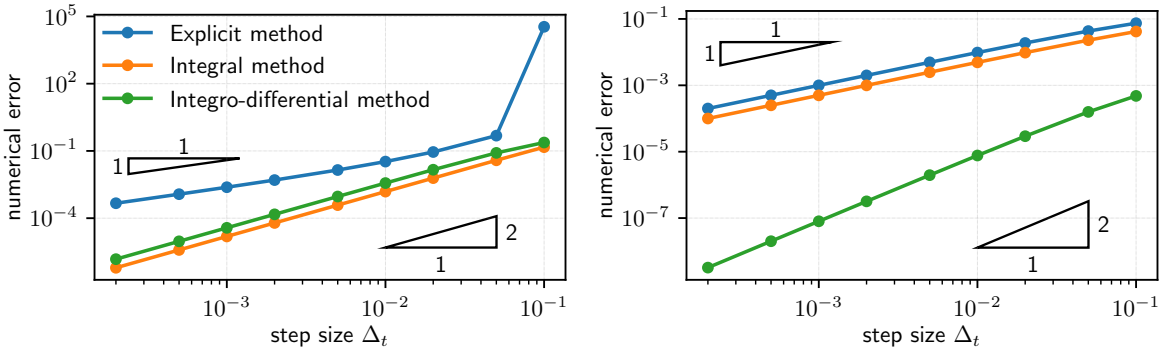

(a) Error for linear integral equation with $A(t) = 1 + t(1/4 + 4\pi^2)$, $B(t) = 1$

(b) Error for nonlinear integral equation with $A(t) = X(t)$, $B(t) = (1 + t)\exp(-t)$

Figure 3.5.: Convergence order of the different numerical schemes. The panels show the maximum error of the numerical solution as a function of step size Δ_t. All integral equations were solved on the interval $t \in [0, 10]$.

that there could be room for improvement in the initialization part of the algorithm. The integro-differential moment method however provides an exact solution for the case $B(t) = t + 1$ and quadratic convergence for $B(t) = (t + 1)\exp(-t)$. Therefore, it is the superior algorithm for the nonlinear integral equations.

3.6.2. Convergence order of the decimation algorithms

In this section, we check the convergence order if we extend the methods using the decimation scheme (Sec. 3.5.3). We choose the same interval $[0, 10]$ for the final solution to easily compare the errors and 10 decimation steps. Then we again compare the methods from Sec. 3.5.1 for the different integral equations, now using the decimation scheme.

For the linear integral equations we find the same convergence order as without decimation: The moment algorithms are of order two, while the explicit method has order 1 with the exception of the integral equation with $A(t) = 1$, where it is also of order 2. The absolute errors decrease by 20 % to 50 % for the integral equation with $A(t) = 1$. Overall, the explicit method and the integro-differential method benefit more from the decimation than the integral method. The best improvement is a factor of 10 for the integral method for $A(t) = \exp(-t)$, while the error reduces by a factor of 30 with the explicit method and by a factor of 250 for the integro-differential method for the same integral equation. The result for $A(t) = a + bt$ is shown in Figure 3.6a. There, the integral method improves by a factor of 2, while the explicit method and the integro-differential method improve by a factor of 8. This causes the integro-differential method to give the best results.

For the nonlinear integral equations with $A(t) = X(t)$, there is a remarkable change. The integral method, which was of convergence order 1 for the uniform grid, now shows convergence order 2. This finding confirms that we can indeed improve the convergence order by refining the initialization as suggested in the previous section. This remarkable finding is shown in Figure 3.6b. The absolute error decreases by a factor of 20 for the explicit method, by a factor of 50 for the integro-differential method. Due to the change in convergence order, the results

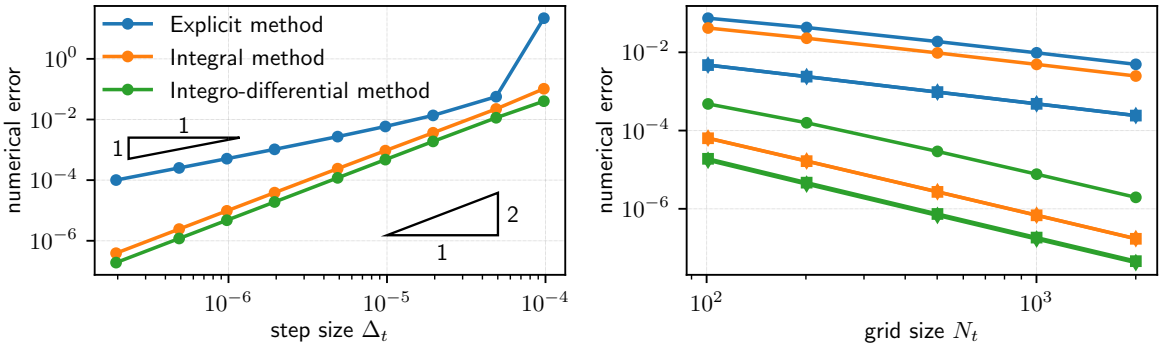

(a) Error for linear integral equation with $A(t) = 1 + t(1/4 + 4\pi^2)$, $B(t) = 1$

(b) Error comparison for nonlinear integral equation with $A(t) = X(t)$, $B(t) = (1+t)\exp(-t)$

Figure 3.6.: Convergence order of the decimation scheme with the different methods on the uniform grid. Panel (a) shows the maximum error of the numerical solution as a function of the initial step size, which is doubled 10 times to cover the interval [0,10]. Panel (b) compares the maximum error as function of grid size (number of points in the time grid) for the uniform scheme (circles) on [0,10], the decimation scheme with the trapezoidal rule (3.50a) (squares) and the decimation scheme with Simpsons rule (3.50b) (diamonds). The colors correspond to the numerical methods as introduced in panel (a). The errors for both decimation methods are basically the same such that the lines collapse onto each other.

integral equation	convergence order		
	explicit	integral	integro-differential
linear (uniform)	1	2	2
nonlinear (uniform)	1	1	2
linear (decimation)	1	2	2
nonlinear (decimation)	1	2	2

Table 3.1.: Convergence order of the *explicit*, the *integral* and the *integro-differential* method for solving linear and nonlinear integral equations on a uniform grid and using the decimation algorithm. Details on the tested integral equations and the numerical parameters can be found in the text.

by the integral method improve by a factor of 15000 or more (depending on the number of grid points N_t). Finally, we do not notice any difference using the Simpson rule (3.50b) or the composite trapezoidal rule (3.50a) for the decimation of the moments, which is also illustrated in Figure 3.6b. A summary of the convergence orders for the integral equations is shown in Table 3.1.

For the sake of completeness, we will also briefly discuss the properties of the decimation algorithm for the integro-differential equation (3.43). This equation can be recast into a Volterra integral equation of second type. Some particular cases can be solved analytically, which is done in Section E.2. These solutions can then be used to determine the convergence order as above.

Initializing the decimation algorithm with the short time expansion $X(t) \approx X_0(1 - \Gamma t)$ for $0 \leq i \leq N_{\text{init}} := N_t$ leads to an error which does not vary with step size. This indicates that the use of the short time expansion is systematically wrong. Therefore, we can try to initialize the decimation scheme by solving the integro-differential equation on the initial grid without the use of any short time expansion ($N_{\text{init}} = 0$). We then obtain an algorithm of convergence

order 1. This is not surprising, because the first step of our methods to solve integral equations is always of order 1 as described at the end of Sec. 3.5.1. As a combination of both approaches one can initialize the first two values for t_0 and t_1 with the short time expansion ($N_{\text{init}} = 1$) and solve the integro-differential equations for t_i with $i \geq 2$. This procedure then shows numerically a convergence of order 2 and is therefore preferable.

From this section we can conclude that the moment algorithms (integral and integro-differential) both have convergence order 2 and a similar error level. It depends on the details of the integral equation which of those algorithms works best. There is no advantage of using the Simpson rule over the composite trapezoidal rule for the decimation of the moments. For the integro-differential method it is advantageous to use the short time expansion for the very first data points until all data for the numerical scheme of order 2 is available.

3.6.3. Stability

In this section, we discuss the stability of the proposed algorithms for different integral equations. For ordinary differential equations, stability is assessed by the following question: Does the numerical solution decay for an arbitrary step size, provided the analytical solution does so? This feature is then discussed looking at the differential equation $\dot{X}(t) = \lambda X(t)$ [But08, Sec. 238, p. 100] and this question can be answered by looking at a single step. For integral equations there is no such simple equivalent, because we always have to take the full history of the function into account. Therefore, we test different analytically solvable integral equations with our decimation schemes.

In the spirit of the stability analysis for ordinary differential equations, we focus on these two questions: Does the numerical solution stay bounded if the analytical solution is bounded? If so, do we obtain the proper long time limit (provided it exists)? If any of these conditions is violated, the use of the numerical solution is limited and one has to employ other methods to verify the correctness of the solution.

We start with the interval $[0, 0.1]$, which is decimated up to 40 times so that we cover the interval $[0, 1.1 \cdot 10^{11}]$. This initial interval is then discretized using different number of grid points. With this procedure we can ensure that the coarser time grids are contained in all finer time grids for the complete decimation algorithm.

To measure the stability of an algorithm, we choose a very pragmatic approach. All test integral equations fulfill that the analytical solution is bounded by 1. Therefore, we consider an algorithm unstable, if any absolute value of the numerical solution exceeds 2. The first time at which this happens will be called the *stability time* t^s.

We consider the following test cases

(a) $A(t) = a\exp(-\lambda t)$, $B(t) = 1$ (cf. (E.5)),

(b) $A(t) = (1 + t(1/4 + 4\pi^2))$, $B(t) = 1$ (cf. (E.4))

and $A(t) = X(t)$ with right hand sides

(c) $B(t) = t + 1$ (cf. (E.8)),

(d) $B(t) = (1 + t)\exp(-t)$ (cf. (E.9)),

for the nonlinear equations. As a special challenge, we consider also $A(t) = 4\pi^2 t, B(t) = 1$,

because its solution is $\cos(2\pi t)$ (cf. (E.2)), which will become problematic for the algorithm, when the step size Δ_t gets comparable to the periodicity.

In the first case (a), all algorithms are stable in the sense of the definition above. However, the explicit method decays (discontinuously) to 0 instead of the nonzero long time limit. The errors in the long time limit of the other algorithms decrease quadratically with the number of grid points, as expected from the convergence analysis.

In the second case (b), all algorithms are unstable, probably due to the oscillatory nature of the analytic solution — even though it is exponentially damped. The best algorithm for this test case is the integro-differential method. It blows up one to three decades later than the other algorithms, which cease to work between $t = 10$ and $t = 100$ (the finer the grids, i.e. the more points they have, the better the performance). It is also worth to note that the stability times for the integro-differential algorithm grow approximately like $(N_t)^{1.8}$ with the number of points N_t in the grid, while the stability time grows only roughly with the number of grid points. This indicates that the step size of the calculation in the uniform grid is the limiting factor for the stability. If this minimal step size exceeds a certain threshold (0.1 for the explicit method, 0.2 for the integral method), these two algorithms become unstable.

Even though the solution for the nonlinear integral equation (c) with $A(t) = X(t)$ and $B(t) = t + 1$ is just a constant, only the integro-differential method behaves stable. The integral method is the best of the unstable methods. Its stability time is $t^s \approx 8000$ for $N_t = 101$ and grows approximately like $N_t^{0.7}$. The stability time is inversely proportional to the prefactor of t in $B(t)$; the larger this prefactor, the smaller the stability time. The explicit method is about one decade worse.

For the variant (d) $B(t) = (t + 1)\exp(-t)$ with $A(t) = X(t)$, the behavior reverses: Both the explicit method and the integral method are stable, while the integro-differential method becomes unstable. Its stability time is $t^s \approx 10^6$ for $N_t = 101$ and grows quadratically $(N_t)^2$ with the number of points. Even though this instability is somewhat milder, we have to conclude that there is no single algorithm, which solves any integral equation properly. Instead, one has to carefully choose the algorithm according to the specific integral equation. It can be even worse (anticipating from the experience with the full MCT integro-differential equations): The proper algorithm could depend on the long-time limit of the solution. If the long-time limit is nonzero one algorithm is stable and the other unstable, while their stability is reversed if the long-time limit is zero in the same way as for these two variants.

Finally, we test the behavior with purely oscillatory solutions as obtained for $A(t) = 4\pi^2 t, B(t) = 1$. As expected, all algorithms break down for long times. However, their break down behavior is different. The integral method and the explicit method become unstable when their minimal step size exceeds 0.1 to 0.2 (the period length is 1) irrespective of the number of grid points. Of course, the time corresponding to the minimal step size exceeding this threshold is larger for grids with more points. The integro-differential method becomes unstable when the minimal step size exceeds 1 to 2, which is one order of magnitude larger than for the other methods. This result does not correspond to a better performance. It is due to the fact that the numerical solution first decays to 0 before it blows up. This yields an extra decade of stability, but is nevertheless far from the real solution.

To summarize, we find that there is no *golden algorithm*, which solves all integral equations equally well (see Table 3.2 for an overview). Since the integral method and the integro-

equation type	explicit	integral	integro-differential
linear (a)	stable[a]	stable	stable
linear (b)	unstable	unstable	unstable
nonlinear (c)	unstable	unstable	stable
nonlinear (d)	stable	stable	unstable

[a] Wrong long time limit

Table 3.2.: Stability of the *explicit*, the *integral* and the *integro-differential* methods using the decimation scheme to cover the time interval $[0,1.1 \cdot 10^{11}]$. The letters in brackets refer to the different integral equation test cases as introduced in the text and further numerical parameters can be found there as well.

differential method often behave complementary, we will implement both of them and trust our solutions as long as both algorithms give the same result. Finally, we find that oscillatory solutions always cause problems for long times, even if they are exponentially damped.

3.6.4. Consistency

Our main motivation to solve the full problem numerically is the lack of an analytical solution. Therefore, we have no direct way of checking the validity of our solutions and the correct implementation of the algorithms. We can, however, do indirect tests in the sense that we should obtain the same results for different (independent) calculations. First of all, the different algorithms to solve the integral equation should give the same results (cf. Sec. 3.5.1). Furthermore, we can check if the long time limit of the dynamical calculation matches the result for the direct long time limit calculation (cf. Sec. 3.3) and finally, we can compare the solutions for the constant bath approximation in Laplace space (cf. Sec. 3.4). Any deviation of these equalities gives us a hint where the numerics breaks down and how far we can trust our results.

Since the wave vector discretization determines the critical force (see Chapter 4), we use the same wave vector grid throughout this section. Both q_x and q_z are discretized using the `unilog10`-grid with a cutoff of $q_{\max} = 20$ and a total of $N_q = 51$ grid points. The difference wave vectors q_d (see Sec. 3.2) are discretized using a `uni`-grid with $q_{\max} = 40$ and a total of $N_q = 401$ points, corresponding to a step size which is five times smaller than the step size in the uniform part of the `unilog10`-grid.

The time grid has an initial time step size of $\Delta_t = 10^{-8}$, ranging from 0 to $1024\Delta_t$ inclusively. This time grid is decimated for 45 times. In addition, we need the input of the bath correlation function $\phi_q(t)$, which is calculated with the standard algorithms for a packing fraction of $\varphi = 0.537$ with a cutoff of $q_{\max} = 65$ and 512 grid points. The decimation scheme is the same as for the tracer correlation function calculation.

A comparison of the results of the integral method and the integro-differential method for the solution of the memory kernel integral equation is shown in Figure 3.7. This comparison is done for a force of $F_{\text{ex}} = 42\, k_{\text{B}}T/d$ which is slightly below the critical force and the depicted wave vectors are $qd = 1$ and $qd = 7$. This picture is characteristic for all forces below the critical force. We notice that the curves collapse onto each other for $tD_0^s/d^2 < 10^3$. A calculation shows that the relative difference between both curves is smaller than 10^{-6} for $tD_0^s/d^2 < 10^2$ and grows to 10^{-2} for $tD_0^s/d^2 = 10^3$. After that, we can see that the solutions for the integral method go crazy and become unphysical, i.e. $|\phi_q^s(t)| > 1$, which violates the boundedness of

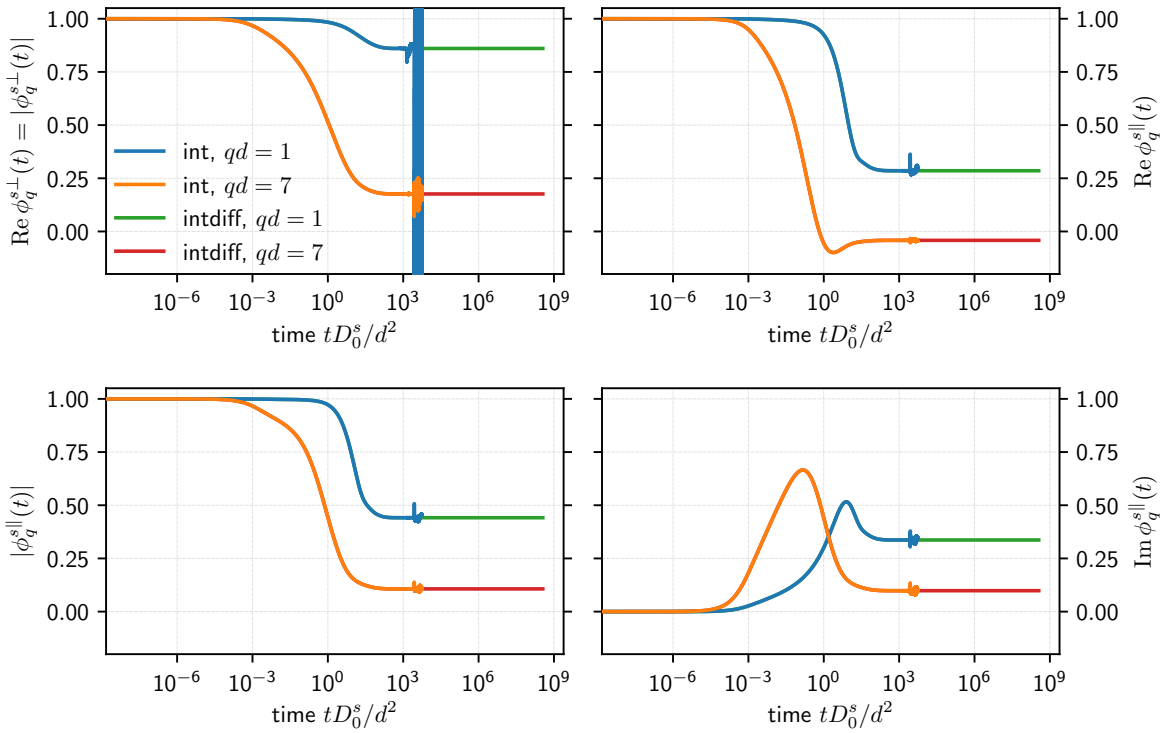

Figure 3.7.: Comparison of the solutions of the MCT equations with the integral method (int) and the integrodifferential method (intdiff) for two wave vectors $qd = 1$ (blue/green) and $qd = 7$ (orange/red) at an external force of $42\,k_\mathrm{B}T/d$ below the critical force. Since $\phi_q^{s\perp}$ is real and positive, it can be naturally compared to $|\phi_q^{s\parallel}(t)|$ (left column). Real and imaginary part of $\phi_q^{s\parallel}(t)$ are shown in the right column. The curves collapse for $tD_0^s/d^2 < 10^3$. Details on the numerical parameters can be found in the text.

the auto-correlation functions (2.88). This behavior is most prominent for the small wave vectors in the perpendicular direction, but is also present for every other wave vector. In fact, these values become arbitrarily large so that we decided to show only these solutions as long as $\phi_q^s(t) < 100$. In contrast, the solutions for the integro-differential method stay bounded and reach a constant plateau for all times.

Hence, the integrodifferential method is stable for forces below the critical force while the integral method is unstable. This finding is in line with the test case $A(t) = X(t)$ and $B(t) = t + 1$ of the stability analysis (Sec. 3.6.3). Having a closer look at the integral equation for the effective memory kernel (2.159b), we notice that this integral equation has similar features. In particular we find for the case $m_{\boldsymbol{q}^*}^{\alpha\beta} \to \mu_{\boldsymbol{q}^*}^{\alpha\beta} \neq 0$ that $M_{\boldsymbol{q}^*}^{(3)} \approx c' + c''t$ looks similar to $B(t) = t + 1$. On the other hand, the equivalent of $A(t)$ is not directly related to $m_{\boldsymbol{q}^*}^{\mathrm{eff}}(t)$.

Above the critical force both algorithms are unstable as can be seen for $F_\mathrm{ex} = 43\,k_\mathrm{B}T/d$ in Figure 3.8. The real part of the correlation function in the direction perpendicular to the force $\phi_q^{s\perp}$ decays monotonously, while we find prominent oscillations in the real part of the correlation function $\phi_q^{s\parallel}$ with the first minima at $tD_0^s/d^2 = 1.5$ for $qd = 7$, $tD_0^s/d^2 = 11$ for $qd = 1$ and $tD_0^s/d^2 = 80$ for $qd = 0.25$. Again, the relative error is below 10^{-6} for $tD_0^s/d^2 < 10^2$ and increases then until both solutions diverge at around $tD_0^s/d^2 = 10^3$.

This resembles the results of second test case in Sec. 3.6.3 with $A(t) = (1 + t)$ and $B(t) = 1$,

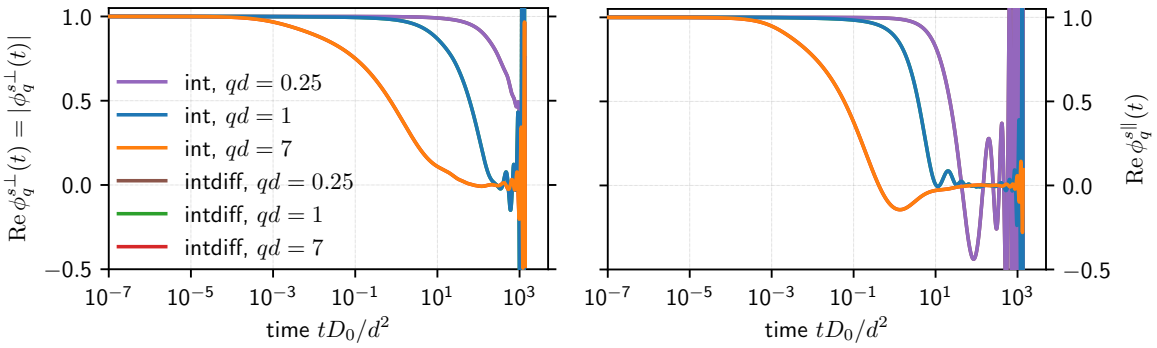

Figure 3.8.: Comparison of the solutions of the MCT equations with the integrodifferential method (intdiff) and the integral method (int) for three wave vectors $qd = 0.25$ (violet/brown), $qd = 1$ (blue/green) and $qd = 7$ (orange/red) at an external force of $43\,k_\mathrm{B}T/d$ above the critical force. The curves for the same wavevector overlap for both methods for all times until they diverge at around $tD_0^s/d^2 < 10^3$. $\phi_q^{s\perp}$ decays rather monotonously, while $\phi_q^{s,\parallel}$ shows oscillations. The oscillations for $tD_0^s/d^2 \gtrsim 10$ are also visible, but less prominent for the imaginary part and the modulus of $\phi_q^{s\parallel}$. The numerical parameters are the same as in Figure 3.7.

where the analytic solution also exhibits damped oscillations while all numerical schemes diverge. In contrast to the previous discussion, it is not possible to identify similarities between the corresponding integral equations. For the test case we found that the solution blows up when the minimal step size exceeds about 10 % of the oscillation period. Reading off a period of order 10 for $qd = 1$ and taking the 10^3 grid points, we find consistently that our full calculation should diverge at around 10^3. This is a strong indication that these oscillations are the cause for the failure of our algorithm. Unfortunately, there is not much we can do about it numerically. Shifting the divergence by one decade requires consequently ten times more points in the uniform time grid.

Naively, these oscillations are caused by a motion with velocity v of the probability density in real space, which translates into a prefactor $e^{\mathrm{i}tvq_z}$ in Fourier space (see (2.52) for the drift diffusion of a single Brownian particle). This implies that larger wave numbers show faster oscillations, but they are at the same time damped more strongly such that one cannot observe a full period. In our case the wave vectors with q_z of the order 1 are the largest wave vectors which show a second maximum. This also explains why $qd = 1$ was suitable to determine the time scale for the instability of the algorithm. All these features can be seen in the right panel of Figure 3.8. Therefore there might be a chance to circumvent this problem by removing the oscillations mathematically by choosing an appropriate frame of reference. It remains to solve the problem that the velocity v is not known beforehand and that it is not necessarily the same for all times, even though we expect it to become constant for long times.

To summarize, this test has shown that both methods to determine the effective memory kernel give the same results. For long times only the integrodifferential method is stable below the critical force. Above the critical force, when the particle delocalizes, we find strong indications that the associated oscillations cause the break-down of both algorithms.

In the next test, we will investigate whether the dynamical calculations lead to the same long time limit as the nonergodicity parameter calculations as introduced in Sec. 3.3. We use

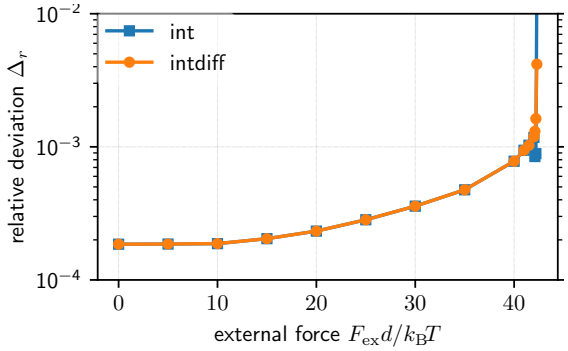

(a) Relative deviation Δ_r as defined in (3.55))for the integral method (int, blue squares) and the integrodifferential method (intdiff, orange circles).

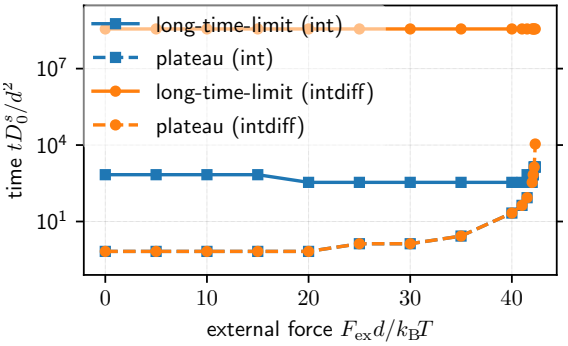

(b) Time at which the nonergodicity parameter was extracted (solid lines) and when the plateau value is reached (dashed lines).

Figure 3.9.: Comparison of nonergodicity parameter determined from the dynamical calculations and the fixed point iteration. The left panel shows the relative deviation, which increases towards the critical force. The right panel shows the times at which the nonergodicity parameter was extracted and at which the plateau value is reached. The errors get large, when the plateau is not reached at the time of the extraction.

the long time limit of the dynamical bath correlation function as input for the nonergodicity parameter to eliminate differences due to different input data. The wave vector grid is the same as for the dynamical calculations (see beginning of this section). We iterate the fixed point equation until the error (3.14) is smaller than 10^{-10}, which is the same accuracy level as for the iteration in the dynamic calculation.

Plotting the resulting nonergodicity parameters as function of wave vector does not show any visual differences. Therefore, we then define the *relative deviation*

$$\Delta_r := \left\| \frac{\boldsymbol{f}^s_{\mathrm{dyn}} - \boldsymbol{f}^s_{\mathrm{fp}}}{\boldsymbol{f}^s_{\mathrm{fp}}} \right\|_\infty , \tag{3.55}$$

where $\boldsymbol{f}^s_{\mathrm{fp}}$ is the nonergodicity parameter obtained by the fixed point iteration and $\boldsymbol{f}^s_{\mathrm{dyn}}$ the one obtained from the dynamical calculation. For the integro-differential method we can directly use the last value, while we have to take some care in choosing the nonergodicity parameters from the integral method calculation due to its instability. The following procedure has shown to give reasonable results. From the time, where the solution becomes unphysical in the sense that $|\phi^s_q(t)| > 1$, we go back two decimation steps, i.e. we divide this time by 4 and define the value of the correlation function at that time to be the nonergodicity parameter.

This works well as long as the plateau of the long time limit is reached before the algorithm becomes unstable as can be seen in Figure 3.9. In this case both algorithms give the same errors. Close to the critical force, however, the plateau value is reached for larger and larger times such that the integral method diverges before the plateau value is reached. The situation is better for the integrodifferential method, because we can extract the nonergodicity parameters at the very end of the calculation.

When approaching the critical force, one finds that the error also increases for the integrodifferential to about 1 % for the forces shown and might grow even larger. A systematic analysis of the features of the correlation function around the critical force will follow in Chapters 4 and

5. Therefore, we only remark that care has to be taken for the results close to the critical force, because the timescales grow very large so that numerical errors can accumulate. In addition, the convergence of the iterations slows down for the dynamical as well as for the fixed point iteration, which has already been noted in [Gru14, Sec. 5.3, p. 55ff]. Hence, we can conclude that the dynamical calculations and the fixed point iterations give the same results as long as the numerical challenges are not too big.

As a last test for this comparison, we change the number of time steps in the uniform grid from 1024 to 512 to 256. This does not change the relative errors, indicating that these errors arise from minor differences in the implementation of the memory kernels or a generic problem of the algorithm which leads to systematic deviations from the long time limit.

Finally, we want to test whether the numerical results for the dynamics are not only consistent in themselves, but also describe the proper dynamics. For this purpose, we use the constant bath approximation. This yields solutions, which are qualitatively the same and have the same long time behavior. Only the relaxation timescale at which the long-time limit is reached reduces by a factor of 3 to 5. With this approximation, we can directly compare the solutions obtained in time space with the explicit solution in Laplace space as introduced in Sec. 2.4.7.

The solution in Laplace space is obtained using the fixed point algorithm described in Sec. 3.4. We discretize the interval $[10^{-10}, 10^5]$ for the Laplace frequency s into 300 points, which are uniformly distributed on a logarithmic grid. Even though the solutions for different s are independent of each other, we calculate the Laplace solution sequentially going from large s to small s using the solution from the previous s as starting point for the next fixed point iteration.

The solutions in the time domain are transformed to the Laplace domain via numerical integration (cf. Section B.2). Since the numerical solutions in the time domain only exist up to a maximum time $t_{\max}$, the numerical integration is also only useful for a finite range of Laplace frequencies. As the correlation functions are bounded and the exponential kernel decays with rate s to zero, we get an acceptable approximation when $t = 5/s$ is in the integration range[5]. This leads to the condition $s > 5/t_{\max}$.

The following consideration might be helpful to understand and interpret the Laplace transformed correlation functions: On a logarithmic scale, the exponential function $\exp(-st)$ can be approximated by 1 for $st \ll 1$ and by 0 for $st \gg 1$. This approximation is of course very crude, but it tells us that the Laplace transform at frequency s can be interpreted as the integral of the correlation function from $t = 0$ to $t = 1/s$. Laplace transforming a constant function $f(t) = c$ then leads to $\tilde{f}(s) = cs^{-1}$, because the integral over a constant c from 0 to $1/s$ is given by cs^{-1}. By chance we recover the exact result in this case.

To clarify these considerations we compare Figure 3.7 (time domain) with Figure 3.10 (Laplace domain). Both figures show the same data in the time domain and the Laplace domain[6]. The left panels in Figure 3.7 show the decay of the modulus of the correlation functions from 1 for $tD_0^s/d^2 < 10^{-3}$ to a non-trivial plateau value for $tD_0^s/d^2 > 10^3$. Consequently we find that the Laplace transform behaves like s^{-1} with prefactor 1 for $sd^2/D_0^s > 10^3$ and with the nontrivial prefactors corresponding to the plateau values for $sd^2/D_0^s < 10^{-3}$. More interesting is the

[5]For bounded functions $|f(t)| \leq 1$ there holds $\left| \int_{5/s}^{\infty} \exp(-st) f(t) \mathrm{d}t \right| \leq \int_{5}^{\infty} \exp(-t') \mathrm{d}t' = \exp(-5) < 0.01$

[6]The constant bath approximation changes the data in Figure 3.7 only slightly.

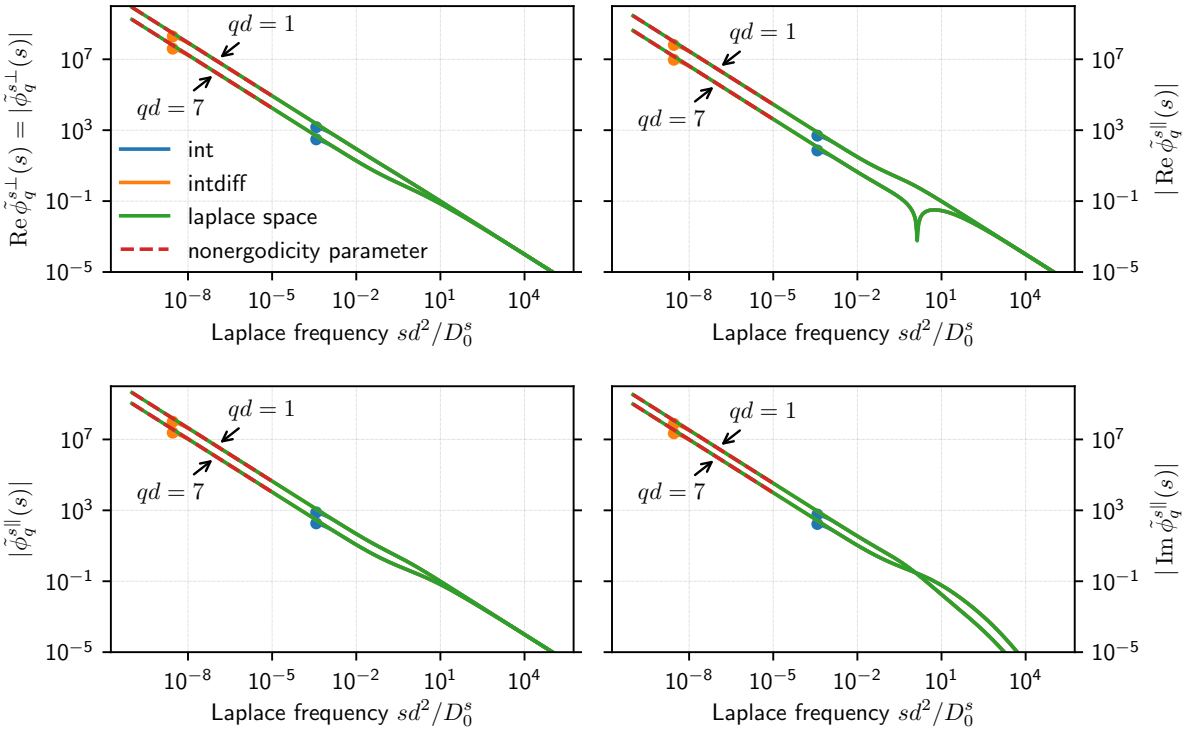

Figure 3.10.: Comparison of the Laplace space solutions of the MCT equations with the integral method (int, blue), the integrodifferential method (intdiff, orange), the Laplace space iteration (green) and the long-time limit solution (dashed, red) for two wave vectors $qd = 1$ and $qd = 7$ as indicated at an external force of $42\,k_\mathrm{B}T/d$. For a proper comparison between the solutions in time and Laplace domain, we used the constant bath approximation. Since the curves collapse almost everywhere, circles indicate, where the Laplace transform of the solution of the integral method and the integrodifferential method starts deviating. This figure corresponds to the Laplace transform of the data in Figure 3.7. The numerical parameters for the wave vector discretization are the same as there and more details can be found in the text.

case of the top right panel ($\mathrm{Re}\,\phi_q^{s\parallel}$). While the long time limit is positive for $qd = 1$, it is negative for $qd = 7$ and consequently there is a change of sign for the Laplace transform, which manifests itself by a kink in the log-log plot. Considering $\mathrm{Im}\,\phi_q^{s\parallel}(t)$, we find that for small times ($tD_0^s/d^2 < 10^0$) the Laplace integral is larger for $qd = 7$ than for $qd = 1$, while this behavior changes in the long time limit (for $tD_0^s/d^2 > 10^3$). This results in a crossing of the curves in the Laplace domain around $sd^2/D_0^s \approx 10^0$. Even though the considerations look very crude, they allow us to get some ideas to connect the features of the correlation functions in time domain to the Laplace domain.

With this understanding of the correlation functions in Laplace space we can discuss the comparison of the different methods in Figure 3.10 for $F_\mathrm{ex} = 42\,k_\mathrm{B}T/d$ in the localized regime. We note that there is no visual difference between the results obtained by the different methods. To indicate the regime of validity for the Laplace transforms, we add circles in the corresponding colors at the smallest Laplace frequency. Zooming in at those points, one would see deviations from the Laplace space solution due to the incomplete numerical integration for the numerical Laplace transform. The dashed red lines for the long time limit are obtained from the

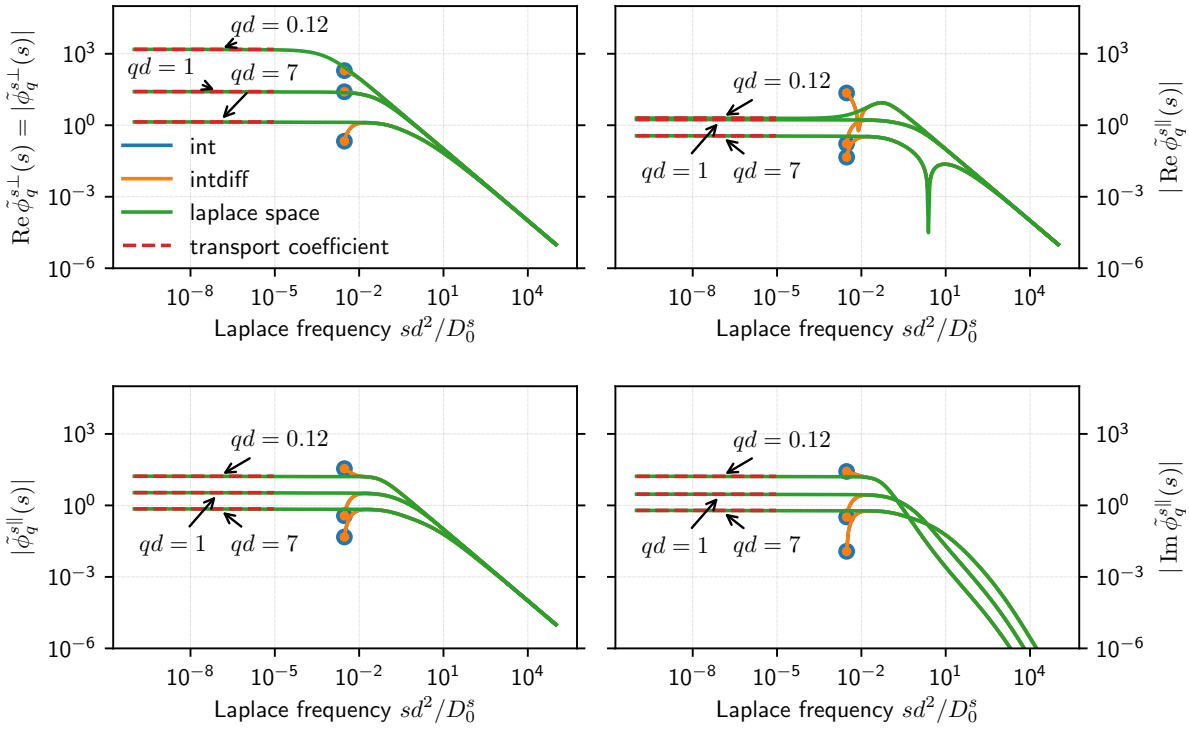

Figure 3.11.: Comparison of the Laplace space solutions of the MCT equations with the integral method (int, blue), the integrodifferential method (intdiff, orange), the Laplace space iteration (green) and the transport coefficients (dashed, red) for three wave vectors $qd = 0.125$, $qd = 1$ and $qd = 7$ as indicated at an external force of $43\,k_\mathrm{B}T/d$. For a proper comparison between the solutions in time and Laplace domain, we used the constant bath approximation. Since the curves collapse almost everywhere, circles indicate, where the Laplace transform of the solution of the integral method and the integrodifferential method starts deviating. This figure corresponds to the Laplace transform of the data in Figure 3.8. The numerical parameters for the wave vector discretization are the same as there and more details can be found in the text.

nonergodicity parameter solution multiplied by s^{-1} as indicated above. They also agree very nicely with the Laplace space solutions.

Figure 3.11 shows the Laplace transforms of the correlation functions for $F_\mathrm{ex} = 43\,k_\mathrm{B}T/d$ in the delocalized regime. Since the nonergodicity parameters are zero everywhere in this regime, we consider the transport coefficients (see Sec. 2.4.8) for the proper $s \to 0$ limit. They are determined from the fixed point equation (2.172) with the same discretization of the wave-vectors and memory kernels as introduced in (3.11). The iteration is stopped if the relative or absolute error becomes smaller than 10^{-10}.

We notice that the solutions agree quite nicely as long as they exist. However, the deviations for small s are larger. For smaller wave vectors this deviation tends to be positive, while it is negative for larger wavevectors. In contrast to the localized regime, the integral and the integro-differential method stop working at about the same time and unfortunately also before the plateau values are reached. Having a closer look one finds also that the plateau for $sd^2/D_0^s < 10^{-4}$ ultimately consists of two plateaus, one for $10^{-4} < sd^2/D_0^s < 10^{-3}$ and one for $sd^2/D_0^s < 10^{-9}$, where the first plateau is smeared out for small wave vectors. The value of

the final plateau corresponds to the value obtained for the transport coefficients, while the first plateau has slightly smaller values. Remarkable is the behavior of the real part in the parallel direction (upper right panel). While the behavior for large wave vectors is similar to the one in the localized regime, e.g. showing the change of sign for large wave vectors, we find a non-monotonic behavior for the smallest wave vectors. The time scale associated with the peak is comparable to the time scale at which the oscillations appeared in the time domain (see upper right panel of Figure 3.8). We also note that this peak becomes more pronounced for smaller wave vectors.

To check whether the numerical solution solves the original equation of motion as well, we reformulate equation (2.158) in the following way

$$\frac{\tilde{\phi}^s_{\boldsymbol{q}^*}(s)}{1 - s\tilde{\phi}^s_{\boldsymbol{q}^*}(s)} = \frac{1 + \tilde{m}^{\text{eff}}_{\boldsymbol{q}^*}(s)}{\Gamma_{\boldsymbol{q}^*}} = \left(\tilde{\mathcal{M}}_{\boldsymbol{q}^*}(s)\right)^{-1}, \tag{3.56}$$

where we used the definition of the effective memory equation (2.157) for the last equality with the combined memory function (2.154b). Even though there is no obvious physical meaning of these quantities, they have to agree for any Laplace frequency s and wave vector $\boldsymbol{q}^*$. This relation also holds in the general case, without the constant bath approximation. These quantities are labeled by $A^{(0)}_{\boldsymbol{q}}(s)$, $A^{(1)}_{\boldsymbol{q}}(s)$ and $A^{(2)}_{\boldsymbol{q}}(s)$ from left to right in [GAPF16, Eq. (E2), (E3)]. For the comparison it is necessary to compute the Laplace transform of those quantities. This was implemented by Gustavo Abade using Filon's integration formula [AS70, p. 890/891, Eq. (25.4.47)] for the Fourier-Laplace transform, which allows the to use full decimated grid. Another possibility would be the use of [AS70, p. 890, Eq. (25.4.45)] for the direct calculation of the Laplace transform using Laguerre polynomials. However, this has not been tested. The analysis shows that the equality is fulfilled for most Laplace frequencies. There is deviations only at the end of the calculation, i.e. for small s in the same way as for the previous analysis. A figure of these quantities as function of the Laplace frequency is shown in [GAPF16, Fig. 14].

In summary, we find that both methods to solve for the time evolution of the correlation functions yield basically the same results. These results agree with the numerical solution of the nonergodicity parameter (the long time limit) and with the direct solution in Laplace space. In the localized regime, the integro-differential method is stable, while the integral method yields unphysical results after some time. In the delocalized regime both algorithms behave unstable, but as long as the solution is physical (i.e. bounded by 1), it agrees with the Laplace solution. The Laplace solution also recovers the proper behavior in the limit $s \to 0$ for the localized as well as the delocalized regime.

3.6.5. Moment calculation

In this section we will briefly discuss the methods for calculating the moments as introduced in Section 2.4.9. They can be obtained via numerical differentiation (3.52). Alternatively, the equations of motion for the moments (2.185b)-(2.185d) can be solved numerically as described in Section 3.5.5. Since the memory kernels for the moments are derived from the correlation functions, we are facing the same problems concerning the stability as described above. The integral method causes the moments to oscillate wildly before diverging, while the integro-differential method yields stable solutions. When reducing the number of points for which

the short time expansion is employed, we find only minor differences at short times. Long times are not affected. We notice that the second cumulant $\langle \Delta z^2 \rangle$ oscillates and may become negative for larger forces and long times. This is unphysical and indicates some problems with the numerics.

Comparing the moments obtained by numerical differentiation with the solutions of the equations of motion, we find relative deviations of about 10 % for short times, when the moments are small and the correlation function is still very close to 1. For longer times, the relative deviations are between 10^{-4} for the first moment in z-direction and 10^{-2} for the second moment in x-direction. Even though these deviations are small, the differentiation causes the moments to be less smooth. This becomes important when local exponents shall be determined (see for example Figure 4.6). Therefore, we will use the moments obtained from solving the integro-differential equations.

4. The critical force

> [Ich bin] Ein Theil von jener Kraft,
> Die stets das Böse will und stets das Gute schafft.
>
> *(Mephistopheles, Faust I [Goe18, v. 1336f, p. 59])*

A characteristic feature of a glass is that the particles remain localized for all times, see Section 2.1.3. The particles may wiggle around their equilibrium positions, but they can never explore the whole system, because they are hindered by their neighbors. This has two measurable consequences: The mean displacement and the variation around this mean position, the variance of the position, remain finite even for infinite times (as for the harmonically bound particle in Sec. 2.3.2). In Fourier space this implies that the correlation functions do not decay to zero, i.e. the intermediate scattering functions $\phi_{\boldsymbol{k}}(t)$ and $\phi^s_{\boldsymbol{k}}(t)$ have a non-trivial long time limit.

If we do microrheology in a glass, this is our equilibrium configuration. Applying an external force, we can move the particle. Does it still remain localized, so that we just shift its equilibrium position or will it start moving? If the force is strong enough, we expect the probe particle to move through the system, because the force is strong enough to push the neighbor particles away, breaking the cage. This qualitative change of the probe particle's motion will be called the *delocalization transition* and the force, at which the particle motion changes from localized to delocalized will be called the *critical force*.

In the following we will use two characterizations of the critical force. Phenomenologically it is easy and convenient to look at the mean displacement of the probe particle. If it saturates for long times, the probe particle is called *localized*. If the mean displacement diverges for long times, the probe particle is called *delocalized*. From a theoretical (and also scatterer's) point of view we can also look at the correlation functions (intermediate scattering functions). If their long time limit is nonzero, the system is nonergodic and the probe particle is *localized*. On the other hand, if the long time limit is nonzero, the probe particle is *delocalized*. In this chapter we will first characterize the critical force according to these definitions in Sections 4.1 and 4.2. With this knowledge, we determine the critical force for various packing fractions to evaluate the phase diagram in Section 4.3. Finally, we characterize the delocalization transition and analyze the behavior of moments, transport coefficients, correlation functions and van Hove functions in Section 4.5. This includes a comparison to simulations of quasi hard spheres.

4.1. Identification of the critical force for the correlation functions

In this section we use the theoretical definition of the critical force, which looks at the long time limits of the correlation functions. If the correlations decay to zero for long times, the system behaves ergodic and the probe particle delocalizes. If there remain finite correlations even for infinite times, the probe particle is localized. These correlations are also called nonergodicity

parameters. We can employ four different calculations, which contain information about the long time limit: The transport coefficients (see Sec. 2.4.8), the nonergodicity parameters (see Sec. 2.4.6) and the limiting behavior in the dynamical calculations in Laplace space (see Sec. 2.4.7) and in time space (see Sec. 2.4.5). Each of those methods has its advantages and drawbacks as we will see in the following.

4.1.1. ... via transport coefficients

It was already noted in [Gru14, Chapter 5] that it is difficult to find the proper critical force. This difficulty arises from the slowing down of the convergence of the fixed point iteration combined with the fact that the nonergodicity parameters are finite but small below the critical force. In consequence one has to iterate very long to see the difference between "small, but finite" and "small, and decaying".

To circumvent this problem, we have a look at the transport coefficients $D^s_{\boldsymbol{q}}$ as introduced in (2.171). If $f^s_{\boldsymbol{q}} \neq 0$ they diverge, while they converge to some finite value if $f^s_{\boldsymbol{q}} = 0$. Numerically, this is easier to detect: In the latter case, the difference between subsequent iterations decreases, while it must not decrease in the divergent case. In terms of the contraction factor c (3.15) this implies $c < 1$ for $D^s_{\boldsymbol{q}} < \infty$ (and $f^s_{\boldsymbol{q}} = 0$) and $c \geq 1$ for $D^s_{\boldsymbol{q}} = \infty$ (and $f^s_{\boldsymbol{q}} \neq 0$). This distinct behavior appears quite reliably after a few fixed point iterations according to (2.172). Therefore, it is sufficient to calculate only the first 200 to 500 iterations for the transport coefficient to determine whether this force causes a localized ($c > 1$) or delocalized ($c < 1$) behavior. Then a bisection method is applied to find the critical force. Since the number of iterations does not depend on the distance to the critical force, the time to find it at a given precision depends only on the number of bisections. In contrast, distinguishing between localized and delocalized results for $f^s_{\boldsymbol{q}}$ needs an increasing number of iterations (roughly $|\delta|^{-1}$, where δ is the relative distance to the critical force $\delta := (F - F_\mathrm{c})/F_\mathrm{c}$).

If this method yields results, which are consistent with the values obtained by the other methods, this is the method of choice, because it yields the critical force with high numerical accuracy and low numerical effort. Testing the consistency is the purpose of the following sections.

4.1.2. ... via nonergodicity parameters

Determining the critical force via the nonergodicity parameter is conceptually simple, but numerically demanding. The task is to find the smallest force F_c for which all nonergodicity parameters $f^s_{\boldsymbol{q}}$ are zero. The numerically demanding task is to determine whether $f^s_{\boldsymbol{q}}$ is really zero, because we can only do a finite number of iterations and on top of that the speed of convergence is slowing down when approaching the critical force. Therefore, a bisection method is not very reliable (see also [Gru14, Sec. 5.1, p. 49-54]). Furthermore, it is also very slow, because it cannot be parallelized as it requires the result at the midpoint to determine the next force. Instead, we calculate the nonergodicity parameter for many forces at the same time and refine the force-grid where the nonergodicity parameter shows interesting behavior. A good guide is the reduced contraction factor $c^r := 1 - c$, which shows minima at critical points [Gru14, Sec. 5.3, p. 55-58]. This is still true for the logarithmic grid, which can be seen in Figure 4.1.

There, we show the nonergodicity parameters as function of the force. We used the `unilog10`-grid with $N = 51$ grid points and a cutoff $q_{\max}d = 20$ for the q_x and q_z direction. The difference grid q_d was discretized uniformly with 401 grid points for $qd \in [0, 40]$. As input for the bath nonergodicity parameter the long time limit of the dynamical calculation with a cutoff of $qd = 65$ and a total of $N = 512$ grid points was used. The physical parameters are a packing fraction of $\varphi = 0.537$ and the forces as specified.

The left column of Figure 4.1 shows the nonergodicity parameters in the directions perpendicular and parallel to the force for a broad force range. We find that the nonergodicity parameter $f_q^{s\perp}$ (which is real by symmetry) in the perpendicular direction decreases monotonously to zero around the critical force. In the parallel direction we find non-monotonic behavior for large wave vectors in the real part and very pronounced peaks for smaller wave vectors in the imaginary part. Having a closer look at the part, where the nonergodicity parameters vanish, we find some interesting behavior. The reduced contraction factor c^r, for example, shows two minima. And for each minimum we find that the structure of the nonergodicity parameters change.

At the first minimum (smaller force) the parallel nonergodicity parameter $f_q^{s\parallel}$ jumps to very small values, while the perpendicular one also jumps, but remains at quite large values for the small wave vectors. This behavior can be observed very clearly in the top right panel for $qd = 0.05$, but is also present for the other wave vectors.

At the second minimum all nonergodicity parameters are going continuously to zero irrespective of direction or magnitude of the wave vector. The position of this minimum also coincides with the critical force obtained by the transport coefficient method introduced in the previous section. This value is shown as red dashed line.

The critical force seems to split into two critical forces with different critical behavior. At the smaller force, we have a discontinuous transition, where many nonergodicity parameters essentially jump to zero, but some remain finite. At the larger force all nonergodicity parameters go continuously to zero. This leaves us with the question whether there are actually two critical forces with associated partial transitions.

Similar features can be found in [Gru14, Fig. 5.5, p. 56], but on a much larger scale. While the difference between the different critical forces and the different grid types there were of the order of several $k_{\mathrm{B}}T/d$, we now find this behavior on a scale of $10^{-2}\, k_{\mathrm{B}}T/d$. This suggests to analyze the grid-dependency of these features. With this analysis we can also try to separate the numerical features of this transition from the physical features (which should not depend on the numerics).

The main difference to the results obtained in [Gru14] is the introduction of the logarithmically spaced grids, which improved the resolution for the small wave vectors. Since it is the nonergodicity parameters for the small wave vectors, which show the strongest anomalies, we will use the `unilogX`-type grid and vary the number of points in the logarithmic part from 6 over 10 to 14, while keeping the number of points in the uniform part and the spacing Δ_q the same. An important characterizing quantity is the minimal nonzero wave vector $q_{\min}$. Additionally, we vary the cutoff $q_{\max}$ keeping the spacing in the uniform part the same. With this comparison we can make sure that the features in the smaller and therefore low-computational-cost grids are the same as for the larger ones. The parameters of those grids are shown in Table 4.1.

The values of the critical forces for different cutoffs with the same base grid of type `unilog10`

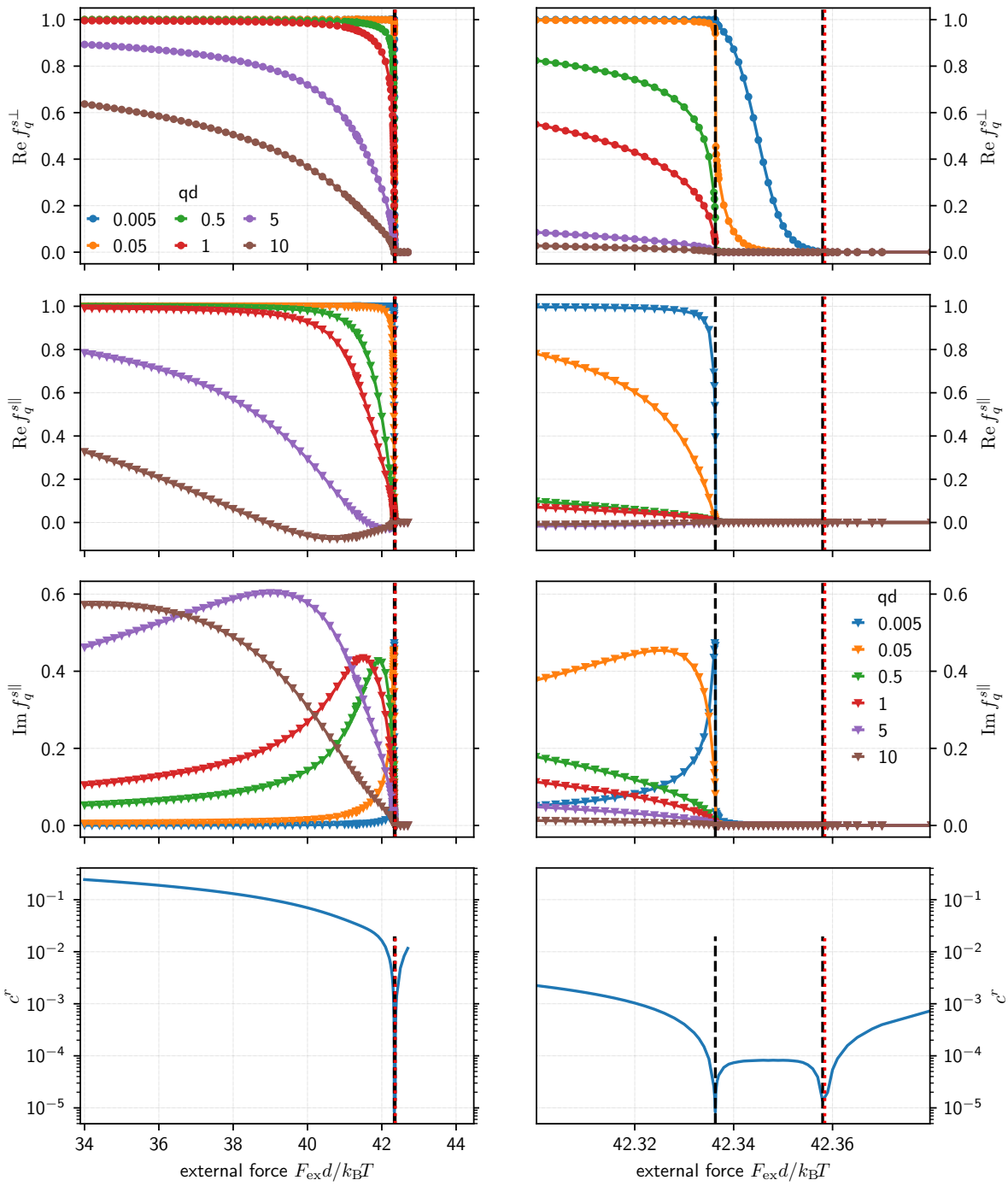

Figure 4.1.: Nonergodicity parameter when approaching the critical force. The dashed black lines indicate the minima of the reduced contraction factor c^r. The right column shows a close up of the same data in the vicinity of the critical forces. The red dotted line indicates the criticial force obtained by the transport coefficient method. **A cutoff of $q_{\max}d = 20$ is used**; further details on the numerical parameters can be found in the text.

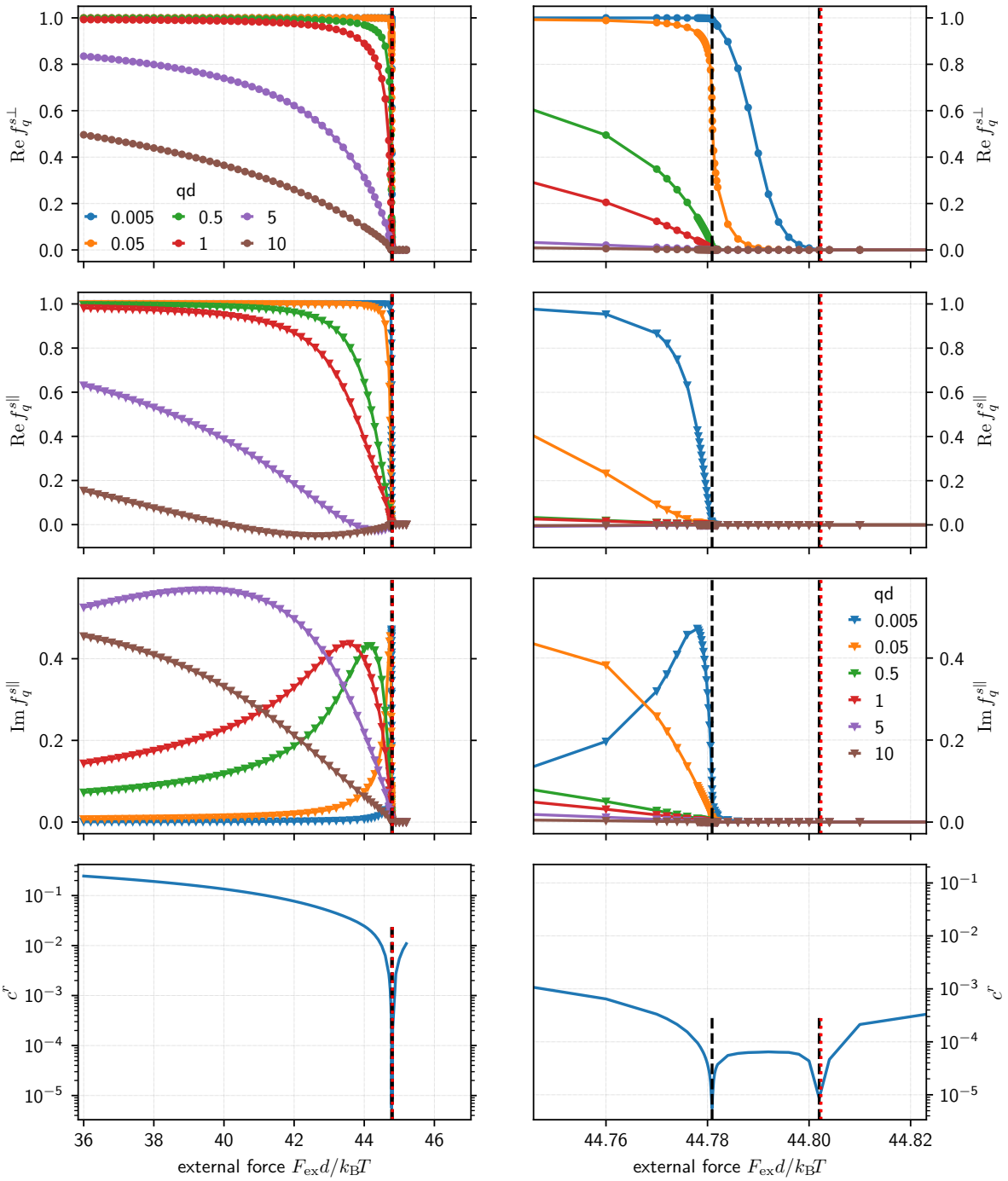

Figure 4.2.: Nonergodicity parameter when approaching the critical force. The dashed black lines indicate the minima of the reduced contraction factor c^r. The right column shows a close up of the same data in the vicinity of the critical forces. The red dotted line indicates the criticial force obtained by the transport coefficient method. The difference to Figure 4.1 is the use of a **cutoff of** $q_{\max}d = 14$. Further details on the numerical parameters can be found in the text.

Table 4.1.: Grid choices and corresponding uniform step sizes Δq and minimal nonzero wave vector $q_{\min}$. These values apply for the q_r and q_z grids. For the corresponding q_d grid we use a uniform discretization of $[0, 2q_{\max}]$ with step size of 0.05 for $q_{\max} = 10$ and 0.1 in the other cases. The unit of the wave vector is d^{-1}.

$q_{\max}$	type	N_q	Δ_q	$q_{\min}$
10	`unilog6`	27	0.50	$7.812{\cdot}10^{-3}$
	`unilog10`	31	0.50	$4.883{\cdot}10^{-4}$
	`unilog14`	35	0.50	$3.052{\cdot}10^{-5}$
14	`unilog6`	35	0.50	$7.812{\cdot}10^{-3}$
	`unilog10`	39	0.50	$4.883{\cdot}10^{-4}$
	`unilog14`	43	0.50	$3.052{\cdot}10^{-5}$

$q_{\max}$	type	N_q	Δ_q	$q_{\min}$
20	`unilog6`	47	0.50	$7.812{\cdot}10^{-3}$
	`unilog10`	51	0.50	$4.883{\cdot}10^{-4}$
	`unilog14`	55	0.50	$3.052{\cdot}10^{-5}$
24	`unilog6`	55	0.50	$7.812{\cdot}10^{-3}$
	`unilog10`	59	0.50	$4.883{\cdot}10^{-4}$
	`unilog14`	63	0.50	$3.052{\cdot}10^{-5}$

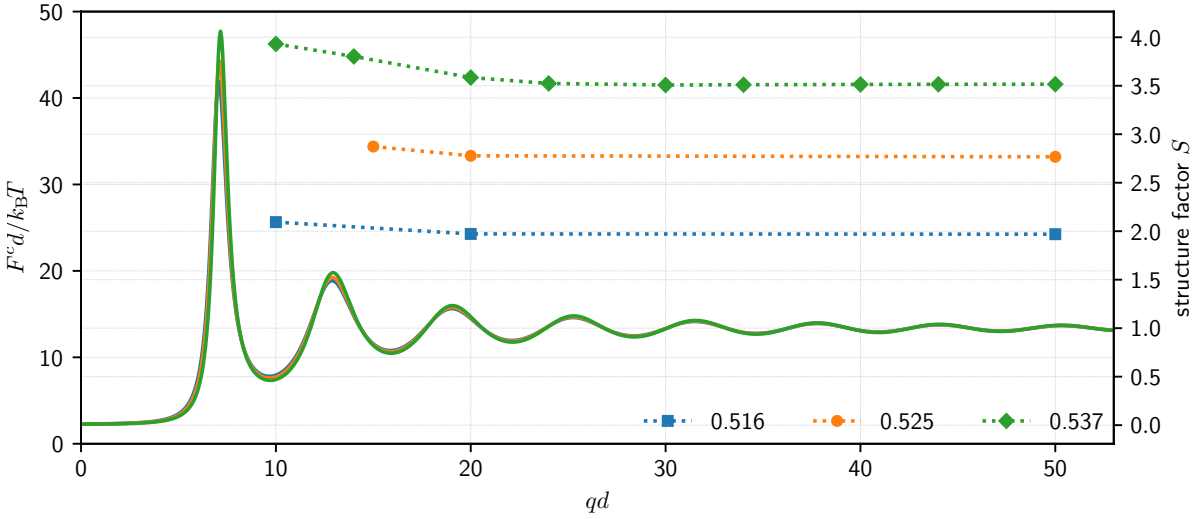

Figure 4.3.: Critical force variation with grid cutoff. The symbols connected by the dashed lines show the critical forces (left axis) obtained by the transport coefficient method for different grid cutoffs as indicated on the x-axis. For comparison we show the static structure factor (solid lines, right axis) for the corresponding packing fractions. After the third peak is included ($qd \gtrsim 20$) the critical force values change only slightly.

with a uniform grid spacing of $\Delta qd = 0.5$ are shown in Figure 4.3. Since the maximum cutoff is $qd = 50$, we calculated the bath nonergodicity parameter on a grid with cutoff $qd = 120$ and 4096 points. We note that once the third peak is included ($qd \gtrsim 20$) the critical force variation is smaller than the symbol size. Nevertheless this variation is important when analyzing the features close to the critical force. Therefore, we will normalize in the following all forces by a reference critical force F_{ref}, which is defined as the critical force obtained by the transport coefficient method using a `unilog25` grid. This choice will be justified later on in this section, when we discuss the quantitative qrid-dependency of the critical forces.

For each grid type, we determine the critical force via the transport coefficient method. By calculating the nonergodicity parameters we determine the two critical forces via the minima

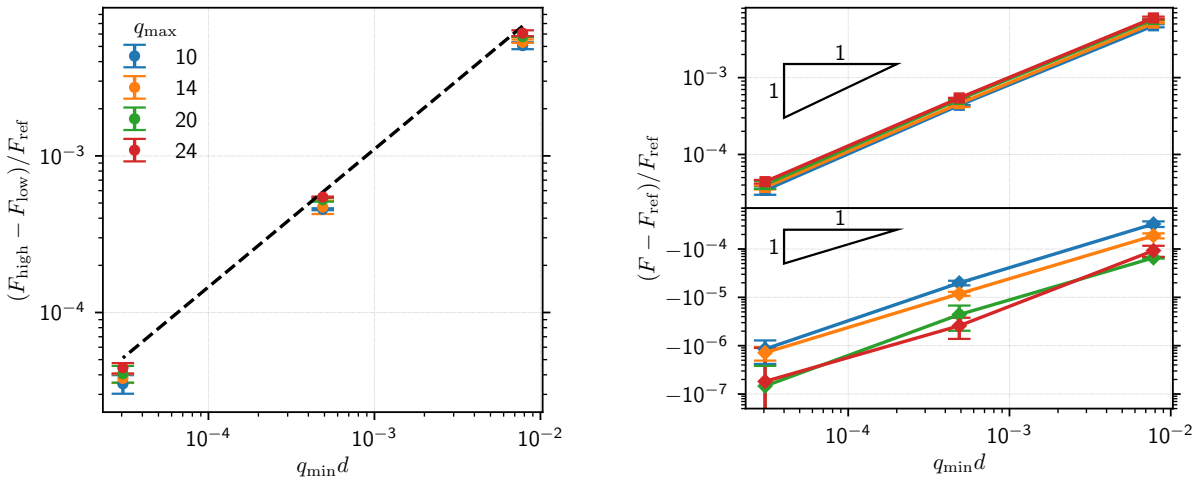

(a) Critical force difference

(b) Difference to the reference critical force

Figure 4.4.: Grid dependency of the critical forces. Panel (a): Difference between the critical forces as function of the minimal nonzero wave vector $q_{\min}$. The dashed black line is a power law with exponent 0.87. Panel (b): Distance of F_{high} (upper panel) and F_{low} (lower panel) from the reference critical force F_{ref}. The color code is the same in both plots. The definitions of the different forces can be found in the text.

in the contraction factors, which we will call F_{low} and F_{high} (such that $F_{\text{low}} < F_{\text{high}}$). The first result is that F_{high} agrees with the critical force obtained by the transport coefficient method within the resolution of the nonergodicity parameter calculation. Second, we analyze how the distance between these forces evolves as a function of the minimal step size $q_{\min}$. This is shown in Figure 4.4a. We find that these data collapse roughly on one line. Based on this data we find the following empirical estimate

$$\frac{F_{\text{high}} - F_{\text{low}}}{F_{\text{ref}}} \lesssim 0.45\,(q_{\min})^{0.87} \tag{4.1}$$

(black dashed line in Figure 4.4a). Extrapolating this finding, we have to conclude $F_{\text{high}} = F_{\text{low}}$ in the limit $q_{\min} \to 0$. While the analytical limit $q_{\min} \to 0$ might propose additional challenges, we can use this relationship to estimate how closely we can approach the critical force before noticing the features of the splitting of the critical force. As a rule of thumb this yields: results for relative distances to the critical forces of $\delta = (F - F_{\text{c}})/F_{\text{c}}$ with $\delta < q_{\min} d$ have to be handled with care, because they might be unphysical.

The second question of this analysis concerns the value of the critical force in the limit infinitely small $q_{\min}$. When analyzing the minima of c^r for decreasing $q_{\min}$ we find that F_{low} increases slightly, while F_{high} decreases. Furthermore, we notice that F_{low} is rather close to F_{ref}. This suggests that all critical forces indeed converge to the same value. To make this statement quantitative we show the distance to the reference force F_{ref} in Figure 4.4b. The upper panel shows the evolution of F_{high}, while the lower panel shows the evolution of F_{low} when $q_{\min}$ is decreased. Both critical forces decrease with an exponent close to 1, i.e. almost proportional to $q_{\min}$. The relative distance of F_{low} is about one to two orders of magnitudes smaller than that of F_{high}. Since both relative forces decrease in the same way as the difference, we can conclude that they indeed converge to F_{ref}. This justifies labeling F_{ref} the reference

force and normalizing by this reference force.

In conclusion we find that the splitting of the critical force seems to be of numerical nature, because the splitting decreases as $q_{\min}$ decreases. This allows a computationally inexpensive way to determine the critical force in the limit of infinitely small $q_{\min}$, namely calculating the critical force by the transport coefficient method for a grid with sufficiently small $q_{\min}$. The value of $q_{\min}$ also gives a rough estimate on which relative distance δ to the critical force we may see effects due to the splitting of the critical force.

4.1.3. ... via Laplace space calculations

In the previous section we found that there are potentially two critical forces, based on the slowing down of the convergence. This is a hint that the solution changes qualitatively, but to answer the question how this limit is approached, we need to look at the full dynamical solution. We start by analyzing the Laplace space solution, because the nonergodicity parameter studied in the previous section is given by the $s \to 0$ limit of this equation. Therefore, we can use basically the same numerical fixed point iteration (3.18). Since the Laplace space solution becomes quite large in the limit $s \to 0$, we can apply the extrapolation (3.19) to speed up the convergence. As the solution is always finite for finite Laplace frequency s, the numerical scheme will always converge. For this reason, we will start with 200 iterations to determine the contraction factor and perform another 100 iterations until the contraction factor is conclusively indicating a contraction ($0 < c < 1$).

For a good and easy comparison, we use again the same wave vector discretizations as in the previous section and start by discussing the system with $q_{\max} = 20$ and the `unilog10`-type grid (see Table 4.1 for the details). The solutions of the correlation functions in Laplace space for $qd = 0.05$ are shown in Figure 4.5. To interpret these figures, we can use the following reasoning: Short times correspond to large Laplace frequencies at the right side, while long times correspond to small Laplace frequencies on the left side. Furthermore, a divergence like s^{-1} corresponds to a nonzero long time limit, while a constant value for $s \to 0$ indicates that the correlation functions decay to zero. To visualize the different regimes, we use blue for forces below F_{low}, red for forces above F_{high} and green for forces in between. The two critical forces F_{low} and F_{high} as identified in the previous section are shown as black lines. For short times, i.e. large frequencies $sd^2/D_0 \gtrsim 10^{-1}$ all curves basically collapse. Even though the short time behavior is force dependent, this cannot be seen here, because the forces cover only a small range, while the correlation functions cover many orders of magnitude.

In the long time limit or small frequency limit, the behavior changes dramatically for different forces. For small forces the curves diverge like s^{-1}, while large forces reach a plateau, as expected. More interesting is the behavior of the green curves between the two critical forces. We find that F_{high} separates the curves which remain finite for $s \to 0$ from those which diverge. Hence, F_{high} is indeed the critical force, which separates ergodic from non-ergodic behavior. This also explains why F_{high} coincides with the critical force obtained by the transport coefficient method. All curves for forces larger than F_{high} show a maximum for $\operatorname{Re} \phi_q^{s\parallel}$ at intermediate frequencies.

The appearance of this maximum is connected to the lower critical force F_{low}. Forces above this threshold show this maximum, while forces below do not, as can be seen on the right hand side of Figure 4.5. The numerics also suggests that this maximum appears discontinuously,

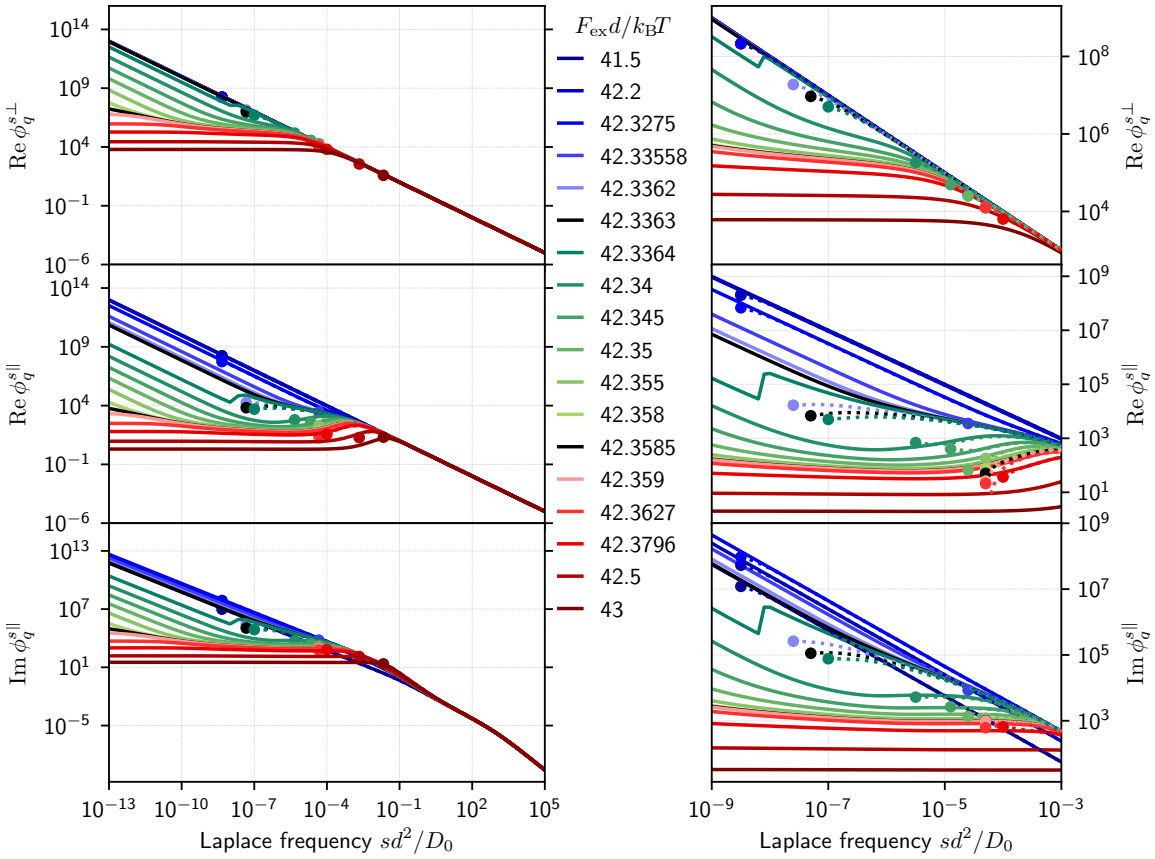

Figure 4.5.: Laplace space solutions close to the critical forces. Left: Correlation functions perpendicular (top panel) and parallel (real part middle panel, imaginary part bottom panel) to the force as function of the Laplace frequency sd^2/D_0 for $qd = 0.05$ and forces as indicated. Forces below F_{low} are colored in blue, forces between F_{low} and F_{high} are colored in green and forces above F_{high} are colored in red. The critical forces $F_{\text{low}} = 42.3363\, k_BT/d$ and $F_{\text{high}} = 42.3585\, k_BT/d$ as obtained from Figure 4.1 are shown in black. Dashed lines show the Laplace transform of the solutions obtained in time space using the constant bath approximation. Circles indicate the Laplace frequency corresponding to the end of those calculations. Right: close up of the discontinuity region with the same color code. For the numerical details see text.

which is compatible with the finding that the nonergodicity parameters jump as well. On the other hand this can also just be an artifact of the extrapolation scheme. Nevertheless, whether this is discontinuous in s or not, we need a discontinuity in the $s \to 0$ limits as function of F_{ex} as obtained by the nonergodicity parameter calculations. A second feature of this first critical force can be observed in the perpendicular direction. Below F_{low}, basically all curves fall on top of each other, describing the straight line s^{-1} in the double-logarithmic plot, while they start to deviate only for forces greater than F_{low}. This coincides with the results for the nonergodicity parameters, which are close to one in the perpendicular direction for small wave vectors below F_{low} (see Figure 4.1).

It is difficult to find some features connected to the lower critical force for the imaginary part of the correlation function parallel to the force, because the curves do not vary monotonously with the force. This is also visible for the nonergodicity parameters.

How do the features described above change with the discretization? Increasing the number of grid points in the logarithmic part of the grid, we find that the appearance of the peak in the real part of the correlation function in the parallel direction shifts to smaller Laplace frequencies. There is roughly a one to one correspondence: decreasing the smallest grid point by one decade induces a shift of the peak by about one decade. The curves around F_{high} are basically not affected by the refinement of the grid. Even though the numerical value of this force changes, the curves at the same relative distance to the critical force look very similar, not only qualitatively but also quantitatively. The same findings apply to the grid with a cutoff of $q_{\max}d = 24$.

Lowering this cutoff to $q_{\max}d = 14$ changes these findings. While the peak in the real part of the correlation function parallel to the force still exists for forces close to and above F_{high}, it appears now continuously. On top of that, the appearance of the peak is not directly connected to F_{low} anymore, it appears somewhere between F_{low} and F_{high}, also depending on the wave vector. Furthermore, we find that the correlation function in the perpendicular direction already shows some decay close to F_{low}, in contrast to the behavior for $q_{\max}d \geq 20$. This makes it therefore difficult to pinpoint this critical force based on the Laplace space solution. For the larger critical force the behavior is still the same: F_{high} separates the forces where the Laplace space solution diverges like s^{-1} from those, where it remains constant for $s \to 0$. The continuous transition at F_{low} is in line with the finding of the nonergodicity parameter calculation, where there is also no discontinuity in the nonergodicity parameter.

To summarize, we find that F_{high} does indeed separate nonergodic from ergodic behavior, also for the Laplace space calculation. The critical force F_{low} can be associated with the appearance of a peak in the real part of the correlation function parallel to the force for small wave vectors. This appearance is discontinuous for and directly related to the critical force for $q_{\max}d \geq 20$, while it is continuous and smeared out for $q_{\max}d \leq 14$. Decreasing the minimal step size in the grid shifts the splitting to smaller Laplace frequencies or larger times. This points again to a numerical origin of this behavior. A more careful analysis of the behavior close to the critical force will be carried out in Chapter 5.

4.1.4. . . . via solving the integro-differential equations

Since the representation of the solution in Laplace space is not very convenient and can cause some headaches when trying to interpret it, we will use these results to benchmark our solution scheme in time space. Hence, we will solve the corresponding integro-differential equations in time space and Laplace transform them to compare them to the solutions obtained above. The reason for this comparison scheme is that the Laplace transform is numerically a one way road. The Laplace transform is straightforward and stable, but its inverse is neither straightforward nor stable, because it involves an improper integral in the complex plane [BMMS08, p. 775, Eq. (15.8)].

In Section 2.4.7 we have shown that the Laplace space solution is equivalent to the solution in time, when the bath correlation function is approximated by its long time limit. Throughout this section, we will use this approximation to check the validity of our solution in time space, since we already know from the numerical tests in Section 3.6 that the algorithms can be unstable or yield wrong results for long times. To allow for an easy comparison with the long time limit and the Laplace space solutions, we choose the same discretization of the wave

vectors as before. The time dependent solution is obtained using a 45-fold decimation starting with a uniform grid with step size $\Delta t = 10^{-8}$ and 1024 points, which covers times from 10^{-8} to $3.6 \cdot 10^{8}$. The solutions are typically obtained using the integro-differential method, unless specified otherwise, because it proves to be the most stable algorithm. Nevertheless, there appear non-physical solutions[1] for larger forces and longer times. In these cases, we stop the calculation whenever this violation is too strong (typically $|\phi^s_{\boldsymbol{q}}(t)| > 1.2$ or $1 + 10^{-10}$).

We start the analysis by comparing the Laplace transformed solutions (dashed lines) in time space to the solutions in Laplace space in Figure 4.5. The minimum value for the Laplace frequency s (indicated by circles) is given by the inverse of the maximum time available in the solution in time space (see Appendix B.2 for details). For large Laplace frequencies ($sd^2/D_0 \gtrsim 10^{-2}$) the relative error is below 10^{-3}, indicating a quite good agreement, for all forces. There is a trend of larger relative errors for increasing wave vectors, which might be related to the fact that the absolute values become smaller for increasing wave numbers. For forces below F_{low} we find only very small deviations over the whole range of Laplace frequencies. The largest deviations can be found at the smallest s, also due to the truncation problem of the Laplace transformation. Very close to F_{low} we find strong deviations of the time-solution from the Laplace solution. It is interesting to observe that we enter the regime of unphysical and unstable solutions in the time domain at forces around F_{low}. This causes the Laplace transforms to end at larger frequencies s. Nevertheless, we find good agreement (a relative error smaller than 10^{-2}) up to that point, which confirms that this break condition is useful. The unphysical solutions appear at decreasing times for increasing forces and prevent us from observing all features of the Laplace space calculations. In particular it is not possible to analyze the behavior between the different critical forces in time space. Defining a relative error threshold we can determine the time until which we trust the solutions. As a rule of thumb, a threshold of 5 % indicates that we should not trust data one decade before the modulus of the correlation function exceeds 1. Close to F_{low} one has to be more careful, because the time solution may deviate from the Laplace solution without becoming unphysical.

In summary, this analysis confirms that the solution in time space is indeed almost correct as long as the solution remains physically sensible. We find that the algorithm becomes unstable for the long time limit for forces around F_{low} and above. Therefore, it is not possible to investigate the long time limit at the different critical forces from these calculations. For the solution with the dynamical bath we cannot check the results this way, but we hope that these findings can be translated, because the dynamic bath mostly affects the solutions at short times.

4.2. Identification of the critical force for the mean displacement

In this section, we will characterize the critical force according to the second definition based on the long time behavior of the mean displacement $\langle z \rangle (t)$. If this mean displacement is finite for long times, we call the probe *localized*; if it diverges for long times, we call it *delocalized*. The critical force separates these two regimes as before. We calculate the mean displacement of the probe particle according to (2.185b) using the methods described in Section 3.5.5. We start by calculating the mean displacement in the constant bath approximation, which will be

[1] $|\phi^s_{\boldsymbol{q}}(t)| > 1$ in contrast to the property that auto-correlation functions are bounded by their initial value $\phi^s_{\boldsymbol{q}}(0) = 1$, see (2.88)

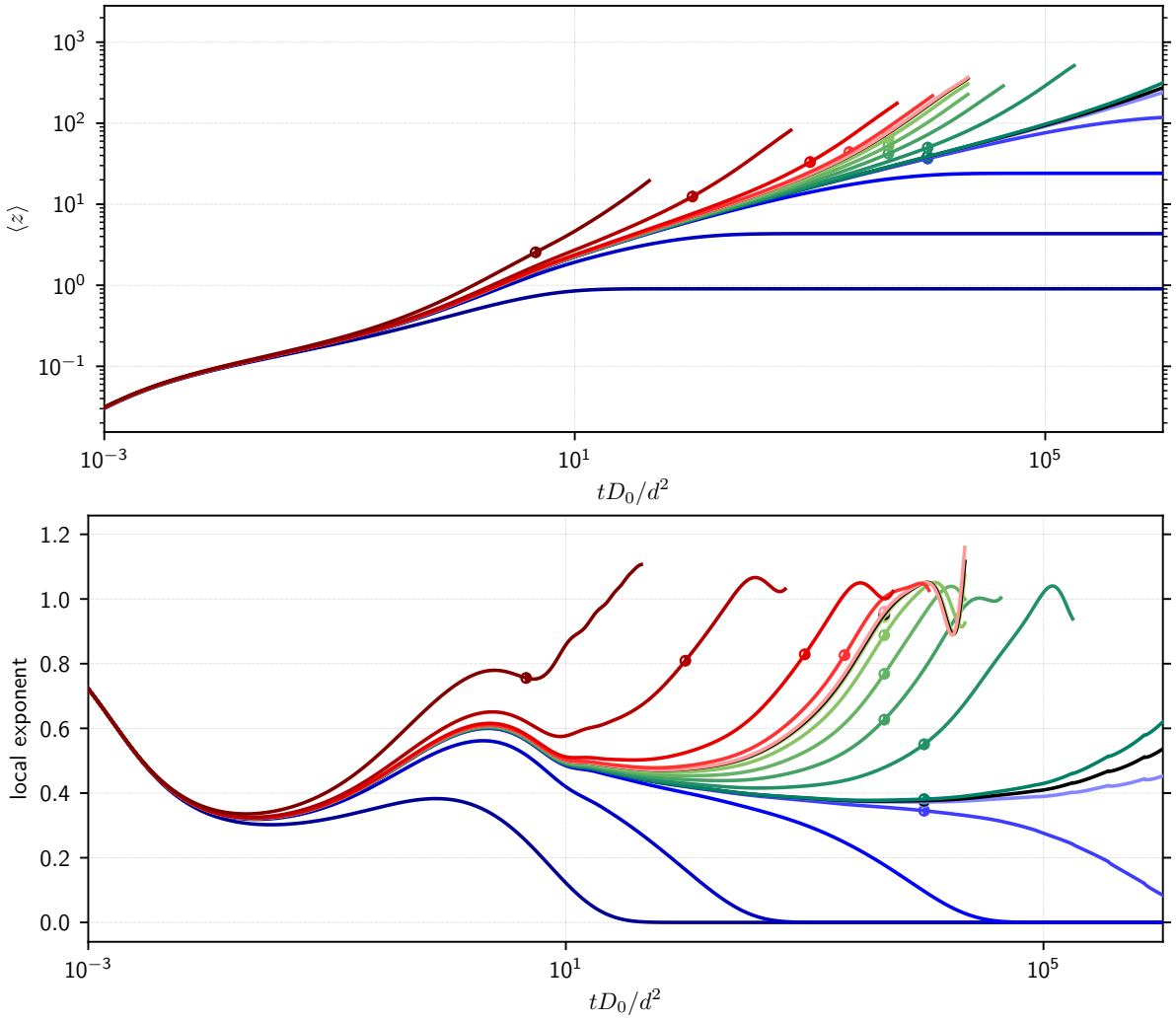

Figure 4.6.: Top: Mean displacement for different forces close to the critical forces. Bottom: Local exponent of the mean displacements. The color code in both panels is the same as in Figure 4.5: blue curves are forces below F_{low}, red curves above F_{high} and green curves in between. Circles indicate the time after which the Laplace transform of these curves deviates from the Laplace space solution by more than 5 %.

compared to the full dynamical solution and the Laplace space solution. In Laplace space, the moments can be calculated using special combinations of memory functions as introduced in Section 2.4.9.

We use the same discretization as in the previous section, namely the `unilog10`-grid with a cutoff of $q_{\max}d = 20$ for the wave vector discretization and a 45-fold decimation of a uniform time grid with 1024 points and a minimal time of 10^{-8}. For the beginning we use the constant bath input with a wave vector discretization of 512 points and a maximum wave vector of $q_{\max}d = 65$ obtained from the long time limit on the same time grid. The mean displacement obtained from these calculations is shown in the top panel of Figure 4.6.

We find that the mean displacement diverges for forces above F_{high} and saturates for forces

below approximately F_{low}. This confirms that the critical force obtained by this method is not too different from the critical force obtained by the previous method. Having a closer look at the data we do not find two critical forces which separate qualitatively different mean displacements, but only one, which differs from F_{low} on the 4th decimal digit. Forces above this value all show a diverging behavior for large times. As mentioned before, our calculations become unphysical for long times for forces above F_{low} so that we cannot access very long times for those forces. Therefore, we cannot rule out that the mean displacement saturates at longer times and even larger displacements, as suggested by the Laplace space solutions, see Figure 4.7. There, a saturation of the mean displacement for $t \to \infty$ corresponds to a saturation of $sM_z^{(1)}(s)$ for $s \to 0$, whereas a divergence proportional to t for $t \to \infty$ corresponds to a pole s^{-1} for $s \to 0$. The existence of two different power laws can be easily seen, but a more quantitative analysis will follow below. We also note that the critical force is exact for the Laplace space solutions in the sense that the critical forces separate solutions with qualitatively different behavior. For forces below F_{low} we can only identify one power law for small Laplace frequencies. For forces above F_{high}, there is a different power law for large times. Forces in between first follow a s^{-1} power law for intermediate Laplace frequencies while they cross over to s^0 for small Laplace frequencies. We again observe a kink in the data for $F_{\mathrm{ex}}d/k_{\mathrm{B}}T = 42.3364$ as before.

To make the comparison of the possible power-laws more quantitative, we calculate the local power-law-exponent

$$\alpha_f(x) := \frac{\partial \log f(x)}{\partial(\log x)} = \frac{x}{f(x)}\partial_x f(x), \tag{4.2}$$

which is effectively the slope of $f(x)$ in the log-log-plot. The first definition is easy to implement numerically via

$$\alpha_f(x_i) := \frac{\log f(x_{i+1}) - \log f(x_i)}{\log(x_{i+1}) - \log(x_i)}. \tag{4.3}$$

In our case f will be the mean displacement as a function of the time t or the Laplace frequency s. The Laplace transform applied to a power law t^τ leads to a power law s^σ in Laplace space with $\sigma = -\tau - 1$ (cf. Table B.1). In particular there is the correspondence $t^0 \leftrightarrow s^{-1}$ and $t^1 \leftrightarrow s^{-2}$. To facilitate comparison of the power laws we multiply the Laplace transformed functions with the Laplace frequency. Then the exponents are simply the negative values of each other.

With this knowledge we can compare the local exponents for the time solution and the Laplace solution as shown in the lower panels of Figure 4.6 and Figure 4.7. Starting with the local exponents in the time domain, we notice, that the diverging mean displacements are easy to spot, because the local exponent starts growing, while it decays to 0 when the final mean displacement is finite. For forces close to F_{low} we find a different behavior than expected: While forces below F_{low} should show an exponent decaying to 0, we find that it grows instead. This indicates that F_{low} is not exactly the desired critical force for the time space calculation. The true critical force should be a little bit smaller. On the other hand we observe that the time at which time and Laplace space solutions disagree by more than 5 % (indicated by circles in the plot) is about two decades before the separation of these curves becomes visible. Therefore, we may attribute this unexpected behavior to the errors introduced by the numerical solution in time space. The same argument applies to the non-monotonic parts in the local exponents for larger forces, which may also be numerically questionable. In this plot we find that the

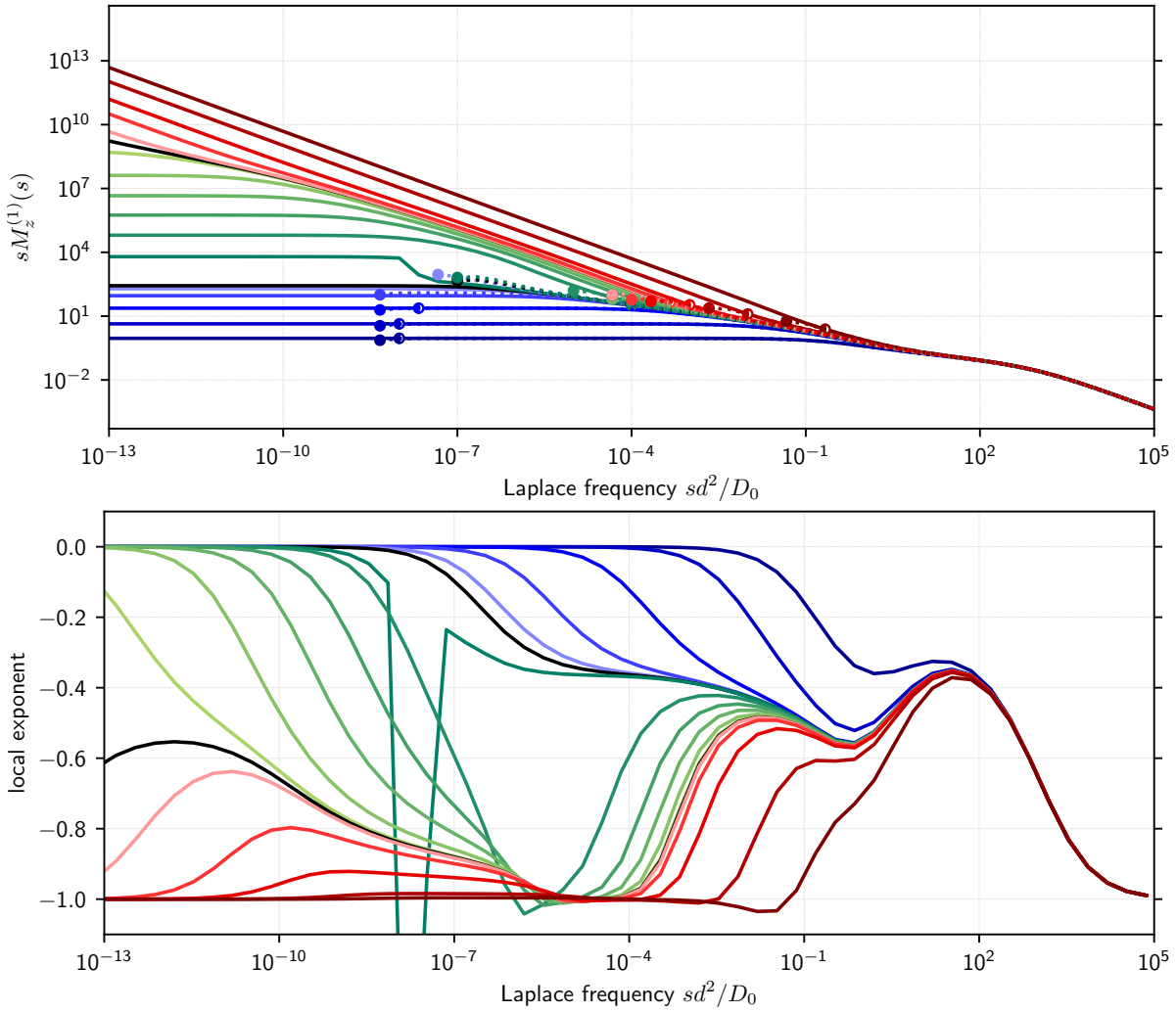

Figure 4.7.: Top: Laplace space solution of the mean displacement for different forces close to the critical forces. For easier comparison the mean displacements are multiplied by the Laplace frequency. Then, the power law s^α translates to $t^{-\alpha}$ in time domain. For example, curves in Laplace space which become flat for $s \to 0$ correspond to curves in time domain which become flat for $t \to \infty$. Circles indicate the time after which the Laplace transform of the curves in Figure 4.6 deviates from the Laplace space solution by more than 5 %. Bottom: Local exponent of $sM_z^{(1)}(s)$. The colors in both panels are the same as in Figure 4.5: blue curves are forces below F_{low}, red curves above F_{high} and green curves in between.

forces above F_{low} show the same qualitative behavior: after some initial variation of the local exponent, which is very similar for all forces close to the critical forces, the local exponent stays between 0.35 and 0.5 for some decades and then rises towards a value of 1. The larger the force, the earlier this rise starts. We also note that this exponent is not constant over time, but decays slowly.

From this data we conclude that the relevant critical force is F_{low}, which is consistent with the findings from the time evolution of the correlation functions in Section 4.1.2. However, the

numerical value of F_{low} is not entirely accurate due to the discretization errors in the time evolution algorithm.

Looking at the local exponents of the Laplace space solutions in Figure 4.7, the different behavior in the different force regimes is eye-catching: Below F_{low} the local exponent increases monotonically from a value of -0.5 at a Laplace frequency of about $sd^2/D_0 = 10^{-1}$ to 0 in the limit $s \to 0$. For forces between F_{low} and F_{high}, the local exponent decays to -1 at around $sd^2/D_0 = 10^{-5}$ before increasing to 0 for $s \to 0$. For forces above F_{high}, the local exponent also decreases to -1 before growing slightly and decay again to -1 for $s \to 0$. There are therefore two frequency ranges, where the solutions follow a critical law with different critical exponents. The first window between $sd^2/D_0 \in [10^{-5}, 10^{-1}]$ with exponents between -0.5 and -0.35 corresponds exactly to the critical law seen in the time domain. Both, the corresponding time window $[10^1, 10^5]$ and the corresponding exponents agree nicely. The second critical behavior for Laplace frequencies $sd^2/D_0 \in [10^{-11}, 10^{-7}]$ is not accessible with the current algorithms for the time domain.

Finally, there is one curve which behaves specially. It is the same curve which exhibits a kink in the Laplace space solution. This kink leads to even more pronounced jump in the local exponent. An interesting observation is that this curve follows the shape of the curves for F_{low} for frequencies to the right of the jump, even though its force is larger than F_{low}. This may indicate that our solution scheme in Laplace space with the extrapolation of the iterations does not always find the proper solution when these solutions are very close. Only once the solutions are sufficiently different, the solution scheme suddenly picks the proper solution, which then causes the jump.

To summarize, we find the same critical force using the more phenomenological approach of characterizing the long time limit of the mean displacement. In time space, the lower critical force F_{low} is the relevant one. At least in the time window, which is accessible with our algorithm. The Laplace space solution suggests that there should be a finite mean displacement for long times for forces between F_{low} and F_{high} even though they grow like t for intermediate times. For the time space calculations F_{low} is not perfectly the critical force (only up to five digits in this case), possibly due to the discretization errors. In Laplace space the critical forces do indeed separate regimes with qualitatively different behavior. These values are the same as in the previous analysis. Therefore, we can assume that these methods to determine the critical force(s) are equivalent.

4.3. Phase diagram

Based on the preceding analysis of the critical force, we can now determine the critical force for various packing fractions. This allows us to draw a phase diagram. In the previous sections we have worked out that the theoretical and the phenomenological definition of the critical force are basically the same. We also learned that the difference between F_{low} and F_{high} decreases with decreasing grid step size. A larger influence on the value of the critical force has the cutoff for the wave vector discretization, when it is not large enough.

We therefore choose the following discretization to determine the critical force for different packing fractions: $q_{\max}d = 50$ to be on the safe side, $\Delta_q = 0.5$ to have enough resolution for the oscillations in the structure factor and a `unilog10`-grid to reduce the relative difference of the

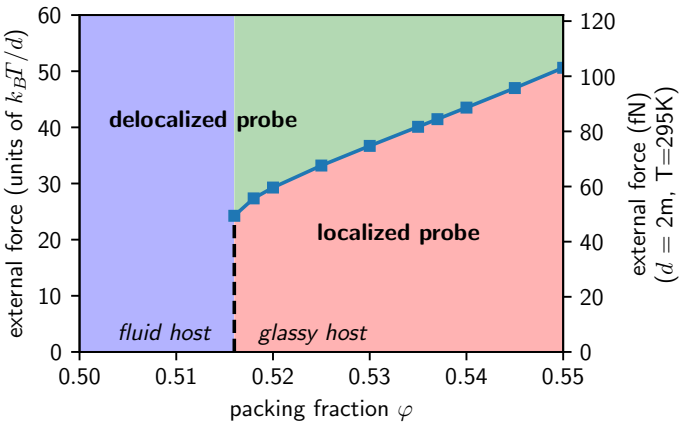

Figure 4.8.: Phase diagram of active microrheology in dense systems. The blue line separates the parameters for which the probe remains localized from those, where the probe delocalizes. The MCT glass transition is at $\varphi = 0.515\,815\,6$. The left axis shows the external force in dimensionless units, the right axis the external force for probe and bath particles with a diameter of 2 µm at room temperature.

critical forces below a per mil. This leads to a grid with 111 grid points in each direction. We choose 201 points to discretize the q_d vectors and calculate the bath nonergodicity parameter on a grid with 4096 points and a cutoff which varies between $qd = 90$ for the packing fraction $\varphi = 0.516$ and $qd = 160$ for $\varphi = 0.55$. This choice is necessary because the particles are localized more strongly for denser systems. A stronger localization implies a broader bath nonergodicity parameter, i.e. it extends to larger wave numbers. Then, we determine the critical forces using the transport coefficient method and obtain the phase diagram as shown in Figure 4.8.

Above the glass transition, which occurs at $\varphi = 0.5158156\ldots$ in our MCT approximation, there is always a finite critical force, which increases with packing fraction. The critical force varies between $24.246\,k_\mathrm{B}T/\mathrm{d}$ for $\varphi = 0.516$ and $50.607\,k_\mathrm{B}T/\mathrm{d}$ for $\varphi = 0.55$. In dimensional units this corresponds to forces of 49.3 fN and 103 fN for particles with a diameter of 2 µm at room temperature (295 K). By definition, we will find a critical force only for systems in which the probe remains localized in equilibrium (i.e. without external force). The phase diagram obtained by Harrer (see [Har13, p. 32, Fig. 3.12]) is very similar, but it shows systematically smaller values for the bifurcation.

4.4. Correlations between the critical force, yield stress and quiescent MSDs

In the following we will present an intuitive picture for the existence of the critical force and characterize this model quantitatively. At high packing fractions the particles' motion is hindered by their neighbors. In the (ideal) glass, this so called *cage effect* [DH98] is so strong that the particles can never leave this cage. In their simulation Doliwa and Heuer found that this cage can be characterized by a harmonic potential [DH98, p. 4917] even though the interaction between the particles is hard sphere like. The van Hove function for a single particle in a harmonic trap has been evaluated in Section 2.3.2. In this model, the long time limit of the mean square displacement (obtained from (2.39)) is inversely proportional to the spring constant. However, when considering linear response of our or other nonergodic systems, we find that the cage strength κ (defined as the spring constant of the harmonic potential in units of $k_\mathrm{B}T/d^2$) is related to the long time limit of the mean square displacement via an additional

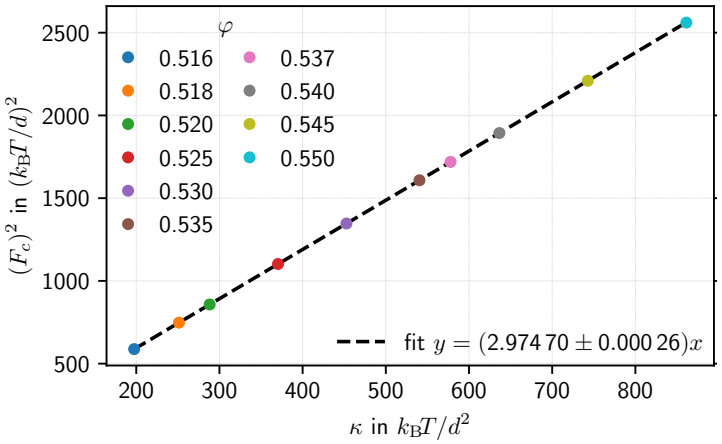

Figure 4.9.: Critical force squared over cage strength κ as defined in the text. The dashed line is a linear fit with almost perfect integer number 3.

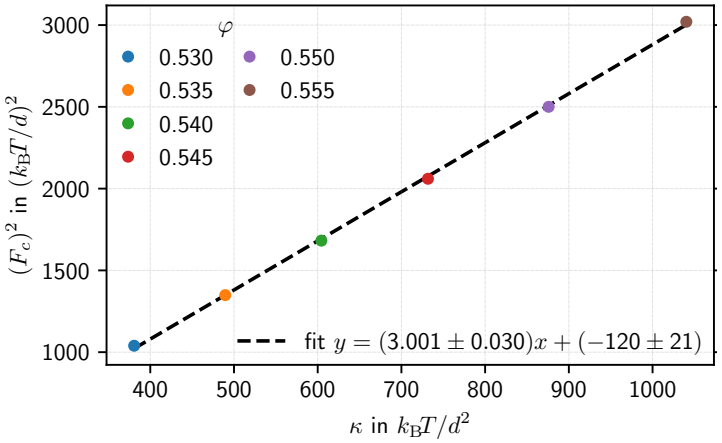

Figure 4.10.: Critical force squared over cage strength κ using the Verlet-Weis structure factor. The dashed line is an affine linear fit.

factor of 2

$$\kappa = \frac{2}{\langle \Delta x^2(t \to \infty) \rangle_{F_{ex}=0}}. \tag{4.4}$$

With this relation we can estimate the cage strength from the long time limit of the mean square displacement.

In Figure 4.9 we show the square of the critical force over the cage strength as defined above for all available packing fractions. We find a proportionality with an almost perfect integer number 3 as coefficient. This leads to the following empirical relation

$$F_c^2 = 3\kappa = \frac{6}{\langle \Delta x^2 \rangle_{F_{ex}=0}}. \tag{4.5}$$

The square of the critical force is proportional to the cage strength. With this result we can also speculate about the critical force directly at the glass transition: Since the glass transition is a discontinuous transition, the nonergodicity parameter jumps from zero to a finite value. This implies that the mean displacement also jumps to a finite value. Using the relation above, we conclude that there is a finite critical force at the glass transition.

This simple relationship between the critical force and the quiescent mean square displacement rises of course the question whether this behavior is universal or just an artifact of our numerics. We can take two routes to investigate this question: first, we can use a different structure factor

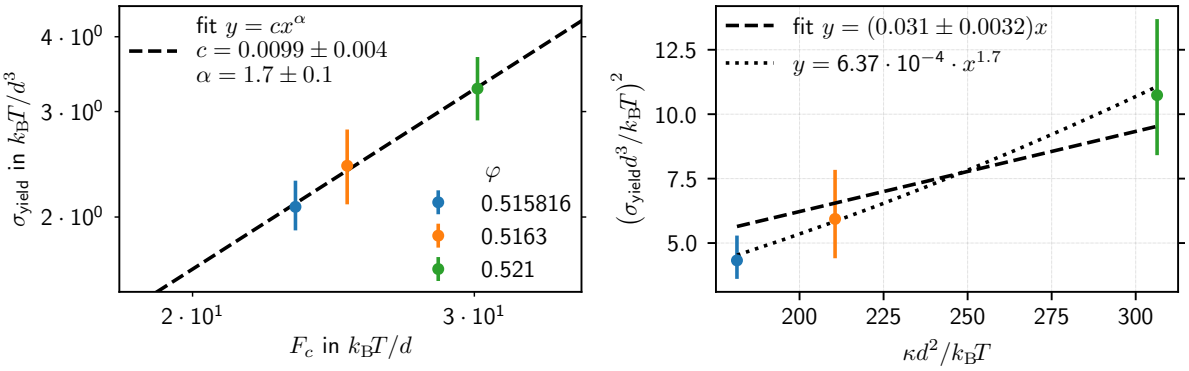

Figure 4.11.: Yield stress relations for the macroscopic yield stress from [AF14, p. 1200, Fig. 4] for the packing fractions as indicated. Error bars indicate readoff uncertainties. Left: yield stress over microscopic critical force. The dashed line is a power law fit. Right: macroscopic yield stress squared over cage strength κ. The dashed line is a proportionality fit, the dotted line is obtained from the fit in the left panel. See text for details.

for our calculations, second we can check the literature for similar features. For the former, we use the Verlet-Weis structure factor [VW72], which is calculated for different packing fractions via a program provided by Gustavo Abade. We then calculate again the critical forces as described in the previous sections together with the mean square displacements without external force. Then we show the square of the critical forces over the corresponding spring constants in Figure 4.10. Again, we find a linear relationship with the same proportionality constant, but we have to allow for a small offset to obtain a good agreement. This emphasizes that there is a close connection between the critical force and the quiescent mean displacement, but the relation is not as simple and universal as suggested by our findings using the Percus-Yevick structure factor as input.

As there is no much literature about the critical force in active microrheology, we will take a little detour to check if there is a connection between the mean square displacement and the critical force. Going back to the roots of microrheology, we want to measure microscopic viscoelastic responses to determine the macroscopic properties. Active microrheology allows us to probe nonlinear properties as well and the macroscopic equivalent for our critical force is the yield stress. When shearing a glass, it reacts elastically like a solid for small stresses. For larger stresses, it will shear melt and respond like a fluid. This problem has been analyzed for hard spheres within an MCT model [AF14]. Since the main focus of this work has not been the determination of the yield stress, there is only data points for three different packing fractions available. Nevertheless it allows a first comparison.

From Fig. 4 in [AF14, p. 1200] we can extract yield stresses for relative packing fractions of $\varepsilon = 0, 10^{-3}, 10^{-2}$. Since they used a different discretization their glass transition is slightly different. For a useful comparison, we take the same relative packing fractions with respect to our glass transition value. This leads to $\varphi = 0.515\,815\,6, 0.5163, 0.521$ for which we determine the critical forces as described in the previous section. In Figure 4.12 we show the yield stresses as a function of the critical forces. The errorbars show the uncertainties of the yield stresses

when reading them off. Fitting a power-law, we find that the yield stress follows approximately

$$\frac{\sigma_{\text{yield}} d^3}{k_\text{B} T} = 10^{-2} \left(\frac{F_\text{c} d}{k_\text{B} T} \right)^{1.7}, \tag{4.6}$$

where the uncertainties are of the order 10 % and given in Figure 4.11. This fractal exponent indicates some fundamental differences between the physical mechanisms for macroscopic yielding and microscopic delocalization.

With this finding, we should not expect a similar simple relation between the yield stress and the cage strength as found in (4.5). To check this, we plot the square of the yield stress over the cage strength in the right panel of Figure 4.11. Fitting a proportionality does not lead to a satisfactory result (see dashed line). Instead, we can take the relation between the yield stress and the critical force (4.6) and the relation between the critical force and the cage strength (4.5) to express the squared yield stress as function of the cage strength (dotted line) and find

$$\frac{\sigma_{\text{yield}} d^3}{k_\text{B} T} = 2.5 \cdot 10^{-2} \left(\frac{\kappa d^2}{k_\text{B} T} \right)^{0.85}. \tag{4.7}$$

This line fits much better to the data than the proportionality fit. Since the data cover only a very narrow range in yield stresses and critical forces, we have to be careful in extrapolating these findings. Nevertheless we can pose the hypothesis that the yield stress is connected to the MSD in the quiescent system.

To check this hypothesis we first have to find data, where yield stresses and mean square displacements are published together. Even though there is many simulations (e.g. [Fri18; PVP04]) and experiments which determine yield stresses in different systems (see the reviews [BFO14] and [BDB+17]), there is only two publications with yield stresses and MSDs for different packing fractions or temperatures: simulations and MCT calculations for harmonic spheres [IB13] and simulations on Lennard-Jones glasses [VBB04].

Ikeda and Berthier study a system of repulsive hard spheres where particle interactions are given by a harmonic potential when they are closer than a distance a, cf. [IB13, p. 2, Eq. (2)]. The energy scale ε of this potential changes the particle behavior from soft to hard in the limit $\varepsilon / k_\text{B} T \to \infty$. This system shows a glass transition and a jamming transition for low temperatures. In the glassy regime, entropic forces govern the physics, while in the jammed state the repulsive forces are the relevant forces [IB13, p. 2]. They study this system using Langevin dynamics simulations for simple shear flow [IB13, p. 3, Eq. (4)] and MCT using the static structure factor from the simulations as input [IB13, Sec. C, p. 2f]. To account for the shear they use the isotropic approximation for shear flow of Fuchs and Cates [FC02]. In this case, the shear stress can be obtained by a memory integral of the intermediate scattering function [IB13, p. 3, Eq. (14)].

The long time limits of the MSDs without shear for both simulations and MCT for different packing fractions are given in [IB13, p. 6, Fig. 2]. From those MSDs we calculate the nondimensional spring constants κ according to (4.11). The yield stress obtained for simulations and MCT for different packing fractions is given in [IB13, p. 9, Fiq. 5]. Note that we have to convert their data from the length scale radius to the length scale diameter. The yield stress as function of the spring constant is shown in Figure 4.12. We find that those data collapse quite nicely on a single line spanning about six orders of magnitude for the spring constants. While

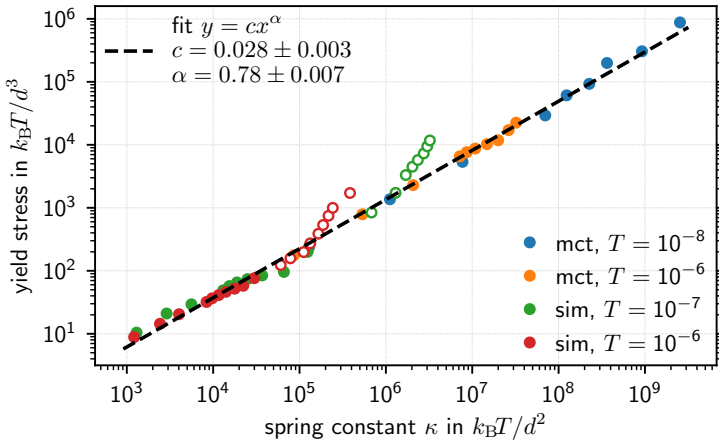

Figure 4.12.: Yield stress over cage strength κ for harmonic spheres calculated from simulations and MCT results in [IB13] (see text for details). The open symbols indicate packing fractions above the jamming transition. The dashed line is a power law fit.

MCT predict MSDs which are one to three magnitudes smaller than the ones in the simulations, it also predicts yield stresses which are one to three magnitudes larger. Major deviations can be found only for packing fractions above the jamming transition (open symbols). This is not surprising, because interactions are dominated by the repulsion forces rather than entropic ones. Fitting the power law, we find

$$\frac{\sigma_{\text{yield}} d^3}{k_B T} = 2.8 \cdot 10^{-2} \left(\frac{\kappa d^2}{k_B T} \right)^{0.78} . \tag{4.8}$$

This is surprisingly close to the values in (4.7) obtained from Amann *et al.* above. This shows impressively, that there is a tight connection between the mean square displacements or the cage strength and the yield stress.

The second system for which both MSDs and yield stresses were published is a 80:20 binary mixture of particles interacting with a Lennard-Jones potential [VBB04, Sec. II, p. 2790f]. In this molecular dynamics simulation the control parameter for the glass transition is the temperature rather than the density. The yield stress is determined from a simulation, where the particles in the sheared wall are subject to an external force [VBB04, Sec. IV, p. 2796]. The static yield stress is then determined "as the smallest stress at which a flow in the system is observed" [VBB04, Sec. V, p. 2798] for a range of temperatures below the glass transition temperature. Its values are given in [VBB04, p. 2799, Fig. 17] and its unit is given by $\varepsilon/\sigma_{AA}^3$, where ε is the Lennard-Jones energy (for interactions of particles of type A with particles of type A) and σ_{AA} is the corresponding Lennard-Jones radius [VBB04, Sec. II, p. 2790f]. Conversion to our unit for stresses k_BT/d^3 is done by dividing through the nondimensional temperature and by eight to convert from radius to diameter. The MSDs for a system in absence of shear are given in [VBB04, p. 2800, Fig. 18] as function of time.

Since most of those curves do not show a clear plateau for long times, we calculate the effective cage strengths for different times according to (4.11) and compare them to the yield stresses[2] for the different temperatures in Figure 4.13. We find that we can fit a power law for each time with different exponents ranging from 1.5 for $t = 10^2$ Lennard-Jones time units to 0.52 for $t = 2 \cdot 10^4$ Lennard-Jones time units. The curves for $t \geq 5 \cdot 10^3$ show a very similar behavior so that we decide to fit a power law for all of them. We find an exponent of 0.55 ± 0.03

[2] for $v_{\text{cm,min}} = 10^{-4}$

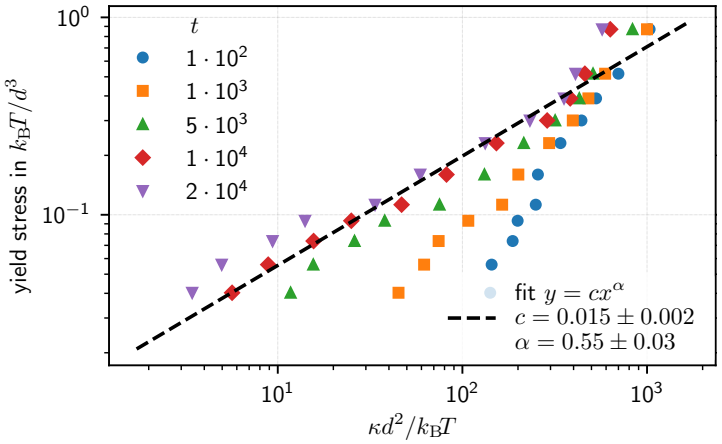

Figure 4.13.: Yield stress over cage strength κ for Lennard-Jones glasses from [VBB04] (see text for details). The different colors correspond to different times (in LJ time units) for which the MSD has been extracted to calculate κ. The dashed line shows a fit to the data for $t \geq 5 \cdot 10^4$.

and deviations from this fit mostly for small cage strengths. The weak cages correspond to high temperatures at which the long time limit of the MSD is not well defined, because it does not show a plateau. At the same time the yield stress is rather sensitive to the procedure of its determination (see [VBB04, p. 2799, Fig. 17]). For the strong cages equilibration is important because of the long relaxation times. The yield stress as well as the MSD may depend on the history (waiting time) of the system. Nevertheless the power law extends over more than one decade. Its value is smaller than in the previous cases, most likely due to the attractive contribution in the Lennard-Jones potential.

4.5. Characterization of the delocalization transition

In the following we will characterize different quantities around the critical force to characterize the delocalization transition. Most of the following comparison to simulations has already been published in [GAPF16]. In addition to that we also compare to predecessors of this theory [HPVF12].

For the simulations, the dynamics of $N = 1000$ particles subject to the Langevin equation (2.9) and interacting through an r^{-36} quasi-hard sphere potential have been analyzed by Antonio Puertas. On one particle[3] there is an additional external force as in our theory. The details on the numerical algorithm can be found in [Gru14, Sec. III]. It is known that the MCT value of $\varphi_g = 0.516\ldots$ for the glass transition [FFG+97, p. 7156] is smaller than the glass transition observed at around $\varphi_g = 0.58$ in experiments [vMU93; ZGM+16] and simulations [VPF04; WPFV10]. Therefore, we cannot compare our models for the same numerical value of the packing fraction. Instead, we match the systems so that the relative distance

$$\varepsilon = \frac{\varphi - \varphi_g}{\varphi_g} \tag{4.9}$$

to the glass transition is the same. For the simulated system, the glass transition is at $\varphi_g^{\text{sim}} = 0.596$ [VPF04; WPFV10] so that the packing fraction of $\varphi = 0.62$ in the simulation corresponds to a packing fraction of $\varphi = 0.537$ within MCT. This will be the standard packing fraction in this chapter unless specified otherwise.

[3] randomly selected for each run

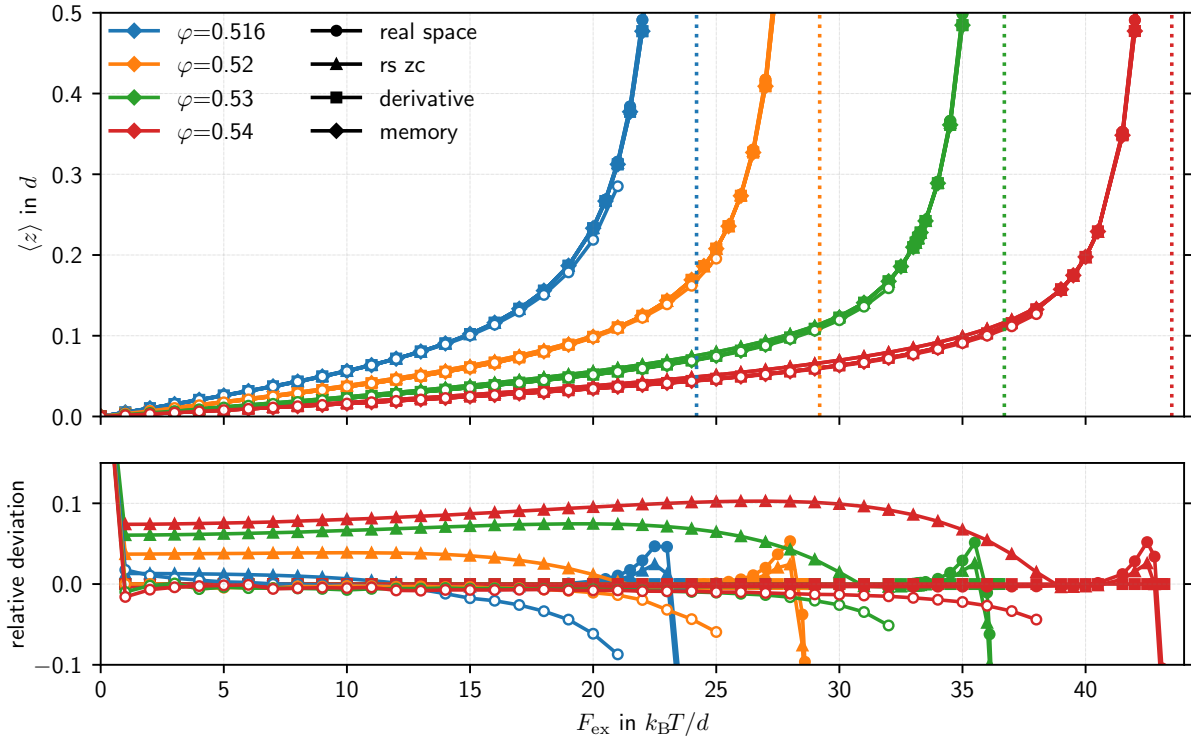

Figure 4.14.: Long time mean displacements over external force. Top: mean displacement obtained from the nonergodicity parameter calculation for different packing fractions with different methods as described in the text. Dotted lines indicate the critical forces. Open symbols are uncorrected data from [HPVF12, Fig. 3]. Bottom: relative deviation of the mean displacements with respect to the memory moment calculation. The symbols and colors are the same as in the top panel.

4.5.1. Moments and transport coefficients

The quantities which are easiest to measure and compare are the mean displacement and the other moments. Nevertheless there are different methods to derive those quantities from our Fourier space solutions. We can take the numerical derivative (3.52) (method *derivative*), use the $q \to 0$ limit of the memory kernels as described in Section 2.4.9 (method *memory*) or calculate the inverse Fourier transform and perform the real space integration for the moments (method *real space*). Note that one-dimensional Fourier transforms are sufficient to calculate the moments, because we only need the marginal probability distributions, see Appendix A.3. Doing the inverse Fourier transform poses additional challenges. One of them is choosing the proper parameters to obtain smooth curves in the range of interest. The other is the problem that we cannot guarantee that our solution is the Fourier transform of a probability distribution. This results in slightly negative parts of the van Hove function. These unphysical features were already present in the work of Christian Harrer, where he decided to ad-hoc correct for this effect by setting these parts to zero and renormalize the probability function [Har13, p. 45]. We will call this method *zero correction* or abbreviated *rs zc*.

We start by comparing the long time limits of the mean displacements for different packing fractions and different methods as a function of the applied force. The parameters for the

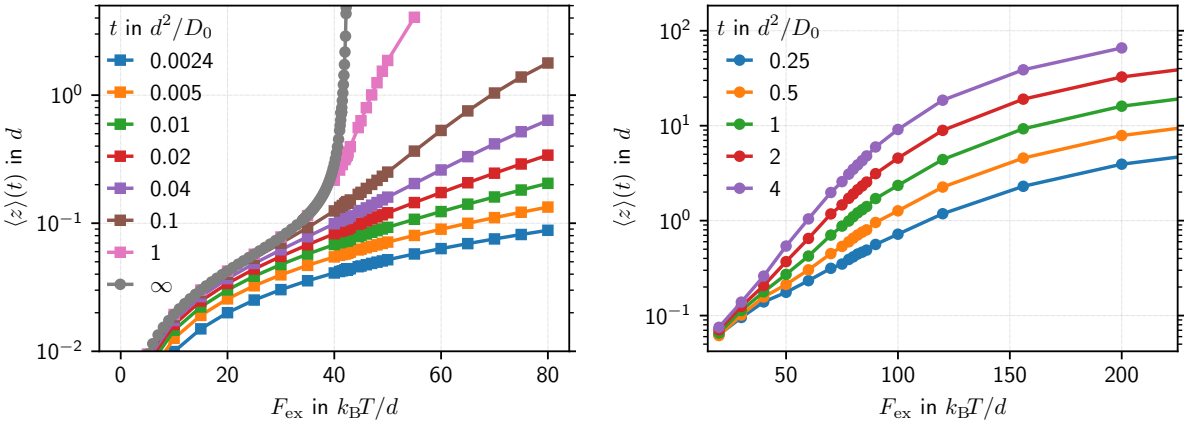

Figure 4.15.: Mean displacement for theory (left) and simulations (right) at different times as labeled as function of the external force.

numerical solution are the same as in Section 4.3 and the solutions are shown in Figure 4.14. We notice that all methods give almost the same results in the range shown. To make the differences more visible, we also plot the relative deviation of the mean displacements with respect to the value of the memory method (defined via $\langle z \rangle_{\text{method}} / \langle z \rangle_{\text{memory}} - 1$) in the lower panel. The largest differences are found for the zero corrected method. This is to be expected because this method modifies the probability distribution, while all other methods ideally access the same quantity. We also note that the deviations grow with increasing packing fraction. This was also found in the previous theory [Har13, p. 45]. Close to the critical force we observe that the methods based on the real space values start to deviate. This is due to the fact that for this calculation we always use the same grid for the Fourier transform and no artificial intelligence to adapt for the very different shapes of the van Hove function. This problem has to be addressed when analyzing the van Hove function close to the critical force. An interesting observation is also that there is always a range of forces slightly below the critical force, where all methods give basically the same results.

In Figure 4.14 we also show the mean displacements (without zero correction) from [HPVF12, Fig. 3] as open symbols. Sufficiently far from the critical force, there is no difference to our results. For increasing force the mean displacements obtained by the previous theory are smaller. Furthermore, with the revised formulation we can approach the critical force without getting unphysical results.

Comparing the long-time mean displacement to the simulations is more challenging, because the simulations always end at a finite time. Therefore, we show in Figure 4.15 not only the theoretical long time limit, but also the values of the mean displacement after finite times. While the mean displacement diverges at the critical force, it remains finite at finite times and smears out the transition. For the simulations we find that the displacements systematically larger than the predictions from theory. Nevertheless, for small force values we find similar values for the mean displacement. Unlike for the theory, there is no sudden increase for longer times above a certain force and additionally there is no saturation visible for long times and small forces, i.e. the mean displacement in the simulations keeps growing. We have to keep in mind that the simulation data covers only one magnitude in time, while it is about three orders of magnitude in the simulations. Therefore it might be possible that the largest time

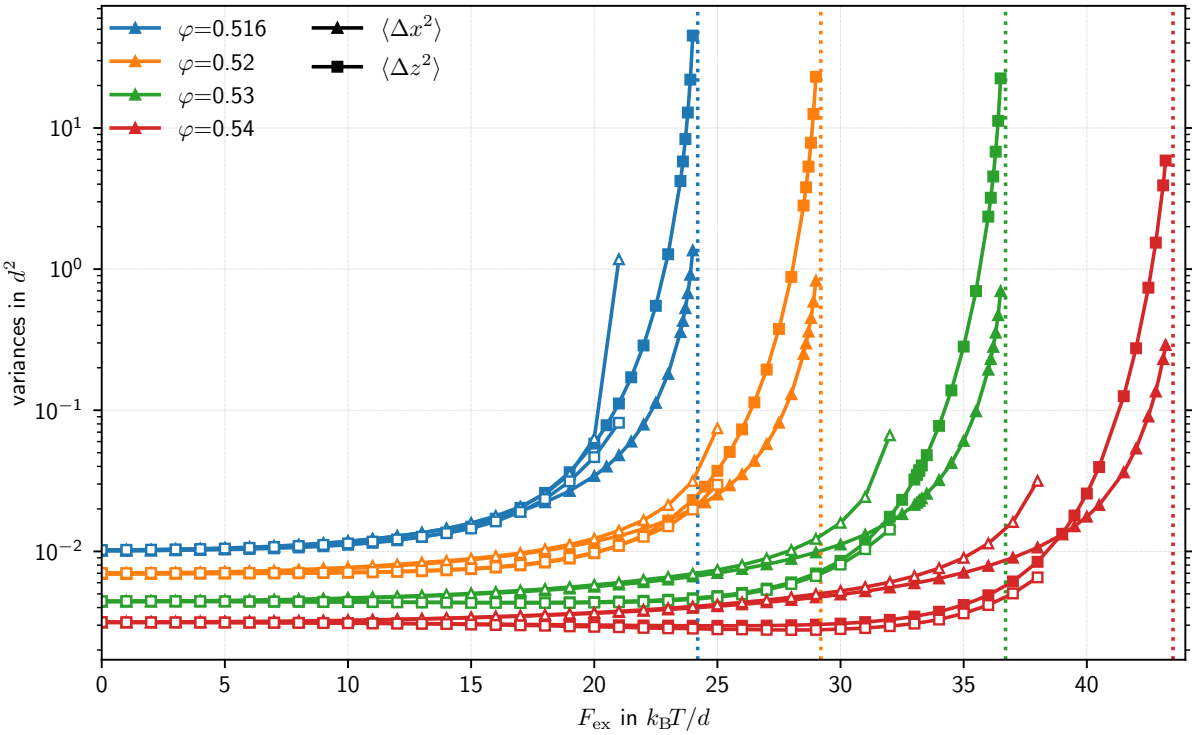

Figure 4.16.: Long time variances over external force. The variances parallel ($\langle \Delta z^2 \rangle$, squares) and perpendicular ($\langle \Delta x^2 \rangle$, triangles) to the external force are calculated using the memory kernels. Dotted lines indicate the critical forces. Open symbols are uncorrected data from [HPVF12, Fig. 4].

in the simulation is not long enough to see reach its final value. The behavior resembles the finite time displacements for the smallest times for the theory ($tD_0/d^2 \leq 4 \cdot 10^{-2}$). On the other hand, it might also be that the simulations do not show an ideal glass as well as an ideal delocalization transition, meaning that the displacements and mean square displacements will slow down, but never saturate.

For the calculation of the variances perpendicular $\langle \Delta x^2 \rangle = \langle x^2 \rangle$ and parallel $\langle \Delta z^2 \rangle = \langle z^2 \rangle - (\langle z \rangle)^2$ to the critical force, we can use the same methods as above - from derivatives in Fourier space or integrals in real space. As second derivative or integral weighted by a parabola these moments are more sensitive to numerical errors. Consequently the differences between the different methods are more pronounced. For small forces, the derivative method and the moment method give essentially the same results, while the real space methods yield about 10 % (zero correction) to 20 % larger values. For intermediate forces even the Fourier space methods give slightly different values. This effect is more pronounced for larger packing fractions. The values obtained for the parallel variance in real space are in this regime up to 60 % larger than those obtained from Fourier space. For large forces, the zero corrected variances agree with those obtained by the Fourier space methods, before it fails completely in the parallel direction close to the critical force. The raw variance calculated in real space yields systematically too large values.

From all methods, determining the moments using the memory functionals requires the smallest amount of numerical approximations, because it is based on the Fourier space data and

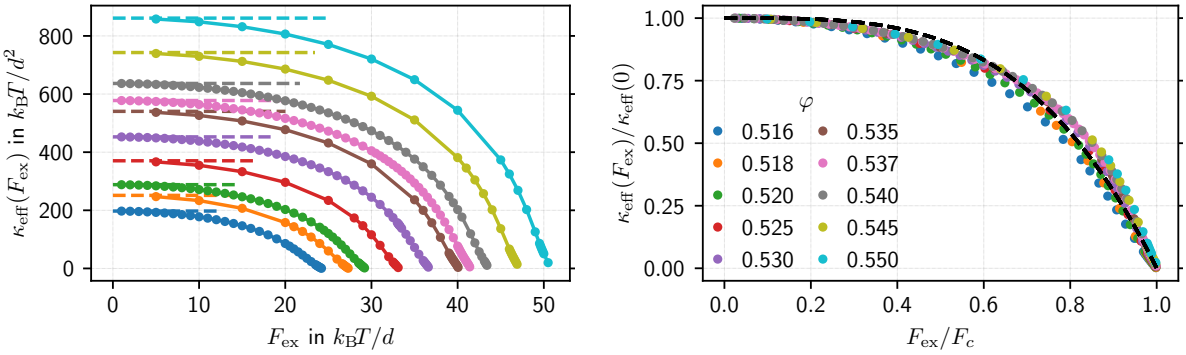

Figure 4.17.: Force softening for different packing fractions. Left: Effective spring constant (4.10) over force for different packing fractions as labeled in the right plot. Dashed lines indicate the linear response value obtained by (4.11) from the equilibrium system. Right: same data as in the left plot, but spring constants are normalized by $\kappa(F_{\mathrm{ex}}=0)$ and forces are normalized by F_{c}. The dashed black line is given by $1-(F_{\mathrm{ex}}/F_{\mathrm{c}})^{3.5}$.

it uses analytical expressions for the derivatives. Therefore, we decide to show only those values in Figure 4.16 as function of the external force for different packing fractions. For small forces up to 30 % of the critical force value there is basically no change of the variance. Then the variance grows faster in the perpendicular direction than in the parallel. For the largest packing fractions the variance in the parallel direction even decreases a little. For large forces there is a crossover, when the variance parallel to the external force grows larger than the variance in the perpendicular direction. This difference can be more than one order of magnitude close to the critical force.

Our results agree fairly well with the data from the previous version, taken from [HPVF12, Fig. 4] and shown as open symbols in Figure 4.16. This includes the observation that the perpendicular variance gets larger than the parallel one. Only towards the critical force of the previous theory deviations become apparent. While the previous theory became unstable, we can now observe much larger variances. Additionally, we now observe that the parallel variance grows larger than the perpendicular one close to the critical force. This was not visible in the previous theory, not even a hint of it. A more detailed analysis on how different lengths evolve when approaching the delocalization transition (as done in [GAPF16, Fig. 10]) will follow in Section 4.5.3, where we analyze the van Hove functions in real space.

Since higher moments are even more sensitive to small numerical differences, we skip the comparison of skewness and kurtosis. Instead, we analyze how the effective spring constant

$$\kappa(F_{\mathrm{ex}}) = \frac{F_{\mathrm{ex}}}{\langle z \rangle} \tag{4.10}$$

varies with force, where $\langle z \rangle$ is the long time limit of the mean displacement at force F_{ex}. This is shown in Figure 4.17 for different packing fractions. As in [HPVF12, Fig. 10] we find a force thinning, where the effective spring constant decreases monotonically with the force. The initial value coincides with the spring constant derived from the linear response result (2.206) as (4.4) in the limit $t \to \infty$, here repeated for reference

$$\kappa_{\mathrm{lr}} = \frac{2}{\langle \Delta z^2 \rangle_{F_{\mathrm{ex}}=0}}, \tag{4.11}$$

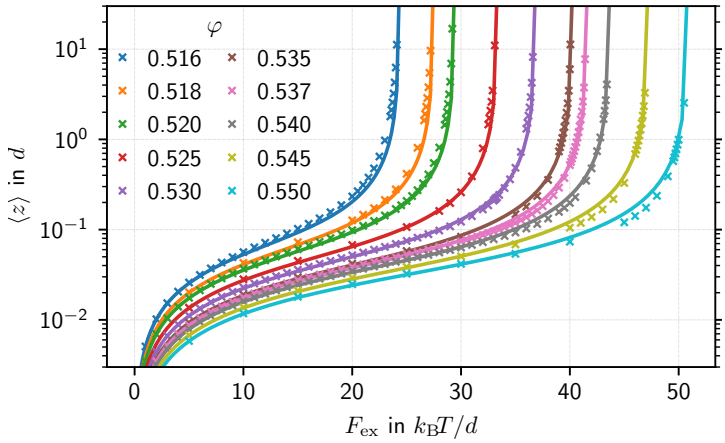

Figure 4.18.: Mean displacement (crosses) and prediction (solid lines) according to (4.13). The only input for the prediction is the MSD from the quiescent calculation.

where the mean square displacement $\langle \Delta z^2 \rangle_{F_{ex}=0} = \langle \Delta x^2 \rangle_{F_{ex}=0}$ is evaluated for the equilibrium system. This value is shown as dashed line on the left hand side of Figure 4.17. The new result is now that we can extend those curves all the way up to the critical force, where the spring constant vanishes. As those curves look very similar, we rescale the spring constants by their quiescent value $\kappa_{\text{eff}}(0)$ and the forces by the critical force, as shown on the right hand side of Figure 4.17. Even though there is some spread, the points fall quite close to a curve described by

$$\frac{\kappa_{\text{eff}}(F_{ex})}{\kappa_{\text{eff}}(0)} = 1 - \left(\frac{F_{ex}}{F_c}\right)^{3.5}, \tag{4.12}$$

where the exponent has been determined by a least squares fit, shown as black dashed line. The ansatz $(1 - F_{ex}/F_c)^{\alpha}$ has also been tested but found to give less agreement. The critical force is related to the equilibrium mean square displacement via (4.5). This leads to the interesting observation that the effective spring constant and consequently the mean displacement is approximately described by a single system property: the quiescent mean square displacement

$$\langle z \rangle = \frac{\langle \Delta z^2 \rangle}{2} \left(1 - \left(\frac{\langle \Delta z^2 \rangle F_{ex}^2}{6}\right)^{1.75}\right)^{-1} F_{ex}. \tag{4.13}$$

Notwithstanding that this equation is purely empiric, it works surprisingly well to describe the mean displacements of our theory as can be seen in Figure 4.18.

To characterize the behavior not only below but across the delocalization transition, we have to analyze the full dynamics. A comparison of the time dependent mean displacements with theory and simulations is shown in Figure 4.19. Those calculations were performed by Gustavo Abade using a `unilog10` grid with cutoff $q_{\max} d = 10$ and $N = 61$ points. This low cutoff leads to a critical force of about $F_c \approx 46.0\, k_B T/\text{d}$. The two different critical forces are not relevant for the comparison to the simulations, because they are so close that they cannot be resolved by the simulations.

Qualitatively, the simulation data agrees very well with the MCT calculations. For small forces the mean displacements stay approximately constant for long times, while they grow linearly for large forces. As the simulated glass is not ideal, there will be no perfect caging of the particles and therefore a decay of correlations and a small drift in the mean displacement. Unfortunately this makes it very difficult to identify the critical force in simulations, because

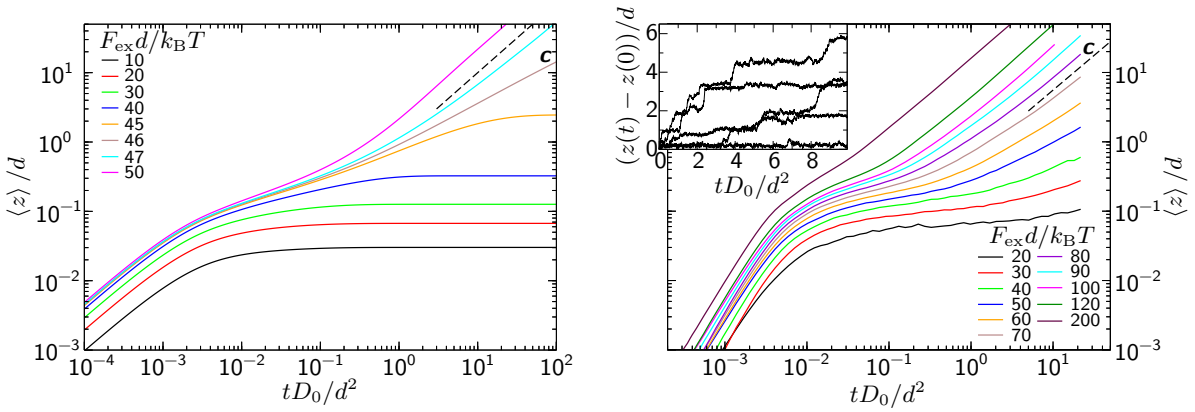

Figure 4.19.: Mean displacement of the probe particle as function of time for MCT (left) and simulations (right). The critical force for MCT is $F_c = 46.0\,k_BT/d$, while we estimate it to be around $F_c \approx 80\,k_BT/d$ for the simulations as indicated by the label c. The dashed lines show a $\propto t$ behavior, which is expected for viscous drag. In the inset we show some example trajectories for $50\,k_BT/d$, see [GAPF16, Fig. 4].

the transition is not as sharp as predicted by theory. There, the curves for $45\,k_BT/d$ and $47\,k_BT/d$ show completely different behavior. For the simulations the curves between $60\,k_BT/d$ and $100\,k_BT/d$ look very similar and differ only in the magnitude of the mean displacement for long times. From this data alone we cannot determine the critical force unambiguously. Instead, we have to look at the time evolution of the correlation functions as discussed in Section 5.9 to identify the critical force as $80\,k_BT/d$.

Below this critical force the mean displacement increases sublinearly. The reason for this can be seen in the inset of Figure 4.19. There, some typical individual trajectories for $50\,k_BT/d$ are shown. They exhibit many jumps with a distance of about d followed by a longer period where they wiggle around some mean (equilibrium) position. Other trajectories also look as if they were completely stuck. We interpret this step-like trajectories as particle escaping its cage by switching places with the particle in front of it [GAPF16, p. 8]. Then the probe particle is trapped again by its new neighbors for some time. For the mean displacement the whole ensemble with arrested trajectories and very mobile trajectories is averaged giving rise to the sublinear growth. These features have also been observed for active microrheology in hard disk glasses [Har13, p. 92, Fig. 7.8] and a Yukawa-mixture [WH13, p. 7, Fig. 7]. Even in quiescent systems, jumps between cages have been identified [Vol04] and it looks as if we can make these heterogeneous dynamics visible by breaking the symmetry of the jump direction via the external force. This heterogeneous dynamics also indicates that the mean displacement on its own is probably not the best measure to describe the motion of the probe particles. This problem will be addressed in Section 4.5.3 when analyzing the van Hove functions.

Another frequently studied quantity is the mean square displacement. In our case we should call it more precisely the variance as defined in (2.176), which is obtained by subtracting the square of the mean displacement from the second moment. For quiescent systems, where the mean displacement vanishes, these two quantities coincide, but in our case they are in general different. The variances for MCT calculations (discretization as before: `unilog10` with cutoff $q_{max}d = 20$, constant bath approximation) are shown in Figure 4.20. To highlight the differences between the variance perpendicular to the force direction ($\langle \Delta x^2 \rangle$, solid line) and

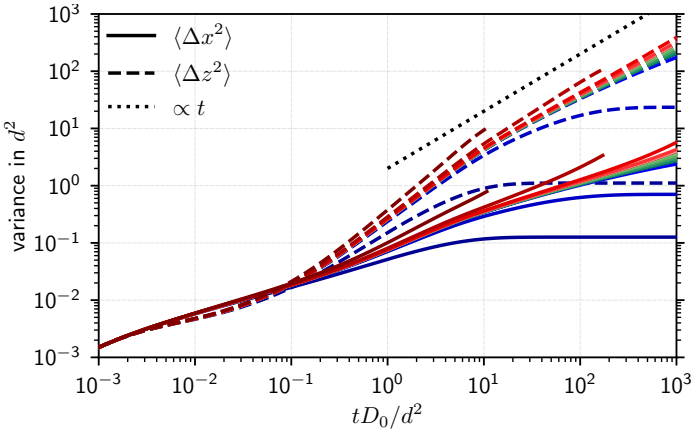

Figure 4.20.: Variance parallel (dashed lines) and perpendicular (solid lines) to the force direction for different forces close to the critical forces. The dotted line visualizes regular diffusion. The colors are the same as in Figure 4.5: blue curves are forces below F_{low}, red curves above F_{high} and green curves in between. For the numerical details see text.

the variance parallel to the force direction ($\langle \Delta z^2 \rangle$, dashed line) we show both curves in the same graph. We only show those parts of the curves, where the Laplace solutions differ by no more than 5 %.

For times $tD_0/d^2 \lesssim 10^{-3}$ the variances in both directions agree. While the variance $\langle \Delta x^2 \rangle$ keeps growing approximately like $t^{1/2}$ until $tD_0/d^2 \approx 10^0$, we find surprisingly that the variance $\langle \Delta z^2 \rangle$ is first growing slower and for $tD_0/d^2 \gtrsim 10^{-1}$ growing faster. An interpretation of this behavior could be that the particle is pushed to the boundary of its cage in force direction, while its motion is not affected in the perpendicular direction. With increasing time, the probability for a particle to escape its initial cage increases as well. Since it is stuck in some configurations while it has jumped in others, the spread and therefore the variance increases. So far, this is just an interpretation, but this picture can be justified when looking at the van Hove functions in Section 4.5.3.

Similarly to the mean displacement, we find that the variance saturates below the critical force F_{low} and increases more or less linearly for forces above F_{high}. Again, we cannot determine the long time behavior of the forces in between. It is however intriguing that the times when the variances saturate are the same for both directions. This suggests that the motion in the perpendicular direction is strongly coupled to the motion in force direction. In the picture sketched above, we imagine the particles escaping their cage by going around their obstacle instead of pushing it away. Since these jumps always occur in force direction, but with equal probability in any of the perpendicular directions, it looks reasonable that $\langle \Delta z^2 \rangle$ is larger than the variance in perpendicular direction. For the longest times shown it is up to two decades larger than the variance in the perpendicular direction (and grows even more for longer times).

Looking at the time dependence of the variance reveals that it is quite different from the regular diffusion. While the latter predicts that the variance increases proportional to t (as indicated by the dotted line), we find that the variance $\langle \Delta x^2 \rangle$ grows like $t^{1/2}$ close to the critical forces. The variance $\langle \Delta z^2 \rangle$ shows clearly superlinear behavior for tD_0/d^2 between 10^{-1} and 10^1, which crosses over to a behavior, which is close to linear for long times. Whether this is exactly linear or truly larger than one (so called *superdiffusion* [MM80; BGK+90]) is pure speculation, because our numerics breaks down for long times. The same applies to the question whether $\langle \Delta x^2 \rangle$ grows linearly or sublinearly for large forces and long times.

Finally, we can evaluate the friction and diffusion coefficients. We can obtain them directly from the time evolution of the mean displacement and the variances. Taking the derivative with

respect to the time, we get the instantaneous average velocity or the double of the diffusion coefficient. In the long time limit these values should be independent of the time provided the evolution is linear in time. We check this, by calculating the local exponent via (4.2). If it is close to one (i.e. $\alpha \in [0.7, 1.3]$), we calculate the corresponding transport coefficient for the data in the interval $[t_{\max}/5, t_{\max}]$ and take the mean of those results as value and the standard deviation as measure for the uncertainty. This method will be referred to as *time*.

Alternatively, we can use the expressions for those transport coefficients in terms of the memory functions as introduced in (2.190), (2.192) and (2.196). Those equations allow for both an evaluation with the time dependent memory functions and an evaluation in Laplace space using the constant bath approximation. To do so, we just need to replace the memory integrals in the equations referenced above by their Laplace space limit: $\int_0^\infty \mathrm{d}t'\, m_0^{\alpha\beta}(t') = m_0^{\alpha\beta}(s=0)$ and similarly $\int_0^\infty \mathrm{d}t'\, t' m_0^{\alpha\beta}(t')\mathrm{d}t' = \partial_s m_0^{\alpha\beta}(s=0)$. Since the time dependent solutions become unphysical for longer times above the critical force, we will only evaluate the time integrals up to the time, where the solution is still valid. Therefore the upper integration limit of the memory integrals is $t_{\max}$ rather than ∞. For a fair comparison of the methods, we should also account for this finite time effect in the Laplace space calculation. We can approximately treat the integral

$$\int_0^{t_{\max}} \mathrm{d}t'\, f(t') \approx \int_0^\infty \mathrm{d}t'\, \mathrm{e}^{-t'/t_{\max}} f(t') = \mathcal{L}\left[f\right](t_{\max}^{-1}) \tag{4.14}$$

as Laplace transform at frequency $t_{\max}^{-1}$, because the exponential function suppresses all contributions from f for $t \gtrsim t_{\max}$ if f is exponentially bounded. The method using the time integrals of the memory function will be called *memory*. Using the $s \to 0$ limit of the Laplace memory functions is referred to as *Laplace*, while the Laplace memory functions at $s = t_{\max}^{-1}$ will be called *Laplace finite*. As before we will also do the same for different end-times and Laplace frequencies to quantify the uncertainties. For the *memory* method we calculate the transport coefficients for all upper integral limits in $[t_{\max}/5, t_{\max}]$ and take the mean as result and the standard deviation as measure for the uncertainty. Similarly, we take $s \in [t_{\max}^{-1}, 5t_{\max}^{-1}]$ for the method *Laplace finite* to estimate the uncertainty. For the method *Laplace*, we choose $s \in [10^{-15}, 10^{-12}]$. Since the numerical derivative $\partial_s m_0^{zz}$ is very sensitive to numerical artifacts for these small s values, we determine it using the median of the numerical derivatives in this range. We also checked that memory functions in the $s \to 0$ limit and the derivative are well defined, i.e. these limits exist and are independent of s as long as s is small enough.

The coefficients obtained by the different methods are shown in Figure 4.21. The friction coefficients are within the errorbars almost the same for all finite time methods. Only the *Laplace* method, evaluating the friction coefficient for true $t \to \infty$ yields significantly larger values for forces close to the critical force. This can be easily understood with the help of Figure 4.19. There, we find the mean displacement to increase sublinearly close to the critical force. Our equations for the friction coefficient are based on a linear increase. Therefore, we overestimate the final velocity and consequently underestimate the friction coefficient. For larger forces the crossover to a linear increase of the mean displacement happens at shorter times so that the estimate for the velocity and friction coefficients are better. This also explains why we find a finite friction coefficient below F_{high} for all finite time methods: It is simply not possible to distinguish between a localized and a delocalized behavior at this finite time.

Similar features can be observed for the diffusion coefficients in the perpendicular direction.

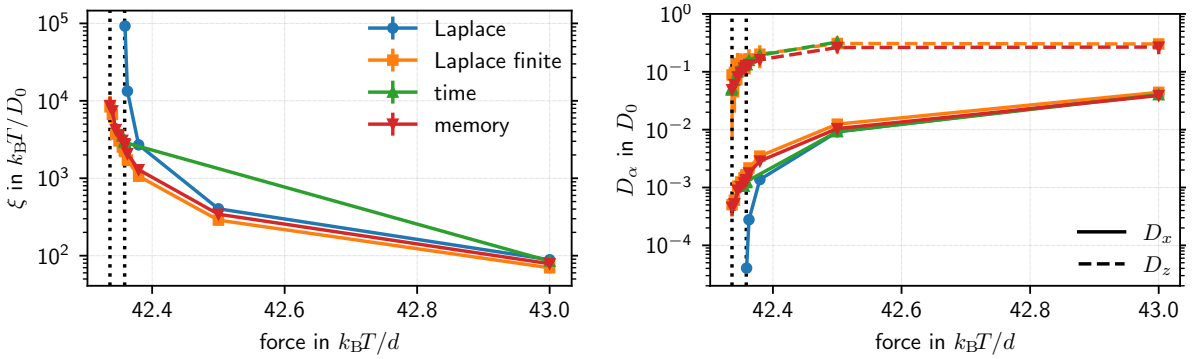

Figure 4.21.: Transport coefficients as function of the force. Dotted vertical lines indicate the critical forces $F_{\text{low}} < F_{\text{high}}$. Left: friction coefficient calculated by different methods as labeled and described in the text. Right: diffusion coefficients parallel to the force direction (dashed) and perpendicular to it (solid lines) for different methods as labeled in the left panel. Not shown are the values for the *Laplace* method, which are of the order 10^5.

The variance also increases sublinearly close to the critical force so that we overestimate the mobility, leading to a diffusion coefficient which is larger for the finite time methods than for the true long time limit values. For the same reasons we find a finite diffusion coefficient below F_{high} for the finite time methods, while the diffusion coefficient obtained from the long time limit vanishes already for F_{high}.

For the diffusion coefficients in direction of the force, there is quantitative agreement for the finite time methods with large uncertainties below F_{high}. The diffusion coefficients obtained by the *Laplace* method however are about six orders of magnitudes larger. This huge difference is at first sight very surprising, because the Laplace method at finite times is based on the same data and yields comparable results. Having a closer look at Figure 4.20 might explain this result. Even though the variance grows approximately linearly in time it is technically slightly superlinear ($\propto t^\alpha$ with $\alpha > 1$). For the same reasons as above, we therefore underestimate the diffusion coefficient by extrapolating this value. This gives a hint, but does not yet fully explain the large deviation. Of the three terms in (2.196), it is the last one involving $\partial_s m_0^{zz}(s=0)$ (or $\int_0^\infty t' m_0^{zz}(t')\mathrm{d}t'$ in the time domain), which is the main contribution to the diffusion coefficient. This naturally rises the question whether this derivative is well defined in the limit $s \to 0$. As discussed after the derivation of (2.196), a non-analytic behavior, which would not allow a power series expansion, could lead to superdiffusion. This cannot be confirmed numerically. In our calculations, we find that the derivative approaches a constant value in the limit $s \to 0$. This implies that we find diffusion in the long time limit. Nevertheless, the timescale to reach this diffusive regime is very large, the derivative $\partial_s m_0^{zz}(s)$ reaches its $s \to 0$ value only for $sd^2/D_0 \lesssim 10^{-10}$ even for the larger forces. The corresponding time scale is about seven decades larger than the times accessible by our algorithm to solve the MCT equations in time. If we want to explain the large diffusivities with a superlinear evolution of the variance, we need exponents of about 1.5 to 1.7, which is much more than we observe in our calculations in the time domain. Such exponents have been observed in a driven lattice Lorentz gas [LF17, p. 2, Fig. 1(b)], in simulations of active microrheology in a glass-forming Yukawa fluid [WHVB12, p. 4, Fig. 4], [WH13, p. 6, Fig. 5(b)], in event-driven simulations of dilute suspensions of hard

sphere colloids [LMF+18, p. 13, Fig. 3], for a continuous time random walk [SH13] and in simulations of a glass of quasi-hard spheres (see Figure 5.23). Unfortunately there is no means to confirm these findings within our theory unless a more stable algorithm for the time evolution or a stable inverse Laplace transform is invented and implemented.

To summarize the common features, we find that the friction coefficient shows a force thinning behavior as it becomes smaller for larger forces. Reciprocally, the diffusion coefficient becomes larger for larger forces. This trend holds for all methods, even for the *Laplace* method. While the friction coefficient decreases to 1 for large forces (as determined in the constant bath approximation), the diffusion coefficient in the direction perpendicular to the force grows to a value of $2.58D_0$ for a force of $200\,k_\mathrm{B}T/d$ and decreases slightly for even larger forces.

4.5.2. Correlation functions

In the preceding section, we characterized the moments of the van Hove function, which are the $q \to 0$ limits of the derivatives of the correlation function $\phi^s_{\boldsymbol{q}}$. In this section we will compare briefly the features of the correlation functions for various wave vectors. Their long-time limits are shown in Figure 4.22.

Within MCT these nonergodicity parameters can be obtained directly without solving the dynamics as described in Section 2.4.6. Since these static calculations are less expensive in time and memory, we can use a grid with a larger cutoff. In this case we chose $q_\mathrm{max}d = 50$ using a `unilog10`-grid with 111 grid points for each direction. Without external force, all the nonergodicity parameters are real valued and can be approximately described by a Gaussian. When a force is applied in our system, isotropy with respect to the force direction is lost. Therefore the correlation functions are complex valued for $q_z \neq 0$. The imaginary part $\mathrm{Im}\, f_q^{s\parallel}$ in force direction starts at 0 for $qd = 0$ and decays to 0 for $qd \to \infty$. In between there is a peak, which shifts to smaller wave vectors for increasing force. Both real parts show a narrowing for larger forces, where the real part in the parallel direction becomes negative for wave vectors larger than $qd \gtrsim 7$. Qualitatively these features can also be found in the simulations. There the nonergodicity parameters have been obtained by fitting the long time plateau of the correlation functions. Since small wave vectors describe correlations over large distances, these correlation functions decay rather slowly so that their long time plateau has not been reached at the end of the simulations. As it is not possible to determine their plateau value unambiguously, we omit those wave vectors in the plot. Therefore, the peak in the imaginary part cannot be properly resolved, but the part which can be seen is very similar to the theoretical predictions. The trends for increasing force are also the same.

The comparison of the dynamics of the correlators has been performed by Gustavo Abade and can be found in [GAPF16, Fig. 5] (which is reproduced as Figure 4.23), where one wave vector is compared for different forces and in [GAPF16, Fig. 6], where different wave vectors are compared for one force. The simulations show the same qualitative features as the theory: The real part in the parallel direction becomes negative for large forces, the imaginary part in the parallel direction shows a peak and the long time limit first increases and then decreases again for increasing force. A major difference can be found at long times: while the correlation functions for the simulation decay, the theory finds an ideal glass where they remain constant. This is similar to what we already found for the mean displacements in Section 4.5.1.

From the theory perspective it is also interesting to study the behavior of the nonergodicity

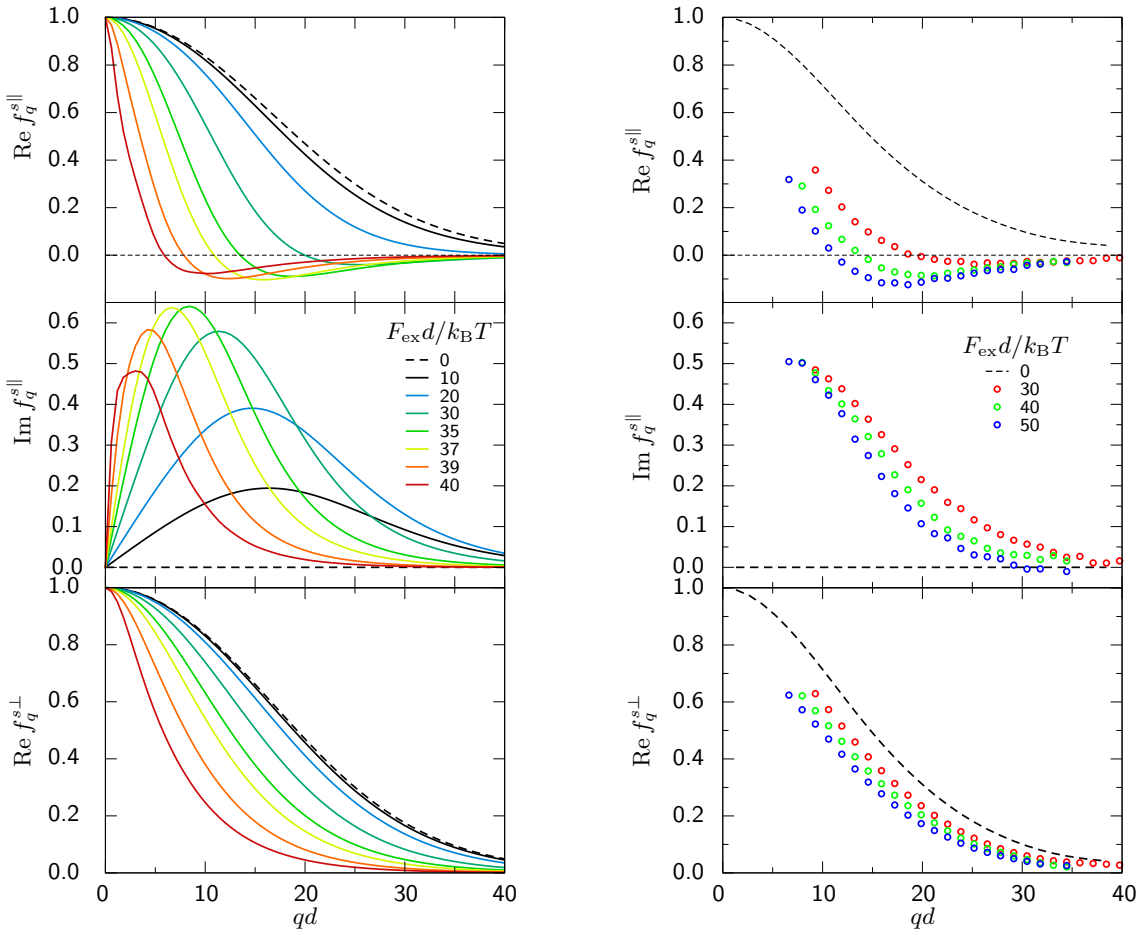

Figure 4.22.: Nonergodicity parameters for MCT (left) and simulations (right) for different forces as labeled. The MCT solution was calculated on a `unilog10`-grid with $q_{\max}d = 50$ and 111 grid points, which has a critical force of $41.57\,k_{\mathrm{B}}T/d$ [GAPF16, Fig. 7].

parameters (the long time limit of the correlation functions) close to the delocalization transition. Even though this regime is not accessible by simulations and experiments due to the large time scales, our theory can give insights in the mechanisms of the delocalization transition.

Some nonergodicity parameters close to this transition are shown in Figure 4.24. They are obtained on a `unilog10`-grid with $q_{\max}d = 20$ and 51 grid points in each direction. In the perpendicular direction they are all real valued and positive so that we can easily show them on a log-scale. For the perpendicular direction, we show the modulus and the phase[4]. For small forces, the shape is approximately Gaussian with a width of the order $qd \approx 10^1$ in both directions, which corresponds roughly to the unperturbed cage size of about $\sigma \approx 10^{-1}d$ (see Figure 4.16). We note, however, that nonergodicity parameters for large wave vectors decay exponentially and not Gaussian, similarly to the exponential decay large wave vectors for forces with $\delta > -10^{-2}$. When approaching the critical force F_{low}, the modulus is monotonously

[4]The phase is defined via the argument function $\arg\left(|z|\mathrm{e}^{\mathrm{i}\phi}\right) = \phi$ [WeiCom].

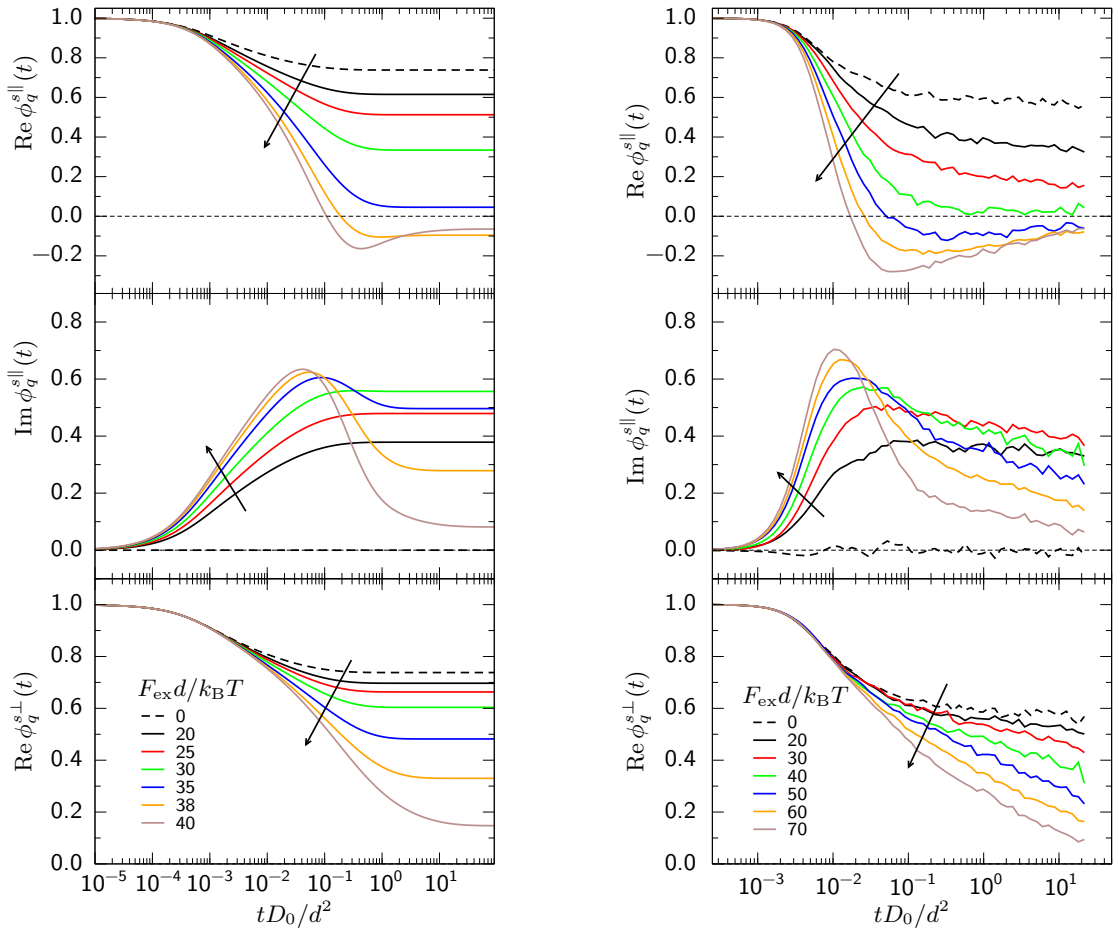

Figure 4.23.: Correlation functions for different forces parallel (top: real part, middle: imaginary part) and perpendicular (bottom) to the direction of the force for MCT (left) and simulations (right) [GAPF16, Fig. 5].

decreasing. Since $f_{\mathbf{0}}^s = 1$ by definition, this causes the curves to narrow. Interestingly, the shape of the curves for $qd \gtrsim 3$ does not change anymore for forces $\delta \geq -10^{-2}$, only its magnitude decreases. This applies to the perpendicular direction as well as to the parallel direction, which shows more pronounced features. This leads to the hypothesis that the shape of the nonergodicity parameter is a combination of two curves, whose relative contribution changes when approaching the critical force. Before testing this hypothesis, we have to analyze the features for small wave vector. For this purpose, we plot the same data over the wave vectors on a logarithmic scale (lower panels of Figure 4.24). This reveals that there is a power law for small wave vectors close to the critical force. For the perpendicular direction there is a q_r^{-2} scaling, while for the parallel direction there is a q_z^{-1} scaling. This observation will also support the choice of the models in the course of this section.

It remains to discuss the features of the phase of the nonergodicity parameter in the parallel direction. For small forces, it increases linearly as one would expect for a constant shift in real space. For larger forces, it changes into an arctan shape, which increases linearly as well but flattens for larger wave vectors. For $\delta > -10^{-3}$ a peak for small wave vectors develops, which

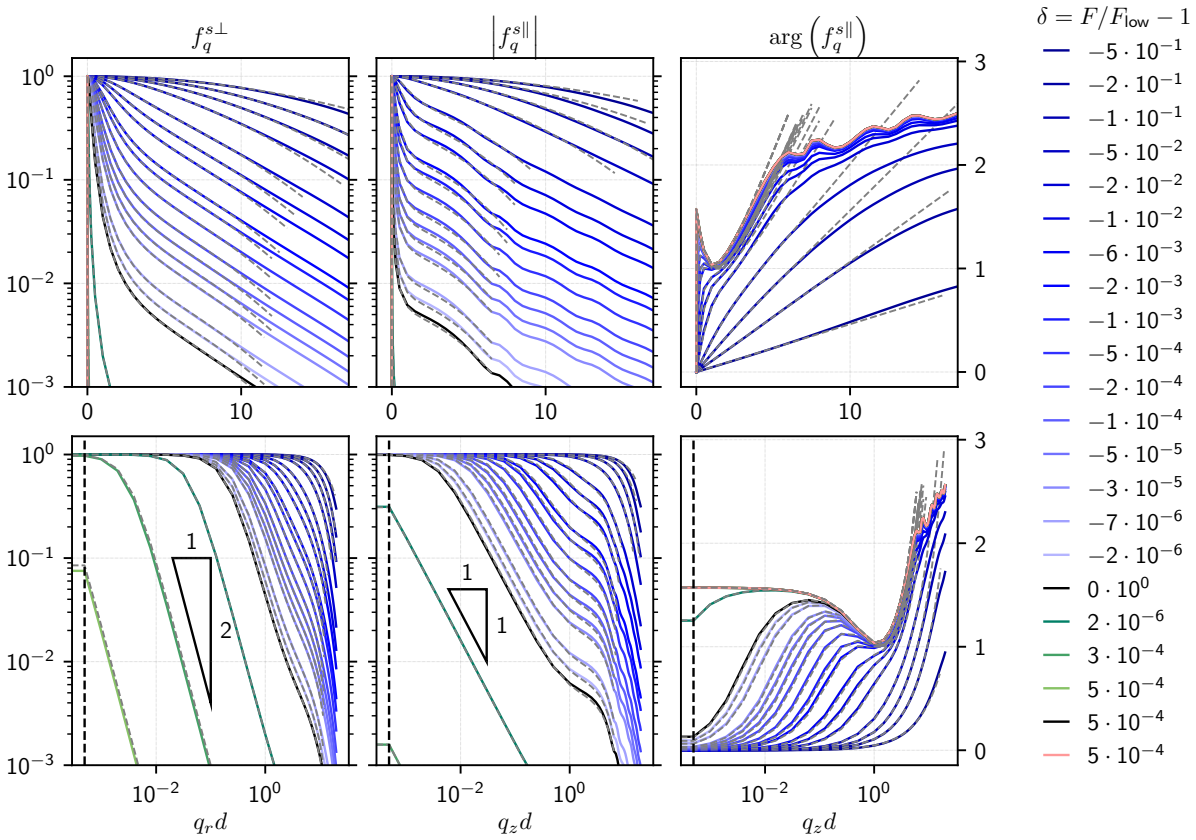

Figure 4.24.: Nonergodicity parameters over wave vector for different forces close to the critical force as labeled. The forces are given relative to the lower critical force $\delta = F/F_{\text{low}} - 1$, the critical forces are colored black and the forces in between in green. Left: $f^{s\perp}$ perpendicular to the force direction. These nonergodicity parameters are real due to the symmetry. Center: Modulus of $|f^{s\parallel}|$ parallel to the force direction. Right: Argument or phase $\arg(f^{s\parallel})$ parallel to the force direction. The lower panels show the same data on a log-scale for the wave vectors to visualize the narrowness close to the critical force. The dashed vertical line indicates the minimal nonzero wave vector. The dashed grey lines are fits according to the model (4.16). Numerical details are given in the text.

moves to smaller wave vectors when getting closer to the critical force.

The discontinuity, i.e. the large gap between the curves for F_{low} (black) and the next larger force (green) exists only for grids with $q_{\max} d \geq 20$, while this transition is continuous for $q_{\max} d \leq 14$. Furthermore, the data for $F > F_{\text{high}}$ are nonzero, because we can only iterate a finite time, but it is apparent that these values are even smaller than what we see here. We also have the impression that at F_{low} the grid in force direction is not fine enough to capture the behavior of $|f_q^{s\parallel}|$ (look at the lower center panel of Figure 4.24). Again, this is not so apparent in grids with $qd \leq 14$. In the following, we will use F_{low} to calculate the relative distance $\delta = F_{\text{ex}}/F_{\text{low}} - 1$ to the critical force, since the nonergodicity parameters above F_{low} are very small and will yield strange results. This choice will also be justified by the following results.

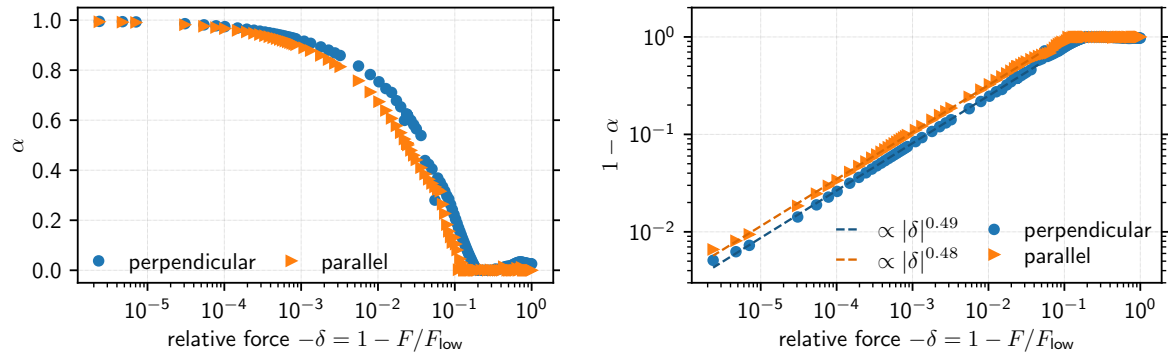

Figure 4.25.: Weight of the small wave vector function obtained from fitting (4.16) shown over relative force $-\delta = 1 - F_{\mathrm{ex}}/F_{\mathrm{low}}$. Since $F_{\mathrm{ex}} < F_{\mathrm{low}}$, δ is negative. Left: weight α on a linear scale. Right: reduced weight $(1-\alpha)$ on a logarithmic scale. The dashed lines are power law fits as indicated.

Let us now come back to evaluate the hypothesis of a two-function combination quantitatively. Since f_q^s is bounded for $q \to 0$ (and should decay to 0 for $q \to \infty$), we propose the following approximate forms close to the critical force

$$f_q^{s\perp} \approx \frac{\alpha}{1+(\ell q)^2} + (1-\alpha), \qquad (4.15a) \qquad \left|f_q^{s\parallel}\right| \approx \frac{\alpha}{\sqrt{1+(\ell q)^2}} + (1-\alpha) \qquad (4.15b)$$

where α describes the contribution of this small wave vector function and ℓ is a length scale for this function. The summand $(1-\alpha)$ is a zero-order approximation for the contribution from the function describing the large wave vector behavior. Motivated from the small force limit, we assume this function to be Gaussian. One might argue that this gives a completely wrong behavior for large wave vectors, but since these values are very small, this will not matter. A detailed analysis of this and other choices has been carried out by Sophia Henckell [Hen16]. The approaches

$$f^{\perp}(q,\sigma,\ell,\alpha) = \left(\frac{\alpha}{1+(\ell q)^2} + (1-\alpha)\right) \mathrm{e}^{-\frac{(\sigma q)^2}{2}}, \qquad (4.16a)$$

$$\begin{aligned} f^{\parallel}(q,\sigma,\ell,\alpha,\mu) &= \left(\frac{\alpha}{1-\mathrm{i}\ell q} + (1-\alpha)\right) \mathrm{e}^{-\frac{(\sigma q)^2}{2}+\mathrm{i}\mu q} \\ &= \left(\frac{\alpha}{\sqrt{1+(\ell q)^2}} \mathrm{e}^{\mathrm{i}\arctan(\ell q)} + (1-\alpha)\right) \mathrm{e}^{-\frac{(\sigma q)^2}{2}+\mathrm{i}\mu q} \end{aligned} \qquad (4.16b)$$

proved to show a good agreement for $qd \lesssim 6$, as can be seen as dashed grey lines in Figure 4.24. Furthermore their counterpart in real space can be motivated by physical arguments, namely a hopping and caging process [Gru14, Sec. 6.4, p. 66-68]. Note that the model for $f_q^{s\parallel}$ has to explain modulus and phase simultaneously.

Fitting these functions is less trivial than it seems to be. Therefore, we will give some details on how we proceed to extract the length scales of the models (4.16) from the data. Since those models are nonlinear, a wise choice for the initial parameters is crucial. The starting values for the fitting procedures were obtained by extracting (fitting) the length scale ℓ from the log-log-plots and by a fit of a Gaussian in the range $3 \leq qd \leq 6$. Then we have to minimize the

least squares error function

$$e_\perp(\sigma,\ell,\alpha) = \sum_{i=1}^{N_{qr}} \left(\frac{f^\perp(q_i,\sigma,\ell,\alpha) - f^{s\perp}_{q_i}}{f^{s\perp}_{q_i}} \right)^2 \tag{4.17}$$

for the perpendicular direction and

$$e_\parallel(\sigma,\ell,\alpha,\mu) = \sum_{i=1}^{N_{qz}} \left(\frac{\left|f^\parallel(q_i,\sigma,\ell,\alpha,\mu)\right| - \left|f^{s\parallel}_{q_i}\right|}{\left|f^{s\parallel}_{q_i}\right|} \right)^2 + \left(\arg(f^\parallel(q_i,\sigma,\ell,\alpha,\mu)) - \arg(f^{s\parallel}_{q_i})\right)^2 \tag{4.18}$$

for the perpendicular direction. The choice of the relative errors of the moduli ensures a good fit on a logarithmic scale. The additional term for $e_\parallel$ ensures a simultaneous fit of modulus and phase. These error functions are minimized using the SLSQP method implemented in the `scipy` module for `python` [Kra19] (see [PJM12] for an overview of minimizers). This method allows constraints for the parameters, which prevents the minimizer from going wild with the parameters. We take all data points with $q_r d < 10$ for the perpendicular direction and $q_z d < 7$ for the parallel direction into account. The lines in Figure 4.24 are shown until the deviation from the real data becomes larger than 20 % (relative to $|f^s_q|$). This range is in most cases larger than the actual fit range, which confirms the suitability of these models.

The results from these fits for different forces are shown in Figure 4.25 for α and in Figure 4.26 for the length scales. Considering α, the contribution of the small wave vector function, we find that it increases monotonically from 0 for small forces to 1 at the critical force. Since we fitted the parallel and the perpendicular direction separately, different values for α are possible, but we find that they agree quite well. The value for the perpendicular direction are systematically higher and start to increase earlier. We observe that the contribution of the small wave vector function only gives significant contributions, when we approach the critical force closer than 10 %. For $\delta > -10^{-3}$ it is the main contribution. In order to characterize its behavior close to the critical force, we also analyze the reduced weight $1-\alpha$ (or equivalently the weight of the large wave vector function). On the logarithmic scale the differences between the two values are more apparent, but also more consistent. We find $(1-\alpha^\parallel)/(1-\alpha^\perp) = 1.28$ over the whole range from $-\delta = 10^{-6}$ to $-\delta = 5 \cdot 10^{-2}$. Both reduced weights follow a power law with an exponent of approximately 0.5. Unfortunately, this exponent is somewhat model dependent. This exponent is also obtained for a cutoff $q_{\max} d = 24$, while for cutoffs $q_{\max} d \leq 14$, one obtains an exponent of approximately 0.8. Additionally, these small cutoff models also show deviations from this power law for $-\delta < 10^{-4}$.

The length scale ℓ obtained from the short wave vector function diverges when approaching the critical force like a power law: $\ell^\perp \propto |\delta|^{-0.27}$, $\ell^\parallel \propto |\delta|^{-0.54}$. Interestingly, the exponent for the parallel direction is twice the exponent for the perpendicular direction. While this relation is also true for the grid with $q_{\max} d = 14$, the numbers for the exponents are different, 0.4 for the perpendicular direction and 0.8 for the parallel (the curves flatten for $\delta > -10^{-5}$). Overall, this length scale increases about two to four orders of magnitude. On the other hand, the length scale σ, which can be associated with a cage size remains finite at the critical force. It increases from $0.07\,d$ for both directions to about $0.16\,d$ for the perpendicular direction and about $0.24\,d$ for the parallel direction. Surprisingly, also the phase factor μ, which corresponds to a shift by μ in real space, remains finite at the critical force. This is astonishing, because the

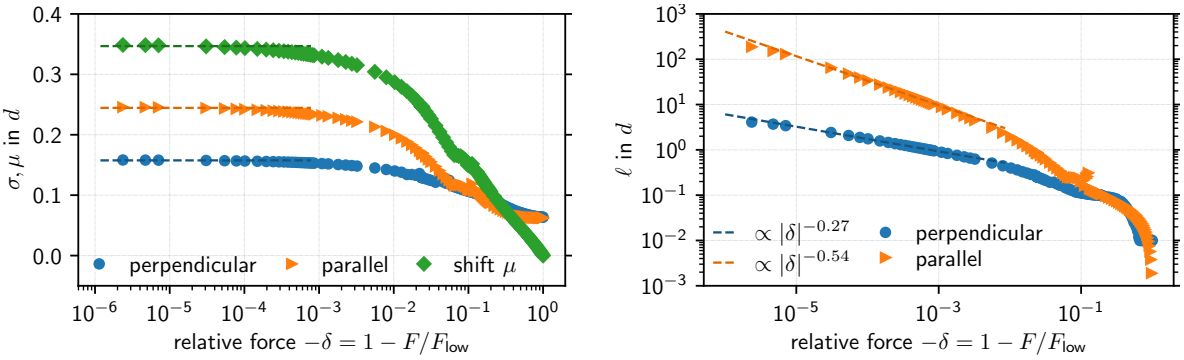

Figure 4.26.: Length scales obtained from fitting (4.16) shown over relative force $-\delta = 1 - F_{\mathrm{ex}}/F_{\mathrm{low}}$. Since $F_{\mathrm{ex}} < F_{\mathrm{low}}$, δ is negative. Left: Length scales for the large wave vector function perpendicular (blue, circles) and parallel (orange, triangles) to the force direction, as well as the phase factor μ (green, diamonds). The dashed lines show the $|\delta| \to 0$ limit. Right: Length scales for the small wave vector function. The dashed lines are power law fits as labeled.

first idea for large displacements is to move the whole probability distribution, as for the drift diffusion model (2.42), which was discussed at the end of Section 2.3.2. Instead, this model achieves these large displacements by a strong distortion of the probability distribution, as the small wave vector function is the Fourier transform of a (one- and two-sided) exponential function in real space (see Table A.1).

4.5.3. van Hove functions

More intuitive than the correlation functions is their Fourier transform, the van Hove function, as introduced in (2.85). $G^s(\boldsymbol{r}, t)$ describes the probability to find the probe particle in the volume $[\boldsymbol{r}, \boldsymbol{r} + \mathrm{d}\boldsymbol{r}]$ at time t, when it started at position $\boldsymbol{r} = 0$ at time $t = 0$. Since one-dimensional functions are easier to discuss, we start with the analysis of the marginal van Hove functions (2.163), where the other directions are integrated out. They can be directly obtained by one-dimensional Fourier transforms of $f_q^{s\perp}$ and $f_q^{s\parallel}$, respectively. We perform this transformation numerically, as discussed in Appendix A.5.

Figure 4.27 shows the marginal van Hove functions for different forces. They correspond to the nonergodicity parameters shown in Figure 4.22, i.e. they were calculated for a `unilog10`-grid with $q_{\max} d = 50$ and 111 grid points, which has a critical force of $41.57\, k_{\mathrm{B}}T/d$. A large cutoff proves to be advantageous for this representation on a logarithmic scale, because the Fourier transform introduces *ringing*, oscillations in a signal as a response to discontinuities [Ols17, Sec. 2.7, p. 63ff and Sec. 4.6, p. 143ff]. Such discontinuities happen inevitably at the maximum wave vector, where the calculated signal drops to zero. Fortunately, the smaller the discontinuity, the smaller the ringing effect. We also employ methods to extrapolate our data to reduce this effect when the cutoff is smaller, see Appendix A.5.

For forces below $35\, k_{\mathrm{B}}T/d$, we observe a roughly Gaussian shape. For symmetry reasons it is centered at the origin for $G^{s\perp}$. In the parallel direction, this Gaussian is shifted in force direction. For $F_{\mathrm{ex}} = 35\, k_{\mathrm{B}}T/d$ this shift is roughly $0.1\, d$. Furthermore, we observe a broadening of the Gaussian in both directions. For larger forces, an exponential tail develops. In the

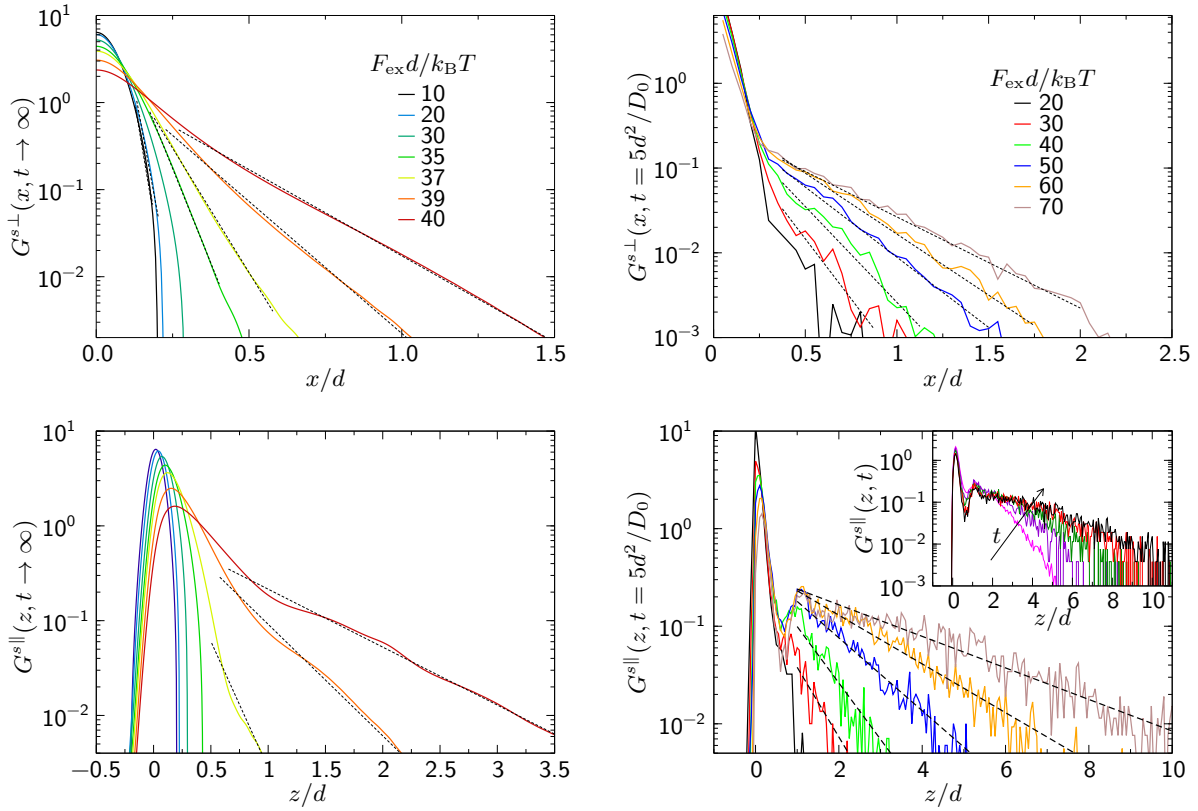

Figure 4.27.: Marginal probability distributions of the probe particle for MCT (left) and simulations (right), perpendicular (top) and parallel (bottom) to the direction of the force. The MCT results were obtained by Fourier transforming the nonergodicity parameters shown in Figure 4.22, while the simulation data is a histogram of the individual probe positions at time $tD_0/d^2 = 5$. Dashed lines are obtained by exponential fits at large distances. The inset shows the evolution of these tails for the $F_{\mathrm{ex}} = 70\,k_{\mathrm{B}}T/d$ and $tD_0/d^2 = 1, 2, 3, 4, 5$ (increasing from bottom to top) [GAPF16, Fig. 9].

direction perpendicular to the force this tail is symmetric to both sides. In force direction, this tail only extends to large positive displacements. The exponential nature is visualized by a semilogarithmic plot and a fit (dashed black lines). This reveals some additional structures for $G^{s\parallel}$, which might or might not be artifacts from the Fourier transform. They could arise from the features, which we have seen in the correlation functions in Figure 4.24.

The van Hove functions obtained from simulations by Antonio Puertas show similar effects, as shown in the right hand side panels of Figure 4.27. For small forces, the particle stays localized around the origin. For larger forces there is also exponential tails evolving as shown by the dashed lines. The time evolution in the inset suggests that even for $F_{\mathrm{ex}} = 70\,k_{\mathrm{B}}T/d$ the distribution becomes stationary. Therefore, we can consider those plots as good approximation for the long time limit. A minor difference is the appearance of a peak in $G^{s\parallel}$ for the simulations at about $z \approx 1.5d$ before the exponential decay starts. One can interpret this as the distance the probe particle has to travel to leave its cage. But to leave its cage, it has to move its neighbors. The closes configuration of the particle and its three neighbors in force direction is a tetrahedron (in 3D). To pass, the probe has to move from the tip of the tetrahedron through

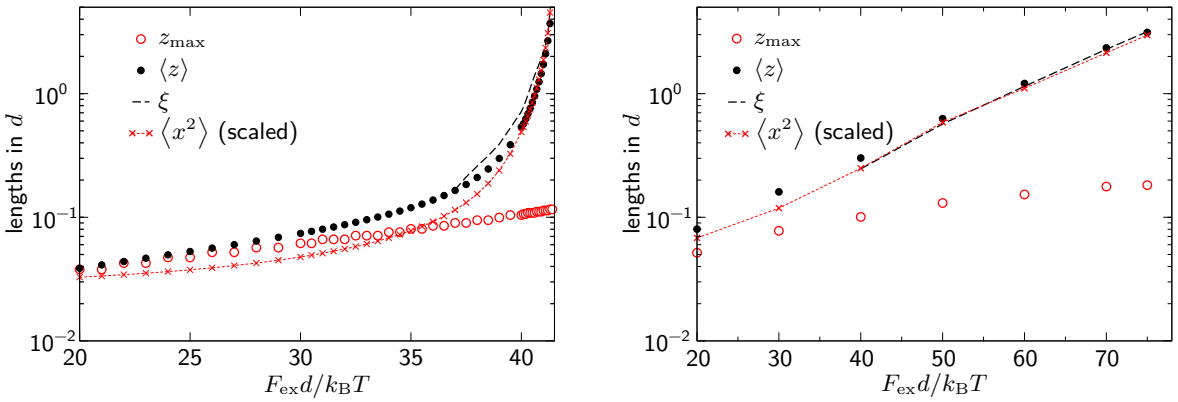

Figure 4.28.: Length scales in MCT (left) and simulations (right). $\langle z \rangle$ is the mean displacement in force direction, $\langle x^2 \rangle$ the variance perpendicular to it, ξ is the length scale extracted from the fit of the exponential tails in Figure 4.27 and $z_{\max}$ the position of the maximum of the probability distribution. The variance is scaled by a constant factor to highlight the similarities to $\langle z \rangle$ and ξ [GAPF16, Fig. 10].

its base face to the other side. Having moved the distance $\sqrt{6}d/3 \approx 0.82\,d$ into the base face, it created a void behind it, in which the neighbors are driven by the pressure of the other particles. Therefore, they push the probe into the new cage center at the tip of the tetrahedron. This process is relatively fast, see inset of Figure 4.19. As a consequence there are very little particles at distances between $0.8\,d$ and $1.6\,d$. The upper bound is twice the tetrahedron height and does not take into account that the neighbor particle moves so that this value should be smaller. Since our theory does not include a coupling from the probe to the bath, we cannot see this effect there.

A major difference to our MCT calculations is the quantitative force range. While the exponential tails only appear very close the critical force in MCT, they are already visible in the simulations for rather small forces. On top of that, MCT predicts delocalized behavior for $F_{\mathrm{ex}} > 41.6\,k_{\mathrm{B}}T/d$, where simulations still show localized behavior up to $F_{\mathrm{ex}} = 70\,k_{\mathrm{B}}T/d$. Such quantitative differences are known for MCT concerning the numerical value for the glass transition (see the introduction of this section for references). Hence, the critical force in the simulations seems to be at least about twice as large as in our calculations and the delocalization transition is not as sharp as in theory.

Since simulations and theory show many similarities, we can analyze the scaling behavior of some properties, which characterize the probability distributions. In Figure 4.28 we show the mean $\langle z \rangle$ in force direction, the variance $\langle x^2 \rangle$ perpendicular to it and the length scale ξ obtained by the fit of the exponential tails of the probability distributions. All quantities grow monotonously with increasing force. Again, the increase is more pronounced for MCT calculations than for simulations. Nevertheless, the variation of those three quantities with the external force is very similar. This is a hint that these quantities share a common cause. Considering the close relation between $\langle z \rangle$ and ξ, we can conclude that the tails of the probability distribution dominate the calculation of the mean. Even if the probability to find a particle at large distances is small, their large displacement has a strong effect on the mean. This is also important to keep in mind when doing experiments.

Furthermore, we find that $\langle z \rangle$ and $\langle x^2 \rangle$ collapse close to the critical force in theory and also over a broader range in simulations. This is similar to what we found in the previous section for the small wave vector length scales. There, we noticed $\ell^{\parallel} \propto (\ell^{\perp})^2$. Calculating the first and second moment from those models (4.16) according to (2.174), neglecting the large wave vector function (i.e. setting $\alpha = 1$), we find $\langle z \rangle \approx \ell^{\parallel} + \mu$ and $\langle x^2 \rangle \approx (\ell^{\perp})^2$. Since μ remains bounded at the critical force, while $\ell^{\parallel}$ diverges, this also implies $\langle z \rangle \approx \ell^{\parallel} \propto (\ell^{\perp})^2 \approx \langle x^2 \rangle$. This allows us to interpret $\ell^{\parallel}$ as the tail length scale ξ. Since these exponential tails appear over a broad range of forces in simulations, this also explains the nice agreement of those quantities over a broad range of forces.

In the previous section we have also seen that the shift μ remains finite at the critical force and we concluded that the large displacements are caused by a strong distortion of the van Hove function. By now, we have verified the distortion of the van Hove functions by the appearance of the exponential tails. To check for the shift μ, we analyze position of the peak of the van Hove function $z_{\max}$, which is also shown in Figure 4.28. For MCT calculations as well as for simulations, the peak position remains finite with values of about $0.1\,d$ to $0.2\,d$, which is about a factor two to four smaller than μ.

Finally, we can also have a look at the three-dimensional van Hove function. Since three-dimensional plots are too difficult to fold into two dimensions, we only show a two-dimensional cut $G^s(x, 0, z, t \to \infty)$ in Figure 4.29. As the van Hove function describes the probability distribution for the probe positions, we can also interpret it as the cage for the probe particle. For $F_{\text{ex}} \leq 30\,k_{\text{B}}T/d$ the shape of the cage is symmetric, but displaced from the origin. This corresponds to the finding that the small wave vector function does not play a role far from the critical force. Its effect is more pronounced for $F_{\text{ex}} = 40\,k_{\text{B}}T/d$: While the peak of the distribution has not moved much more, the cage extends comparatively far into the force direction so that it looks egg shaped. The results for the simulations are similar even though the forces have to be larger to achieve comparable effects.

4.6. Conclusions

In this chapter we have found that there is indeed a transition from elastic to viscous behavior of the probe particle, the so called delocalization transition. This definition is consistent with the finding that the nonergodicity parameters vanish at this transition. However, numerically there are two critical forces. At the lower critical force F_{low} most of the nonergodicity parameters vanish, except for those for small wave vectors perpendicular to the direction of the force force. At the larger critical force F_{high} finally all nonergodicity parameters vanish. The difference between both forces decreases with decreasing step size, indicating a numerical origin of this behavior. With this, we can calculate the phase diagram, i.e., the critical force as function of the packing fraction. Our model shows a linear relation between the square of the critical force and the inverse of the long time limit of the mean square displacement without external force. Furthermore, we find a power law relation between the yield stress and the critical force. Consequently there is another power law connecting the yield stress and the long time limit of the mean square displacement in the quiescent system, which is verified with some data from simulations. Finally, we have characterized moments, transport coefficients and correlation functions approaching the critical force (not too closely). The long time limits of the correlation function can be explained by a simple model, which shows diverging and

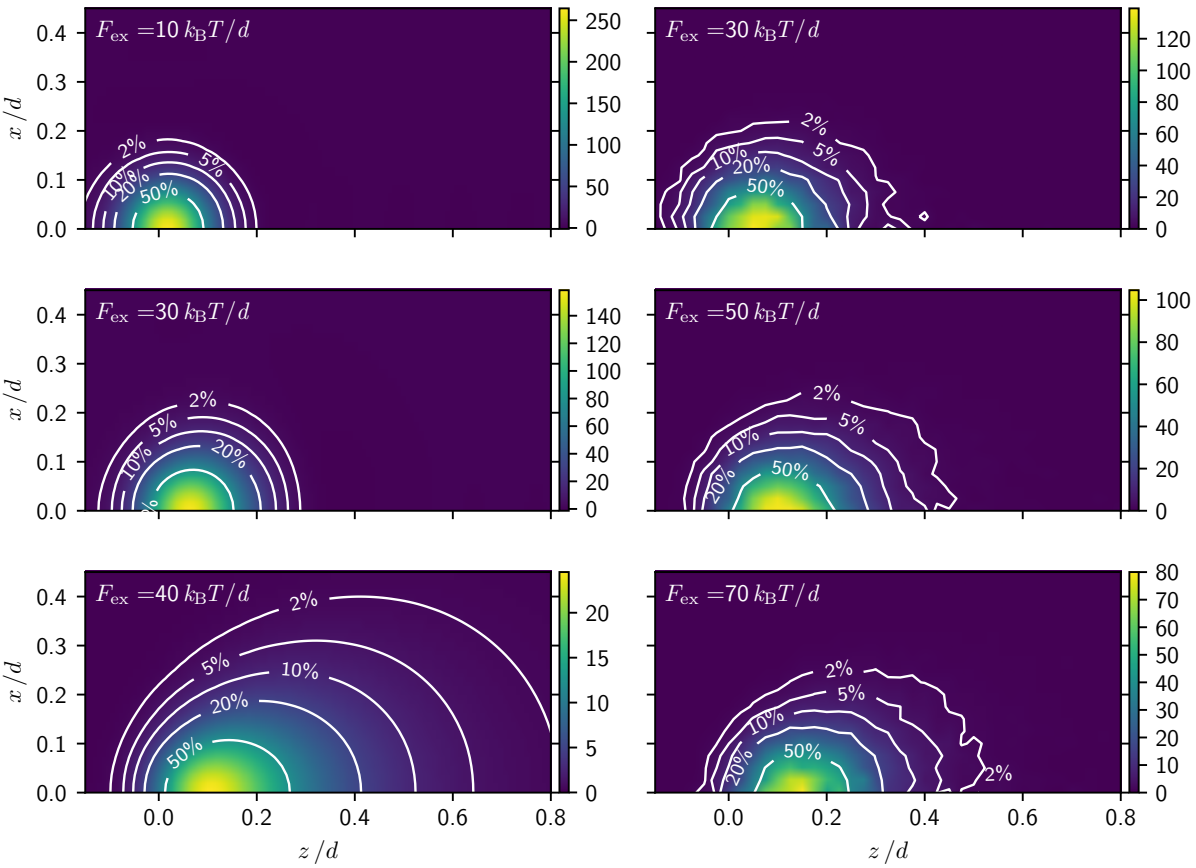

Figure 4.29.: Long time limit of the van Hove function $G^s(x, 0, z, t)$ for different forces, increasing from top to bottom. The force is applied in z direction to the right. Left column: MCT calculations for $t \to \infty$ obtained by inverse Fourier transformation of the nonergodicity parameters. Right column: Probe displacement probability distribution of the simulations for $tD_0/d^2 = 1$. The contour line labels indicate the percentage of the peak value and are used to illustrate the shape [GAPF16, Fig. 8].

non-diverging length scales when approaching the critical force. The comparison to simulations exhibits a good qualitative and also a fair quantitative agreement, even though the critical force in the simulations is about twice as large.

5. Bifurcation analysis

> The deepest and most interesting problem in solid state theory is probably the theory of the nature of glass and the glass transition.
>
> *(P.W. Anderson, [And95])*

In this chapter we will have a closer look at the delocalization transition. This includes a semi-analytical analysis of the critical point and the critical behavior at and close to the critical point. The measure for the distance to the critical force, also called *separation parameter*, is the relative force

$$\delta = \frac{F_{\mathrm{ex}} - F_{\mathrm{c}}}{F_{\mathrm{c}}}, \tag{5.1}$$

which is negative below the critical force F_{c} and positive above.

We will follow the extensive discussions of glass-transition singularities in mode-coupling theory by Götze [Göt09, Chap. 4.3-4.5] for the bifurcation and [Göt09, Chap. 6, p. 437] for the asymptotic dynamics. Originally, mode-coupling theory was formulated with polynomial memory functionals with real, non-negative coefficients [Göt09, p. 192, Eq. (4.15a,b)], which is frequently exploited for proofs of certain properties. For our equations there are two important differences: our memory functionals are not given by multivariate polynomials but multivariate rational functions and their coefficients are not real but complex valued. Therefore one has to check carefully whether the proofs still apply and how to adapt them to our case.

Starting point for this analysis are the equations of motion for the probe correlation function (2.154) in Laplace space, which we repeat here for reference

$$0 = (s\tilde{\phi}^s_{\boldsymbol{q}^*}(s) - 1) + \tilde{\phi}^s_{\boldsymbol{q}^*}(s)\tilde{\mathcal{M}}_{\boldsymbol{q}^*}(s), \tag{5.2a}$$

$$\tilde{\mathcal{M}}_{\boldsymbol{q}^*}(s) = \frac{\Gamma^x_{\boldsymbol{q}^*}\left(\tilde{m}^{zz}_{\boldsymbol{q}^*}(s)+1\right) + \Gamma^z_{\boldsymbol{q}^*}\left(\tilde{m}^{xx}_{\boldsymbol{q}^*}(s)+1\right) - \Gamma^{xz}_{\boldsymbol{q}^*}\tilde{m}^{xz}_{\boldsymbol{q}^*}(s)}{\left(\tilde{m}^{xx}_{\boldsymbol{q}^*}(s)+1\right)\left(\tilde{m}^{zz}_{\boldsymbol{q}^*}(s)+1\right) - \left(\tilde{m}^{xz}_{\boldsymbol{q}^*}(s)\right)^2}, \tag{5.2b}$$

where the primitive memory functionals $m^{xz}_{\boldsymbol{q}^*}(t)$ are defined in (2.160). For the moment it is sufficient to know that they are linear functionals in the bath correlation function $\boldsymbol{\phi}(t)$ and the probe correlation function $\boldsymbol{\phi}^s(t)$. The prefactors $\Gamma_{\boldsymbol{q}^*}$ were introduced in (2.155) and read with the use of the separation parameter (5.1)

$$\Gamma^x_{\boldsymbol{q}^*} = (q^*_x)^2, \tag{5.3a}$$

$$\Gamma^z_{\boldsymbol{q}^*} = q^*_z(q^*_z - \mathrm{i}F_{\mathrm{c}}) - \mathrm{i}\delta q^*_z F_{\mathrm{c}} =: \Gamma^{z,c}_{\boldsymbol{q}^*} - \mathrm{i}\delta\Gamma^{z,d}_{\boldsymbol{q}^*}, \tag{5.3b}$$

$$\Gamma^{xz}_{\boldsymbol{q}^*} = q^*_x(2q^*_z - \mathrm{i}F_{\mathrm{c}}) - \mathrm{i}\delta q^*_x F_{\mathrm{c}} =: \Gamma^{xz,c}_{\boldsymbol{q}^*} - i\delta\Gamma^{xz,d}_{\boldsymbol{q}^*}. \tag{5.3c}$$

For the analysis of the asymptotic scaling laws in conventional MCT it turns out to be beneficial to introduce the S-transform, which is derived from the Laplace transform (B.1) by

multiplication with the Laplace argument

$$\mathcal{S}\left[t \mapsto f(t)\right](s) := s\mathcal{L}\left[f\right](s) \tag{5.4}$$

(cf. [Göt09, p. 439, Eq. (6.2)]). This definition has the advantage over the simple Laplace transform that constants map onto the same constants, which can be verified using Table B.1. Another advantage is that the limit $s \to 0$ of the S-transform corresponds directly to the limit $t \to \infty$, which allows us to directly identify the nonergodicity parameters. To keep the notation concise, we label the S-transformed correlation functions and memory kernels with a hat

$$\hat{\phi}^s_{\boldsymbol{q}^*}(s) := s\tilde{\phi}^s_{\boldsymbol{q}^*}(s), \tag{5.5a}$$

$$\hat{m}^{\alpha\beta}_{\boldsymbol{q}^*}(s) := s\tilde{m}^{\alpha\beta}_{\boldsymbol{q}^*}(s). \tag{5.5b}$$

With this notation, the equation of motion (5.2) can be transformed into

$$\frac{\hat{\phi}^s_{\boldsymbol{q}^*}(s)}{1-\hat{\phi}^s_{\boldsymbol{q}^*}(s)} = \frac{\hat{m}^{xx}_{\boldsymbol{q}^*}(s)\hat{m}^{zz}_{\boldsymbol{q}^*}(s) - (\hat{m}^{xz}_{\boldsymbol{q}^*}(s))^2 + s(\hat{m}^{xx}_{\boldsymbol{q}^*}(s) + \hat{m}^{zz}_{\boldsymbol{q}^*}(s)) + s^2}{\Gamma^x_{\boldsymbol{q}^*}\hat{m}^{zz}_{\boldsymbol{q}^*}(s) + \Gamma^z_{\boldsymbol{q}^*}\hat{m}^{xx}_{\boldsymbol{q}^*}(s) - \Gamma^{xz}_{\boldsymbol{q}^*}\hat{m}^{xz}_{\boldsymbol{q}^*}(s) + s(\Gamma^x_{\boldsymbol{q}^*} + \Gamma^z_{\boldsymbol{q}^*})}, \tag{5.6}$$

which is the equivalent of [Göt09, p. 439, Eq. (6.3b)], the starting point of Götze's asymptotic expansion. In contrast to his case, we cannot separate the Laplace frequencies s from the memory functionals. Furthermore, our right hand side is still a rational function rather than a polynomial. As a consequence, the change of variable around the critical correlator $\boldsymbol{f}^{sc}$ via

$$\hat{\phi}^s_{\boldsymbol{k}^*}(s) = f^{sc}_{\boldsymbol{q}^*} + (1 - f^{sc}_{\boldsymbol{q}^*})\hat{g}_{\boldsymbol{q}^*}(s) \tag{5.7}$$

does not reduce to the same problem with different coefficients as in [Göt09, p. 439, Eq. (6.3c)]. Another difference, which might be more advantageous for us, is the fact that the primitive memory functionals are independent of the force. This force only enters via the prefactors $\Gamma^z_{\boldsymbol{q}^*}$ and $\Gamma^{xz}_{\boldsymbol{q}^*}$.

Since we are only interested in the delocalization transition of the probe correlation function, we will again apply the constant bath approximation as introduced in Section 2.4.7, which consists in replacing all time-dependent bath correlation functions by their long time limit. Then, the primitive memory kernels are linear functionals in $\boldsymbol{\phi}^s$ only. We will denote them as $\mu^{\alpha\beta}_{\boldsymbol{k}^*}$ as defined in (2.166).

In the following, we will first introduce some basic concepts for the bifurcation analysis in Section 5.1. Since our mode-coupling functional is different from the usual one, we analyze the bifurcation for the long time limit numerically in Section 5.2. As this bifurcation does not allow for a unambiguous classification, we will have a look at the bifurcations of some simple models in Section 5.3 before diving into the bifurcation analysis of the full model in Section 5.4. Then, we turn to the analysis of the asymptotic relaxation laws in Section 5.6. These analytical predictions will be tested in Section 5.7 and from these results, we can derive critical laws for the moments, which are discussed in Section 5.8. Finally, we compare the findings for the bifurcation to data from simulations in Section 5.9.

5.1. Preliminaries for the bifurcation analysis

We start by analyzing the long time limits or nonergodicity parameters $f^s_{\boldsymbol{q}^*} := \lim_{t\to\infty} \phi^s_{\boldsymbol{q}^*} = \lim_{s\to 0} \hat{\phi}^s_{\boldsymbol{q}^*}$, which will set the stage for the analysis of the asymptotic scaling laws. The implicit equations for the nonergodicity parameters are given by the $s \to 0$ limit of (5.6) (see also (2.167) and Section 2.4.6 for a derivation). This problem can be mapped onto finding the common roots of the functions

$$J'_q(F_{\text{ex}}, \boldsymbol{v}) = v_q - \frac{\mathcal{F}_q(F_{\text{ex}}, \boldsymbol{v})}{1 + \mathcal{F}_q(F_{\text{ex}}, \boldsymbol{v})} \tag{5.8}$$

(cf. [Göt09, p. 220]) with

$$\mathcal{F}_q(F_{\text{ex}}, \boldsymbol{v}) = \frac{\mu^{xx}_q(\boldsymbol{v})\mu^{zz}_q(\boldsymbol{v}) - (\mu^{xz}_q(\boldsymbol{v}))^2}{\Gamma^x_q \mu^{zz}(\boldsymbol{v}) + \Gamma^z_q(F_{\text{ex}})\mu^{xx}_q(\boldsymbol{v}) - \Gamma^{xz}(F_{\text{ex}})\mu^{xz}_q(\boldsymbol{v})} \tag{5.9}$$

being our equivalent of the mode-coupling memory functional [Göt09, p. 192, Eq. (4.15)]. The index q labels the two-dimensional grid of wave vectors (q^x_i, q^z_j) with $0 \le i < N_{q_x}$ and $0 \le j < N_{q_z}$. The primitive memory functions $\mu^{\alpha\beta}_q$ as defined in (2.166) are linear functionals in $\boldsymbol{v}$ and the prefactors Γ^α_q are given in (2.155). We explicitly highlight the dependence on the external force F_{ex}, which is the parameter driving the transition. All other couplings (arising from the memory integrals with the structure factors) are constant in this model. The memory functional $\mathcal{F}_q$ is a rational function with a quadratic form in the numerator and a linear form in the denominator. As we will need their derivatives, we introduce the following shorthands

$$\boldsymbol{v}^T A_q \boldsymbol{w} = \frac{1}{2}\left(\mu^{xx}_q(\boldsymbol{v})\mu^{zz}_q(\boldsymbol{w}) + \mu^{xx}_q(\boldsymbol{w})\mu^{zz}_q(\boldsymbol{v})\right) - \left(\mu^{xz}_q(\boldsymbol{v})\mu^{xz}_q(\boldsymbol{w})\right), \tag{5.10a}$$

$$B^T_q(F_{\text{ex}})\boldsymbol{v} = \Gamma^x_q \mu^{zz}_q(\boldsymbol{v}) + \Gamma^z_q(F_{\text{ex}})\mu^{xx}_q(\boldsymbol{v}) - \Gamma^{xz}_q(F_{\text{ex}})\mu^{xz}_q(\boldsymbol{v}), \tag{5.10b}$$

which express the quadratic form through a symmetric matrix A_q and the linear form through a vector B_q with the usual conventions for matrix multiplication. Then

$$\mathcal{F}_q(F_{\text{ex}}, \boldsymbol{v}) = \frac{\boldsymbol{v}^T A_q \boldsymbol{v}}{B^T_q(F_{\text{ex}})\boldsymbol{v}}. \tag{5.11}$$

The implicit function theorem guarantees that a solution $\boldsymbol{f}^s$ of $J'_q(F_{\text{ex}}, \boldsymbol{f}^s) = 0$ can be uniquely extended to forces in an open set around F_{ex}, if the Jacobian of J'_q with respect to the variables $\boldsymbol{v}$ is invertible. On the other hand, if two (or more) solutions coalesce, the Jacobian is not invertible, which gives us a necessary condition for searching for bifurcations. For $B^T_q \boldsymbol{v} \neq 0$, we can rewrite the implicit function equation fraction free as

$$0 = (v_q - 1)\boldsymbol{v}^T A_q \boldsymbol{v} + v_q B^T_q(F_{\text{ex}})\boldsymbol{v} =: J_q(F_{\text{ex}}, \boldsymbol{v}). \tag{5.12}$$

In this representation it is immediately clear that $v_q = 0$ is a solution. More interesting is the other, nontrivial, solution of this equation and the condition, when it appears or disappears as discussed in the previous chapter. As shown above, we have to analyze the Jacobian of J_q at a

solution $\boldsymbol{f}^s(F_{\text{ex}})$ of $J_q(F_{\text{ex}}, \boldsymbol{f}^s) = 0$. It is given by

$$\begin{aligned} S_{qp}(F_{\text{ex}}, \boldsymbol{f}^s) = \frac{\partial}{\partial v_p} J_q(F_{\text{ex}}, \boldsymbol{f}^s) =& \delta_{qp}((\boldsymbol{f}^s)^T A_q \boldsymbol{f}^s + B_q^T(F_{\text{ex}})\boldsymbol{f}^s) + f_q^s B_q^T(F_{\text{ex}})\hat{\boldsymbol{p}} \\ &+ (f_q^s - 1)\left((\boldsymbol{f}^s)^T A_q \hat{\boldsymbol{p}} + (\hat{\boldsymbol{p}})^T A_q \boldsymbol{f}^s\right), \end{aligned} \tag{5.13}$$

where $\hat{\boldsymbol{p}}$ is the unit vector in p-direction, i.e. $\hat{\boldsymbol{p}}_i = \delta_{ip}$. In particular, we get for any vector $\boldsymbol{v}$

$$\begin{aligned} (S(F_{\text{ex}})\boldsymbol{v})_q =& v_q((\boldsymbol{f}^s)^T A_q \boldsymbol{f}^s + B_q^T(F_{\text{ex}})\boldsymbol{f}^s) + f_q^s B_q^T(F)\boldsymbol{v} \\ &+ (f_q^s - 1)\left((\boldsymbol{f}^s)^T A_q \boldsymbol{v} + \boldsymbol{v}^T A_q \boldsymbol{f}^s\right). \end{aligned} \tag{5.14}$$

Hence we have found a critical point, when S is not invertible, i.e. where S has an eigenvalue 0. An obvious solution is again $\boldsymbol{f}^s = 0$, which leads to the problem that there is not only one zero eigenvalue but all. Such a bifurcation does not fall into the classical categories of bifurcations as introduced by Arnol'd [Arn84]. It is found in a schematic model as discussed in [Göt09, p. 231], where it can be understood as result of a sequence of regular bifurcations. However, "a more detailed discussion of the specified problem is not yet available" [Göt09, p. 242].

Based on relation (5.8) we can define the stability matrix[1] (as Jacobian of this equation)

$$S'_{qp}(F_{\text{ex}}, \boldsymbol{f}^s) = \delta_{qp} - (1 - f_q^s)^2 \left(\frac{\hat{\boldsymbol{p}}^T A_q \boldsymbol{f}^s + (\boldsymbol{f}^s)^T A_q \hat{\boldsymbol{p}}}{B_q^T \boldsymbol{f}^s} - \frac{\boldsymbol{f}^s A_q \boldsymbol{f}^s}{(B_q^T \boldsymbol{f}^s)^2} B_q^T \hat{\boldsymbol{p}} \right). \tag{5.15}$$

For this calculation, we used that $\boldsymbol{f}^s$ fulfills the fixed point equation given by the root of (5.8). This representation has the advantage that this stability matrix does not necessarily vanish completely if $\boldsymbol{f}^s \to 0$, because the norm of $\boldsymbol{f}^s$ cancels in the fractions. However, the limit of this stability matrix in the limit of vanishing $\boldsymbol{f}^s$ may depend on the limiting procedure. We will choose $\boldsymbol{f}^s$ according to the solution of (5.8) for $F_{\text{ex}} \to F_{\text{c}}$. For further reference we will call $S_{pq} - \delta_{pq}$ the reduced stability matrix.

For classical MCT equations, where $\mathcal{F}_q$ is a multivariate polynomial with positive coefficients, the glass-transition singularities are generic and degenerate A_l bifurcations [Göt09, Sec. 4.3.3, p. 235]. The index l refers to the multiplicity of the root. Characteristic for generic bifurcations are discussed in detail in [Göt09, Sec. 4.3.4(i), p. 242-247]. Their characteristic feature is a discontinuity, $f_q^c > 0$ and a $\sqrt{|\delta|}$ variation of the nonergodicity parameters as a function of the distance δ to the bifurcation [Göt09, p. 245, Eq. (4.91a)]. For a degenerate bifurcation, which is discussed in [Göt09, Sec. 4.3.4(ii), p. 247ff], the nonergodicity parameters vanish continuously at the critical point, $f_q^c = 0$, and therefore vary like $|\delta|$ with the distance to the critical point [Göt09, p. 249]. Degenerate bifurcations are also referred to as *type A* and generic bifurcations as *type B* transitions [Göt09, p. 228].

Glass-glass transitions, where only a subset of the correlation function changes from ergodic to nonergodic can be mapped to liquid-glass transitions by subtracting the critical nonergodicity parameters [Göt09, Sec. 4.3.4(iii), p. 249]. There is also the possibility of more exotic bifurcations, for example a simultaneous type A transition for some correlators and a type B transition for

[1] Götze defines a slightly different stability matrix $\mathcal{A}_{q,p}$ (cf. [Göt09, p. 222, Eq. (4.60a)]), which is related to our stability matrix via $(\mathcal{A}(F_{\text{ex}}))_{q,p} = \delta_{pq} - (1 - f_p^s)(1 - f_q^s)^{-1} S'(F_{\text{ex}})_{pq}$. Consequently, the bifurcation condition that an eigenvalue of $S(F_{\text{ex}})$ has to be zero translates into the condition that $\mathcal{A}(F_{\text{ex}})$ has to have an eigenvalue of one [Göt09, p. 221].

others, if the stability matrix is reducible [Göt09, Sec. 4.3.4(iv), p. 250]. A matrix is called reducible, if it is block-triangular after a possible permutation of indexes.

A distinction based on the fixed point equations is usually not possible, because the solutions are only known numerically. However, the different scenarios have different consequences for the behavior close to the transition. It affects also the analytical approach. For this reason, we will first have a look at the numerical results.

5.2. Numerical findings for the bifurcation

We start by analyzing the numerical solution of our MCT equations close to the critical force. As already noted earlier in Sec. 4.1.2, there is in fact two forces where the solution changes qualitatively. We will now study this more quantitatively. In Figure 5.1 we show the nonergodicity parameter f^s for a variety of wave vectors. The discretization is the same as for Figure 4.1, namely a packing fraction of $\varphi = 0.537$, a `unilog10`-grid with 51 points and a cutoff of $q_{\max}d = 20$ and the bath input from the dynamical calculations on a grid of 512 points with a cutoff of $q_{\max}d = 65$.

Focusing on the modulus $|f^s_{\boldsymbol{q}^*}|$ first, we find that the nonergodicity parameter for almost all wave vectors drops to zero at the first critical force as shown in Figure 5.1. Larger wave vectors even show the same functional behavior: They approach the lower critical force like $\sqrt{-\delta}$. This is the generic *type B* behavior. Nevertheless, the prefactor of this law can be negative for large wave vectors, which is expected from Figure 4.22, where we observed negative real parts of the nonergodicity parameters for large wave vectors. This is different from the usual glass transition analysis, where all nonergodicity parameters have to be non negative.

What is also very different from the usual type B transition is the behavior for small wave vectors. $f^s(q_x, 0)$ for $q_x d \leq 6.2 \cdot 10^{-2}$ is visibly nonzero above the first critical force. A closer look in particular at the imaginary part reveals that also $f^s(q_x, q_z)$ for $q_x d \leq 6.2 \cdot 10^{-2}$ and $q_z d \leq 3.9 \cdot 10^{-3}$ is measurably different from zero above the lower critical force. We say *measurably different*, because after a finite number of iterations none of the nonergodicity parameters will be exactly zero. Therefore we use the concept of the *confidence level* [Gru14, p. 44, Eq. (4.7)] to determine which values are most likely nonzero. It is interesting to note that the maxima in the imaginary part for those small wave vectors appear above the lower critical force. Since it is hard to see, we also mention that for $q_z d = 4.9 \cdot 10^{-4}$ and small q_x the imaginary part exhibits a kink as in the letter Λ, while the imaginary part for $q_z d = 3.9 \cdot 10^{-3}$ as well as the real parts for small q_x and q_z exhibit a large discontinuity (up to 0.8). Approaching this discontinuity could be modeled by a square root law for both $\delta < 0$ as well as for $\delta > 0$ with different prefactors for each side. It is however difficult to test because the discontinuity cannot be determined accurately. These findings suggest that there is a type B glass-glass transition at the lower critical force, where the larger wave vectors decouple.

The same qualitative behavior can be found for a discretization with $q_{\max}d = 24$. Unfortunately, there is a qualitative change when the cutoff is reduced to $q_{\max}d = 14$ or $q_{\max}d = 10$. In both cases, we find a type-A-like transition at the first critical force, which manifests itself by a finite slope at the transition as can be observed in Figure 5.2. In addition to that there is no discontinuities anymore. These qualitative changes will be reflected in many critical scaling laws. To summarize, this bifurcation shows a very rich phenomenology, which makes it difficult

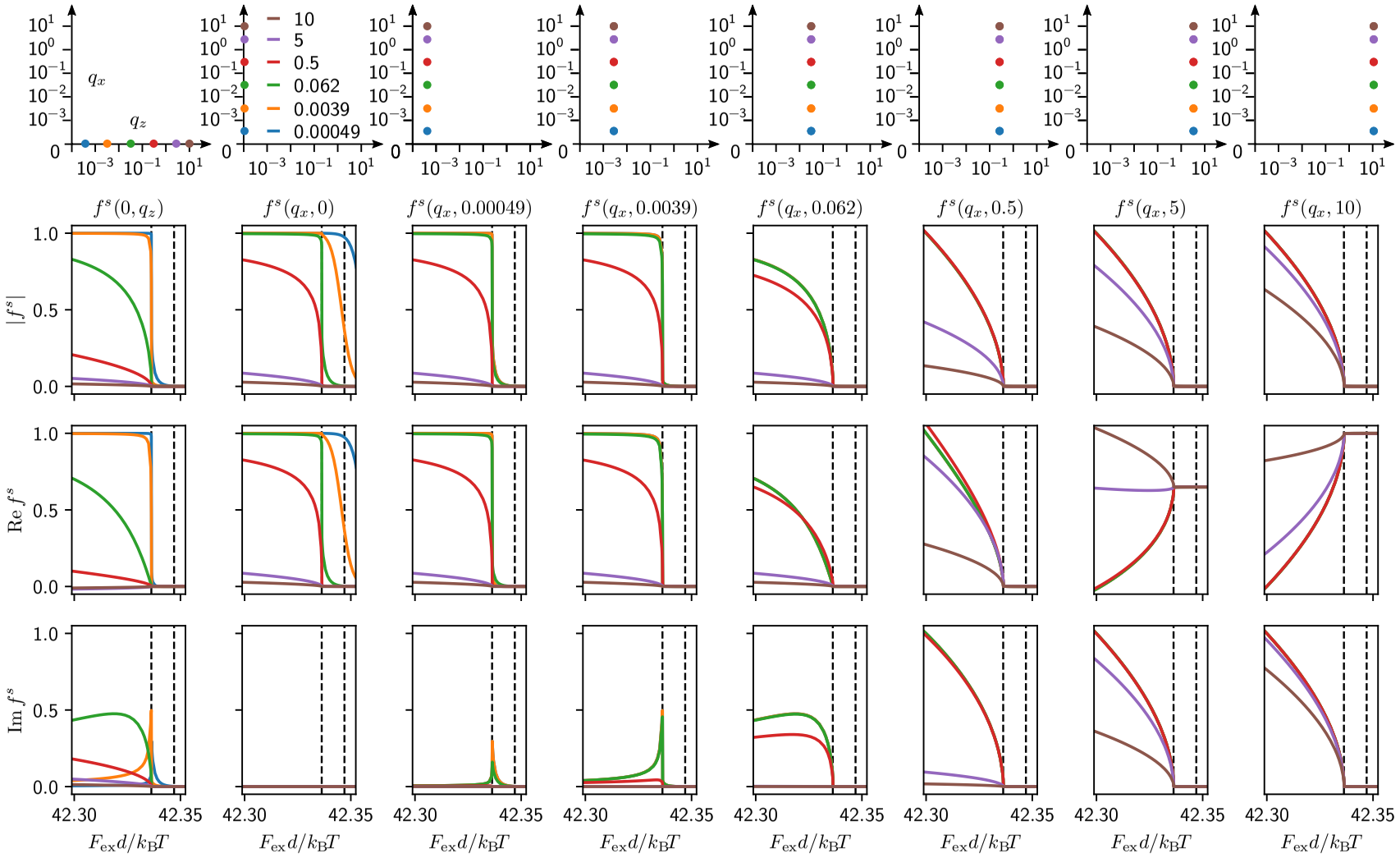

Figure 5.1.: Nonergodicity parameters $f^s_{\boldsymbol{q}^*} = f^s(q_x, q_z)$ as function of the external force for different wave vectors as labeled. The top row sketches the positions of the wave vectors in the (q_x, q_z) plane for the panels below. For the three rightmost columns ($q_z d \geq 0.5$) we zoomed in on the y-axis. The dashed lines indicate the critical forces. The cutoff is $q_{\max} d = 20$, more details can be found in the text.

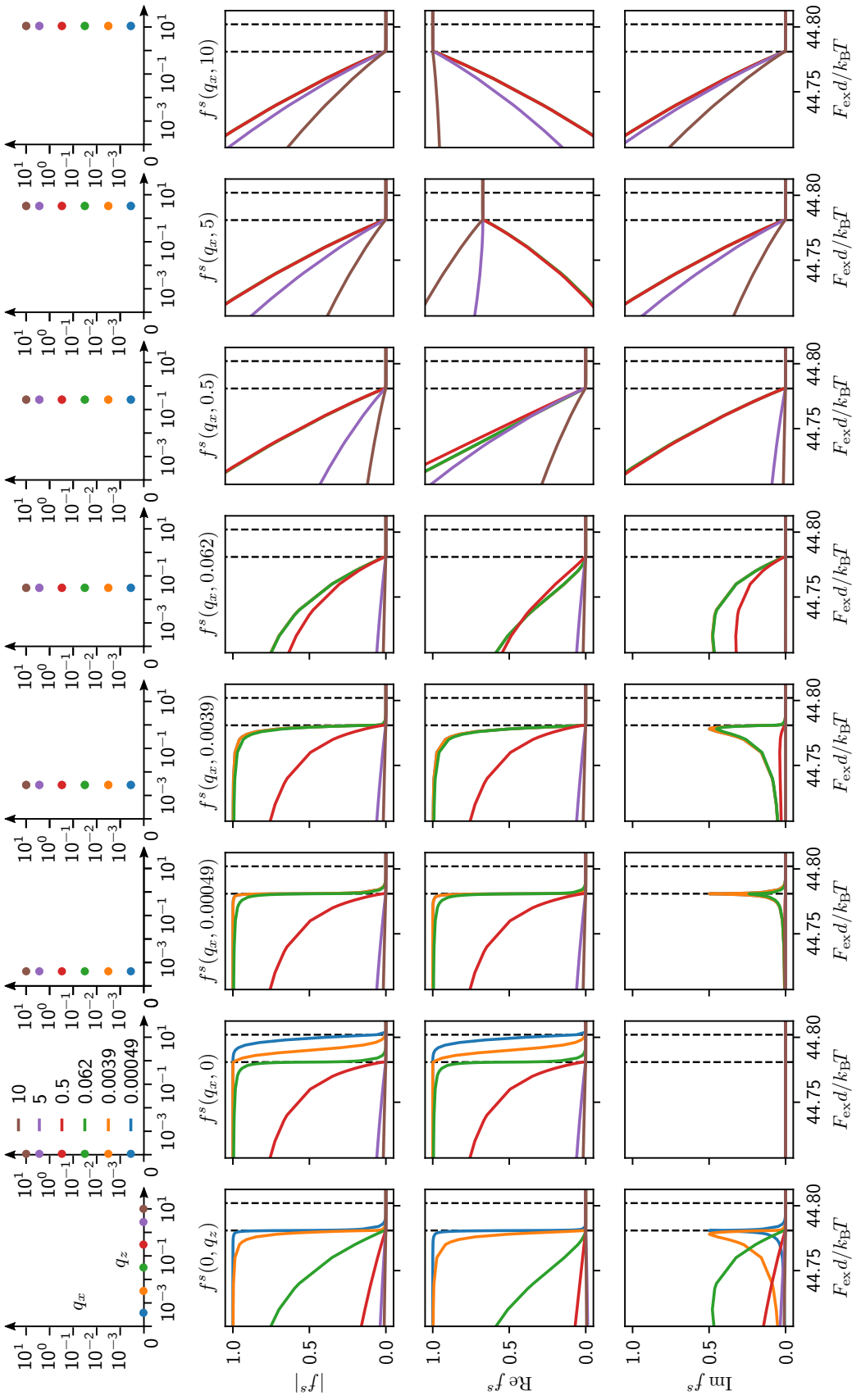

Figure 5.2.: Nonergodicity parameters $f^s_{\boldsymbol{q}^*} = f^s(q_x, q_z)$ as function of the external force for different wave vectors as labeled. The top row sketches the positions of the wave vectors in the (q_x, q_z) plane for the panels below. For the three rightmost columns ($q_z d \geq 0.5$) we zoomed in on the y-axis. The dashed lines indicate the critical forces. The cutoff is $q_{\mathrm{max}} d = 14$, more details can be found in the text.

to classify it as either type A or type B. Therefore, we will look into simple models first, to learn about the possibilities for the bifurcation.

5.3. Models for the bifurcation

In this section, we will explore the transitions of different models for the nonergodicity parameters to shine light on the possible bifurcation types. Since previous theories [Gaz08; Har13] became unphysical before reaching the delocalization transition, there is no prediction or expectation about the type of the transition. It might therefore be instructive to look at simple models so see what can happen. The first schematic model is motivated by the observation, that there are two critical forces, with some glass-glass transition. The harmonically bound particle is analyzed because it successfully reproduced the mean displacements. Finally, we analyze the hopping model with the power laws extracted in Section 4.5.2.

5.3.1. Schematic model for a combined transition

A schematic model for mode-coupling theory replaces the full wave-vector dependence by a few typical wave vectors. The memory functionals are replaced by multivariate polynomials, which take these typical wave vectors as input. For our model, we need at least two typical wave vectors: one in the parallel direction $\phi_\parallel$ and one in the perpendicular one $\phi_\perp$, which show a glass-glass transition. Since the bath correlators only enter as constant prefactors, which do not change with the force, we can ignore them here. Such a model is already among the simplest schematic models, but in a different context [Göt09, p. 232, Fig. 4.4]. The equations of motion are given by

$$\partial_t \phi_i + \int_0^t \mathcal{F}_i[\boldsymbol{\phi}(t')] \partial_t \phi_i(t-t') \mathrm{d}t' \tag{5.16}$$

with $i \in \{\parallel, \perp\}$ and the following memory functionals

$$\mathcal{F}_\parallel[\boldsymbol{x}] = v_\parallel x_\parallel x_\perp, \tag{5.17a}$$

$$\mathcal{F}_\perp[\boldsymbol{x}] = v_1 x_\perp + v_2 (x_\perp)^2. \tag{5.17b}$$

The coefficients $v_\parallel$, v_1 and v_2 are called *coupling coefficients*, because they determine the coupling between the different correlation functions. In the long time limit for the nonergodicity parameters $f_i := \lim_{t\to\infty} \phi_i(t)$ we obtain the following fixed point equations

$$\frac{f_i}{1-f_i} = \mathcal{F}_i[\boldsymbol{f}]. \tag{5.18}$$

This is the F_{12}-model for the perpendicular component and a probe-correlator coupling for the parallel component [Göt09, p. 231]. The F_{12}-model shows a type A glass transition for $v_1 = 1$, $v_2 \in (0,1)$ and a type B glass transition at $v_1 = (2(v_2)^{-1/2} - 1)v_2$, $v_2 \in (1,4)$. Based on v_2, we can therefore choose the type of transition for $\phi_\perp$. We will move through this transition on the following path, parametrized by $\xi \in [0,2]$

$$v_1(\xi) = \begin{cases} 2-\xi, & v_2 < 1, \\ 2-(2-\xi)v_2\left(2(v_2)^{-1/2}-1\right), & v_2 > 1. \end{cases} \tag{5.19}$$

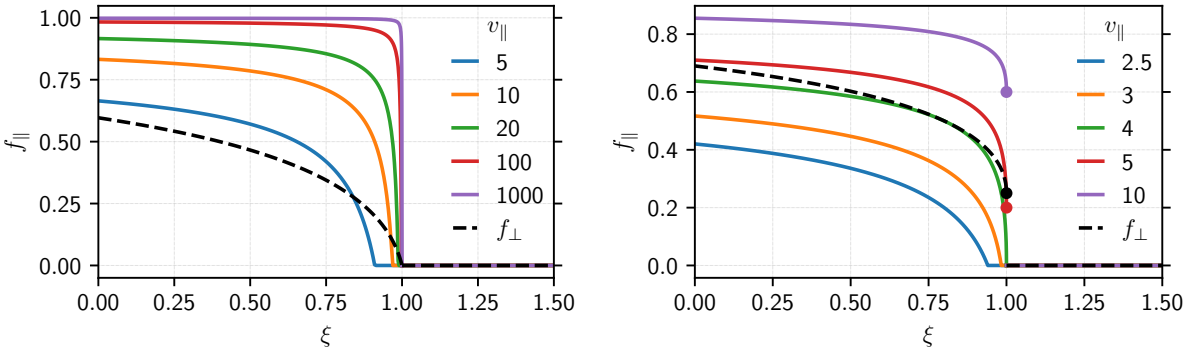

Figure 5.3.: Nonergodicity parameters of the schematic model for $v_2 = 2$ (left) and $v_2 = 16/9$ (right) for different coupling strengths $v_\parallel$. The dashed black line shows $f_\perp$, which is independent of the choice of $v_\parallel$. Discontinuities are shown by circles.

By definition, the solution is nonergodic for $\xi < 1$ and becomes ergodic for $\xi > 1$. Therefore, a "critical force" of this model is $\xi_\perp^c = 1$. The nonergodic solution is given by

$$f_\perp(\xi) = \begin{cases} 0, & \xi > 1, \\ \frac{v_2 - v_1(\xi) \pm \sqrt{(v_2 - v_1(\xi))^2 - 4(1 - v_1(\xi))v_2}}{2v_2}, & \xi \leq 1 \end{cases} \tag{5.20}$$

(cf. [Göt09, p. 226]). With this solution, we can calculate the nonergodicity parameter for the parallel direction by solving (5.18) with (5.17a) for $f_\parallel$

$$f_\parallel(\xi) = \begin{cases} 1 - (v_\parallel f_\perp(\xi))^{-1}, & v_\parallel f_\perp(\xi) \geq 1, \\ 0, & \text{else.} \end{cases} \tag{5.21}$$

(cf. [Göt09, p. 231]). This implies that the critical force for this component is given by the condition $v_\parallel f_\perp(\xi_\parallel^c) = 1$. We can expand $f_\perp(\xi)$ around $\xi = 1$ to analyze the bifurcation of $f_\parallel$.

For $v_2 < 1$, the perpendicular component exhibits a type A bifurcation, i.e. we can expand $f_\perp(\xi_\perp^c + \delta) \approx -h_\perp \delta$ for $\delta < 0$ with some prefactor $h_\perp > 0$. This leads to a critical force $\xi_\parallel^c = 1 - (v_\parallel h_\perp)^{-1}$ for the parallel component. This critical force is smaller than the critical force for the perpendicular component as shown in the left panel of Figure 5.3. For large couplings $v_\parallel$, these two forces agree. This feature is similar to what we find, when extending the logarithmic grid. Since $f_\perp$ is approaching zero continuously, $f_\parallel$ will do the same. Expanding it around $\xi_\parallel^c$, we find $f_\parallel(\xi_\parallel^c + \delta) = -h_\perp \delta$ with $h_\perp = v_\parallel h_\perp$. This implies that the slope of $f_\parallel(\xi)$ becomes steeper and steeper, when approaching its critical force. This feature is observed in our system as well, when we consider the small wave vectors.

For $v_2 > 1$, $f_\perp$ shows a type B bifurcation, i.e. is can be described asymptotically by $f_\perp(1+\delta) \approx f_\perp^c + h_\perp \sqrt{-\delta}$ for $\delta < 0$. The transition type of $f_\parallel$ depends now on the value of $v_\parallel f_\perp^c$. If $v_\parallel f_\perp < 1$, we find a type A behavior with a critical force of $\xi_\parallel^c = 1 - \left((v_\parallel f_\perp^c - 1)/(v_\parallel h_\perp)\right)^2$. For $v_\parallel f_\perp > 1$ both correlators show a type B bifurcation at $\xi_\parallel^c = \xi_\perp^c = 1$. This is illustrated in the right panel of Figure 5.3. The asymptotic behavior is given by $f_\parallel(\delta) = f_\parallel^c + \sqrt{-\delta} h_\perp / v_\parallel f_\perp$. This change from type A to type B upon increasing the coupling, can also be observed in our full system, when we increase the cutoff from $q_{\max} d = 14$ to $q_{\max} d = 20$.

With the model above, we can have combinations of type $A - A$ and $A - B$ and $B - B$ for $f_\parallel$ and $f_\perp$, respectively. We can also construct a $B - A$ transition if we change the memory functional for the parallel correlator to

$$\mathcal{F}_\parallel(\boldsymbol{x}) = x_\parallel + v_\parallel x_\perp(1 + x_\parallel) \tag{5.22}$$

This leads to $f_\parallel = \sqrt{v_\parallel f_\perp/(1 + v_\parallel f_\perp)}$. The critical force here coincides with the critical force $\xi_\perp^c$. This result is nevertheless remarkable, because $f_\parallel$ scales like $\sqrt{-\delta}$ if $f_\perp$ scales like δ close to the transition, but $f_\parallel$ does not exhibit a discontinuity and goes continuously to zero. Therefore it shows features for both bifurcation types, type A and type B. If $f_\perp$ shows a type B transition, then $f_\parallel$ shows a typical type B transition with a jump as well.

These models show that there is a huge variety of bifurcation scenarios. They arise from the fact that the stability matrix is reducible [Göt09, p. 250], i.e. the eigenvalue 0 (or 1 in Götze's definition) in the stability matrix has a multiplicity larger than one [Göt09, p. 242]. They rarely appear in classical mode-coupling theory, because "such a peculiarity must have a special reason like, for example, some symmetry of the microscopic equations of motion" [Göt09, p. 242]. An example is a dumbbell system [Göt09, Sec. 5.3.2, p. 416].

In the models above, there was no coupling of $f_\parallel$ to $f_\perp$. If one extends the model to allow for small couplings as done in by Franosch and Götze, the sharp glass-glass transition is smeared out (cf. [FG94, p. 4811, Fig. 1]). This feature can also explain our observations for $F_{\text{low}} < F_{\text{ex}} < F_{\text{high}}$, where the values for $f^s_{(q_x,q_z)}$ for $q_z > 0$ are small but finite. We will elaborate on this in Section 5.4.

5.3.2. A harmonically bound particle

In Section 4.5.1, we successfully described the mean displacement as function of the external force for various packing fractions using the harmonic trap model from Section 2.3.2 with a force dependent spring constant. We will now analyze if this model can also describe the behavior of the correlation functions close to the critical force.

Recall that the long time limit of the harmonically trapped particle was given by

$$f_q^s = \exp\left(\mathrm{i}q\frac{F_{\text{ex}}}{\kappa} - \frac{q^2}{2\kappa}\right), \tag{5.23}$$

(see (2.43)) with the nondimensional force F_{ex} and the nondimensional spring constant κ. According to (4.12) we model the spring constant as

$$\kappa(F_{\text{ex}}) = \kappa_0\left(1 - \left(\frac{F_{\text{ex}}}{F_{\text{c}}}\right)^\alpha\right) \tag{5.24}$$

with some exponent α and a quiescent spring constant κ_0. The exponent α is 3.5 for our data, but to keep the discussion more general, we allow for arbitrary exponents $\alpha > 0$. F_{c} is the critical force in this system. In our case it is related to the quiescent spring constant via (4.5), $F_{\text{c}} = \sqrt{3\kappa_0}$. Since we are interested in the behavior close to the critical force for a fixed κ_0, its

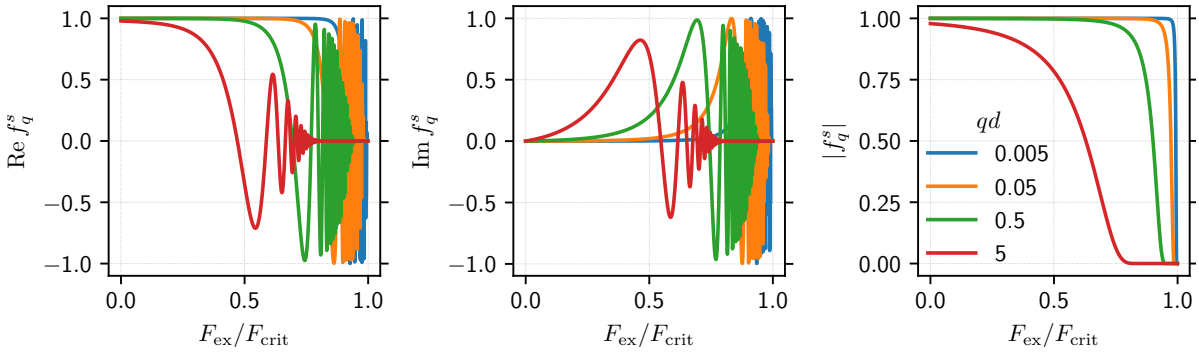

Figure 5.4.: Real part (left), imaginary part (middle) and modulus (right) of the nonergodicity parameters as function of the force for the harmonic spring model described by (5.25) for $\kappa_0 = 580\, k_B T/d^2$, $F_c = \sqrt{3\kappa_0}$, $\alpha = 3.5$.

precise value does not matter and we just keep F_c. Inserting (5.24) into (5.23) we obtain

$$f_q^s(F_{ex}) = \exp\left(-\frac{q(q-2iF_{ex})}{2\kappa_0}\left(1-\left(\frac{F_{ex}}{F_c}\right)^{\alpha}\right)^{-1}\right). \tag{5.25}$$

This function is shown in Figure 5.4 for different wave vectors and the choices $\kappa_0 = 580\, k_B T/d^2$, $F_c = \sqrt{3\kappa_0}$, $\alpha = 3.5$. These values are chosen such that they match the parameters of the MCT calculations in Figure 4.1. For $F_{ex}/F_c \lesssim 0.5$ we find the same qualitative behavior for the model as the MCT results. For example the real part starts close to one and decreases below zero, while large wave vectors decay earlier. The imaginary part starts at zero and the first peak is moving towards the critical force for smaller wave vectors. Closer to the critical force the differences cannot be overlooked. While the simple model shows very strong oscillations, they are not present for the MCT results. Furthermore we notice that the decay of the correlators from close to one to zero happens in a much smaller force range for MCT than for the model.

At first, this result is puzzling, because the model described the mean displacements very well for any force, but now fails to describe the features at large forces. Having a closer look, we find that the modulus $|f_q^s|$ is determined by $\kappa(F_{ex})$ only. The displacement $F/\kappa(F_{ex})$ drops out because it affects only the phase. What is needed instead is an appropriate model for the variance of the distribution, given by $\kappa(F_{ex})$. This implies that a pure force softening of the cage is not a good model system and the softening of the cage should be independent from the growth of the mean displacement.

Nevertheless, we can study the limit $F \to F_c$ of this model. We find $f_q^s \to 0$ continuously for $q \neq 0$, because f_q^s is by definition a smooth function and $\kappa(F_{ex})$ goes continuously to zero. This is an argument for a *type A* transition. However, when expanding $f_q^s(F_{ex})$ around F_c, we find that all derivatives are zero. Consequently, no linear behavior as expected for this type of transition can be found. This function is nonanalytic at the critical force. This finding is true for any $\kappa(F_{ex})$ which decays not faster to zero for $F_{ex} \to F_c$ than a power law.

5.3.3. Hopping model

A model to describe the full wave vector dependency was introduced in Section 4.5.2. There, we have shown that the nonergodicity parameters can be modeled by two relatively simple models for the perpendicular (4.16a) and the parallel direction (4.16b). Furthermore, we have seen that the fit parameters follow power laws close to the critical force. In this section, we will analyze the behavior of the nonergodicity parameter described by these models and their scaling laws.

For the ease of reference, we repeat those models here. For the perpendicular direction, we have

$$f^{\perp}(q,\sigma_{\perp},\ell_{\perp},\alpha_{\perp}) = \left(\frac{\alpha_{\perp}}{1+(\ell_{\perp}q)^2} + (1-\alpha_{\perp})\right) \mathrm{e}^{-\frac{(\sigma_{\perp}q)^2}{2}}, \tag{5.26a}$$

where the parameters follow these power laws

$$\sigma_{\perp}(\delta) \approx \sigma_0, \tag{5.26b}$$
$$\ell_{\perp}(\delta) \approx \ell_0|\delta|^{-\beta_\ell}, \tag{5.26c}$$
$$\alpha_{\perp}(\delta) \approx 1-\alpha_0|\delta|^{\beta_\alpha}, \tag{5.26d}$$

with $\beta_\ell \approx 0.27$ and $\beta_\alpha \approx 0.49$ for the discretization with $q_{\max}d \geq 20$ and $\beta_\ell \approx 0.4$ and $\beta_\alpha \approx 0.8$ for $q_{\max}d \leq 14$. For the parallel direction we have the complex valued model

$$f^{\parallel}(q,\sigma_{\parallel},\ell_{\parallel},\alpha_{\parallel},\mu) = \left(\frac{\alpha_{\parallel}}{1-\mathrm{i}\ell_{\parallel}q} + (1-\alpha_{\parallel})\right) \mathrm{e}^{-\frac{(\sigma_{\parallel}q)^2}{2}+\mathrm{i}\mu q}, \tag{5.27a}$$

where the coefficients follow these power laws

$$\sigma_{\parallel}(\delta) \approx \sigma_0, \tag{5.27b}$$
$$\mu(\delta) \approx \mu_0, \tag{5.27c}$$
$$\ell_{\parallel}(\delta) \approx \ell_0|\delta|^{-\beta_\ell}, \tag{5.27d}$$
$$\alpha_{\parallel}(\delta) \approx 1-\alpha_0|\delta|^{\beta_\alpha}, \tag{5.27e}$$

with $\beta_\ell \approx 0.54$ and $\beta_\alpha \approx 0.48$ for the discretization with $q_{\max}d \geq 20$ and $\beta_\ell \approx 0.8$ and $\beta_\alpha \approx 0.8$ for $q_{\max}d \leq 14$. Note that we have defined the exponents such that their numerical values are positive. Since we will analyze both models separately, we will use the same symbols, even if their values are different.

Inserting the power laws (5.26b)-(5.26d) into the model for the perpendicular direction (5.26a), we find

$$f^{\perp}(q,\delta) = \left(\frac{1}{1+|\delta|^{-2\beta_\ell}(\ell_0 q)^2} + \frac{\alpha_0|\delta|^{\beta\alpha}}{1+|\delta|^{2\beta_\ell}(\ell_0 q)^{-2}}\right) \mathrm{e}^{-\frac{(\sigma_0 q)^2}{2}}. \tag{5.28}$$

As $|\delta|^{-2\beta_\ell}$ diverges for $\delta \to 0$, we find in the limit $|\delta|^{-2\beta_\ell}(\ell_0 q)^2 \gg 1$

$$f^{\perp}(q,\delta) \approx \left(\frac{|\delta|^{2\beta_\ell}}{(\ell_0 q)^2} + \alpha_0|\delta|^{\beta_\alpha}\right) \mathrm{e}^{-\frac{(\sigma_0 q)^2}{2}}. \tag{5.29}$$

Consequently, we get a superposition of two power laws with exponents $2\beta_\ell$ and β_α, which are in this case both approximately 0.5. This would correspond to a type B transition, but without a discontinuity, because the nonergodicity parameters go to zero. This is in line with the finding for the schematic model for a combined transition. For a visual comparison we

show the nonergodicity parameters corresponding to Figure 5.1 in Figure 5.5. Below F_{low} these curves resemble the full solution qualitatively. Due to the model, the second critical force cannot be reproduced, but we can think of it as limiting case, when both critical forces collapse. Quantitatively they also look similar even though the values for large wave vectors are overestimated. For the discretization with $q_{\max}d \leq 14$, we find both exponents to be approximately 0.8, which is right in between 1, the exponent for a type A and 0.5, the exponent for a type B transition.

For the parallel direction, we find after inserting the power laws (5.27b)-(5.27e) for the parameters into the model (5.27a)

$$f^{\parallel}(q,\delta) = \left(\frac{1-\alpha_0|\delta|^{\beta_\alpha}}{1-\mathrm{i}\ell_0 q|\delta|^{\beta_\ell}} + \alpha_0|\delta|^{\beta_\alpha}\right) \mathrm{e}^{-\frac{(\sigma_0 q)^2}{2}+\mathrm{i}\mu_0 q}. \tag{5.30}$$

Separating the fractions into real and imaginary part and using $|\delta|^{-2\beta_\ell}(l_0 q)^2 \gg 1$ as above, we find

$$\begin{aligned} f^{\parallel}(q,\delta) \approx \mathrm{e}^{-\frac{(\sigma_0 q)^2}{2}} &\left(\cos(\mu_0 q)\left(\frac{|\delta|^{2\beta_\ell}}{(\ell_0 q)^2} + \alpha_0|\delta|^{\beta_\alpha}\right) - \frac{\sin(\mu_0 q)}{\ell_0 q}\left(|\delta|^{\beta_\ell} - \alpha_0|\delta|^{\beta_\alpha+\beta_\ell}\right)\right), \\ + \mathrm{i}\mathrm{e}^{-\frac{(\sigma_0 q)^2}{2}} &\left(\frac{\cos(\mu_0 q)}{\ell_0 q}\left(|\delta|^{\beta_\ell} - \alpha_0|\delta|^{\beta_\alpha+\beta_\ell}\right) + \sin(\mu_0 q)\left(\frac{|\delta|^{2\beta_\ell}}{(\ell_0 q)^2} + \alpha_0|\delta|^{\beta_\alpha}\right)\right) \end{aligned} \tag{5.31}$$

where we neglected terms proportional to $|\delta|^{\beta_\alpha+2\beta_\ell}/(\ell_0 q)^2$. In this case, there is a superposition

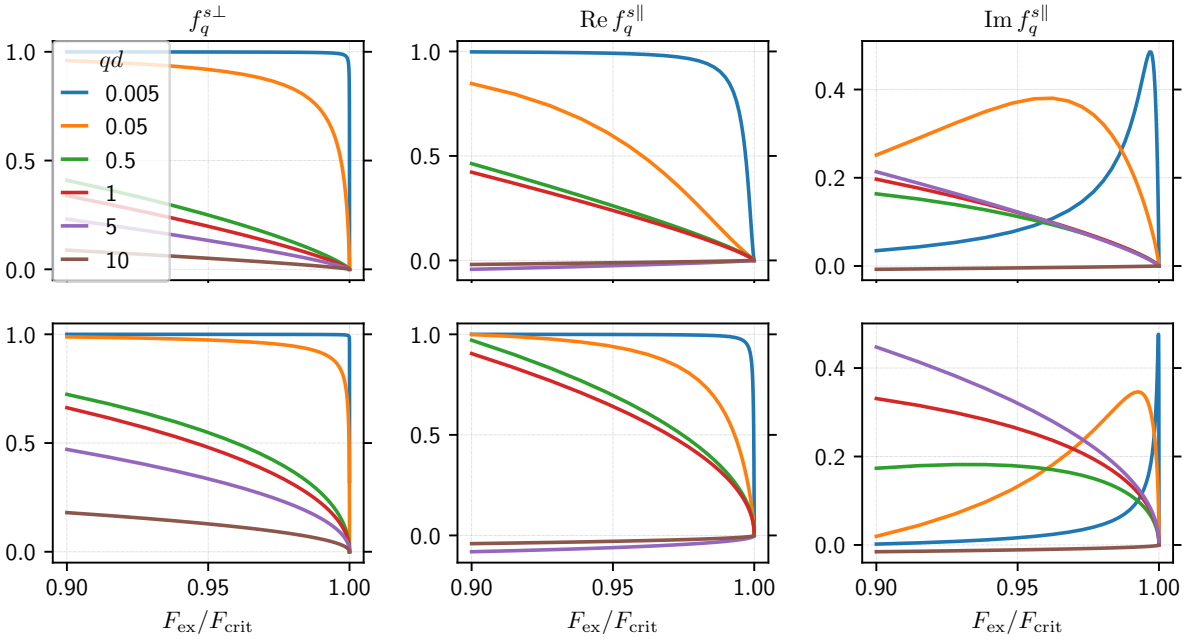

Figure 5.5.: Nonergodicity parameter for the perpendicular direction (left column), real part (center column) and imaginary part (right column) for the parallel direction for the hopping model described by (5.26) and (5.27) with the parameters obtained from the results for $q_{\max}d = 14$ (top row) and $q_{\max}d = 20$ (bottom row) as described in the text. The color code is the same in all panels.

of four different power laws for real and imaginary part, respectively, with the exponents β_ℓ, β_α, $2\beta_\ell$ and $\beta_\alpha + \beta_\ell$. The terms in the last line are negligible for small $|\delta|$. With the numbers from above, we have two distinct exponents, $\beta_\alpha \approx \beta_\ell \approx 0.5$ and $2\beta_\ell \approx \beta_\alpha + \beta_\ell \approx 1$. As $x^{0.5}/x^1 = x^{-0.5} \to \infty$ for $x \to 0$, the contribution associated with the exponent 0.5 will always dominate close to the bifurcation. But it can also be noted that for large wave vectors q (and fixed δ) the term with exponent $\beta_\ell + \beta_\alpha$ becomes more prominent.

Using the values for the grids with $q_{\max} d \leq 14$, we obtain a transition with a critical exponent of 0.8 (and 1.6), which is again in between type A and type B. Even though this power law has also a diverging derivative for $\delta = 0$, it resembles a linear behavior not too close to the transition as can be seen in the top row of Figure 5.5.

5.4. Static bifurcation analysis

The preceding analysis showed that some of the features of our bifurcation can be reproduced by a schematic model with a reducible stability matrix. Therefore, we will analyze the structure of our stability matrix. All physically motivated models from the previous section suggest that there is a continuous transition, i.e. the critical nonergodicity parameter vanishes $f_q^{sc} = 0$. In this case the fraction free stability matrix (5.13) is identically zero, we will first focus on the stability matrix (5.14).

Since we will need to decide which elements of the stability matrix are nonzero, we will repeat the definition of the discrete memory kernels (3.11) from Section 3.2

$$m_{mn}^{\alpha\beta} = \sum_{j=0}^{N_{qz}-1} \sum_{i=0}^{N_{qx}-1} w_j^z w_i^x k_i^x \left(f_{ij}^s J^{\alpha\beta}(k_m^x, k_i^x, k_n^z - k_j^z) + (f_{ij}^s)^* J^{\alpha\beta}(k_m^x, k_i^x, k_n^z + k_j^z) \right). \quad (5.32)$$

The indices m, n, i, j specify the numbers of the discretized wave vectors. The first index corresponds to the x direction, while the second corresponds to the z direction.

The first observation is that all memory functionals are independent of f_{0j}^s, because of the multiplication with the radial prefactor $k_0^x = 0$. This already implies that our stability matrix is reducible, because all derivatives with respect to any f_{0j}^s yield zero identically. This is similar to the scenario in Section 5.3.1, where the parallel component does not couple to the perpendicular component either. In the full model, however, we have to consider also the nonergodicity parameters, which are off-axis. Numerically, we find that they behave like the parallel components, even though they do couple in general to all other nonergodicity parameters. Numerically, we observe that the nonergodicity parameters for $q_z > 0$ almost show a glass-liquid transition at the lower critical force. This resembles the smearing effect of small couplings, studied by Franosch and Götze (cf. [FG94, p. 4811, Fig. 1]). In their spirit, we start by analyzing the couplings for the case $f_{ij}^s = f_i^{s\perp} \delta_{j0}$, i.e., when all nonergodicity parameters with $q_z > 0$ ($j > 0$) are set to zero. This leads to

$$\mu_{mn}^{\alpha\beta} = \sum_{i=0}^{N_{qx}-1} w_0^z w_i^x k_i^x \left((f_i^{s\perp} + (f_i^{s\perp})^*) J^{\alpha\beta}(k_m^x, k_i^x, k_n^z) \right). \quad (5.33)$$

For the perpendicular components, we need to evaluate these memory functions for $n = 0$,

which implies to study $J^{\alpha\beta}(k_m^x, k_i^x, 0)$. Inspecting their definitions (3.9), we find $J^{zz}(q_x, k_x, 0) = J^{xz}(q_x, k_x, 0) = 0$, but

$$J^{xx}(q_x, k_x, 0) = \left(\frac{k_x^2}{2} + q_x^2\right) \int_0^{2\pi} \mathrm{d}\theta \, g\left(\sqrt{q_x^2 + k_x^2 - 2q_x k_x \cos(\theta)}\right), \tag{5.34}$$

which is nonzero as $g(p)$ (as defined in (3.9e)) is always positive. By symmetry, $f_i^{s\perp}$ is real so that we obtain

$$\mu_{m0}^{xx} = 2w_0^z \sum_{i=0}^{N_{qx}-1} w_i^x k_i^x f_i^{s\perp} J^{xx}(k_m^x, k_i^x, 0). \tag{5.35}$$

Note that this memory functional is proportional to the weight w_0^z for the memory integral in z-direction. Its value is given by $w_z^0 = q_1^z/2$, i.e. it is directly proportional to the smallest nonzero wave vector. For the full memory functional, we find then

$$\mathcal{F}_{m0}(\boldsymbol{f}^{s\perp}) = \frac{\mu_{m0}^{xx}(\boldsymbol{f}^{s\perp})}{(k_m^x)^2}. \tag{5.36}$$

This is a linear memory functional, which suggests a type A transition. Interestingly, this memory functional does not depend on the external force anymore. Hence, a coupling to the other wave vectors is necessary to drive it through the bifurcation. If $f^\perp$ was one dimensional with $\mathcal{F}(f^\perp) = af^\perp$ the solution would be $f^\perp = 1 - a^{-1}$ and the bifurcation would happen for $a^{-1} = 1$. It is intriguing that this memory functional is proportional to the smallest nonzero wave vector, as the difference between both critical forces also scales with q_1^z (see Figure 4.4). Hence, we can speculate that this memory functional is the reason for this scaling and we would therefore expect the two critical forces to collapse in the limit of infinitely small grid spacings.

Analyzing the full stability matrix (5.14) for `unilog10` with $q_{\max} d = 20$ with 51 grid points with $F_{\mathrm{ex}} = 42.336\, k_{\mathrm{B}}T/d$ close to F_{low} numerically, we find that the only identically vanishing components are indeed found for $q_x = 0$. However, the absolute values of the other components range from 10^{-19} to 10^6. Nevertheless of those $51 \times 51 = 2601$ variables there are only 16, which have couplings larger than $10^{-4} A_{\max}$ and 93 larger than $10^{-5} A_{\max}$, where $A_{\max}$ is the maximum value of the stability matrix. Hence, the matrix is basically zero. The ten largest entries of the stability matrix are found for $(q_i^x, q_j^z) \in \{(1,0), (2,0), (3,0), (4,0), (5,0), (6,0), (7,0), (0,1), (1,1), (2,1)\}$ (in decreasing order), which are the seven smallest wave vectors along the x axis and adjacent ones. This remains true, when analyzing the stability matrix at F_{high}.

Analyzing the eigenvalues of the reduced stability matrix, we find complex numbers with magnitudes 2.65, 1.16, 0.87 and smaller, which does not fit to the expectation that this stability matrix has an eigenvalue of 1 close to the bifurcation. This might be related to the fact, that we treated the complex correlators as single variables. We can also interpret one complex correlator as two real correlators so that we get twice as many real variables. Splitting the equations is a rather tedious task because of the quotients involved. Rewriting the root problem (5.8) we obtain

$$J_q'^{\mathrm{re}}(F_{\mathrm{ex}}, \boldsymbol{v}^{\mathrm{re}}, \boldsymbol{v}^{\mathrm{im}}) = v_q^{\mathrm{re}} - \frac{a^{\mathrm{re}}(a^{\mathrm{re}} + b^{\mathrm{re}}) + a^{\mathrm{im}}(a^{\mathrm{im}} + b^{\mathrm{im}})}{(a^{\mathrm{re}} + b^{\mathrm{re}})^2 + (a^{\mathrm{im}} + b^{\mathrm{im}})^2}, \tag{5.37a}$$

$$J_q'^{\mathrm{im}}(F_{\mathrm{ex}}, \boldsymbol{v}^{\mathrm{re}}, \boldsymbol{v}^{\mathrm{im}}) = v_q^{\mathrm{im}} - \frac{a^{\mathrm{im}} b^{\mathrm{re}} - a^{\mathrm{re}} b^{\mathrm{im}}}{(a^{\mathrm{re}} + b^{\mathrm{re}})^2 + (a^{\mathrm{im}} + b^{\mathrm{im}})^2}, \tag{5.37b}$$

with $v_q^{\mathrm{re}} := \operatorname{Re} v_q$, $v_q^{\mathrm{im}} = \operatorname{Im} v_q$ and

$$a^{\mathrm{re}} = \operatorname{Re} \boldsymbol{v}^T A_q \boldsymbol{v}, \tag{5.38a}$$
$$b^{\mathrm{re}} = \operatorname{Re} B_q^T(F_{\mathrm{ex}})\boldsymbol{v}, \tag{5.38b}$$
$$a^{\mathrm{im}} = \operatorname{Im} \boldsymbol{v}^T A_q \boldsymbol{v}, \tag{5.38c}$$
$$b^{\mathrm{im}} = \operatorname{Im} B_q^T(F_{\mathrm{ex}})\boldsymbol{v}. \tag{5.38d}$$

The reduced stability matrix then consists of the four blocks

$$\begin{aligned}
\frac{\partial J_q'^{\mathrm{re}}}{\partial v_p^{\mathrm{re/im}}} = c \Bigg(& \left(\frac{\partial a^{\mathrm{re}}}{\partial v_p^{\mathrm{re/im}}}\right) \left(2a^{\mathrm{im}}b^{\mathrm{im}}a^{\mathrm{re}} - (a^{\mathrm{im}})^2 b^{\mathrm{re}} + b^{\mathrm{re}}(a^{\mathrm{re}} + b^{\mathrm{re}})^2 + (b^{\mathrm{im}})^2(2a^{\mathrm{re}} + b^{\mathrm{re}})\right) \\
& + \left(\frac{\partial a^{\mathrm{im}}}{\partial v_p^{\mathrm{re/im}}}\right) \left(b^{\mathrm{im}}((a^{\mathrm{im}})^2 + (b^{\mathrm{im}})^2 - (a^{\mathrm{re}})^2 + (b^{\mathrm{re}})^2) + 2a^{\mathrm{im}}((b^{\mathrm{im}})^2 + b^{\mathrm{re}}(a^{\mathrm{re}} + b^{\mathrm{re}}))\right) \\
& + \left(\frac{\partial b^{\mathrm{re}}}{\partial v_p^{\mathrm{re/im}}}\right) \left(-2a^{\mathrm{im}}b^{\mathrm{im}}b^{\mathrm{re}} - (a^{\mathrm{im}})^2(a^{\mathrm{re}} + 2b^{\mathrm{re}}) - a^{\mathrm{re}}(-(b^{\mathrm{im}})^2 + (a^{\mathrm{re}} + b^{\mathrm{re}})^2)\right) \\
& + \left(\frac{\partial b^{\mathrm{im}}}{\partial v_p^{\mathrm{re/im}}}\right) \left(-(a^{\mathrm{im}})^3 - 2(a^{\mathrm{im}})^2 b^{\mathrm{im}} - 2b^{\mathrm{im}}a^{\mathrm{re}}(a^{\mathrm{re}} + b^{\mathrm{re}}) - a^{\mathrm{im}}((b^{\mathrm{im}})^2 + (a^{\mathrm{re}})^2 - (b^{\mathrm{re}})^2)\right) \Bigg)
\end{aligned} \tag{5.39}$$

$$\begin{aligned}
\frac{\partial J_q'^{\mathrm{im}}}{\partial v_p^{\mathrm{re/im}}} = c \Bigg(& \left(\frac{\partial a^{\mathrm{re}}}{\partial v_p^{\mathrm{re/im}}}\right) \left(b^{\mathrm{im}}((a^{\mathrm{re}})^2 - (a^{\mathrm{im}})^2 - (b^{\mathrm{im}})^2 - (b^{\mathrm{re}})^2) - 2a^{\mathrm{im}}((b^{\mathrm{im}})^2 + b^{\mathrm{re}}(a^{\mathrm{re}} + b^{\mathrm{re}}))\right) \\
& + \left(\frac{\partial a^{\mathrm{im}}}{\partial v_p^{\mathrm{re/im}}}\right) \left(2a^{\mathrm{im}}b^{\mathrm{im}}a^{\mathrm{re}} - (a^{\mathrm{im}})^2 b^{\mathrm{re}} + b^{\mathrm{re}}(a^{\mathrm{re}} + b^{\mathrm{re}})^2 + (b^{\mathrm{im}})^2(2a^{\mathrm{re}} + b^{\mathrm{re}})\right) \\
& + \left(\frac{\partial b^{\mathrm{re}}}{\partial v_p^{\mathrm{re/im}}}\right) \left((a^{\mathrm{im}})^3 + 2(a^{\mathrm{im}})^2 b^{\mathrm{im}} + 2b^{\mathrm{im}}a^{\mathrm{re}}(a^{\mathrm{re}} + b^{\mathrm{re}}) + a^{\mathrm{im}}((b^{\mathrm{im}})^2 + (a^{\mathrm{re}})^2 - (b^{\mathrm{re}})^2)\right) \\
& + \left(\frac{\partial b^{\mathrm{im}}}{\partial v_p^{\mathrm{re/im}}}\right) \left(-2a^{\mathrm{im}}b^{\mathrm{im}}b^{\mathrm{re}} - (a^{\mathrm{im}})^2(a^{\mathrm{re}} + 2b^{\mathrm{re}}) - a^{\mathrm{re}}(-(b^{\mathrm{im}})^2 + (a^{\mathrm{re}} + b^{\mathrm{re}})^2)\right) \Bigg)
\end{aligned} \tag{5.40}$$

with $c = ((a^{\mathrm{re}})^2 + (a^{\mathrm{im}})^2 + (b^{\mathrm{re}})^2 + (b^{\mathrm{im}})^2)^{-2}$. After calculating the derivatives of $a^{\mathrm{re}}, a^{\mathrm{im}}, b^{\mathrm{re}}, b^{\mathrm{im}}$ with respect to the variables v_p^{re} and v_p^{im}, we are ready to construct the stability matrix as

$$S(F_{\mathrm{ex}}, \boldsymbol{v}^{\mathrm{re}}, \boldsymbol{v}^{\mathrm{im}}) = \mathbb{1} - \begin{pmatrix} \frac{\partial J_q'^{\mathrm{re}}(\boldsymbol{v}^{\mathrm{re}}, \boldsymbol{v}^{\mathrm{im}})}{\partial v_p^{\mathrm{re}}} & \frac{\partial J_q'^{\mathrm{im}}(\boldsymbol{v}^{\mathrm{re}}, \boldsymbol{v}^{\mathrm{im}})}{\partial v_p^{\mathrm{re}}} \\ \frac{\partial J_q'^{\mathrm{re}}(\boldsymbol{v}^{\mathrm{re}}, \boldsymbol{v}^{\mathrm{im}})}{\partial v_p^{\mathrm{im}}} & \frac{\partial J_q'^{\mathrm{im}}(\boldsymbol{v}^{\mathrm{re}}, \boldsymbol{v}^{\mathrm{im}})}{\partial v_p^{\mathrm{im}}} \end{pmatrix}. \tag{5.41}$$

Since a and b are holomorphic functions, there hold the Cauchy-Riemann differential equations as long as $\boldsymbol{v} \neq 0$

$$\frac{\partial J_q'^{\mathrm{re}}}{\partial v_p^{\mathrm{re}}} = \frac{\partial J_q'^{\mathrm{im}}}{\partial v_p^{\mathrm{im}}} \qquad \text{and} \qquad \frac{\partial J_q'^{\mathrm{re}}}{\partial v_p^{\mathrm{im}}} = -\frac{\partial J_q'^{\mathrm{im}}}{\partial v_p^{\mathrm{re}}}. \tag{5.42}$$

Evaluating this matrix confirms that still no couplings for the real and imaginary part of the $f^{s\parallel}$ component to the others. Furthermore, there is also no coupling for the imaginary

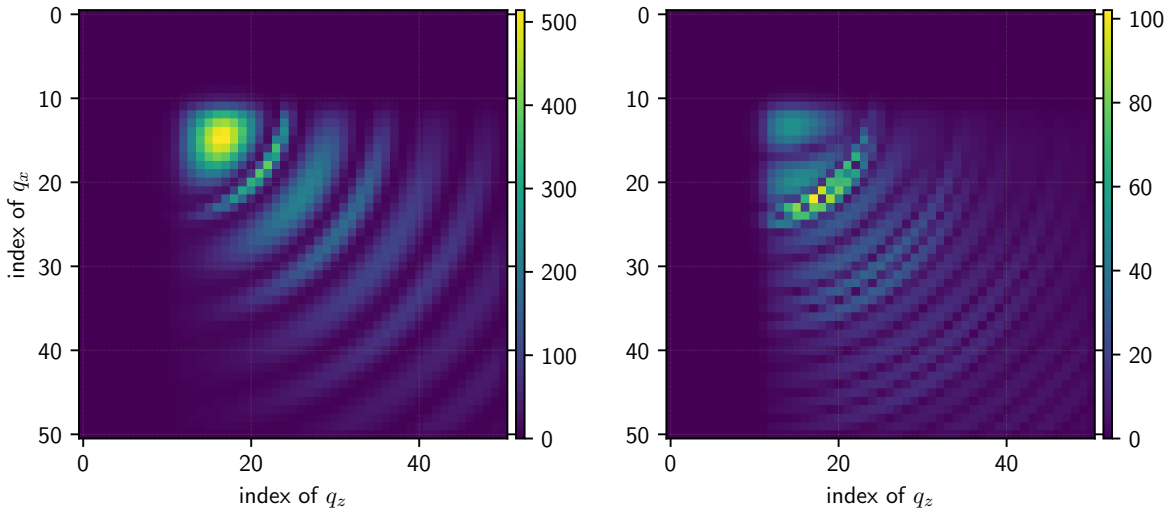

Figure 5.6.: Coupling strength $s_q = \sum_p |S_{pq} - \delta_{pq}|$ for $F_{\mathrm{ex}} = 42.336\, k_{\mathrm{B}}T/d$ (close to but below F_{low}) for `unilog10` with $q_{\max}d = 20$ and 51 grid points. The indexes 1-11 are part of the logarithmic grid. Left: couplings to v_q^{re}. Right: couplings to v_q^{im}.

part in the perpendicular direction. This is not surprising, because it is always zero due to symmetry. All other components are in general nonzero with values ranging from 10^{-20} to 10^{1}. Cutting at a value of 10^{-4} retains 3786 nonzero couplings (of 5202 variables). Hence, this stability matrix is much denser than its complex counterpart. Weak couplings are found in the logarithmic part of the grid, i.e. for small wave vectors close to the axes. It should be noted that the coupling close to the x-axis (i.e. small q_z) is much stronger than close to the z-axis (i.e. small q_x). Looking at the coupling strength defined as sum over the rows of the reduced stability matrix,

$$s_q := \sum_p |S_{pq} - \delta_{pq}| \tag{5.43}$$

we find the strongest coupling for the real parts around $(q_x d, q_z d) = (2, 3)$ and in shells around the origins with radii $qd = 7.2, 10, 13, 16, 20, 22$ as shown in Figure 5.6. For the imaginary part the maximum coupling strength occurs on a shell with radius $qd = 7$ and on shells with radius $qd = 9, 11, 13, 14, 15, 17$. There is also a larger coupling strength for $(q_r d, q_z d) = (2, 2)$ and $(q_r d, q_z d) = (5, 2)$ with a minimum in between.

The summation over the columns of the reduced stability matrix can be a measure for the impact of the corresponding variable on the result. We find that the most relevant variables in this sense are all located in the logarithmic part of the grid. For the real part the nonergodicity parameters with $q_z d = 7.8 \cdot 10^{-3}$ and $q_r d \leq 0.5$ as well as with $q_r d = 0.25$ and $q_z d \leq 7.8 \cdot 10^{-3}$ are most relevant. For the imaginary part it is all nonergodicity parameters with $q_z d \in [1 \cdot 10^{-3}, 6.3 \cdot 10^{-2}]$ and $q_r d \leq 0.25$ except the line with $q_z d = 7.8 \cdot 10^{-3}$. Hence, the structure of the stability matrix is highly nontrivial and could prove difficult to construct a schematic model with important wave vectors only. Above F_{low}, the coupling strength does not change, while the impact reduces to a single point $(q_x d, q_z d) = (3.1 \cdot 10^{-2}, 0)$ for the real parts and the line $q_r d \leq 6.3 \cdot 10^{-2}$, $q_z d = 5 \cdot 10^{-4}$.

The largest eigenvalues of this reduced stability matrix are real and given by 0.999 974 322

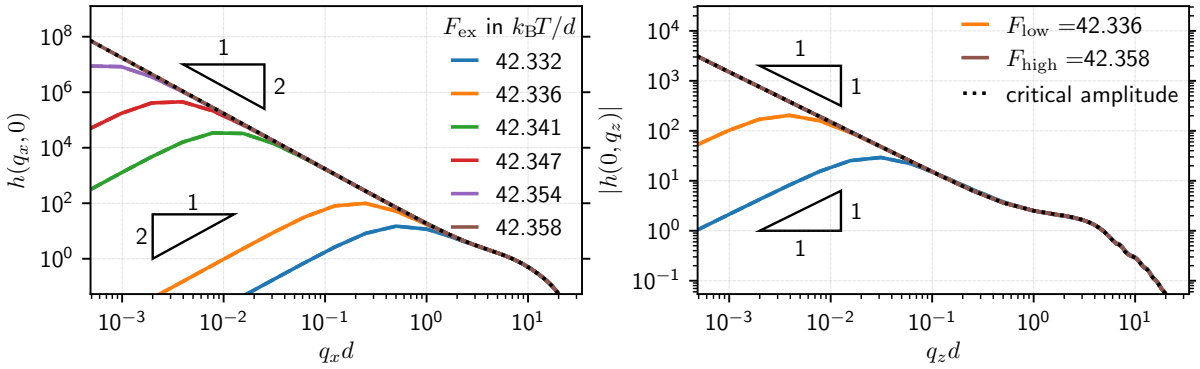

Figure 5.7.: Eigenvector of the reduced stability matrix for the largest eigenvalue for different forces. The dashed line shows the critical amplitude obtained from (5.45). Left: real part components of the eigenvectors perpendicular to the force direction. Since this component is real and positive, this equals also the modulus of this component. Right: modulus of the components of the eigenvectors parallel to the force direction. The color code is the same for both panels and the critical force values are shown in the right panel. The results were obtained for the grid `unilog10` with $q_{\max} d = 20$ and 51 grid points.

and 0.680 927 32. The largest eigenvector is very close to 1 as expected for a bifurcation. Hence, this is the appropriate stability matrix. We also note that this eigenvalue has multiplicity 1. The value of this largest eigenvalue coincides with the value of the contraction factor determined by the iteration. The eigenvector for this largest eigenvalue is also called the *critical amplitude* $\boldsymbol{h} = (h_q)_q$ and it determines in classical mode-coupling theory the wave vector dependency of the nonergodicity parameters close to the critical point via

$$f_q - f_q^c = h_q g(\delta) \tag{5.44}$$

[Göt09, p. 239, Eq. (4.78a)], where $g(\delta)$ describes the scaling behavior close to the critical force depending on the type of the transition: $g(\delta) \propto \sqrt{|\delta|}$ for a type B transition [Göt09, p. 245, Eq. (4.91a)] and $g(\delta) \propto \delta$ for a type A transition [Göt09, p. 248, Eq. (4.98)]. Since eigenvectors are only unique up to a scalar multiple, some normalization condition has to be obeyed to fix the amplitude of the scaling law (5.44).

In the case of vanishing nonergodicity parameters at the critical point, it is also possible to evaluate the eigenvector to the largest eigenvalue of the reduced stability matrix directly from the fixed point iteration scheme. Using (5.44) with $f_q^c = 0$ in the iteration equation (5.8) and dividing by $g(\delta)$ we find in the limit $g(\delta) \to 0$

$$h_q = \frac{a^{\mathrm{re}}(\boldsymbol{h}) b^{\mathrm{re}}(\boldsymbol{h}) - a^{\mathrm{im}}(\boldsymbol{h}) b^{\mathrm{im}}(\boldsymbol{h}) + \mathrm{i}\left(a^{\mathrm{im}}(\boldsymbol{h}) b^{\mathrm{re}}(\boldsymbol{h}) - a^{\mathrm{re}}(\boldsymbol{h}) b^{\mathrm{im}}(\boldsymbol{h})\right)}{(b^{\mathrm{re}}(\boldsymbol{h}))^2 + (b^{\mathrm{im}}(\boldsymbol{h}))^2}. \tag{5.45}$$

This is a fixed point iteration for the critical amplitude. Since this equation is scale free, meaning that any multiple of a solution $\boldsymbol{h}$ is again a solution, we have to normalize $\boldsymbol{h}$ after each iteration. This is a general method to obtain the largest eigenvalues and the corresponding eigenvector, called *power iteration method* [Boo06]. It also has the potential to be used as fast iteration scheme to determine the critical force (probably F_{high} only) as it also provides the eigenvalue, which is exactly one at the critical force.

As the former derivation of the critical amplitude h_q relies on the validity of the stability analysis of the classical MCT as well as on the fact that the critical nonergodicity parameters vanish, we will compare the different approaches for the critical amplitude in the following. We normalize the eigenvectors such that the value at the position of the first peak of the structure factor in the perpendicular direction is one, i.e. we require the normalization condition $h_{q_s} = 1$ with $q_s d = (7, 0)$. For the critical amplitude obtained by (5.45) the force enters only through the coefficients for $B_q^T(F_{\mathrm{ex}})$. Since the difference between F_{low} and F_{high} is very small, the critical amplitude is basically the same for both cases. For the determination of the eigenvalues and vectors from the stability matrix, the strongly force dependent nonergodicity parameters will enter the calculation. Therefore, the eigenvectors will also be strongly force dependent. This is shown in Figure 5.7. Since the critical amplitude has the same dimensionality as the nonergodicity parameters, we only show the values along the axes. We find that the components of the eigenvectors for large wave vectors are force independent and coincide with the result from (5.45) (shown as dashed black line). The agreement holds for $q_z d \geq 10^{-1}$ for the parallel component and for $q_x d \geq 1$ for the perpendicular component for the forces shown. For smaller wave vectors the critical amplitude depends on the force. Below F_{low} the modulus of the parallel component scales like $(qd)^1$ for small wave vectors. Above F_{low} this behavior disappears and we find agreement with the critical amplitude from the iteration, which scales like $(q_z d)^{-1}$. For the perpendicular direction we find a $(q_z d)^2$ scaling for small wave vectors below F_{low}, but also below F_{high}. It will only follow the critical amplitude from the iteration for all wave vectors for forces equal to and above F_{high}. This critical amplitude scales like $(q_x d)^{-2}$ for small wave vectors.

To summarise, the parallel component of the eigenvectors of the stability matrix follow the critical amplitude at F_{low} and above, while the perpendicular component follows the critical amplitude for F_{high} only. This behavior can not only be found for the grid with $q_{\max} d = 20$, but also for the grid $q_{\max} d = 14$, which could allow to characterize the two different critical forces other than through their contraction factors only. This comparison also shows that the critical amplitude is well defined for large wave vectors, while strong variations can be found for small wave vectors. We also note that any normalization which incorporates all elements of the eigenvector (such as taking the Euclidean norm) will cause the large wave vectors to vanish because of the divergence for small wave vectors in both parallel and perpendicular direction. The scaling of the nonergodicity parameters as function of the relative distance to the critical force with the prefactor determined by the critical amplitude will be tested in comparison with the experimens in Section 5.9 and Figure 5.17.

5.5. Static scaling laws

In this section, we will analyze the scaling of the moments and the corresponding friction and diffusion coefficients close to the critical force. The scaling parameter is the relative distance to the critical force $\delta = (F - F_c)/F_c$, which is negative below and positive above the critical force. So far it remains unclear which of our critical forces is the appropriate critical force for this scaling.

We will start with the case $\delta < 0$, analyzing the moments of the nonergodicity parameters. Remember that we have two methods available for their calculation: the memory integral (2.187) (referred to as *memory*) and the finite difference method (3.52) (referred to as *diff*).

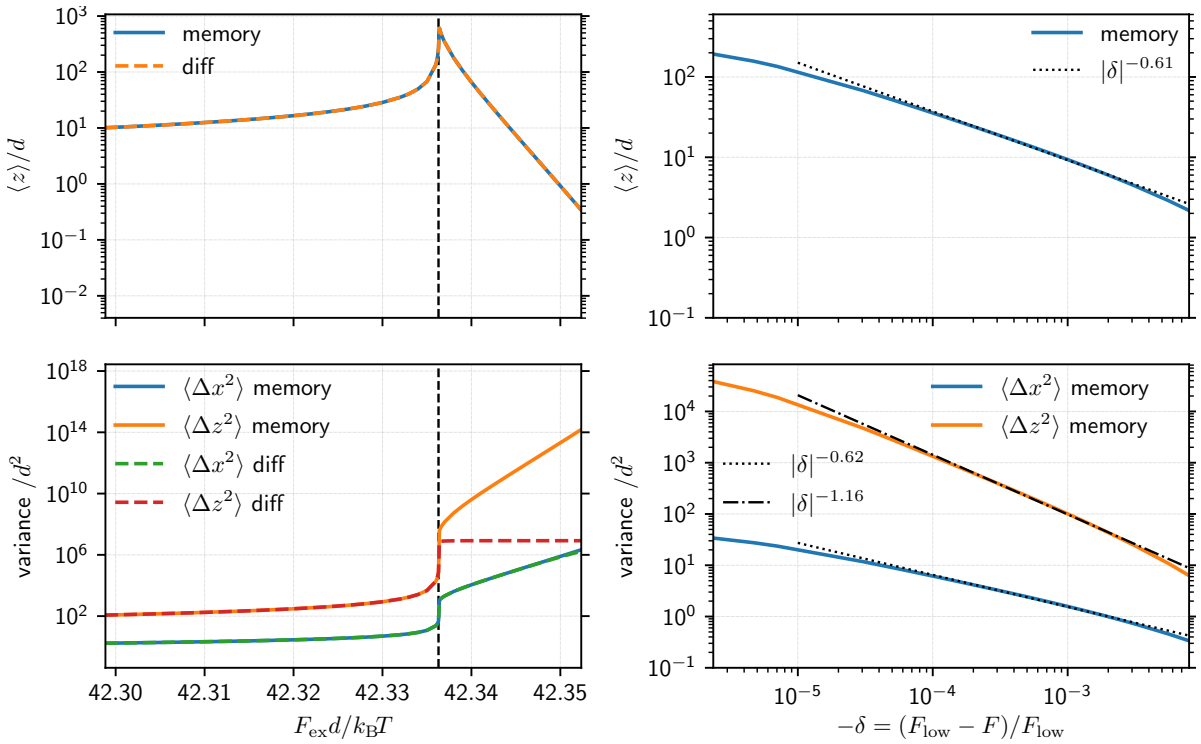

Figure 5.8.: Variation of the first and second moments close to the critical force on a `unilog10`-grid with $q_{\max} d = 20$. Solid lines show the moments obtained by the memory integral (2.187), while dashed lines show the result for the finite difference method (3.52). The right column shows the same moments over the relative distance to the lower critical force F_{low}.

We have already shown that they agree for small and moderate forces. In Figure 5.8 we show the mean displacement and the variances for both methods for forces crossing the critical force values. For the mean displacement both methods agree for all forces. The mean displacement increases up to the F_{low}, before it decreases again, reaching values of 10^{-7} at F_{high}. The behavior above F_{low} is clearly unphysical as there is no reason for the particles to move less with larger forces. Approaching the F_{low} becomes quite large. To visualize this, we show the mean displacement over the relative distance to the critical force in a log-log plot (top right panel). We find a power law with exponent -0.61, which holds over one decade but flattens for $-\delta \to 0$. This can be an effect of the theory, but it can also be an artifact since we know the critical force only to a finite precision.

For the variances in the bottom row of Figure 5.8 we find agreement of both methods for forces below F_{low}. For larger forces, the variance obtained by the finite difference method saturates. This is easy to understand, because the enumerator in our finite difference quotient is bounded by 1 and the denominator is given by $(q_1^x)^{-1}$, which yields the maximum variance. This effect can also be observed for the variance in the perpendicular direction just before the strong increase at F_{high}. Therefore, it is advisable to use the memory integral method when the variances are expected to become very large. For the variances there is a strong increase at the first critical force as well as for the second critical force. But since the mean displacement is unphysical above F_{low}, we will also analyze its scaling only with respect to the

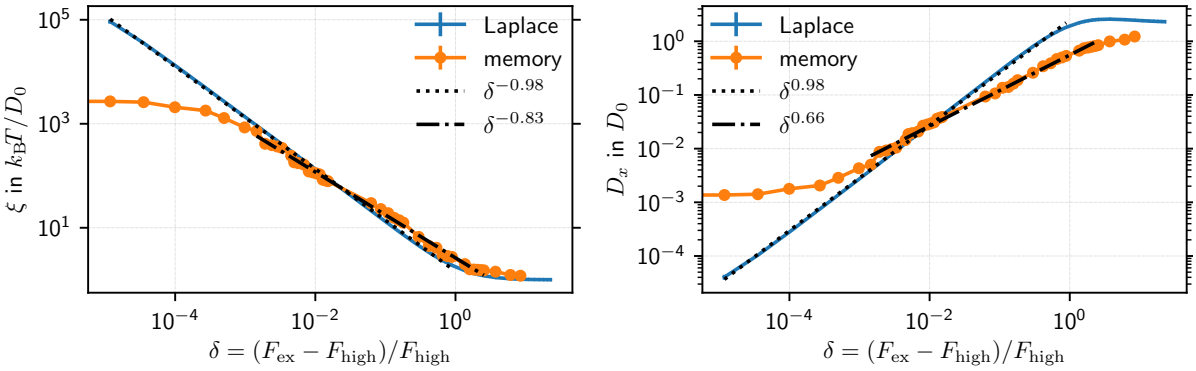

Figure 5.9.: Friction coefficient ξ (left) and perpendicular diffusion coefficient D_x (right) close to the critical force in the constant bath approximation. These coefficients were determined using the Laplace method (blue) and the memory method (orange)as introduced in Section 4.5.1. Errorbars denote the uncertainties about the values as introduced in the text, but are smaller than the symbol sizes. The results are shown for the `unilog10`-grid with $q_{\max}d = 20$.

lower critical force. We find that the variance perpendicular to the force direction increases with an exponent -0.62 similarly to the mean displacement. There is again deviations for very small relative distances. The variance parallel to the force direction increases with an exponent -1.16, which is approximately twice as large as the other exponents. This agrees with the findings of Section 4.5.3, where we fitted a model to the van Hove functions. These numbers apply to the grid with $q_{\max}d = 20$. Choosing the cutoff $q_{\max}d = 14$, we obtain the exponents -0.91, -0.93 and -1.78 for the mean displacement, the variance perpendicular and the variance parallel to the force direction, respectively. This power law is valid for $-\delta \in [10^{-4}, 10^{-2}]$, but the flattening for $-\delta < 10^{-5}$ is more pronounced. The other features are the same.

Above the critical force, the long time limit of the moments diverges (unless they are zero by symmetry). What remains typically finite is the velocity and the diffusion coefficients, which characterize the linear divergence of the first and second moments. Instead of the velocity v one can also consider the friction coefficient $\xi = F_{ex}/v$, which would be the fluid equivalent of the spring constant in a solid as analyzed in Section 4.4. Their long-time limits can be directly calculated in the constant bath approximation as introduced in Section 2.4.9 in (2.190), (2.192) and (2.196) and elaborated in Section 4.5.1, where also the details for the calculation can be found. In Figure 5.9 we show the data from Figure 4.21 as function of the relative distance to F_{high}. Since the expression for the variance in force direction is only approximate and yields very different results, we will focus on the diffusion coefficient in the perpendicular direction only. We employ the Laplace space result and compare also to the long time limit of the solution in time space using the memory method as introduced in Section 4.5.1, where we also define the measures for the uncertainties. The friction coefficient obtained from the Laplace space solution shows little uncertainties and a nice power law with exponent -0.98. For the diffusion coefficient D_x we have little uncertainties as well and again a power law, which extends from $\delta = 10^{-5}$ to almost $\delta = 10^{0}$ with an exponent of 0.98. Again, the power law exponents associated with the first moment in force direction and the second moment perpendicular to the force direction are the same. Note that we have defined the relative distance δ with respect to F_{high}.

Using the memory method these relations are modified. First of all, we note that there is a saturation for the friction and the diffusion coefficient for small relative distances. This is related to the fact that the memory method considers large, but not infinite times, which leads to a underestimation of the friction coefficient and an overestimation of the diffusion coefficient as discussed in Section 4.5.1. Nevertheless, there is a power law behavior for $\delta \in [10^{-3}, 10^{0}]$ with an exponent of -0.83 for the friction coefficient and an exponent 0.66 for the diffusion coefficient. In this case, the exponent for the friction coefficient is not simply the negative of the exponent for the diffusion coefficient. The reason for this modification remains unclear, even though we can speculate that it is associated with the break down of the numerics of the time dependent solution for large times.

Doing the analysis for the discretization with $q_{\max}d = 14$ yields the same qualitative behavior, but slightly different exponents: -1.04 and 1.04 for the friction and diffusion coefficient obtained by the Laplace method and -0.90 and 0.86 for the memory method. In this case we did only fit data with $\delta \in [2 \cdot 10^{-3}, 3 \cdot 10^{-2}]$, because we have not calculated larger forces. This might explain, why those results show less spread. These exponents seem to be less affected by the change of cutoff than the exponents below the bifurcation.

Finally, we analyze the behavior of the nonergodicity parameters themselves at the lower critical force. Since some nonergodicity parameters remain finite at this transition, we subtract the values of the critical nonergodicity parameters $f^{s\perp,c}$ and $f_q^{s\parallel,c}$ at F_{low}. As we do not now the critical value exactly, this leads to errors very close to the critical force. Therefore, we show only relative forces, which are one magnitude larger than the smallest available. For the grid with cutoff $q_{\max}d = 20$ we find for many wave vectors a scaling which is close to $\sqrt{-\delta}$ as can be seen in the top row of Figure 5.10. It appears for all large wave vectors ($qd \geq 1$). However, the nonergodicity parameters at small wave vectors remain constant for $-\delta \geq 10^{-4}$ and then start to decrease. With our data it is not possible to decide whether they will eventually follow the same power law.

For the grid with cutoff $q_{\max}d = 14$ we find a scaling of the nonergodicity parameters which is close to $(-\delta)^1$ as shown in the bottom row of Figure 5.10. Again, this scaling can be observed for all wave vectors in the parallel direction, but the lowest and for the large wave vectors ($qd \geq 0.5$) in the perpendicular direction. The nonergodicity parameters at the smallest wave vectors in the perpendicular direction again behave roughly constant. A close look reveals that the power law is slightly smaller than linear, $|\delta|^{-0.9}$. This does not fit to any of the classical MCT bifurcations, but it is similar to what we obtained for the corresponding hopping model at the end of Section 5.3.3. The reason for this remains unclear, but we can rule out that it is due to an insufficient number of iterations. Those errors only play a role, when we are even closer to the critical force.

To summarize the static analysis, our model exhibits technically two bifurcations. At the first one, all correlation functions with $q_z d > 0$ become very small, at the second all correlation functions disappear completely. Power laws for the moments, transport coefficients and nonergodicity parameters can be found when approaching the critical force F_{low} from below and F_{high} from above. In between we observe unphysical behavior of the mean displacement. In Figure 4.4b we showed that these two bifurcations converge to the same value in the limit of infinitely small step sizes. For this reason, we can ignore the results in between these two critical forces. However, it remains unclear how the combined (higher order) bifurcation looks like. On top of that we find that the power laws (below F_{low}) differ between systems with a

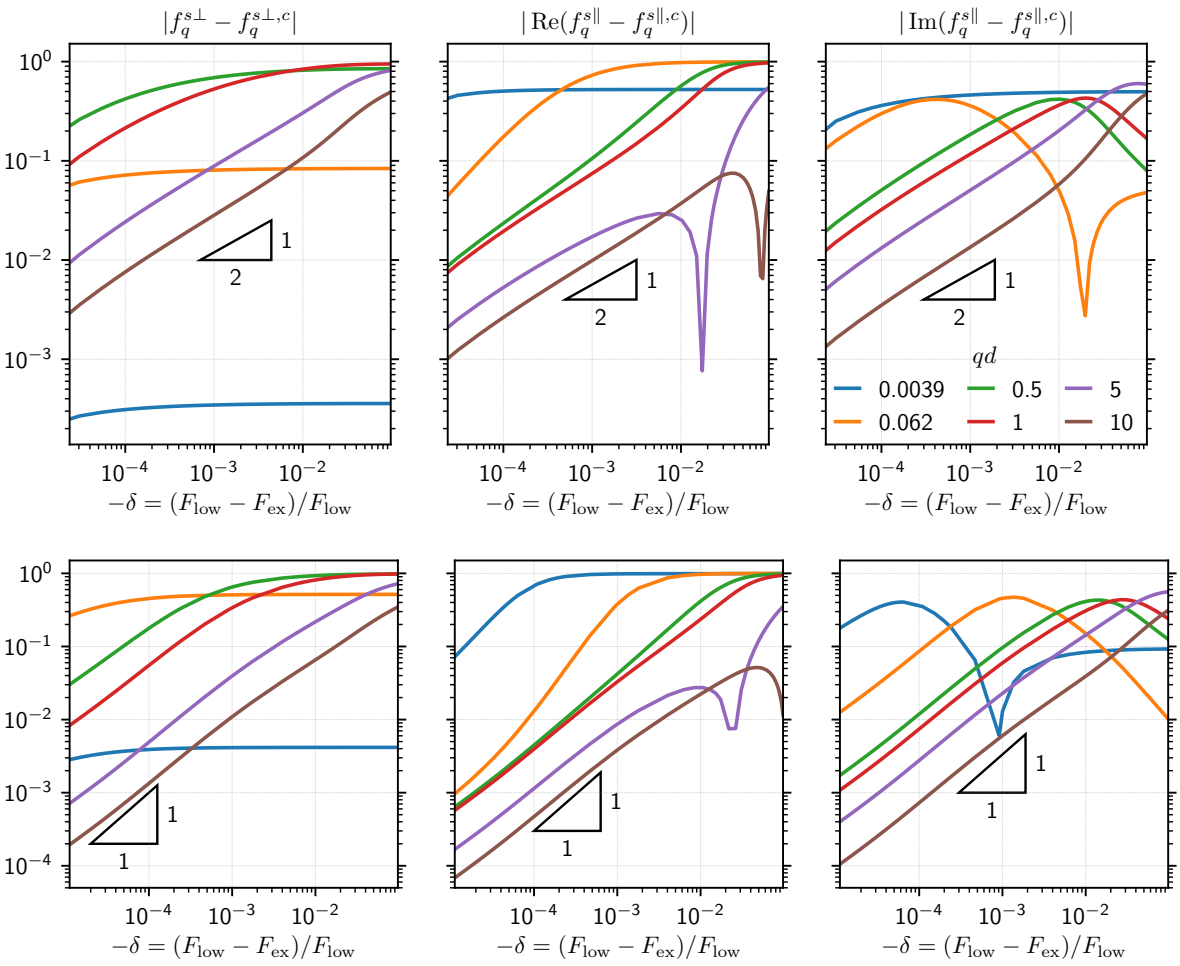

Figure 5.10.: Scaling of the nonergodicity parameters close to F_{low} for different wave vectors as labeled. The values of the nonergodicity parameter at the critical force are subtracted. Left column: nonergodicity parameter perpendicular to the force. Center column: real part of the nonergodicity parameter parallel to the force. Right column: imaginary part of the nonergodicity parameter parallel to the force. Top row: for the grid `unilog10` with $q_{\max}d = 20$. Bottom row: for the grid `unilog10` with $q_{\max}d = 14$.

cutoff $q_{\max}d \leq 14$ from those with a cutoff $q_{\max}d \geq 20$. While the former resembles a type A bifurcation with a linear scaling of the nonergodicity parameters, the latter resembles a type B bifurcation with a square root scaling.

5.6. Dynamic bifurcation analysis: beta-scaling

In the following, we will give an analytical reasoning for the critical law of the dynamics of the correlation function. We will first follow the procedures outlined in [Göt09, Chapter 6, p. 437], even though it is based on the classical real-valued MCT equations and on the assumption that the critical point is an A_2 bifurcation singularity [Göt09, p. 438]. From the analysis in the previous section, it remained unclear whether the nonergodicity parameters are zero or just

very small at the bifurcation(s). To cover both cases, we separate the critical nonergodicity parameter via

$$\phi_q^s(t) = f_q^{sc} + g_q(t), \tag{5.46}$$

f_q^{sc} is the solution of the fixed point equation (5.8) at the critical force. $g_q(t)$ is the small parameter for which the expansion will be done. With the S-transform as introduced in (5.4) this translates directly to

$$\hat{\phi}_q^s(s) = f_q^{sc} + \hat{g}_q(s). \tag{5.47}$$

(cf. [Göt09, p. 439, Eq. (6.1b)], but mind the different normalization of $\hat{g}$). The next step is to rewrite the equation of motion (5.6) in terms of $\hat{g}_q$. Since the conventional mode-coupling theory deals with polynomials only, there are now two options: We can proceed with the quotient in (5.6) and try to expand the resulting equations, or we can multiply this equation with the denominator and analyze the fraction free case as already done for the stability matrix. We will follow both approaches in the following two sections.

5.6.1. Asymptotic analysis for the quotient representation

In this section, we use the equations of motion as stated in (5.6). We have to rewrite this equation in terms of $\hat{g}_q$. For the left hand side, we use the identity

$$\frac{\hat{\phi}_q^s(s)}{1-\hat{\phi}_q^s(s)} = \frac{f_q^{sc}}{1-f_q^{sc}} + \frac{1}{1-f_q^{sc}} \frac{\hat{g}_q(s)}{(1-f_q^{sc}) - \hat{g}_q(s)} = \frac{f_q^{sc}}{1-f_q^{sc}} + \frac{\hat{g}_q(s)}{(1-f^{sc})^2} + \sum_{n=2}^{\infty} \frac{(\hat{g}_q(s))^n}{(1-f_q^{sc})^{n+1}}. \tag{5.48}$$

The right hand side requires a two-fold expansion: around the critical force F_c with $F_\mathrm{ex} = F_\mathrm{c}(1+\delta)$ and for long times, i.e. around $s = 0$. In analogy to the static bifurcation analysis, we introduce the following shorthands

$$(A_q^{(1)})^T \boldsymbol{v} = \mu_q^{xx}(\boldsymbol{v}) + \mu_q^{zz}(\boldsymbol{v}), \tag{5.49a}$$
$$(B_q^c)^T \boldsymbol{v} = \Gamma_q^x \mu_q^{zz}(\boldsymbol{v}) + \Gamma^{z,c} \mu_q^{xx}(\boldsymbol{v}) - \Gamma_q^{xz,c} \mu_q^{xz}(\boldsymbol{v}), \tag{5.49b}$$
$$(B_q^d)^T \boldsymbol{v} = \Gamma_q^{z,d} \mu_q^{xx}(\boldsymbol{v}) - \Gamma_q^{xz,d} \mu_q^{xz}(\boldsymbol{v}), \tag{5.49c}$$
$$B_q^{(1),c} = \Gamma_q^{z,c} + \Gamma_q^x, \tag{5.49d}$$
$$B_q^{(1),d} = \Gamma_q^{z,d}. \tag{5.49e}$$

Note that $\boldsymbol{v}^T A_q \boldsymbol{w}$ (from (5.10a)) is not affected by the force and $B_q^T(F_\mathrm{ex})\boldsymbol{v}$ is split into $(B_q^c)^T \boldsymbol{v} + \mathrm{i}\delta (B_q^d)^T \boldsymbol{v}$. This allows us to rewrite (5.6) as

$$\frac{\hat{\phi}_q^s(s)}{1-\hat{\phi}_q^s(s)} = \frac{(\hat{\boldsymbol{\phi}}^s(s))^T A_q \hat{\boldsymbol{\phi}}^s(s) + s(A_q^{(1)})^T \hat{\boldsymbol{\phi}}^s(s) + s^2}{(B_q^c)^T \hat{\boldsymbol{\phi}}^s(s) + sB_q^{(1),c} - \mathrm{i}\delta \left((B_q^d)^T \hat{\boldsymbol{\phi}}^s(s) + sB_q^{(1),d} \right)} \tag{5.50a}$$

$$= \frac{(\hat{\boldsymbol{\phi}}^s(s))^T A_q \hat{\boldsymbol{\phi}}^s(s) + s(A_q^{(1)})^T \hat{\boldsymbol{\phi}}^s(s) + s^2}{(B_q^c)^T \hat{\boldsymbol{\phi}}^s(s) + sB_q^{(1),c}} \sum_{n=0}^{\infty} \left(\mathrm{i}\delta \frac{(B_q^d)^T \hat{\boldsymbol{\phi}}^s(s) + sB_q^{(1),d}}{(B_q^c)^T \hat{\boldsymbol{\phi}}^s(s) + sB_q^{(1),c}} \right)^n, \tag{5.50b}$$

where we used the geometric series in the second line, which requires the condition

$$\left|\delta\left((B_q^d)^T\hat{\boldsymbol{\phi}}^s(s)+sB_q^{(1),d}\right)\left((B_q^c)^T\hat{\boldsymbol{\phi}}^s(s)+sB_q^{(1),c}\right)^{-1}\right|<1. \tag{5.51}$$

This condition becomes problematic for $\hat{\boldsymbol{\phi}}^s\to 0$ and $s\to 0$ as it depends on the order of the limiting procedures. If either of them is finite, there is no problem and δ can always be chosen so small that this condition is fulfilled.

For this chapter, we will proceed with the critical behavior without possible corrections, i.e. $\delta=0$. We still have to express the right hand side in terms of $\hat{\boldsymbol{g}}$. Inserting its definition (5.47), we find

$$\frac{\hat{\phi}_q^s(s)}{1-\hat{\phi}_q^s(s)}=\frac{(\boldsymbol{f}^{sc})^TA_q\boldsymbol{f}^{sc}+2\boldsymbol{f}^{sc}A_q\hat{\boldsymbol{g}}(s)+(\hat{\boldsymbol{g}}(s))^TA_q\hat{\boldsymbol{g}}(s)+s(A_q^{(1)})^T\boldsymbol{f}^{sc}+s(A_q^{(1)})^T\hat{\boldsymbol{g}}(s)+s^2}{(B_q^c)^T\boldsymbol{f}^{sc}+(B_q^c)^T\hat{\boldsymbol{g}}(s)+sB_q^{(1),c}}. \tag{5.52}$$

Our aim is to identify in this equation the equation for the long time limit as well as the stability matrix as in [Göt09, p. 439, Eq. (6.4)]. We therefore expand simultaneously in $\hat{\boldsymbol{g}}$ and s with the geometric series

$$\frac{1}{(B_q^c)^T\boldsymbol{f}^{sc}+(B_q^c)^T\hat{g}(s)+sB_q^{(1),c}}=\frac{1}{(B_q^c)^T\boldsymbol{f}^{sc}}\sum_{n=0}^{\infty}\left(-\frac{(B_q^c)^T\hat{g}(s)+sB_q^{(1),c}}{(B_q^c)^T\boldsymbol{f}^{sc}}\right)^n. \tag{5.53}$$

This requires the condition

$$\left|\left((B_q^c)^T\hat{g}(s)+sB_q^{(1),c}\right)\left((B_q^c)^T\boldsymbol{f}^{sc}\right)^{-1}\right|<1, \tag{5.54}$$

which again becomes tricky for $\boldsymbol{f}^{sc}\to 0$. With this expansion and the identity (5.48) we can summarize our expansion as follows

$$\begin{aligned}0=&\frac{f_q^{sc}}{1-f_q^{sc}}-\frac{(\boldsymbol{f}^{sc})^TA_q\boldsymbol{f}^{sc}}{(B_q^c)^T\boldsymbol{f}^{sc}}-s\frac{(A_q^{(1)})^T\boldsymbol{f}^{sc}}{(B_q^c)^T\boldsymbol{f}^{sc}}-\frac{s^2}{(B_q^c)^T\boldsymbol{f}^{sc}}\\&+\frac{sB_q^{(1),c}}{(B_q^c)^T\boldsymbol{f}^{sc}}\left(\frac{(\boldsymbol{f}^{sc})^TA_q\boldsymbol{f}^{sc}}{(B_q^c)^T\boldsymbol{f}^{sc}}+s\frac{(A_q^{(1)})^T\boldsymbol{f}^{sc}}{(B_q^c)^T\boldsymbol{f}^{sc}}+\frac{s^2}{(B_q^c)^T\boldsymbol{f}^{sc}}\right)\\&+\frac{\hat{g}_q(s)}{(1-f_q^{sc})^2}-\frac{2\boldsymbol{f}^{sc}A_q\hat{\boldsymbol{g}}}{(B_q^c)\boldsymbol{f}^{sc}}+\frac{(\boldsymbol{f}^{sc})^TA_q\boldsymbol{f}^{sc}}{\left((B_q^c)^T\boldsymbol{f}^{sc}\right)^2}(B_q^c)^T\hat{\boldsymbol{g}}(s)-s\frac{(A_q^{(1)})^T\hat{\boldsymbol{g}}(s)}{(B_q^c)^T\boldsymbol{f}^{sc}}+\frac{s^2(B_q^c)^T\hat{\boldsymbol{g}}(s)}{\left((B_q^c)^T\boldsymbol{f}^{sc}\right)^2}\\&+\sum_{n=2}^{\infty}\frac{(\hat{g}_q(s))^n}{(1-f_q^{sc})^{n+1}}+\mathcal{O}(\hat{g}^2,s^2).\end{aligned} \tag{5.55}$$

The Landau symbol $\mathcal{O}$ summarizes all contributions of higher order from the expansion. We recognize the fixed-point equation for the critical nonergodicity parameter (blue) and the stability matrix J' (as defined in (5.15)) applied to $\hat{\boldsymbol{g}}$ (orange). Further calculation with this representation is cumbersome, because we can get any combination of powers of s and $\hat{\boldsymbol{g}}$. As

we have no knowledge about the s-dependency of $\hat{\boldsymbol{g}}$ it impossible to decide which terms are important in the limit $s \to 0$. Therefore, we do not follow this approach any further.

5.6.2. Asymptotic analysis for the fraction-free representation

In this section, we will do the asymptotic analysis based on a fraction free version of the equations of motion in Laplace space (5.6). Keeping the concept of the S-transform, and the abbreviations as introduced in (5.49), we find

$$\begin{aligned} 0 = {} & s^2(\hat{\phi}_q^s(s) - 1) + s\left(\left(B^{(1),c} + \mathrm{i}\delta B^{(1),d}\right)\hat{\phi}_q^s(s) - (\hat{\phi}_q^s(s) - 1)(A_q^{(1)})^T\hat{\boldsymbol{\phi}}^s\right) \\ & + \hat{\phi}_q^s\left((B_q^c)^T\hat{\boldsymbol{\phi}}^s + \mathrm{i}\delta(B_q^d)^T\hat{\boldsymbol{\phi}}^s\right) + (\hat{\phi}_q^s - 1)(\hat{\boldsymbol{\phi}}^s)^T A_q\hat{\boldsymbol{\phi}}^s. \end{aligned} \tag{5.56}$$

As in the previous section, we expand the correlation function around the critical nonergodicity parameter via $\hat{g}_q(s)$ as introduced in (5.47).

Inserting this relation into the equation of motion above leads to the following equations of motion for $\hat{g}_q$

$$\begin{aligned} 0 = {} & s^2(f_q^{sc} - 1) + s^2\hat{g}_q(s) \\ & + s\left(B_q^{(1),c}f_q^{sc} - (f_q^{sc} - 1)(A_q^{(1)})^T\boldsymbol{f}^{sc} + \mathrm{i}\delta\left(B^{(1),d}f_q^{sc} + B^{(1),d}\hat{g}_q(s)\right)\right. \\ & \quad \left. + B_q^{(1),c}\hat{g}_q(s) + \hat{g}_q(s)(A_q^{(1)})^T\boldsymbol{f}^{sc} + (f^{sc} - 1)(A_q^{(1)})^T\hat{\boldsymbol{g}}(s) + \hat{g}_q(s)(A_q^{(1)})^T\hat{\boldsymbol{g}}(s)\right) \\ & + f_q^{sc}(B_q^c)^T\boldsymbol{f}^{sc} + (f_q^{sc} - 1)(\boldsymbol{f}^{sc})^T A_q\boldsymbol{f}^{sc} + \mathrm{i}\delta f_q^{sc}(B_q^d)^T\boldsymbol{f}^{sc} \\ & + f_q^{sc}(B_q^c)^T\hat{\boldsymbol{g}}(s) + \hat{g}_q(s)(B_q^c)^T\boldsymbol{f}^{sc} + \hat{g}_q(s)(\boldsymbol{f}^{sc})^T A_q\boldsymbol{f}^{sc} + \hat{g}_q(s)(B_q^c)^T\hat{\boldsymbol{g}}(s) \\ & + \mathrm{i}\delta\left(f_q^{sc}(B_q^d)^T\hat{\boldsymbol{g}}(s) + \hat{g}_q(s)(B_q^d)^T\boldsymbol{f}^{sc} + \hat{g}_q(s)(B_q^d)^T\hat{\boldsymbol{g}}(s)\right) \\ & + (f_q^{sc} - 1)\left(\hat{\boldsymbol{g}}(s))^T A_q\boldsymbol{f}^{sc} + (\boldsymbol{f}^{sc})^T A_q\hat{\boldsymbol{g}}(s)\right) \\ & + (f_q^{sc} - 1)(\hat{\boldsymbol{g}}(s))^T A_q\hat{\boldsymbol{g}}(s) + \hat{g}_q(s)\left((\boldsymbol{f}^{sc})^T A_q\hat{\boldsymbol{g}}(s) + (\hat{\boldsymbol{g}}(s))^T A_q\boldsymbol{f}^{sc}\right) \\ & + \hat{g}_q(s)(\hat{\boldsymbol{g}}(s))^T A_q\hat{\boldsymbol{g}}(s) \end{aligned} \tag{5.57}$$

Since this is a lot of terms, we highlight a few. The terms in blue describe the fixed-point equation for f_q^{sc} and cancel therefore. The terms in orange consist of the stability matrix (5.13) evaluated at the critical point and applied to $\hat{\boldsymbol{g}}(s)$. Finally, the terms in red describe the correction terms if the force deviates from the critical one. After this identification, we now order the terms in powers of $\hat{g}_q(s)$, which yields

$$\begin{aligned} 0 = {} & \mathrm{i}\delta f_q^{sc}(B_q^d)^T\boldsymbol{f}^{sc} + s\left(B_q^{(1),c}f_q^{sc} + (f_q^{sc} - 1)(A_q^{(1)})^T\boldsymbol{f}^{sc} + \mathrm{i}\delta B_q^{(1),d}f_q^{sc}\right) + s^2(f_q^{sc} - 1) \\ & + (S^c\hat{\boldsymbol{g}}(s))_q + \mathrm{i}\delta\left(\hat{g}_q(s)(B_q^d)^T\boldsymbol{f}^{sc} + f_q^{sc}(B_q^d)^T\hat{\boldsymbol{g}}(s)\right) \\ & + s\left(\hat{g}_q(s)(B_q^{(1),c} + (A_q^{(1)})^T\boldsymbol{f}^{sc}) + (f_q^{sc} - 1)(A_q^{(1)})^T\hat{\boldsymbol{g}}(s) + \mathrm{i}\delta B_q^{(1),d}\hat{g}_q(s)\right) + s^2\hat{g}_q(s) \\ & + \hat{g}_q(s)\left((B_q^c)^T\hat{\boldsymbol{g}}(s) + (\hat{\boldsymbol{g}}(s))^T A_q\boldsymbol{f}^{sc} + (\boldsymbol{f}^{sc})^T A_q\hat{\boldsymbol{g}}(s)\right) + (f_q^{sc} - 1)(\hat{\boldsymbol{g}}(s))^T A_q\hat{\boldsymbol{g}}(s) \\ & + \mathrm{i}\delta\hat{g}_q(s)(B_q^d)^T\hat{\boldsymbol{g}}(s) + s\hat{g}_q(s)(A_q^{(1)})^T\hat{\boldsymbol{g}}(s) \\ & + \hat{g}_q(s)\left((\hat{\boldsymbol{g}}(s)^T A_q\hat{\boldsymbol{g}}(s)\right). \end{aligned} \tag{5.58}$$

This equation corresponds to the end result of the previous section, with the main difference that this result is still exact, since we did not apply any approximations here.

To proceed with the asymptotic analysis, we have to identify the terms which are most important for the long time behavior. This corresponds to the $s \to 0$ limit, which suggests to retain only the lowest powers in s. Therefore, we drop all terms, which are of higher order in s (highlighted in blue). We keep the first term linear in s, because the zero-order term vanishes at the critical force. Furthermore, we drop all terms which are cubic in $\hat{g}(s)$ (orange), which also yield higher order contributions.

In order to find the critical law, we follow the power-counting ansatz of Götze [Göt09, Sec 6.1.2(i), p. 444] using the factorization

$$g_q(t) = h_q g_0^\sigma(t), \tag{5.59a}$$

$$\hat{g}_q(s) = h_q \hat{g}_0^\sigma(s), \tag{5.59b}$$

where the wave vector and time dependency is split into a time-independent wave-vector-dependent prefactor h_q and a wave-vector-independent evolution $g_0^\sigma(t)$, which only depends on the parameter σ which characterizes the distance to the critical point (σ will be specified later on). While this ansatz yields useful results in classical MCT, it cannot be proved that there is always such a separation of wave vector and time dependency. This assumption will be checked later on numerically. This results in the following equations

$$\begin{aligned} -(S^c \boldsymbol{h})_q \hat{g}_0^\sigma(s) = {} & \mathrm{i}\delta D_q^{(0)} + s\left(E_q^{(0)} + \mathrm{i}\delta \overline{D}_q^{(0)}\right) + \mathrm{i}\delta D_q^{(1)} \hat{g}_0^\sigma(s) \\ & + \left(E_q^{(2)} + \mathrm{i}\delta D_q^{(2)}\right) (\hat{g}_0^\sigma(s))^2, \end{aligned} \tag{5.60}$$

with

$$D_q^{(0)} = f_q^{sc} (B_q^d)^T \boldsymbol{f}^{sc}, \tag{5.61a}$$

$$E_q^{(0)} = \Gamma_q^c f_q^{sc} + (f_q^{sc} - 1) C_q^T \boldsymbol{f}^{sc}, \tag{5.61b}$$

$$\overline{D}_q^{(0)} = \Gamma_q^d f_q^{sc}, \tag{5.61c}$$

$$D_q^{(1)} = h_q (B_q^d)^T \boldsymbol{f}^{sc} + f_q^{sc} (B_q^d)^T \boldsymbol{h} \tag{5.61d}$$

$$E_q^{(2)} = h_q ((B_q^c)^T h_q + \boldsymbol{h}^T A_q \boldsymbol{f}^{sc} + (\boldsymbol{f}^{sc})^T A_q \boldsymbol{h}) + (f_q^{sc} - 1) \boldsymbol{h}^T A_q \boldsymbol{h}, \tag{5.61e}$$

$$D_q^{(2)} = h_q (B_q^d)^T \boldsymbol{h}. \tag{5.61f}$$

The critical stability matrix S^c is by definition not invertible, as it has an eigenvalue 0. Let us denote the corresponding right eigenvector by $\boldsymbol{e}$ and the corresponding left eigenvector by $\boldsymbol{e}^*$, i.e. $S^c \boldsymbol{e} = 0$ and $(\boldsymbol{e}^*)^T S^c = 0$. We can nevertheless find a solution of (5.60) if we make sure that the right hand side has no component in the kernel of S^c. This is achieved by projecting on the left eigenvector $\boldsymbol{e}^*$ (see Appendix C.4 for a proof). This yields the following solubility condition

$$\begin{aligned} 0 = {} & \mathrm{i}\delta \sum_q e_q^* D_q^{(0)} + \mathrm{i}\delta \sum_q e_q^* D_q^{(1)} \hat{g}_0^\sigma(s) \\ & + s \sum_q e_q^* (E_q^{(0)} + \mathrm{i}\delta \overline{D}_q^{(0)}) + \left(\sum_q e_q^* \left(E_q^{(2)} + \mathrm{i}\delta D_q^{(2)}\right) \right) (\hat{g}_0^\sigma(s))^2 . \end{aligned} \tag{5.62}$$

Following again Götze [Göt09, Sec. 6.1.3(i), p. 471], the first term is the so called separation parameter and has to be of order $\hat{g}^2$ for a generic A_2 bifurcation. For a degenerate A_2 bifurcation, it is of order $\hat{g}$, which implies that we can either neglect the second term or combine it with the last term. What remains is an equation of the form

$$0 = -\sigma - s\tau + (\hat{g}_0^\sigma(s))^2 = \sigma + s\tau + (s\tilde{g}_0^\sigma(s))^2 \tag{5.63}$$

with

$$\sigma = -\frac{\mathrm{i}\delta \sum_q e_q^* D_q^{(0)}}{\sum_q e_q^* \left(E_q^{(2)} + \mathrm{i}\delta D_q^{(2)}\right)}, \tag{5.64a}$$

$$\tau = -\frac{\sum_q e_q^* (E_q^{(0)} + \mathrm{i}\delta \overline{D}_q^{(0)})}{\sum_q e_q^* \left(E_q^{(2)} + \mathrm{i}\delta D_q^{(2)}\right)}. \tag{5.64b}$$

After translating this equation into time space we obtain

$$\int_0^t g_0^{\sigma,\tau}(t-t') g_0^{\sigma,\tau}(t') \mathrm{d}t' = \sigma t + \tau. \tag{5.65}$$

We change the notation from g_0^σ to $g_0^{\sigma,\tau}$ because we find that the solution depends on the two parameters σ and τ (which, however, need not be independent).

This result is only useful, if $\boldsymbol{f}^{sc} \neq 0$, because most of the coefficients above vanish in the case $\boldsymbol{f}^{sc} = 0$. In particular, (5.58) simplifies to

$$\begin{aligned} 0 = {} & (S^c \hat{\boldsymbol{g}}(s))_q - s^2 + s\left(\hat{g}_q(s) B_q^{(1),c} - (A_q^{(1)})^T \hat{\boldsymbol{g}}(s) - \mathrm{i}\delta B_q^{(1),d} \hat{g}_q(s)\right) + s^2 \hat{g}_q(s) \\ & + \hat{g}_q(s)(B_q^c)^T \hat{\boldsymbol{g}}(s) - (\hat{\boldsymbol{g}}(s))^T A_q \hat{\boldsymbol{g}}(s) + \mathrm{i}\delta \hat{g}_q(s)(B_q^d)^T \hat{\boldsymbol{g}}(s) + s\hat{g}_q(s)(A_q^{(1)})^T \hat{\boldsymbol{g}}(s) \\ & + \hat{g}_q(s)((\hat{\boldsymbol{g}}(s))^T A_q \hat{\boldsymbol{g}}(s)). \end{aligned} \tag{5.66}$$

Note that the stability matrix S^c will vanish.

5.6.3. Scaling law

Starting from (5.65), we can find a scaling law: Let $g_0^{1,1}(t)$ be a solution of (5.65) with $\tau = \sigma = 1$. Then $g_0^{\sigma,\tau}(t) := \sqrt{|\sigma|} g_0^{1,1}(|\sigma| t/\tau)$ is a solution of (5.65) with general $\sigma, \tau > 0$.

Proof. We have

$$\begin{aligned} \int_0^t g_0^{\sigma,\tau}(t-t') g_0^{\sigma,\tau}(t') \mathrm{d}t' &= \int_0^t |\sigma| g_0^{1,1}\left(\frac{|\sigma|(t-t')}{\tau}\right) g_0^{1,1}\left(\frac{|\sigma| t'}{\tau}\right) \mathrm{d}t' \\ &= |\sigma| \int_0^{t|\sigma|/\tau} g_0^{1,1}\left(\frac{|\sigma| t}{\tau} - x\right) g_0^{1,1}(x) \frac{\tau}{|\sigma|} \mathrm{d}x = \tau\left(\frac{t|\sigma|}{\tau} + 1\right) \\ &= +|\sigma| t + \tau \end{aligned} \tag{5.67}$$

□

The sign of σ could be incorporated by considering solutions $g_{\pm}^{1,1}(t)$ for $\sigma = \pm 1$.

5.6.4. Solution of beta scaling equation

This paragraph is dedicated to find a solution of the beta-scaling-equation (5.65). First, we have to find out more about the parameters σ and τ as specified in (5.64). As a first step we do another approximation: Since we are interested in the solution for small δ, we can neglect this contribution compared to the (assumed) nonzero force-independent terms. Then, the equations reduce to

$$\sigma = -\mathrm{i}\delta \frac{\sum_q e_q^* D_q^{(0)}}{\sum_q e_q^* E_q^{(2)}}, \tag{5.68a}$$

$$\tau = -\frac{\sum_q e_q^* E_q^{(0)}}{\sum_q e_q^* E_q^{(2)}}. \tag{5.68b}$$

So far, we have at least two degrees of freedom left to adjust their properties: We have not fixed the eigenvector $\boldsymbol{e}$ yet and we did not specify the amplitude $\boldsymbol{h}$. However, multiplying $\boldsymbol{e}$ with a constant factor will not change the parameters, because the factor will cancel due to the fact that it shows up in the numerator as well as in the denominator. Furthermore both numerators do not contain h_q, therefore, we can only make the denominator real by choosing the right h_q. To conclude, σ and τ are in general complex numbers.

According to [PM08, p. 393, Eq. 1], (5.65) has the solutions

$$g^{\sigma,\tau}(t) = \pm\sqrt{\tau}\left(\frac{1}{\sqrt{\pi t}}\exp\left(-\frac{\sigma}{\tau}t\right) + \sqrt{\frac{\sigma}{\tau}}\operatorname{erf}\left(\sqrt{\frac{\sigma}{\tau}t}\right)\right), \tag{5.69}$$

where $\operatorname{erf}(z)$ is the error function defined via

$$\operatorname{erf}(z) = \frac{2}{\sqrt{\pi}}\int_0^z \exp\left(-x^2\right)\mathrm{d}x\,. \tag{5.70}$$

Both, the exponential function as well as the error function can be extended to complex arguments. Now we can distinguish three cases

$\operatorname{Re}\sigma/\tau > 0$ The first term vanishes for $t \to \infty$ and the error function converges towards 1, i.e. the long time limit is $\sqrt{\sigma}$. Since $\sigma \propto \delta$ this finding indicates a type B transition.

$\operatorname{Re}\sigma/\tau = 0$ At the transition, only the power law $t^{-1/2}$ remains, because the exponential term is one and the error function is 0. The exponent $-1/2$ is typically found for type A transitions.

$\operatorname{Re}\sigma/\tau < 0$ Both, the exponential term and the error function diverge for $t \to \infty$, which indicates a breakdown of the small $\hat{g}$-expansion.

Hence, we find a power law with exponent $-1/2$ for the critical dynamics. Due to the complications with vanishing nonergodicity parameters, which appear in the denominator as well as the enumerator of fractions, we cannot rigorously prove a scaling law. Most of the preceding calculations were only formal, waiting for a numerical approval.

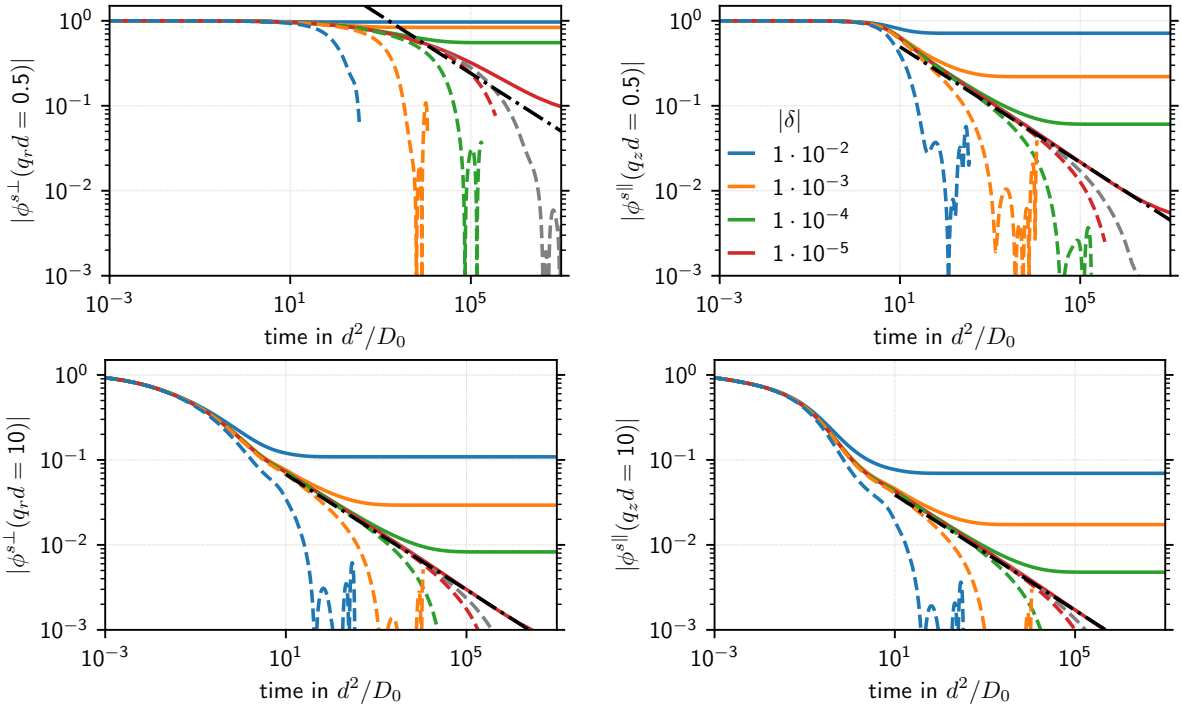

Figure 5.11.: Critical dynamics for the correlation functions for a small wave number ($qd = 0.5$, top row) and a large wave number ($qd = 10$, bottom row) perpendicular (left column) and parallel (right column) to the direction of the force. Forces below F_c are shown as solid lines, forces above as dashed lines. A power law with exponent -0.34 is shown as dash-dotted black line matched to the values of the correlation functions at $t = 10^4\ d^2/D_0$. This result is obtained for a cutoff $q_{\max} d = 20$.

5.7. Numerical results for critical dynamics

In this section, we will numerically check the analytical predictions from the previous section. Since the time window, where the critical law can be observed increases when approaching the critical force, we would like to approach the critical force as close as possible. However, we cannot approach it arbitrarily close, because there are two critical forces as worked out in Section 4.1.2 with unphysical behavior (like decreasing mean displacement) in between as seen in Section 5.5. The difference between both critical forces is determined by the smallest nonzero wave vector in the grid as shown in Figure 4.4 and sets the scale how close we can approach the critical force. We therefore choose to extend the number of points in the logarithmic part of our grids. In comparison to the grids introduced at the beginning of Section 5.2, we choose a `unilog25`-grid with cutoff $q_{\max} d = 20$ and 66 grid points as well as a `unilog25`-grid with cutoff $q_{\max} d = 14$ with 54 grid points. These grids have a smallest nonzero wave vector of $qd = 1.5 \cdot 10^{-8}$ and we can therefore safely approach the critical force up to a relative distance of $1 \cdot 10^{-7}$. The critical force for $q_{\max} d = 20$ is $42.336\,486\ k_B T/d$ and for $q_{\max} d = 14$ $44.781\,432\,0\ k_B T/d$.

In Figure 5.11 we show the correlation functions obtained from the time space calculations in the constant bath approximation close to the critical force for the grid with cutoff $q_{\max} d = 20$. We find that there emerges a power law decay for the correlation functions parallel and

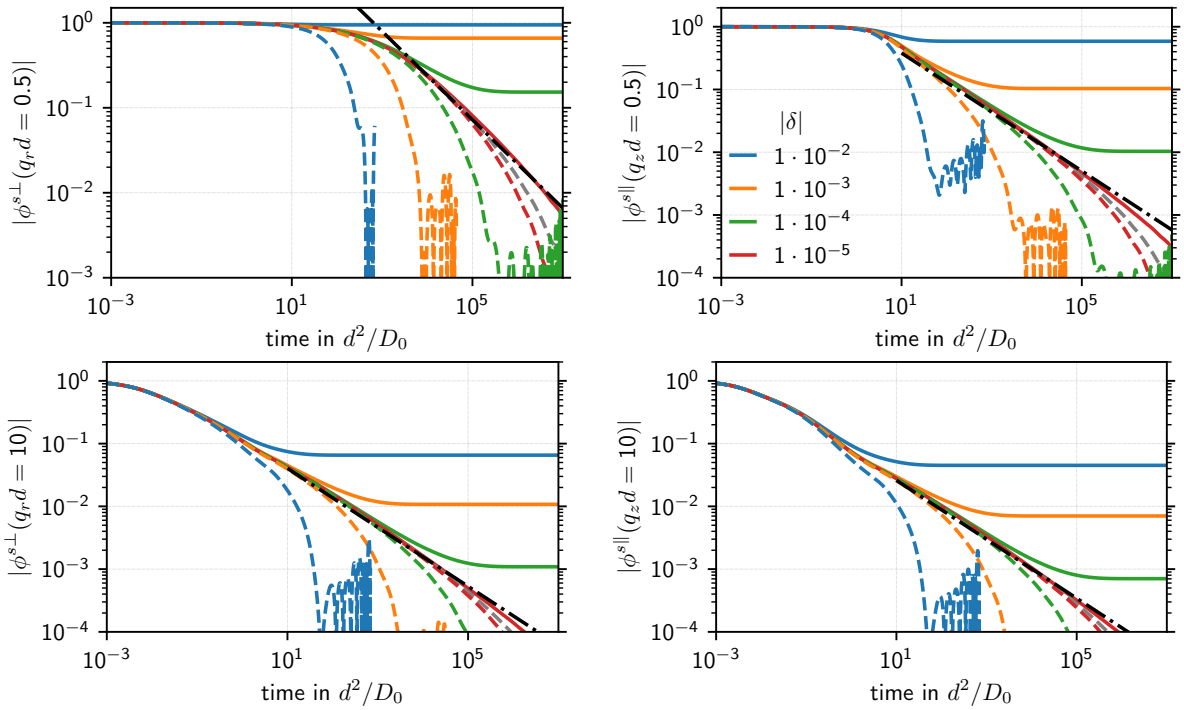

Figure 5.12.: Critical dynamics for the correlation functions for a small wave number ($qd = 0.5$, top row) and a large wave number ($qd = 10$, bottom row) perpendicular (left column) and parallel (right column) to the direction of the force. Forces below F_c are shown as solid lines, forces above as dashed lines. A power law with exponent -0.52 is shown as dash-dotted black line matched to the values of the correlation functions at $t = 10^4\, d^2/D_0$. The difference to Figure 5.11 is only the grid: This result is obtained for a cutoff $q_{\max} d = 14$.

perpendicular to the force. The time window in which this power law can be observed ranges from $10^1\, d^2/D_0$ to $10^7\, d^2/D_0$ for large wave vectors, but is reduced to $10^5\, d^2/D_0$ to $10^7\, d^2/D_0$ for the small wave vector in the perpendicular direction. Even though this power law extends over several decades, analyzing the local exponent reveals that it is slightly changing over time. This is not shown, but similar to Figure 4.6 and Figure 4.5 for the first moments. A plateau value of about -0.34 is reached for the larger wave vectors, while the local exponent for $qd = 0.5$ in the perpendicular direction is still evolving. We also notice that the correlation functions are not symmetric with respect to this power law for small distances to the critical force. This indicates that the critical force for the time-based calculation is slightly smaller than obtained from the Laplace calculation, possibly due to numerical inaccuracies.

To summarize, we find for the grid with cutoff $q_{\max} d = 20$ an approximate critical power law with an exponent of about -0.34, which deviates from what we predicted. For the grid with cutoff $q_{\max} d = 14$ we find the same qualitative behavior as shown in Figure 5.12. There, the exponent of the power law is given by -0.52, which fits better to our prediction. In both cases we find that the time at which this power law sets in shifts to longer times for smaller wave vectors, most prominent in the perpendicular direction.

The analysis of the time-based calculation has the drawback of accumulating numerical errors when reaching large times through round-off errors and the decimation procedure. The latter

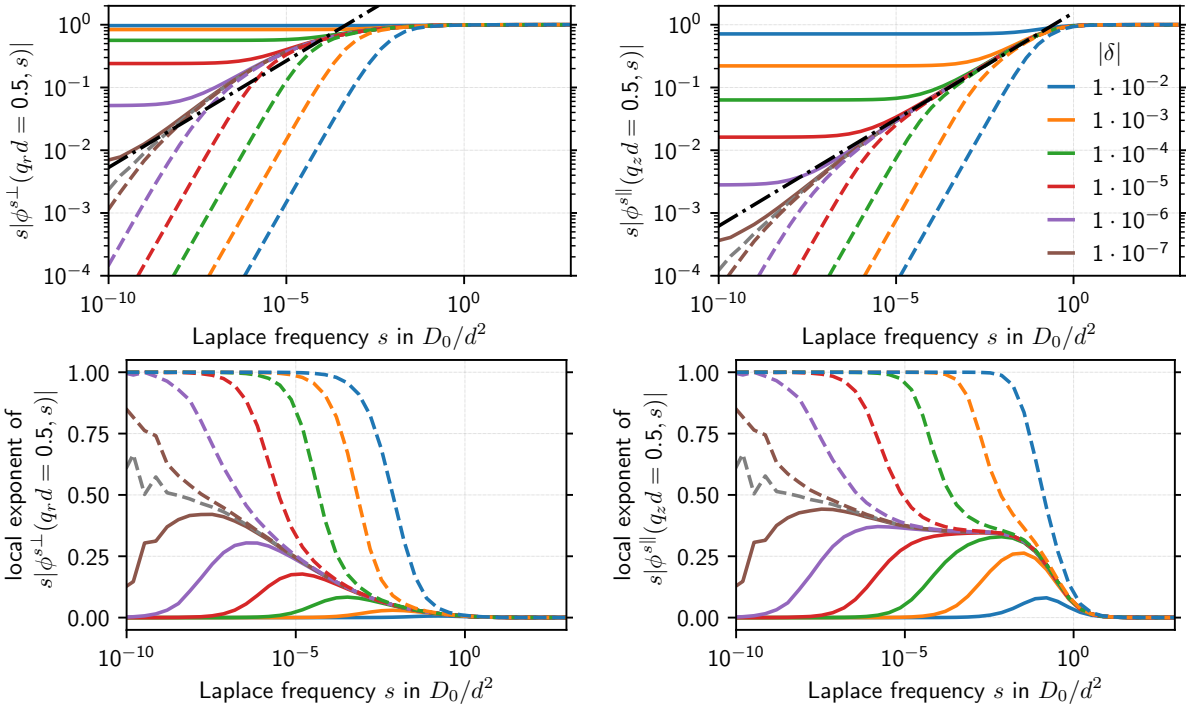

Figure 5.13.: Critical behavior of the S-transform of the correlation functions in Laplace space (top row) for small wave vectors perpendicular (left) and parallel (right) to the force direction for different forces close to the critical force. Forces below the critical force are shown as solid lines, while forces above are shown as dashed lines. The critical power law from the time domain with exponent 0.34 is shown as black, dash dotted line and matched to the values at $sd^2/D_0 = 10^{-4}$. The panels below show the local exponents of these correlation functions. These results are obtained for a grid with $q_{\max}d = 20$.

might be hold responsible for the variation of the power law exponent, because it introduces discontinuities in the time step by the decimation. To overcome these problems, we resort again to the Laplace space calculations, where the solution for each Laplace frequency is independent of the others and no solution of an evolution equation is required. This is shown in Figure 5.13 for the grid with $q_{\max}d = 20$. For better comparison we show the S-transform of the correlation functions, because they avoid the divergence for $s \to 0$ and the critical laws translate to each other by a change of sign. For large wave vectors (not shown) and small wave vectors in the parallel direction we find a power law, which corresponds to the one in the time domain with an exponent of 0.34. It fits over approximately four decades to the critical behavior, but deviates for very small frequencies. Analyzing the local exponent as defined in (4.2), we find that there is no true power law, but a gradual change of the exponent. At the smallest frequencies the exponents become noisy, indicating the onset of numerical inaccuracies.

For small wave vectors in the direction perpendicular to the force, the picture is completely different. There is no power law visible at all even though this wave number is still in the uniform part of the grid. All curves collapse onto the critical law (shown as dashed grey line), the longer, the closer to the critical force. This critical local exponent increases monotonously from 0 at $sd^2/D_0 = 10^0$ to 0.4 at $sd^2/D_0 = 10^{-6}$. For this reason there is no agreement with the corresponding critical law from the time domain. For the grid with $q_{\max}d = 14$ the qualitative

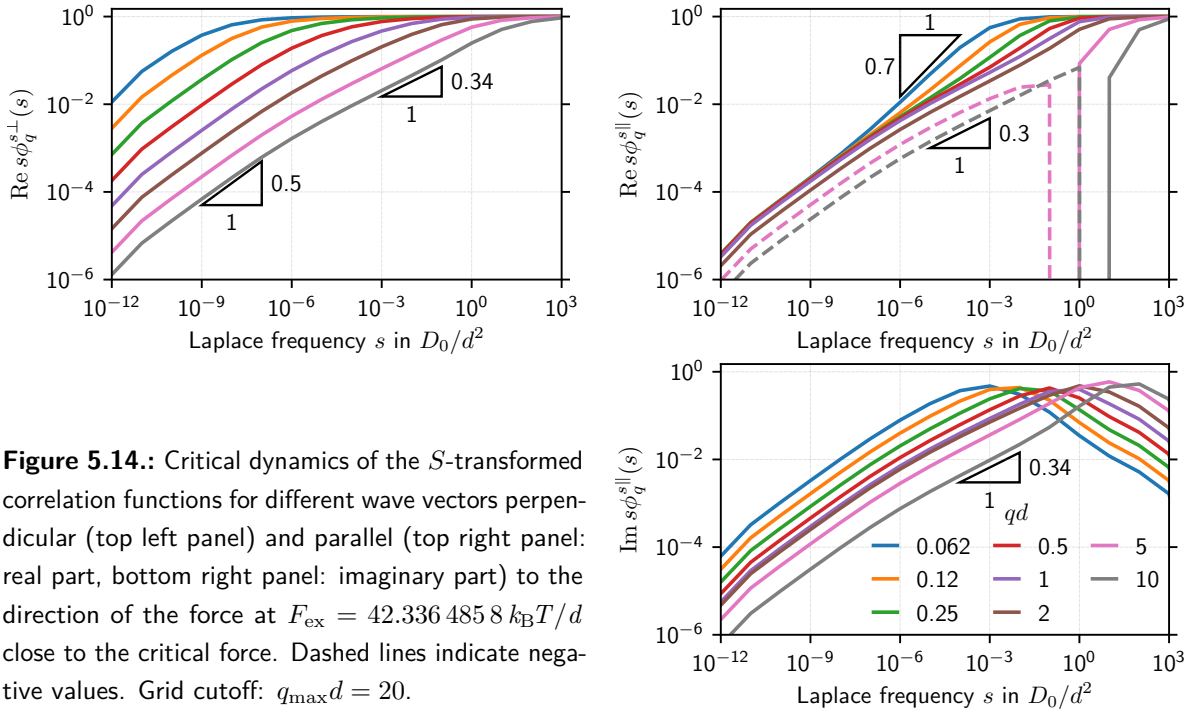

Figure 5.14.: Critical dynamics of the S-transformed correlation functions for different wave vectors perpendicular (top left panel) and parallel (top right panel: real part, bottom right panel: imaginary part) to the direction of the force at $F_{\mathrm{ex}} = 42.336\,485\,8\,k_{\mathrm{B}}T/d$ close to the critical force. Dashed lines indicate negative values. Grid cutoff: $q_{\max}d = 20$.

behavior is the same with the only difference, that the critical exponent has a plateau at around 0.50. Furthermore, the onset of the non-power-law behavior in the perpendicular correlation functions shifts to smaller wave numbers.

This finding has two important consequences. First, a factorization ansatz separating the dynamics into a common time (or Laplace frequency) dependence and a wave vector dependent prefactor is not adequate to describe the small wave vector behavior. Second, we may ask what sets the length scale for the crossover between power-law-like critical behavior and the non-power law like?

To answer the latter question, we analyze the wave vector dependent behavior of the correlation functions for the critical force as shown in Figure 5.14. Again, we show the S-transform of the correlation functions. Furthermore, we split the parallel correlation functions into real and imaginary part. We find that the behavior for all three functions is very different. For the perpendicular direction, we find that the appearance of the power law is shifted to smaller and smaller frequencies when decreasing the wave number. This shift is rather strong: A reduction of the wave number by a factor of ten (from $qd = 10$ to $qd = 1$) yields a shift in the Laplace frequency from $sd^2/D_0 = 10^{-4}$ to $sd^2/D_0 = 10^{-8}$, i.e. by four orders of magnitude, if we want to achieve the same value of $\phi_q^{s\perp}(s) = 10^{-2}$. Furthermore, the power law changes from 0.34 for large frequencies (and large wave vectors) to approximately 0.5 for very small Laplace frequencies. As we cannot go even closer to the critical force, it remains unclear if all correlators would follow an ultimate power law with exponent 0.5 if we could analyze the exact critical force. On top of that there remains the problem that even in this case we could choose wave vectors so small that they would remain close to one and not follow any power law if we extrapolate the scaling observed above.

The real part of the parallel direction dos not show such a scaling law. Instead the curves

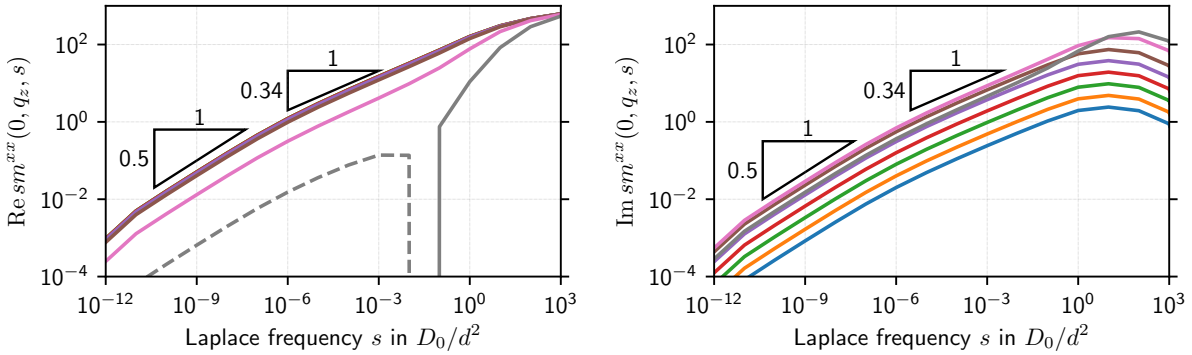

Figure 5.15.: Critical behavior of the S-transform of the real part (left) and the imaginary part (right) of the memory functional m^{xx} along the q_z-axis in Laplace space at $F_{\mathrm{ex}} = 42.336\,485\,8\, k_{\mathrm{B}}T/d$ close to the critical force. The other memory functionals show the same Laplace frequency dependency for frequencies $sd^2/D_0 < 10^{-5}$. The color code for the different wave vectors is the same as in Figure 5.14. Grid cutoff: $q_{\max}d = 20$.

collapse for all small wave vectors, However, for intermediate frequencies, the small wave numbers show a different scaling. They remain close to one for large frequencies and then have to bend down more strongly to reach the values of the other correlators for small frequencies. For large wave vectors, we find negative values in the real part of the parallel correlation functions as already observed for the nonergodicity parameters. The imaginary part exhibits a peak, which moves to smaller Laplace frequencies for smaller wave vectors. For the small wave vectors there seems to be again a scaling law: decreasing the wave number by a factor of ten one has to reduce the Laplace frequency by a factor of 100 to superimpose those curves approximately.

The fact that the correlation functions for small frequencies stay close to one for a very long time (for very small frequencies) destroys the idea that there could be a time window, in which all curves can be collapsed onto a master curve. This behavior is not specific for our case. For simple diffusion, as discussed in Section 2.3.1, the time scale associated with the decay is proportional to q^{-2}. This translates to $s\phi_q(s) = s/(s+q^2)$ in Laplace space (in dimensionless form), which changes from constant behavior to s^1-scaling around $s \approx q^2$. In the case of a driven diffusing particle moving with velocity v as discussed at the end of Section 2.3.3 we obtain

$$s\phi_q(s) = s\frac{s+q^2}{(s+q^2)^2+q^2v^2} + \mathrm{i}\frac{vq}{(s+q^2)^2+q^2v^2} \approx s\frac{1}{q^2+v^2} + \mathrm{i}s\frac{vq}{q^4+q^2v^2} \tag{5.71}$$

with the approximation for $s \ll q^2$. This yields an explanation for the observation that the real part collapses for small wave vectors and also for the $1/q$-scaling of the imaginary part for fixed s, which we observe at least for small wave vectors. Furthermore, the imaginary part exhibits a maximum as well. However, the behavior of the correlation functions perpendicular to the force direction cannot be rationalized with these simple models.

Since the correlation function is a nontrivial combination of memory functions, we can also check whether there is a master curve for the memory functionals. This is visualized in Figure 5.15. We show as an example real and imaginary part of $sm^{xx}(0, q_z, s)$. The other

memory functionals show similar behavior. The real parts typically show little wave vector dependence, while the imaginary parts usually decrease with decreasing wave vector. Dividing by the $\mathrm{Re}\, sm^{xx}(0,q,s)$ for some fixed q we find that all memory functionals become constant for $sd^2/D_0 < 10^{-5}$. Hence, we can separate the Laplace space dependency from the wave vector dependency for the memory functionals for long times, but this critical behavior is only an approximate power law. The exponent changes gradually between 0.34 at the upper validity range of the master curve and 0.5 at the lower end of the validity range.

With this knowledge, we can at least explain the behavior of the correlation functions for small frequencies. Let $\hat{g}(s)$ be the master function and $h_q^{\alpha\beta}$ such that $m_q^{\alpha\beta}(s) = h_q^{\alpha\beta}\hat{g}(s)$. Then, we can solve (5.6) for $\hat{\phi}_q^s(s)$ and find

$$\hat{\phi}_q^s(s) = \left(1 + \frac{\hat{g}(s)\left(\Gamma_q^x \hat{h}_q^{zz} + \Gamma_q^z \hat{h}_q^{xx} - \Gamma_q^{xz}\hat{h}_q^{xz}\right) + s(\Gamma_q^x + \Gamma_q^z)}{(\hat{g}(s))^2\left(\hat{h}_q^{xx}\hat{h}_q^{zz} - (\hat{h}_q^{xz})^2\right) + s\hat{g}(s)(\hat{h}_q^{xx} + \hat{h}_q^{zz}) + s^2}\right)^{-1} \tag{5.72}$$

Power counting with the assumption $\hat{g}(s) \propto s^\alpha$ for $\alpha < 1$ leads in the limit of $s \to 0$ to

$$\hat{\phi}_q^s(s) = \frac{\hat{g}_q(s)\left(\hat{h}_q^{xx}\hat{h}_q^{zz} - (\hat{h}_q^{xz})^2\right)}{\left(\Gamma_q^x \hat{h}_q^{zz} + \Gamma_q^z \hat{h}_q^{xx} - \Gamma_q^{xz}\hat{h}_q^{xz}\right) + \hat{g}_q(s)\left(\hat{h}_q^{xx}\hat{h}_q^{zz} - (\hat{h}_q^{xz})^2\right)}. \tag{5.73}$$

This representation suppresses the critical law, whenever

$$\left|\left(\Gamma_q^x \hat{h}_q^{zz} + \Gamma_q^z \hat{h}_q^{xx} - \Gamma_q^{xz}\hat{h}_q^{xz}\right)\right| \ll \left|\hat{g}_q(s)\left(\hat{h}_q^{xx}\hat{h}_q^{zz} - (\hat{h}_q^{xz})^2\right)\right|, \tag{5.74}$$

as it cancels in this case. Along the axes there holds numerically $\hat{h}_q^{xz} \ll \hat{h}_q^{xx}$ and $\hat{h}_q^{xz} \ll \hat{h}_q^{zz}$. Therefore, we find

$$\hat{\phi}_{q_z}^{s\parallel}(s) = \frac{\hat{g}_{q_z}(s)\hat{h}_{q_z}^{zz}}{\Gamma_{q_z}^z + \hat{g}_q(s)\hat{h}_{q_z}^{zz}}, \tag{5.75}$$

$$\hat{\phi}_{q_x}^{s\perp}(s) = \frac{\hat{g}_{q_x}(s)\hat{h}_{q_x}^{xx}}{q_x^2 + \hat{g}_{q_x}(s)\hat{h}_{q_x}^{xx}} \tag{5.76}$$

and the condition to observe the critical law becomes in the perpendicular direction

$$\hat{g}_q(s) < \frac{q_x^2}{\hat{h}_q^{xx}}. \tag{5.77}$$

In the case of $\hat{g}_q(s) \propto s^{1/2}$ we recover the scaling $sq^{-4} = \text{const}$ for the onset of the power law as discussed with Figure 5.11. For the parallel direction, we find structurally similar equations like for the driven diffusive particle.

In the case of the grid $q_{\max}d = 14$ we find a master curve for the memory functionals, too. In this case it is simpler and shows a power law with exponent 1/2 over the whole range for $sd^2/D_0 < 10^{-4}$.

In summary, we find that the factorization ansatz holds for the memory functionals, but not for the correlation functions. The reason for this is an interplay between small Laplace frequencies and small wave vectors. Furthermore, we find that the master curve is a power law with exponent 1/2 for the grid with $q_{\max}d = 14$. For $q_{\max}d = 20$ the master curve is more

complicated, it starts out with an exponent of 0.34 and then crosses over to an exponent of 0.5 for very small Laplace frequencies. As a consequence, we will only see the 0.34 exponent in the time domain calculations, as they cannot reach such tremendous time scales. The exponent of 1/2 matches the prediction of Section 5.6, but it remains unclear what to expect in an experiment as we have seen the exponent changing over time.

5.8. Scaling laws for the moments

As we now know that there is a critical law for the memory functionals, we can apply this to the equations of motion for the moments as well. Within this setting, we can find the critical laws for the moments. Since the critical law is somewhat model-dependent (whether the cutoff is larger or equal than $q_{\max}d = 20$ or smaller equal than $q_{\max}d = 14$), we will do the derivation with a general master function $\hat{g}(s) = s^{\alpha}$ with $0 < \alpha < 1$. Again, we choose $h_0^{\alpha\beta}$ such that $\hat{m}_0^{\alpha\beta}(s) = h_0^{\alpha\beta}\hat{g}(s)$ and likewise for the derivative $\partial_{q_\gamma}\hat{m}_0^{\alpha\beta}(s) = h^{\alpha\beta,\gamma}\hat{g}(s)$. With (2.183b) we find for the mean displacement

$$\mathcal{M}_z^{(1)}(s) = \frac{1}{s^2}F_{\mathrm{c}}\frac{1}{1 + h_0^{zz}s^{-1}\hat{g}(s)} \approx F_{\mathrm{c}}\frac{1}{h_0^{zz}}s^{-(1+\alpha)} \tag{5.78}$$

for small s, which translates to

$$\langle z \rangle (t) = \frac{F_{\mathrm{c}}}{\Gamma(1+\alpha)h_0^{zz}}t^{\alpha} \tag{5.79}$$

in the time domain. Hence, there should be a sublinear increase in the mean displacement with exponents between 0.34 and 0.5 when comparing to experiments or simulations.

For the seconds moments, we find for small Laplace frequencies according to (2.184a) and (2.184b)

$$\mathcal{M}_x^{(2)}(s) \approx \left(\frac{2}{h_0^{xx}} + \frac{2\mathrm{i}F_{\mathrm{c}}h_0^{xz,x}}{h_0^{xx}h_0^{zz}}\right)s^{-(\alpha+1)}, \tag{5.80}$$

$$\mathcal{M}_z^{(2)}(s) = \frac{2F_{\mathrm{c}}^2}{(h_0^{zz})^2}s^{-(2\alpha+1)} + 2\left(\frac{1}{h_0^{zz}} + \frac{\mathrm{i}F_{\mathrm{c}}h_0^{zz,z}}{(h_0^{zz})^2}\right)s^{-(\alpha+1)}. \tag{5.81}$$

This translates to

$$\left\langle x^2 \right\rangle (t) = \frac{2}{\Gamma(\alpha+1)}\left(\frac{1}{h_0^{xx}} + \frac{\mathrm{i}F_{\mathrm{c}}h_0^{xz,x}}{h_0^{xx}h_0^{zz}}\right)t^{\alpha}, \tag{5.82}$$

$$\left\langle z^2 \right\rangle (t) = \frac{2F_{\mathrm{c}}^2}{\Gamma(2\alpha+1)(h_0^{zz})^2}t^{2\alpha} + \frac{2}{\Gamma(\alpha+1)}\left(\frac{1}{h_0^{zz}} + \frac{\mathrm{i}F_{\mathrm{c}}h_0^{zz,z}}{(h_0^{zz})^2}\right)t^{\alpha} \tag{5.83}$$

for the long time limit in the time domain. With these results, we can also calculate the critical mean square displacement in force direction

$$\left\langle \Delta z^2 \right\rangle (t) = \frac{F_{\mathrm{c}}^2}{(h_0^{zz})^2}\left(\frac{2}{\Gamma(2\alpha+1)} - \frac{1}{(\Gamma(\alpha+1))^2}\right)t^{2\alpha} + \frac{2}{\Gamma(\alpha+1)}\left(\frac{1}{h_0^{zz}} + \frac{\mathrm{i}F_{\mathrm{c}}h_0^{zz,z}}{(h_0^{zz})^2}\right)t^{\alpha} \tag{5.84}$$

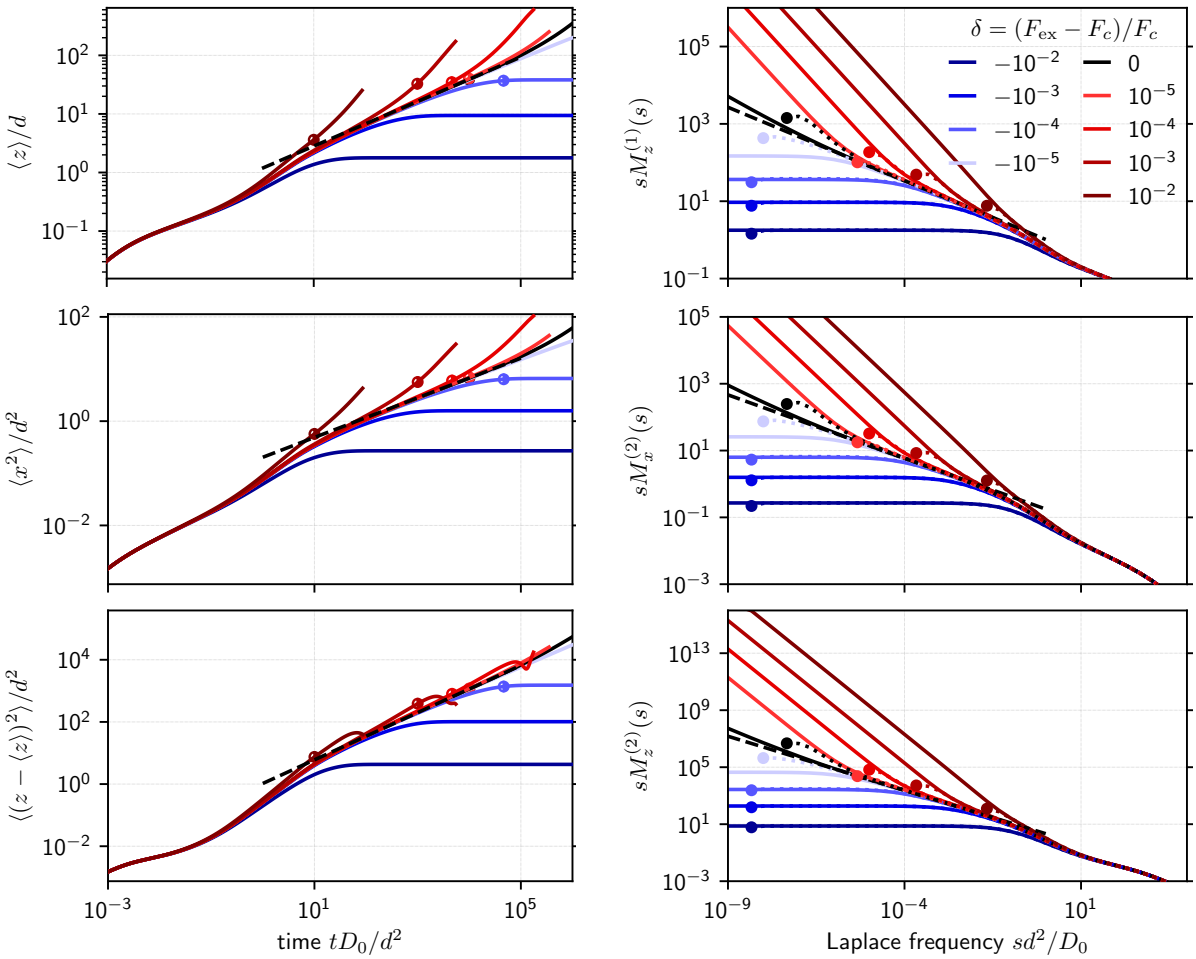

Figure 5.16.: Critical dynamics for the mean displacement (top row) and the variances ($\langle x^2 \rangle$ and $\langle (z - \langle z \rangle)^2 \rangle$ center and bottom row) as function of time (left column) and Laplace frequency (right column). The dashed lines visualize a critical law with exponent 0.38 (top and middle row) and 0.76 (bottom row) in the time domain and the negative exponents for the S-transforms. The color code is the same in all panels. Circles in the left column indicate the times up to which the difference between Laplace space solutions and Laplace transform of the time solution (shown as dotted lines in the right column) is smaller than 5 %. In the right column they indicate $s_{\min} := t_{\max}^{-1}$. Grid cutoff: $q_{\max} d = 20$.

Hence, there is the same critical power laws with exponent α for the mean displacement as for the mean square displacement perpendicular to the force direction and a power law with an exponent 2α for the variance in force direction. This is shown in Figure 5.16 for $q_{\max} d = 20$. We find a critical power law for the mean displacement and for the variance perpendicular to the force with exponent $\alpha = 0.38$. In agreement with our prediction, the exponent of the critical power law for the variance in force direction has the value $2\alpha = 0.76$. The exponents can be directly translated from the time domain to the Laplace domain. This is matches our predictions. The critical exponent used here is slightly larger than the one obtained for the correlation functions. For the discretization with $q_{\max} d = 14$ we find the same qualitative behavior, but a critical law with exponent 0.5. This exponent is well defined (constant) over at

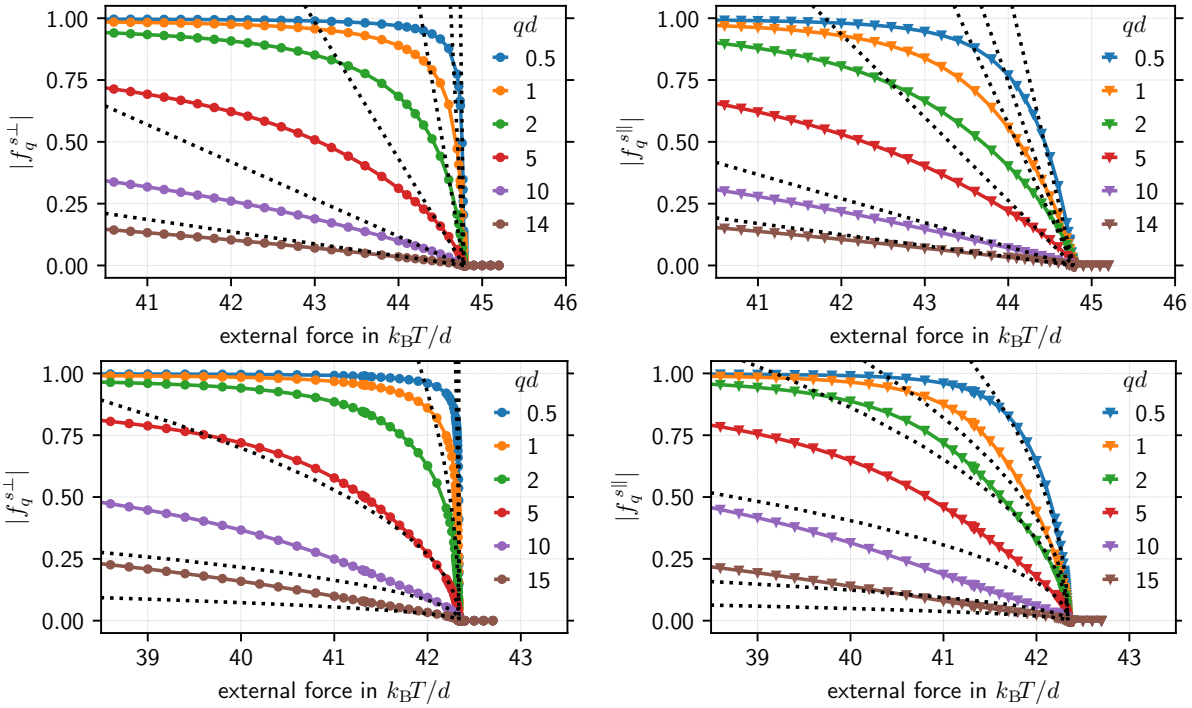

Figure 5.17.: Nonergodicity parameters perpendicular (left) and parallel (right) to the direction of the force as function of the force for different wave vectors as given. The top row shows the results for a grid with $q_{\max}d = 14$, the bottom row for $q_{\max}d = 20$. The dotted lines are the predictions based on the critical amplitude with a linear (top row, type A) and square-root-like (bottom row, type B) scaling. The agreement is best close to the critical force since it is an asymptotic expansion.

least four decades in Laplace space and about two decades for the time solution very close to the critical force.

5.9. Comparison to MD simulations

In the previous sections, we worked out the predictions of the theory about the scalings and dynamics around the critical force. This chapter is dedicated to the verification of these asymptotic laws in simulations. These simulations have been performed by Antonio Puertas, using the same system as described in Section 4.5. For this analysis we focus on forces around the critical force, which we estimated to be at around $80\,k_BT/d$. Here, we will provide an alternative means to determine the critical force based on the scaling of the nonergodicity parameters.

For the nonergodicity parameters we have seen in Section 5.5 that the nonergodicity parameters for large wave vectors decrease to zero at the critical force as shown in Figure 5.17. Even though we have a different asymptotic behavior for type A (which occur for $q_{\max}d \leq 14$) and type B transitions (which occur for $q_{\max}d \geq 20$), this is not relevant anymore for relative distances larger than 1 %. The qualitative and quantitative behavior for both discretizations is very similar not too close to the critical force. Furthermore, we could approximate the

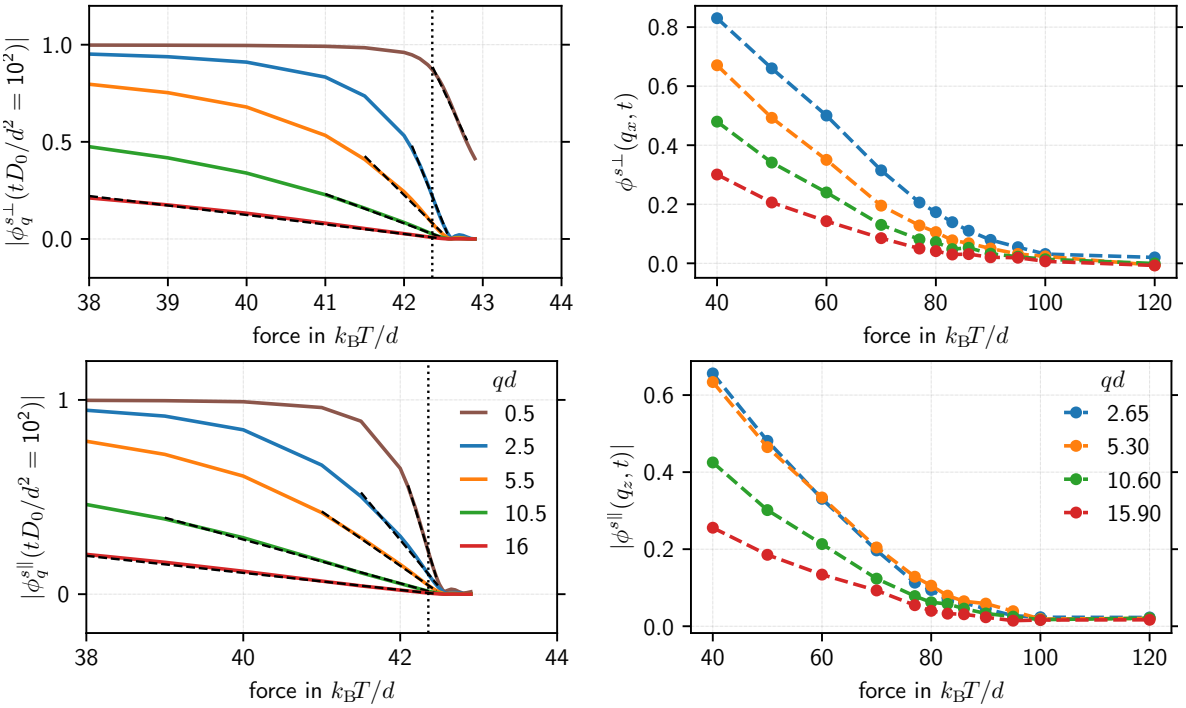

Figure 5.18.: Finite time nonergodicity parameters as function of the force for larger wave vectors for theory (left column) and simulations (right column) in the direction of the force (top row) and in the direction perpendicular to it. For the simulations, the values are obtained by averaging the correlation functions for $tD_0/d^2 \in [10, 25]$. The dashed lines in the left column show the fits to extrapolate for the critical force and the dotted vertical line shows the true critical force.

asymptotic behavior on this scale with a straight line. This works best for the large wave vectors, irrespective of the precise type of the transition. These long-time limits are of course not accessible in simulations. Therefore, we check how the values of the correlation functions behave at long, but finite times. This is shown in Figure 5.18. We find that there is still a strong, roughly linear change, even though the correlation functions are not zero above the critical force.

For the simulations, we find a very similar behavior, which is depicted in Figure 5.18. The smallest wave vector is determined by the box size. Longer wavelengths may introduce artifacts due to the periodic boundary conditions. For each wave vector, we find an approximately linear decrease, which flattens in the region, where we expect the critical force. The main difference to the calculations is again the force scale. For the theory it all happens within a few $k_\mathrm{B}T/d$, while this behavior extends from $40\,k_\mathrm{B}T/d$ to $80\,k_\mathrm{B}T/d$ in the simulations.

These values can be used to approximate the critical force by extrapolating the linear part. Since the slope is steepest directly at the critical force for the long time limit, we fit the linear part in a region around the maximum (negative) slope as shown in Figure 5.18. From those fits, we can also obtain a measure of the uncertainty depending on how closely the curve resembles a straight line and how many points were included. The result of this procedure is shown in Figure 5.19 for the theory (left) and the simulations (right). Since we know the exact value of the critical force for the theory, we can estimate the range of validity of this procedure. We

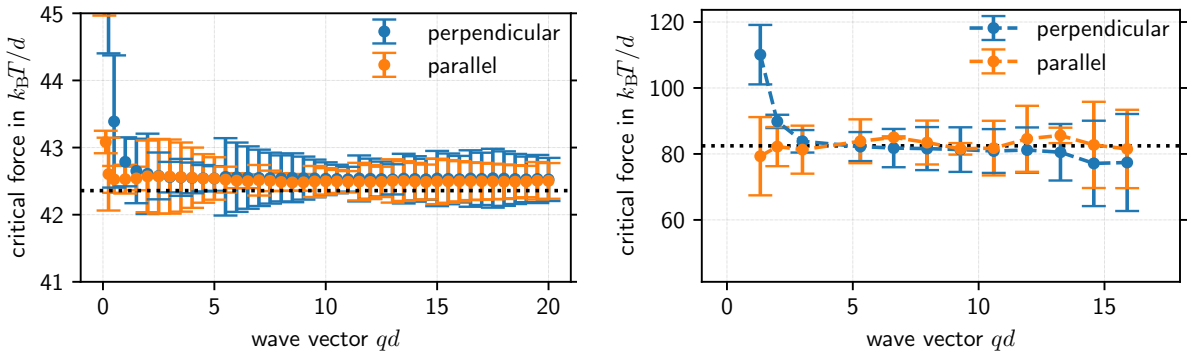

Figure 5.19.: Critical force obtained by extrapolating the density correlation functions ϕ^s at long, but finite times (as shown in Figure 5.18) linearly to zero for the theory (left) and the simulations (right). The uncertainties are determined from the fit. The dotted black horizontal line shows the true critical force for the theory (left) and the average for $qd > 2.5$ with $82.4\,k_BT/d$ in the simulations (right).

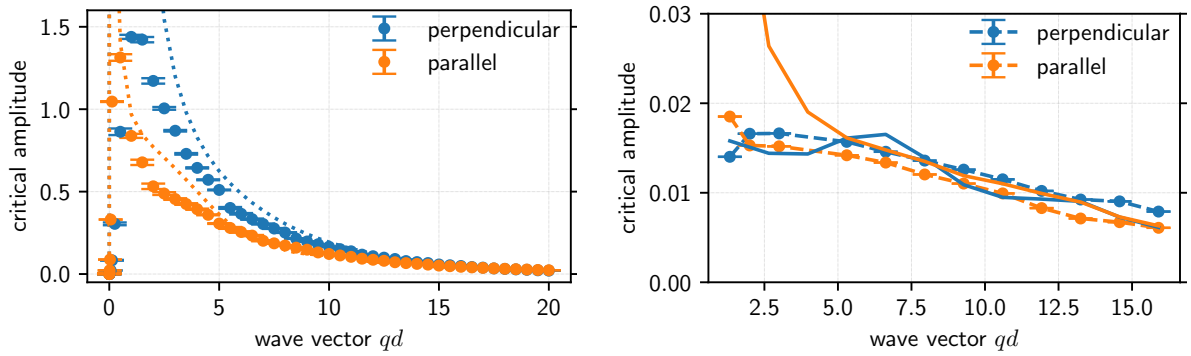

Figure 5.20.: Critical amplitudes as function of wave vector for MCT (left) and simulations (right). The symbols show the critical amplitudes obtained from the linear fits of the long time values of the correlation functions. The dashed lines in the left panel show the true critical amplitude obtained from the long time limit. The solid lines in the right panel show the critical amplitude obtained from the long time limit of the prefactor of the critical law as presented in Figure 5.22 (averaged in the time window $[10, 25]d^2/D_0$).

find that this method systematically overestimates the critical force. Nevertheless, the exact critical force is within the error bars. The strongest deviations are observed for the small wave vectors, also with the largest uncertainties as they bend down quite strongly.

For the simulations, the strongest test of this prediction is the question of consistency, i.e. whether the critical force obtained for all wave vectors yields the same result. This is confirmed in the right hand panel of Figure 5.19 for both parallel and perpendicular directions, we obtain the same critical force within the uncertainties. The smallest uncertainties are obtained for wave vectors between $qd = 5$ and $qd = 10$. We can also confirm the finding of the theory, that the predictions for small wave vectors perpendicular to the force direction yield large systematic deviations and large uncertainties. Averaging those results for $2.5 < qd < 12.5$, we obtain a critical force of $(83.1 \pm 5.8)\,k_BT/d$ from the parallel direction and $(81.5 \pm 5.8)\,k_BT/d$ for the perpendicular direction, where the uncertainties are also averaged. Taking into account that this procedure systematically overestimates the critical force, we can claim that there is an upper limit of the critical force of $81.5\,k_BT/d$.

From those fits, we can evaluate not only the intersection, but also the slope. This corresponds to the critical amplitude for a type A transition as introduced in (5.44). The eigenvector of the stability matrix is also proportional to this critical amplitude, but it is only defined up to a scalar multiple. Therefore, we have to multiply the eigenvector by a constant factor (given by the ratio of critical amplitude and eigenvector at a given wave vector) for the comparison. This comparison is shown in Figure 5.20. For the theory, we can compare the fit values (symbols with error bars) with the prediction for the long time limit obtained from the eigenvector of the stability matrix (shown as dashed line). There is a fair agreement for large wave vectors, but the deviations grow for small wave vectors. This is also a consequence of the fact that the critical eigenvector diverges for $q \to 0$.

For the simulations, we find a similar qualitative behavior. While the values of this critical amplitude are about two orders of magnitude smaller, we find also the trend that the critical amplitude becomes larger for smaller wave vectors. For the theory, the critical amplitude in the perpendicular direction is typically larger than the parallel direction. This behavior can be observed in the simulations as well even though the noise is more pronounced there. However, the increase for small wave vectors is not as pronounced as in theory.

With this, we have established that we can obtain the critical force from the vales of the correlation functions at long, but finite times. The prediction works best for intermediate wave vectors. Furthermore, we have also shown that the critical amplitude in theory and simulations shows a qualitative similar behavior. In the remainder of this chapter, we will analyze the critical dynamics.

To check the critical scaling, we multiply the correlation functions by t^α as shown in Figure 5.21. This procedure is called rectification, because in this representation, the curves become flat as long as they follow the critical law. If they decay faster than the critical law (above the critical force) the curves will bend downwards for long times, while they will bend upwards, if they decay slower than the critical law (below the critical force). The plateau value is given by the critical amplitude up to a scale factor if a factorization ansatz holds [Göt09, p. 440, Eq. (6.5d)]. This is visualized and verified by the dash-dotted black line in Figure 5.21, where the critical amplitude is obtained via (5.45). The scale is determined such that it fits to the critical law of the top left panel for $\phi^{s\perp}(q_r d = 2.5)$. Then, the height of the plateaus for the other panels is fixed and we find a good, but not perfect agreement of the actual critical laws with the prediction. We note that the critical law emerges only very close to the critical force and appears earlier for larger wave vectors. The correlation function perpendicular to the force for $q_x d = 2.5$ only shows a plateau for forces closer than $|\delta| < 10^{-4}$.

We will use the same rectification to check which simulations belong to forces above or below the critical force as shown in Figure 5.22. We choose the exponent 0.5 for the critical law, as it is the exponent found for both numerical systems for very long times and has some foundation by the analytical calculations. By separating the curves into upwards-bending and downwards-bending, we can again determine the critical force. The most flat behavior can be observed for $80\,k_\mathrm{B}T/\mathrm{d}$ for wave vectors $qd \geq 5.30$ in agreement with the prediction of the critical force using the extrapolation method. This justifies the choice of the critical exponent 0.5 as it leads to a consistent definition of the critical force. We also observe that for the small wave vector $qd = 2.65$, the splitting of the curves appears about a factor 5 to 10 later as for the largest wave vector and there is barely a plateau visible in the perpendicular direction. This agrees with the findings from the theoretical calculations shown in Figure 5.21.

Finally, we have a look at the scaling of the moments as observed in the simulations. They are shown as function of time in Figure 5.23 for different forces. Since they behave quite similarly, we determine their local exponent using (4.2), which is shown in the center column. Even though the data is noisy, we find that there is definitely no critical exponent between 0.34 and 0.5 as expected from theory for the mean displacement and the variance perpendicular to the force. It is rather approximately 0.8. For the variance parallel to the force direction the exponents are with 1.8 also much larger than 1, the exponent predicted by theory. Nevertheless, we find that the critical exponent for the variance in force direction is twice as large as the critical exponent for the variance perpendicular to the force direction. This property is shared with the prediction from theory even though the absolute exponents are different. To confirm these exponents, we also show the rectified moments in the right column of Figure 5.22. These curves do indeed flatten for large times, confirming the critical exponents. In contrast to the MCT calculations in Figure 5.16 almost all curves show the same exponent for long times, i.e. there is no strong force dependence of this critical behavior.

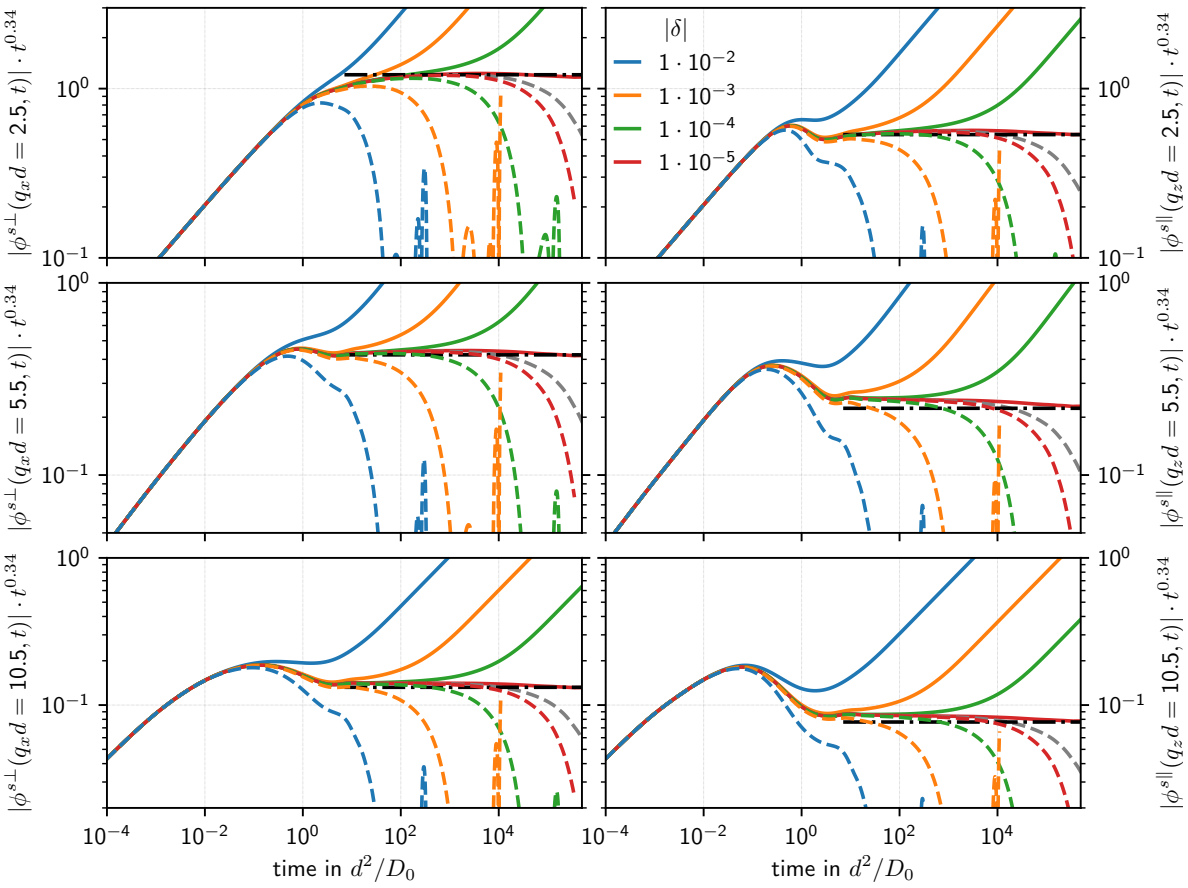

Figure 5.21.: Rectification plot of probe correlation functions for wave vectors perpendicular (left) and parallel (right) to the direction of the force for MCT calculations with $q_{\max} d = 20$. The numerically determined critical exponent is -0.34. The different forces are given by their relative distance the relative distance $\delta = (F_{\text{ex}} - F_{\text{low}})/F_{\text{low}}$. Solid lines show forces below F_{low}, dashed lines forces above. The dash-dotted black line is the critical amplitude, scaled such that it matches the critical behavior in the top left panel.

5.10. Conclusions

A detailed analytical and numerical analysis of the delocalization transition revealed critical power laws for the nonergodicity parameters as a function of the relative distance to the critical force as well as for the time evolution of the correlation functions and moments at the critical force. Since our memory functional is a multivariate rational function instead of a simple multivariate polynomial as in classical MCT, there are multiple representations of the problem with different consequences. One challenge with the analytical approach via the stability matrix as introduced by Götze concerns the limit of a multivariate rational function when both enumerator and denominator go to zero. Another consequence is that the factorization ansatz is only valid for the primitive memory functionals, but not for the correlation functions. While it still holds approximately for large wave vectors, it breaks down for small wave vectors, which finds its expression in a divergence of the critical amplitude (the eigenvector of the stability matrix corresponding to the eigenvalue 0) for $q \to 0$ with a q_x^{-2} scaling for the perpendicular and q_z^{-1} scaling for the parallel direction.

The type of the transition cannot be determined analytically and is therefore investigated

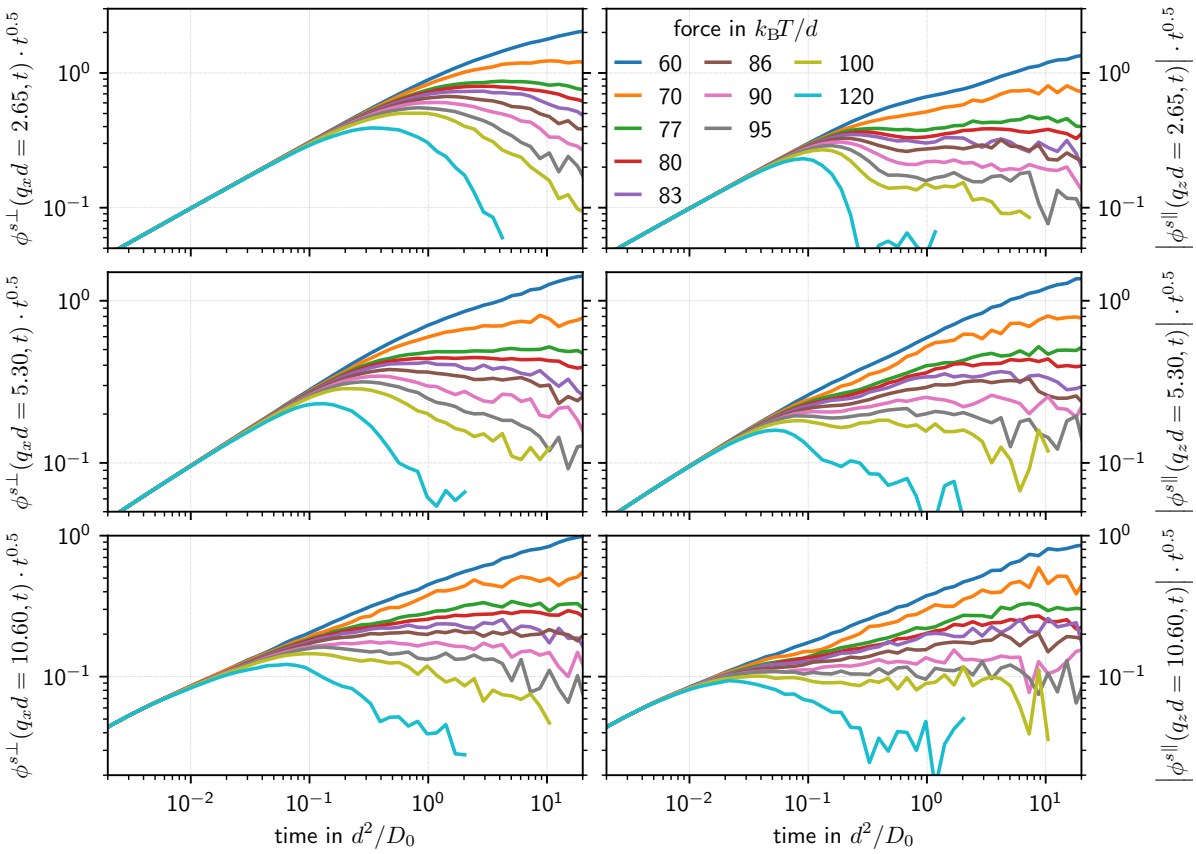

Figure 5.22.: Rectification plot of probe correlation functions for wave vectors perpendicular (left) and parallel (right) to the direction of the force for the simulations. The forces range from $60\,k_BT/d$ to $120\,k_BT/d$ as labeled and the wave numbers are $qd = 2.65$ (top row), $qd = 5.30$ (center row) and $qd = 10.60$ (bottom row).

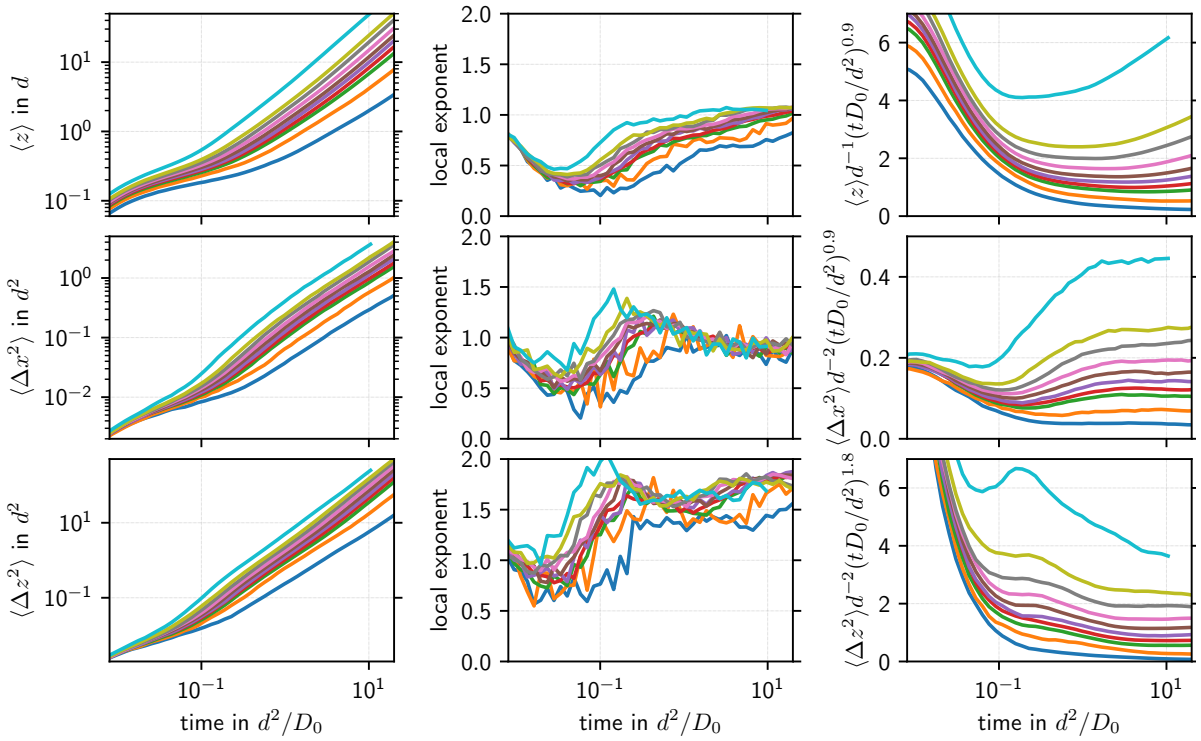

Figure 5.23.: Critical laws for mean displacement (top row), variance $\langle x^2 \rangle$ perpendicular to the force (center row) and variance $\langle \Delta z^2 \rangle$ parallel to the force (bottom row) in the simulations for different forces (color code as in Figure 5.22). The left column shows the evolution, the center row their local exponent and the right row the rectified moments scaled with exponent 0.9 for the mean displacement and the perpendicular variance and 1.8 for the variance parallel to the force.

numerically for the full model as well as numerically for different models for the bifurcation. Most of the calculations suggest a continuous decrease to zero at the critical force, but the asymptotic behavior is different in every model. Even for the full model, we find a type A like behavior (i.e. linear decrease to 0, critical exponent of 1/2) for a grid-cutoff of $q_{\max} d \leq 14$, while a discretization with a grid-cutoff of $q_{\max} d \geq 20$ exhibits a type B like behavior (square-root-like decrease to 0, critical exponent different from 1/2). The numerical results in Laplace space suggest that even in this case there is a crossover to an exponent of 1/2 at very long times. Assuming a power law scaling for the correlation functions, we can derive a critical law for the dynamics of the moments. We predict that the exponent for the variance parallel to the force is twice as large as the exponent for the variance perpendicular to the force and for the mean displacement. These findings are supported by the analysis of simulations. This analysis provides another consistent way to determine the critical force in non-ideal systems. The exponents for the moments are larger than predicted by MCT, but there is a good qualitative agreement with the simulation.

6. Schematic model

Nature has a great simplicity and, therefore, a great beauty.

(Richard Feynman [Fey80, p. 176])

Since solving the full microscopic model is demanding and time consuming, we also look at schematic models, which are designed to reproduce the time evolution for some characteristic wave vectors, see [Göt09, p. 209ff, Sec. 4.2.4]. Unfortunately there is no general recipe how to design those schematic models. Their utility can only be justified afterwards. In this section, we will analyze a schematic model for our MCT equations for active microrheology in dense suspensions developed by Gustavo Abade.

6.1. Equations of motion

The schematic model by Gustavo Abade contains three correlator modes: the bath correlation function ϕ_b, the probe correlator perpendicular to the force direction $\phi_\perp$ and the complex valued probe correlator in the force direction $\phi_\parallel$. The bath correlator is determined by the F_{12} model, see [Göt09, p. 203, Eq. (4.32b)] for the definition and [Göt09, Sec. 4.3.2, p. 224-228] for a discussion of the features.

6.1.1. Equations of motion in time domain

The equations of motion are given by the classical equations for an overdamped 3-component schematic model

$$\tau_i \partial_t \phi_i + \phi_i(t) + \int_0^t m_i(t-t')\partial_{t'}\phi_i(t')\mathrm{d}t' = 0 \tag{6.1}$$

for $i \in \{b, \parallel, \perp\}$ (cf. [Göt09, p. 202]). The integro-differential equation for the bath correlator mode ϕ_b is given by the F_{12} model [Göt09, p. 203. Eq. (4.32b)]. Its time scale is τ_b and its memory kernel is given by the memory functional $\mathcal{F}_b$ via $m_b(t) = \mathcal{F}_b(\boldsymbol{\phi}(t))$ and

$$\mathcal{F}_b(x_b, x_\parallel, x_\perp) = v_1 x_b + v_2 x_b^2. \tag{6.2}$$

The parameters v_1 and v_2 determine the properties of the bath correlation function, for example the glass transition of the F_{12} model. As in the full model there is no coupling from the probe correlation functions to the bath. This model can be solved analytically. For $v_1 = 1$ and $v_2 \in [0, 1]$ it exhibits at continuous type A glass transition [Göt09, p. 226, Eq. (4.67a)], while there is a discontinuous type B glass transition for $v_1 = (2\lambda - 1)\lambda^{-2}$ and $v_2 = \lambda^{-2}$ for $\lambda \in [0.5, 1]$ [Göt09, p. 226, Eq. (4.67b)]. At $v_1 = v_2 = 1$, where both glass transition lines meet, there is a higher order glass transition singularity [Göt09, p. 226, Eq. (4.67c)].

The equations of motion for the probe correlator modes are inspired by the effective memory equations given in (2.159). This leads to the following relaxation times for the tagged-particle correlator

$$\tau_{\parallel} = \frac{\tau^s}{1 - \mathrm{i}\kappa_{\parallel} F_{\mathrm{ex}}} \tag{6.3a}$$

$$\tau_{\perp} = \tau^s, \tag{6.3b}$$

where τ^s describes the relaxation time without external force. The memory functions are given via the memory functional $m_{\parallel}(t) = \mathcal{F}_{\parallel}(\boldsymbol{\phi}(t))$ in the parallel direction

$$\mathcal{F}_{\parallel}(\boldsymbol{x}) = \frac{(v_1^s(x_{\parallel})^* + v_2^s x_{\perp}) x_b}{1 - \mathrm{i}\kappa_{\parallel} F_{\mathrm{ex}}}, \tag{6.4a}$$

where v_1^s and v_2^s describe the coupling of the perpendicular and the parallel component to the bath mode, while $\kappa_{\perp}$ (in the next equation) and $\kappa_{\parallel}$ describe the coupling of the probe correlators to the force. The star * denotes complex conjugation.

For the perpendicular direction, the memory kernel $m_{\perp}(t)$ is nonlocal in time, because it has to fulfill

$$\begin{aligned}
&\tau_{\perp} m_{\perp}(t) + \int_0^t m_{\perp}(t - t') \left(m_{\perp}^{zz}(t) + \mathrm{i}\kappa_{\perp} F_{\mathrm{ex}} m_{\perp}^{xz}(t)\right) \\
=&\tau_{\perp} \left(m_{\perp}^{xx}(t) - \mathrm{i}\kappa_{\perp} F_{\mathrm{ex}} m_{\perp}^{xz}(t)\right) + \int_0^t m_{\perp}^{xx}(t - t') m_{\perp}^{zz}(t') \mathrm{d}t' - \int_0^t m_{\perp}^{xz}(t - t') m_{\perp}^{xz}(t') \mathrm{d}t',
\end{aligned} \tag{6.4b}$$

with the local memory functionals

$$\mathcal{F}_{\perp}^{xx}(\boldsymbol{x}) = (v_1^s x_{\perp} + v_2^s \operatorname{Re}(x_{\parallel})) x_b, \tag{6.4c}$$

$$\mathcal{F}_{\perp}^{xz}(\boldsymbol{x}) = -\mathrm{i} v_2^s \operatorname{Im}(x_{\parallel}) x_b, \tag{6.4d}$$

$$\mathcal{F}_{\perp}^{zz}(\boldsymbol{x}) = v_2^s \operatorname{Re}(x_{\parallel}) x_b. \tag{6.4e}$$

This definition mimics the equations of motion for the effective memory kernel of the full model.

6.1.2. Equations of motion in Laplace domain

Using the Laplace transform (B.1), the equations of motion transform into

$$\tau_i (s\tilde{\phi}_i(s) - 1) + \tilde{\phi}_i(s) + \tilde{m}_i(s)(s\tilde{\phi}_i(s) - 1) = 0. \tag{6.5}$$

The nonlocal integral condition (6.4b) transforms into

$$\tilde{m}_{\perp}(s) \left(\tau_{\perp} + \tilde{m}_{\perp}^{zz}(s) + \mathrm{i}\kappa_{\perp} F_{\mathrm{ex}} \tilde{m}_{\perp}^{xz}(s)\right) = \tilde{m}_{\perp}^{xx}(s) \left(\tau_{\perp} + \tilde{m}_{\perp}^{zz}(s)\right) - \tilde{m}_{\perp}^{xz}(s) \left(\mathrm{i}\kappa_{\perp} F_{\mathrm{ex}} \tau_{\perp} + \tilde{m}_{\perp}^{xz}(s)\right). \tag{6.6}$$

For the ease of notation, we drop the tilde for the Laplace transformed quantities and only use the argument s to indicate the Laplace frequency. It will be clear from the context in which domain we operate.

The Laplace transforms of the local memory functions are nontrivial, because they always contain a product of bath correlator and tagged-particle correlator. However, if one assumes the bath correlator to be constant and equal to its long time limit $\phi_b(t) \approx f := \lim_{t\to\infty} \phi_b(t)$, the memory functionals are linear in the remaining correlators. This corresponds to the constant bath approximation in Section 2.4.7. Then, the Laplace transform of the memory functionals is given by the memory functionals applied to the Laplace transform of the correlators

$$\tilde{m}_i(s) = \mathcal{F}_i(f, \tilde{\phi}_\parallel(s), \tilde{\phi}_\perp(s)). \tag{6.7}$$

For the beta-scaling analysis it will be convenient to rewrite the equations of motion in Laplace space for the constant bath case in terms of the real quantities $\phi_1 := \operatorname{Re}\phi_\parallel$, $\phi_2 := \operatorname{Im}\phi_\parallel$ and $\phi_3 := \phi_\perp$:

$$-\frac{\phi_1(s)\left(\phi_1(s)s-1\right)+\phi_2^2(s)s}{\phi_2^2(s)s^2+\left(\phi_1(s)s-1\right)^2} = \sum_{i\in I}\left(V_\parallel^{\mathrm{re}}\right)_i \phi_i(s) + \tau_1 \tag{6.8a}$$

$$\frac{\phi_2(s)}{\phi_2^2(s)s^2+\left(\phi_1(s)s-1\right)^2} = \sum_{i\in I}\left(V_\parallel^{\mathrm{im}}\right)_i \phi_i(s) + \tau_2 \tag{6.8b}$$

$$\frac{\phi_3(s)}{1-s\phi_3(s)} = \frac{\sum_{i,j\in I}\left(W_\perp\right)_{ij}\phi_i(s)\phi_j(s) + \sum_{i\in I}\left(V_\perp\right)_i\phi_i(s)}{\tau_3 + \sum_{i\in I}\left(U_\perp\right)_i\phi_i(s)} + \tau_3 \tag{6.8c}$$

with the abbreviations $I := \{1,2,3\}$,

$$V_\parallel^{\mathrm{re}} = \frac{f}{F_{\mathrm{ex}}^2\kappa_\parallel^2+1}\begin{pmatrix} v_1^s \\ F_{\mathrm{ex}}\kappa_\parallel v_1^s \\ v_2^s \end{pmatrix}, \tag{6.9a}$$

$$V_\parallel^{\mathrm{im}} = \frac{f}{F_{\mathrm{ex}}^2\kappa_\parallel^2+1}\begin{pmatrix} F_{\mathrm{ex}}\kappa_\parallel v_1^s \\ -v_1^s \\ F_{\mathrm{ex}}\kappa_\parallel v_2^s \end{pmatrix}, \tag{6.9b}$$

$$W_\perp = f^2\begin{pmatrix} (v_2^s)^2 & 0 & \frac{v_1^s v_2^s}{2} \\ 0 & (v_2^s)^2 & 0 \\ \frac{v_1^s v_2^s}{2} & 0 & 0 \end{pmatrix}, \tag{6.9c}$$

$$V_\perp = \tau_3 f\begin{pmatrix} v_2^s \\ -\kappa_\perp F_{\mathrm{ex}} v_2^s \\ v_1^s \end{pmatrix}, \tag{6.9d}$$

$$U_\perp = v_2^s f\begin{pmatrix} 1 \\ \kappa_\perp F_{\mathrm{ex}} \\ 0 \end{pmatrix}, \tag{6.9e}$$

$$\tau_1 = \frac{\tau_s}{\kappa_\parallel^2 F_{\mathrm{ex}}^2+1}, \tag{6.9f}$$

$$\tau_2 = \frac{\tau^s\kappa_\parallel F_{\mathrm{ex}}}{\kappa_\parallel^2 F_{\mathrm{ex}}^2+1}, \tag{6.9g}$$

$$\tau_3 = \tau^s. \tag{6.9h}$$

Since the main feature of the bath correlator is the glass transition, we fix $v_2 = 2$ for the F_{12} model and choose v_1 according to ε, the relative distance to the glass transition, via

$$v_1 = 2(\sqrt{2}-1) + \frac{\varepsilon}{\sqrt{2}-1}, \tag{6.10}$$

unless specified otherwise. Furthermore, we fix $\kappa_\parallel = \kappa_\perp = 1$ and $\tau^s = \tau_b = 1$ unless stated otherwise to reduce the parameter space.

6.1.3. Solution methods

The problem stated above is tackled using both analytical and numerical approaches. For the numerical solutions, we employ all the techniques presented in Chapter 3, since the structure of the equations is the same. The major simplification with the schematic models is the reduction of dimensionality. Instead of 50×50 complex valued wave vectors, we only have to deal with three. Furthermore, the memory integrals are replaced by polynomials, which eliminates another time consuming task. The computer program to solve the time evolution of the schematic model has been implemented by Gustavo Abade, while the Laplace space solution and nonergodicity parameter calculations have been implemented by myself.

6.2. Bifurcation analysis

The following bifurcation analysis follows the same path as the full analysis in Chapter 5. We start with some analytical calculations to characterize the bifurcation of this model. These predictions will be tested in the following sections.

6.2.1. Nonergodicity parameters

The nonergodicity parameters are defined via the long time limits of the correlation functions $f_i := \lim_{t\to\infty} \phi_i(t)$. They have to fulfill the following set of equations, which can be obtained by multiplying (6.8) with s and then taking the $s \to 0$-limit using the relation (B.3) as discussed in Section 2.4.6. The equations read

$$-\frac{f_1\left(f_1-1\right)+f_2^2}{f_2^2+\left(f_1-1\right)^2} = \sum_{i\in I}\left(V_\parallel^{\mathrm{re}}\right)_i f_i, \tag{6.11a}$$

$$\frac{f_2}{f_2^2+\left(f_1-1\right)^2} = \sum_{i\in I}\left(V_\parallel^{\mathrm{im}}\right)_i f_i, \tag{6.11b}$$

$$\frac{f_3}{1-f_3} = \frac{\sum_{i,j\in I}\left(W_\perp\right)_{ij} f_i f_j}{\sum_{i\in I}\left(U_\perp\right)_i f_i}. \tag{6.11c}$$

These equations do not rely on the constant bath approximation, because this long time limit is exact. From a mathematical point of view, we have to find the roots of the following set of nonlinear equations

$$J_1(\boldsymbol{x}) = -\frac{x_1\left(x_1-1\right)+x_2^2}{x_2^2+\left(x_1-1\right)^2} - \sum_{i\in I}\left(V_\parallel^{\mathrm{re}}\right)_i x_i, \tag{6.12}$$

$$J_2(\boldsymbol{x}) = \frac{x_2}{x_2^2+\left(x_1-1\right)^2} - \sum_{i\in I}\left(V_\parallel^{\mathrm{im}}\right)_i x_i, \tag{6.13}$$

$$J_3(\boldsymbol{x}) = \frac{x_3}{1-x_3} - \frac{\sum_{i,j\in I}\left(W_\perp\right)_{ij} x_i x_j}{\sum_{i\in I}\left(U_\perp\right)_i x_i}. \tag{6.14}$$

The implicit function theorem guarantees a solution, if the Jacobian of this system is invertible. On the other hand, when multiple solutions coalesce at a bifurcation, this Jacobian is not invertible as we will see in the following. Anticipating that the nonergodicity parameters will go

to zero at the critical point, we can simplify the fractions by $x_i \ll 1$ and neglecting quadratic terms. This allows us to define the critical Jacobian matrix

$$S^c(\boldsymbol{x})_{1j} = \frac{\partial}{\partial x_j} J_1^c(\boldsymbol{x}) = \delta_{1j} - \left(V_\parallel^{\mathrm{re}}\right)_j, \tag{6.15a}$$

$$S^c(\boldsymbol{x})_{2j} = \frac{\partial}{\partial x_j} J_2^c(\boldsymbol{x}) = \delta_{2j} - \left(V_\parallel^{\mathrm{im}}\right)_j, \tag{6.15b}$$

$$S^c(\boldsymbol{x})_{3j} = \frac{\partial}{\partial x_j} J_3^c(\boldsymbol{x}) = \delta_{3j} - \frac{2\sum_{i\in I}(W_\perp)_{ij}\, x_j - x_3\,(U_\perp)_j}{\sum_{i\in I}(U_\perp)_i\, x_i}, \tag{6.15c}$$

where the symmetry $W_\perp = (W_\perp)^T$ and the condition for the root $F_3^c(\boldsymbol{x}) = 0$ have been used to identify parts of the derivatives with x_3. S^c is also called *stability matrix*.

6.2.2. Ergodic integrals

We can also evaluate the limit $s \to 0$ for the equations (6.5) in the ergodic case. In contrast to the nonergodic cases before, we now must rely on the constant bath assumption to keep the memory functionals linear in the tagged-particle correlator. This limit provides us with the time integral over the correlation function, according to

$$\lim_{s\to 0}\phi_i(s) = \lim_{s\to 0}\int_0^\infty \phi_i(t)\mathrm{e}^{-st}\mathrm{d}t = \int_0^\infty \phi_i(t)\mathrm{d}t\,, \tag{6.16}$$

which holds when $\phi_i(t)$ decays sufficiently fast (such that the integral is finite) according to Lebesgue's dominated convergence theorem. The corresponding equations can be obtained from (6.8) by setting $s = 0$, which results in

$$\phi_1(0) = \sum_{i\in I}\left(V_\parallel^{\mathrm{re}}\right)_i \phi_i(0) + \tau_1, \tag{6.17a}$$

$$\phi_2(0) = \sum_{i\in I}\left(V_\parallel^{\mathrm{im}}\right)_i \phi_i(0) + \tau_2, \tag{6.17b}$$

$$\phi_3(0) = \frac{\sum\limits_{i,j\in I}(W_\perp)_{ij}\,\phi_i(0)\phi_j(0) + \sum\limits_{i\in I}(V_\perp)_i\,\phi_i(0)}{\tau_3 + \sum\limits_{i\in I}(U_\perp)_i\,\phi_i(0)} + \tau_3. \tag{6.17c}$$

6.2.3. Critical dynamics

In order to derive equations for the critical dynamics, we can approximate (6.8) for small s and large ϕ_i. Summarizing, we get the following approximate equations of motion close to the critical force

$$\phi_1(s) + s(\phi_1^2(s) - \phi_2^2(s)) \approx \sum_{i\in I}\left(V_\parallel^{\mathrm{re}}\right)_i \phi_i(s) + \tau_1, \tag{6.18a}$$

$$\phi_2(s) + 2s\phi_1(s)\phi_2(s) \approx \sum_{i\in I}\left(V_\parallel^{\mathrm{im}}\right)_i \phi_i(s) + \tau_2, \tag{6.18b}$$

$$\phi_3(s) + s\phi_3^2(s) \approx \frac{\mathcal{W}(\boldsymbol{\phi}(s))}{\mathcal{U}(\boldsymbol{\phi}(s))} + \frac{\mathcal{V}(\boldsymbol{\phi}(s))}{\mathcal{U}(\boldsymbol{\phi}(s))} - \tau_3 \frac{\mathcal{W}(\boldsymbol{\phi}(s))}{(\mathcal{U}(\boldsymbol{\phi}(s)))^2} + \tau_3, \tag{6.18c}$$

with the abbreviations

$$\mathcal{W}(\boldsymbol{x}) = \sum_{i,j\in I} (W_\perp)_{ij}\, x_i x_j, \tag{6.19a}$$

$$\mathcal{V}(\boldsymbol{x}) = \sum_{i\in I} (V_\perp)_i\, x_i, \tag{6.19b}$$

$$\mathcal{U}(\boldsymbol{x}) = \sum_{i\in I} (U_\perp)_i\, x_i. \tag{6.19c}$$

Next, we use the ansatz as obtained for the full model

$$\phi_i(s) = h_i s^{-1/2} + c_i + \mathcal{O}(s^{1/2}) \tag{6.20}$$

to find an approximate solution for $\phi_i(s)$. This ansatz implies $s^2\phi^3(s) = \mathcal{O}(s^{1/2})$ and $\phi^{-1} = \mathcal{O}s^{1/2}$ and results in

$$0 = s^{-1/2}\left(h_1 - \sum_{i\in I}\left(V_\parallel^{\mathrm{re}}\right)_i h_i\right) + \left(c_1 + h_1^2 - h_2^2 - \sum_{i\in I}\left(V_\parallel^{\mathrm{re}}\right)_i c_i - \tau_1\right) + \mathcal{O}(s^{1/2}), \tag{6.21a}$$

$$0 = s^{-1/2}\left(h_2 - \sum_{i\in I}\left(V_\parallel^{\mathrm{im}}\right)_i h_i\right) + \left(c_2 + 2h_1h_2 - \sum_{i\in I}\left(V_\parallel^{\mathrm{im}}\right)_i c_i - \tau_2\right) + \mathcal{O}(s^{1/2}), \tag{6.21b}$$

$$\begin{aligned} 0 = {} & s^{-1/2}\left(h_3 - \frac{\sum_{i,j\in I}(W_\perp)_{ij}\, h_i h_j}{\sum_{i\in I}(U_\perp)_i\, h_i}\right) \\ & + \left(c_3 + h_3^2 - \frac{\sum_{i,j\in I} 2\,(W_\perp)_{ij}\, h_i c_j + \sum_{i\in I}(V_\perp)_i\, h_i - h_3(\tau_3 + \sum_i (U_\perp)_i\, c_i)}{\sum_{i\in I}(U_\perp)_i\, h_i} - \tau_3\right) + \mathcal{O}(s^{1/2}), \end{aligned} \tag{6.21c}$$

where we used again the symmetry of $W_\perp$ in the last equation and made use of the determining equation for h_3, as introduced below in (6.22c) to simplify the last equation. A solution now has to fulfill the brackets for the different powers of s. The factor $s^{-1/2}$ yields a fixed point equation for the critical amplitude $\boldsymbol{h}$

$$h_1 = \sum_{i\in I}\left(V_\parallel^{\mathrm{re}}\right)_i h_i, \tag{6.22a}$$

$$h_2 = \sum_{i\in I}\left(V_\parallel^{\mathrm{im}}\right)_i h_i, \tag{6.22b}$$

$$h_3 = \frac{\sum_{i,j\in I}(W_\perp)_{ij}\, h_i h_j}{\sum_{i\in I}(U_\perp)_i\, h_i}. \tag{6.22c}$$

Note that any multiple of a solution is again a solution of this fixed point equation. If such a solution is found, we can use the bracket for s^0 and the solution for $\boldsymbol{h}$ to find a system of linear equations for $\boldsymbol{c}$

$$c_1 - \sum_{i\in I}\left(V_\parallel^{\mathrm{re}}\right)_i c_i = \tau_1 - h_1^2 + h_2^2, \tag{6.23a}$$

$$c_2 - \sum_{i\in I}\left(V_\parallel^{\mathrm{im}}\right)_i c_i = \tau_2 - 2h_1h_2, \tag{6.23b}$$

$$c_3 - \frac{\sum_{i,j\in I} 2\,(W_\perp)_{ij}\, h_i c_j - h_3 \sum_i (U_\perp)_i\, c_i}{\sum_{i\in I}(U_\perp)_i\, h_i} = \tau_3 - h_3^2 + \frac{\sum_{i\in I}(V_\perp)_i\, h_i - h_3\tau_3}{\sum_{i\in I}(U_\perp)_i\, h_i}. \tag{6.23c}$$

The left hand side can be identified as the stability matrix (6.15) at the value $\boldsymbol{x} = \boldsymbol{h}$ applied to $\boldsymbol{c}$. Evaluating $S^c(\boldsymbol{h})\boldsymbol{h}$, we find that $S^c(\boldsymbol{h})\boldsymbol{h} = 0$, i.e. $\boldsymbol{h}$ is an eigenvector of the critical stability matrix $S^c(\boldsymbol{h})$ to the eigenvalue 0. This implies that $S^c(\boldsymbol{h})$ is not invertible. As we want to solve the system of linear equations (6.23), we need to make sure that the right hand side lies in the invertible subspace. This can be achieved by tuning the magnitude of the critical amplitude $\boldsymbol{h}$ such that the projection of the right hand side lies in the image of $S^c(\boldsymbol{h})$. It can be shown that this is accomplished by making the projection on a left eigenvector $\boldsymbol{e}_l$ corresponding to the eigenvalue 0 vanish (see Section C.4 for a proof). A left eigenvector fulfills $\boldsymbol{e}_l^T A = \lambda \boldsymbol{e}_l^T$ or equivalently $A^T \boldsymbol{e}_l = \lambda \boldsymbol{e}_l$. Let $\tilde{\boldsymbol{h}}$ be such a left eigenvector of $S^c(\boldsymbol{h})$ (which could be determined numerically), $\boldsymbol{h}$ a somehow normalized solution of (6.22) and α the magnitude of $\boldsymbol{h}$, which shall be determined. Then the solubility condition reads

$$0 = (\tau_1 + \alpha^2(-h_1^2 + h_2^2))\tilde{h}_1 + (\tau_2 - \alpha^2 2h_1h_2)\tilde{h}_2 + \left(\tau_3 - \alpha^2 h_3^2 + \frac{\sum_{i\in I}(V_\perp)_i h_i - h_3\tau_3}{\sum_{i\in I}(U_\perp)_i h_i}\right)\tilde{h}_3. \quad (6.24)$$

This is a quadratic equation for α and solved by

$$\alpha = \pm\sqrt{\frac{\left(\tilde{h}_1\tau_1 + \tilde{h}_2\tau_2 + \tilde{h}_3\tau_3\right)\mathcal{U}(\boldsymbol{h}) + \tilde{h}_3\mathcal{V}(\boldsymbol{h}) - h_3\tilde{h}_3\tau_3}{\left(h_1^2\tilde{h}_1 - h_2^2\tilde{h}_1 + 2h_1h_2\tilde{h}_2 + h_3^2\tilde{h}_3\right)(\mathcal{U}(\boldsymbol{h}))}}, \quad (6.25)$$

using the abbreviation (6.19).

6.2.4. Critical force

In this section, we will show how to derive an analytical expression for the critical force and the critical amplitude in the case $\kappa_\parallel = \kappa_\perp =: \kappa$. Starting point are the iteration equations for the critical amplitude (6.22). For the sake of simplicity, we replace v_1^s by βv_2^s. The iteration equations then read

$$h_1 = \frac{f v_2^s}{F_{\text{ex}}^2\kappa^2 + 1}\left(F_{\text{ex}}\kappa\beta h_2 + \beta h_1 + h_3\right), \quad (6.26a)$$

$$h_2 = \frac{f v_2^s}{F_{\text{ex}}^2\kappa^2 + 1}\left(F_{\text{ex}}\kappa\beta\left(\beta h_1 + h_3\right) - \beta h_2\right), \quad (6.26b)$$

$$h_3 = f v_2^s \frac{\beta h_1 h_3 + h_1^2 + h_2^2}{F_{\text{ex}}\kappa h_2 + h_1}. \quad (6.26c)$$

First, we want to rewrite the denominator in (6.26c). By combining (6.26a) and (6.26b), we find

$$h_1 + F_{\text{ex}}\kappa h_2 = f v_2^s(\beta h_1 + h_3). \quad (6.27)$$

Substituting this back into (6.26c), we get

$$h_3 = \frac{\beta h_1 h_3 + h_1^2 + h_2^2}{\beta h_1 + h_3} \Leftrightarrow h_3^2 = h_1^2 + h_2^2. \quad (6.28)$$

Using again (6.26a) and (6.26b) we can find an expression for the right hand side

$$h_1^2 + h_2^2 = \frac{f^2 \left(v_2^s\right)^2}{F_{\mathrm{ex}}^2 \kappa^2 + 1} \left(\beta^2 (h_1^2 + h_2^2 + 2\beta h_1 h_3 + h_3^2\right). \tag{6.29}$$

Solving this equation for $h_1^2 + h_2^2$, we get

$$h_1^2 + h_2^2 = \frac{\left(f v_2^s\right)^2 \left(2\beta h_1 h_3 + h_3^2\right)}{F_{\mathrm{ex}}^2 \kappa^2 + 1 - \left(f v_2^s\right)^2 \beta^2}. \tag{6.30}$$

Now this equation is substituted into (6.28) leading to

$$h_3^2 = \frac{\left(f v_2^s\right)^2 \left(2\beta h_1 h_3 + h_3^2\right)}{F_{\mathrm{ex}}^2 \kappa^2 + 1 - \left(f v_2^s\right)^2 \beta^2}. \tag{6.31}$$

Here, we have eliminated the variable h_2. In the next step we make use of the fact, that the iteration equation is scale invariant, i.e. any multiple of a solution is again a solution. This allows us to fix $h_3 = 1$ and we obtain a linear equation for h_1. Its solution is

$$h_1 = \frac{F_{\mathrm{ex}}^2 \kappa^2 + 1}{2\beta \left(f v_2^s\right)^2} - \frac{1 + \beta^2}{2\beta}. \tag{6.32}$$

Inserting this solution together with $h_3 = 1$ into (6.26a) and (6.26b), we get two equations to be solved for h_2

$$h_2 = \left(2F_{\mathrm{ex}} \kappa \left(f v_2^s\right)^3\right)^{-1} \left(F_{\mathrm{ex}}^4 \kappa^4 + \left(\beta f v_2^s\right)^3 - 1 - \left(F_{\mathrm{ex}}^2 \kappa^2 + 1\right) \left(\left(\beta f v_2^s\right)^2 + \beta f v_2^s + \left(f v_2^s\right)^2 - 2\right)\right), \tag{6.33a}$$

$$h_2 = \frac{F_{\mathrm{ex}} \kappa}{2 f v_2^s} \frac{F_{\mathrm{ex}}^2 \kappa^2 + 1 - \left(f v_2^s\right)^2 \left(1 - \beta^2\right)}{F_{\mathrm{ex}}^2 \kappa^2 + \beta f v_2^s + 1}. \tag{6.33b}$$

Since both equations must give the same result at the critical force, we can obtain an equation for the critical force by equating these two equations:

$$\begin{aligned} 0 =& F_{\mathrm{ex}}^6 \kappa^6 + F_{\mathrm{ex}}^4 \kappa^4 \left(3 - \left(f v_2^s\right)^2 (1 + 2\beta)\right) \\ &+ F_{\mathrm{ex}}^2 \kappa^2 \left(\left(f v_2^s\right)^4 \left(\beta^4 - \beta^2\right) - 2\beta \left(f v_2^s\right)^3 - 2 \left(f^2 v_2^s\right)^2 \left(2\beta^2 + 1\right) + 3\right) \\ &+ \left(f v_2^s\right)^4 \left(\beta^4 - \beta^2\right) - 2\beta \left(f v_2^s\right)^3 - \left(f v_2^s\right)^2 \left(2\beta^2 + 1\right) + 1. \end{aligned} \tag{6.34}$$

This is a third order polynomial in $F_{\mathrm{ex}}^2 \kappa^2$, which has the following three solutions

$$\left\{-1, \left(f v_2^s\right)^2 \left(\beta^2 + \frac{1}{2}\right) - 1 \pm \frac{\left(f v_2^s\right)^2}{2} \sqrt{8\beta^2 + 1 + \frac{8\beta}{f v_2^s}}\right\}. \tag{6.35}$$

As we want the critical force to be real, we have to choose the largest (positive) solution, which

is

$$F_\mathrm{c} = \frac{1}{\kappa}\left(\frac{(fv_2^s)^2}{2}\left(2\beta^2+1+\sqrt{8\beta^2+1+\frac{8\beta}{fv_2^s}}\right)-1\right)^{\frac{1}{2}}. \tag{6.36}$$

This solution can now be plugged into (6.32) and (6.33b) to find

$$h_1 = \frac{1}{4\beta}\left(\sqrt{8\beta^2+1+\frac{8\beta}{fv_2^s}}-1\right) \tag{6.37a}$$

$$h_2 = \frac{1}{2}\frac{F_\mathrm{c}\kappa\left(3+\sqrt{8\beta^2+1+8\beta/fv_2^s}\right)}{fv_2^s\left(2\beta^2+1+\sqrt{8\beta^2+1+8\beta/fv_2^s}\right)+2\beta}. \tag{6.37b}$$

By definition, we had $h_3 = 1$. Finally, one has to replace β by v_1^s/v_2^s to get the result in terms of v_1^s and v_2^s, which will be discussed in Section 6.3.2 for the critical force and in Section 6.4 for the critical dynamics.

6.3. Static analysis

In this section we cover the aspects which can be accessed by solving only the equations for the long time limit. As their solution is only nontrivial in the glassy state, we are restricted to the regime $\varepsilon > 0$, which implies $f > 0$. Their determining equations are given in (6.11), which can be solved analytically in the cases $v_1^s = 0$ or $v_2^s = 0$, but has to be determined numerically in the other cases.

6.3.1. Phase diagram

As a primer, we present the phase diagram of the schematic model with respect to the delocalization transition in Figure 6.1. The critical force can be determined analytically as shown in Section 6.2.4. For forces smaller than the critical force, we find nonergodic solutions, while forces larger than the critical force have again ergodic solutions. The dashed line there shows $\varepsilon = 0.1$, for which we show the following beta scaling analysis. An interesting feature of the parameter set $v_1^s = 0$, $v_2^s = 2$ is that the critical force at the glass transition is zero. This implies that the coupling of the tagged particle to the bath is so weak, that it is still delocalized although the bath is already frozen. Only deep in the glass ($\varepsilon > 0.07$) the tagged particle will also localize and thus one finds a finite critical force. This could describe the case of a probe particle, which is smaller than the bath particles. They can delocalize in a glass as well if the voids between the bath particles are large enough [BB98; BT87].

6.3.2. Critical force

In Section 6.2.4 we derived an analytical expression for the critical force for $\kappa_\parallel = \kappa_\perp =: \kappa$. It is given as

$$F_\mathrm{c} = \frac{\sqrt{2}}{2\kappa}\left(f^2\left(2\left(v_1^s\right)^2+\left(v_2^s\right)^2\right)-2+\sqrt{8f^4\left(v_1^s v_2^s\right)^2+\left(fv_2^s\right)^4+8f^3v_1^s\left(v_2^s\right)^2}\right)^{\frac{1}{2}}. \tag{6.38}$$

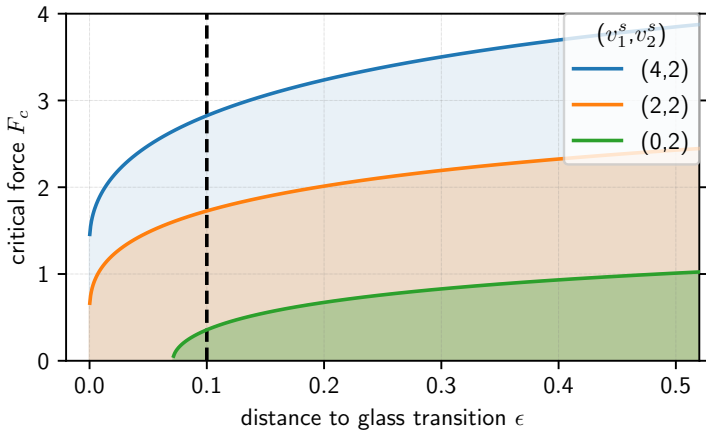

Figure 6.1.: Phase diagram for the schematic model for different coupling parameters v_1^s, v_2^s. For the other model parameters see text. The solutions are nonergodic in the shaded regions. The dashed line indicates the glass parameter for the bifurcation analysis.

We show the value of the critical force as function of v_1^s and v_2^s for $\varepsilon = 0.1$ in Figure 6.2. The contour lines in the (v_1^s, v_2^s)-plane can be obtained by solving (6.38) for v_2^s

$$v_2^s = \frac{\left|F_c^2\kappa^2 - (fv_1^s)^2 + 1\right|}{f\sqrt{F_c^2\kappa^2 + (fv_1^s)^2 + 2fv_1^s + 1}}. \tag{6.39}$$

Specifying $F_{\text{ex}} = 0$, we find the condition for a nonzero critical force to be

$$\frac{1}{f} < v_1^s + v_2^s \tag{6.40}$$

and the line for the onset of a nonzero critical force is drawn in red. Even though this figure is based on the analytical results, we verified that it coincides with the numerical solution. To strengthen this analytical finding, we will always use the analytical value of the critical force to determine the distance δ from the critical force. If there were deviations between the numerical and analytical solutions, the results would not be consistent.

6.3.3. Transition type

An important question is the type of the transition, i.e. the question how do the nonergodicity parameters behave close to the critical force. If they go continuously (and linearly) to zero, we call it a *type A* transition. If they jump from a finite value to zero (and behave squarerootlike in the vicinity of the jump), we call it a *type B* transition. The transition is shown exemplarily for $v_1^s = v_2^s = 2$ and $\varepsilon = 0.1$ in Figure 6.3a. Hence, we find numerically a textbook example of a type A transition.

For other parameters this transition looks similar. Conversion from the critical parameter δ to the external force is done by $F_{\text{ex}} = (1+\delta)F_{\text{c}}$, i.e. the transition occurs at $\delta = 0$. For $v_1^s = 0$, we can even proof that this is a type A transition, because we can find analytical expressions

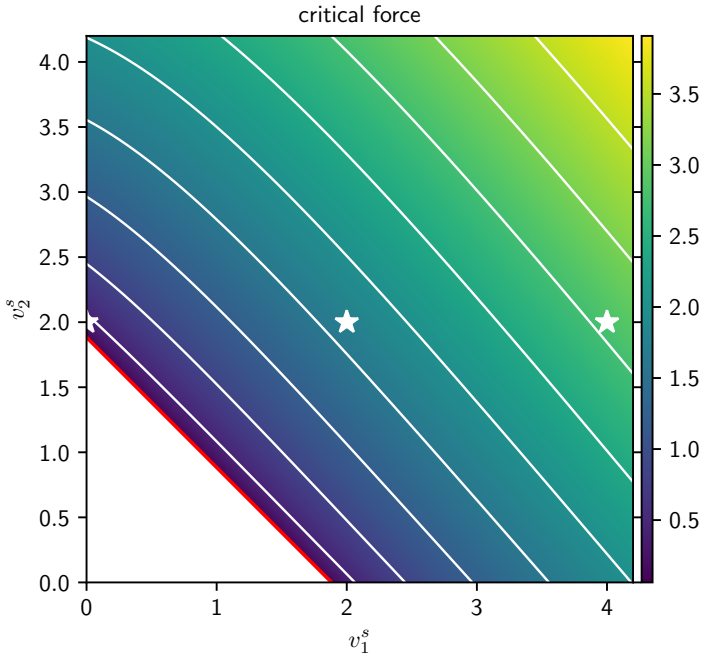

Figure 6.2.: Critical force value as function of the coupling parameters v_1^s and v_2^s for $\varepsilon = 0.1$. In the white region there is no critical force. The red boundary is given by $v_1^s + v_2^s = 1/f$. The parameters as in Figure 6.1 are shown as stars.

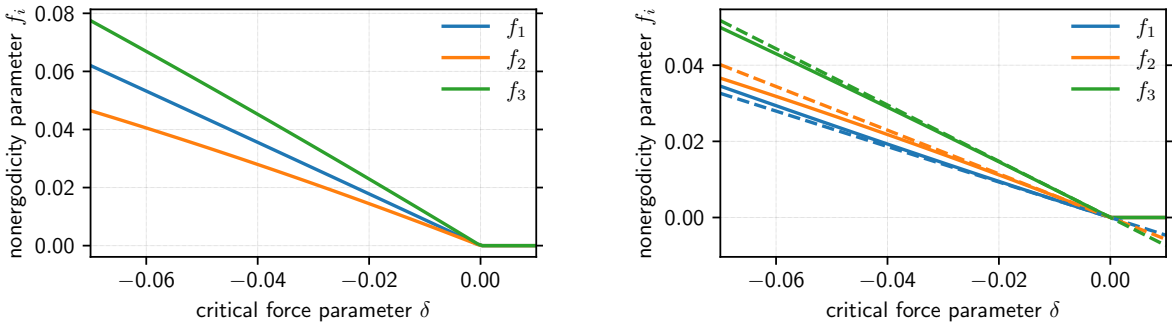

(a) Numerical solution for $v_1^s = v_2^s = 2$

(b) Analytical solution for $v_1^s = 0$, $v_2^s = 2$

Figure 6.3.: Nonergodicity parameters close to the critical force F_c for $\varepsilon = 0.1$. The distance to the critical force is given by $\delta = (F_{ex} - F_c)/F_c$. (a) Numerical solution. (b) Analytic solution (solid) and first order expansion around $\delta = 0$ (dashed).

for the nonergodicity parameters. They are given by

$$f_1 = \frac{\left(F_{ex}^2\kappa_\parallel\kappa_\perp - (fv_2^s)^2 + 1\right)\left(F_{ex}^2\kappa_\parallel\kappa_\perp - (fv_2^s)^2 - fv_2^s\right)}{F_{ex}^4{\kappa_\parallel}^2{\kappa_\perp}^2 - 2F_{ex}^2f\kappa_\parallel\kappa_\perp v_2^s\left(fv_2^s+1\right) + \left(F_{ex}^2{\kappa_\parallel}^2 + (fv_2^s)^2\right)\left(fv_2^s+1\right)^2}, \tag{6.41a}$$

$$f_2 = -\frac{F_{ex}\kappa_\parallel\left(fv_2^s+1\right)\left(F_{ex}^2\kappa_\parallel\kappa_\perp - f^2{v_2^s}^2 + 1\right)}{F_{ex}^2{\kappa_\parallel}^2\left(fv_2^s+1\right)^2 + \left((fv_2^s)^2 + fv_2^s - F_{ex}^2\kappa_\parallel\kappa_\perp\right)^2}, \tag{6.41b}$$

$$f_3 = -\frac{F_{ex}^2\kappa_\parallel\kappa_\perp - (fv_2^s)^2 + 1}{fv_2^s\left(fv_2^s+1\right)}. \tag{6.41c}$$

Expansion around $F_\mathrm{c} = \sqrt{((fv_2^s)^2 - 1)/\kappa_\parallel \kappa_\perp}$ via $F_\mathrm{ex} = F_\mathrm{c}(1+\delta)$ for $\delta < 0$ yields in first order

$$f_1 = -\frac{2\kappa_\perp (fv_2^s - 1)}{f^2 \kappa_\parallel v_2^{s2} - \kappa_\parallel + \kappa_\perp}\delta + \mathcal{O}(\delta^2), \tag{6.42a}$$

$$f_2 = -\frac{2\kappa_\parallel \kappa_\perp F_\mathrm{c}\,(fv_2^s - 1)}{f^2 \kappa_\parallel v_2^{s2} - \kappa_\parallel + \kappa_\perp}\delta + \mathcal{O}(\delta^2), \tag{6.42b}$$

$$f_3 = -\frac{2(fv_2^s + 1)}{fv_2^s}\delta + \mathcal{O}(\delta^2). \tag{6.42c}$$

These results are illustrated in Figure 6.3b. We find agreement between the expansion and the exact result for $-0.01 < \delta \leq 0$.

We also note that this model for $v_1^s = 0$ does not permit arbitrarily large prefactors in (6.42). To achieve this, one needs to fulfill $\kappa_\perp = \kappa_\parallel(1 - (fv_2^s)^2)$, but $1 - (fv_2^s)^2$ is negative (for a real valued critical force) and as a result $\kappa_\perp$, too. In the case $\kappa_\parallel = \kappa_\perp$ one needs $v_2^s \to 0$ for a diverging derivative. But this implies also $F_\mathrm{c} \to 0$. Therefore, there is no set of parameters $v_2^s, \kappa_\parallel, \kappa_\perp$, which could lead to diverging large prefactors as found in the full model (cf. Figure 5.7).

6.3.4. Ergodic integrals

Finally, the equations (6.17) for the ergodic integrals as introduced in Section 6.2.2 can be solved by a fixed point iteration as well. We expect $\phi_i(s=0)$ to diverge at the critical force, because nonergodic functions are not integrable. Numerically, we find for $v_1^s = v_2^s = 2$ and $\varepsilon = 0.1$ that $\phi_i(s=0)$ diverges like δ^{-1} when approaching the bifurcation.

To visualize this power law, we plot $\phi_i(s=0)\delta$ for $v_1^s = v_2^s = 2$ and $\varepsilon = 0.1$ in Figure 6.4, which results in a constant value for $\delta < 10^{-3}$. The reciprocal power law can be found in the nonergodic case. If we plot f^s/δ, we also find a constant value for $|\delta| < 10^{-3}$. Surprisingly, the relative weight of the constants for the three correlators is the same for both cases, the ergodic and the nonergodic. This is illustrated by normalizing the values by $\lim_{\delta\to 0}\delta\phi_3(s=0)$ in the ergodic case and by $\lim_{\delta\to 0} f_3/|\delta|$ in the nonergodic case as shown in Figure 6.4. The quotient of the absolute amplitudes is $(\lim_{\delta\to 0} f_i/|\delta|)/(\lim_{\delta\to 0}\delta\phi_i(s=0)) = 1.60$ in this case.

6.4. Dynamic analysis

Now, we solve the full equations in time space and Laplace space under the constant bath assumption. Furthermore, we test the predictions of the critical law from Section 6.2.3.

6.4.1. Laplace space calculations

In Laplace space, the Laplace frequency s enters the equations of motion (6.8) only as a parameter. Therefore, we can use the same iteration scheme as for the static calculations to solve the problem. We can check the solution in two limiting cases $s \to 0$ and $s \to \infty$. The

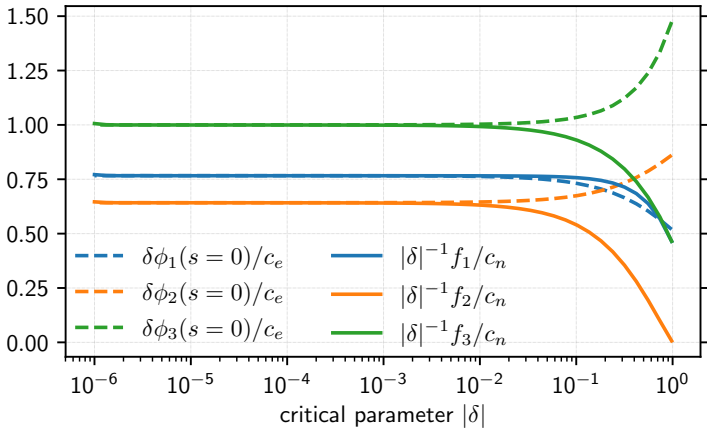

Figure 6.4.: Rectified scaling for ergodic $\phi_i(s=0)$ (dashed, $\delta > 0$) and nonergodic f^s (solid, $\delta < 0$) solutions for $v_1^s = v_2^s = 2$ and $\varepsilon = 0.1$. The data for $\delta > 0$ is normalized by $c_e := \lim_{\delta\to 0} \delta\phi_3(s=0)$, the data for $\delta < 0$ is normalized by $c_n := \lim_{\delta\to 0} f_3/|\delta|$.

case $s \to 0$ was solved in the previous section and provides the following asymptotic behaviour

$$\phi_i(s\to 0) \approx \begin{cases} f_i/s, & F_{\mathrm{ex}} < F_{\mathrm{c}}, \\ \phi_i(s=0), & F_{\mathrm{ex}} > F_{\mathrm{c}}. \end{cases} \tag{6.43}$$

In the case $s \to \infty$ (corresponding to short times), we obtain the following asymptotic results

$$\phi_1(s) \approx \frac{1}{s}, \tag{6.44a}$$

$$\phi_2(s) \approx \frac{1}{s^2}\frac{F_{\mathrm{ex}}\kappa_{\parallel}}{\tau^s}, \tag{6.44b}$$

$$\phi_3(s) \approx \frac{1}{s}. \tag{6.44c}$$

Two examples for the Laplace space solution for $\varepsilon = 0.1$, $v_1^s = v_2^s = 2$, $\delta = \pm 10^{-2}$ are shown in Figure 6.5a and Figure 6.5b. We note that the solution basically consists of three different power law regimes. The small s expansion is valid for $s \lesssim 10^{-5}$, then there is a regime which is approximately described by the critical law $\phi_i(s) = \alpha h_i s^{-1/2}$ as introduced in Section 6.2.3 and finally the large s expansion is valid for $s \gtrsim 10^{1}$.

For the special case $\kappa_{\parallel} = \kappa_{\perp} =: \kappa$ we found analytical expressions for the critical amplitude $\boldsymbol{h}$ in Section 6.2.4

$$h_1 = \frac{1}{4v_1^s}\left(\sqrt{8\left(v_1^s\right)^2 + 8v_1^s f^{-1} + \left(v_2^s\right)^2} - v_2^s\right), \tag{6.45a}$$

$$h_2 = \frac{F_{\mathrm{c}}\kappa}{2}\frac{3v_2^s + \sqrt{8\left(v_1^s\right)^2 + \left(v_2^s\right)^2 + 8v_1^s f^{-1}}}{\sqrt{8f^2\left(v_1^s v_2^s\right)^2 + f^2\left(v_2^s\right)^4 + 8fv_1^s\left(v_2^s\right)^2} + f\left(2\left(v_1^s\right)^2 + \left(v_2^s\right)^2\right) + 2v_1^s}, \tag{6.45b}$$

$$h_3 = 1. \tag{6.45c}$$

The magnitude α is determined via (6.25). This analytical result fits to the numerical solutions shown in Figure 6.5 and Figure 6.6.

Next, we will focus on the change of the solution as we approach the critical force. In order to keep the plots simple, we will just show $\phi_1(s)$, since the behaviour of the other correlators follows the same power laws for intermediate and small s. The numerical results are shown in Figure 6.6. We find that the correlation function follows the critical law, the closer it is to the critical force. Decreasing δ by one order of magnitude extends the critical law regime by roughly two decades.

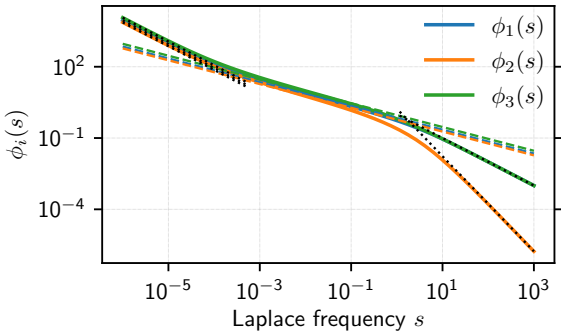

(a) Nonergodic Laplace space solution, $\delta = -10^{-2}$

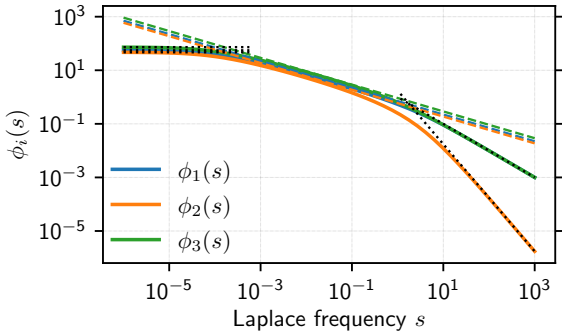

(b) Ergodic Laplace space solution, $\delta = 10^{-2}$

Figure 6.5.: Laplace space solutions for $\varepsilon = 0.1$, $v_1^s = v_2^s = 2$, $\kappa_\parallel = \kappa_\perp = 1$. The limiting cases for small s from (6.43) and large s from (6.44) are shown as dotted black lines. The colored dashed lines are obtained by the beta scaling analysis and indicate the critical law.

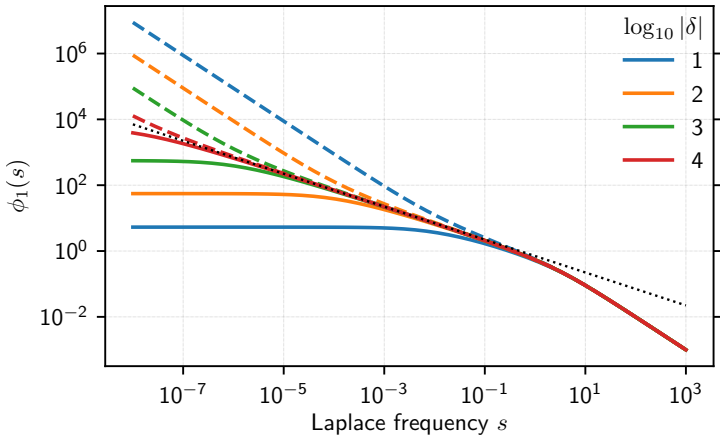

Figure 6.6.: $\phi_1(s)$ for $\varepsilon = 0.1$, $v_1^s = v_2^s = 2$, $\kappa_\parallel = \kappa_\perp = 1$ and different distances δ from the critical force. For $\delta < 0$ (dashed) the curves show a s^{-1} scaling for small s, while for $\delta > 0$ (solid) they reach a plateau. The critical law is drawn as a dotted line.

6.4.2. Time space calculations

In this section, we compare the critical law to the time space solution, obtained by the integro-differential method by Gustavo Abade. The conversion of the power law from Laplace space to time space introduces a factor $\pi^{-1/2}$ for the critical amplitude in time space and is given by $h_i' = \pi^{-1/2}\alpha h_i$. The results are shown in Figure 6.7 together with the critical law.

We observe that the critical law emerges on approaching the critical force from either side, from above or from below. In order to make the deviations from the critical law better visible, we plot the relative deviation, given by

$$\Delta_i(t) := \phi_i(t)/(h_i' t^{-1/2}) - 1, \tag{6.46}$$

which is zero for perfect agreement. These plots are shown in the right column of Figure 6.7. The agreement is good and one notices that the interval with good agreement grows upon approaching the critical force. As in Laplace space, a decrease of δ by one order of magnitude increases this region by about two decades. However, we should mention that the agreement is not perfect. Comparing the values at $\bar{t} = 10^3$, we have $\Delta_i(\bar{t}) \approx 4 \cdot 10^{-3}$ for $\delta = 10^{-4}$,

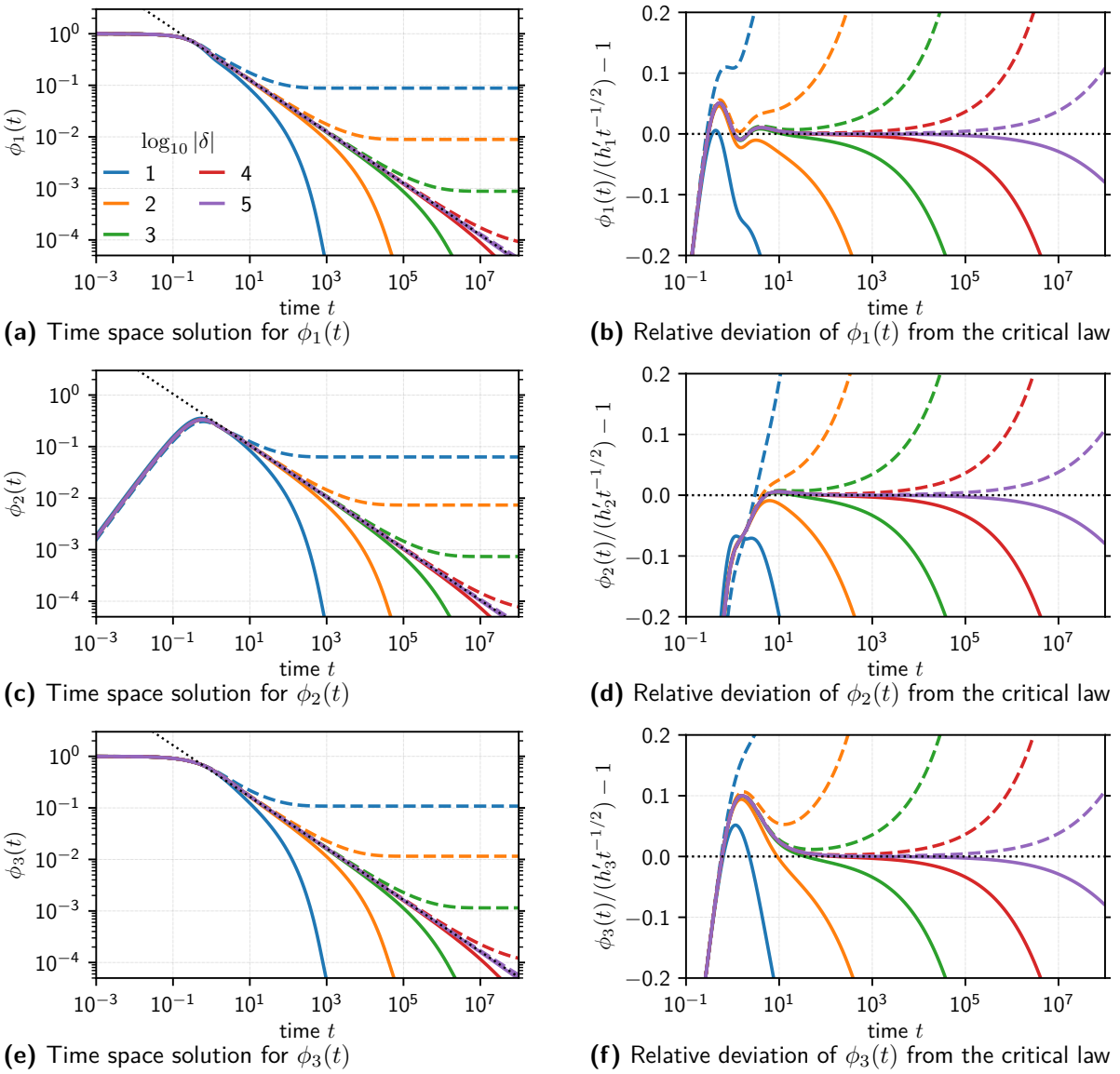

(a) Time space solution for $\phi_1(t)$

(b) Relative deviation of $\phi_1(t)$ from the critical law

(c) Time space solution for $\phi_2(t)$

(d) Relative deviation of $\phi_2(t)$ from the critical law

(e) Time space solution for $\phi_3(t)$

(f) Relative deviation of $\phi_3(t)$ from the critical law

Figure 6.7.: Correlation functions for $\varepsilon = 0.1$, $v_1^s = v_2^s = 2$, $\kappa_\parallel = \kappa_\perp = 1$, constant bath and different distances δ to the critical force as labeled. Dashed lines indicate $\delta < 0$, while solid lines indicate $\delta > 0$. The critical law is shown as dotted line. Left column: Time space solution. Right column: Relative deviation of the time space solution $\phi_i(t)$ from the critical law as introduced in (6.46). The line color and style is the same across all panels.

$\Delta_i(\bar{t}) \approx 8 \cdot 10^{-4}$ for $\delta = 10^{-5}$ and $\Delta_i(\bar{t}) \approx 5 \cdot 10^{-4}$ for $\delta = 10^{-6}$. While for $|\delta| \geq 10^{-4}$ the differences for $\delta > 0$ are negative and for $\delta < 0$ are positive, these differences are always positive for $|\delta| \leq 10^{-5}$.

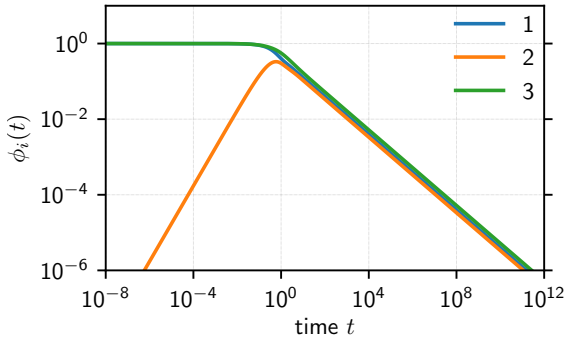

(a) Time space solution (integro-differential)

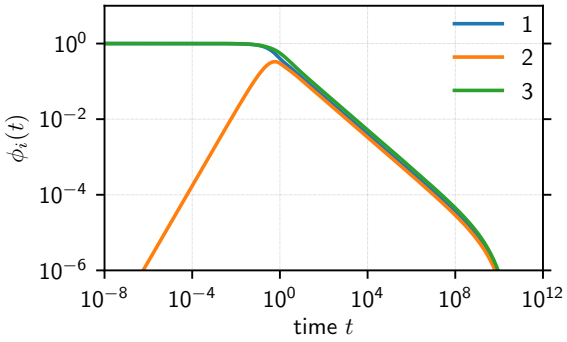

(b) Time space solution (integral method)

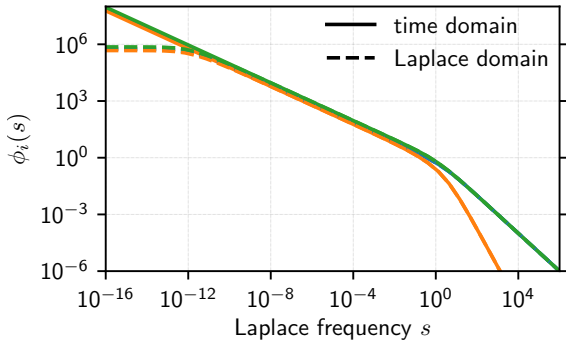

(c) Laplace space solutions (integro-differential)

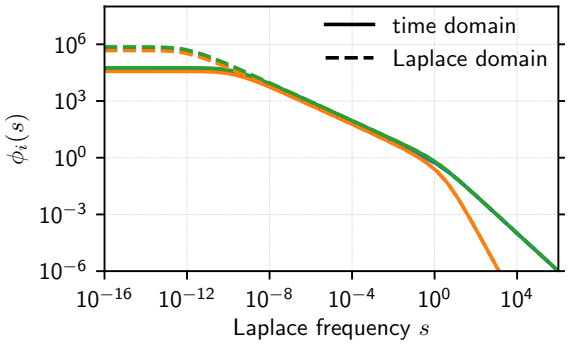

(d) Laplace space solutions (integral method)

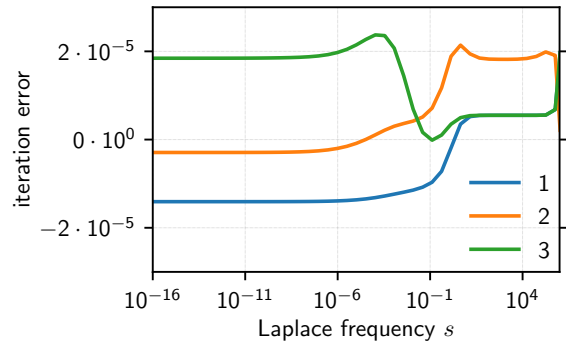

(e) Iteration difference (integro-differential method)

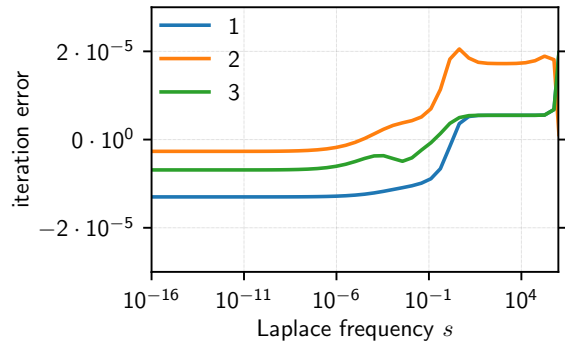

(f) Iteration difference (integral method)

Figure 6.8.: Comparison of correlation functions close to the critical force for $\varepsilon = 0.1$, $v_1^s = v_2^s = 2$, $\delta = 10^{-6}$ in the constant bath approximation for the integro-differential method (left column) and the integral method (right column). The Laplace space solution is shown as dashed line in the center row. The legend indicates the index of the corresponding correlator.

6.4.3. Comparison in Laplace space

Finally, we want to compare the solutions obtained by different integration schemes in time space, namely the *integral method* and the *integro-differential method*. We compare both to the solution in Laplace space by doing the numerical Laplace transform as introduced in Section B.2. We therefore again require a constant bath. The solution in time space for both methods for $\varepsilon = 0.1$, $v_1^s = v_2^s = 2$ and $\delta = 10^{-6}$ (above the critical force) is shown in Figure 6.8a and Figure 6.8b respectively. The solutions differ only in the long time behaviour. While the

integral method decays to zero at some time, the integro-differential method continues decaying with the critical power law.

This behaviour is also reflected in the Laplace transform. While all solutions agree for large Laplace frequencies, they disagree at small Laplace frequencies, as can be seen in Figure 6.8c and Figure 6.8d, respectively. The integro-differential method seems to diverge like $s^{-1/2}$ at small frequencies, while the integral method converges to a plateau value, like the Laplace space solution. However, the plateau value of the integral method is roughly one order of magnitude smaller than the Laplace space solution. Calculating the relative error of the time solution with respect to the Laplace space solution, one finds that the error exceeds the 1% threshold only for frequencies smaller than $5 \cdot 10^{-9}$ for the integro-differential method and for frequencies smaller than $5 \cdot 10^{-7}$ for the integral method.

The last question, we try to answer is why do the integration algorithms find such different solutions. As an indication for the validity of the time solution, we take the Laplace transformed solution and do one iteration using the Laplace space iteration scheme. The difference between those values normalized to the input data is shown in Figure 6.8e and Figure 6.8f. Surprisingly this relative difference is only of the order of 10^{-5}. Hence, we could conclude that the solution is not that bad. However, one should take into account that the convergence of the iteration is rather slow close to the critical force. In this case we find reduced contraction factors of the order 10^{-6}. This means that the a-priori estimation of Banach's fixed point theorem would guarantee the exact solution to be within a factor of $10^{-5}/(1-(1-10^{-6})) = 10$. Even using this error estimate, the solutions disagree for small s. This indicates that there is a convergence problem for both time space algorithms for long times.

6.5. Conclusions

For this schematic model we find analytically a type A bifurcation and the asymptotic dynamical behavior at the transition is governed by a power law with exponent 1/2. We can even find an explicit expression for the critical force and the critical amplitude in a restricted parameter space. This model does not allow for a diverging critical amplitude by tuning the coupling parameters, but it could possibly allow for scenarios with different probe sizes. The analytical findings are confirmed by numerical solutions.

7. Heterogeneous dynamics

> Le vrai point d'honneur [d'un scientifique] n'est pas d'être toujours dans le vrai. Il est d'oser, de proposer des idées neuves, et ensuite de les vérifier.
>
> *(Pierre-Gilles de Gennes [dGen07, p. 13])*

This chapter is dedicated to the comparison with an experiment, performed by Nesrin Senbil, which revealed strongly heterogeneous dynamics in the motion of the probe particle. We start by describing the experimental setup. Then we map the experimental time-scales to the theoretical ones by collapsing the mean square displacements (MSD). We establish a new method to calibrate the force via a linear response experiment, which is also verified via simulations. With this knowledge, we can discuss the features of the experiment and compare quantitatively with our MCT predictions. Finally, we will discuss different methods to identify the critical force. Part of these results have already been published in [ŞGZ+19]. As the experimentalists prefer to call the force direction the x axis, we have to choose to be either consistent with the notation in the paper or within this thesis. We choose to have this thesis self-consistent, i.e. the force is also in this chapter along the z direction. This implies that one has to swap the x and z axis when comparing the figures (with the same data) to the paper.

7.1. Experimental setup

Nesrin Senbil, Chi Zhang and Frank Scheffold have established an experimental system, which is very close to our model and therefore suitable to test and check our predictions. The colloidal glass of hard spheres is realized by an oil-in-water emulsion [ZGM+16]. The oil droplets have a diameter $d = 2.01\,\mu\text{m}$ with a polydispersity of about $12\,\%$ to prevent crystallization. They are sterically stabilized to inhibit coalescence of droplets. The solvent is a 6:4:1 mixture of water, dimethylacetamid and formamide to match the buoyancy and the refractive index of the emulsion droplets (see the supplemental material of [ŞGZ+19] for the details of the sample preparation). This system has the advantage, that it can be reversible jammed and unjammed. This allows a precise control of the packing fraction by taking the jamming transition as reference and then diluting the sample in well defined steps. The accuracy of the packing fraction is about $5 \cdot 10^{-3}$ [ZGM+16, Sec. 1.2, p. 6]. The glass transition of this system has been determined to occur at $\varphi_g = 0.59$ [ZGM+16, Sec. 4.1.1, p. 9]. Even though the colloidal particles are made of fluid droplets, they essentially behave like hard spheres. For volume fractions below $\varphi \leq 0.61$ they do not touch, which ensures that they are not deformed and that they will not coalesce.

The probe particle will be moved by optical tweezers [Ash70], which requires optical contrast to the medium. Therefore, a small amount of polystyrene particles of the same size is added to the sample. Typically, laser tweezers trap the particles so strongly that we would have

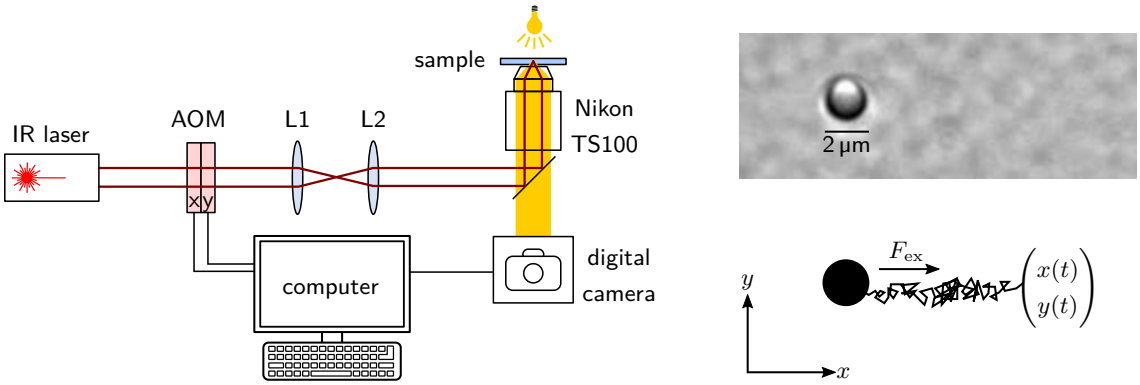

Figure 7.1.: Left: Experimental setup for active microrheology in an emulsion glass. The optical tweezers are created by an infrared laser with $\lambda = 1064\,\text{nm}$ and up to 10 W output power. The laser beam is modified by acousto optic modulators (AOM) to achieve a line trap as described in the text. Then, the beam is focused using two lenses L1 and L2 with focal lengths $L_1 = 100\,\text{mm}$ and $L_2 = 250\,\text{mm}$ and then coupled into the inverted microscope with an infrared reflective dichroic mirror. The microscope is equipped with a 60X/1.30 Nikon objective. The sample is placed above the objective on a xy translation stage. White background lighting allows recording of the bright field image with a digital camera. (adapted from [ŞGZ+19, Fig. S3]) Right: Data processing. From the microscope image (courtesy of Nesrin Senbil) the position of the probe particle is extracted for each frame to obtain a trajectory (sketched).

a constant velocity rather than a constant force experiment [SB05, Sec. VIII, p. 10]. To circumvent this, the optical tweezers are used as a line trap. This means that the position of the tweezers is randomly distributed along a line using acousto-optic modulators. If the probability density varies linearly along this line, the force on the probe will be independent of the position, as long as one stays away from the ends of the line (see supplemental material of [ŞGZ+19] for a derivation). This allows to apply a constant force in one direction on the probe particle. For the other directions, it implies that the particle is trapped to the line, i.e. is cannot diffuse or move beyond the trap size perpendicular to the line. This motivated the description of the semi-harmonic trap (2.73b) in Section 2.4. The value of this force is determined by the optical parameters of the setup, which makes a calibration necessary. Irrespective of the absolute values of the force, one expects a linear increase of the force with the laser power [Ash70, p. 157, Eq. (1)]. This applies to the constant force along the line as well as to the confining force perpendicular to the line. Since this line trap has a fixed position, a single beam point trap is used to align the particle position and the optical tweezers.

The setup is controlled with a computer as shown in Figure 7.1 and the probe particle trajectory is recorded through a digital camera and evaluated using a particle tracking algorithm. An example of a microscope image is also shown in this figure. For the comparison with the experiment, the force will be applied into the x-direction. A typical trajectory is recorded for about 1200 s with five frames per second and the accuracy of the positions is approximately $\pm 30\,\text{nm}$. Some uncertainty arises for the time at which the force is switched on, since this has to be done manually. It is about 0 s to 0.2 s for the smaller forces and 0.5 s to 1 s for the larger ones. With this experiment we can obtain trajectories of the probe particle for different line forces.

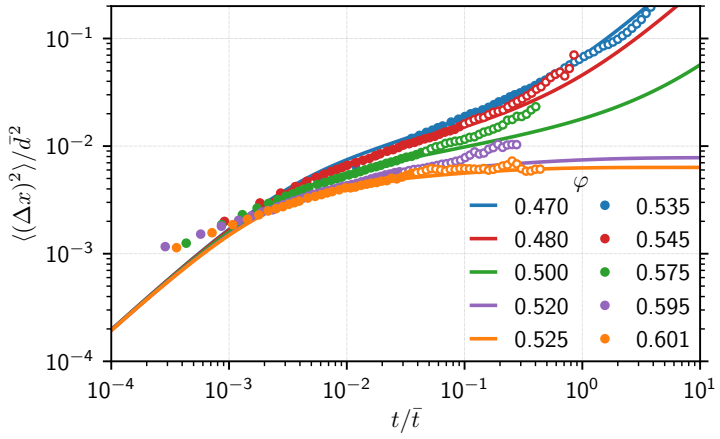

Figure 7.2.: 1D mean square displacement of the emulsion droplets (symbols) for different packing fractions ($\langle(\Delta x)^2\rangle = \langle(\Delta y)^2\rangle = \langle(\Delta z)^2\rangle$). Full symbols show the data included in the fit. Solid lines show MCT results. We use the same color for packing fractions corresponding via (7.1) [ŞGZ+19, Fig. S2].

7.2. Mapping between experiment and theory

Our theory just needs the length- and timescale of the experiment together with the volume fraction as input. At first sight, this looks trivial, but some care has to be taken for the choice of the parameters as we will elaborate in the following.

The packing fraction can be determined accurately, as described above. However, MCT does not predict the experimental value for the glass transition. Therefore, we will have to scale the packing fractions with the ratios of the glass transition packing fractions, as in the comparison with the simulations in Section 4.5. The conversion is given by

$$\varphi^{\mathrm{MCT}} = \varphi^{\mathrm{exp}} \frac{\varphi_g^{\mathrm{MCT}}}{\varphi_g^{\mathrm{exp}}} = \frac{0.516}{0.59} \varphi^{\mathrm{exp}}. \tag{7.1}$$

While previous works found this scaling only below the glass transition [Spe05, Fig. 3, p. 3], we will see that this simple scaling also works above the glass transition.

The length scale is generally given by the particle diameter $d = 2\,\mu\mathrm{m}$. As the MCT glass transition occurs at smaller packing fractions than in the experiment, the resulting localization length (i.e. the long time limit of the MSD in the glass) is larger in MCT than in experiments (see [Spe05, Fig. 3, p. 3]). Therefore, we will allow for a slight modification of this length scale as described in the following.

The time scale is given via $\bar{t} = d^2/D_0$ through the short time diffusion coefficient D_0, which describes the diffusion of the particles before they start to interact. In dilute systems, this is equal to the diffusion coefficient of a single sphere. For dense systems, however, the particles can feel each other through steric or hydrodynamic interactions even if they are not touching. This leads to a slowing down of the dynamics. Since our theory does not account for these effects, we will treat them effectively by adjusting D_0. Any slowing down due to hydrodynamic or other effects will be reflected in a reduction of D_0.

The time scale $\bar{t}$ as well as the length scale $\bar{d}$ are determined for each packing fraction by matching the MSDs in a quiescent system. The experimental MSD is given by $\langle \Delta z^2(t_i)\rangle_{\mathrm{exp}}$ for the times t_i with $1 \leq i \leq N$. Note that the choice of the axis does not matter as long as no force is applied. What is important is the dimensionality of the MSD, it can be one-, two- or three-dimensional. The 2D and 3D MSDs equal the double or the triple of the one-dimensional

φ_{exp}	φ_{MCT}	$\bar{t}$ (s)	D_0 (µm^2/s)	$\bar{d}/d$
0.535	0.47	167	0.0237	0.795
0.545	0.48	1090	0.003 66	0.965
0.575	0.50	2310	0.001 73	1.21
0.595	0.52	3480	0.001 15	1.0
0.601	0.525	2790	0.001 44	1.12

Table 7.1.: Parameters for matching mode-coupling theory to experiments. Packing fractions are calculated, the time scale $\bar{t}$ and the length scale $\bar{d}$ are fitted. The short time diffusion coefficient is determined via $D_0 = d^2/\bar{t}$, where d =2 µm is the particle diameter.

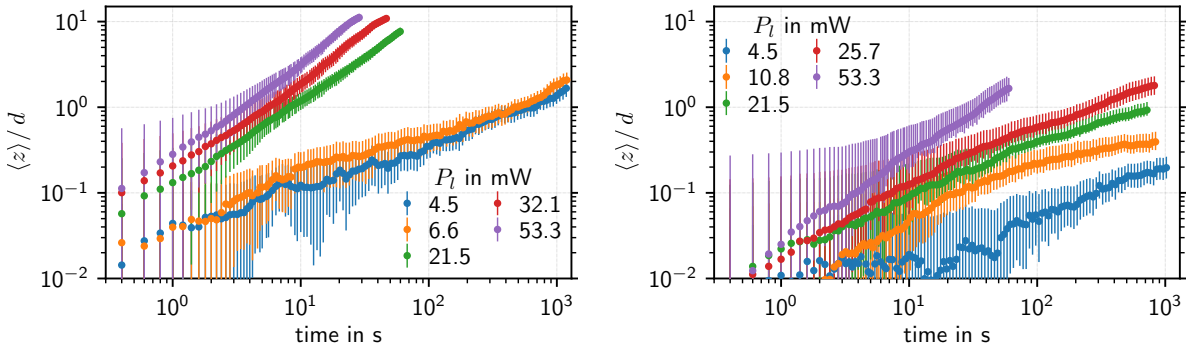

Figure 7.3.: Experimental mean displacement of the probe particle for different laser powers P_l in the fluid (left, $\varphi = 0.535$) and the glass (right, $\varphi = 0.601$). The error bars contain statistical and systematic errors as described in the text [ŞGZ+19, Fig. S5].

MSD in the isotropic case. For this comparison, we choose the one-dimensional MSD: The mean square displacement for MCT is determined at the equivalent packing fraction as described above and denoted by subscript MCT. To find the best agreement, we minimize the function

$$f(\bar{t}, \bar{d}) = \sum_{i=1}^{N} \left(\ln\left(\left\langle \Delta z^2(t_i) \right\rangle_{\mathrm{exp}} \right) + \ln\left(\left\langle \Delta z^2(t_i/\bar{t}) \right\rangle_{\mathrm{MCT}} \right) \right)^2, \tag{7.2}$$

which is a least squares fit in a logarithmic representation of the data. The result is shown in reduced units in Figure 7.2. Clearly, the glass transition between $\varphi = 0.575$ and $\varphi = 0.601$ can be observed: While the MSD for $\varphi = 0.575$ keeps increasing, it saturates for $\varphi = 0.601$. The data for 0.595 is inconclusive. The agreement with the MCT curves after adjusting the time and the length scale is quite good for the lowest and the highest packing fractions. There is always a deviation at short times so that the short time diffusion regime is not visible in the experiment. This might be related to the tracking accuracy and the experimental setup, which can have subtle effects on the MSD at short times and small displacements [FS17, Chap. 4.8, p. 166-175]. The parameters obtained from the fit are summarized in Table 7.1. The time scale $\bar{t}$ increases from 167 s for $\varphi = 0.535$ to 2790 s for 0.601. The effective particle diameter $\bar{d}$ is about 20 % smaller in the fluid phase, indicating a weaker localization, and about 20 % larger in the glass, indicating a stronger localization as in theory. In the following, we will not make use of this length scale factor anymore and use the particle diameter $d = 2\,\mu$m instead. Furthermore, we will restrict our analysis to two packing fractions: $\varphi = 0.535$ in the fluid phase and $\varphi = 0.601$ in the glass.

In Figure 7.3 we show the raw experimental data for the mean displacements for different

laser powers in the fluid and in the glass. In order to allow for a thorough analysis, we show the uncertainties of the data. They arise from different sources. First, there is the statistical uncertainty. For each packing fraction and laser power, Nesrin Senbil obtained 15 to 40 probe particle trajectories (which are shown exemplarily in Figure 7.7). From these trajectories, the mean displacement is obtained by averaging the probe positions at each time. More precisely for the mean displacement at time t_i, we average the values in the time window $[t_i(1+10^{-4})^{-1}, t_i(1+10^{-4})]$ to reduce the noise. This finite number of observations introduces the statistical uncertainty of the mean value and is characterized by the variance divided by the number of observations [DM83, p. 48]. Second, there is an uncertainty for the values at short times as the exact time of the power-on of the line trap is not known and differs between individual trajectories as described above. These errors are estimated using linear response and add to the statistical errors at small times as visualized by the error bars in Figure 7.3.

Finally, we need to map the laser power P_l to a physical force on the particle. This can be done by measuring the velocity of the probe particle in a simple liquid (1:1.15 mixture of water and dimethylacetamid with a viscosity of 4 mPa s). The velocity as function of the laser power is shown in [ŞGZ+19, Fig. S4], where they find a linear relation between the velocity and the laser power[1]. This relation can be converted to the force-laser power relation

$$F_{\mathrm{ex}} = 12.8 \frac{\mathrm{fN}}{\mathrm{mW}} P_l = 6.31 \frac{k_{\mathrm{B}}T}{d} \frac{P_l}{\mathrm{mW}} \tag{7.3}$$

with the help of the Stokes drag. The force scale for the nondimensionalization is given by $k_{\mathrm{B}}T/d = 2.03\,\mathrm{fN}$.

These measurements also confirm that the instantaneous velocity of the probe is constant over the whole length of the trap (shown in the inset of [ŞGZ+19, Fig. S4]). As the motion of the probe is overdamped, this implies that the force is constant over the whole length of the trap as well. This establishes a relation between the laser power P_l and the force F_{ex} on the probe particle in a simple liquid. It remains unclear if the same conversion factor also holds in the dense suspension, where it could be reduced due to attenuation through the bath particles, since perfect refractive index matching is not possible. This will be addressed in the next section.

7.3. Linear response

To access the relation between the laser power and the force in situ, we will check the linear response relation (2.206), which was predicted in Section 2.4.10. It relates the time-dependent mean displacement after application of a constant external force to the time-dependent mean square displacement in the quiescent system

$$\langle z \rangle (t) = \frac{F_{\mathrm{ex}}}{2k_{\mathrm{B}}T} \left\langle \Delta z^2 \right\rangle_{\mathrm{eq}} (t). \tag{7.4}$$

An easy check of this relation can be performed by dividing the mean displacement through the force. The result should then equal half of the (one-dimensional) MSD of the quiescent case. This is shown for simulations of Antonio Puertas in Figure 7.4. The system is the same as for

[1] Do not assume that a controller, which ranges from 0 % to 100 % has a linear relationship to the laser power.

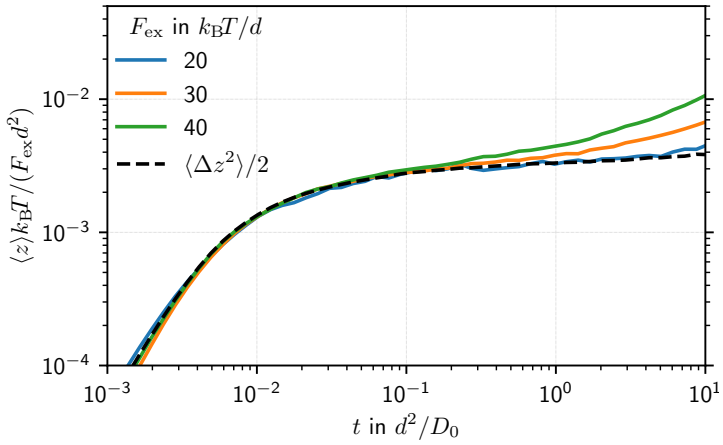

Figure 7.4.: Check of the linear response prediction (7.4) for quasi-hard spheres at $\varphi = 0.62$. The simulation has been performed by Antonio Puertas. The dashed black line shows the 1D-MSD of the quiescent system divided by two.

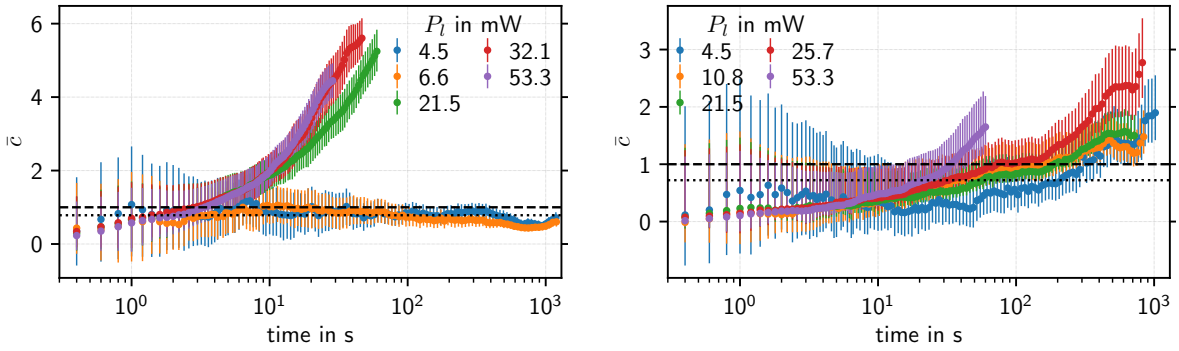

Figure 7.5.: Time resolved linear response coefficient in the fluid (left, $\varphi = 0.535$) and the glass (right, $\varphi = 0.601$) as introduced in (7.5). The theoretical prediction is $\bar{c} = 1$ (dashed line) and the average over all forces, where linear response holds ($P_l < 21.5\,\mathrm{mW}$ in the fluid and $P_l < 53.3\,\mathrm{mW}$ in the glass) is shown as dotted line [ŞGZ+19, Fig. S7].

the comparison with MCT in Section 4.5, i.e. quasi-hard spheres above the glass transition at a packing fraction of $\varphi = 0.62$. For $F_{ex} = 20\,k_BT/d$ the reduced mean displacement $\langle z \rangle / F_{ex}$ coincides with the MSD for all times. For larger forces, deviations are visible at long times, while the short time behavior up to the plateau is still nicely described by the quiescent MSD.

To make this comparison more quantitative, we divide (7.4) by the right hand side and obtain

$$\bar{c}(t) = \frac{2\,\langle z \rangle\,(t) k_B T}{\langle \Delta z^2 \rangle_{eq}\,(t) F_{ex}}, \tag{7.5}$$

with $\bar{c}(t) = 1$ if the prediction is correct. This is done with the experimental data in the fluid and in the glass as shown in Figure 7.5, where the mean displacements have been presented in Figure 7.3 and the quiescent MSDs in Figure 7.2. For the force values, we assume that the calibration (7.3) also holds in the complex fluid. The data for the fluid agrees for small forces with the predicted value of $\bar{c}(t) = 1$ for almost all times. For the longest times it is systematically smaller than predicted, which causes the average over all times to be $\langle \bar{c}(t) \rangle_t = 0.74$ in the fluid and $\langle \bar{c}(t) \rangle_t = 0.78$. For long times, there is the possibility that the system changes slightly due to drift or heating through the line trap laser, while for short times the errors from the experimental setup are more important. Therefore, the uncertainty is smallest in a window

between 10 s and 400 s. For forces above or equal to $135\,k_\mathrm{B}T/d$ ($P_l = 21.5\,\mathrm{mW}$) the linear response relation only holds for times shorter than 10 s within the large uncertainty range. Hence, it does not allow for a definite answer if the linear response relation holds for large forces at short times.

In the glass, the experiment is more challenging, because the uncertainties are large as the displacements are small. Nevertheless, there is a time window from 60 s to 200 s, where the data for $F_\mathrm{ex} \leq 162\,k_\mathrm{B}T/d$ ($P_l \leq 25.7\,\mathrm{mW}$) collapse and fall closely to 1. This time window falls in the same range as for the fluid. Hence, we assume that the uncertainties due to long time stability of the system are not important here as well. For longer times, the data is always larger than the expected value, while for short times it is systematically smaller. Again, the results are compatible with the hypothesis $\bar{c} = 1$ for short times, but the uncertainty is large. The overall average for those curves with linear response is $\langle \bar{c}(t) \rangle_t = 0.7$. Hence, we confirm that the linear response relation (7.4) holds in the complex fluid and is compatible with the data in the glass.

This relation can consequently also be used to calibrate the force in situ. Assuming a linear relation between the force and the laser power $F_\mathrm{ex} = cP_l$, we obtain for the proportionality constant

$$c = \frac{2\,\langle z \rangle\,(t) k_\mathrm{B}T}{\langle \Delta z^2 \rangle_\mathrm{eq}\,(t) P_l}, \tag{7.6}$$

which is 9.46 fN/mW for the liquid and 9.96 fN/mW in the glass. Both values are about 25 % smaller than the value obtained from the calibration in the simple liquid in (7.3). This could be caused by additional losses in the emulsion due to scattering as discussed above.

7.4. Mean displacement comparison

A parameter free comparison (except for the time scale) beyond the linear response prediction is shown in Figure 7.6. The MCT calculations are performed for a packing fraction of $\varphi = 0.47$ for the fluid and of $\varphi = 0.525$ for the glass. For the forces we choose the same numerical values as obtained in the experiment. Hence, no fitting to the experimental data has been done except for the matching of the time scales in the quiescent system. MCT shows the same qualitative behavior as the experiment. There is also a similar scaling of the mean displacements with the force. However, the time scale seems to be off by a factor 10 in the fluid and a factor 5 in the glass. In the glass, we additionally observe a different value for the delocalization transition, because the mean displacement seems to saturate for $F_\mathrm{ex} = 68\,k_\mathrm{B}T/d$, while the theory curve already increases linearly. Furthermore, the experimental mean displacements for $135\,k_\mathrm{B}T/d$ and $162\,k_\mathrm{B}T/d$ do increase sublinearly, but do not seem to approach a plateau. This makes it difficult to classify them as above or below the delocalization transition. We can take this result as an indication that the transition from localized to delocalized behavior is not as sharp as observed in theory, where a small change from $42.2\,k_\mathrm{B}T/d$ to $42.5\,k_\mathrm{B}T/d$ of the force around the critical force makes a huge difference in the mean displacement (see Figure 4.6). In simulations, the transition is not as sharp either (for example comparing the length scales in Figure 4.28 or comparing the forces for comparable van Hove functions in Figure 4.27).

Dividing the mean displacements by the force (bottom row in Figure 7.6), we can compare to the experimental mean square displacement (dashed black line) and visualize the deviations

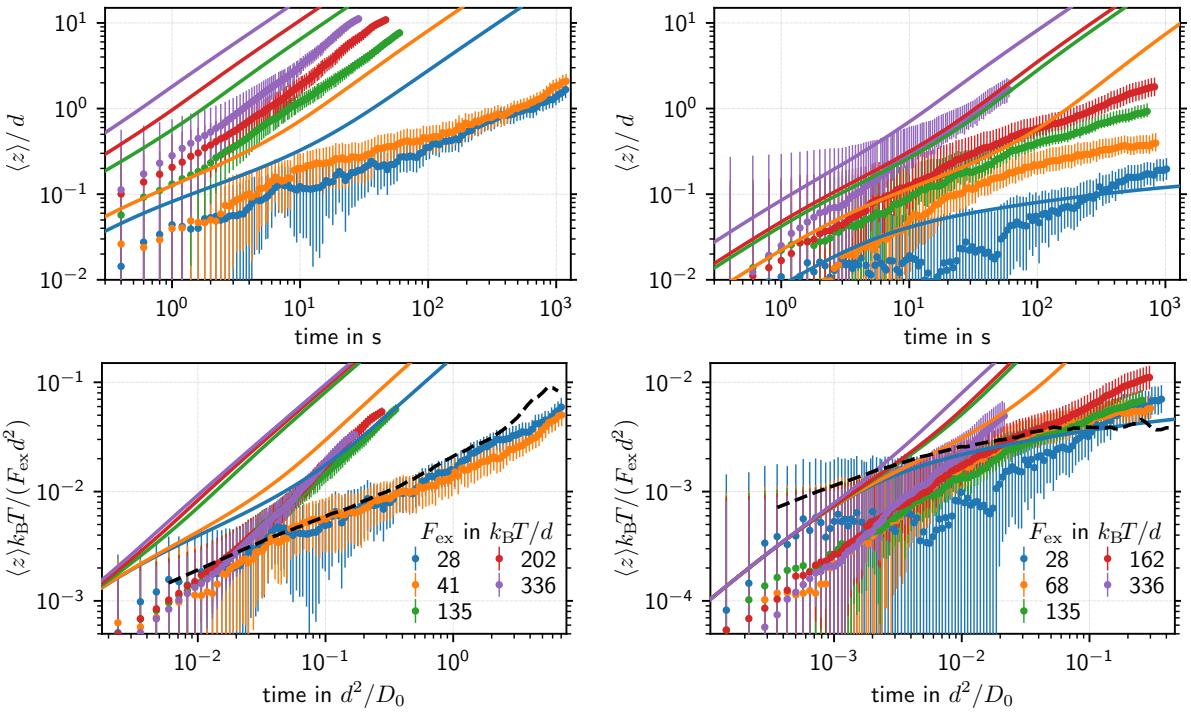

Figure 7.6.: Comparison of experimental mean displacement (symbols) with MCT calculations (lines) for the fluid (left column) and the glass (right column). The top row shows the mean displacement, while the bottom row shows the rescaled mean displacement $\langle x \rangle / d$ to allow for the comparison with the linear response prediction (shown as dashed black line, experimental data). The color code is the same in each column. To allow for the easy comparison of experimental and theoretical time scales, we show the same time window in both columns. In the upper row in units of seconds and in the lower row in units of d^2/D_0 [ŞGZ+19, Fig. 2, Fig. S5, Fig. S6].

from this relation for large forces. We notice that the deviations in the experiment happen about one order of magnitude later as predicted in theory. Hence, the motion of the probe is slower than in theory. This could be an effect of the line trap, because it forces the probe particle to stay on this line, while in the theory, there is no such lateral forces. This implies that in theory, the probe can go around an obstacle, while in the experiment it has to push it away. From everyday life experience this process is much slower and from a physical point of view it should be slower as well as the number of possibilities to go around the obstacle is reduced. We also should not forget that the theoretical packing fraction is smaller than the experimental one. Even though this does not cause huge differences in quiescent systems, we can imagine that the lower bath particle density facilitates the motion of the probe particle.

Finally, we note that the theoretical lines do not collapse onto the experimental MSD for small forces. This is the effect of ignoring the length scale $\overline{d}$. Changing d to $\overline{d}$ also requires to change the forces from $k_B T/d$ to $k_B T/\overline{d}$ to be consistent. This has been done, but no significant improvement of the comparison has been found. The main reason is that this scaling only shifts the curves on the y-axis, but we would need a shift in the time axis for a better comparison. From the theory side, such improvement could be a theory for the line trap with lateral confinement. For the experiments the implementation of a homogeneous force field (for

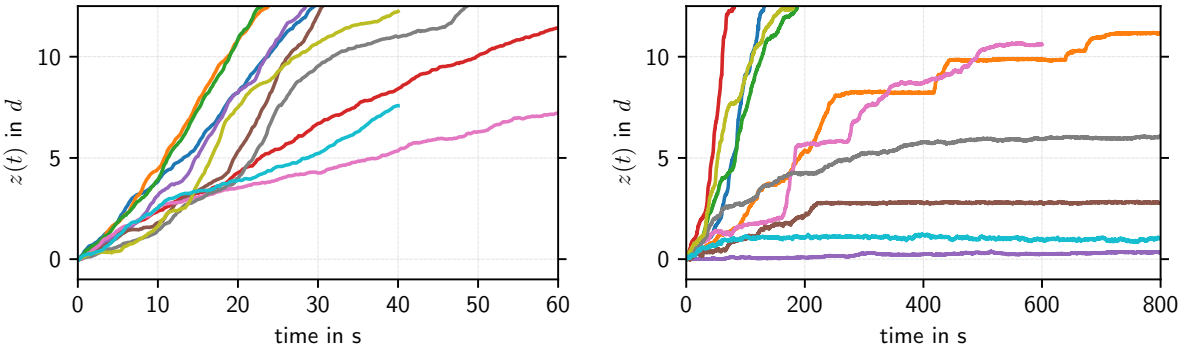

Figure 7.7.: Ten random trajectories in the fluid (left, $\varphi = 0.535$) and glass (right, $\varphi = 0.601$) for the largest force of 682 fN (336 $k_\mathrm{B}T/d$). Note the different time scales [ŞGZ+19, Fig. 3].

example by adjusting the position of the trap relative to the position of the probe) would be beneficial for the comparison.

7.5. Heterogeneous dynamics

A challenge for the experiments is the finding that the trajectories of the particles appear to be very different for different runs of the experiment as illustrated in Figure 7.7. In view of these data one may worry about the reproducibility of the experiment, in particular for experiments in the glass. In this section, we will show that this is not a problem of the experimental setup, but a feature of this model system.

7.5.1. Bimodal van Hove functions

Within our theory, we cannot predict individual trajectories. Instead, we know the probability distribution of the probe positions, the van Hove function $G^s(\boldsymbol{r}, t)$ as introduced in (2.85). Since the experiment is limited to a one-dimensional motion, we will mostly consider the parallel marginal van Hove function $G^{s\parallel}(z, t)$ as introduced in (2.163), where the perpendicular degrees of freedom are integrated out. Before we start to compare to the experiment, we will analyze the pure theoretical predictions.

For the experiment, we will need to calculate the van Hove functions in real space with sufficient resolution and with as little artifacts as possible. This makes it mandatory to use a grid in Fourier space with a small step size so that we can at least cover a range of about ten particle diameters in real space. Therefore, we choose a grid with `unilog10`, $q_\mathrm{max}d = 15$ and $N_q = 111$ for q_x and q_z. The maximum time accessible in experiments also allows us to shorten the upper time limit of the calculation to 27 decimation steps, starting with a uniform grid with step size $10^{-8}\, d^2/D_0$ and $N_t = 1024$ steps. This corresponds to a maximum time of $1.4 \cdot 10^3\, d^2/D_0$. The packing fractions for the comparison were already specified in Table 7.1. For $\varphi_\mathrm{exp} = 0.601$ (corresponding to $\varphi_\mathrm{MCT} = 0.525$) we find for this discretization a critical force of $34.386\, k_\mathrm{B}T/d$. A cutoff $q_\mathrm{max}d = 20$ with 91 grid points yields a critical force of $33.316\, k_\mathrm{B}T/d$. Since we cannot access the critical dynamics experimentally, the type of the transition does not enter this discussion.

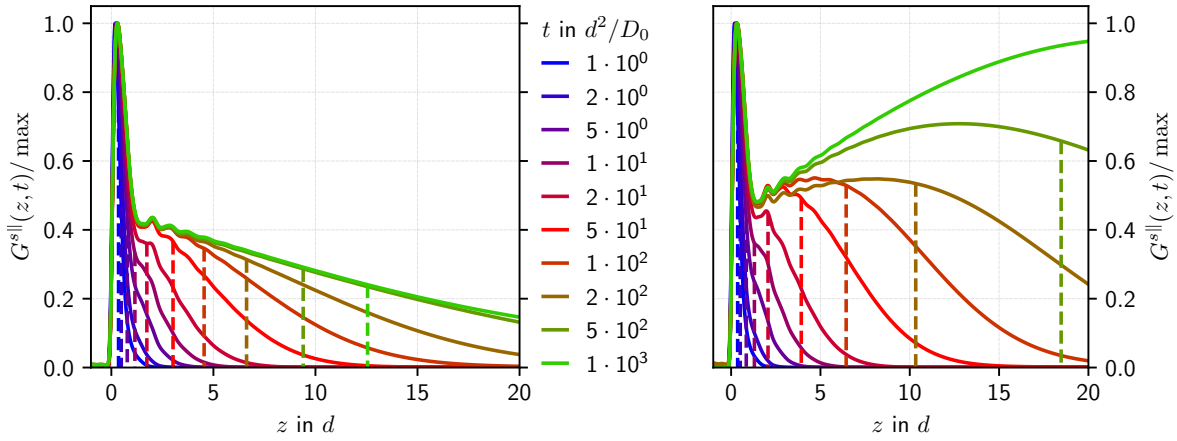

Figure 7.8.: Time evolution of the van Hove function in the glass ($\varphi_{\mathrm{MCT}} = 0.525$) for $F_{\mathrm{ex}} = 34.3\,k_{\mathrm{B}}T/d$ (left) slightly below the critical force and $F_{\mathrm{ex}} = 34.5\,k_{\mathrm{B}}T/d$ (right) slightly above the critical force. Time increases from blue over red to green as indicated. The van Hove functions are normalized to their maximum value. The dashed vertical lines show the mean of the distribution. Numerical details can be found in the text.

First, we want to get an idea how the probability distribution evolves over time. This is shown in Figure 7.8. To highlight the evolution of the shape, we normalize by the maximum of the distribution. Below the critical force there is the majority of the particles localized at the origin. With increasing time a shoulder develops in force direction, which gets more and more prominent until it saturates at its final exponential shape as discussed in Section 4.5.3. We also show the means at the different times, which illustrate that the mean is mainly determined by the width of the shoulder. Above the critical force the short time evolution is still the same, but for times larger than $50\,d^2/D_0$ the shoulder no longer tends to a long time limit, but instead converts into a second peak, which moves in force direction and grows in width with time. Even though these distributions do not provide individual trajectories, we can interpret them qualitatively on a single particle level: with increasing time the probe particle can escape the first cage of neighboring particles in more and more realizations of the experiments, while it is still stuck in many others. In the glass below the critical force, a there is a finite probability that the probe particle gets trapped forever in some cage. This results in the exponential tail (see [Gru14, Sec. 6.4, p. 66ff]). Above the delocalization transition the probe particle will eventually move in all experiments if one waits long enough, which leads to the very broad Gaussian probability distribution (due to the central limit theorem). Nevertheless even at $10^3\,d^2/D_0$ there is still some experiments, where the particle is sitting basically at the origin. This is exactly what we have observed in the experimental trajectories in Figure 7.7. A more quantitative comparison will be done in the following section.

From our theory, we can also calculate the full three dimensional van Hove function. It is shown for $F_{\mathrm{ex}} = 35\,k_{\mathrm{B}}T/d$ in Figure 7.9. We observe that the maximum of the threedimensional probe–particle distribution is still located close to the origin, even though the maximum of the marginal probability distribution is found at around $z = 6\,d$. This is related to the fact that the probe particle distribution extends not only into the z direction, but also perpendicular to it. Integrating these directions out yields the new maximum at $z \gg d$. For large distances, we

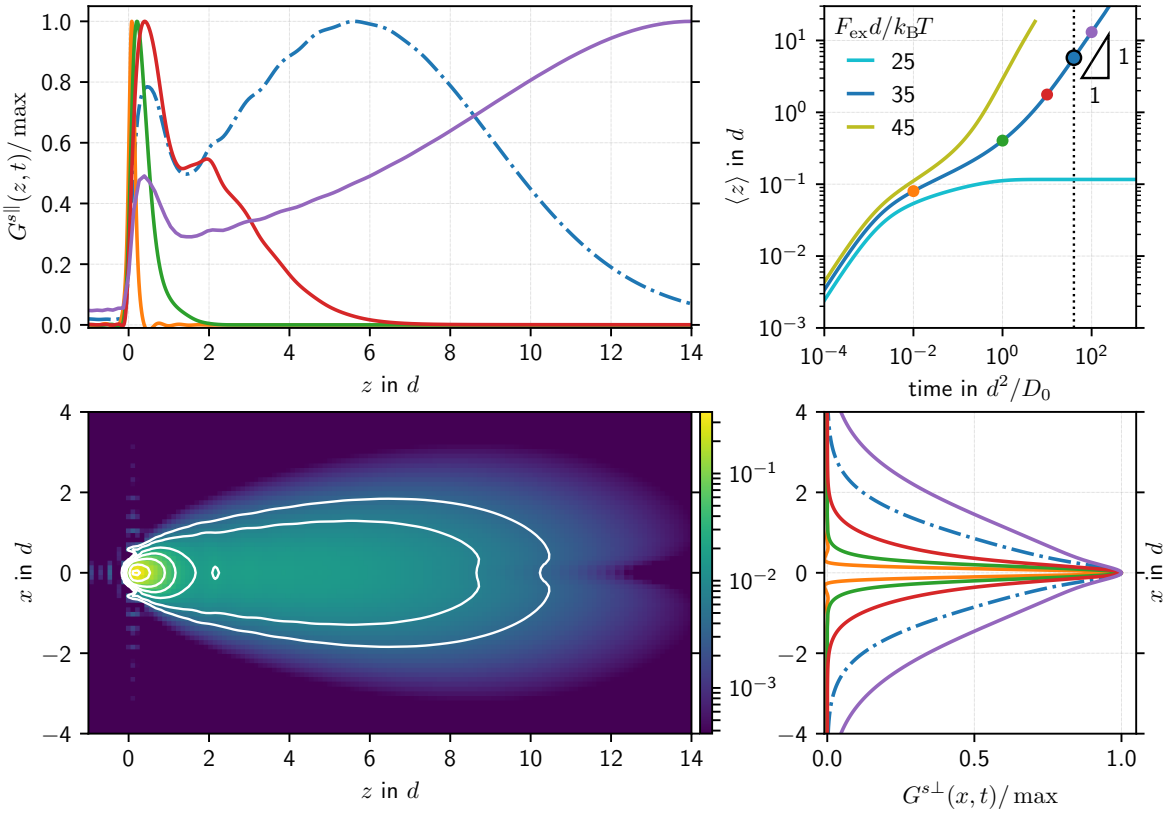

Figure 7.9.: Van Hove function for $\varphi_{\mathrm{MCT}} = 0.525$. The bottom left panel shows $G^s(x, 0, z, t)$ for $tD_0/d^2 = 50$. The full van Hove function is cylindrically symmetric around the z axis. The white lines label points with an equal probability density. The adjacent panels show the marginal probability distributions $G^{s\parallel}(z,t)$ at the top and $G^{s\perp}(x,t)$ to the right for different times. The dash-dotted line is the marginal probability distribution corresponding to the full van Hove function. The times for the other marginal van Hove functions are depicted by circles with the same color in the top right panel, which shows the mean displacement as function of the time.

observe that the probability density along the z axis is smaller than off-axis. This could mean that the particle indeed passes its neighbors by moving sideways instead of pushing them away. As there is an equal probability for going left or right (or up or down) this effect is only seen for the distances, which have been reached by a few realisations only. For smaller distances the largest probability is in the center, because it can be reached from all sides on different paths. As this effect is very small, we also have to consider that it might be just a numerical artifact, which is definitely present as small oscillations along the axes at the origin.

Together with the three-dimensional solution, we also show the corresponding marginal van Hove functions in parallel $G^{s\parallel}(z,t)$ and perpendicular direction $G^{s\perp}(z,t)$ (dash-dotted line). For comparison we also show them for different times together with the mean displacement. The width of the perpendicular van Hove function keeps increasing with time, highlighting that in the case of a spatially homogeneous force, there is indeed a particle transport perpendicular

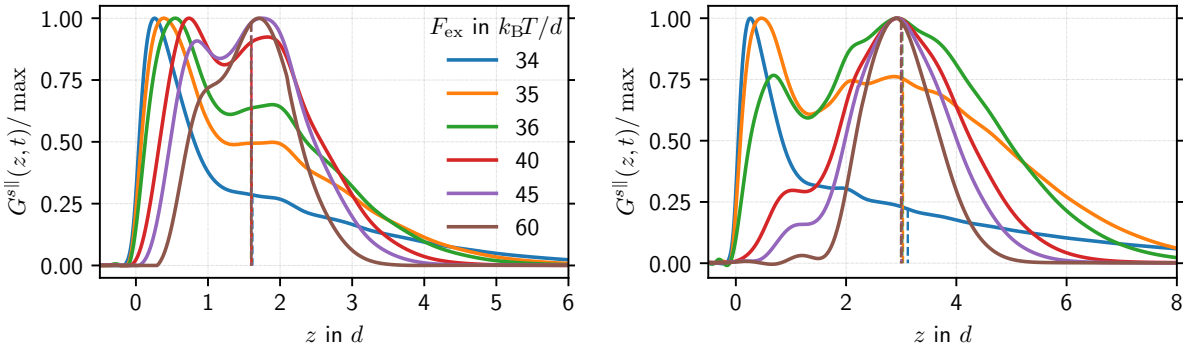

Figure 7.10.: Comparison of the van Hove functions for different forces at a mean displacement of $\langle z \rangle = 1.6\,d$ (left) and $\langle z \rangle = 3\,d$ (right). The critical force for $\varphi_{\mathrm{MCT}} = 0.525$ is $F_c = 34.386\,k_BT/d$.

to the force. In the parallel we observe this bimodal structure, which appears at times of about $10\,d^2/D_0$. Interestingly, this first peak arises at $z = 2d$, very close to an integer multiple of the probe diameter. This small maximum already appears below the critical force as can be seen in Figure 7.8 and Figure 4.27. In the simulations there, however, this peak arises at a position of about $1.5\,d$.

Finally, we note that almost nothing of this interesting behavior is reflected in the mean displacement. The only signature is an almost invisible sublinear increase of the mean displacement.

Since this heterogeneous dynamics with the bimodal van Hove function is interesting, but not seen in the mean displacement, we would like to know under which conditions it appears. A necessary condition is a mean displacement larger than 1 and not too large as we want to analyze a situation, where some particles have already left their cage but have not traveled too far. For the following analysis, we compare the van Hove functions for different forces at times, which lead to the same mean displacement, in particular $\langle z \rangle = 1.6\,d$ and $\langle z \rangle = 3\,d$ as shown in Figure 7.10. It is interesting to note that these mean displacements are realized by very different van Hove functions. The displacement $\langle z \rangle = 1.6\,d$ shown in the left panel is chosen to highlight the bimodal structure, because we have noticed that the probe position probability density shows peaks at approximately integer multiples of the particle diameter. Choosing the mean in between imposes the condition that those peaks are of similar height. We indeed find such a bimodal structure for a broad range of forces. With increasing force the probability to find the probe particle close to the origin decreases and a second peak arises above the critical force at around $z = 2\,d$, causing a bimodal structure for a broad force range. For the largest force however, this second peak moves to a value of about $z = 1.7\,d$ and grows at the expense of the first peak, which is only visible as a shoulder at around $z = 1\,d$ for $F_{ex} = 60\,k_BT/d$.

For a mean displacement of $\langle z \rangle = 3\,d$ there is still a bimodal structure for forces above the critical force. While the separation of the peaks is more pronounced for forces close to the critical force, it decreases for larger forces so that these van Hove functions show a reduced width. The minimum between the peaks is in this case at around $z = 1.5\,d$, while it was around $z = 1.2\,d$ for the smaller displacement. Hence, we conclude that this bimodal structure is most prominent at the delocalization transition. For large forces it reduces to an approximately Gaussian form.

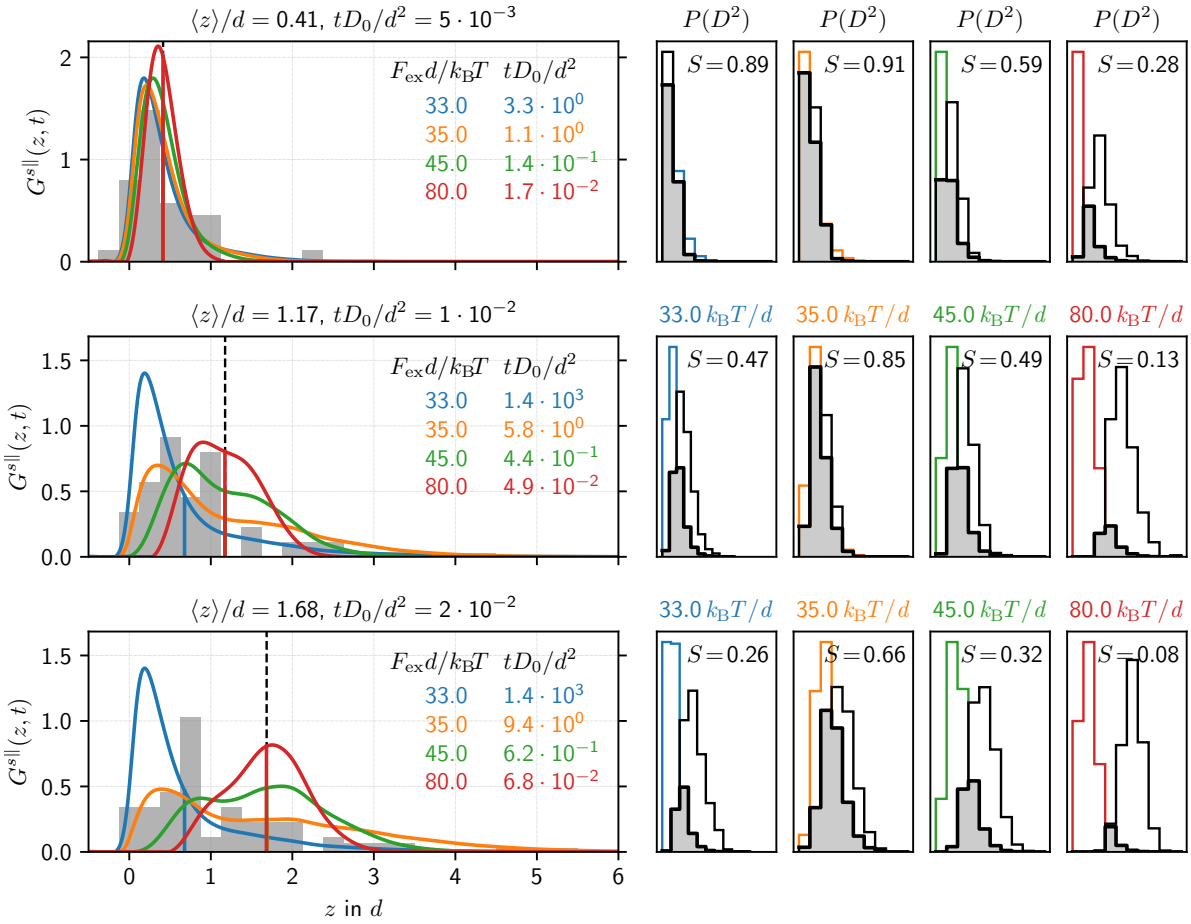

Figure 7.11.: Example for similarity analysis. Left column: Experimental histograms (grey bars) for $\varphi = 0.601$ and the largest force of 335 k_BT/d. MCT results for $G^{s\parallel}(x,t)$ for different forces as indicated in the panels. The times are chosen such that all probability distributions have the same mean as indicated in the titles ($\langle x\rangle/d$ =0.41,1.17,1.68 from top to bottom). The mean is visualized by vertical lines (dashed black for the experiment and solid colored for the theory). The time at which these mean displacements are reached are given in the title for the experiment and in the panel for the different MCT calculations. Right column: Difference distributions $P(D^2)$ for the histograms sampled from the given MCT results (colored lines) and of the experimental histogram with the MCT samples (black lines). The similarity measure S is highlighted in grey and given as number in the panels.

7.5.2. Similarity analysis

Since the experiments are very time consuming, we cannot obtain large statistics. Therefore, a direct comparison of the histograms with our MCT calculations would always lack the confidence that the result is not just pure coincidence. Fortunately, there is a possibility to check if a given sample is compatible with a certain probability density. This is achieved by comparing the probability distribution of distances between histograms, which will be presented in the following. We follow the procedure outlined in the supporting information of [FESS17, Sec. Similarity Function, p. 3f]. This analysis is summarized and visualized in Figure 7.11.

For the nomenclature let us call the histogram of the probe particle positions at a given time $P^{\text{exp}}(z)$. This histogram shall be normalized such that $P^{\text{exp}}(z)$ can be regarded as a (stepwise defined) probability density distribution. In particular we ask for the normalization condition

$$\int_{-\infty}^{\infty} P^{\text{exp}}(z)\mathrm{d}z = 1. \tag{7.7}$$

Therefore, we can treat $P^{\text{exp}}(z)$ as a regular probability distribution, which approximates the underlying (unknown) probability distribution. For this reason we will call these functions also *finite-sampling distributions*. They are shown as grey bars in the left hand side panels of Figure 7.11.

The squared distance between two arbitrary probability distributions $P_i(z)$ and $P_j(z)$ is given by

$$D_{i,j}^2 = \int_{-\infty}^{\infty} \left(P_i(z) - P_j(z)\right)^2 \mathrm{d}z \tag{7.8}$$

[FESS17, Eq. [S22], p. S3], which is the L^2-norm on the vector space of square-integrable functions and therefore indeed a measure for the distance between two probability distributions. Since we cannot access the full probability distributions directly in the experiment, we have to use their closest statistical counterpart, the histogram $P^{\text{exp}}(z)$. Since they are only a finite sample of the full probability distribution, they will differ even if drawn from the same underlying probability distribution.

On the other hand, we know the theoretical probability distribution P^{theo} (shown as colored lines in the left hand side of Figure 7.11) from which we can draw as many histograms as we need. This allows us to characterize the distribution of squared distances $P(D^2)$ between all finite-sampling distributions (histograms) $P_i(z)$ obtained independently from the same probability distribution. More precisely, the distribution of squared distances $P^D_{\text{hist}}(D^2)$ is the histogram of $D^2_{i,j}$ for all combinations of histograms with $i \neq j$. It is shown as histogram with the colored frame in the right hand side of Figure 7.11.

The key point is now the assumption that the experimental histogram was sampled from the probability distribution $P^{\text{theo}}(z)$ if it produces the same distribution of squared distances $P^D_{\text{exp}}(D^2)$ using the squared distances (cf. [FESS17, Eq. [S23], p. S4])

$$D^2_{\text{exp},i} = \int_{-\infty}^{\infty} \left(P^{\text{exp}}(z) - P_i(z)\right)^2 \mathrm{d}z \tag{7.9}$$

with the same synthetic finite-sampling distributions $P_i(z)$ as used to compute $P^D_{\text{hist}}(D^2)$. They are visualized as histograms with the black frame in the right hand side of Figure 7.11. To quantify the similarity of these distance distribution functions, we introduce the similarity S via

$$S = \int_{0}^{\infty} \min\left(P^D_{\text{hist}}(x), P^D_{\text{exp}}(x)\right) \mathrm{d}x \tag{7.10}$$

(cf. [FESS17, Eq. [S24], p. S4]). This is the overlapping area of both probability distributions, shown as grey shaded area in the right hand side of Figure 7.11. If they are the same we obtain

$S = 1$, while there holds $S = 0$ if they do not overlap at all.

For the numerical evaluation of the similarity, we take $N = 1000$ histograms from the theoretical probability distribution. Each histogram consists of the same number of samples as the experimental histogram and the same bins as well, since "[t]his procedure [...] is particularly sentitive to subtle variations in the parameters controlling the sampling and histogramming procedures" [FESS17, p. S4]. The bins for the position histogram are the same for all forces, times and packing fractions. To account for the different distributions, we use small bins (with width $0.125\,d$) around the origin which increase up to $1\,d$ for $z \geq 3.5\,d$ until the end of the line trap at $12\,d$. The bins for the histograms of $P(D^2)$ are determined automatically for P^D_{hist} and then applied to P^D_{exp}.

With this procedure, we can objectively find the theory curve, which fits best to the experimental data by maximizing the similarity.

7.5.3. Histogram comparison

The preceding analysis allows us to quantify the agreement between theory and experiment. However, there remains the question how to compare. In Section 7.4 we have already seen that the time-scale of the MCT calculations with respect to the mean displacements is off by at least one order of magnitude. On the other hand, we have seen in this section, that there are many qualitatively similar features. To eliminate the time scale, we compare the histograms at times, which exhibit the same mean displacement. This allows us to investigate the structural features of the histograms, which are connected to the length scale of the bath particles rather than the time scale.

With this procedure, we can unveil the structural differences between a fluid state and a glass as shown in Figure 7.12. We compare histograms for the glass with the histograms of the fluid at the same mean displacement. Since we find always smaller displacements in the glass, they set the scale for the comparison. This comparison is carried out for different forces. They are the same or at least comparable for both experiments. For small forces there is little difference between the behavior in a fluid or a glassy host. These data agree also very well with the zero-order approximation: A Gaussian with the same mean and the variance obtained from the quiescent MSD at the same time (shown as red dashed line). With increasing force, the mean increases and the histograms become right-skewed, i.e. they extend more in force direction. For a force of $135\,k_{\text{B}}T/d$ the van Hove function is already much broader than the zero-order approximation, which says in other words that we have a force-induced broadening of the van Hove function.

It is remarkable that for forces larger than $135\,k_{\text{B}}T/d$ there are some trajectories in the glass state, which reach quite large displacements (labeled by arrows). This is in contrast to the fluid state, where the van Hove function is narrower and does not exhibit any of these outlier-like trajectories. Even if they look like outliers, they are just a simple consequence of the long exponential tail of the van Hove function (shown as black lines). This experiment shows that there is a strongly heterogeneous dynamics in the glass and a force-induced broadening of the van Hove function in the fluid state. A reason for this could be the intrinsic dynamical heterogeneities in a glass [Sil99]. Through the application of an external force, the jumps between cages [Vol04] do not occur with equal probability in each direction anymore, but they are biased in force direction. This allows us to make them visible through the asymmetric and

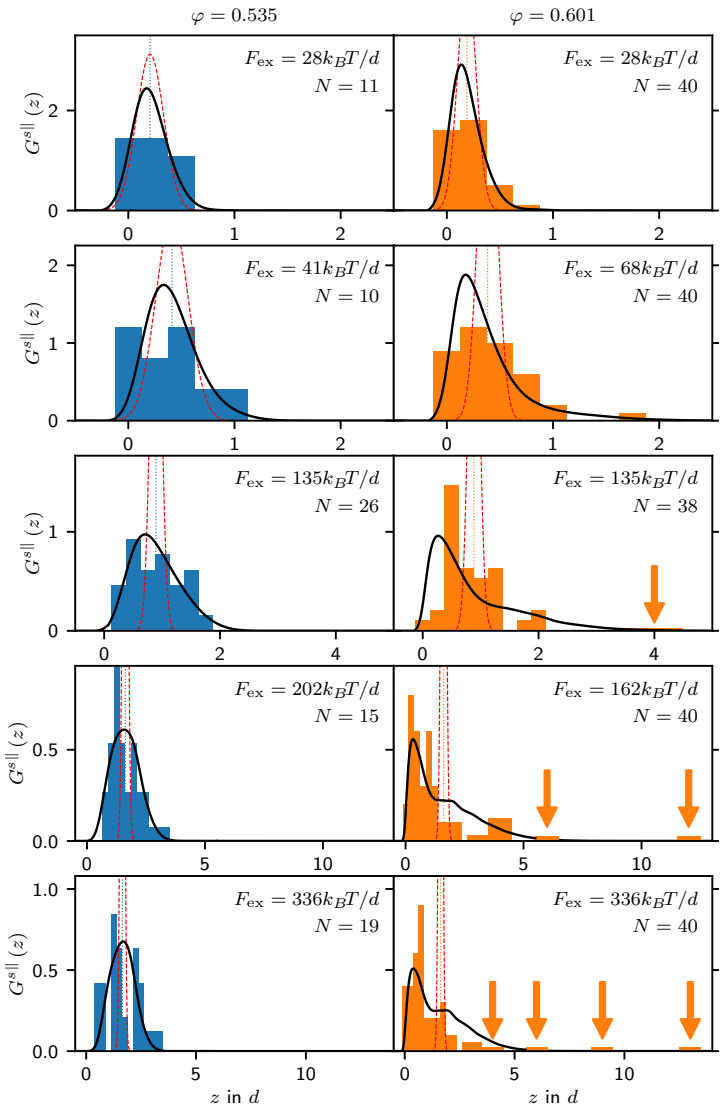

Figure 7.12.: Comparison of the probe position histograms (of N observations) for different forces (rows, increasing from top to bottom) in the fluid (left column, $\varphi = 0.535$) and the glass (right column, $\varphi = 0.601$). For each force we compare the histograms at times, which show the same mean displacement. This displacement (dotted vertical lines) is determined by the largest displacement available in the glass: $\langle z \rangle / d = 0.2, 0.4, 0.9, 1.6, 1.6$. Arrows label single observations. The theory curves (black lines) are chosen such that their similarity (as introduced in (7.10)) is maximal. For comparison we plot a Gaussian with the same mean and the variance of the quiescent MSD (red dashed line) at the same time. The times at which the histograms are taken are: 32.2 s, 64.8 s, 7.6 s, 9.0 s, 5.8 s for the fluid and 973 s, 801 s, 644 s, 642 s, 59 s for the glass from top to bottom [ŞGZ+19, Fig. 4].

bimodal structure in the van Hove function.

7.6. Critical force

Finally, we want to address the question: What is the critical force in the experimental system? In Chapter 4 and Chapter 5 we have found different features, which are characteristic at the critical force. The determining phenomenon was the question whether the mean displacement saturates for long times or not. For this analysis we focus on the packing fraction $\varphi = 0.601$. The experimental mean displacements were already shown in Figure 7.6. Since there is only one trajectory with a linear increase at long times in the glass, we can only conclude that $F_c < 336\, k_B T/d$. The other trajectories may or may not saturate at long times. If we check if the local exponents of the mean displacements are smaller or larger than the critical exponent, the situation is even worse, because of the noise in the data. This gets amplified so much that exponents cannot be determined reliably. On top of that, we do not know what the real critical

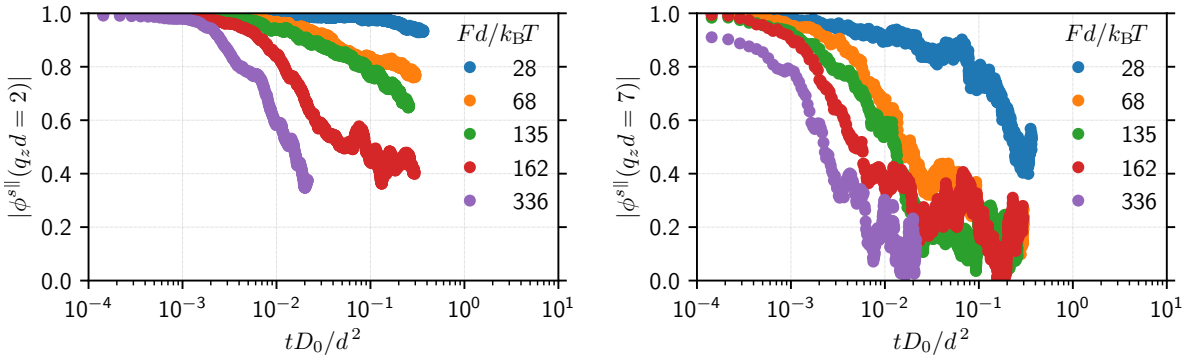

Figure 7.13.: Intermediate scattering function $\phi^{s\parallel}(q_z, t)$ obtained from the experimental trajectories for $q_z d = 2$ (left) and $q_z d = 7$ (right) for different forces as labeled. The average becomes ill-defined as soon as the first particle leaves the trap. This explains the early end time for large forces.

exponents are, as we find different values in MCT and simulations (cf. Sec. 5.9).

More promising is the calculation of the correlation functions, which are obtained from the trajectories by definition (2.98) via

$$\phi^{s\parallel}(q_z, t) = \left\langle \mathrm{e}^{\mathrm{i}q_z(z(t)-z(0))} \right\rangle = \frac{1}{N} \sum_{i=1}^{N} \mathrm{e}^{\mathrm{i}q_z(z(t)-z(0))}. \tag{7.11}$$

They are shown for two wave vectors in Figure 7.13. For $q_z d = 7$ all correlation functions basically decay, which suggests that the probe particle can move more than the associated length scale of the order $0.1\,d$. Since the peak of the structure factor is around this value, we can associate this with the motion in the cage. For the smaller wave vector $q_z d = 2$ the decay of the correlation functions resembles more closely, what we found for the MCT solutions for the correlation function in Figure 5.11: The correlation functions for $F_{\mathrm{ex}} \leq 68\,k_{\mathrm{B}}T/d$ seem to saturate at a finite value, while the correlation functions for $F_{\mathrm{ex}} \geq 162\,k_{\mathrm{B}}T/d$ decay quite fast. One could argue that the correlation function for $F_{\mathrm{ex}} = 135\,k_{\mathrm{B}}T/d$ looks very similar to the critical behavior. However, one has to take into account that in this figure, there is a linear scale on the y axis and the effect of the noise on the correlation functions is not clear. From these observations, we would conclude $68\,k_{\mathrm{B}}T/d < F_{\mathrm{c}} < 162\,k_{\mathrm{B}}T/d$.

The last method to determine the critical force is based on the observation, that the particles escape their cage above the delocalization transition. Therefore, calculate the probability to find particles outside their cage. In a close packed hexagonal lattice, the next cage would be a distance $\sqrt{3}d$ away (two times the height of an equilateral triangle with side length d). In 3D this distance could be a little bit smaller ($\sqrt{249}d$ two times the height of a tetrahedron with side length d), but with disorder slightly larger. Therefore it seems to be a good choice to define particles, which have travelled a distance larger than $\sqrt{3}d$ to have escaped their cage. From the van Hove function, this probability is obtained via

$$P_{\mathrm{escaped}}(t) = \int_{\sqrt{3}d}^{\infty} G^{\parallel}(z, t)\mathrm{d}z \tag{7.12}$$

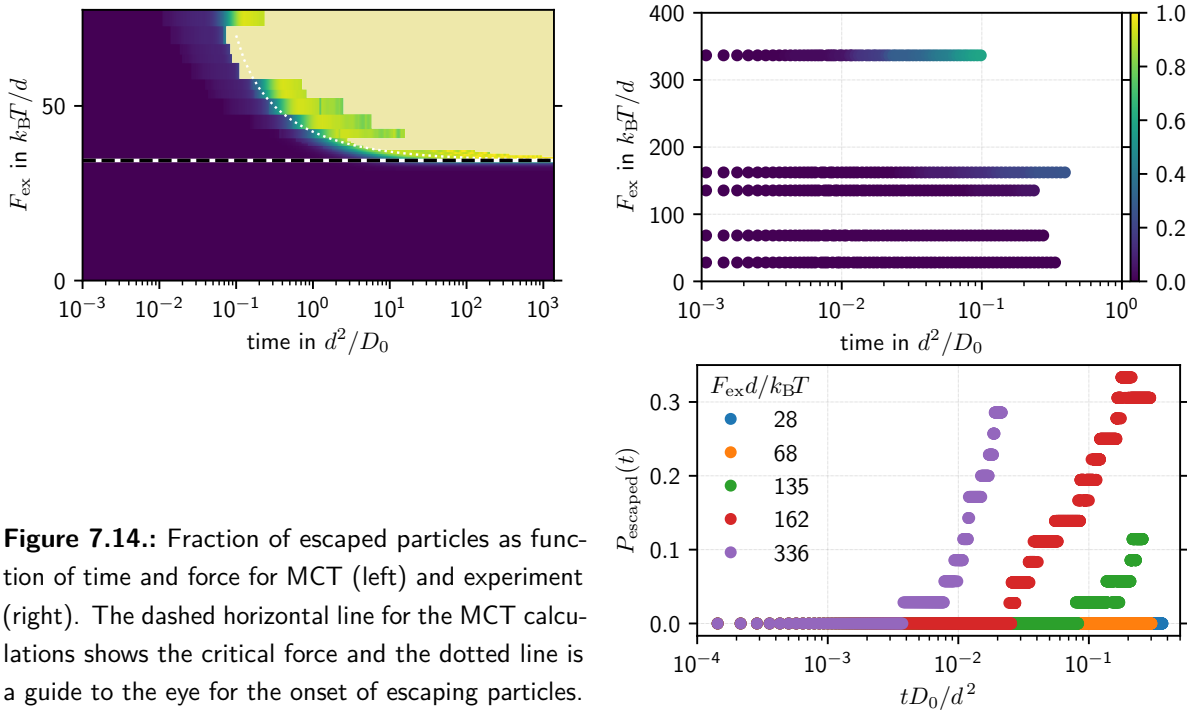

Figure 7.14.: Fraction of escaped particles as function of time and force for MCT (left) and experiment (right). The dashed horizontal line for the MCT calculations shows the critical force and the dotted line is a guide to the eye for the onset of escaping particles.

and from the experiments via

$$P_{\text{escaped}}(t) = \frac{1}{N}\sum_{i=1}^{N}\begin{cases}1, & r_i(t) > \sqrt{3}d,\\ 0, & r_i(t) \leq \sqrt{3}d.\end{cases} \tag{7.13}$$

To verify the claim that the particles only leave their cages above the critical force, we show a 2D map of $P_{\text{escaped}}(t)$ for different forces in Figure 7.14 as obtained by MCT calculations ($\varphi = 0.525$, `unilog10` with 111 grid points and $q_{\max}d = 15$). At long times, we find a very sharp transition from all particles caged to all particles escaped. If one has a very close look the transition is smooth and compatible with our findings for the correlation functions in Section 4.5. The experimental equivalent is shows next to it in the same figure. The particles noticeably escape for $F_{\text{ex}} \geq 162\,k_BT/d$. Since we have only five different forces for the experiment, they are easier to analyze, if we show the probability of escaped particles directly as function of time as shown in the bottom panel of Figure 7.14. This confirms that there are many particles escaping for $F_{\text{ex}} \geq 162\,k_BT/d$ and no particles escaping for $F_{\text{ex}} \leq 68\,k_BT/d$. For $F_{\text{ex}} = 135\,k_BT/d$ there is a small, but finite probability that the probe particle can escape. This is again a behavior, which resembles the one close to the critical force. Hence, we can consistently conclude that the critical force is in the interval $F_cd/k_BT \in [68, 162]$ and probably close to, but slightly smaller than $135\,k_BT/d$. The values in this range are larger than what we observe in our MCT calculations, but are comparable to the findings of the simulations.

7.7. Conclusions

We compared our theoretical calculations to an experiment using a dense suspension of emulsion droplets as host and an optical line trap to exert a constant force on a probe particle made of polystyrene. The time scale is mapped by comparing the quiescent mean square displacements for theory and experiment to account for hydrodynamic interactions. The packing fractions are converted directly without any fit. For the calibration of the force, we establish a linear response relation between the mean displacement under force and the quiescent mean square displacement. This relation holds for small forces below the glass transition and is also compatible with the data in the glass. A parameter free comparison of the MCT solutions with the experimental mean displacements shows the same qualitative features, but on different time scales.

The experimental trajectories exhibit a large variety of behaviors: in some experiments the probe is stuck for the whole duration of the experiment, while it moves quite far in others. This is not a problem of the experimental setup, but an intrinsic feature of the probe dynamics in the glass. We show that the van Hove function obtained from the MCT calculations shows a bimodal structure, with a peak close to the origin, which accounts for the trajectories which are stuck, and a peak, which arises at a distance of about $2\,d$, which moves towards infinity for long times, which accounts for the trajectories which can leave their cages. The comparison between theory and experiment is made quantitative by a similarity analysis the histograms. We find a broadening of the van Hove function as compared to the quiescent case, which is more pronounced in the glass. Finally, we apply different methods to find the critical force, which is estimated to be in the interval $F_{\mathrm{c}}d/k_{\mathrm{B}}T \in [68, 162]$, probably close to $135\,k_{\mathrm{B}}T/d$.

8. Active microrheology in active suspensions

Life is like riding a bicycle.
To keep your balance you must keep moving.

(Albert Einstein, Letter to his son Eduard (5.2.1930))

In this chapter we will analyze the predictions of active microrheology in a dilute suspension of active particles. The equations of motion for the pair correlation function have been derived in Section 2.5. We consider a constant velocity experiment with an ellipsoid of fixed orientation to keep the complicated equations as simple as possible. Furthermore, we only analyze the stationary limit to calculate the friction coefficient of the probe. The resulting partial differential equations for the bath particle density n and the polar order field $\boldsymbol{m}$ are given in Cartesian coordinates in (2.256) with no-flux boundary condition for the fluxes (2.255) and in spheroidal coordinates in (2.259) with boundary conditions (2.261).

We will start by analyzing some special cases, which can be solved analytically to evaluate the different solution strategies. Then, we establish a finite-difference scheme to solve the partial differential equation numerically. We verify this scheme by reproducing results from literature for different special cases. Then we analyze the effect of activity on the friction coefficient for different activities, run lenghts, aspect ratios and activities. For small activities there is always a reduction of the friction coefficient, but for large activities it depends strongly on the shape. Therefore, we analyze for non-moving spheroids the particle fluxes on the surface and the swim pressure or density at the surface based on the curvature. Finally, we can relate the particle transport due to the symmetry breaking of the flow to the observed changes in the friction coefficient.

8.1. Analytic solutions for special cases

We approach the solution of the full partial differential equation (2.259) with the no-flux boundary conditions (2.261) step by step. This allows us to learn about the features of the equation and to explore different solution strategies.

8.1.1. Solution for isotropic, quiescent, passive systems

In the isotropic ($\Delta D = 0$), quiescent ($\mathrm{Pe}^{\mathrm{ext}} = 0$), passive ($\mathrm{Pe}^{\mathrm{act}} = 0$) case, the equations of motion read

$$\partial_t n(\boldsymbol{r}, t) = \left(1 + \frac{\overline{D}}{s}\right) \boldsymbol{\partial}_r^2 n(\boldsymbol{r}, t), \tag{8.1a}$$

$$\partial_t m_i(\boldsymbol{r}, t) = \left(1 + \frac{\overline{D}}{s}\right) \boldsymbol{\partial}_r^2 m_i(\boldsymbol{r}, t), \tag{8.1b}$$

Using the representation in spheroidal coordinates, we have to solve

$$0 = \left(\frac{\cosh(\xi)}{\sinh(\xi)}\partial_\xi + \frac{\cos(\eta)}{\sin(\eta)}\partial_\eta + \partial_\xi^2 + \partial_\eta^2 + \left(\frac{1}{\sinh^2(\xi)} + \frac{1}{\sin^2(\eta)}\right)\partial_\phi^2\right) n(\xi,\eta,\phi) \tag{8.2a}$$

$$0 = \left(\frac{\cosh(\xi)}{\sinh(\xi)}\partial_\xi + \frac{\cos(\eta)}{\sin(\eta)}\partial_\eta + \partial_\xi^2 + \partial_\eta^2 + \left(\frac{1}{\sinh^2(\xi)} + \frac{1}{\sin^2(\eta)}\right)\partial_\phi^2\right) m_i(\xi,\eta,\phi) \tag{8.2b}$$

for the stationary case, subject to the boundary conditions

$$0 = \partial_\xi n(\xi,\eta,\phi) \quad \text{for } \xi = \xi_0, \tag{8.3a}$$

$$n_b = \lim_{\xi\to\infty} n(\xi,\eta,\phi), \tag{8.3b}$$

$$0 = \partial_\xi m_i(\xi,\eta,\phi) \quad \text{for } \xi = \xi_0, \tag{8.3c}$$

$$0 = \lim_{\xi\to\infty} m_i(\xi,\eta,\phi). \tag{8.3d}$$

The last condition expresses the fact, that this system should not show any polar order for large distances.

The ansatz $n(\xi,\eta,\phi) = X(\xi)E(\eta)\Phi(\phi)$ for separation of variables yields the following ordinary differential equations

$$0 = \partial_\phi^2\Phi(\phi) + k^2\Phi(\phi), \tag{8.4a}$$

$$0 = \sinh^2(\xi)\partial_\xi^2 X(\xi) + \cosh(\xi)\sinh(\xi)\partial_\xi X(\xi) + l\sinh^2(\xi)X(\xi) + k^2, \tag{8.4b}$$

$$0 = \sin^2(\eta)\partial_\eta^2 + \cos(\eta)\sin(\eta)\partial_\eta E(\eta) - l\sin^2(\eta)E(\eta) + k^2, \tag{8.4c}$$

with the separation constants k and l. The requirement $\Phi(0) = \Phi(2\pi)$ implies $k \in \mathbb{N}_0$, because the general solution for $\Phi(\phi)$ reads

$$\Phi(\phi) = A_\phi\cos(k\phi) + B_\phi\sin(k\phi). \tag{8.5a}$$

The isotropic nature of the problem suggests $k = 0$ and we are therefore only looking for solutions for $X(\xi)$ and $E(\eta)$ with $k = 0$. For $l = 0$ we find the solutions

$$X(\xi) = A_\xi + B_\xi\ln(\tanh(\xi/2)), \tag{8.5b}$$

$$E(\eta) = A_\eta + B_\eta\cos(-\eta). \tag{8.5c}$$

The boundary conditions imply $B_\xi = B_\eta = B_\phi = 0$ and $A_\xi = A_\eta = A_\phi = n_b$ resulting in the homogeneous solution

$$n(\xi,\eta,\phi) = n_b. \tag{8.6a}$$

With the same reasoning one can conclude

$$\boldsymbol{m}(\xi,\eta,\phi) = 0. \tag{8.6b}$$

Hence, the passive bath particles are homogeneously distributed without a particular orientation.

8.1.2. Solution for quiescent spherical probe in active bath

The density profile of active particles and their polar order field around a fixed spherical obstacle has already been solved by Yan and Brady [YB15a]. In our case, we want to find a solution for a diffusing spherical probe. For this, we follow [YB15a, Sec. 3, p. 4-7], but there are not many

details of the calculation given. Furthermore, they use a different set of dimensionless variables. Therefore, we will derive the intermediate steps by ourselves. The equations of motion here read

$$\partial_t n(\boldsymbol{r},t) + \boldsymbol{\partial}_r \cdot \boldsymbol{j}_n(\boldsymbol{r},t) = 0, \tag{8.7a}$$

$$\partial_t m_i(\boldsymbol{r},t) + \boldsymbol{\partial}_r \cdot \boldsymbol{j}_{m,i}(\boldsymbol{r},t) + 2\frac{\mathrm{Pe}^{\mathrm{act}}}{\overline{\ell}} m_i(\boldsymbol{r},t) = 0, \tag{8.7b}$$

with the fluxes

$$\boldsymbol{j}_n = -\tilde{D}\boldsymbol{\partial}_r n + \mathrm{Pe}^{\mathrm{act}}\boldsymbol{m}, \tag{8.8a}$$

$$\boldsymbol{j}_{m,i} = -\tilde{D}\boldsymbol{\partial}_r m_i + \hat{\boldsymbol{i}}\frac{\mathrm{Pe}^{\mathrm{act}}}{3} n, \tag{8.8b}$$

where $\tilde{D} = (1 + \overline{D}(1)/s)$. The main difference to [YB15a, p. 3, Eqs. (2.3), (2.4)] is the diffusion coefficient $\tilde{D}$ vs D_T, which accounts for the diffusive motion of the probe. The quotient $\mathrm{Pe}^{\mathrm{act}}/\overline{\ell}$ can be interpreted as dimensionless rotation diffusion coefficient due to

$$\frac{\mathrm{Pe}^{\mathrm{act}}}{\overline{\ell}} = \frac{u_0 d}{D_b}\frac{d}{u_0\tau_0} = D_R\frac{d^2}{D_b}. \tag{8.9}$$

To account for the spherical geometry of the boundary condition, we convert the equation to spherical coordinates via

$$\begin{aligned} x &= r\sin\theta\cos\phi \\ y &= r\sin\theta\sin\phi \\ z &= r\cos\theta. \end{aligned} \tag{8.10}$$

Following the procedures of Section 2.5.3 and Appendix D we find

$$Q = \begin{pmatrix} \sin(\theta)\cos(\phi) & \cos(\theta)\cos(\phi) & -\sin(\phi) \\ \sin(\theta)\sin(\phi) & \sin(\phi)\cos(\theta) & \cos(\phi) \\ \cos(\theta) & -\sin(\theta) & 0 \end{pmatrix} \tag{8.11}$$

and

$$\partial_x = \sin(\theta)\cos(\phi)\partial_r - \frac{\cos(\theta)\cos(\phi)}{r}\partial_\theta + \frac{\sin(\phi)}{r\sin(\theta)}\partial_\phi, \tag{8.12a}$$

$$\partial_y = \sin(\theta)\sin(\phi)\partial_r + \frac{\cos(\theta)\sin(\phi)}{r}\partial_\theta + \frac{\cos(\phi)}{r\sin(\theta)}\partial_\phi, \tag{8.12b}$$

$$\partial_z = \cos(\theta)\partial_r - \frac{\sin(\theta)}{r}\partial_\theta. \tag{8.12c}$$

Inserting these results into the equations above, we find

$$\begin{aligned} \partial_t n =& \tilde{D}\left(\partial_r^2 + \frac{2}{r}\partial_r + \frac{1}{r^2}\frac{\cos(\theta)}{\sin(\theta)}\partial_\theta + \frac{1}{r^2}\partial_\theta^2 + \frac{1}{r^2\sin^2\theta}\partial_\phi^2\right) n \\ &- \mathrm{Pe}^{\mathrm{act}}\left(\frac{2}{r}m_r + \partial_r m_r + \frac{\cos(\theta)}{r\sin(\theta)}m_\theta + \frac{1}{r}\partial_\theta m_\theta + \frac{1}{r\sin(\theta)}\partial_\phi m_\phi\right), \end{aligned} \tag{8.13a}$$

$$\begin{aligned}\partial_t m_r =&\tilde{D}\left(\left(\partial_r^2+\frac{2}{r}\partial_r+\frac{1}{r^2}\frac{\cos(\theta)}{\sin(\theta)}\partial_\theta+\frac{1}{r^2}\partial_\theta^2+\frac{1}{r^2\sin^2\theta}\partial_\phi^2-\frac{2}{r^2}\right)m_r\right.\\&\left.-\frac{2\cos(\theta)}{r^2\sin(\theta)}m_\theta-\frac{1}{r^2\sin(\theta)}m_\phi-\frac{2}{r^2}\partial_\theta m_\theta-\frac{2}{r^2\sin(\theta)}\partial_\phi m_\phi\right)\\&-2\frac{\mathrm{Pe}^{\mathrm{act}}}{\bar{\ell}}m_r-\frac{\mathrm{Pe}^{\mathrm{act}}}{3}\partial_r n,\end{aligned}\tag{8.13b}$$

$$\begin{aligned}\partial_t m_\theta =&\tilde{D}\left(\left(\partial_r^2+\frac{2}{r}\partial_r+\frac{1}{r^2}\frac{\cos(\theta)}{\sin(\theta)}\partial_\theta+\frac{1}{r^2}\partial_\theta^2+\frac{1}{r^2\sin^2\theta}\partial_\phi^2-\frac{1}{r^2\sin^2(\theta)}\right)m_\theta\right.\\&\left.+\frac{2}{r^2}\partial_\theta m_r-\frac{2}{r^2\sin^2\theta}\cos(\theta)\partial_\phi m_\phi\right)-2\frac{\mathrm{Pe}^{\mathrm{act}}}{\bar{\ell}}m_\theta-\frac{\mathrm{Pe}^{\mathrm{act}}}{3r}\partial_\theta n,\end{aligned}\tag{8.13c}$$

$$\begin{aligned}\partial_t m_\phi =&\tilde{D}\left(\left(\partial_r^2+\frac{2}{r}\partial_r+\frac{1}{r^2}\frac{\cos(\theta)}{\sin(\theta)}\partial_\theta+\frac{1}{r^2}\partial_\theta^2+\frac{1}{r^2\sin^2\theta}\partial_\phi^2-\frac{1}{r^2\sin^2(\theta)}\right)m_\phi\right.\\&\left.+2(\sin(\theta)\partial_\phi m_r+\cos(\theta)\partial_\phi m_\theta)\right)-2\frac{\mathrm{Pe}^{\mathrm{act}}}{\bar{\ell}}m_\phi-\frac{\mathrm{Pe}^{\mathrm{act}}}{3}\frac{1}{r\sin(\theta)}\partial_\phi n,\end{aligned}\tag{8.13d}$$

and the no-flux boundary conditions transform into

$$0=\hat{\boldsymbol{r}}\cdot\boldsymbol{j}_n=-\tilde{D}\partial_r n+\mathrm{Pe}^{\mathrm{act}}m_r,\tag{8.14a}$$

$$0=\hat{\boldsymbol{r}}\cdot\boldsymbol{j}_{m_i}=-\tilde{D}\partial_r m_i+\hat{\boldsymbol{r}}\cdot\hat{\boldsymbol{i}}\frac{\mathrm{Pe}^{\mathrm{act}}}{3}n\tag{8.14b}$$

for $i\in\{r,\theta,\phi\}$ at $r=(s+1)/2$.

Assuming symmetry in ϕ, we find that the equation for m_ϕ decouples from the others and $m_\phi=0$ is a stationary solution, which fulfills the boundary condition. Similarly, if there is additional symmetry in θ, we find that $m_\theta=0$ is a stationary solution, which fulfills the boundary condition. It remains to solve the stationary equations for n and m_r

$$0=\tilde{D}\left(\partial_r^2+\frac{2}{r}\partial_r\right)n-\mathrm{Pe}^{\mathrm{act}}\left(\frac{2}{r}m_r+\partial_r m_r\right),\tag{8.15a}$$

$$0=\tilde{D}\left(\partial_r^2+\frac{2}{r}\partial_r-\frac{2}{r^2}\right)m_r-2\frac{\mathrm{Pe}^{\mathrm{act}}}{\bar{\ell}}m_r-\frac{\mathrm{Pe}^{\mathrm{act}}}{3}\partial_r n,\tag{8.15b}$$

subject to the boundary conditions

$$0=-\tilde{D}\partial_r n+\mathrm{Pe}^{\mathrm{act}}m_r,\tag{8.16a}$$

$$0=-\tilde{D}\partial_r m_r+\frac{\mathrm{Pe}^{\mathrm{act}}}{3}n\tag{8.16b}$$

on $r=(s+1)/2$ and $\lim_{r\to\infty}n(r)=n_b$, $\lim_{r\to\infty}m_r(r)=0$. We start with the ansatz

$$m_r(r)=M_1\partial_r n(r)\tag{8.17}$$

to get equations for $n(r)$ only. This implies

$$0=(\tilde{D}-M_1\mathrm{Pe}^{\mathrm{act}})\frac{1}{r}\left(r\partial_r^2 n(r)+2\partial_r n(r)\right),\tag{8.18a}$$

$$0=\frac{\tilde{D}^2}{\mathrm{Pe}^{\mathrm{act}}}\left(\partial_r^2+\frac{2}{r}\partial_r-\frac{2}{r^2}-\lambda^2\right)\partial_r n(r)\tag{8.18b}$$

where we already inserted the solution condition for the first equation

$$M_1 = \frac{\tilde{D}}{\mathrm{Pe}^{\mathrm{act}}} \tag{8.19}$$

into the second equation and defined

$$\lambda^2 = 2\left(\frac{\alpha}{\overline{\ell}} + \frac{\alpha^2}{6}\right), \tag{8.20a}$$

$$\alpha = \frac{\mathrm{Pe}^{\mathrm{act}}}{\tilde{D}}. \tag{8.20b}$$

The boundary conditions transform into

$$\partial_r^2 n(R) = \frac{\alpha^2}{3} n(R), \tag{8.21a}$$

$$\lim_{r\to\infty} n(r) = n_b. \tag{8.21b}$$

for $R = (s+1)/2$. The general solution of (8.18b) is given by

$$n(r) = c_1 + c_2 \frac{\mathrm{e}^{-\lambda r}}{r} + c_3 \frac{\mathrm{e}^{\lambda r}}{r}. \tag{8.22}$$

The boundary condition (8.21b) implies $c_3 = 0$ and $c_1 = n_b$. From (8.21a) we can deduce

$$c_2 = n_b \frac{\alpha^2}{3}\left(\lambda^2 + 2\frac{\lambda}{R} + \frac{2}{R^2} - \frac{\alpha^2}{3}\right)^{-1} R\mathrm{e}^{\lambda R} \tag{8.23}$$

for $R = (s+1)/2$. Hence, the final result is

$$\frac{n(r)}{n_b} = 1 + \frac{\alpha^2 R^2}{3(\lambda R+1)^2 + 3 - \alpha^2 R^2} \frac{R}{r} \mathrm{e}^{-\lambda(r-R)}, \tag{8.24a}$$

$$\frac{m_r(r)}{n_b} = -\frac{\alpha R(\lambda r+1)}{3(\lambda R+1)^2 + 3 - \alpha^2 R^2} \frac{R^2}{r^2} \mathrm{e}^{-\lambda(r-R)}. \tag{8.24b}$$

Active particles accumulate at the boundary, because of the no-flux boundary conditions and the finite reorientation time [EG13]. Since particles pointing away from the surface will swim away immediately, while particles pointing into the surface have to wait until they reorient, there is a net orientation of the particles towards the surface (m_r is negative).

8.1.3. Analytical solution for a quiescent ellipsoid in an active bath

We try to find a stationary solution for the following system of equations based on (2.256):

$$0 = \tilde{D}\boldsymbol{\partial}_r^2 n(\boldsymbol{r}) - \mathrm{Pe}^{\mathrm{act}} \boldsymbol{\partial}_r \cdot \boldsymbol{m}(\boldsymbol{r}), \tag{8.25a}$$

$$0 = \left(\tilde{D}\boldsymbol{\partial}_r^2 - 2\frac{\mathrm{Pe}^{\mathrm{act}}}{\overline{\ell}}\right) m_i(\boldsymbol{r}) - \frac{\mathrm{Pe}^{\mathrm{act}}}{3} \partial_{r,i} n(\boldsymbol{r}). \tag{8.25b}$$

fulfilling the no-flux boundary conditions on the surface $\partial\mathcal{V}$ of the excluded volume

$$\boldsymbol{n}\cdot\boldsymbol{j}_n = 0, \tag{8.26a}$$
$$\boldsymbol{n}\cdot\boldsymbol{j}_{m,i} = 0, \tag{8.26b}$$

where $\boldsymbol{n}$ is the surface normal and the fluxes are given by

$$\boldsymbol{j}_n = \tilde{D}\boldsymbol{\partial}_r n(\boldsymbol{r}) - \mathrm{Pe}^{\mathrm{act}}\boldsymbol{m}(\boldsymbol{r}), \tag{8.26c}$$
$$\boldsymbol{j}_{m,i} = \tilde{D}\boldsymbol{\partial}_r m_i(\boldsymbol{r}) - \frac{\mathrm{Pe}^{\mathrm{act}}}{3}\hat{\boldsymbol{i}}n(\boldsymbol{r}), \tag{8.26d}$$

with the abbreviation $\tilde{D} = (1 + D(\hat{a})s^{-1})$. Instead of solving for the fields n and $\boldsymbol{m}$ directly, we rewrite the equations (8.25) in terms of the auxiliary function

$$f(\boldsymbol{r}) = \boldsymbol{\partial}_r \cdot \boldsymbol{m}(\boldsymbol{r}) = \sum_i \partial_i m_i(\boldsymbol{r}) \tag{8.27}$$

and obtain

$$\boldsymbol{\partial}_r^2 n = \frac{\mathrm{Pe}^{\mathrm{act}}}{\tilde{D}} f, \tag{8.28a}$$
$$m_i = \frac{\bar{\ell}\tilde{D}}{2\mathrm{Pe}^{\mathrm{act}}}\left(\boldsymbol{\partial}_r^2 m_i - \frac{\mathrm{Pe}^{\mathrm{act}}}{3\tilde{D}}\partial_i n\right). \tag{8.28b}$$

Substituting the equations (8.28b) into (8.27) and making use of relation (8.28a) we find

$$0 = \boldsymbol{\partial}_r^2 f(\boldsymbol{r}) + \kappa^2 f(\boldsymbol{r}) \tag{8.29}$$

with

$$\kappa^2 = -2\frac{\mathrm{Pe}^{\mathrm{act}}}{\bar{\ell}\tilde{D}} - \frac{1}{3}\left(\frac{\mathrm{Pe}^{\mathrm{act}}}{\tilde{D}}\right)^2, \tag{8.30}$$

which is called *Helmholtz* equation. This equation is separable in spheroidal coordinates. According to [MS71, p. 30] the equations for the separation $f(\xi,\eta,\phi) = R(\xi)S(\eta)\Phi(\phi)$ read

$$0 = R''(\xi) + \frac{\cosh(\xi)}{\sinh(\xi)}R'(\xi) + \left(c^2\sinh^2(\xi)\kappa^2 - \alpha_2 - \frac{\alpha_3}{\sinh^2(\xi)}\right)R(\xi), \tag{8.31a}$$
$$0 = S''(\eta) + \frac{\cos(\eta)}{\sin(\eta)}S'(\eta) + \left(c^2\sin^2(\eta)\kappa^2 + \alpha_2 - \frac{\alpha_3}{\sin^2(\eta)}\right)S(\eta), \tag{8.31b}$$
$$0 = \Phi'(\phi) + \alpha_3\Phi(\phi), \tag{8.31c}$$

where α_2 and α_3 are separation parameters. Considering only cylindrically symmetric solutions, we set $\alpha_3 = 0$. The two remaining equations can be simplified using the substitutions

$$x = \cosh(\xi), \tag{8.32a}$$
$$y = \cos(\eta), \tag{8.32b}$$

and read then

$$0 = (x^2-1)R''(x) + 2xR'(x) + (x^2c^2\kappa^2 - c^2\kappa^2 - \alpha_2)R(x), \tag{8.33a}$$
$$0 = (1-y^2)S''(y) - 2yS'(y) + (-y^2c^2\kappa^2 + c^2\kappa^2 + \alpha_2)S(y). \tag{8.33b}$$

Based on the separation constant α_2 we obtain a set of solutions for the angle function S and the radial function R, which can be expanded in different ways [Fla57, Ch. 3, Ch. 4]. For the

moment we will just label them with an index n. Thus, the general axisymmetric solution then reads

$$f(\xi,\eta,\phi) = \sum_l f_l R_l(\kappa,\xi) S_l(\kappa,\eta), \tag{8.34}$$

with some constant coefficients f_l.

Now we can use (8.28a) to find the general solution for n. The homogeneous problem (with zero on the right hand side) is the Laplace equation for n, which is separable as well (set $\kappa = 0$ in the case above). The homogeneous solution n^h is given by *Legendre functions* [Fla57, p. 13], [MS71, p. 28, p. 201ff]

$$n^h(\xi,\eta) = \sum_{l=0}^{\infty} n_l Q_l(\cosh(\xi)) P_l(\cos(\eta)), \tag{8.35}$$

where Q_l are the Legendre functions of the second kind and P_l are the Legendre polynomials (see [BMMS08, Sec. 9.1.2.6.3, p. 569f] for definitions and properties). For the particular solution, we use the ansatz $n(\xi,\eta) = c_n f(\xi,\eta)$. This implies

$$\boldsymbol{\partial}_r^2 n = c_n \boldsymbol{\partial}_r^2 f = -c_n \kappa^2 f = \frac{\mathrm{Pe}^{\mathrm{act}}}{\tilde{D}} f \tag{8.36}$$

if we choose $c_n = -\mathrm{Pe}^{\mathrm{act}}/(\tilde{D}\kappa^2)$. Hence, the general solution for n is given by

$$\begin{aligned} n(\xi,\eta) &= -\frac{\mathrm{Pe}^{\mathrm{act}}}{\tilde{D}\kappa^2} f(\xi,\eta) + n^h(\xi,\eta) \\ &= \sum_l \left(n_l Q_l(\cosh(\xi)) P_l(\cos(\eta)) - \frac{\mathrm{Pe}^{\mathrm{act}}}{\tilde{D}\kappa^2} R_l(\kappa,\xi) S_l(\kappa,\eta) \right). \end{aligned} \tag{8.37}$$

To obtain the fields $\boldsymbol{m}$ we realize that (8.28b) is a Helmholtz equation as well for each component of m_i

$$\boldsymbol{\partial}_r^2 m_i + (\kappa')^2 m_i = \frac{\mathrm{Pe}^{\mathrm{act}}}{3\tilde{D}} \partial_i n \tag{8.38}$$

with $(\kappa')^2 = -2\mathrm{Pe}^{\mathrm{act}}/\bar{\ell}\tilde{D}$ and an inhomogeneity proportional to the gradient of n. The homogeneous solutions m_i^h can be obtained as described above, which yields

$$m_i^h = \sum_l m_{i,l} R_l(\kappa',\xi) S_l(\kappa',\eta). \tag{8.39}$$

For the particular solution, we employ the ansatz

$$m_i = c_h \partial_i n^h + c_p \partial_i f, \tag{8.40}$$

where c_h and c_p can be determined as follows. Inserting this ansatz into (8.38) and using the defining equations for n^h, $\boldsymbol{\partial}_r^2 \partial_i n^h = \partial_i \boldsymbol{\partial}_r^2 n^h = 0$, and f, $\boldsymbol{\partial}_r^2 \partial_i f = \partial_i \boldsymbol{\partial}_r^2 f = -\kappa^2 \partial_i f$, we obtain

$$0 = \partial_i n^h \left(c_h \frac{2\mathrm{Pe}^{\mathrm{act}}}{\bar{\ell}\tilde{D}} + \frac{\mathrm{Pe}^{\mathrm{act}}}{3\tilde{D}} \right) + \partial_i f \left(c_p \left(\frac{2\mathrm{Pe}^{\mathrm{act}}}{\bar{\ell}\tilde{D}} + \kappa^2 \right) - \frac{(\mathrm{Pe}^{\mathrm{act}})^2}{3\tilde{D}^2\kappa^2} \right), \tag{8.41}$$

which is fulfilled for any solution n^h and f if $c_h = -\bar{\ell}/6$ and $c_p = -\kappa^{-2}$. Therefore, the general

solution for the fields m_i reads

$$m_i = -\frac{\overline{\ell}}{6}\partial_i n^h - \frac{1}{\kappa^2}\partial_i f + m_i^h. \tag{8.42}$$

Transformation to spheroidal coordinates according to (D.6) and (D.10) leads to

$$m_\xi = -\frac{\overline{\ell}}{6}h_\xi^{-1}\partial_\xi n^h - \frac{1}{\kappa^2}h_\xi^{-1}\partial_\xi f + (Q^T\boldsymbol{m}^h)_\xi, \tag{8.43a}$$

$$m_\eta = -\frac{\overline{\ell}}{6}h_\eta^{-1}\partial_\eta n^h - \frac{1}{\kappa^2}h_\eta^{-1}\partial_\eta f + (Q^T\boldsymbol{m}^h)_\eta, \tag{8.43b}$$

$$m_\phi = -\frac{\overline{\ell}}{6}h_\phi^{-1}\partial_\phi n^h - \frac{1}{\kappa^2}h_\phi^{-1}\partial_\phi f + (Q^T\boldsymbol{m}^h)_\phi. \tag{8.43c}$$

For a cylindrically symmetric solution of f and n also the ϕ component of the polar order field has to vanish identically, $m_\phi = 0$. This requires $m_x^h = m_y^h = 0$. Consequently

$$\begin{aligned} m_\xi &= -\frac{\overline{\ell}}{6}h_\xi^{-1}\partial_\xi n^h - \frac{1}{\kappa^2}h_\xi^{-1}\partial_\xi f + ch_\xi^{-1}\sinh(\xi)\cos(\eta)m_z^h \\ &= \frac{1}{h_\xi}\sum_l \left(-\frac{\overline{\ell}}{6}n_l Q_l'(\cosh(\xi))\sinh(\xi)P_l(\cos(\eta)) - \frac{f_l}{\kappa^2}R_l'(\kappa,\xi)S_l(\kappa,\eta) \right. \\ &\qquad \left. + c\sinh(\xi)\cos(\eta)m_{z,l}R_l(\kappa',\xi)S_l(\kappa',\eta)\right), \end{aligned} \tag{8.44a}$$

$$m_\eta = -\frac{\overline{\ell}}{6}h_\eta^{-1}\partial_\eta n^h - \frac{1}{\kappa^2}h_\eta^{-1}\partial_\eta f - ch_\eta^{-1}\cosh(\xi)\cos(\eta)m_z^h \tag{8.44b}$$

$$\begin{aligned} &= \frac{1}{h_\xi}\sum_l \left(-\frac{\overline{\ell}}{6}n_l Q_l(\cosh(\xi))P_l'(\cos(\eta))\sin(\eta) - \frac{f_l}{\kappa^2}R_l(\kappa,\xi)S_l'(\kappa,\eta) \right. \\ &\qquad \left. - c\cosh(\xi)\cos(\eta)m_{z,l}R_l(\kappa',\xi)S_l(\kappa',\eta)\right). \end{aligned} \tag{8.44c}$$

The final task is now to adjust the parameters f_l, n_l and $m_{z,l}$ so that the boundary conditions (8.26) are fulfilled. The general boundary conditions in prolate spheroidal coordinates are given in (2.261) and for this case they read

$$0 = \tilde{D}C\partial_\xi n(\xi_0,\eta) - \mathrm{Pe}^{\mathrm{act}}m_\xi(\xi_0,\eta), \tag{8.45a}$$

$$0 = \tilde{D}C\left(\frac{\sin(2\eta)}{\cosh(2\xi_0)-\cos(2\eta)}m_\eta(\xi_0,\eta) + \partial_\xi m_\xi(\xi_0,\eta)\right) - \frac{\mathrm{Pe}^{\mathrm{act}}}{3}n(\xi_0,\eta), \tag{8.45b}$$

$$0 = -\frac{\sin(2\eta)}{\cosh(2\xi_0)-\cos(2\eta)}m_\xi(\xi_0,\eta) + \partial_\xi m_\eta(\xi_0,\eta). \tag{8.45c}$$

In order to isolate the coefficients, we would like to employ the orthogonality relation

$$\int_{-1}^{1} P_n(x)P_m(x)\mathrm{d}x = \delta_{mn}\frac{2}{2n+1} \tag{8.46}$$

(cf. [BMMS08, p. 570, Eq. (9.60d)]) of the Legendre polynomials. This requires to expand the

angle functions $S_l(\kappa,\eta)$ in terms of these polynomials according to

$$S_l(\kappa,\eta) = \sum_{r=0,1}^{\infty}{}' d_r^{0l}(c\kappa) P_r(\cos(\eta)) \tag{8.47}$$

(cf. [Fla57, p. 16, Eq. (3.1.3a)][1]), where the prime indicates summation over all even numbers if l is even and over all odd numbers if l is odd. $d_r^{0l}(c\kappa)$ fulfills a recurrence relation [Fla57, p. 17, Eq. (3.1.4)]. Furthermore, we have to replace the derivatives $S_l'(\kappa,\eta)$ and $P_l'(\kappa,\eta)$ in terms of the Legendre polynomials. Even though one can express the derivative of a Legendre polynomial in terms of Legendre polynomials, this includes η-dependent coefficients, which will render the orthogonality relation useless. Therefore, we have to give up this analytical approach and continue with a numerical solution.

8.2. Numerical solution

In this section we describe the numerical solution of our problem. To reveal the structure of the partial derivatives, we introduce new variables, which collect all those terms. The boundary value problem then reads

$$\begin{aligned}
0 &= \left(A_\xi^n \partial_\xi + A_\eta^n \partial_\eta + A_{\xi\xi}^n \partial_\xi^2 + A_{\eta\eta}^n \partial_\eta^2\right) n(\xi,\eta) \\
&\quad + \left(A_\xi^{m_\xi} \partial_\xi + A^{m_\xi}\right) m_\xi(\xi,\eta) + \left(A_\eta^{m_\eta} \partial_\eta + A^{m_\eta}\right) m_\eta(\xi,\eta) && \text{(8.48a)} \\
0 &= \left(B_\xi^{m_\xi} \partial_\xi + B_\eta^{m_\xi} \partial_\eta + B_{\xi\xi}^{m_\xi} \partial_\xi^2 + B_{\eta\eta}^{m_\xi} \partial_\eta^2 + B^{m_\xi}\right) m_\xi(\xi,\eta) \\
&\quad + \left(B_\xi^{m_\eta} \partial_\xi + B_\eta^{m_\eta} \partial_\eta + B^{m_\eta}\right) m_\eta(\xi,\eta) + B_\xi^n \partial_\xi n(\xi,\eta) && \text{(8.48b)} \\
0 &= \left(C_\xi^{m_\eta} \partial_\xi + C_\eta^{m_\eta} \partial_\eta + C_{\xi\xi}^{m_\eta} \partial_\xi^2 + C_{\eta\eta}^{m_\eta} \partial_\eta^2 + C^{m_\eta}\right) m_\eta(\xi,\eta) \\
&\quad + \left(C_\xi^{m_\xi} \partial_\xi + C_\eta^{m_\xi} \partial_\eta + C^{m_\xi}\right) m_\xi(\xi,\eta) + C_\eta^n \partial_\eta n(\xi,\eta) && \text{(8.48c)}
\end{aligned}$$

subject to the boundary conditions

$$\begin{aligned}
\partial_\xi n(\xi,\eta) &= N_n n(\xi,\eta) + N_{m_\xi} m_\xi(\xi,\eta) && \text{(8.49a)} \\
\partial_\xi m_\xi(\xi,\eta) &= M_{m_\xi}^\xi m_\xi(\xi,\eta) + M_{m_\eta}^\xi m_\eta(\xi,\eta) + M_n^\xi n(\xi,\eta) && \text{(8.49b)} \\
\partial_\xi m_\eta(\xi,\eta) &= M_{m_\eta}^\eta m_\eta(\xi,\eta) + M_{m_\xi}^\eta m_\xi(\xi,\eta) && \text{(8.49c)}
\end{aligned}$$

for $\xi = \xi_0$,

$$n(\xi,\eta) = n_b, \qquad \text{(8.50a)} \qquad m_\xi(\xi,\eta) = 0, \qquad \text{(8.50b)} \qquad m_\eta(\xi,\eta) = 0, \qquad \text{(8.50c)}$$

for $\xi \to \infty$ and

$$\partial_\eta n(\xi,\eta) = 0, \qquad \text{(8.51a)} \qquad \partial_\eta m_\xi(\xi,\eta) = 0, \qquad \text{(8.51b)} \qquad m_\eta(\xi,\eta) = 0, \qquad \text{(8.51c)}$$

[1] Mind the different definitions: $\eta \hat{=} \cos(\eta)$, $c \hat{=} c\kappa$.

for $\eta \in \{0, \pi\}$ due to cylindrical symmetry with the abbreviations A_α^f, B_α^f, C_α^f and N_f, M_f^ξ, M_f^η as given in Section D.7.

8.2.1. Finite differences scheme

For the finite differences scheme, we establish a uniform grid in ξ and η given by

$$\xi_i = ih_\xi + \xi_0, \qquad (0 \leq i < N_\xi), \tag{8.52a}$$
$$\eta_j = jh_\eta, \qquad (0 \leq j < N_\eta), \tag{8.52b}$$

where N_ξ and N_η are the number of grid points in each direction and

$$h_\xi = \frac{\xi_{\max} - \xi_0}{N_\xi - 1}, \tag{8.53a}$$
$$h_\eta = \frac{\pi}{N_\eta - 1} \tag{8.53b}$$

are the step sizes. In order to obtain the spheroid of excluded volume with semiaxes $(s+1)/2$ and $(s\hat{a}+1)/2$, we have to determine c, the free parameter of the spheroidal coordinates, and ξ_0

$$c = \frac{1}{2}\sqrt{|s^2(\hat{a}^2-1) + 2s(\hat{a}-1)|}, \tag{8.54}$$
$$\xi_0 = \frac{1}{2}\log\left(\left|\frac{s(\hat{a}+1)+2}{s(\hat{a}-1}\right|\right). \tag{8.55}$$

As the size of the spheroid defined by $\xi = \xi_{\max}$ changes for different shapes, we will define $\xi_{\max}$ conveniently through its minimum distance to the origin $r_{\max}$ via

$$\xi_{\max} = \operatorname{arsinh}\left(\frac{r_{\max}}{c}\right). \tag{8.56}$$

arsinh is the area hyperbolic sine, the inverse of the hyperbolic sine sinh.

Furthermore, we introduce the notation

$$n^{i,j} := n(\xi_i, \eta_j) \tag{8.57}$$

and correspondingly we define $m_\xi^{i,j}$ and $m_\eta^{i,j}$. We use central differences to approximate the derivatives to second order

$$\partial_\xi f(\xi_i, \eta_j) = \frac{f^{i+1,j} - f^{i-1,j}}{2h_\xi} + \mathcal{O}(h_\xi^2) \tag{8.58a}$$
$$\partial_\xi^2 f(\xi_i, \eta_j) = \frac{f^{i+1,j} - 2f^{i,j} + f^{i-1,j}}{h_\xi^2} + \mathcal{O}(h_\xi^2) \tag{8.58b}$$

for $1 \leq i < N_\xi - 1$ and $1 \leq j < N_\eta - 1$ and correspondingly for the derivatives in η.

At the boundaries, we have to incorporate the boundary condition into this second order difference scheme. For $\xi = \xi_{\max}$ we have to fulfill the conditions $n(\xi_{\max}, \eta) = n_b$ and $m_\xi(\xi_{\max}, \eta) = m_\eta(\xi_{\max}, \eta) = 0$ which translates into

$$n^{N_\xi-1,j} = n_b, \qquad (8.59a) \qquad m_\xi^{N_\xi-1,j} = 0, \qquad (8.59b) \qquad m_\eta^{N_\xi-1,j} = 0, \qquad (8.59c)$$

for $0 \leq j < N_\eta$. For $\xi = \xi_0$ we have to fulfill a boundary condition, which incorporates the derivative of n, which also has to be determined numerically. This is achieved as follows: Let the boundary condition for the field $f(\xi, \eta)$ be specified by some functional Φ via

$$\partial_\xi f(\xi_0, \eta) = \Phi[n, m_\xi, m_\eta](\xi_0, \eta), \tag{8.60}$$

where the functional Φ contains on all fields and their derivatives except for $\partial_\xi f$ at the boundary. The approximation scheme (8.58a) yields

$$\frac{f^{1,j} - f^{-1,j}}{2h_\xi} = \Phi_j := \Phi[n, m_\xi, m_\eta](\xi_0, \eta_j), \tag{8.61}$$

which can be solved for $f^{-1,j}$

$$f^{-1,j} = f^{1,j} - 2h_\xi \Phi_j. \tag{8.62}$$

This result can be inserted into the approximation for the second derivative (8.58b) at $i = 0$, which requires the knowledge of $f^{-1,j}$. Then we find

$$\partial_\xi^2 f^{0,j} \approx 2\frac{f^{1,j} - h_\xi \Phi_j - f^{0,j}}{h_\xi^2}. \tag{8.63}$$

If Φ_j contains derivatives, they have to be discretized via (8.58) as well.

For the boundary conditions at $\eta = 0, \pi$ we apply symmetry considerations. First of all, we require $n(\xi, \eta + 2\pi) = n(\xi, \eta)$ for all $\xi \in [\xi_0, \infty)$ and $\eta \in [0, 2\pi)$ and similarly for m_ξ and m_η, since η and $\eta + 2\pi$ describe the same points in space. Furthermore, it can be shown that the equations of motion (8.48) are invariant under the transformations

$$n(\xi, \eta) \mapsto n(\xi, -\eta), \tag{8.64a}$$
$$m_\xi(\xi, \eta) \mapsto m_\xi(\xi, -\eta), \tag{8.64b}$$
$$m_\eta(\xi, \eta) \mapsto -m_\eta(\xi, -\eta). \tag{8.64c}$$

As a consequence $m_\eta(\xi, 0) = m_\eta(\xi, \pi) = 0$ and $\partial_\eta n(\xi, 0) = \partial_\eta n(\xi, \pi) = 0$, $\partial_\eta m_\xi(\xi, 0) = \partial_\eta m_\xi(0, \pi) = 0$. For the discretization, this implies for $\eta = 0$

$$n^{i,-1} = n(\xi_i, -h_\eta) = n(\xi_i, h_\eta) = n^{i,1}, \tag{8.65a}$$
$$m_\xi^{i,-1} = m_\xi(\xi_i, -h_\eta) = m_\xi(\xi_i, h_\eta) = m_\xi^{i,1}, \tag{8.65b}$$
$$m_\eta^{i,-1} = m_\eta(\xi_i, -h_\eta) = -m_\eta(\xi_i, h_\eta) = -m_\eta^{i,1}, \tag{8.65c}$$

and for $\eta = \pi$ (which corresponds to $\eta_{N_\eta - 1}$)

$$n^{i,N_\eta} = n(\xi_i, \pi + h_\eta) = n(\xi_i, -\pi - h_\eta) = n(\xi_i, \pi - h_\eta) = n^{i,N_\eta - 2}, \tag{8.66a}$$
$$m_\xi^{i,N_\eta} = m_\xi^{i,N_\eta - 2}, \tag{8.66b}$$
$$m_\eta^{i,N_\eta} = -m_\eta^{i,N_\eta - 2}. \tag{8.66c}$$

Collecting all fields at all grid-points into one $(3N_\xi N_\eta)$-dimensional vector v via

$$v^{3(iN_\eta+j)} = n^{i,j}, \quad (8.67a) \qquad v^{3(iN_\eta+j)+1} = m_\xi^{i,j}, \quad (8.67b) \qquad v^{3(iN_\eta+j)+2} = m_\eta^{i,j}, \quad (8.67c)$$

we transform our partial differential equation into a large system of linear equations, which can be expressed in the form

$$Av = b \tag{8.68}$$

with a $(3N_\xi N_\eta) \times (3N_\xi N_\eta)$-matrix A and a $(3N_\xi N_\eta)$-dimensional vector b. The rows of A are given by (8.48), where the derivatives have been substituted by the finite differences (8.58). The vector b contains all terms which are not related to the fields and which typically arise from the boundary conditions. The order of the equations is arbitrary, but can have significant effects on the performance of the algorithms to solve the matrix equation (8.68). The challenge is to fit this equation into a computer, because even a coarse discretization with $N_\xi = N_\eta = 100$ requires with double precision about 2 GB of memory. Doubling the number of points in each direction, will increase the required memory by a factor of 16. This requirement can be reduced significantly, when looking at the structure of the matrix A. The finite differences only couple neighboring points so that there are only $\mathcal{O}(N_\xi N_\eta)$ nonzero entries. Therefore, the matrix consists mainly of zeros. It is consequently very efficient to store only the non-zero entries. For these sparse matrices there exist special solution algorithms, which perform better, the smaller the bandwidth of the matrix [Tew73, Sec. 3.3, p. 40f]. The bandwidth is determined by the largest side-diagonal with nonzero entries [Tew73, Sec. 3.3, p. 40]. To keep the bandwidth of the sparse matrix small, we sort the equations in the same way as the variables, i.e. the fist row contains the discretized version of (8.48a) for $i, j = 0$, the second (8.48b), the third (8.48c). Then, we continue with the same sequence of equations for $i = 0$, $j = 1$.

After filling the sparse matrix on a computer, the solution is found by the standard method for solving systems of linear equations of the `scipy.linalg.sparse` module for python (python 2.7, scipy version 0.16.0).

When the bath particle density n is known, we can calculate the force on the probe and the corresponding change of the friction coefficient $\Delta\eta$ according to (2.270).

8.2.2. Grid effects

It is known from the active microrheology of ellipsoids in a passive bath that there forms a boundary layer $\propto (\mathrm{Pe}^{\mathrm{ext}})^{-1}$ [KB08, Appendix B, p. 190]. As we use a uniform grid for the discretization, we expect our numerics to break down or give grid-dependent results for large $\mathrm{Pe}^{\mathrm{ext}}$. To check for these grid-dependencies, we compare the results for the microviscosity increment for two different grids: $N_\xi \times N_\eta = 400 \times 100$ and $N_\xi \times N_\eta = 800 \times 200$. We choose $r_{\max} d = 10$ and for convenience, we set $\mathrm{Pe}^{\mathrm{act}} = 0$ and $\overline{D} = 0$. We calculate $\delta\eta$ for each grid and $\mathrm{Pe}^{\mathrm{ext}} \in [10^{-2}, 10^2]$.

In Figure 8.1 we show the relative error

$$\varepsilon_{\mathrm{rel}} = \left| \frac{\Delta\eta(400 \times 100) - \Delta\eta(800 \times 200)}{\Delta\eta(800 \times 200)} \right| \tag{8.69}$$

as a function of the external Péclet number $\mathrm{Pe}^{\mathrm{ext}}$. While this error is of the order 10^{-4} for

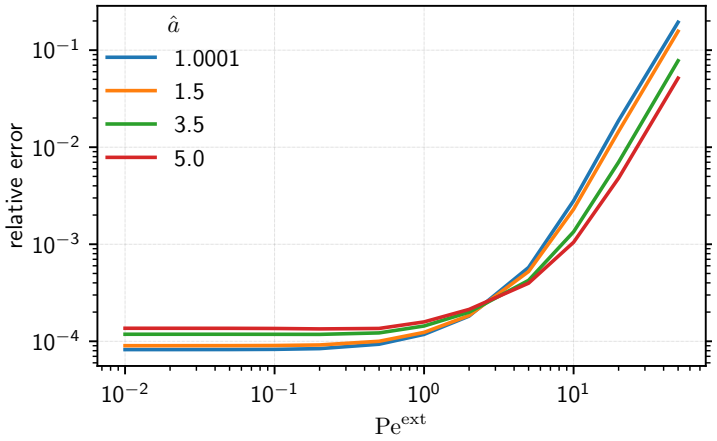

Figure 8.1.: Grid effect for the microviscosity increment. The relative error of the microviscosity increments as defined in (8.69) between a grid with $N_\xi \times N_\eta = 400 \times 100$ and $N_\xi \times N_\eta = 800 \times 200$ as a function of $\mathrm{Pe}^{\mathrm{ext}}$ for different aspect ratios $\hat{a}$ for prolate spheroids. Other numerical details are given in the text.

$\mathrm{Pe}^{\mathrm{ext}} < 1$, it increases up to order 10^{-1} for $\mathrm{Pe}^{\mathrm{ext}} = 50$. For $\mathrm{Pe}^{\mathrm{ext}} = 100$ we cannot obtain a valid solution on the grid 400×100. Hence, the microviscosity increments are well defined only for Péclet numbers $\mathrm{Pe}^{\mathrm{ext}} \lesssim 10$ and $\mathrm{Pe}^{\mathrm{act}} \lesssim 10$. In the following, we will find interesting behavior for large activities. To avoid numerical artifacts, we will implement a nonuniform grid, which adjusts to the boundary layer as discussed in the next section.

8.2.3. Nonuniform mapping finite differences scheme

Khair and Brady introduce a nonuniform grid to capture the boundary layer at large $\mathrm{Pe}^{\mathrm{ext}}$ by the following mapping from $[0, 1]$ to $[\xi_0, \infty]$

$$p(\xi) = \exp\left(-y\left(w + \frac{1-w}{1+y}\right)\right), \tag{8.70}$$

where $y = s_{\mathrm{Pe}}(\xi - \xi_0)$ and w is a parameter to adjust the spacing of the grid [KB08, Sec. V.B, p. 181]. There, $s_{\mathrm{Pe}} = \mathrm{Pe}^{\mathrm{ext}}$, but we leave this Péclet number scale more general, because we have more than one Péclet number in our problem. Our choice will be $s_{\mathrm{Pe}} = \max(1, \mathrm{Pe}^{\mathrm{act}}, \mathrm{Pe}^{\mathrm{ext}})$.

Solving (8.70) for ξ we obtain

$$\xi = \xi_0 + \frac{1}{s_{\mathrm{Pe}}}\left(-\frac{\ln(p)+1}{2w} + \sqrt{\left(\frac{\ln(p)+1}{2w}\right)^2 - \frac{\ln(p)}{w}}\right). \tag{8.71}$$

Choosing p on a linear grid in $[0, 1]$ with N_ξ points yields values of ξ in $[\xi_0, \infty]$. $p = 1$ corresponds to $\xi = \xi_0$ and $p = 0$ corresponds to $\xi = \infty$, which allows the exact implementation of the boundary condition. On the other hand, these values are difficult to visualize. Therefore, we want to control the largest finite value for ξ. This can be achieved by adjusting w. A value of

$$w = \log(N_\xi - 1)\frac{1+y}{y^2} - \frac{1}{y} \tag{8.72}$$

guarantees $\xi_{N_\xi - 2} = \xi_{\max}$, where we used the abbreviation y as introduced above.

With the change of variables, we have to rewrite the derivatives via

$$\partial_\xi = \frac{\partial p}{\partial \xi}\partial_p, \tag{8.73a}$$

$$\partial_\xi^2 = \frac{\partial^2 p}{\partial \xi^2}\partial_p + \left(\frac{\partial p}{\partial \xi}\right)^2 \partial_p^2, \tag{8.73b}$$

where

$$\frac{\partial p}{\partial \xi} = -s_{\mathrm{Pe}} \frac{wy^2 + 2wy + 1}{(1+y)^2} p \tag{8.74a}$$

$$\frac{\partial^2 p}{\partial \xi^2} = (s_{\mathrm{Pe}})^2 \frac{2(1-w)(1+y) + (wy^2 + 2wy + 1)^2}{(y+1)^4} p \tag{8.74b}$$

Keeping the scheme and notation of (8.48) and (8.49) but ξ by p, we find

$$A_p^n = \frac{\partial p}{\partial \xi} A_\xi^n + \frac{\partial^2 p}{\partial \xi^2} A_{\xi\xi}^n, \tag{8.75a}$$

$$A_{pp}^n = \left(\frac{\partial p}{\partial \xi}\right)^2 A_{\xi\xi}^n, \tag{8.75b}$$

$$A_p^{m_\xi} = \frac{\partial p}{\partial \xi} A^{m_\xi}, \tag{8.75c}$$

$$B_p^n = \frac{\partial p}{\partial \xi} B_\xi^n, \tag{8.76a}$$

$$B_p^{m_\xi} = \frac{\partial p}{\partial \xi} B_\xi^{m_\xi} + \frac{\partial^2 p}{\partial \xi^2} B_{\xi\xi}^{m_\xi}, \tag{8.76b}$$

$$B_{pp}^{m_\xi} = \left(\frac{\partial p}{\partial \xi}\right)^2 B_{\xi\xi}^{m_\xi}, \tag{8.76c}$$

$$C_p^{m_\xi} = \frac{\partial p}{\partial \xi} C_\xi^{m_\xi}, \tag{8.77a}$$

$$C_p^{m_\eta} = \frac{\partial p}{\partial \xi} C_\xi^{m_\eta} + \frac{\partial^2 p}{\partial \xi^2} C_{\xi\xi}^{m_\eta}, \tag{8.77b}$$

$$C_{pp}^{m_\eta} = \left(\frac{\partial p}{\partial \xi}\right)^2 C_{\xi\xi}^{m_\eta}, \tag{8.77c}$$

and the coefficients for the boundary conditions have to be scaled

$${}^pN_n = \left(\frac{\partial p}{\partial \xi}\right)^{-1} N_n \tag{8.78}$$

and analogously for the coefficients ${}^pN_{m_\xi}$, ${}^pM_{m_\xi}^\xi$, ${}^pM_{m_\eta}^\xi$, ${}^pM_n^\xi$, ${}^pM_{m_\eta}^\eta$, ${}^pM_{m_\xi}^\eta$.

Doing the same comparison as in the previous section (now using $r_{\max} = 100$), we find that the relative error stays below $5 \cdot 10^{-4}$ for all tested Péclet numbers $\mathrm{Pe}^{\mathrm{ext}} \leq 10^2$. Hence, this parametrization of the problem is superior to the naive approach with a uniform grid.

8.2.4. Comparison to microrheology of ellipsoids in a passive suspension

In order to test our implementation, which involves many terms, we compare to results known from literature. The microviscosity increment in a passive bath has been evaluated by Khair and Brady for oblate and prolate spheroids [KB08]. For the comparison, we need to set $\overline{D} = \Delta D = 0$ in our equations. We choose $r_{\max} d = 100$, $N_\xi = 800$, $N_\eta = 200$ and the new non-uniform grid with $r_{\max} d = 100$ (which is used to calculate $\xi_{\max}$ and w). The corresponding numerical results are shown in Figure 8.2. We also show the values extracted from [KB08, Fig. 12, p. 182] for oblate spheroids and [KB08, Fig. 13, p. 183] for prolate spheroids as open symbols. All curves fall nicely on top of each other. There is only minor deviations for intermediate $\mathrm{Pe}^{\mathrm{ext}}$ for the prolate spheroid with $\hat{a} = 3.5$. The reason for this remains unclear, because the extraction of the values has been double checked. In addition to the previous section, we can state that this nonuniform grid keeps the relative differences between the two grids at a level of 10^{-4}.

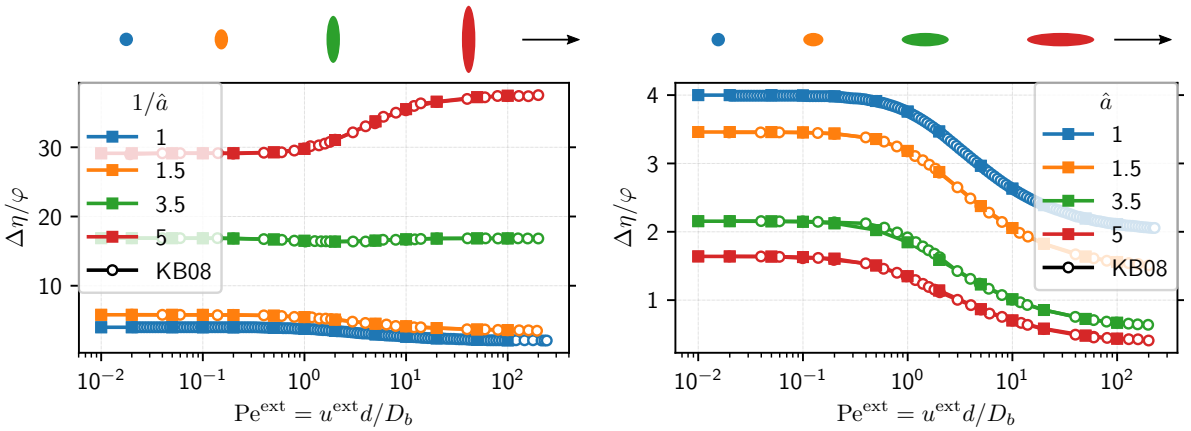

Figure 8.2.: Comparison of the microviscosity increment for oblate spheroids (left) and prolate spheroids (right) in a passive bath with the results of [KB08, Fig. 12, p. 182] for oblate and [KB08, Fig. 13, p. 183] for prolate spheroids (open circles). The spheroids are sketched above the graphs. Their motion is along their symmetry axis to the right.

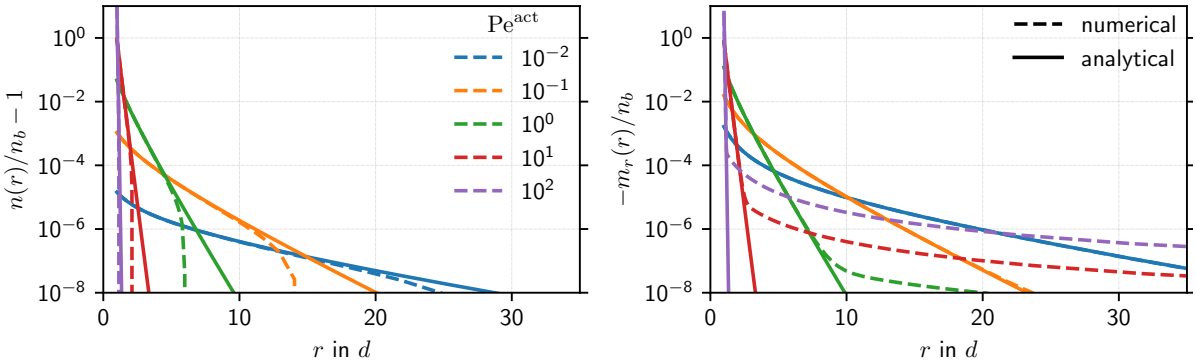

Figure 8.3.: Relative excess density $n(r)/n_b - 1$ and radial component of the polar order field $m_r(r)$ around a spherical obstacle for different activities $\mathrm{Pe}^{\mathrm{act}}$ with constant run length $\ell = 1$. The distance r is measured from the center of the sphere, where the excluded volume surface is at $r = 1$. Numerical solutions are shown as dashed lines, analytical results as solid lines. Details on the numerical parameters can be found in the text.

8.2.5. Comparison to spherical probe in active bath

To check the validity of our numerical calculations, we compare to the known analytical results of [YB15a, p. 5, Eq. (3.4)], where they analyzed the particle density around a fixed spherical obstacle. The results for the particle density as well as the polar order field are given in (8.24), specifying $\overline{D} = 0$. for the numerical solution, we employ an aspect ratio of $\hat{a} = 1.0001$, since the spheroidal coordinates are not well-defined for $\hat{a} = 1$. We choose $N_\xi \times N_\eta = 200 \times 200$ and a cutoff $r_{\max} d = 100$ for the nonuniform grid. For an aspect ratio close to one, the ξ axes become radial axes. The radius can be obtained by $r = c \sinh(\xi)$. Similarly, the ξ component of a vector field transforms into the radial component. To check the effect for a change of activity, we fix $\ell = 1$ and vary $\mathrm{Pe}^{\mathrm{act}}$ from 10^{-2} to 10^{2}. Those results are shown in Figure 8.3 as dashed lines together with the analytical solutions as solid lines. For any nonzero activity the particles

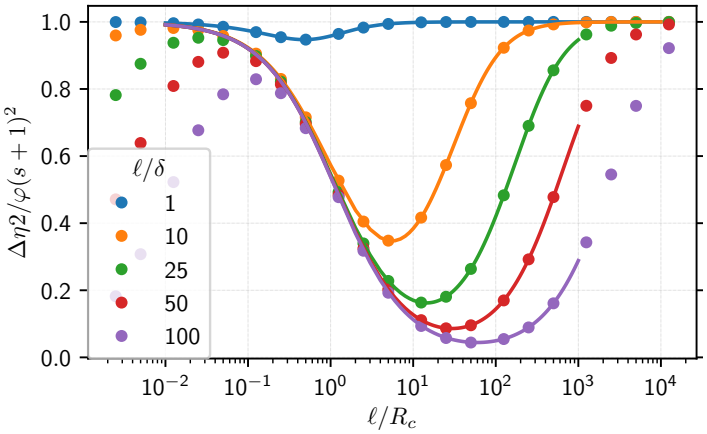

Figure 8.4.: Comparison of the numerical solution for the microviscosity increment (symbols) of spheres with the analytical results (solid lines).

accumulate at the surface of the sphere. This effect becomes more and more pronounced when the activity is increased. The reason for this behavior is generic for any kind of barrier as already discussed at the end of Section 8.1.2. Since the active swimmers need a finite time to reorient, when they hit the wall they are stuck there for this period of time, while particles pointing away from the wall will swim away immediately. This also explains the nonzero polar order of the particles at the wall, which points into the wall. The length scale, over which this effect is visible is given by (8.20a). The analytical results can be reproduced over a range of more than three decades before visible inaccuracies appear. The maximum of the field m_η is of the order 10^{-8} to 10^{-7} and therefore negligible compared to m_r (or m_ξ) as expected.

8.2.6. Comparison to microrheology of spherical probe in active bath

For a sphere in an active bath, it is possible to find the microviscosity increment $\Delta\eta$ in linear response analytically. This has been done by Eric Burkholder. As the equations are quite lengthy, he kindly shared his data for some parameters with me. He expresses the run length ℓ in terms of the excluded volume radius R_c of probe and bath particles and the activity in terms of the width of the activity layer δ

$$\frac{\ell}{R_c} = \frac{\ell}{d}\frac{2}{(s+1)}, \tag{8.79}$$

$$\frac{\delta}{d} = \sqrt{\frac{\overline{\ell}\left(1+\frac{1}{s}\right)}{\mathrm{Pe}^{\mathrm{act}}}}. \tag{8.80}$$

This leads to the following measures for the microviscosity increment and the activity level

$$\frac{\Delta\eta}{\frac{1}{2}\left(\frac{R_c}{a}\right)^2} = \Delta\eta\frac{2}{(s+1)^2}, \tag{8.81}$$

$$\frac{\ell}{\delta} = \sqrt{\frac{\overline{\ell}\mathrm{Pe}^{\mathrm{act}}}{\left(1+\frac{1}{s}\right)}}, \tag{8.82}$$

which are visualized in Figure 8.4. We compare the analytical results for spheres with the numerical results for $\hat{a} = 1.0001$, $\overline{D} = 1$, $\mathrm{Pe}^{\mathrm{ext}} = 0.01$ on the grid $N_\xi \times N_\eta = 800 \times 200$ with $r_{\max} d = 100$. ℓ and $\mathrm{Pe}^{\mathrm{act}}$ are determined according to the relations above. The agreement for large ℓ/R_c is very good. For small ℓ/R_c and large δ/ℓ, however, we obtain different results. We can only speculate about these differences. One possible explanation is the following: keeping ℓ/δ constant implies keeping the product $\overline{\ell}\mathrm{Pe}^{\mathrm{act}}$ constant. But as we are decreasing ℓ, we have

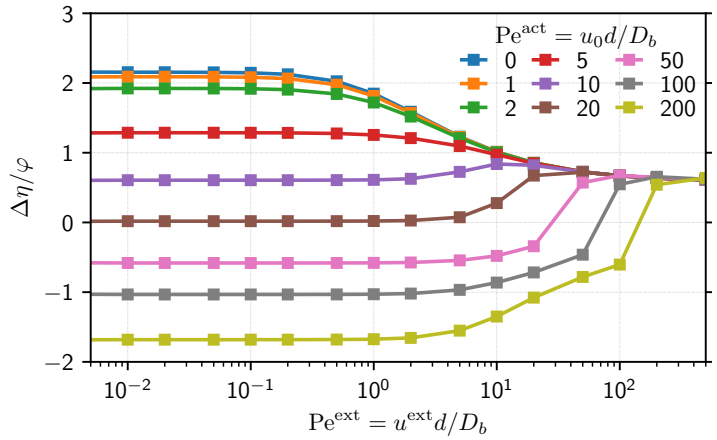

Figure 8.5.: Microviscosity increment $\Delta\eta$ as function of the external motion $\mathrm{Pe}^{\mathrm{ext}}$ and the activity $\mathrm{Pe}^{\mathrm{act}}$. The run length is coupled to the activity via $\overline{\ell} = \mathrm{Pe}^{\mathrm{act}}/3$ assuming the rotational diffusion of a sphere. The aspect ratio of the ellipsoid is $\hat{a} = 3.5$.

to increase $\mathrm{Pe}^{\mathrm{act}}$. Larger activities require a finer grid around the boundary. Even though we use the refinement of the nonuniform grid, this may not be sufficient anymore for very large activities. It is also possible that for these large activities the effect of the external pulling is comparatively small. Nevertheless this asymmetric contribution is the important change for the viscosity increment.

In summary, we tested our numerics for ellipsoids without activity, for quiescent spheres in an active bath and for spherical probes moving slowly through an active bath. In any case, we can reproduce the analytical results with our numerical solution up to some small errors arising from the discretization. Care has to be taken for large activities, where boundary layers may become very small.

8.3. Activity dependent friction coefficient

In this section, we will explore how the friction coefficient or microviscosity increment $\Delta\eta$ of an ellipsoid changes, when we pull it in an active suspension. Since diffusion is not possible in a fixed velocity microrheology experiment we will use $\overline{D} = \Delta D = 0$ throughout this section. We start by analyzing the equivalent of Figure 8.2, the microviscosity increment as a function of the external pulling $\mathrm{Pe}^{\mathrm{ext}}$ for different activities. In Figure 8.5 we show these curves for an ellipsoid with aspect ratio $\hat{a} = 3.5$ and size ratio $s = 1$. The nondimensional run length is inferred from the rotational diffusion of a sphere and given by $\ell = \mathrm{Pe}^{\mathrm{act}}/3$. The results for a grid with $N_\xi \times N_\eta = 400 \times 400$ and $r_{\max} d = 100$ are shown. This will be the default grid for this section, unless specified otherwise. Those results are not different from the ones on a grid with $N_\xi \times N_\eta = 200 \times 200$.

We find that $\Delta\eta$ decreases with increasing activity for small external pulling. For $\mathrm{Pe}^{\mathrm{ext}} \gtrsim \mathrm{Pe}^{\mathrm{act}}$ we find a crossover to the values without activity. This indicates that in this regime the activity is no longer important. For $\mathrm{Pe}^{\mathrm{ext}} \lesssim 0.1$ the microviscosity increment $\Delta\eta$ is constant. Thus, the friction coefficient does not depend on the pulling strength and is therefore well defined. With increasing activity $\Delta\eta$ seems to get arbitrarily small. Values smaller than 0 indicate that the friction coefficient is reduced compared to a bath without particles. The strength of the reduction is given by $\phi\Delta\eta$, i.e. it depends additionally on the packing fraction of the bath particles. This reduction of friction is a surprising feature and not intuitive at first sight. It

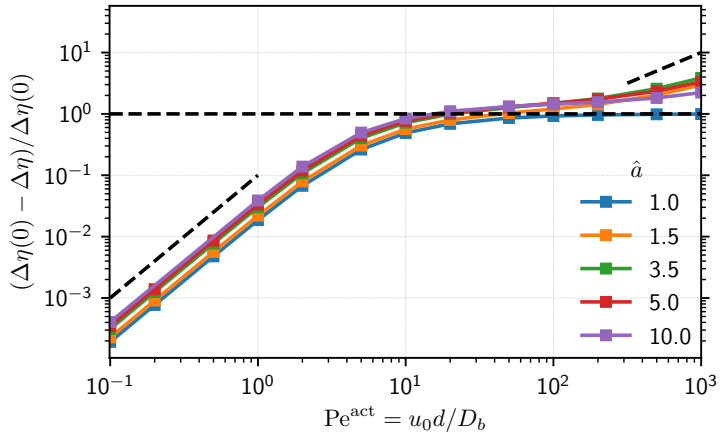

Figure 8.6.: The relative change in the microviscosity increment as function of activity for $\mathrm{Pe}^{\mathrm{ext}} = 0.01$ and different aspect ratios $\hat{a}$. For $\mathrm{Pe}^{\mathrm{act}} \gtrsim 1$, the microviscosity increment becomes negative. The dashed line on the left hand side visualizes a power law with exponent 2, while the dashed line on the right visualizes a power law with exponent 1.

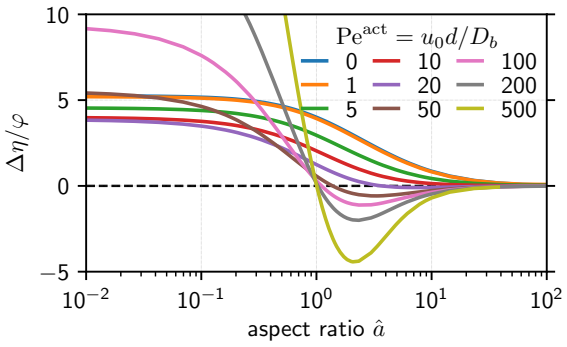

(a) Size ratio $s = 1$. Aspect ratios of $\hat{a} < 1$ correspond to oblate and $\hat{a} > 1$ to prolate spheroids.

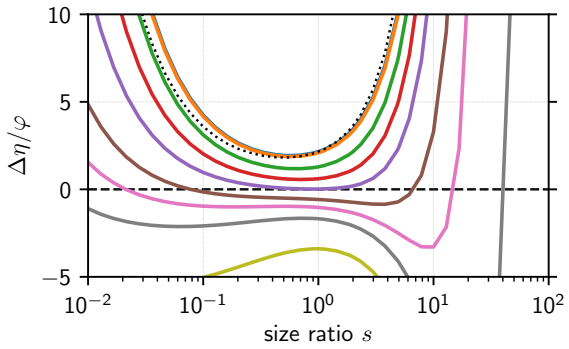

(b) Aspect ratio $\hat{a} = 3.5$. The dotted line shows the scaling behavior of a sphere.

Figure 8.7.: The microviscosity increment for small $\mathrm{Pe}^{\mathrm{ext}} = 10^{-2}$ for different activities as a function of the aspect ratio $\hat{a}$ (left) and the size ratio s (right). The color code for the activity is the same in both figures.

is also not completely unreasonable, because we consider a non-equilibrium system. Naively, this looks like the active particles are pushing the probe particle so that we need a smaller force to move it with a certain velocity. In the following we want to address the question of this driving mechanism. Since this effect does not depend on the external velocity $\mathrm{Pe}^{\mathrm{ext}}$ if it is small enough, we will focus on this linear response regime and set $\mathrm{Pe}^{\mathrm{ext}} = 10^{-2}$ for all following evaluations.

To analyze the reduction of the friction coefficient compared to the case without activity in the linear regime, we plot the relative change in the viscosity increment $(\Delta\eta(0) - \Delta\eta(\mathrm{Pe}^{\mathrm{act}}))/\Delta\eta(0)$ as a function of activity in Figure 8.6 for different aspect ratios in the linear response regime for $\mathrm{Pe}^{\mathrm{ext}} = 10^{-2}$. The value of the external velocity does not matter as long as it is small enough. Note that a decrease of the viscosity increment corresponds to a positive value. A relative change larger than 1 implies $\Delta\eta(\mathrm{Pe}^{\mathrm{act}}) < 0$. We find that the relative change increases as $(\mathrm{Pe}^{\mathrm{act}})^2$ for $\mathrm{Pe}^{\mathrm{act}} \lesssim 5$. For larger activities there is some saturation around a value of the relative change of about 1. While the value for the sphere is always smaller than 1, there is a sub-linear increase for prolate spheroids. Although the relative change increases monotonically with the aspect ratio for small activities, this ordering is lost for large activities, where we find a non-monotonic behavior.

The microviscosity increment as a function of the aspect ratio is shown in Figure 8.7a to reveal the structure of this non-monotonic behavior. We find that for $\mathrm{Pe}^{\mathrm{act}} \lesssim 20$ the microviscosity decreases monotonically for all aspect ratios. However, for larger activities it increases for oblate spheroids ($\hat{a} < 1$), while it continues to decrease for prolate spheroids ($\hat{a} > 1$). A minimum appears, which shifts to $\hat{a} \approx 2$ for large activity. While we have roughly $\Delta\eta \propto \mathrm{Pe}^{\mathrm{act}}$ in the limit $\hat{a} \to 0$ (platelets), we find $\Delta\eta \to 0$ for $\hat{a} \to \infty$ (rods) as well as for $\hat{a} = 1$ (spheres). For large activities this limit is approached from below. The negative microviscosity increment is most prominent for $\hat{a} \in (1, 10)$ with a minimum at around $\hat{a} = 2$. Hence, the effect of the activity on the microviscosity increment is strongly shape dependent. For oblate spheroids, it increases the friction of the probe, while is decreasing the friction of the probe for prolate spheroids. For spheres and rods as limiting cases of prolate spheroids, however, the friction increment decreases to 0 only for large activities, while it can become strongly negative for aspect ratios in between.

In order to trace down the mechanisms for the negative microviscosity increment, we did also some calculations for different size ratios. Keeping the aspect ratio at $\hat{a} = 3.5$ we vary the size of the probe compared to the bath particles. This is shown in Figure 8.7b. Checking for grid effects with a $N_\xi \times N_\eta = 800 \times 400$ grid, we find only minor quantitative deviations for the largest activities and aspect ratios. Furthermore, we increase the grid cutoff for large size ratios to $r_{\max} d = 500$ for $s \geq 10$.

For spheres, Squires and Brady obtained the following scaling

$$\frac{\Delta\eta}{\varphi} = \frac{(1+s)^3}{2s}, \tag{8.83}$$

cf. [SB05, p. 7, Eq. (40)]. Even though the dependence of the microviscosity increment on the aspect ratio was discussed in [KB08], they do not give a corresponding result for the scaling with the size ratio for ellipsoids. To visualize the similarity to the result of spheres, we rescale (8.83) such that it matches the curve for $\mathrm{Pe}^{\mathrm{act}} = 0$ at $s = 1$, as shown as dotted line in Figure 8.7b. Despite that an aspect ratio of $\hat{a} = 3.5$ is already far from a sphere, there is a fair agreement for no and small activities. The microviscosity increment is minimal, if bath and probe particle have roughly the same size. If the probe diameter is larger than the bath particles' diameter, the microviscosity increment is slightly smaller than expected for a spherical particle. For probes smaller than the bath particles, the effect is reversed: The microviscosity increment is larger than expected from the scaling of a sphere. Again, the microviscosity increment is reduced with increasing activity. For this aspect ratio it becomes negative for $\mathrm{Pe}^{\mathrm{act}} \gtrsim 20$. Furthermore, for activities $\mathrm{Pe}^{\mathrm{act}} \gtrsim 50$ the minimum shifts towards a size ratio of about $s \approx 10$ and larger and for even larger activities another minimum develops at around $s \approx 10^{-1}$ with a trend to smaller size ratios for larger activities. In the limit of large size ratios, there seems to occur a crossover to positive microviscosity increments. Hence, there is not only an optimal aspect ratio, but also an optimal size ratio, when trying to minimize the friction increment for a given activity. The microviscosity increment can become as small as $\Delta\eta/\varphi = -90$ for $\mathrm{Pe}^{\mathrm{act}} = 500$ and $s = 40$.

So far, we have observed that the microviscosity increment decreases for increasing activity for prolate spheroids. But the activity has two parameters, the swim speed u_0 and the run length ℓ. For thermal rotational motion, they are coupled as shown at the beginning of this section. However, for certain microswimmers like bacteria, these properties can be decoupled. Therefore,

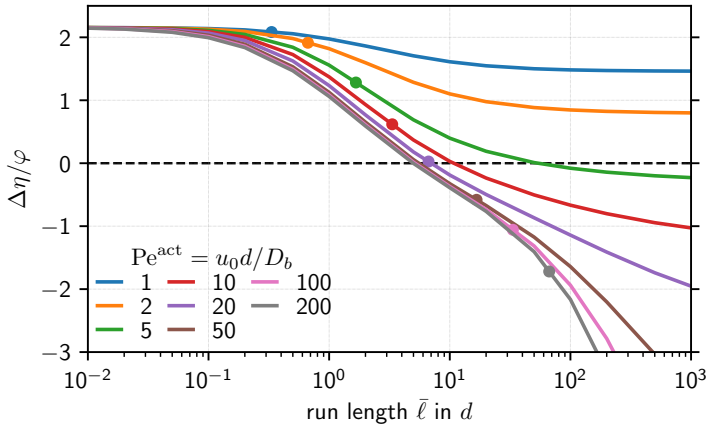

Figure 8.8.: Microviscosity increment as function of the run length $\bar{\ell}$ for different activities $\mathrm{Pe}^{\mathrm{act}}$ for an aspect ratio $\hat{a} = 3.5$ and a size ratio $s = 1$. The circles indicate the run length for a thermal swimmer $\bar{\ell} = \mathrm{Pe}^{\mathrm{act}}/3$.

we ask whether a large swimming speed u_0 (characterized by the Péclet number $\mathrm{Pe}^{\mathrm{act}}$) or a large run length (a slow reorientation) is more important. To answer this question, we perform calculations for an aspect ratio $\hat{a} = 3.5$, a size ratio of $s = 1$ and different combinations of run lengths $\bar{\ell}$ and activities on a grid with $N_\xi \times N_\eta = 400 \times 400$ with $r_{\max} d = 100$. These results are shown as function of run length in Figure 8.8. We checked for grid effects with $N_\xi \times N_\eta = 800 \times 400$ for large activities and run lengths, but did not find any visual differences.

We find that the microviscosity increment for small run lengths $\bar{\ell} \lesssim 10^{-1}$ is basically independent of the activity. For intermediate run lengths of the order 10^0 to 10^1, there is a strong effect for small activities, but a saturation for $\mathrm{Pe}^{\mathrm{act}} \gtrsim 20$. For large run lengths $\bar{\ell} \gtrsim 10^2$ the microviscosity increment saturates for small activities ($\mathrm{Pe}^{\mathrm{act}} \lesssim 10$), while it continues to decrease for larger activities. Hence, fast swimmers are not sufficient for a substantial decrease in $\Delta\eta/\phi$ if the run length is small. On the other hand, moderate swim speeds of $\mathrm{Pe}^{\mathrm{act}} = 5$ to 10 can make the microviscosity increment negative, if the run length is large. When both run length and swim speed are large, the reduction of $\Delta\eta$ is also very large. If the swim speed and the run length have to be coupled, a ratio of $\mathrm{Pe}^{\mathrm{act}}/\bar{\ell} \approx 100$ would be more beneficial than the thermal motion, which is shown as circles in Figure 8.8.

8.4. Surface fluxes

In the previous section we have shown that the microviscosity increment for prolate spheroids can become negative for large activities. This implies that the friction coefficient of the probe is reduced as compared to the pure solvent. It is, however, not clear yet, which mechanism causes this effect, we just know that a large run length $\bar{\ell}$ is beneficial. Since the microviscosity increment for spheres just decreases to zero for large activities, but does not become negative, it seems likely to search for the pushing mechanism in the anisotropic shape of the probe particle.

In the following, we will discuss the features of a fixed spheroidal probe ($\overline{D} = \Delta D = 0$) without external motion ($\mathrm{Pe}^{\mathrm{ext}} = 0$). We use a grid with $N_\xi \times N_\eta = 400 \times 400$ and $r_{\max} d = 100$ unless specified otherwise. Since the microviscosity increment is determined by the particle density at the excluded volume surface, we will have a closer look on the processes on this surface. Since we have cylindrical symmetry, it is sufficient to examine the properties along one meridian from fore to aft. To cast this into numbers, the simplest choice is the parameter η

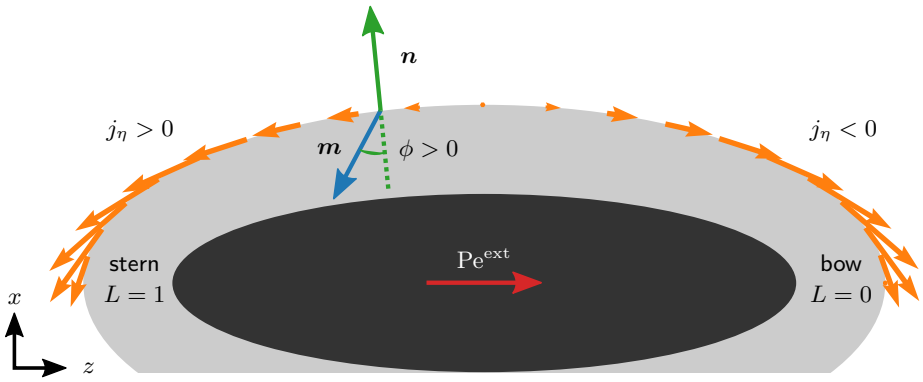

Figure 8.9.: Sketch of the terms and angles to describe the surface flux j_η (orange, only upper half is shown). It is positive if it points towards the stern of the ellipsoid. The angle of the polar order field $\boldsymbol{m}$ with the surface normal $\boldsymbol{j}$ is denoted by ϕ and positive if $\boldsymbol{m}$ points towards the stern of the ellipsoid. The dark area is a spheroid with aspect ratio $\hat{a} = 3.5$ and the light grey area is the approximate excluded surface volume.

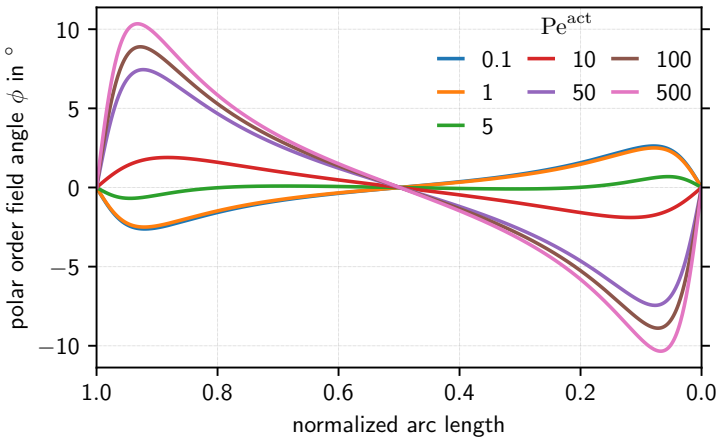

Figure 8.10.: Mean angle between polar order field and surface normal at the surface for a prolate ellipsoid with $\hat{a} = 3.5$, $s = 1$ without external pulling. For a positive value the polar order field points towards the stern of the ellipsoid. The normalized arclength of 0 corresponds to the bow of the particle while 1 is the stern of the ellipsoid.

from the spheroidal coordinates. The drawback of this simple choice appears, when we want to analyze gradients along the meridian. The derivative with respect to η will not only include the variation of the function, but also the variation of the distance to the origin. This issue can be resolved, if we choose the arc length of the meridian as parameter. It is given by

$$L(\eta) = \int_0^\eta \sqrt{a^2 \sin^2(\eta') + c^2 \cos^2(\eta')} \mathrm{d}\eta' \,, \tag{8.84}$$

where $a = (s\hat{a} + 1)/2$ and $c = (s + 1)/2$ are the semiaxes of our ellipsoid. Since there is no closed form for this integral available, we will do this calculation numerically using a simple Riemann sum on the available grid points. For the plots we will normalize the arc length with the distance from bow to stern, where a value of 0 corresponds to the bow and a value of 1 corresponds to the stern. As the probe particles are moving to the right throughout this thesis, we show the bow (value 0) at the right and the stern (value 1) at the left, see Figure 8.9 for a sketch of the quantities.

The first quantity we have a look at is the angle ϕ between the polar order field $\boldsymbol{m}$ and the

surface normal $\boldsymbol{n}$ for different activities (with thermal run length $\overline{\ell} = \mathrm{Pe}^{\mathrm{act}}/3$) as shown in Figure 8.10. This angle is calculated via

$$\phi = \arcsin\left(\frac{m_\eta}{\sqrt{m_\eta^2 + m_\xi^2}}\right), \tag{8.85}$$

which allows us to determine the direction of the deviation. A positive angle indicates that the polar order field points into the positive η-direction, i.e. towards the stern of the ellipsoid, while a negative angle occurs if the polar order field points towards the bow of the ellipsoid.

While the polar order field points towards the equator of the spheroid for small activities, it points towards the ends for activities larger than $\mathrm{Pe}^{\mathrm{act}} \gtrsim 10$. The maxima or minima of the angle are observed at around normalized arc lengths of $L = 0.08$ and $L = 0.92$ with slight deviations only close to the crossover from positive to negative. Furthermore, the magnitude of this angle increases with activity and saturates above $\mathrm{Pe}^{\mathrm{act}} \gtrsim 500$. There seems to be an activity threshold for this crossover, because for $\mathrm{Pe}^{\mathrm{act}} \leq 1$ we do not find a crossover even for large run lengths (long reorientation times, small rotational diffusion). In this configuration the magnitude of the angle increases up to $\ell \approx 10$ and decreases for larger run lengths (not shown). For activities above this threshold, we find that the angle reverses its sign for $\mathrm{Pe}^{\mathrm{act}}\overline{\ell} \gtrsim 10$. These findings hold for $\hat{a} = 1.5$ as well as for $\hat{a} = 5$, although the magnitude of the angles is larger for larger aspect ratios. These results are at first sight in contrast to the findings of Fily *et al.* [FBH15], who find that the particles align with the surface normal. Their system, however, differs in two aspects: Their particles do not show translational diffusion. i.e. their results correspond to the large $\mathrm{Pe}^{\mathrm{act}}$ limit. Second, they consider particles inside a box with convex and concave regions, while we consider particles outside an obstacle, which is completely concave. This is the crucial difference, because convex regions act as particle traps, while concave regions drive the particles away [FBH15, p. 2, Fig. 2]. In their stationary case there is consequently only particles in the convex regions [FBH15, p. 4, Eq. (8)]. Since our system does not exhibit particle traps but an infinite reservoir of active particles, their argument cannot be applied to our system. Instead, there should be a stationary flux of particles along the surface.

For this purpose we look at the particle flux $\boldsymbol{j}_n$ as introduced in (2.255a) or (8.26c). For convenience, we separate this flux into its diffusive $\boldsymbol{j}_d$, convective $\boldsymbol{j}_c$ and active $\boldsymbol{j}_a$ contribution via

$$\boldsymbol{j}_n = \boldsymbol{j}_d + \boldsymbol{j}_c + \boldsymbol{j}_a, \tag{8.86a}$$

$$\boldsymbol{j}_d = -\boldsymbol{\partial}_r n, \tag{8.86b}$$ $$\boldsymbol{j}_c = -\mathrm{Pe}^{\mathrm{ext}}\hat{\boldsymbol{z}} n, \tag{8.86c}$$ $$\boldsymbol{j}_a = \mathrm{Pe}^{\mathrm{act}}\boldsymbol{m}, \tag{8.86d}$$

assuming fixed velocity microrheology $\overline{D} = \Delta D = 0$ (which changes only $\boldsymbol{j}_d$). Without external pulling there is only the diffusive and the active contribution. Since, we have no-flux boundary conditions, the ξ component of those fluxes vanishes as well as the ϕ component due to the symmetry. What remains to be analyzed is the η component of those fluxes.

The surface flux as a function of the normalized arc-length and its contributions from diffusive and active motion are shown in Figure 8.11. We use again the coupling of the run length to the activity via rotational diffusion. For small activities, the surface flux is also quite small. Interestingly, the contribution from the activity points to the equator and has a different direction than the diffusive contribution to the flux, which reduces the total flux. For activities

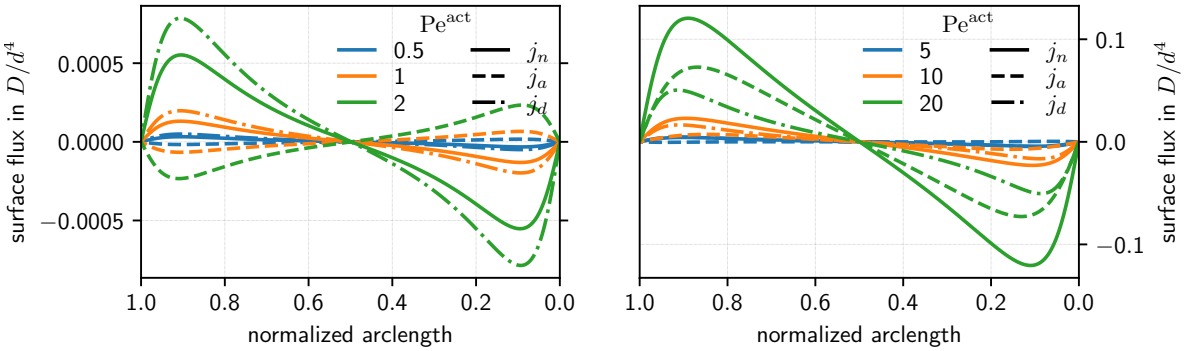

(a) Small activities **(b)** Larger activities

Figure 8.11.: Particle flux density along the surface of the spheroid with aspect ratio $\hat{a} = 3.5$ and $s = 1$ for different activities. Solid lines show the total flux $(\boldsymbol{j}_n)_\eta$, dashed lines the contribution from the active flux $(\boldsymbol{j}_a)_\eta$, while dash-dotted lines show the contribution from the diffusive flux $(\boldsymbol{j}_d)_\eta$.

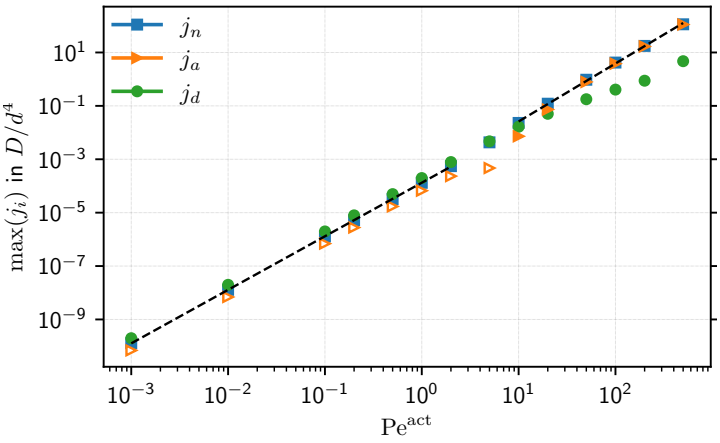

Figure 8.12.: The maximum of the total (squares, blue), active (triangles, orange) and diffusive (circles, green) surface fluxes shown in Figure 8.11. Open symbols visualize a flux towards the equator, filled ones a flux towards the poles. The dashed line is a power law fit below and above the sign change of j_a with exponents of 2.0 and 2.2, respectively.

$\mathrm{Pe}^{\mathrm{act}} \gtrsim 5$ we find that all surface fluxes point towards the poles of the prolate ellipsoid. Hence, the surface flux due to the activity reverses its direction above a certain activity level. Since it is proportional to the polar order field, this is exactly what we have observed for the angle of the polar order field in the previous paragraph. Since the magnitudes of the fluxes span several orders of magnitude, we plot the maximum of the fluxes as function of the activity in Figure 8.12.

For small activities the total flux is dominated by the diffusive flux $\boldsymbol{j}_d$. Since diffusive and active flux have different signs, the total flux is smaller than the diffusive flux. For large activities the flux is dominated by the active flux $\boldsymbol{j}_a$. Below the sign change, the maximum of the total particle flux $\boldsymbol{j}_n$ scales like $(\mathrm{Pe}^{\mathrm{act}})^2$. Above the sign change, we find that the maximum scales like $(\mathrm{Pe}^{\mathrm{act}})^{2.2}$, i.e. a little bit stronger. If the run length $\overline{\ell}$ is fixed, the scaling of the maxima for large activities is reduced to $(\mathrm{Pe}^{\mathrm{act}})^{1.5}$ for $\overline{\ell} = 1$ and to $(\mathrm{Pe}^{\mathrm{act}})^{2.0}$ for $\overline{\ell} = 1000$.

We now change to an oblate spheroid. The fluxes for a spheroid with aspect ratio of $\hat{a} = (3.5)^{-1}$ and a size ratio of $s = 3.5$ (to keep the arc length of the spheroid the same) are shown in Figure 8.13a. We find that the directions of all surface fluxes are reversed as compared to the prolate ellipsoid (shown in Figure 8.11). The total flux always points into the direction of the equator. The minima and maxima of the total flux $\boldsymbol{j}_n$ appear at a normalized arc length of

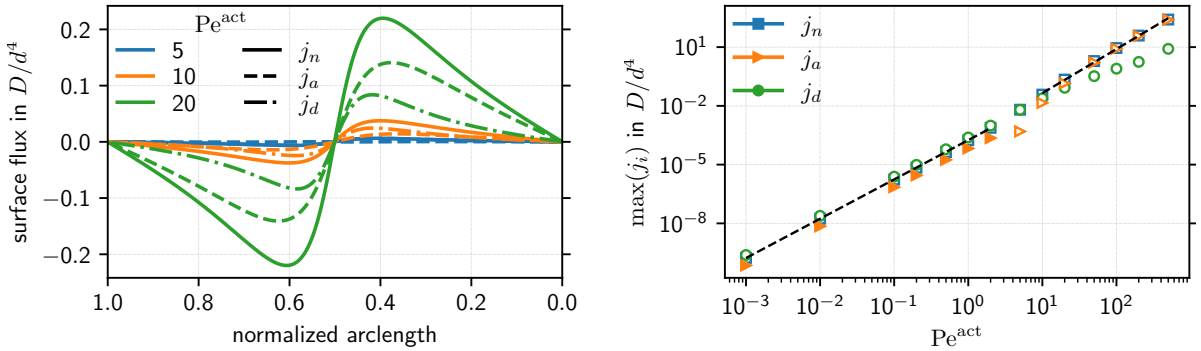

(a) Surface fluxes, see Figure 8.11 for explanations. **(b)** Maximum of the surface fluxes, see Figure 8.12.

Figure 8.13.: The surface flux for an oblate spheroid with $\hat{a} = (3.5)^{-1}$ and $s = 3.5$ for selected activities (left) and its maximum as a function of activity (right). The dashed black lines are power law fits to the total flux j_d below and above the inversion of j_a with exponents 2.0 and 2.3, respectively.

about 0.4 and 0.6. These maxima show a very similar scaling as in the oblate case as shown in Figure 8.13b. For small activities the diffusive flux dominates and is counteracted by the active flux. For an activity of $\mathrm{Pe}^{\mathrm{act}} \approx 5$, the direction of the active flux changes and points towards the equator. For large activities, the active flux dominates the total flux. The maximum of these fluxes scales like $(\mathrm{Pe}^{\mathrm{act}})^2$ for activities below the flow inversion of the active flux and like $(\mathrm{Pe}^{\mathrm{act}})^{2.3}$ above. Furthermore, the magnitudes of these fluxes are essentially the same as in the prolate case.

In summary, we find that there is a steady state flux of particles along the surface towards the poles of a prolate spheroid and towards the equator of an oblate spheroid. For both objects these are the regions with the largest curvature. The maxima of these fluxes scale like $(\mathrm{Pe}^{\mathrm{act}})^2$ for large run lengths or slightly stronger if the run length is coupled to the activity via rotational diffusion. The curvature dependence of these fluxes will be examined in the next section.

8.5. Swim pressure at curved surfaces

In the preceding section, we found that there is a steady state flow of active particles along the surface towards the regions with the largest curvature, even in the absence of external flow. In this section, we will test several hypotheses about the curvature dependence of these fluxes. The cause for a flux is typically a gradient. For example the diffusive flux is driven by a gradient in density. Macroscopically, we can also associate a flow with a gradient in pressure. This concept can be transferred to active particles, which generate a so called *swim pressure* [YB15b; TYB14]. It is given in the ideal gas limit (dilute, no interactions between particles) by

$$P^{\mathrm{swim}} = n\gamma \frac{u_0^2}{6D^R} = nk_{\mathrm{B}}T \frac{\mathrm{Pe}^{\mathrm{act}}\overline{\ell}}{6} \tag{8.87}$$

in 3D (cf. [TYB14, p. 2, Eq. (2)]). Since the friction coefficient γ, the swim velocity u_0 and the rotational diffusion coefficient D^R are constant in the system, there is a direct proportionality of the particle density n and the swim pressure. However, unlike the usual pressure, it may depend on the geometry, as we will see below. In the following, we will present some results

from the literature.

Fily *et al.* studied active particles without translational diffusion in a 2D box [FBH14; FBH15]. Their approach considers the strong confinement limit, where the run length $\overline{\ell}$ is much larger than the box such that the particles essentially stay at the boundary of the box. They define the pressure of the active particles on the wall via

$$P = n\gamma u_0 \frac{\langle \hat{\boldsymbol{q}} \cdot \boldsymbol{n} \rangle}{|\hat{\boldsymbol{q}}|}, \tag{8.88}$$

(cf. [FBH14, p. 5611, Eq. (10)]), where $\hat{\boldsymbol{q}} \cdot \boldsymbol{n}/|\hat{\boldsymbol{q}}|$ is the component of the normalized polar order field $\hat{\boldsymbol{q}}$ parallel to the surface normal $\boldsymbol{n}$. For a circle of radius R they find

$$P(R) = \frac{N\gamma u_0}{2\pi R} \exp\left(-\frac{RD^R}{2u_0}\right) = Nk_\mathrm{B}T \frac{\mathrm{Pe}^\mathrm{act}}{2\pi\overline{R}} \exp\left(-\frac{\overline{R}}{2\overline{\ell}}\right), \tag{8.89}$$

(cf. [FBH14, p. 5611, Eq. (13)]), where N is the number of particles in the circle (and on the boundary). The particle density at the boundary is given by

$$n(L) = \frac{N}{2\pi R(L)}, \tag{8.90}$$

(cf. [FBH15, p. 3, Eq. (6)]), where L is the arc length and $R(L) = 1/\kappa(L)$ is the local radius of curvature the interior of a convex box.

Smallenburg and Löwen discuss the swim pressure caused by active particles at curved walls [SL15]. Their model system consists of self-propelled particles in 2D with rotational, but without translational diffusion inside ($R < 0$) and outside a circular boundary ($R > 0$). They find the following empirical expression for the curvature dependence of the pressure characterized by the radius R of the circle

$$\frac{P(R)}{P_0} = \alpha e^{-2\ell/R} + (1-\alpha)\frac{\ln 2}{\ln(1+\exp(\ell/R))} \tag{8.91}$$

(cf. [SL15, p. 2, Eq. (4)]) with $\alpha \approx 0.0893$ and $P_0 = n_\infty \gamma u_0^2/2D^R$. n_∞ is the particle number density in the bulk, which vanishes for large activities.

A system of active particles with translational diffusion in and outside of circular (2D) and spherical (3D) boundaries was studied by Yan and Brady [YB15a]. They find analytical expressions for the swim pressure at curved surfaces. Outside circles they find

$$\frac{P(R)}{P_0} = \frac{1}{1+(\ell/R)/\sqrt{2}} \tag{8.92}$$

(cf. [YB15a, p. R1-6, Eq. (3.7)] and outside spheres they find

$$\frac{P(R)}{P_0'} = \frac{1}{1+(\ell/R)\sqrt{3}} \tag{8.93}$$

(cf. [YB15a, p. R1-5, Eq. (3.6)]) with $P_0' = n_\infty \gamma u_0^2/6D^R$ and in both cases in the limit of vanishing translational diffusion.

This result, however, is somewhat different from Smallenburg's results. Even though the qualitative result for $\ell/R > 0$ is the same, the numbers are larger for Yan's results. The prefactor in the limit $\ell/R \to \infty$ is different: $\sqrt{2} \approx 1.41$ for Yan vs $(1-\alpha)\ln(2) \approx 0.63$ for Smallenburg. Similarly, the expansion around $\ell/R = 0$ gives a prefactor $-1/\sqrt{2} \approx -0.71$ for Yan and $(\alpha - 4\alpha\ln(2) - 1)/\ln(4) \approx -0.836$ for Smallenburg. A possible explanation for this discrepancy could be the approximate nature of the analytical solution. It is shown in [YB15a, p. R1-6, Fig. 2] that the use of a higher order closure leads to smaller values for the density and therefore, for the swim pressure.

Furthermore there is the possibility to define the pressure on a surface via hydrodynamic equations as introduced by Steffenoni *et al.* [SFK17, Eq. (44)]. This approach combines the swim pressure (8.87) with the divergence of the polar order field. Care has to be taken, when applying these predictions to 3D, because many of the definitions above were introduced and tested for 2D systems only, even though they could possibly be extended to 3D. Since all those equations were derived under different assumptions, they are not equivalent despite a similar qualitative behavior.

All those concepts have in common that there is a well defined radius. In two dimensions, such a radius can be uniquely generalized to arbitrary shapes by the inverse of the curvature (essentially the second derivative) of a curve [Yat74, p. 62]. For an ellipse with semiaxes a and c parametrized by $(x(\eta), z(\eta)) = (a\sin(\eta), c\cos(\eta))$ the curvature is given by

$$\kappa(\eta) = \frac{ac}{(c^2\sin^2(\eta) + a^2\cos^2(\eta))^{3/2}}. \tag{8.94}$$

However, for 3D objects such as spheroids there are different concepts of curvature, for example the *mean curvature* or the *Gaussian curvature*. For spheroids with semiaxes $a = b \neq c$, the *mean curvature* is given by

$$H(\eta) = \frac{a^2c(6a^2 + 2c^2 + 2(a^2 - c^2)\cos(2\eta))}{8(a^4\cos^2(\eta) + a^2c^2\sin^2(\eta))^{3/2}} \tag{8.95}$$

and the *Gaussian curvature* by

$$K(\eta) = \frac{a^4c^2}{(a^4\cos^2(\eta) + a^2c^2\sin^2(\eta))^2} \tag{8.96}$$

(cf. [WeiEll, Eq. (12), (13)]). The Gaussian curvature has units of inverse length squared, while the other measures have just inverse lengths as units. Therefore, we will use the square root of the Gaussian curvature for a better comparison. As introduced in 2.5.1, the semiaxes are in our case $a = (s+1)/2$, $c = (s\hat{a}+1)/2$.

The relation (8.90) suggests a simple relationship between the density and the curvature in the limit of large activities. To check for a similar relationship in our case, we want to compare the density as function of the different definitions of a curvature. Two things have to be taken into account. First, the swim pressure arises in addition to the usual pressure from the thermal motion. Therefore, we have to subtract the bulk bath particle density. Second, since we model an infinite reservoir of bath particles, their density at the surface increases with increasing

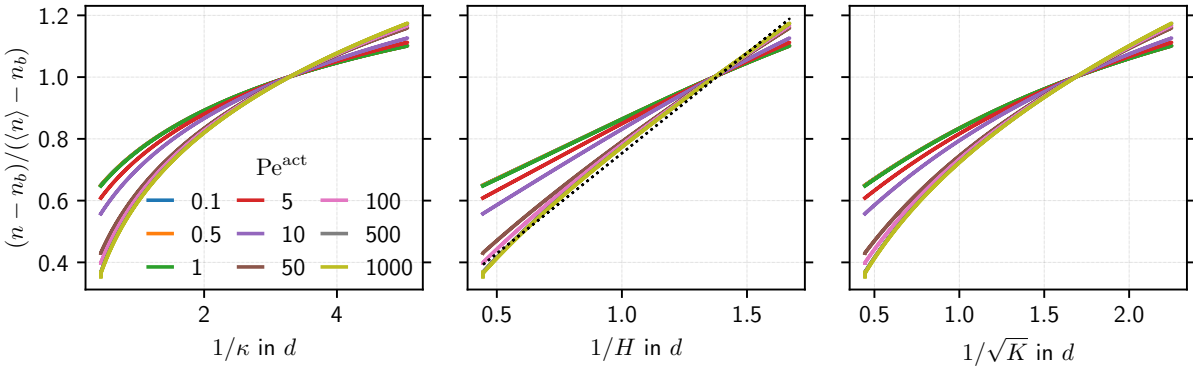

Figure 8.14.: The normalized excess density of active particles at the surface plotted over the inverse of the local curvature for different activities without external forcing for a spheroid with $\hat{a} = 3.5, s = 1$. Left: inverse curvature κ of the ellipse (8.94), Center: inverse mean curvature H (8.95) Right: square root of the inverse Gaussian curvature K (8.96). The dashed black line in the center panel shows a linear fit to $\mathrm{Pe}^{\mathrm{act}} = 1000$ with $y = 0.65x + 0.1$.

activity. Therefore, we normalize by the average particle density on the surface

$$\langle n \rangle_S = \frac{1}{|\partial \mathcal{V}^{\mathrm{exc}}|} \int_{\partial V^{\mathrm{exc}}} n(\boldsymbol{r}) \mathrm{d}\boldsymbol{r} = \frac{1}{A} \int_0^\pi n(\xi_0, \eta) \sqrt{\sinh^2(\xi_0) + \sin^2(\eta)} \sin(\eta) \mathrm{d}\eta \tag{8.97}$$

with[2]

$$A = \int_0^\pi \sin(\eta) \sqrt{\sinh^2(\xi_0) + \sin^2(\eta)} \mathrm{d}\eta \,. \tag{8.98}$$

With this, we can define the normalized excess density $(n - n_b)/(\langle n \rangle - n_b)$, which is shown for different activities in Figure 8.14. As the relations with the curvature do not show anything close to a linear behavior, we show the normalized excess density as function of the inverse curvature, which can be interpreted as the radius of an osculating sphere[3]. We find that there are limiting distributions of the normalized excess density for small activities and large activities. For large activities, the difference in excess density for different curvatures is more pronounced. This is independent of the choice of the curvature definition, since they are all monotonic. However, there is no simple relationship between any of the curvature definitions and the excess density. The most linear dependence can be found for the inverse of the mean curvature. A linear fit is shown as dotted black line, which reveals that the curve is not perfectly straight. Additionally, we find that there is always a smaller particle density for smaller radii (larger curvatures). This is opposite to the findings (8.90) in the interior of a sphere, where the density is larger for smaller radii. If we assign different signs to the curvature of concave and convex regions as done in [SL15, Sec. III, p. 2], we can summarize both behaviors with the statement that the active particles accumulate in regions with larger curvature (convex > 0, concave < 0). A quantitative statement is not trivial.

[2] Note that A is only proportional to the surface area $|\partial \mathcal{V}^{\mathrm{exc}}|$, since we already cancelled some terms in the integral.

[3] As the curvature can differ for different directions, the osculating sphere can intersect with the surface and is not necessarily osculating in all directions.

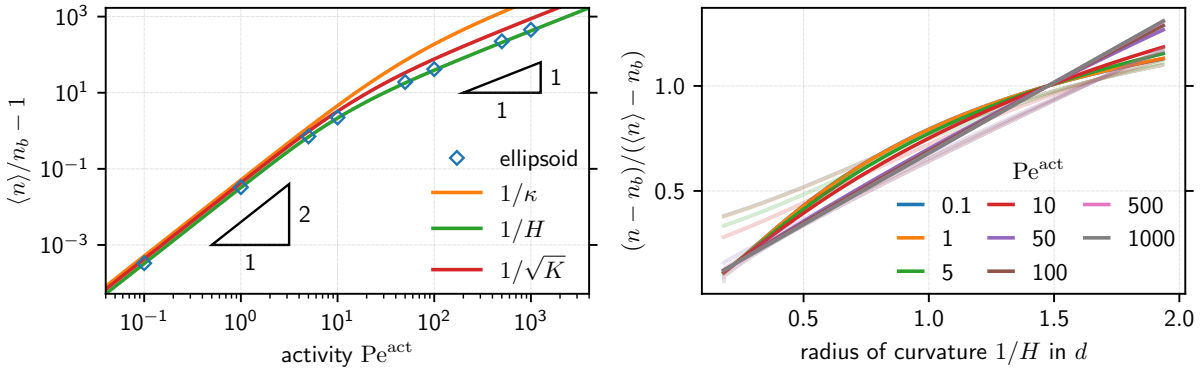

Figure 8.15.: Predictions for the excess density of active (with thermal run length) at the surface ($\hat{a} = 10$, $s = 1$). Left: Mean excess density as function of activity predicted from (8.99) with the radius obtained as inverse from the surface averages of the ellipse curvature κ (orange), the mean curvature H (green) and the Gaussian curvature K (red). Open squares are the numerical values for the ellipsoid. Right: Prediction of the curvature dependence based on the local mean curvature for different activities. The semitransparent curves show the actual values for the ellipsoid.

For a non-trivial model, we can try to use the prediction for the density of active particles around a sphere, as derived in (8.24a). It yields for the excess density on the surface (for $\tilde{D} = 1$)

$$n(R) - n_b = \frac{n_b}{6} \frac{(\mathrm{Pe}^{\mathrm{act}} R)^2}{R^2 \mathrm{Pe}^{\mathrm{act}}/\overline{\ell} + R\lambda + 1} \tag{8.99}$$

with $\lambda^2 = 2(\mathrm{Pe}^{\mathrm{act}}/\overline{\ell} + (\mathrm{Pe}^{\mathrm{act}})^2/6)$ (see (8.20)). This leads to the relation

$$n(R) - n_b = n_b \frac{\sqrt{3}}{6} \mathrm{Pe}^{\mathrm{act}} R \tag{8.100}$$

in the limit of large activities ($\mathrm{Pe}^{\mathrm{act}} \gg 6/\overline{\ell}$ in the general case or $\mathrm{Pe}^{\mathrm{act}} \gg \sqrt{3}$ for active spheres). Hence, in the limiting case of a spherical surface and large activities, we find that the excess density on the surface is indeed proportional to the radius of curvature. But our finding from the previous paragraph indicates that the behavior is more complex on objects with varying curvature. In the case of a sphere, all definitions for the curvature agree such that this does not give us a hint on the choice of a curvature.

We can also use relation (8.99) to predict the average excess density based on an effective curvature of the ellipsoid. We will again calculate the curvature for the ellipse (8.94), the mean curvature (8.95) and the square root of the Gaussian curvature (8.96) and average them the same way as the density (8.97). Then, we take the inverse of this average curvature as value for the prediction. This is shown for different activities in the left panel of Figure 8.15. We find that the overall agreement is quite good for any of these averaged curvatures. For low activities the excess density increases quadratically with the activity, while it increases linearly for large activities. The differences between the different average curvatures become more pronounced for large activities and larger aspect ratios. This is why we show the data for $\hat{a} = 10$ as the differences are more visible. Having a close look, we find the best agreement for the average mean curvature, which deviates only about 5 %, while the other measures deviate by 15 % or

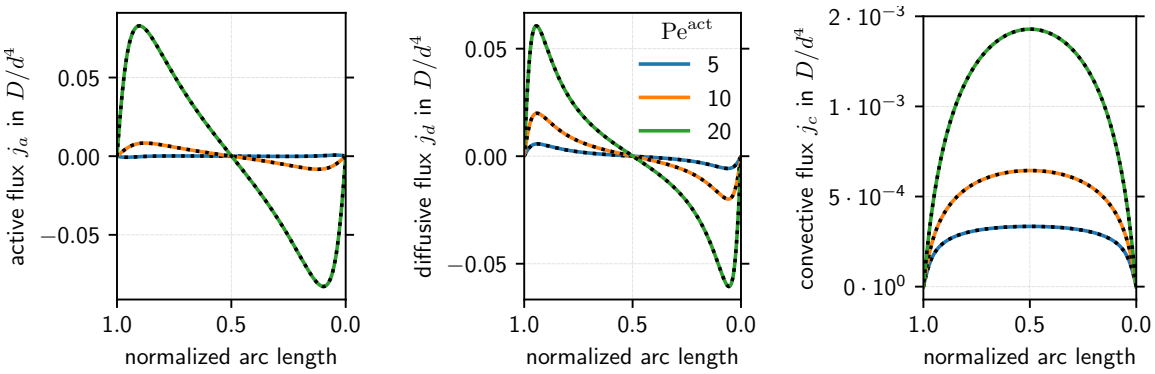

Figure 8.16.: The fluxes on the surface of an ellipsoid with $\hat{a} = 5$. while pulling with $\mathrm{Pe}^{\mathrm{ext}} = 0.01$ for different activities. The black dotted lines indicate the prediction of the fluxes based on the data for $\mathrm{Pe}^{\mathrm{ext}} = 0$ as introduced in the text.

more. Interestingly, for oblate spheroids, we find the best agreement with the average Gaussian curvature. Furthermore, we find that for large size ratios, the agreement is getting worse.

The nice agreement for the prolate spheroids encourages us to also check the curvature dependence of this prediction based on the mean curvature. This is shown in the right panel of Figure 8.15. The prediction shows qualitatively the same behavior as the data, which was presented in Figure 8.14. The excess density increases monotonically with the radius of curvature and the difference between the extremal radii becomes more pronounced for larger activities. The quantitative agreement, however, is not so good. At small radii, the density is underestimated, while at large radii it is overestimated. This suggests that there are some transport processes on the surface, which we did not take into account by the flux-free solution of the sphere. To summarize, we find that there is a curvature dependent particle density. The translation of this density into a local pressure depends on the model employed as introduced in the beginning of this section. This changes the magnitude of the pressure, but a curvature dependence of this local pressure will remain.

8.6. Symmetry breaking through external pulling

The interesting question is now, how do things change, when we pull the probe externally. In order to keep the analysis simple, we stay in the linear response regime with small external pulling, $\mathrm{Pe}^{\mathrm{ext}} = 0.01$. Small pulling implies that the number density is only slightly changed. In Figure 8.16 we find that the active and diffusive fluxes on the surface remain almost unchanged, while the convective flux on the surface is given by $\boldsymbol{j}_c \cdot \hat{\boldsymbol{\eta}} = n_0 \mathrm{Pe}^{\mathrm{ext}} \hat{\boldsymbol{z}} \cdot \hat{\boldsymbol{\eta}}$, where n_0 is the particle number density on the surface without external pulling. Since this convective flux has the same direction on the whole surface of the ellipsoid, it creates an asymmetric particle density around the ellipsoid, because it counteracts the already existing fluxes in the front part of the probe, while it adds to those fluxes in the rear part of the ellipsoid. This non-symmetric particle density causes the net force on the probe as introduced in (2.263). (Symmetric contributions cancel out because of the multiplication with the surface normal).

From the same figure we find that the strength of this flux increases with the activity, because

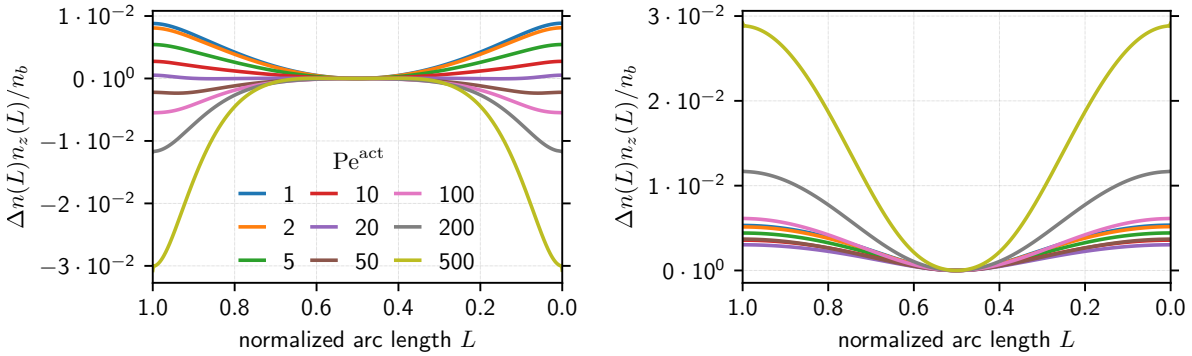

Figure 8.17.: The density difference $\Delta n = n(\mathrm{Pe}^{\mathrm{act}}, \mathrm{Pe}^{\mathrm{ext}}) - n(\mathrm{Pe}^{\mathrm{act}}, \mathrm{Pe}^{\mathrm{ext}} = 0)$ at the surface weighted by the z component of the surface normal, which causes the net force on the probe. Left: density difference for a prolate ellipsoid with $\hat{a} = 3.5$, $s = 1$, Right: panel density difference for an oblate ellipsoid with $\hat{a} = (3.5)^{-1}$, $s = 1$.

the particle density at the surface increases with the activity. A larger flux can create larger density asymmetries. However, the interplay between particle flux and particle density is nontrivial and the effect of the fluxes on the microviscosity increment cannot be inferred easily.

As a final analysis, we look at the difference of the particle density at the surface with for $\mathrm{Pe}^{\mathrm{ext}} = 0.01$ and $\mathrm{Pe}^{\mathrm{ext}} = 0$, weighted with the z-component of the surface normal as shown in Figure 8.17. The integral over this function is exactly the net force on the probe. We find that there is a decrease in the density difference for small activities for both oblate and prolate ellipsoids. However, for activities larger than $\mathrm{Pe}^{\mathrm{act}} \gtrsim 20$ the behavior is different. While the density difference continues to decrease for prolate spheroids, it increases again for oblate spheroids. This turning point roughly coincides with the crossover point found in the fluxes, where the dominant flux contribution changes from diffusive flux to active flux.

8.7. Conclusions

We have investigated the effect of an active bath on the change in the friction coefficient of a spheroidal probe particle. An analytic approach did not lead to closed equations, therefore we studied this problem numerically. We find that small activities reduce the friction coefficient of the probe irrespective of the shape. For large activities, however, there is an increase of the friction coefficient for oblate spheroids and a decrease for prolate spheroids. This can lead to a reduction of the friction coefficient below the value in the pure solvent. The strength of this effect depends on the shape and the size ratio and vanishes for large probes as well as spheres and rods, i.e., they have the same friction coefficient in a system with very active bath particles as in a pure solvent. This effect can be related to the flux of active bath particles along the surface of the probe particle. The symmetry breaking through the external pulling leads to an asymmetry in the bath particle distribution along the probe surface with more particles pushing from behind.

9. Conclusions and Outlook

In this thesis, we have analyzed a theoretical description for active microrheology in two complex liquids: a dense colloidal suspension and a dilute suspension of active Brownian particles. In both cases, the description is based on the Smoluchowski equation as introduced in Section 2.3. For the dense colloidal suspension of hard spheres, we employed the mode-coupling theory framework in Section 2.4 to derive equations of motion for the probe particle density correlation functions for constant force microrheology. From these equations, we obtained a fixed point equation for the long time limit and expressions for the transport coefficients and moments. Furthermore, we could derive a linear response relation, which connects the mean displacement for small forces to the mean square displacement without external force.

For the dilute suspension of active Brownian particles, we could reduce the problem to solving a two-body Smoluchowski-equation as described in Section 2.5. Considering the constant velocity mode for active microrheology, we found that the force on the probe is determined by the bath particle density distribution on its surface. This density, together with the polar order field for the bath particles associated with their average swimming direction, has been obtained by a moment expansion of the probe-bath pair correlation function.

The main part of this thesis is the analysis of the MCT equations for the active microrheology in a colloidal glass. These equations have been solved numerically. The required numerical methods were developed in Chapter 3. We described the discretization of the memory integrals, which are required for the long-time-limit calculation, the Laplace space solution as well as the full time-dependent solution. For the time-dependent solution, we had to numerically solve integral equations of the Volterra type and associated integro-differential equations. In order to cover a large time window, a decimation scheme is introduced which allows to find the solutions spanning many orders of magnitude in time without excessive memory consumption. Three different algorithms, two based on solving an integral equation and the third based on solving an integro-differential equation are introduced, since the numerical solution behaves unstable for large forces and long times. To compare these algorithms, we test their numerical performance with respect to convergence order and stability by comparing to analytically known solutions. While the moment-based methods perform best by achieving convergence of order 2, their stability depends on the type of equation. There is no algorithm, which is stable for all tested integral equations. For the full numerical solution, we verified that all methods yield the same results as long as they operate in their stable regimes, which is cross-checked by calculating independently the Laplace space solution. We find that the integro-differential method is stable for the full solution below a threshold force, but becomes unstable for long times for larger forces. The integral method is unstable for long times for any force. The comparison of both methods allows us to estimate the reliability of the solution.

Since a colloidal glass behaves dynamically like a solid, the motion of the probe shows two qualitatively different motions. For small forces, the mean displacement of the probe is finite in the limit of long times, while it increases proportional to the time for large forces. The

force separating these two regimes is called the critical force and the corresponding phase transition, the delocalization transition. In Chapter 4, we investigate this transition using two defining properties, first using the theoretical approach of looking at long time limits of the probe density correlation functions and second the phenomenological definition looking at the mean displacements. Since the convergence speed of the numerical scheme is proportional to the relative distance from the critical force, i.e. we need more and more iterations to find the solution for a given accuracy, efficient methods to determine the critical force are essential. Such a method is established and verified. Moreover, we find that there is numerically two critical forces: At the lower critical force basically all but the correlation functions perpendicular to the force vanish. At the upper critical force the long time limits of all correlation functions vanish, which coincides with the critical force obtained by the efficient critical force method using the transport coefficients. This is a numerical feature, because the difference between both critical forces is approximately proportional to the value of the smallest nonzero wave vector. Evaluating the mean displacement, we find that the lower critical force is relevant for the qualitative change from finite to diverging long time limit. The corresponding critical force for the time domain calculations differs slightly from the values obtained in Laplace space, possibly due to a loss in accuracy.

Having identified the relevant numerical parameters, we can construct a phase diagram to study the critical force as function of the packing fraction. We find that the square of the critical force is proportional to the long time limit of the mean square displacement obtained without any external force. We also relate the critical force to the yield stress and find a power law with exponent 1.7 ± 0.1. This establishes a power law between the yield stress and the long time limit of the quiescent mean square displacement, which is checked for two different simulations.

Finally, we characterize the behavior of different observables around the delocalization transition in Section 4.5. We analyze the moments below the critical force and friction as well as diffusion coefficients above the critical force. We find a force-thinning behavior of the elastic constant below the critical force, i.e. the long time limit of the mean displacement becomes very large close to the critical force. The variances at long times become also very large close to the critical force. While the variance perpendicular to the force direction grows faster for intermediate forces, the variance parallel to the force direction overtakes close to the critical force. The friction coefficient diverges when approaching the critical force from above and the diffusion coefficient vanishes. In the time domain we find slight superdiffusion for intermediate times, but not as strongly as in simulations. Furthermore, we analyze the long time limit of the probe density correlation functions and establish a description through a simple model with a few fit parameters. While some parameters obtained from the fit diverge like power-laws at the critical force, others approach a constant value.

Analyzing the van Hove function (in real space), we observe exponential tails extending in force direction, but also perpendicular to the force. The length of these exponential tails increases when approaching the critical force and dominates the value of the mean displacement. In contrast, the peak of the van Hove function remains close to the origin. This behavior is also observed in simulations.

A more thorough analysis of the bifurcation together with analytical calculations is given in Chapter 5. Numerically we find that the nonergodicity parameters close to the upper critical force go continuously to zero. At the lower critical force, the behavior for $q_{\max} d \leq 14$

is qualitatively different than that for $q_{\max}d \geq 20$. In the former case the nonergodicity parameters behave continuously, while in the latter they exhibit a discontinuity together with a square-root-like behavior. Since this type of transition is not observed in classical MCT, we analyze models for the bifurcation based on schematic models and simple physical ideas, which can reproduce some of the features. This is followed by a systematic analysis of the stability matrix, which reveals a divergence of the critical eigenvector (the critical amplitude) for $q \to 0$, like q_x^{-2} perpendicular and like q_z^{-1} parallel to the direction of the force. The mean displacement and the variances as well as the friction and diffusion coefficients scale like power laws. Their exponents are different for $q_{\max}d \leq 14$ and $q_{\max}d \geq 20$, but they share the property that the mean displacement and the variance perpendicular to the force have the same exponent, which is half of the exponent of the variance parallel to the force.

For the asymptotic dynamical critical behavior we expand different representations of the equations of motion in Laplace space. With some approximations, we can derive a critical power law with exponent $-1/2$ for the correlation functions in time space. This exponent is confirmed for numerical solutions in the time domain for $q_{\max}d \leq 14$, but has to be replaced by -0.34 for $q_{\max}d \geq 20$. We note that the agreement deteriorates for small wave vectors, which impedes the use of a factorization ansatz separating the time from the wave-vector dependency. The analysis of the solution in Laplace space shows that there is a crossover from an exponent of 0.34 for small Laplace frequencies to 0.5 for very small Laplace frequencies, which reestablishes the derived critical law. Even though there is no factorization of the correlation functions possible, such a factorization applies to the primitive memory functionals, which can be used to explain the behavior of the correlation functions as well as the moments. Finally, we compare the critical behavior to simulations, which confirm the critical exponent for the correlation functions, but obtain different exponents for the moments.

As the bifurcation analysis of the full model revealed many peculiarities, we also investigated a schematic model designed by Gustavo Abade in Chapter 6. We can derive a critical power law with exponent $-1/2$ and an analytic expression for the critical force. The bifurcation is of type A. These findings are verified by numerical solutions in the time and Laplace domain.

Apart from the critical phenomena close to the delocalization transition, we also studied the implications of the non-Gaussian van Hove functions in Chapter 7. For this purpose, we compare to an experiment using an emulsion glass and an optical line trap. We test and verify the time-dependent linear response relation, which will allow an in-situ calibration of the force. A parameter-free comparison exhibits the same qualitative features, but a difference in the force and time scale. A major challenge for the experiments is the strongly heterogeneous dynamics in the glass. This is reflected in a bimodal structure of the parallel marginal van Hove function. For a quantitative comparison, we perform a similarity analysis of the experimental histograms and the theoretical predictions for the same mean displacements. We find the same structural features suggesting a bounded cage motion and a hopping between cages. This leads to an anomalous broadening of the van Hove function as compared to equilibrium dynamics. Finally, we give an estimate for the critical force using different characterizations, including the fraction of particles which have left their cages.

In the last project, we investigated active microrheology in active suspensions in Chapter 8. Analytical solutions can be found for special cases. For the full problem, a formal solution can be obtained, but the no-flux boundary conditions make it difficult to solve. Therefore, the finite-difference method is applied to solve the partial differential equations numerically. We

find that small activities of the probe particles reduce the friction coefficient of a spheroidal probe of any shape. For large activities it is increased again for oblate spheroids, but it can become even smaller than the friction coefficient in a particle free bath for prolate spheroids. The magnitude of this effect depends on the aspect ratio and the size ratio. In both cases the effect vanishes if the ratios are too large or too small, hence there is an optimal size. To investigate this phenomenon, we look at the flux of active particles along the surface and the induced swim pressure. The symmetry breaking of these fluxes due to the fixed velocity of the probe leads to a force pushing the probe. This makes it necessary to apply a force in the opposite direction to maintain a constant velocity.

Outlook — We have seen that active microrheology in complex fluids exhibits a broad variety of phenomena, which are beyond the scope of conventional rheometers and macroscopic rheological properties. Nevertheless, there are some questions which require further investigations: The nature of the delocalization transition could be addressed by a continuous schematic model describing the parameters of the hopping model fitted to it. For the numerical solution it would be beneficial to analyze the conditions for stable solutions so that larger times and displacements for large forces can be reached. A possible improvement could be the change to a frame of reference at the mean displacement of the probe. Completely unknown is the behavior on time dependent variations of the force, such as oscillatory motion or relaxation after releasing the force (the microscopic equivalent to shear cessation). The latter could be achieved directly with this theory as it only requires the insertion of the proper initial conditions, for the former the extension to time dependent forces has to be worked out. Another extension could be the incorporation of effects of the probe on the surrounding bath, in particular the structure of the bath particles around the probe. For active microrheology in the dilute regime, this is crucial for the nontrivial friction coefficient for large forces [SB05, Sec. V, p. 6f]. Finally, a theory without experimental verification is more a mathematical riddle than physics. Therefore it would be very interesting to see if very active particles indeed push a spheroidal probe.

In summary, we have seen that active microrheology in complex fluids exhibits a great variety of features, which go beyond what is measurable in classical rheometers. Our analysis suggests that a careful analysis not only of the moments but also of the full van Hove functions is crucial for the understanding of the dynamical behavior of this model system.

10. Zusammenfassung in deutscher Sprache

In dieser Arbeit wurde die theoretische Beschreibung von aktiver Mikrorheologie in zwei komplexen Flüssigkeiten untersucht: in einer dichten kolloidalen Suspension und einer verdünnten Suspension aktiver Brownscher Teilchen. In beiden Fällen basiert die Beschreibung auf der Smoluchowksi-Gleichung, die in Abschnitt 2.3 eingeführt wird. Für die dichte kolloidale Suspension aus harten Kugeln verwenden wir den Rahmen der Modenkopplungstheorie in Abschnitt 2.4, um Bewegungsgleichungen für die Dichtekorrelationsfunktionen des Probenteilchens in einem konstanten Kraftfeld herzuleiten. Ausgehend von diesen Gleichungen erhalten wir eine Fixpunktgleichung für den Grenzfall langer Zeiten sowie Ausdrücke für Transportkoeffizienten und Momente der van Hove Funktion. Schließlich können wir noch eine Beziehung für das lineare Antwortverhalten herleiten, das die mittlere Verschiebung für kleine Kräfte mit der mittleren quadratischen Verschiebung ohne externe Kräfte in Verbindung bringt.

Für das System mit wenigen aktiven Brownschen Teilchen können wir die theoretische Beschreibung, wie in Abschnitt 2.5 ausgeführt, auf die Lösung einer Zwei-Körper-Smoluchowski-Gleichung reduzieren. Für den Fall von Mikrorheologie mit einer konstanten Geschwindigkeit des Probenteilchens können wir die notwendige Kraft anhand der Teilchendichteverteilung auf seiner Oberfläche bestimmen. Diese Dichte kann zusammen mit der durchschnittlichen Ausrichtung der Teilchen aus einer Entwicklung der Proben-Bad-Paarkorrelationsfunktion in Momenten erhalten werden.

Der Hauptteil dieser Arbeit ist die Analyse der MCT-Gleichungen für die aktive Mikrorheologie in einem kolloidalen Glas. Diese Gleichungen wurden numerisch gelöst, wobei die notwendigen Methoden in Kapitel 3 eingeführt wurden. Ein wichtiger Baustein ist die Diskretisierung der Gedächtnisintegrale, die sowohl für den Grenzfall unendlich langer Zeiten als auch für die Lösung im Laplace-Raum sowie für die Berechnung der vollen Zeitabhängigkeit benötigt wird. Für die zeitabhängige Lösung müssen wir Volterra-Integral- und -Integro-Differential-Gleichungen numerisch lösen. Um ein großes Zeitfenster abdecken zu können, führen wir ein Dezimationsverfahren ein, das es erlaubt die Lösung über viele Größenordnungen in der Zeit zu berechnen, ohne einen übermäßigen Speicherverbrauch zu erfordern. Drei verschiedene Algorithmen, zwei basierend auf der numerischen Lösung einer Integralgleichung, der dritte basierend auf einer Transformation in eine Integro-Differentialgleichung werden getestet, da die numerische Lösung für große Kräfte und lange Zeiten instabil wird. Um diese Algorithmen zu vergleichen, testen wir ihre numerische Leistungsfähigkeit bezüglich Konvergenzordnung und Stabilität durch Vergleich mit analytisch bekannten Lösungen. Während die Algorithmen, die Teilintegrale verwenden, mit einer quadratischen Konvergenzordnung am besten funktionieren, hängt ihre Stabilität von der Art der Gleichung ab. Es gibt keinen Algorithmus, der für alle getesteten Integralgleichungen stabil ist. Für die volle numerische Lösung finden wir, dass alle Methoden die selben Ergebnisse liefern, solange sie in ihren stabilen Bereichen verwendet werden. Wir finden, dass die Methode, die die Integro-Differentialgleichung verwendet, unterhalb einer bestimmten Kraft für alle Zeiten stabil ist, aber für größere Kräfte für lange Zeiten instabil

wird. Die Methode basierend auf der Integral-Gleichung is instabil für lange Zeiten für alle Kräfte. Der Vergleich erlaubt uns eine Abschätzung der Verlässlichkeit der Lösung.

Da sich ein kolloidales Glas wie ein Festkörper verhält, finden wir zwei qualitativ verschiedene Verhaltensweisen des Probenteilchens. Für kleine Kräfte ist die mittlere Verschiebung des Teilchens selbst für unendlich lange Zeiten endlich, während sie für große Kräfte linear mit der Kraft anwächst. Die Kraft, die diese beiden Bereiche trennt wird kritische Kraft genannt und der zugehörige Phasenübergang Delokalisationsübergang. In Kapitel 4 untersuchen wir diesen Übergang anhand von zwei definierenden Eigenschaften: dem Verhalten der Nichtergodizitätsparameter, des Langzeitgrenzwertes der Dichtekorrelationsfunktionen, das aus theoretischer Sicht den Phasenübergang beschreibt, sowie dem Verhalten der mittleren Verschiebung des Probenteilchens, was phänomenologisch motiviert ist. Da die Konvergenzgeschwindigkeit des numerischen Verfahrens proportional zum relativen Abstand von der kritischen Kraft ist, sodass wir mehr und mehr Iterationen benötigen, um die Lösung mit einer bestimmten Genauigkeit zu finden, ist es wichtig, effiziente Methoden zu entwickeln, um die kritische Kraft zu bestimmen. Eine solche Methode wird entwickelt und getestet. Zusätzlich finden wir, dass es numerisch zwei kritische Kräfte gibt: Bei der kleineren kritischen Kraft verschwinden für lange Zeiten im Wesentlichen alle Dichtekorrelationsfunktionen mit Ausnahme derer, die Richtungen senkrecht zur äußeren Kraft beschreiben. Oberhalb der größeren kritische Kraft verschwinden dann alle Dichtekorrelationsfunktionen für lange Zeiten. Diese kritische Kraft stimmt mit der kritischen Kraft überein, die mit der effizienten Methode bestimmt wurde. Die Aufspaltung in zwei kritische Kräfte ist ein rein numerisches Phänomen, da die Differenz zwischen beiden Kräften ungefähr proportional zum Wert des kleinsten von Null verschiedenen Wellenvektors ist. Für die Bestimmung der kritischen Kraft anhand des Verhaltens der mittleren Verschiebung findet bei der kleineren kritische Kraft bereits der Übergang von einem endlichen Wert für lange Zeiten zu einem divergierenden Verhalten statt. Die zugehörige kritische Kraft für die Lösungen im Zeitraum unterscheidet sich leicht von den Werten, die für die Gleichungen im Laplaceraum erhalten wurden, was möglicherweise auf eine Summation von Rundungsfehlern im Verlauf der Iterationen zurückzuführen ist.

Nachdem wir die relevanten numerischen Parameter bestimmt haben, können wir ein Phasendiagramm konstruieren, um die kritische Kraft als Funktion des Packungsbruchs zu analysieren. Wir finden, dass das Quadrat der kritischen Kraft proportional zum Langzeitgrenzwerts der mittleren quadratischen Verschiebung ohne äußere Kraft ist. Wir können einen Zusammenhang zwischen der kritischen Kraft und der Fließspannung herstellen, der durch ein Potenzgesetz mit Exponent 1.7 ± 0.1 gegeben ist. Dies erlaubt es, auch ein Potenzgesetz zwischen der Fließspannung und dem Lanzeitgrenzwert der mittleren quadratischen Verschiebung ohne Kraft herzustellen, die für zwei verschiedene Simulationen getestet wird.

Schließlich charakterisieren wir das Verhalten von verschiedenen Größen in der Nähe des Delokalisationsübergangs in Abschnitt 4.5. Wir analysieren die Momente der van Hove Funktion unterhalb der kritischen Kraft sowie die Reibungs- und Diffusionskoeffizienten oberhalb der kritischen Kraft. Wir finden, dass sich die elastische Konstante bezüglich der mittleren Verschiebung für große Kräfte verringert, sodass die mittlere Verschiebung in der Nähe der kritischen Kraft sehr groß wird. Für mittlere Kräfte ist die Varianz senkrecht zur Kraftrichtung größer als in Kraftrichtung, was sich aber in der Nähe der kritischen Kraft wieder ändert, da die Varianz in Kraftrichtung dort schneller wächst. Der Reibungskoeffizient divergiert bei Annäherung an die kritische Kraft von oben und der Diffusionskoeffizient verschwindet. Die

zeitabhängigen Lösungen zeigen ein schwach superdiffusives Verhalten für nicht zu kurze und nicht zu lange Zeiten, aber nicht so ausgeprägt, wie in den Simulationen. Weiterhin analysieren wir den Langzeitgrenzwert der Dichtekorrelationsfunktionen und finden eine Beschreibung durch ein einfaches Modell mit wenigen Fitparametern. Während einige Fitparameter mit verschiedenen Potenzgesetzen an der kritischen Kraft divergieren, gibt es andere, die gegen einen konstanten Wert streben.

Bei der Analyse der van Hove Funktion finden wir eine exponentiell abklingende Verteilung der Probenteilchen sowohl in Kraftrichtung als auch senkrecht dazu. Die zugehörige Längenskala wächst bei Annäherung an die kritische Kraft und bestimmt den Wert der mittleren Verschiebung. Andererseits bleibt das Maximum der van Hove Funktion in der Nähe des Ursprungs. Dieses Verhalten wird auch in Simulationen beobachtet.

Eine detailliertere Analyse des Delokalisationsübergangs wird zusammen mit analytischen Rechnungen in Kapitel 5 gegeben. Numerisch finden wir, dass der Nichtergodizitätsparameter in der Nähe der oberen kritischen Kraft stetig gegen Null geht. An der unteren kritischen Kraft finden wir für $q_{\max}d \leq 14$ ein qualitativ anderes Verhalten als für $q_{\max}d \geq 20$. In ersterem Fall ist das Verhalten der Nichtergodizitätsparameter an der unteren kritischen Kraft stetig, während im letzteren Fall eine Unstetigkeit zusammen mit einem wurzelartigen Verhalten auftritt. Da diese Art des Übergangs in den klassischen Modenkopplungsgleichungen nicht auftritt, untersuchen wir verschiedene Möglichkeiten dieses Übergangs anhand von schematischen Modellen und einfachen physikalischen Überlegungen und können einige Beobachtungen reproduzieren. Danach folgt eine systematische Analyse der Stabilitätsmatrix, die divergentes Verhalten des kritischen Eigenvektors im Grenzfall $q \to 0$ aufzeigt: q_x^{-2} senkrecht zur Kraftrichtung und q_z^{-1} parallel zur Kraftrichtung. Die mittlere Verschiebung und die Varianzen sowie die Reibungs- und Diffusionskoeffizienten zeigen Potenzgesetze. Deren Exponenten unterscheiden sich zwar zwischen $q_{\max}d \leq 14$ und $q_{\max}d \geq 20$, aber in beiden Fällen haben die mittlere Verschiebung und die Varianz senkrecht zur Kraftrichtung den selben Exponenten. Der Exponent der Varianz parallel zur Kraftrichtung ist jeweils doppelt so groß.

Um das asymptotische kritische dynamische Verhalten zu analysieren, entwickeln wir verschiedene Darstellungen der Bewegungsgleichungen im Laplaceraum. Unter gewissen Näherungen können wir ein kritisches Potenzgesetz mit Exponent $-1/2$ für die Zeitentwicklung der Dichtekorrelationsfunktionen herleiten. Dieser Exponent wird von numerischen Lösungen im Fall $q_{\max}d \leq 14$ bestätigt, muss aber durch -0.34 für $q_{\max}d \geq 20$ ersetzt werden. Wir beobachten, dass sich die Übereinstimmung für kleine Wellenvektoren verschlechtert, was die Verwendung eines Faktorisierungsansatzes verhindert, der das zeitliche Verhalten von der Wellenvektorabhängigkeit trennt. Die Lösungen im Laplaceraum zeigen einen Übergang vom Exponent 0.34 für kleine Laplace-Frequenzen zu 0.5 für sehr kleine Laplace-Frequenzen, was das hergeleitete kritische Gesetz wieder bestätigt. Obwohl der Faktorisierungsansatz für die Korrelationsfunktionen nicht möglich ist, finden wir einen solchen für die einfachen Memoryfunktionale. Dies kann dazu verwendet werden, das kritische Verhalten der Korrelationsfunktionen sowie der Momente zu erklären. Schließlich vergleichen wir das kritische Verhalten mit Simulationen. Diese bestätigen den kritischen Exponenten für die Korrelationsfunktionen, zeigen aber andere Werte für die Exponenten der Momente.

Da die Bifurkationsanalyse einige Besonerheiten enthüllt hat, untersuchen wir in Kapitel 6 auch ein schematisches Modell, das von Gustavo Abade entwickelt wurde. Wir erhalten ein kritisches Potenzgesetz für die Zeitentwicklung mit Exponent $-1/2$ und einen analytischen

Ausdruck für die kritische Kraft. Die Bifurkation ist vom Typ A. Diese Ergebnisse werden durch numerische Lösungen im Zeit- und Laplaceraum bestätigt.

Neben den kritischen Phänomenen in der Nähe des Delokalisationsübergangs untersuchen wir in Kapitel 7 auch die Auswirkungen der nicht-Gauss-artigen van Hove Funktionen. Zu diesem Zweck vergleichen wir mit einem Experiment. Das kolloidale Glas aus harten Kugeln wird durch sterisch stabilisierte Emulsionströpfchen realisiert und die konstante Kraft auf das Teilchen durch eine optischen Linienfalle. Wir testen und bestätigen die zeitabhängige Lineare-Antwort-Beziehung, die es erlaubt die Kraft in der eigentlichen Probe zu kalibrieren. Ein parameterfreier Vergleich zwischen Theorie und Experiment zeigt die selben qualitativen Merkmale, aber auch Unterschiede in der Kraft- und Zeitskala. Eine große Herausforderung für die Experimente ist die heterogene Dynamik im Glas. Diese zeigt sich als bimodale Struktur in der van Hove Funktion in Kraftrichtung. Für einen quantitativen Vergleich führen wir eine Ähnlichkeitsanalyse zwischen den experimentell gemessenen Histogrammen und den theoretischen Vorhersagen bei gleicher mittlerer Verschiebung durch. Wir finden die selben strukturellen Merkmale, die eine gebundene Bewegung der Probenteilchen in ihrem Käfig unterbrochen von Sprüngen in Nachbarkäfige nahelegen. Dies führt zu einer anormalen Verbreiterung der van Hove Funktion im Vergleich zur Gleichgewichtsdynamik. Schließlich schätzen wir noch die kritische Kraft im Experiment anhand von verschiedenen characteristischen Funktionen ab. Dies beinhaltet auch die Analyse des Anteils der Teilchen, die ihren Käfig verlassen konnten.

Schließlich untersuchen wir in Kapitel 8 aktive Mikrorheologie in aktiven Suspensionen. Für Spezialfälle können wir analytische Lösungen finden. Für das ganze Problem können wir zwar eine formale Lösung aufschreiben, aber durch die Randbedingungen nicht auflösen. Deswegen verwenden wir die Finite-Differenzen-Methode, um die partiellen Differentialgleichungen numerisch zu lösen. Kleine Aktivitäten führen zu einer Reduktion des Reibungskoeffizienten des Probenteilchens für jede Form. Für große Aktivitäten finden wir wieder einen Anstieg des Reibungskoeffizienten für oblate Spheroide, aber für prolate Spheroide kann der Reibungskoeffizient sogar kleiner werden als im reinen Lösungsmittel. Die Größe dieses Effekts hängt vom Längenverhältnis des Ellipsoids und vom Größenverhältnis zwischen Ellipsoid und aktiven Teilchen ab. In beiden Fällen verschwindet der Effekt, falls die Verhältnisse zu groß oder zu klein sind. Damit gibt es eine optimale Größe und Form des Probenteilchens. Um dieses Phänomen zu untersuchen, schauen wir uns den Fluss von aktiven Teilchen entlang der Oberfläche des Probenteilchens und den dadurch induzierten Schwimmdruck an. Ein Symmetriebruch dieser Flüsse durch die feste Geschwindigkeit des Probenteilchens führt zu einer Kraft, die das Probenteilchen anschiebt. Deswegen muss man gegebenenfalls eine Kraft in die entegengesetzte Richtung anlegen, um die Geschwindigkeit konstant zu halten.

Zusammenfassend haben wir gesehen, dass aktive Mikrorheologie in komplexen Flüssigkeiten eine große Vielfalt an Phänomenen zeigt, die weit über die messbaren Größen in gewöhnlichen Rheometern hinausgehen. Unsere Analyse legt nahe, dass eine sorgfältige Analyse der vollständigen van Hove Funktionen und nicht nur der Momente entscheidend für das Verständnis des dynamischen Verhaltens dieses Modellsystems ist.

A. Fourier transform

As there are different conventions for the definition of the Fourier transform, which in turn have different effects on the calculus, we will provide in this chapter the necessary definitions and calculation rules, which are used throughout this thesis. Many results can be found in [BMMS08, Chap. 15.3, p. 789-798], but we have to adapt these results to match our convention. We define the d-dimensional Fourier transform from real space to Fourier space via

$$\mathcal{F}[f](\boldsymbol{q}) = \int_{\mathbb{R}^d} \mathrm{d}^d\boldsymbol{r}\, \mathrm{e}^{\mathrm{i}\boldsymbol{q}\cdot\boldsymbol{r}} f(\boldsymbol{r}). \tag{A.1}$$

with the abbreviation $\mathrm{d}^d\boldsymbol{r} := \mathrm{d}r_1 \cdots \mathrm{d}r_d$. If the dimensionality of $\boldsymbol{r}$ is known, we will suppress the superscript d. The corresponding inversion formula to get back from Fourier space to real space is given by

$$\mathcal{F}^{-1}[f](\boldsymbol{r}) = \frac{1}{(2\pi)^d} \int_{\mathbb{R}^d} \mathrm{d}^d\boldsymbol{q}\, \mathrm{e}^{-\mathrm{i}\boldsymbol{q}\cdot\boldsymbol{r}} f(\boldsymbol{q}). \tag{A.2}$$

For convenience we introduce the following multiindex notation. This allows to write derivatives in a n-dimensional vector space in a compact way. Let $\boldsymbol{\alpha} \in \mathbb{N}_0^d$ be a multiindex (i.e. a d-dimensional tuple of non-negative integers). Then we define

$$|\boldsymbol{\alpha}| := \sum_{i=1}^{d} \alpha_i, \tag{A.3a}$$

$$\boldsymbol{k}^{\boldsymbol{\alpha}} := \prod_{i=1}^{d} k_i^{\alpha_i}, \tag{A.3b}$$

$$\boldsymbol{\partial}^{\boldsymbol{\alpha}} := \prod_{i=1}^{d} \partial_i^{\alpha_i}. \tag{A.3c}$$

A.1. Relations and important Fourier transformation pairs

In this section we summarize some important relations for the calculation of the Fourier transforms. The second part gives some important Fourier transformation pairs. Even though these rules can be found in many places in literature, there are many different conventions for the Fourier transform. This collection of rules and transformation pairs is compiled to match the definition of the Fourier transform used in this work as given by (A.1) and (A.2).

In the following we consider $f, g : \mathbb{R}^d \to \mathbb{C}$ to be complex valued functions. The argument $\boldsymbol{r}$ indicates that the function is considered in real space, i.e. before a Fourier transform has been applied. Conversely, the argument $\boldsymbol{k}$ indicates a function in Fourier space, i.e. after a Fourier transform has been applied. The following rules only apply if the corresponding Fourier transforms exist.

Linearity Let $a, b \in \mathbb{C}$. Then

$$\mathcal{F}[af + bg](\boldsymbol{k}) = a\mathcal{F}[f](\boldsymbol{k}) + b\mathcal{F}[g](\boldsymbol{k}) \tag{A.4}$$

[BMMS08, p. 793, Eq. (15.83)].

Symmetry If f is real valued, i.e. $f(\boldsymbol{r}) = \operatorname{Re} f(\boldsymbol{r})$ for all $\boldsymbol{r} \in \mathbb{R}^d$, then its Fourier transform obeys the following symmetry

$$\mathcal{F}[f](-\boldsymbol{k}) = \int_{\mathbb{R}^d} \mathrm{d}\boldsymbol{r}\, \mathrm{e}^{-\mathrm{i}\boldsymbol{k}\cdot\boldsymbol{r}} f(\boldsymbol{r}) = \left(\int_{\mathbb{R}^d} \mathrm{e}^{\mathrm{i}\boldsymbol{k}\cdot\boldsymbol{r}} f(\boldsymbol{r}) \mathrm{d}\boldsymbol{r} \right)^* = (\mathcal{F}[f](\boldsymbol{k}))^*, \tag{A.5}$$

where the asterisk * denotes complex conjugation.

Scaling rule For real $\alpha \neq 0$ we have

$$\mathcal{F}[\boldsymbol{r} \mapsto f(\boldsymbol{r}/\alpha)](\boldsymbol{k}) = |\alpha| \mathcal{F}[f](\alpha\boldsymbol{k}), \tag{A.6}$$

cf. [BMMS08, p. 793, Eq. (15.84)].

Shift/Phase rule Shifting a function by $\boldsymbol{a} \in \mathbb{R}^d$ yields

$$\mathcal{F}[\boldsymbol{r} \mapsto f(\boldsymbol{r} - \boldsymbol{a})](\boldsymbol{k}) = \mathrm{e}^{\mathrm{i}\boldsymbol{k}\cdot\boldsymbol{a}} \mathcal{F}[f](\boldsymbol{k}) \tag{A.7a}$$

and vice versa

$$\mathcal{F}\left[\boldsymbol{r} \mapsto \mathrm{e}^{\mathrm{i}\boldsymbol{r}\cdot\boldsymbol{a}} f(\boldsymbol{r})\right](\boldsymbol{k}) = \mathcal{F}[f](\boldsymbol{k} - \boldsymbol{a}), \tag{A.7b}$$

cf. [BMMS08, p. 793, Eq. (15.85) and (15.86)] (note the different convention for the sign in the exponent of the Fourier transform).

Differentiation Let $\boldsymbol{\alpha} \in \mathbb{N}^d$ be a multiindex (see (A.3) for the definitions). Then

$$\mathcal{F}[\boldsymbol{r} \mapsto \boldsymbol{\partial}^{\boldsymbol{\alpha}} f(\boldsymbol{r})](\boldsymbol{k}) = (-\mathrm{i})^{|\boldsymbol{\alpha}|} \boldsymbol{k}^{\boldsymbol{\alpha}} \mathcal{F}[f](\boldsymbol{k}), \tag{A.8}$$

cf. [BMMS08, p. 793, Eq. (15.88)].

Multiplication Let $\boldsymbol{\alpha} \in \mathbb{N}^d$ be a multiindex. Then

$$\mathcal{F}[\boldsymbol{r} \mapsto \boldsymbol{r}^{\boldsymbol{\alpha}} f(\boldsymbol{r})](\boldsymbol{k}) = (-\mathrm{i})^{|\boldsymbol{\alpha}|} \boldsymbol{\partial}^{\boldsymbol{\alpha}} \mathcal{F}[f](\boldsymbol{k}), \tag{A.9}$$

cf. [BMMS08, p. 793, Eq. (15.87)], provided the derivatives exist.

A particular case is the combination of a first order derivative with a multiplication by the variable in one dimension. We find

$$\begin{aligned} \mathcal{F}[x \mapsto \partial_x(x f(x))](k) &= \int e^{\mathrm{i}kx} \partial_x(x f(x)) \mathrm{d}x = -\int x f(x) \partial_x e^{\mathrm{i}kx} \mathrm{d}x = -\int x f(x) (\mathrm{i}k) e^{\mathrm{i}kx} \mathrm{d}x \\ &= (-\mathrm{i}k) \int x f(x) e^{\mathrm{i}kx} \mathrm{d}x = -(\mathrm{i}k) \frac{1}{\mathrm{i}} \partial_k \int f(x) e^{\mathrm{i}kx} \\ &= -k \partial_k \mathcal{F}[f](k). \end{aligned} \tag{A.10}$$

where integration by parts was used in the first line, assuming that the boundary terms vanish.

With the definition (A.1) of the Fourier transform, we obtain the Fourier transformation pairs as shown in Table A.1. We use the following naming conventions

Table A.1.: Important Fourier transformation pairs with convention (A.1). The functions are defined in (A.11). These results are taken from [BMMS08, p. 1135f, Tab. 21.14.3] and adapted to our Fourier convention.

$f(\boldsymbol{r})$	$\mathcal{F}[f](\boldsymbol{k})$	
	d-dimensional	
$\delta(\boldsymbol{r})$	1	
1	$(2\pi)^d\delta(\boldsymbol{k})$	
$\frac{1}{(2\pi\sigma^2)^{d/2}}e^{-r^2/2\sigma^2}$	$e^{-\sigma^2k^2/2}$	$(\sigma>0)$
	1-dimensional	
$\frac{1}{2\lambda}\mathrm{e}^{-\lvert r_x\rvert/\lambda}$	$\frac{1}{1+k_x^2\lambda^2}$	$(\lambda>0)$
$\frac{1}{\lambda}e^{-\lvert r_x\rvert/\lambda}H(r_x)$	$\frac{1}{1-\mathrm{i}k_x\lambda}$	$(\lambda>0)$
$\mathrm{rect}(r_x)$	$2\,\mathrm{sinc}(k_x)$	[Pou96, p. 210, Eq. (2.48)]
$\mathrm{tria}(r_x)$	$\mathrm{sinc}^2(k_x/2)$	[Pou96, p. 212, Eq. (2.55)]

$$H(x)=\begin{cases}1 & x\geq 0,\\ 0 & x<0,\end{cases} \tag{A.11a}$$

$$\mathrm{sinc}(x)=\begin{cases}\frac{\sin(x)}{x} & x\neq 0,\\ 1 & x=0.\end{cases} \tag{A.11b}$$

$$\mathrm{rect}(x)=H(x+1)-H(x-1), \tag{A.11c}$$

$$\mathrm{tria}(x)=\begin{cases}1+x & -1\leq x<0,\\ 1-x & 0\leq x\leq 1,\\ 0 & \text{else},\end{cases} \tag{A.11d}$$

Note that in other literature and software the sinc-function can have πx as argument (for example `numpy`).

A.2. Cylindrical symmetry and Hankel transform

A function $f(\boldsymbol{r})$ is has cylindrical symmetry with respect to the z-axis if for every rotation $\mathcal{R}$ with $\mathcal{R}\hat{\boldsymbol{z}}=\hat{\boldsymbol{z}}$ holds $f(\mathcal{R}\boldsymbol{r})=f(\boldsymbol{r})$. The Fourier transform (and its inverse) preserves this property as can be seen in the following calculation

$$\mathcal{F}[f](\mathcal{R}\boldsymbol{k})=\int\mathrm{d}\boldsymbol{r}\,\mathrm{e}^{\pm\mathrm{i}\mathcal{R}\boldsymbol{k}\cdot\boldsymbol{r}}f(\boldsymbol{r})=\int\mathrm{d}\boldsymbol{r}'\,\mathrm{e}^{\pm\mathrm{i}\boldsymbol{k}\cdot\boldsymbol{r}'}f(\mathcal{R}\boldsymbol{r}')=\mathcal{F}[f](\boldsymbol{k}), \tag{A.12}$$

where we used the identity $\mathcal{R}\boldsymbol{k}\cdot\boldsymbol{r}=\boldsymbol{k}\cdot\mathcal{R}^T\boldsymbol{r}$, the substitution $\boldsymbol{r}'=\mathcal{R}^T\boldsymbol{r}$ and the cylindrical symmetry of f for the last equality. It is therefore sufficient to calculate the Fourier-transform for the particular wave vectors $\boldsymbol{k}^*=(k_\perp,0,k_z)$ only.

This allows us to simplify the three-dimensional Fourier transform into a a one-dimensional Fourier transform along the axis of symmetry and a one-dimensional Hankel transform (definition will follow below) for the perpendicular axis as follows

$$\mathcal{F}\left[f\right]\left(\boldsymbol{k}^*\right) = \int \mathrm{d}\boldsymbol{r}\, \mathrm{e}^{i\boldsymbol{k}^*\cdot\boldsymbol{r}} f(\boldsymbol{r}) = \int \mathrm{d}r_z \int_0^\infty \mathrm{d}r_\perp \int_0^{2\pi} \mathrm{d}\phi\, \mathrm{e}^{\mathrm{i}k_z r_z} r_\perp \mathrm{e}\mathrm{i}k_\perp r_\perp \cos(\phi) f(r_\perp \cos\phi, r_\perp \sin\phi, r_z), \tag{A.13}$$

where we used the transformation to cylindrical coordinates with $(r_x, r_y) = (r_\perp \cos\phi, r_\perp \sin\phi)$. Since f is cylindrically symmetric, we can set $f(r_\perp \cos\phi, r_\perp \sin\phi, r_z) = f(r_\perp, 0, r_z)$ and then perform the integral over ϕ, which yields

$$\int_0^{2\pi} \mathrm{d}\phi\, \cos(\phi) e^{\mathrm{i}k_\perp r_\perp \cos(\phi)} = 2\pi J_0(k_\perp r_\perp), \tag{A.14}$$

(cf. [BMMS08, p. 567, Eq. (9.54f)]), where $J_0(x)$ is the Bessel function of the first kind of order 0. With this result, we obtain

$$\mathcal{F}\left[f\right]\left(\boldsymbol{k}^*\right) = 2\pi \int_{-\infty}^{\infty} \mathrm{d}r_z \int_0^\infty \mathrm{d}r_\perp\, r J_0(r_\perp k_\perp) f(r_\perp, 0, r_z). \tag{A.15}$$

The one-dimensional integral transform

$$\mathcal{H}\left[f\right](k) = \int_0^\infty \mathrm{d}r\, r J_0(kr) f(r) \tag{A.16}$$

is called *Hankel transform* (of order zero) [BMMS08, p. 773]. This allows us to write the Fourier transform in the following way

$$\begin{aligned} \mathcal{F}\left[f\right](k_\perp, 0, k_z) &= 2\pi \mathcal{F}\left[r_z \mapsto \mathcal{H}\left[r_\perp \mapsto f(r_\perp, 0, r_z)\right](k_\perp)\right](k_z) \\ &= 2\pi \mathcal{H}\left[r_\perp \mapsto \mathcal{F}\left[r_z \mapsto f(r_\perp, 0, r_z)\right](k_z)\right](k_\perp). \end{aligned} \tag{A.17}$$

Hence, we need to do a Hankel transform on the perpendicular coordinate $r_\perp$ and a Fourier transform on the parallel coordinate r_z, while keeping the other variable as parameter to obtain the full three-dimensional Fourier transform. The order of these operations does not play a role.

Note that (A.14) does not change when the sign in the exponential is changed. Therefore, the Hankel transform is its own inverse [Pou96, p. 721, Eq. (12)].

Just for further reference, the Fourier transform for functions with spherical symmetry has been worked out in [Göt09, p. 120, Eq. (3.9c)].

Table A.2.: Important Hankel transformation pairs with convention (A.16). These results are taken from [Pou96, p. 742, Table 9.1].

$f(r)$	$\mathcal{H}[f](k)$
$\frac{1}{r}$	$\frac{1}{k}$
$\frac{1}{\sigma^2}\mathrm{e}^{-r^2/2\sigma^2}$	$\mathrm{e}^{-\sigma^2 k^2/2}$
$\frac{1}{\sqrt{r^2+\lambda^2}}$	$\frac{\mathrm{e}^{-k\lambda}}{k}$
$\mathrm{e}^{-\lambda r}$	$\frac{\lambda}{(k^2+r^2)^{3/2}}$

A.3. Marginal distributions

The marginal probability distributions parallel $f_\parallel(r_z)$ and perpendicular $f_\perp(r_x)$ to the external force defined via

$$f_\parallel(r_z) = \int \mathrm{d}r_x \int \mathrm{d}r_y\, f(r_x, r_y, r_z), \tag{A.18}$$

$$f_\perp(r_x) = \int \mathrm{d}r_y \int \mathrm{d}r_z\, f(r_x, r_y, r_z), \tag{A.19}$$

can be directly related to a 1-dimensional Fourier transform along the axes

$$f(0,0,k_z) = \int \mathrm{d}r_x \int \mathrm{d}r_y \int \mathrm{d}r_z\, e^{ik_z r_z} f(r_x, r_y, r_z) = \mathcal{F}\left[f_\parallel\right](k_z), \tag{A.20}$$

$$f(k_x,0) = \int \mathrm{d}r_x \int \mathrm{d}r_y \int \mathrm{d}r_z\, e^{ik_x r_x} f(r_x, r_y, r_z) = \mathcal{F}[f_\perp](k_x). \tag{A.21}$$

A.4. Moments and derivatives

The multiplication rule (A.9) can be used to establish a relation between the moments of a probability distribution p in real space and the derivatives of their Fourier transform at $\boldsymbol{k} = 0$. Let $\boldsymbol{\alpha} \in \mathbb{N}^d$ be a multiindex. Then the corresponding moment is given by

$$\langle \boldsymbol{r}^{\boldsymbol{\alpha}} \rangle_p = \int \boldsymbol{r}^{\boldsymbol{\alpha}} p(\boldsymbol{r}) \mathrm{d}\boldsymbol{r} = \int \mathrm{e}^{\mathrm{i}\boldsymbol{r}\cdot\boldsymbol{0}} \boldsymbol{r}^{\alpha} p(\boldsymbol{r}) \mathrm{d}\boldsymbol{r} = (-\mathrm{i})^{|\alpha|} \boldsymbol{\partial}^{\boldsymbol{\alpha}} \mathcal{F}[p](\boldsymbol{k} = 0). \tag{A.22}$$

It is also possible to define the probability distribution in cylindrical coordinates $\rho \in [0, \infty)$, $\phi \in [0, 2\pi)$ and $z \in \mathbb{R}$ via

$$p_{\mathrm{cyl}}(\rho, \phi, z) = \rho p(\rho, 0, z). \tag{A.23}$$

While the marginal probability distribution in z is the same as before, we obtain the following

marginal probability distribution in ρ

$$p_\rho(\rho) = \int_{-\infty}^{\infty} \mathrm{d}z \int_0^{2\pi} \mathrm{d}\phi \, p_{\mathrm{cyl}}(\rho, \phi, z). \tag{A.24}$$

Naturally the question arises whether the moments of the marginal probability distribution p_ρ contain different information than the moments of p_x. By explicit calculation, one can show

$$\langle |x| \rangle := \int_{-\infty}^{\infty} \mathrm{d}x \, |x| p_x(x) = \frac{2}{\pi} \int_0^{\infty} \mathrm{d}\rho \, p_\rho(\rho) = \frac{2}{\pi} \langle \rho \rangle \,. \tag{A.25}$$

This implies that there is no additional information in the first moment of p_ρ. Similarly, one can work out relations for the higher moments.

A.5. Numerical implementation

Since the solution of our MCT equation is only known numerically, we need to invert the Fourier transform numerically as well. Special care has to be taken for the fact that our numerical solution is given on a non-uniform grid. Interpolating the values on a uniform grid is problematic, because the memory consumption scales with the ratio between the uniform step size and the minimal nonzero wave vector. In other words, a proper interpolation of a `unilog10` grid has 2^{10} times more grid points and needs therefore extra memory with the same factor.

A.5.1. 1D Fourier transform

We start by discretizing the one-dimensional Fourier transform. Since our main interest is the real valued inverse Fourier transform, we already employ the corresponding symmetries. On a uniform grid $k_l = l\Delta_k$ with $0 \leq l \leq N$ we find for the integral

$$\int_{-\infty}^{\infty} \mathrm{d}k \, \mathrm{e}^{-\mathrm{i}rk} f(k) \approx \mathrm{Re}\, \Delta_k \sum_{l=0}^{N} \mathrm{e}^{\mathrm{i}rl\Delta_k} f(l\Delta). \tag{A.26}$$

In order to employ the efficient Fast Fourier Transform (FFT) for the discrete data X_l, which calculates

$$Y_k = \sum_{l=1}^{N} \mathrm{e}^{2\pi \mathrm{i} lk/N} X_l, \tag{A.27}$$

(cf. [BMMS08, p. 999, Eq. (19.211)]) we have to match the exponent, i.e.

$$\frac{2\pi lk}{N} \stackrel{!}{=} rk\Delta_k. \tag{A.28}$$

This imposes some constraints on the choice of the grids before and after the transformation. The spacing and the maximum value of one grid define the spacing and the maximum value of

the other. In particular, we find

$$r_l = \frac{2\pi l}{N\Delta} =: \Delta_r l, \tag{A.29}$$

i.e. the new grid has a spacing of $\Delta_r = 2\pi/N\Delta_k$ and a cutoff of $2\pi/\Delta_k$. Increasing the resolution requires to increase the cutoff $N\Delta_k$ and increasing the cutoff requires to increase the resolution in the original grid. In numbers: for a resolution $\Delta_r = 10^{-2}$, we need a cutoff $N\Delta_k = 2\pi/\Delta_r \approx 628$.

This cutoff value is way beyond what is computationally accessible in our MCT calculations. A common technique is therefore continue the signal with zeros, the so called *zero padding* [SW04, Sec. 5.2.1, p. 136], which effectively interpolates the data to the required resolution. This procedure causes oscillations with an amplitude which is of the order of the jump from the last data point to 0. Therefore this method is fine, when the signal which has to be Fourier transformed is already small. For larger jumps the Fourier transform is basically useless. We therefore need to extrapolate our data.

Empirically, we notice that $|f^s(q)|$ decays roughly like $\exp(-(q/l)^\beta)$ for large q with $1 \leq \beta \leq 2$ and its phase increases linearly with q. Hence, we extrapolate with the following scheme

$$f(q) = f(q_N)\exp\left(\mathrm{i}\alpha(q-q_N)\right)\exp\left(-\left(\frac{q}{\lambda}\right)^\beta + \left(\frac{q_N}{\lambda}\right)^\beta\right), \tag{A.30a}$$

$$\beta = -\frac{\log(|f(q_N)|) - \log(|f(q_{N-1})|)}{\log(q_N) - \log(q_{N-1})}, \tag{A.30b}$$

$$\lambda = \left(\frac{-q_N^\beta + q_{N-1}^\beta}{\log(|f(q_N)/f(q_{N-1})|)}\right)^{1/\beta}, \tag{A.30c}$$

$$\alpha = \frac{\arg(f(q_N)) - \arg(f(q_{N-1}))}{q_N - q_{N-1}}. \tag{A.30d}$$

The function arg determines the phase of the complex number, i.e. for the representation $z = A\mathrm{e}^{i\phi}$ it returns $\phi \in [0, 2\pi)$. Side remark: when determining α, one has to make sure that the phase is continuous and does not jump by 2π.

Another issue arises for small and large mean displacements. By the definitions above, our grid after Fourier transformation always covers the interval $[0, N\Delta_r]$. Shifting this interval implies a multiplication by a phase before the Fourier transform according to (A.7b) and (A.7a). In order to use the grid optimally, we choose the shift such that the mean (or center of mass) of the Fourier transformed curve is in the center of the grid. The mean can be calculated beforehand using numerical differentiation (3.52) or using the corresponding memory functionals as discussed in Sec. 3.5.5. In the code this trick is called `roll`, because it effectively consists in choosing the right window for the periodic Fourier transform.

Finally, we have to Fourier transform for the non-uniform grid. Since we mainly use the grids of type `unilogX` (see Sec. 3.1) and (3.7) therein for the definition), we will specialize the Fourier transform to this grid type and give the equations only for the inverse Fourier transform. The challenge is to Fourier transform the information in the logarithmic part of the grid in a smart way. The grid points are labeled by k_i and $N_{\log}$ gives the number of logarithmic points in the grid. Furthermore, we use the abbreviation $f_i := f(k_i)$.

We start by extending the definition range of the function from the discrete grid to arbitrary

arguments via interpolation. In the uniform part, we use a zero-order interpolation, which assigns to each argument k the value of the grid point to the left of it. For the logarithmic part of the grid, we use linear interpolation as illustrated in Figure A.1, the use of a constant interpolation implies omitting the difference quotient. This way, we can separate the function into a function on a uniform grid, for which the fast Fourier transform can be applied, and a correction function on the logarithmic part of the grid for which the Fourier transform will be calculated analytically:

$$f(k) = f^{\text{uni}}(k) + f^{\log}(k), \tag{A.31a}$$

$$f^{\text{uni}}(k) = f_0 \chi_{[k_0, k_{N_{\log}+1})}(k) + \sum_{i=N_{\log}+2}^{N} f_i \chi_{[k_i, k_{i+1})}(k), \tag{A.31b}$$

$$f^{\log}(k) = \sum_{i=1}^{N_{\log}+1} \left[f_{i-1} + (f_i - f_{i-1}) \frac{k - k_{i-1}}{k_i - k_{i-1}} - f_0 \right] \chi_{[k_{i-1}, k_i)}(k). \tag{A.31c}$$

$\chi_{[a,b)}$ is the characteristic function. It is 1 if $k \in [a, b)$ and 0 otherwise. Since the Fourier transform is linear, we can do the Fourier transforms separately and add them together. For the uniform we apply the methods as introduced above. For the corrections given on the logarithmic grid, we notice that we can rewrite it in terms of the triangle functions (A.11d) with the left corner at the origin

$$f^{\log}(k) = (f_i - f_0) \operatorname{tria}\left(\frac{k}{k_{N_{\log}+1}} - 1 \right) \chi_{[0, k_{N_{\log}+1})}(k) + \sum_{i=1}^{N_{\log}} \left(f_i - \frac{f_{i+1} + f_0}{2} \right) \operatorname{tria}\left(\frac{k}{k_i} - 1 \right). \tag{A.32}$$

Since the grid points grow by a factor of 2, we ensure that the right corner of a triangle falls on the center of the next larger triangle, re-establishing the linear interpolation, see Figure A.1.

The Fourier transform of the triangle function is known analytically (see Table A.1 and [Pou96, p. 213, Eq. (2.56), Eq. (2.57)]) and we find with the help of (A.6) and (A.7a)

$$\begin{aligned} \mathcal{F}^{-1}\left[f^{\log} \right](r) =& \frac{1}{2\pi} \sum_{i=1}^{N_{\log}} 2 \operatorname{Re}\left[\left(f_i - \frac{f_{i-1} + f_0}{2} \right) \mathrm{e}^{\mathrm{i}rk_i} \right] k_i \left(\operatorname{sinc}(k_i r/2) \right)^2 \\ &+ \frac{2}{2\pi} k_{N_{\log}+1} \operatorname{Re}\left[\left(f_{N_{\log}+1} - f_0 \right) \frac{\mathrm{e}^{\mathrm{i}rk_{N_{\log}+1}} (1 - \mathrm{i}rk_{N_{\log}+1}) - 1}{(rk_{N_{\log}+1})^2} \right]. \end{aligned} \tag{A.33}$$

The expression $2\,\mathrm{Re}$ arises from the use of the conjugation symmetry of our problem in Fourier space.

A.5.2. 1D Hankel transform

To do the Hankel transform numerically, we approximate the integral by a Riemann-sum. To deal with the oscillatory nature of the Bessel function, we can rewrite the Hankel transform (A.16) as follows

$$\mathcal{H}[f]\, k = \frac{1}{k^2} \int_0^\infty \mathrm{d}r'\, r' J_0(r') f\left(\frac{r'}{k} \right). \tag{A.34}$$

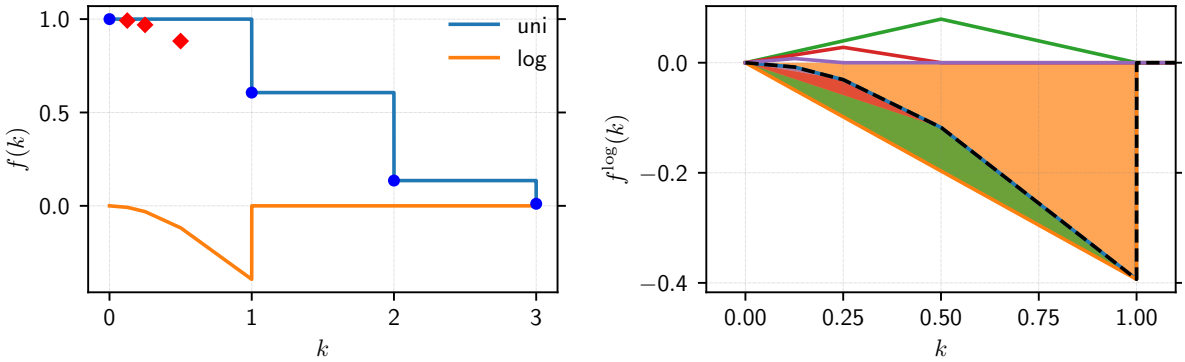

Figure A.1.: Fourier transform on the logarithmic grid. We use a `unilog3`-grid with uniform grid spacing $\Delta k = 1$ for demonstration. Discrete function values on the uniform grid are shown with blue circles, those on the logarithmic part are shown as red squares. Left: Decomposition of the function into the uniform f^{uni} (blue) and logarithmic $f^{\log}$ (orange) contributions. Right: Decomposition of $f^{\log}$ (dashed line) into a sum of triangle functions, shown as lines and as filled triangles in the composition.

Both representations can be approximated by Riemann-sums on a uniform grid $r_i := i\Delta_r$ for $0 \leq i \leq N$ and we obtain

$$\mathcal{H}[f](k) \approx \Delta_r \sum_{i=1}^{N} r_i f(r_i) J_0(k r_i), \tag{A.35a}$$

$$\mathcal{H}[f](k) \approx \frac{\Delta_r}{k^2} \sum_{i=1}^{N} f\left(\frac{r_i}{k}\right) J_0(r_i). \tag{A.35b}$$

While the second representation has the virtue of discretizing the Bessel function properly, it causes problems for small k due to the diverging prefactor. In this case, $f(r)$ varies faster than $J_0(kr)$ so that we can use the first representation. In any case, we need to interpolate the function f on the grid r_i, because the grid spacing from our calculations is usually too coarse. A general truncation error estimate is therefore not possible, because $rJ_0(kr)$ diverges asymptotically like $r^{1/2}$ [BMMS08, p. 568, Eq. (9.56a)]. This implies that $f(r)$ has to decay faster than $r^{-1/2}$, for a well-defined Hankel transform.

A.5.3. 3D cylindrically symmetric Fourier transform

As already shown in the previous section, we can replace the three-dimensional Fourier transform of a cylindrically symmetric function by a Hankel transform and a one-dimensional Fourier transform, see (A.17). For the inverse Fourier transform, we just have to invert the single transforms, which leads to

$$\mathcal{F}^{-1}[f](r_\perp, 0, r_z) = \frac{1}{2\pi} \mathcal{H}\left[k_\perp \mapsto \mathcal{F}^{-1}[k_z \mapsto f(k_\perp, 0, k_z)](r_z)\right](r_\perp). \tag{A.36}$$

Remember that the Hankel transform is its own inverse. We choose to do the inverse Fourier transform first, because the result is then completely real, which simplifies inter- and extrapolations.

B. Laplace transform

The Laplace transform is defined by

$$\mathcal{L}[f](s) = \int_0^\infty \mathrm{e}^{-st} f(t) \mathrm{d}t \tag{B.1}$$

(see [BMMS08, p. 775, Eq. (15.5)]) for piecewise continuous functions f with $|f(t)| < c^{\alpha t}$ for some $c, \alpha > 0$ and all $t > 0$. The following summary of the most important properties used throughout this thesis are taken from [BMMS08, Sec. 15.2, p. 775-789].

B.1. Relations

First of all, the Laplace transform is linear (cf. [BMMS08, p. 776, Eq. (15.9)])

$$\mathcal{L}[t \mapsto (\lambda_1 f(t) + \lambda_2 g(t))](s) = \lambda_1 \mathcal{L}[f](s) + \lambda_2 \mathcal{L}[g](s). \tag{B.2}$$

A convenient property of the Laplace transform is the tight connection of the limiting values to the limits in the time domain. If the following limits exist, then

$$\lim_{\substack{t\to\infty \\ (t\to 0)}} f(t) = \lim_{\substack{s\to 0 \\ (s\to\infty)}} s\mathcal{L}[f](s) \tag{B.3}$$

(cf. [BMMS08, p. 775, Eq. (15.7b)]).

The definitions of the Laplace transform and the Fourier transform are very similar. Therefore, there are many equivalents of the relations for Fourier transform. The most important ones are listed below.

Differentiation The derivative of a function $f(t)$ with initial value $f(t = 0) = f(0)$ is given by

$$\mathcal{L}[\partial_t f](s) = s\mathcal{L}[f](s) - f(0) \tag{B.4}$$

(cf. [BMMS08, p. 777, Eq. (15.13)]).

Multiplication by monomials Let $n \in \mathbb{N}$. Then

$$\mathcal{L}[t \mapsto (-1)^n t^n f(t)] = \partial_s^n \mathcal{L}[f](s) \tag{B.5}$$

(cf. [BMMS08, p. 777, Eq. (15.14)]).

Table B.1.: Important Laplace transformation pairs with convention (B.1). Mostly taken from [BMMS08, Sec. 21.13]

$f(t)$	$\mathcal{L}[f](s)$		
1	s^{-1}		[BMMS08, p. 1118, Nr. 2]
$\frac{t^{n-1}}{(n-1)!}$	s^{-n}		[BMMS08, p. 1118, Nr. 3]
$\frac{1}{\sqrt{\pi t}}$	$\frac{1}{\sqrt{s}}$		[BMMS08, p.1120, Nr. 33]
t^α	$s^{-(1+\alpha)}\Gamma(1+\alpha)$	$(\alpha \geq -1)$	[Pou96, p. 380, Table 5.1, No. 7]
$\sin(\alpha t)$	$\frac{\alpha}{s^2+\alpha^2}$		[BMMS08, p. 1118, Nr. 8]
$\exp(-at)$	$\frac{1}{s+a}$	$\operatorname{Re} s > -a$	[BMMS08, p. 1118, Nr. 4]

Integration

$$\mathcal{L}\left[t \mapsto \int_0^t f(\tau)\mathrm{d}\tau\right](s) = \frac{1}{s}\mathcal{L}[f](s) \tag{B.6}$$

(cf. [BMMS08, p. 777, Eq. (15.17b)])

Multiplication by an exponential function

$$\mathcal{L}[t \mapsto \exp(at)f(t)](s) = \mathcal{L}[f](s-a) \tag{B.7}$$

(cf. [AS70, p. 1024, Eq. (29.2.12)], [BMMS08, p. 776, Eq. (15.12)]),

Convolution and Multiplication Let the convolution be defined via

$$(f_1 * f_2)(t) = \int_0^t f_1(t')f_2(t-t')\mathrm{d}t' \tag{B.8}$$

(cf. [BMMS08, p. 778, Eq. (15.21)]) then

$$\mathcal{L}[f_1 * f_2](s) = \mathcal{L}[f_1](s)\mathcal{L}[f_2](s) \tag{B.9}$$

(cf. [BMMS08, p. 778, Eq. (15.23)]).

The inverse is given by a complex contour integral [BMMS08, p. 775, Eq. (15.8)]. Some important Laplace transformation pairs are listed in Table B.1.

B.2. Numerical Laplace transform

We use the composite trapezoidal rule on a nonuniform grid to obtain

$$\tilde{f}(s) = \int_0^\infty \mathrm{e}^{-st} f(t)\mathrm{d}t \approx \sum_{i=0}^{N-1} \mathrm{e}^{-st_i} w_i f(t_i) \tag{B.10a}$$

with the weights (cf. (3.11c))

$$w_i = \frac{1}{2}\begin{cases} t_1 - t_0, & i = 0 \\ t_{i+1} - t_{i-1}, & 0 < i < N-1, \\ t_{N-1} - t_{N-2}, & i = N-1. \end{cases} \tag{B.10b}$$

The minimal reasonable Laplace frequency is given by (a multiple) of the inverse of the maximum time t_N. As we have $|f(t)| \leq 1$ in our case, the truncation error is given by

$$\varepsilon_{\mathrm{trunc}}(s) = \left| \int_{t_N}^\infty \exp(-st') f(t')\mathrm{d}'t \right| \leq \int_{t_N}^\infty \exp(-st')|f(t')|\mathrm{d}t' \leq \int_{t_N}^\infty \exp(-st')\mathrm{d}t' = \frac{1}{s}\exp\left(-st_N\right). \tag{B.11}$$

Hence, the truncation error is minimized for $s \to \infty$. This limit is of no practical use, because we do not have any information about the Laplace transformed function anymore. Therefore, we need to find a trade-off between the truncation error and the information in Laplace space. Since the maximum time t_N only affects the exponential, we can choose $s_{\min} = t_N^{-1}$ or $s_{\min} = 5t_N^{-1}$ as lower boundaries for the Laplace transform based on the requirements for the accuracy of the Laplace transformed solution.

Another approach is the use of the so called *Filon quadrature method*, which was used by Gustavo Abade in his evaluations [AS70, p. 890f].

C. Details of the MCT calculation

In this chapter, we collect some of the results for the MCT calculations, which are too verbose to fit into the main text.

C.1. Inner products and operator actions

Considering also probe-bath correlations, we obtain an extended version of the Zwanzig-Mori scheme (cf. Section 2.4.3) with the variables $\rho^b_{\boldsymbol{k}} := \rho_{\boldsymbol{k}}$, $\rho^s_{\boldsymbol{k}}$, $\rho^{sb}_{\boldsymbol{k}} := (\rho^s_{\boldsymbol{k}})^* \rho_{\boldsymbol{k}}$. Combining them into a vector $\boldsymbol{A} = (\rho^b_{\boldsymbol{k}_1}, \rho^s_{\boldsymbol{k}_1}, \rho^{sb}_{\boldsymbol{k}_1}, \rho^b_{\boldsymbol{k}_2}, \rho^s_{\boldsymbol{k}_2}, \rho^{sb}_{\boldsymbol{k}_2}, \ldots)$ we can calculate the elements of the orthogonality matrix $(\langle \boldsymbol{A}, \boldsymbol{A} \rangle)^{-1}$ as

$$\left\langle \rho^b_{\boldsymbol{p}}, \rho^b_{\boldsymbol{q}} \right\rangle = \delta_{\boldsymbol{pq}} N S_q, \qquad \text{[Göt09, p. 133, Eq. (3.58c)]} \tag{C.1a}$$

$$\left\langle \rho^b_{\boldsymbol{p}}, \rho^s_{\boldsymbol{q}} \right\rangle = \delta_{\boldsymbol{pq}} S^s_q, \qquad \text{[Göt09, p. 322, Eq. (5.23d)]} \tag{C.1b}$$

$$\left\langle \rho^b_{\boldsymbol{p}}, \rho^{sb}_{\boldsymbol{q}} \right\rangle = \delta_{\boldsymbol{pq}} N S_q, \tag{C.1c}$$

$$\left\langle \rho^s_{\boldsymbol{p}}, \rho^s_{\boldsymbol{q}} \right\rangle = \delta_{\boldsymbol{pq}}, \tag{C.1d}$$

$$\left\langle \rho^s_{\boldsymbol{p}}, \rho^{sb}_{\boldsymbol{q}} \right\rangle = \delta_{\boldsymbol{pq}} S^{sb}_q, \tag{C.1e}$$

$$\left\langle \rho^{sb}_{\boldsymbol{p}}, \rho^{sb}_{\boldsymbol{q}} \right\rangle = \delta_{\boldsymbol{pq}} N S_q, \tag{C.1f}$$

where $\rho^s_{\boldsymbol{q}} = 1$ in equilibrium was used due to our choice of frame of reference; $S^{sb}_q = \left\langle \rho^s_{\boldsymbol{q}}, \rho^{sb}_{\boldsymbol{q}} \right\rangle$. Note that the right hand sides are all real valued such that complex conjugation can be omitted.

This leads to a block-diagonal matrix

$$\begin{aligned}
(\langle \boldsymbol{A}, \boldsymbol{A} \rangle)^{-1}_{\boldsymbol{pq}} &= \begin{pmatrix} \left\langle \rho^b_{\boldsymbol{p}}, \rho^b_{\boldsymbol{q}} \right\rangle & \left\langle \rho^b_{\boldsymbol{p}}, \rho^s_{\boldsymbol{q}} \right\rangle & \left\langle \rho^s_{\boldsymbol{p}}, \rho^{sb}_{\boldsymbol{q}} \right\rangle \\ \left\langle \rho^s_{\boldsymbol{p}}, \rho^b_{\boldsymbol{q}} \right\rangle & \left\langle \rho^s_{\boldsymbol{p}}, \rho^s_{\boldsymbol{q}} \right\rangle & \left\langle \rho^s_{\boldsymbol{p}}, \rho^{sb}_{\boldsymbol{q}} \right\rangle \\ \left\langle \rho^{sb}_{\boldsymbol{p}}, \rho^b_{\boldsymbol{q}} \right\rangle & \left\langle \rho^{sb}_{\boldsymbol{p}}, \rho^s_{\boldsymbol{q}} \right\rangle & \left\langle \rho^{sb}_{\boldsymbol{p}}, \rho^{sb}_{\boldsymbol{q}} \right\rangle \end{pmatrix}^{-1} \\
&= \frac{\delta_{\boldsymbol{pq}}}{N S_q (S^s_q - S^{sb}_q)^2} \begin{pmatrix} (S^{sb}_q)^2 - N S_q & N S_q (S^s_q - S^{sb}_q) & N S_q - S^s_q S^{sb}_q \\ N S_q (S^s_q - S^{sb}_q) & 0 & -N S_q (S^s_q - S^{sb}_q) \\ N S_q - S^s_q S^{sb}_q & -N S_q (S^s_q - S^{sb}_q) & (S^s_q)^2 - N S_q \end{pmatrix}
\end{aligned} \tag{C.2}$$

Furthermore, we need to calculate

$$\Omega^\dagger \rho_{\boldsymbol{k}} = - Dk^2 \rho_{\boldsymbol{k}} - \mathrm{i}D\boldsymbol{k} \cdot \sum_{i=1}^{N} (\boldsymbol{\partial}_i V) e^{\mathrm{i}\boldsymbol{k}\cdot\boldsymbol{r}_i}, \tag{C.3a}$$

$$\Omega^\dagger \rho^s_{\boldsymbol{k}} = (-k^2 - \mathrm{i}\boldsymbol{k} \cdot (\boldsymbol{\partial}_s V) - i\boldsymbol{k} \cdot (\boldsymbol{\partial}_s V^{\mathrm{ext}})) \rho^s_{\boldsymbol{k}}, \tag{C.3b}$$

$$\begin{aligned} \Omega^\dagger (\rho^s_{\boldsymbol{k}})^* \rho_{\boldsymbol{k}} =& (-k^2 D - k^2 + i\boldsymbol{k} \cdot (\boldsymbol{\partial}_s V) + \mathrm{i}\boldsymbol{k} \cdot (\boldsymbol{\partial}_s V^{\mathrm{ext}})) \rho^{sb}_{\boldsymbol{k}} \\ & - iD\boldsymbol{k} \cdot \sum_i (\boldsymbol{\partial}_i V) \mathrm{e}^{-\mathrm{i}\boldsymbol{k}\cdot\boldsymbol{r}_s} \mathrm{e}^{\mathrm{i}\boldsymbol{k}\cdot\boldsymbol{r}_i}, \end{aligned} \tag{C.3c}$$

and use

$$\begin{aligned} \left\langle \rho^b_{\boldsymbol{k}}, \sum_{i=1}^{N} \mathrm{i}\boldsymbol{p} \cdot (\boldsymbol{\partial}_i V) e^{\mathrm{i}\boldsymbol{p}\cdot\boldsymbol{r}_i} \right\rangle &= \sum_{i,j=1}^{N} \mathrm{i}\boldsymbol{p} \cdot \left\langle e^{\mathrm{i}\boldsymbol{k}\cdot\boldsymbol{r}_j}, (\boldsymbol{\partial}_i V) e^{\mathrm{i}\boldsymbol{p}\boldsymbol{r}_i} \right\rangle = \sum_{i,j=1}^{N} \mathrm{i}\boldsymbol{p} \cdot \left\langle \boldsymbol{\partial}_i e^{-\mathrm{i}\boldsymbol{k}\cdot\boldsymbol{r}_j} e^{\mathrm{i}\boldsymbol{p}\cdot\boldsymbol{r}_i} \right\rangle \\ &= \sum_{i,j=1}^{N} \mathrm{i}\boldsymbol{p} \cdot \mathrm{i}\boldsymbol{p} \left\langle e^{-\mathrm{i}\boldsymbol{k}\cdot\boldsymbol{r}_j} e^{\mathrm{i}\boldsymbol{p}\cdot\boldsymbol{r}_i} \right\rangle + \sum_{i=1}^{N} \boldsymbol{p} \cdot (-\mathrm{i}\boldsymbol{k}) \left\langle e^{-\mathrm{i}\boldsymbol{k}\cdot\boldsymbol{r}_i} e^{\mathrm{i}\boldsymbol{p}\cdot\boldsymbol{r}_i} \right\rangle \\ &= - p^2 \left\langle \rho^b_{\boldsymbol{k}}, \rho^b_{\boldsymbol{p}} \right\rangle + \boldsymbol{p} \cdot \boldsymbol{k} N \delta_{\boldsymbol{kp}} = \delta_{\boldsymbol{pk}} p^2 N (1 - S_p) \end{aligned} \tag{C.4}$$

to find (cf. (2.114))

$$\left\langle \rho^b_{\boldsymbol{p}}, \Omega^\dagger \rho^b_{\boldsymbol{k}} \right\rangle = -\delta_{\boldsymbol{pk}} N D k^2, \tag{C.5a}$$

$$\left\langle \rho^s_{\boldsymbol{p}}, \Omega^\dagger \rho^b_{\boldsymbol{k}} \right\rangle = 0, \tag{C.5b}$$

$$\left\langle \rho^{sb}_{\boldsymbol{p}}, \Omega^\dagger \rho^b_{\boldsymbol{k}} \right\rangle = -\delta_{\boldsymbol{pk}} N S_k D k^2, \tag{C.5c}$$

$$\left\langle \rho^b_{\boldsymbol{p}}, \Omega^\dagger \rho^s_{\boldsymbol{k}} \right\rangle = -\delta_{\boldsymbol{pk}} S^s_k \mathrm{i}\boldsymbol{k} \cdot (\boldsymbol{\partial}_s V^{\mathrm{ext}}), \tag{C.5d}$$

$$\left\langle \rho^s_{\boldsymbol{p}}, \Omega^\dagger \rho^s_{\boldsymbol{k}} \right\rangle = \delta_{\boldsymbol{pk}} \left(-k^2 - \mathrm{i}\boldsymbol{k} \cdot (\boldsymbol{\partial}_s V^{\mathrm{ext}}) \right), \tag{C.5e}$$

$$\left\langle \rho^{sb}_{\boldsymbol{p}}, \Omega^\dagger \rho^s_{\boldsymbol{k}} \right\rangle = \delta_{\boldsymbol{pk}} S^{sb}_k \left(k^2 - i\boldsymbol{k} \cdot (\boldsymbol{\partial}_s V^{\mathrm{ext}}) \right), \tag{C.5f}$$

$$\left\langle \rho^b_{\boldsymbol{p}}, \Omega^\dagger (\rho^s_{\boldsymbol{k}})^* \rho_{\boldsymbol{k}} \right\rangle = \delta_{\boldsymbol{pk}} N \left(-k^2 D + S_k \mathrm{i}\boldsymbol{k} \cdot (\boldsymbol{\partial}_s V^{\mathrm{ext}}) \right), \tag{C.5g}$$

$$\left\langle \rho^s_{\boldsymbol{p}}, \Omega^\dagger (\rho^s_{\boldsymbol{k}})^* \rho_{\boldsymbol{k}} \right\rangle = \delta_{\boldsymbol{pk}} S^{sb}_k \left(k^2 + \mathrm{i}\boldsymbol{k} \cdot (\boldsymbol{\partial}_s V^{\mathrm{ext}}) \right), \tag{C.5h}$$

$$\left\langle \rho^{sb}_{\boldsymbol{p}}, \Omega^\dagger (\rho^s_{\boldsymbol{k}})^* \rho_{\boldsymbol{k}} \right\rangle = \delta_{\boldsymbol{pk}} N \left(-k^2 (D + S_k) + S_k \mathrm{i}\boldsymbol{k} \cdot (\boldsymbol{\partial}_s V^{\mathrm{ext}}) \right). \tag{C.5i}$$

This leads in the thermodynamic limit $N \to \infty$ with the definition $\tilde{S}^{sb}_q = S^{sb}_q / N$ to

$$\Gamma_{\boldsymbol{kq}} = \delta_{\boldsymbol{kq}} \begin{pmatrix} \frac{Dk^2}{S_k} & 0 & 0 \\ 0 & i\boldsymbol{k} \cdot (\boldsymbol{\partial}_s V^{\mathrm{ext}}) - k^2 & 0 \\ \frac{k^2}{S_k} (D + S_k) & \frac{S_k k^2}{\tilde{S}^{sb}_k} & -i\boldsymbol{k} \cdot (\boldsymbol{\partial}_s V^{\mathrm{ext}}) - k^2 \end{pmatrix}. \tag{C.6}$$

This result is slightly different from (2.115), where we considered only bath and probe correlators. One reason is that the orthogonality matrix is different. But it could also be that the gremlin did its work. For this thesis, we did not extend the theory to higher order correlations, but if

you want to continue along these lines, you should carefully check the results above.

The adjoint operator Ω^{adj} acting on the densities leads to

$$\Omega^{\mathrm{adj}}\rho^b_{\boldsymbol{k}} \overset{\text{(C.3a)}}{=} -Dk^2\rho_{\boldsymbol{k}} - \mathrm{i}D\boldsymbol{k}\cdot\sum_{i=1}^{N}(\boldsymbol{\partial}_i V)e^{\mathrm{i}\boldsymbol{k}\cdot\boldsymbol{r}_i}, \tag{C.7a}$$

$$\Omega^{\mathrm{adj}}\rho^s_{\boldsymbol{k}} = \left(-k^2 - i\boldsymbol{k}\cdot(\boldsymbol{\partial}_s V) - (\boldsymbol{\partial}_s V^{\mathrm{ext}})\cdot((\boldsymbol{\partial}_s V) + i\boldsymbol{k}) + (\boldsymbol{\partial}_s\cdot\boldsymbol{\partial}_s V^{\mathrm{ext}})\right)\rho^s_{\boldsymbol{k}}, \tag{C.7b}$$

$$\begin{aligned}\Omega^{\mathrm{adj}}\rho^{sb}_{\boldsymbol{k}} =& \left(-k^2 D - k^2 + i\boldsymbol{k}\cdot(\boldsymbol{\partial}_s V) - (\boldsymbol{\partial}_s V^{\mathrm{ext}})\cdot((\boldsymbol{\partial}_s V) - i\boldsymbol{k}) + (\boldsymbol{\partial}_s\cdot\boldsymbol{\partial}_s V^{\mathrm{ext}})\right)\rho^{sb}_{\boldsymbol{k}} \\ & - iD\boldsymbol{k}\cdot\sum_i(\boldsymbol{\partial}_i V)\mathrm{e}^{-\mathrm{i}\boldsymbol{k}\cdot\boldsymbol{r}_s}\mathrm{e}^{\mathrm{i}\boldsymbol{k}\cdot\boldsymbol{r}_i}.\end{aligned} \tag{C.7c}$$

C.2. Irreducible operator

This calculation follows [Gru14, Sec 3.3, p. 19f], but hopefully with less typos. Introducing the projection operator

$$\mathcal{Q}_i = \mathbb{1} - \mathcal{P}_i = \mathbb{1} - \mathrm{e}^{\mathrm{i}\boldsymbol{k}\cdot\boldsymbol{r}_i}\left\langle e^{\mathrm{i}\boldsymbol{k}\cdot\boldsymbol{r}_i,\cdot}\right\rangle \tag{C.8}$$

we define the irreducible Smoluchowski operator $\Omega^\dagger_{\mathrm{irr}}$ by inserting the projection $\mathcal{Q}_i$ after the first gradient operators in $\mathcal{Q}\Omega^\dagger\mathcal{Q}$ as introduced by Cichocki and Hess [CH87]

$$\begin{aligned}\Omega^\dagger_{\mathrm{irr}} =& \mathcal{Q}\left(D\sum_{i=1}^{N}(\boldsymbol{\partial}_i - \boldsymbol{\partial}_i V(\boldsymbol{R}))\cdot\mathcal{Q}_i\boldsymbol{\partial}_i + (\boldsymbol{\partial}_s - \boldsymbol{\partial}_s V(\boldsymbol{R}))\cdot\mathcal{Q}_s\boldsymbol{\partial}_s - \boldsymbol{\partial}_s V^{\mathrm{ext}}(\boldsymbol{r}_s)\cdot\mathcal{Q}_s\boldsymbol{\partial}_s\right)\mathcal{Q} \\ =& \mathcal{Q}\Omega^\dagger\mathcal{Q} - \mathcal{Q}(D\sum_i(\boldsymbol{\partial}_i - \boldsymbol{\partial}_i V)\cdot\mathcal{P}_i\boldsymbol{\partial}_i - (\boldsymbol{\partial}_s + \boldsymbol{\partial}_s V)\cdot\mathcal{P}_s\boldsymbol{\partial}_s - \boldsymbol{\partial}_s V^{\mathrm{ext}}\cdot\mathcal{P}_s\boldsymbol{\partial}_s)\mathcal{Q}\end{aligned} \tag{C.9}$$

To simplify this expression, we use the following identities (which are proved with the help of an arbitrary dynamical observable B)

$$\boldsymbol{\partial}_i\mathcal{P}_i B = \boldsymbol{\partial}_i\left\langle\mathrm{e}^{\mathrm{i}\boldsymbol{k}\boldsymbol{r}_i}, B\right\rangle\mathrm{e}^{\mathrm{i}\boldsymbol{k}\boldsymbol{r}_i} = \mathrm{i}\boldsymbol{k}\left\langle\mathrm{e}^{\mathrm{i}\boldsymbol{k}\boldsymbol{r}_i}, B\right\rangle e^{\mathrm{i}\boldsymbol{k}\boldsymbol{r}_i}, \tag{C.10a}$$

where we used that the inner product does not depend on $\boldsymbol{r}_i$ and is only a number. This can be used to show

$$\mathcal{Q}\boldsymbol{\partial}_s\mathcal{P}_s B = \mathcal{Q}\mathrm{i}\boldsymbol{k}\left\langle\mathrm{e}^{\mathrm{i}\boldsymbol{k}\boldsymbol{r}_s}, B\right\rangle\mathrm{e}^{\mathrm{i}\boldsymbol{k}\boldsymbol{r}_s} = \mathrm{i}\boldsymbol{k}\left\langle\mathrm{e}^{\mathrm{i}\boldsymbol{k}\boldsymbol{r}_s}, B\right\rangle\mathcal{Q}\rho^s_{\boldsymbol{k}} = 0 \tag{C.10b}$$

as well as

$$\begin{aligned}\mathcal{Q}\sum_i\boldsymbol{\partial}_i\mathcal{P}_i B =& \sum_i\mathcal{Q}\mathrm{i}\boldsymbol{k}\left\langle\mathrm{e}^{\mathrm{i}\boldsymbol{k}\boldsymbol{r}_i}, B\right\rangle\mathrm{e}^{\mathrm{i}\boldsymbol{k}\boldsymbol{r}_i} = \mathrm{i}\boldsymbol{k}\sum_i\left\langle\mathrm{e}^{\mathrm{i}\boldsymbol{k}\boldsymbol{r}_i}, B\right\rangle\left(e^{\mathrm{i}\boldsymbol{k}\boldsymbol{r}_i} - \frac{1}{N}\sum_j e^{\mathrm{i}\boldsymbol{k}\boldsymbol{r}_j}\right) \\ =& \mathrm{i}\boldsymbol{k}\left(\sum_i\left\langle\mathrm{e}^{\mathrm{i}\boldsymbol{k}\boldsymbol{r}_i}, B\right\rangle e^{\mathrm{i}\boldsymbol{k}\boldsymbol{r}_i} - \frac{1}{N}\sum_{i,j}\mathrm{e}^{\mathrm{i}\boldsymbol{k}\boldsymbol{r}_j}\left\langle\mathrm{e}^{\mathrm{i}\boldsymbol{k}\boldsymbol{r}_i}, B\right\rangle\right) \\ =& 0,\end{aligned} \tag{C.10c}$$

due to $\left\langle \mathrm{e}^{\mathrm{i}\boldsymbol{k}\boldsymbol{r}_i}, A\right\rangle = \left\langle \mathrm{e}^{\mathrm{i}\boldsymbol{k}\boldsymbol{r}_j}, A\right\rangle$ because the bath particles are indistinguishable. We also used

$$\mathcal{Q}\mathrm{e}^{\mathrm{i}\boldsymbol{k}\boldsymbol{r}_i} = \mathrm{e}^{\mathrm{i}\boldsymbol{k}\boldsymbol{r}_i} - \frac{1}{N}\sum_j \mathrm{e}^{\mathrm{i}\boldsymbol{k}\boldsymbol{r}_j}, \tag{C.10d}$$

which can be found in a straightforward calculation. Furthermore, we need to calculate

$$\boldsymbol{\partial}_i V \cdot \mathcal{P}_i \boldsymbol{\partial}_i B = (\boldsymbol{\partial}_i V)\cdot \left\langle \mathrm{e}^{\mathrm{i}\boldsymbol{k}\boldsymbol{r}_i}, \boldsymbol{\partial}_i B\right\rangle \mathrm{e}^{\mathrm{i}\boldsymbol{k}\boldsymbol{r}_i} = -(\boldsymbol{\partial}_i V)\cdot \left\langle (\boldsymbol{\partial}_i V + \mathrm{i}\boldsymbol{k})e^{\mathrm{i}\boldsymbol{k}\boldsymbol{r}_i}), B\right\rangle \mathrm{e}^{\mathrm{i}\boldsymbol{k}\boldsymbol{r}_i}, \tag{C.10e}$$

where an integration by parts was performed for the second equality. This relation holds for bath particles as well as the probe particle. For the latter we find

$$\mathcal{Q}\boldsymbol{\partial}_s V \cdot \mathcal{P}_s \boldsymbol{\partial}_s \mathcal{Q} B = -\mathcal{Q}(\boldsymbol{\partial}_s V)\mathrm{e}^{\mathrm{i}\boldsymbol{k}\boldsymbol{r}_s}\cdot \left\langle \mathcal{Q}(\boldsymbol{\partial}_s V)\mathrm{e}^{\mathrm{i}\boldsymbol{k}\boldsymbol{r}_s}, B\right\rangle, \tag{C.10f}$$

where we used that $\mathcal{Q}$ is Hermitian to move it in the inner product. This also provides us with $\left\langle \mathrm{e}^{\mathrm{i}\boldsymbol{k}\boldsymbol{r}_s}, \mathcal{Q}B\right\rangle = \left\langle \mathcal{Q}\mathrm{e}^{\mathrm{i}\boldsymbol{k}\boldsymbol{r}_s}, B\right\rangle = 0$, which makes the second term vanish. With the same arguments, we find for the bath particles

$$\begin{aligned}\mathcal{Q}\sum_i \boldsymbol{\partial}_i V \cdot \mathcal{P}_i \boldsymbol{\partial}_i \mathcal{Q} B &= -\sum_i \mathcal{Q}(\boldsymbol{\partial}_i V)e^{\mathrm{i}\boldsymbol{k}\boldsymbol{r}_i}\left\langle \mathcal{Q}(\boldsymbol{\partial}_i V)\mathrm{e}^{\mathrm{i}\boldsymbol{k}\boldsymbol{r}_i}, B\right\rangle \\ &= -\sum_i \mathcal{Q}(\boldsymbol{\partial}_i V)e^{\mathrm{i}\boldsymbol{k}\boldsymbol{r}_i}\frac{1}{N}\left\langle \sum_j \mathcal{Q}(\boldsymbol{\partial}_j V)\mathrm{e}^{\mathrm{i}\boldsymbol{k}\boldsymbol{r}_j}, B\right\rangle.\end{aligned} \tag{C.10g}$$

For the last equality we used that the bath particles are indistinguishable and any index can be used for the overlap $\left\langle \mathcal{Q}(\boldsymbol{\partial}_j V)\mathrm{e}^{\mathrm{i}\boldsymbol{k}\boldsymbol{r}_j}, B\right\rangle$. The last term to discuss includes the external force. We get

$$\mathcal{Q}(\boldsymbol{\partial}_s V^{\mathrm{ext}})\cdot \mathcal{P}_s \boldsymbol{\partial}_s B = (\boldsymbol{\partial}_s V^{\mathrm{ext}})\cdot \mathrm{i}\boldsymbol{k}\left\langle \mathrm{e}^{\mathrm{i}\boldsymbol{k}\boldsymbol{r}_s}, B\right\rangle \mathcal{Q}\mathrm{e}^{\mathrm{i}\boldsymbol{k}\boldsymbol{r}_s} = 0, \tag{C.10h}$$

where in the case of an inhomogeneous external force we have to use $\boldsymbol{\partial}_s V^{\mathrm{ext}}(\boldsymbol{r}_s = 0)$ according to our initial conditions.

Collecting all results, we get

$$\mathcal{Q}\Omega^\dagger \mathcal{Q} = \Omega^\dagger_{\mathrm{irr}} - \mathcal{P}_F \tag{C.11a}$$

with the projector

$$\mathcal{P}_F := \sum_{\substack{\alpha\in\{x,y,z\}\\ \mu\in\{b,s\}}} F^{\mu\alpha}_{\boldsymbol{k}} \left\langle F^{\mu\alpha}_{\boldsymbol{k}}, \cdot\right\rangle \tag{C.11b}$$

and

$$F^{b\alpha}_{\boldsymbol{k}} := \sum_i \sqrt{\frac{D}{N}}\mathcal{Q}(\partial_{i,\alpha}V)e^{\mathrm{i}\boldsymbol{k}\boldsymbol{r}_i}, \tag{C.11c}$$

$$F^{s\alpha}_{\boldsymbol{k}} := \mathcal{Q}(\partial_{s,\alpha}V)\mathrm{e}^{\mathrm{i}\boldsymbol{k}\boldsymbol{r}_s}. \tag{C.11d}$$

Next, the operator identity (cf. [Zwa01, p. 149, Eq. (8.22)])

$$\mathrm{e}^{(A+B)t} = \mathrm{e}^{At} + \int_0^t \mathrm{d}t' \mathrm{e}^{A(t-t')}B\mathrm{e}^{(A+B)t'}, \tag{C.12}$$

can be used to rewrite the evolution operator[1]

$$\mathrm{e}^{\mathcal{Q}\Omega^\dagger\mathcal{Q}t} = \mathrm{e}^{\Omega^\dagger_{\mathrm{irr}}t} - \int_0^t \mathrm{d}t'\, \mathrm{e}^{\Omega^\dagger_{\mathrm{irr}}(t-t')}\mathcal{P}_F \mathrm{e}^{(\mathcal{Q}\Omega^\dagger\mathcal{Q})t'}. \tag{C.13}$$

For two dynamical variables A and B, we then obtain

$$\left\langle A, e^{\mathcal{Q}\Omega^\dagger\mathcal{Q}t}B\right\rangle = \left\langle A, \mathrm{e}^{\Omega^\dagger_{\mathrm{irr}}t}B\right\rangle - \sum_{\mu,\alpha}\int_0^t \mathrm{d}t' \left\langle A, \mathrm{e}^{\Omega_{\mathrm{irr}}(t-t')}F_{\boldsymbol{k}}^{\mu\alpha}\right\rangle \left\langle F_{\boldsymbol{k}}^{\mu\alpha}, e^{\mathcal{Q}\Omega^\dagger\mathcal{Q}t'}B\right\rangle \tag{C.14}$$

For the choice $A = F_{\boldsymbol{k}}^{\mu\alpha}$, $B = F_{\boldsymbol{k}}^{\nu\beta}$ and the definitions

$$m^{\mu\alpha,\nu\beta}(t) := \left\langle F_{\boldsymbol{k}}^{\mu\alpha}, \mathrm{e}^{\mathcal{Q}\Omega^\dagger\mathcal{Q}t}F_{\boldsymbol{k}}^{\nu\beta}\right\rangle \tag{C.15a}$$

$$m^{\mu\alpha,\nu\beta}_{\mathrm{irr}}(t) := \left\langle F_{\boldsymbol{k}}^{\mu\alpha}, \mathrm{e}^{\mathcal{Q}\Omega^\dagger_{\mathrm{irr}}\mathcal{Q}t}F_{\boldsymbol{k}}^{\nu\beta}\right\rangle \tag{C.15b}$$

this leads to

$$m^{\mu\alpha,\nu\beta}(t) = m^{\mu\alpha,\nu\beta}_{\mathrm{irr}}(t) - \sum_{\lambda,\gamma}\int_0^t \mathrm{d}t'\, m^{\mu\alpha,\lambda\gamma}_{\mathrm{irr}}(t-t')m^{\lambda\gamma,\nu\beta}(t'). \tag{C.16}$$

Note also that for A or B in the subspace of the relevant variables (i.e. $\mathcal{Q}A = \mathcal{Q}B = 0$) it follows

$$\left\langle A, \mathrm{e}^{\mathcal{Q}\Omega^\dagger\mathcal{Q}t}B\right\rangle = \left\langle \mathcal{Q}A, \mathrm{e}^{\mathcal{Q}\Omega^\dagger\mathcal{Q}t}\mathcal{Q}B\right\rangle = 0 \tag{C.17}$$

using again the properties of the projection operator.

C.2.1. Symmetry calculations

For the symmetry considerations, we want to derive a condition for the memory kernels, which assert cylindrical symmetry for the correlation function according to (2.141). Using the equations of motion in Laplace space for the correlation function, this symmetry condition translates into

$$\frac{1}{s + L^T_{Q\boldsymbol{q}}(1+\tilde{\boldsymbol{m}}(Q\boldsymbol{q},s))^{-1}R_{Q\boldsymbol{q}}} = \frac{1}{s + L^T_{\boldsymbol{q}}(1+\tilde{\boldsymbol{m}}(\boldsymbol{q},s))^{-1}R_{\boldsymbol{q}}} \tag{C.18a}$$

$$\Leftrightarrow L^T_{\boldsymbol{q}}Q^T(1+\tilde{\boldsymbol{m}}(Q\boldsymbol{q},s))^{-1}QR_{\boldsymbol{q}} = L^T_{\boldsymbol{q}}(1+\tilde{\boldsymbol{m}}(\boldsymbol{q},t))^{-1}R_{\boldsymbol{q}} \tag{C.18b}$$

$$\Leftrightarrow Q^T\tilde{\boldsymbol{m}}(Q\boldsymbol{q},s)Q = \tilde{\boldsymbol{m}}(\boldsymbol{q},s). \tag{C.18c}$$

[1] For an extension of this theory for time dependent forces, it would be required to check whether the identity above holds also for time dependent operator.

Second, we show that the irreducible memory operator, which is obtained by inserting the projection operators $\mathcal{Q}$, is also invariant under the cylindrical symmetry, if the potentials are

$$\begin{aligned}
&\sum_{\alpha} \mathcal{Q}(\boldsymbol{r}_s)\partial_{s,\alpha}V(\boldsymbol{r}_s,\Gamma)\mathrm{e}^{\mathrm{i}\boldsymbol{q}\cdot\boldsymbol{r}_s}\left\langle \mathcal{Q}(\boldsymbol{r}_s)\partial_{s,\alpha}V(\boldsymbol{r}_s,\Gamma)\mathrm{e}^{\mathrm{i}\boldsymbol{q}\cdot\boldsymbol{r}_s},\cdot\right\rangle \\
=&\sum_{\alpha\beta\gamma} \mathcal{Q}(\boldsymbol{r}'_s)\mathcal{R}^{\alpha\beta}\partial_{s,\beta}V(\mathcal{R}\boldsymbol{r}'_s\mathcal{R}\Gamma')\mathrm{e}^{\mathrm{i}\boldsymbol{q}\cdot\mathcal{R}\boldsymbol{r}'_s}\left\langle \mathcal{Q}(\boldsymbol{r}'_s)\mathcal{R}^{\alpha\gamma}\partial_{s,\gamma}V(\mathcal{R}\boldsymbol{r}'_s,\mathcal{R}\Gamma')\mathrm{e}^{\mathrm{i}\boldsymbol{q}\cdot\mathcal{R}\boldsymbol{r}'_s},\cdot\right\rangle \\
=&\sum_{\beta\gamma} \mathcal{Q}(\boldsymbol{r}'_s)\partial_{s,\beta}V(\mathcal{R}\boldsymbol{r}'_s,\mathcal{R}\Gamma')\mathrm{e}^{\mathrm{i}\boldsymbol{q}\cdot\mathcal{R}\boldsymbol{r}'_s}\left\langle \mathcal{Q}(\boldsymbol{r}'_s)\partial_{s,\gamma}V(Q\boldsymbol{r}'_s,\mathcal{R}\Gamma')\mathrm{e}^{\mathrm{i}\boldsymbol{q}\cdot\mathcal{R}\boldsymbol{r}'_s},\cdot\right\rangle \sum_{\alpha}\mathcal{R}^{\alpha\beta}\mathcal{R}^{\alpha\gamma} \\
=&\sum_{\beta} \mathcal{Q}(\boldsymbol{r}'_s)\partial_{s,\beta}V(\mathcal{R}\boldsymbol{r}'_s,\mathcal{R}\Gamma')\mathrm{e}^{\mathrm{i}\boldsymbol{q}\cdot\mathcal{R}\boldsymbol{r}'_s}\left\langle \mathcal{Q}(\boldsymbol{r}'_s)\partial_{s,\beta}V(\mathcal{R}\boldsymbol{r}'_s,\mathcal{R}\Gamma')\mathrm{e}^{\mathrm{i}\boldsymbol{q}\cdot\mathcal{R}\boldsymbol{r}'_s},\cdot\right\rangle,
\end{aligned} \tag{C.19}$$

where we used $\sum_\alpha (\mathcal{R}^T)^{\beta\alpha}\mathcal{R}^{\alpha\gamma} = \delta_{\beta\gamma}$.

C.3. Memory kernels in the limit $q \to 0$

In this section we analyze the behavior of the memory kernels in the limit of vanishing wave vector. This is required for the analysis of the moments as discussed in Section 2.4.9. We will basically follow the notation introduced there. Recall also that the dependency on the time or the Laplace frequency only enters as a parameter. Therefore, it does not matter whether we discuss this limit in time or Laplace space.

First, we have a look at the elementary memory functions, which were defined in (2.139b), and their derivatives

$$m_{\boldsymbol{q}}^{\alpha\beta}(t)\Big|_{\boldsymbol{q}=0} = \int \mathrm{d}\boldsymbol{k}\, \phi_{\boldsymbol{k}}^s(t) k_\alpha k_\beta g(k,t), \tag{C.20a}$$

$$\frac{\partial m_{\boldsymbol{q}}^{\alpha\beta}(t)}{\partial q_\gamma}\bigg|_{\boldsymbol{q}=0} = \int \mathrm{d}\boldsymbol{k}\, \phi_{\boldsymbol{k}}^s(t) \left(-\frac{k_\alpha k_\beta k_\gamma}{k} g'(k,t) - (\delta_{\alpha\gamma}k_\beta + k_\alpha\delta_{\beta\gamma})g(k,t)\right), \tag{C.20b}$$

$$\begin{aligned}
\frac{\partial^2 m_{\boldsymbol{q}}^{\alpha\beta}(t)}{\partial {q_\gamma}^2}\bigg|_{\boldsymbol{q}=0} = &\int \mathrm{d}\boldsymbol{k}\, \phi_{\boldsymbol{k}}^s(t) \left(2\delta_{\alpha\gamma}\delta_{\beta\gamma}g(k,t) + \frac{k_\alpha k_\beta k_\gamma^2}{k^2} g''(k,t)\right. \qquad \text{(C.20c)}\\
&\left. +2\left((\delta_{\alpha\gamma}k_\beta + \delta_{\beta\gamma}k_\alpha)\frac{k_\gamma}{k} + \frac{k_\alpha k_\beta}{k}\left(1-\frac{k_\gamma^2}{k^2}\right)\right) g'(k,t)\right). \qquad \text{(C.20d)}
\end{aligned}$$

The helper function g was introduced in (2.161) or (3.9e)). Notice that the chain rule for g yields

$$\frac{\partial}{\partial q_\gamma} g\left(\sqrt{(\boldsymbol{q}-\boldsymbol{k})^2}, t\right)\bigg|_{\boldsymbol{q}=0} = -g'(k,t)\frac{k_\gamma}{k}, \tag{C.21a}$$

$$\frac{\partial^2}{\partial {q_\gamma}^2} g\left(\sqrt{(\boldsymbol{q}-\boldsymbol{k})^2}, t\right)\bigg|_{\boldsymbol{q}=0} = \frac{g'(k,t)}{k}\left(1-\frac{k_\gamma^2}{k^2}\right) + g''(k,t)\frac{k_\gamma^2}{k^2}. \tag{C.21b}$$

We find that $g(k)$ is bounded, $g'(k)$ is bounded and shows $g'(k) \propto k$ for $k \to 0$ and $g''(k)$ is bounded as well (see Figure C.1). Therefore, there is no divergence of the integrand for $k \to 0$. For $t > 0$ both $\phi_{\boldsymbol{k}}(t)$ and $\phi_{\boldsymbol{k}}^s(t)$ decay at least exponentially so that the memory integrals will

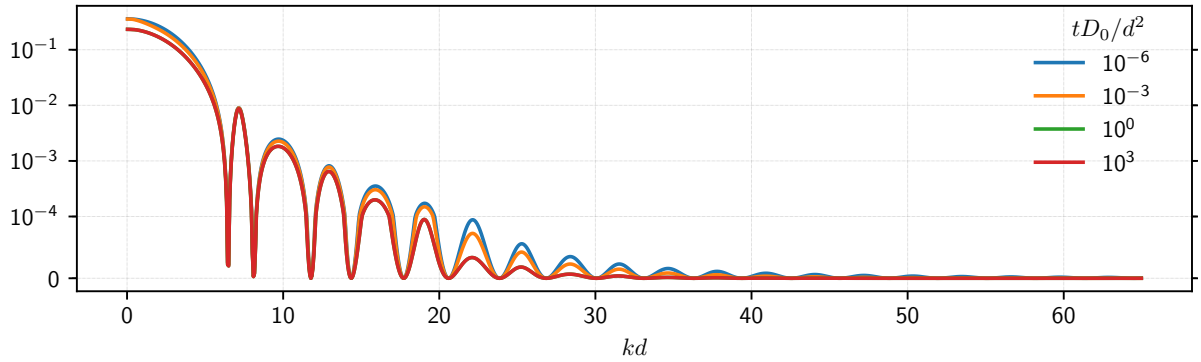

Figure C.1.: $g(k)$ for $\varphi = 0.537$ and different times as indicated. To emphasize the oscillatory behavior of $g(k)$, we choose a combination of a linear and a logarithmic scale: values above 10^{-4} are scaled logarithmically, while values below are scaled linearly to show the zeros. Note that the curves for $tD_0/d^2 = 10^0$ and $tD_0/d^2 = 10^3$ fall on top of each other, because the long time limit has already been reached.

converge[2]. Hence, all memory functionals are finite.

Furthermore, the reflection symmetry $\phi^s_{(k_x,0,k_z)}(t) = \phi^s_{(-k_x,0,k_z)}(t)$ implies $m_0^{xz}(t) = 0$, because g and ϕ^s are even functions in k_x, but the additional k_x in this memory kernel is odd so that all contributions will cancel. With the same argument we can show that $\partial_x m_0^{xx}(t) = 0 = \partial_x m_0^{zz}(t)$.

We can now focus on the elements of M (see (2.177b)). The finding $m^{xz}(0, s) = 0$ yields

$$M_0^{xx}(s) = \frac{1}{1 + m_0^{xx}(s)}, \tag{C.22a}$$

$$M_0^{xz}(s) = 0, \tag{C.22b}$$

$$M_0^{zz}(s) = \frac{1}{1 + m_0^{zz}(s)}. \tag{C.22c}$$

For the derivatives, we find (after simplification for $\boldsymbol{q} = 0$)

$$\frac{\partial M_0^{xx}(s)}{\partial q_\gamma} = -\frac{1}{(1 + m_0^{xx})^2} \frac{\partial m_0^{xx}}{\partial q_\gamma}, \tag{C.23a}$$

$$\frac{\partial M_0^{xz}(s)}{\partial q_\gamma} = -\frac{1}{(1 + m_0^{xx})(1 + m_0^{zz})} \frac{\partial m_0^{xz}}{\partial q_\gamma}, \tag{C.23b}$$

$$\frac{\partial M_0^{zz}(s)}{\partial q_\gamma} = -\frac{1}{(1 + m_0^{zz})^2} \frac{\partial m_0^{zz}}{\partial q_\gamma}, \tag{C.23c}$$

where we omitted the argument s on the right hand sides for clarity. We note that unless $m_0^{xx}(s) = -1$ or $m_0^{zz}(s) = -1$, there will be no divergence. From symmetry we know that both $m_0^{xx}(s)$ and $m_0^{zz}(s)$ are real valued and numerically we find $m_0^{xx}(s) > 0$, $m_0^{zz}(s) > 0$ so that the no-divergence-condition is met. Proving this rigorously faces the problem that $\phi^s_{\boldsymbol{k}}(s)$ is not known and is negative for some $\boldsymbol{k}$.

[2] This argument uses the boundedness of $\phi_{\boldsymbol{k}}(t)$, $\phi^s_{\boldsymbol{k}}(t)$, $c^s_{\boldsymbol{k}}$ and $S_{\boldsymbol{k}}$ and that they are at least two times continuously differentiable.

For the second derivatives, we get

$$\frac{\partial^2 M_0^{xx}(s)}{\partial {q_\gamma}^2} = \frac{\frac{\partial^2 m_0^{zz}}{\partial {q_\gamma}^2}}{(1+m_0^{xx})(1+m_0^{zz})} - \frac{\partial M_0^{xx}}{\partial q_\gamma}\left(\frac{\frac{\partial m_0^{zz}}{\partial q_\gamma}}{1+m_0^{zz}} + \frac{\frac{\partial m_0^{xx}}{\partial q_\gamma}}{1+m_0^{xx}}\right) - M_0^{xx}\left(\frac{\frac{\partial^2 m_0^{xx}}{\partial {q_\gamma}^2}}{1+m_0^{xx}} + \frac{\frac{\partial^2 m_0^{zz}}{\partial {q_\gamma}^2}}{1+m_0^{zz}}\right) - M_0^{xx}\left(\frac{\left(\frac{\partial m_0^{xx}}{\partial q_\gamma}\right)^2 + \left(\frac{\partial m_0^{zz}}{\partial q_\gamma}\right)^2 - 2\left(\frac{\partial m^{xz}}{\partial q_\gamma}\right)^2}{(1+m_0^{xx})(1+m_0^{zz})} - \left(\frac{\frac{\partial m_0^{zz}}{\partial q_\gamma}}{1+m_0^{zz}} + \frac{\frac{\partial m_0^{xx}}{\partial q_\gamma}}{1+m_0^{xx}}\right)^2\right), \tag{C.24a}$$

$$\frac{\partial^2 M_0^{xz}(s)}{\partial {q_\gamma}^2} = \frac{\frac{\partial^2 m^{xz}}{\partial {q_\gamma}^2}}{(1+m_0^{xx})(1+m_0^{zz})} - \frac{\partial M_0^{xz}}{\partial q_\gamma}\left(\frac{\frac{\partial m_0^{zz}}{\partial q_\gamma}}{1+m_0^{zz}} + \frac{\frac{\partial m_0^{xx}}{\partial q_\gamma}}{1+m_0^{xx}}\right), \tag{C.24b}$$

$$\frac{\partial^2 M_0^{zz}(s)}{\partial {q_\gamma}^2} = \frac{\frac{\partial^2 m_0^{xx}}{\partial {q_\gamma}^2}}{(1+m_0^{xx})(1+m_0^{zz})} - \frac{\partial M_0^{zz}}{\partial q_\gamma}\left(\frac{\frac{\partial m_0^{zz}}{\partial q_\gamma}}{1+m_0^{zz}} + \frac{\frac{\partial m_0^{xx}}{\partial q_\gamma}}{1+m_0^{xx}}\right) - M_0^{zz}\left(\frac{\frac{\partial^2 m_0^{xx}}{\partial {q_\gamma}^2}}{1+m_0^{xx}} + \frac{\frac{\partial^2 m_0^{zz}}{\partial {q_\gamma}^2}}{1+m_0^{zz}}\right) - M_0^{zz}\left(\frac{\left(\frac{\partial m_0^{xx}}{\partial q_\gamma}\right)^2 + \left(\frac{\partial m_0^{zz}}{\partial q_\gamma}\right)^2 - 2\left(\frac{\partial m^{xz}}{\partial q_\gamma}\right)^2}{(1+m_0^{xx})(1+m_0^{zz})} - \left(\frac{\frac{\partial m_0^{zz}}{\partial q_\gamma}}{1+m_0^{zz}} + \frac{\frac{\partial m_0^{xx}}{\partial q_\gamma}}{1+m_0^{xx}}\right)^2\right). \tag{C.24c}$$

Again, we find that as long as $m_0^{xx}(s) \neq -1$ and $m_0^{zz}(s) \neq -1$ there will be no divergence. And for the same reasoning as above this is the case.

C.4. Solubility condition for non-invertible matrices

Let $A \in \mathbb{R}^{n\times n}$ and $e \in \mathbb{R}^n \setminus \{0\}$ with $Ae = 0$, i.e. A is not invertible. We search a solution of

$$Ax = b \tag{C.25}$$

on the subspace where A is invertible. What is the condition for b that such a solution exists? In terms of linear algebra this is equivalent to finding the cokernel of A, i.e. $\mathbb{R}^n / \operatorname{img}(A)$.

C.4.1. Solution for symmetric matrices

For symmetric matrices, the spectral theorem holds:

$$A = \sum_{i=1}^{n} \lambda_i \langle e_i, \cdot \rangle e_i = \sum_{i=1}^{n} \lambda_i e_i e_i^T, \tag{C.26}$$

where e_i are the normalized eigenvectors of A, which form an orthonormal basis (with $Ae_i = \lambda_i e_i$, $\|e_i\| = 1$ and $\lambda_i \in \mathbb{R}$). Let $I := \{i \in \{1,\dots,n\} | \lambda_i \neq 0\}$. The subspace on which A is invertible is spanned by $\{e_i | i \in I\}$ and its image is spanned by the same vectors, since the eigenvectors are mapped onto multiples of themselves. Hence, we require

$$b \in \operatorname{span}\{e_i | i \in I\} \tag{C.27}$$

or equivalently

$$\langle b, e_i \rangle = 0 \qquad \text{for } i \notin I. \tag{C.28}$$

If b satisfies this condition, the solution is then given by

$$x = \sum_{i \in I} \frac{1}{\lambda_i} \langle e_i, b \rangle \, e_i = \sum_{i \in I} \lambda_i e_i e_i^T b. \tag{C.29}$$

C.4.2. Pseudo-Inverse-Method

A pseudoinverse A^+ of A fulfills (see [Pen55])

$$AA^+A = A. \tag{C.30}$$

Lemma 1. *If b fulfills $(AA^+ - \mathbb{1})b = 0$, then the system $Ax = b$ can be solved.*

Proof. The condition for b can be reformulated as $AA^+b = b$. Since $AA^+y \in \mathrm{img}(A)$ for any $y \in \mathbb{R}^n$ and $AA^+A = A$, we have $AA^+y \in \mathrm{img}(AA^+A)$ for any $y \in \mathbb{R}^n$. This implies that $AA^+Ax = AA^+b$ can be solved. Let x be such a solution. Then we have

$$Ax = AA^+Ax = AA^+b = b, \tag{C.31}$$

where the first equality is the identity for the pseudoinverse, the second is the solution and the third is the condition for b. □

Lemma 2. *If A has exactly k vanishing eigenvalues, the condition $(AA^+ - \mathbb{1})b = 0$ reduces to*

$$\sum_{i=1}^{k} u_i u_i^T b = 0 \Leftrightarrow u_i^T b = 0 \text{ for } i \in \{1, \ldots, k\}. \tag{C.32}$$

where u_i are an orthonormal basis of the left eigenspace corresponding to the eigenvalue 0, i.e. $A^T u_i = 0$.

Proof. Consider the singular value decomposition of A,

$$A = U \Sigma V^* \tag{C.33}$$

(cf. [BMMS08, Sec. 4.6.3, p. 325, Eq. (4.232)]), where U and V are unitary matrices and Σ a diagonal matrix with the singular values $\sigma_i \geq 0$, the pseudoinverse of A is given as

$$A^+ = V \Sigma^+ U^*, \tag{C.34}$$

where

$$(\Sigma^+)_{ij} = \begin{cases} 1/\sigma_i, & \text{if } i = j \text{ and } \sigma_i \neq 0 \\ 0, & \text{else} \end{cases}. \tag{C.35}$$

Furthermore, we have the following property: Let $U = (u_1, \ldots, u_n)$ with $u_i \in \mathbb{R}^n$ (column vectors) and $V = (v_1, \ldots, v_n)$ with $v_i \in \mathbb{R}^n$. Then

$$M v_i = \sigma_i u_i, \tag{C.36}$$

$$M^T u_i = \sigma_i v_i. \tag{C.37}$$

Evaluating the condition above for b, we get

$$AA^+ - \mathbb{1} = U\Sigma V^* V\Sigma^+ U^* - \mathbb{1} = U(\Sigma\Sigma^+ - \mathbb{1})U^*, \tag{C.38}$$

where we used $VV^* = \mathbb{1} = UU^*$ for unitary matrices. For the product of the diagonal matrices we get

$$\Sigma\Sigma^+ = \begin{cases} 1, & \text{if } i = j \text{ and } \sigma_i \neq 0 \\ 0, & \text{else} \end{cases}. \tag{C.39}$$

Therefore,

$$\Sigma\Sigma^+ - \mathbb{1} = \begin{cases} -1 & \text{if } i = j \text{ and } \sigma_i = 0 \\ 0, & \text{else} \end{cases}. \tag{C.40}$$

Without loss of generality assume that $\sigma_i = 0$ for $i \leq k$. Then

$$AA^+ - \mathbb{1} = (u_1, \ldots, u_n)(\Sigma\Sigma^+ - \mathbb{1}) \begin{pmatrix} u_1^T \\ \vdots \\ u_n^T \end{pmatrix} = -\sum_{i=1}^{k} u_i u_i^T. \tag{C.41}$$

Hence, we get

$$(AA^+ - \mathbb{1})b = 0 \Leftrightarrow \sum_{i=1}^{k} u_i u_i^T b = 0. \tag{C.42}$$

As the u_i are linearly independent, we conclude $u_i^T b = 0$ for $i \in \{1, \ldots, k\}$. □

Corollary 1. *If A has exactly one vanishing eigenvalue, the condition $(AA^+ - \mathbb{1})b = 0$ reduces to*

$$u^T b = 0, \tag{C.43}$$

where u is a left eigenvector to the eigenvalue 0, i.e. $A^T u = 0$.

Proof. Specialize $k = 1$ in the previous lemma. □

Note that in the case of a symmetric matrix, left and right eigenvectors are the same. Therefore, we recover the result of Section C.4.1.

D. Transformation to prolate spheroidal coordinates

As introduced in (2.257), the prolate spheroidal coordinates are given by

$$\begin{aligned} x &= c \sinh \xi \sin \eta \cos \phi \\ y &= c \sinh \xi \sin \eta \sin \phi \\ z &= c \cosh \xi \cos \eta. \end{aligned} \tag{D.1}$$

with $0 \leq \xi < \infty$, $0 \leq \eta \leq \pi$, $0 \leq \phi < 2\pi$. The unit vectors (in Cartesian coordinates) are given by

$$\hat{\boldsymbol{\xi}} = \frac{1}{\sqrt{\sin^2(\eta) + \sinh^2(\xi)}} \begin{pmatrix} \cosh(\xi)\sin(\eta)\cos(\phi) \\ \cosh(\xi)\sin(\eta)\sin(\phi) \\ \sinh(\xi)\cos(\eta) \end{pmatrix}, \tag{D.2a}$$

$$\hat{\boldsymbol{\eta}} = \frac{1}{\sqrt{\sin^2(\eta) + \sinh^2(\xi)}} \begin{pmatrix} \sinh(\xi)\cos(\eta)\cos(\phi) \\ \sinh(\xi)\cos(\eta)\sin(\phi) \\ -\cosh(\xi)\sin(\eta) \end{pmatrix}, \tag{D.2b}$$

$$\hat{\boldsymbol{\phi}} = \begin{pmatrix} -\sin(\phi) \\ \cos(\phi) \\ 0 \end{pmatrix}. \tag{D.2c}$$

The *metric coefficients* or *scale factors* are given by (cf. [MS71, p. 28, Table 1.06], [WeiPro])

$$h_\xi = h_\eta = c\sqrt{\sinh^2(\xi) + \sin^2(\eta)}, \tag{D.3a}$$

$$h_\phi = c \sinh(\xi)\sin(\eta). \tag{D.3b}$$

D.1. Transformation of vector fields

These unit vectors can be used to define the transformation matrix Q,

$$Q(\xi, \eta, \phi) = \left(\hat{\boldsymbol{\xi}}(\xi, \eta, \phi) \quad \hat{\boldsymbol{\eta}}(\xi, \eta, \phi) \quad \hat{\boldsymbol{\phi}}(\xi, \eta, \phi)\right) \tag{D.4}$$

which transforms vectors $\boldsymbol{m}^S = (m_\xi, m_\eta, m_\phi)$ at the point (ξ, η, ϕ) in the prolate spheroidal base to vectors $\boldsymbol{m}^K = (m_x, m_y, m_z)$ in the Cartesian base at the same point via

$$\boldsymbol{m}^K = Q\boldsymbol{m}^S. \begin{pmatrix} m_\xi \\ m_\eta \\ m_\phi \end{pmatrix} = \begin{pmatrix} \hat{\boldsymbol{\xi}}^T \\ \hat{\boldsymbol{\eta}}^T \\ \hat{\boldsymbol{\phi}}^T \end{pmatrix} \begin{pmatrix} m_x \\ m_y \\ m_z \end{pmatrix}. \tag{D.5}$$

Since the transformation is orthonormal, the inverse is given by its transpose

$$\boldsymbol{m}^S = Q^T \boldsymbol{m}^K. \tag{D.6}$$

In particular the components of the vector field along these directions read

$$m_\xi = \boldsymbol{m} \cdot \hat{\boldsymbol{\xi}} = \frac{\cosh(\xi)\sin(\eta)\cos(\phi)m_x + \cosh(\xi)\sin(\eta)\sin(\phi)m_y + \sinh(\xi)\cos(\eta)m_z}{\sqrt{\sin^2(\eta) + \sinh^2(\xi)}}, \tag{D.7a}$$

$$m_\eta = \boldsymbol{m} \cdot \hat{\boldsymbol{\eta}} = \frac{\sinh(\xi)\cos(\eta)\cos(\phi)m_x + \sinh(\xi)\cos(\eta)\sin(\phi)m_y - \cosh(\xi)\sin(\eta)m_z}{\sqrt{\sin^2(\eta) + \sinh^2(\xi)}}, \tag{D.7b}$$

$$m_\phi = \boldsymbol{m} \cdot \hat{\boldsymbol{\phi}} = -\sin(\phi)m_x + \cos(\phi)m_y. \tag{D.7c}$$

The inverse relationship is given by

$$m_x = \frac{\cosh(\xi)\sin(\eta)\cos(\phi)m_\xi + \sinh(\xi)\cos(\eta)\cos(\phi)m_\eta}{\sqrt{\sin^2(\eta) + \sinh^2(\xi)}} - \sin(\phi)m_\phi \tag{D.8a}$$

$$m_y = \frac{\cosh(\xi)\sin(\eta)\sin(\phi)m_\xi + \sinh(\xi)\cos(\eta)\sin(\phi)m_\eta}{\sqrt{\sin^2(\eta) + \sinh^2(\xi)}} + \cos(\phi)m_\phi \tag{D.8b}$$

$$m_z = \frac{\sinh(\xi)\cos(\eta)m_\xi - \cosh(\xi)\sin(\eta)m_\eta}{\sqrt{\sin^2(\eta) + \sinh^2(\xi)}}. \tag{D.8c}$$

D.2. Differential operators in prolate spheroidal coordinates

To transform the derivatives we have to consider the Jacobian matrix of the transformation (D.1) and the metric coefficients (D.3) to find

$$\partial_x = cC^2 \cos\phi \left(\sin(\eta)\cosh(\xi)\partial_\xi + \cos(\eta)\sinh(\xi)\partial_\eta\right) - C'\sin(\phi)\partial_\phi, \tag{D.9a}$$

$$\partial_y = cC^2 \sin\phi \left(\sin(\eta)\cosh(\xi)\partial_\xi + \cos(\eta)\sinh(\xi)\partial_\eta\right) + C'\cos(\phi)\partial_\phi, \tag{D.9b}$$

$$\partial_z = cC^2 \left(\cos(\eta)\sinh(\xi)\partial_\xi - \sin(\eta)\cosh(\xi)\partial_\eta\right), \tag{D.9c}$$

with the abbreviations $1/C = h_\xi = c\sqrt{\sin^2(\eta) + \sinh^2(\xi)}$ and $1/C' = h_\phi = c\sin(\eta)\sinh(\xi)$. These relations can also be expressed in terms of the metric coefficients and the transformation

matrix

$$\begin{pmatrix}\partial_x\\ \partial_y\\ \partial_z\end{pmatrix} = (HQ)^T \begin{pmatrix}\partial_\xi\\ \partial_\eta\\ \partial_\phi\end{pmatrix} \qquad \text{with} \qquad H = \begin{pmatrix} h_\xi^{-1} & 0 & 0\\ 0 & h_\eta^{-1} & 0\\ 0 & 0 & h_\phi^{-1}.\end{pmatrix} \tag{D.10}$$

These expressions can be combined into higher order derivatives, which leads to (see also [MS71, p. 28f, Table 1.06])

$$\begin{aligned}\frac{1}{c^2C^4}\partial_z^2 = &\left(3 - 2\frac{\sin^4(\eta) - \sinh^2(\xi)(\sin^2(\eta) - 2)}{\sin^2(\eta) + \sinh^2(\xi)}\right)\sinh(\xi)\cosh(\xi)\partial_\xi \qquad \text{(D.11a)}\\ &+ \left(3 - 2\frac{\sin^2(\eta)(\sinh^2(\xi) + 2) - \sinh^4(\xi)}{\sin^2(\eta) + \sinh^2(\xi)}\right)\sin(\eta)\cos(\eta)\partial_\eta\\ &+ \cos^2(\eta)\sinh^2(\xi)\partial_\xi^2 + \sin^2(\eta)\cosh^2(\xi)\partial_\eta^2 - 2\sinh(\xi)\cosh(\xi)\sin(\eta)\cos(\eta)\partial_\xi\partial_\eta,\\ \frac{1}{C^2}\boldsymbol{\partial}_r^2 = &\frac{\cosh(\xi)}{\sinh(\xi)}\partial_\xi + \frac{\cos(\eta)}{\sin(\eta)}\partial_\eta + \partial_\xi^2 + \partial_\eta^2 + \left(\frac{1}{\sinh^2(\xi)} + \frac{1}{\sin^2(\eta)}\right)\partial_\phi^2, \qquad \text{(D.11b)}\\ \boldsymbol{\partial}_r \cdot \boldsymbol{m} = &\, C\left(\partial_\xi m_\xi + \partial_\eta m_\eta\right) + C'\partial_\phi m_\phi + c^2C^3\left(\sin^2(\eta) + 2\sinh^2(\xi)\right)\frac{\cosh(\xi)}{\sinh(\xi)}m_\xi \qquad \text{(D.11c)}\\ &+ c^2C^3\left(2\sin^2(\eta) + \sinh^2(\xi)\right)\frac{\cos(\eta)}{\sin(\eta)}m_\eta,\\ \boldsymbol{\partial}_r n = &\frac{\hat{\boldsymbol{\xi}}}{c\sqrt{\sin^2(\eta) + \sinh^2(\xi)}}\partial_\xi n + \frac{\hat{\boldsymbol{\eta}}}{c\sqrt{\sin^2(\eta) + \sinh^2(\xi)}}\partial_\eta n + \frac{\hat{\boldsymbol{\phi}}}{c\sin(\eta)\sinh(\xi)}\partial_\phi n. \qquad \text{(D.11d)}\end{aligned}$$

D.3. Transformation of the equations of motion for a vector field

When we apply a change of variables to a PDE, we have to transform the differentials. For scalar fields this is all to be done. However, for vector fields, a change of variables implies a change of the basis-vectors as well. In this section, we deal with the problem of finding the equation of motion for the vector field in the new (local) basis. Let $\boldsymbol{m} = m_1\hat{\boldsymbol{e}}_1 + m_2\hat{\boldsymbol{e}}_2 + m_3\hat{\boldsymbol{e}}_3$ be the vector field in the old basis $(\hat{\boldsymbol{e}}_1, \hat{\boldsymbol{e}}_2, \hat{\boldsymbol{e}}_3)$. Let Q be the orthogonal transformation matrix from the new to the old coordinate system, i.e.

$$\boldsymbol{m} = Q\boldsymbol{m}' \quad \text{and} \quad \boldsymbol{m}' = Q^T\boldsymbol{m}. \tag{D.12}$$

We assume that the dynamics of the vector field is determined by a single scalar second-order differential operator

$$\partial_i m_i = \Omega m_i \tag{D.13}$$

with

$$\Omega = \sum_l A_l^{(1)}\partial_l + \sum_{m,n} A_{mn}^{(2)}\partial_m\partial_n, \tag{D.14}$$

where the operator is already formulated in the new of variables. We then find find by using relations (D.12)

$$\partial_t m_i' = \partial_t \sum_j Q_{ij}^T m_j = \sum_j Q_{ij}^T \partial_t m_j = \sum_j Q_{ij}^T \Omega m_j = \sum_{j,k} Q_{ij}^T \Omega Q_{jk} m_k. \tag{D.15}$$

Inserting the definition of the operator (D.14) leads to

$$\begin{aligned}\partial_t m_i' &= \sum_{jk} Q_{ij}^T \left(\sum_l A_l^{(1)} \partial_l + \sum_{m,n} A_{mn}^{(2)} \partial_m \partial_n \right) Q_{jk} m_k' \\ &= \sum_{jkl} A_l^{(1)} Q_{ij}^T \left(\partial_l Q_{jk} + Q_{jk} \partial_l \right) m_k' \\ &\quad + \sum_{jkmn} A_{mn}^{(2)} Q_{ij}^T \left(\partial_m \partial_n Q_j + \partial_n Q_{jk} \partial_m + \partial_m Q_{jk} \partial_n + Q_{jk} \partial_m \partial_n \right) m_k'.\end{aligned} \tag{D.16}$$

Using the relation $Q^T Q$ for orthogonal matrices we can simplify this to

$$\partial_t m_i' = \Omega m_i' + \sum_l A_l^{(1)} \sum_{jk} Q_{ij}^T \partial_l Q_{jk} m_k' + \sum_{\substack{mn \\ jk}} A_{mn}^{(2)} Q_{ij}^T \partial_m \partial_n Q_{jk} m_k' + 2 \sum_{\substack{mn \\ jk}} A_{mn}^{(2)} Q_{ij}^T \partial_m Q_{jk} \partial_n m_k' \tag{D.17}$$

or in vector notation

$$\partial_t \boldsymbol{m}' = \Omega \boldsymbol{m}' + \sum_l A_l^{(1)} Q^T \partial_l Q \boldsymbol{m}' + \sum_{mn} A_{mn}^{(2)} Q^T \partial_m \partial_n Q \boldsymbol{m}' + \sum_{mn} A_{mn}^{(2)} Q^T \partial_m Q \partial_n \boldsymbol{m}'. \tag{D.18}$$

Thus, we get additional couplings if the terms $Q^T \partial_l Q$ or $Q^T \partial_m \partial_n Q$ do not vanish. The advantage of this notation is that the terms $Q^T \partial_l Q$ can be easily computed and for many cases there are only a few non-zero entries.

D.4. Vector field transformation matrices for prolate spheroidal coordinates

As shown in the previous section, we need to calculate certain combinations of derivatives of the transformation matrix Q (D.4). Since many entries vanish, we will only show the nonzero components. For the first order derivatives we obtain for $B = Q^T \partial_\xi Q$

$$B_{\xi\eta} = -B_{\eta\xi} = -\frac{\sin(2\eta)}{\cos(2\eta) - \cosh(2\xi)}, \tag{D.19}$$

for $B = Q^T \partial_\eta Q$

$$B_{\xi\eta} = -B_{\eta\xi} = -\frac{\sinh(2\xi)}{2\sin^2(\eta) + \cosh(2\xi) - 1}, \tag{D.20}$$

for $B = Q^T \partial_\phi Q$

$$B_{\phi\eta} = -B_{\eta\phi} = \frac{\sin(\eta)\cosh(\xi)}{\sqrt{\sin^2(\eta)+\sinh^2(\xi)}}, \tag{D.21a}$$

$$B_{\phi\xi} = -B_{\xi\phi} = \frac{\cos(\eta)\sinh(\xi)}{\sqrt{\sin^2(\eta)+\sinh^2(\xi)}}. \tag{D.21b}$$

For the second derivatives we find for $B = Q^T \partial_\xi \partial_\xi Q$

$$B_{\xi\xi} = B_{\eta\eta} = \frac{\cos^2(\eta)\sin^2(\eta)}{(\sin^2(\eta)+\sinh^2(\xi))^2}, \tag{D.22a}$$

$$B_{\eta\xi} = -B_{\xi\eta} = \frac{2\sin(2\eta)\sinh(2\xi)}{(\cos(2\eta)-\cosh(2\xi))^2}, \tag{D.22b}$$

and for $B = Q^T \partial_\eta \partial_\eta Q$

$$B_{\xi\xi} = B_{\eta\eta} = \frac{\sin(\eta)\cos(\eta)\sinh(2\xi)}{2(\sin^2(\eta)+\sinh^2(\xi))^2}, \tag{D.23a}$$

$$B_{\eta\xi} = -B_{\xi\eta} = \frac{\cos^2(\eta)+\cosh^2(\xi)(1-2\cos^2(\eta))}{(\cos^2(\eta)-\cosh^2(\xi))^2}. \tag{D.23b}$$

The other combinations are not relevant in our case.

D.5. Transformation from prolate spheroidal to oblate spheroidal coordinates

In the definition of prolate spheroidal coordinates in Section 2.5.3 we find that the expressions for c and ξ_0 become imaginary for $a < 1$, because the arguments of the root and the logarithm get negative. Thus we can define

$$c = \mathrm{i}\frac{1}{2}\sqrt{s^2(1-\hat{a}^2)+2s(1-\hat{a})} =: \mathrm{i}\tilde{c}, \tag{D.24a}$$

$$\xi_0 = -\frac{\mathrm{i}\pi}{2} + \ln\left(\frac{1}{s}\frac{s(\hat{a}+1)+2}{1-\hat{a}}\right) =: -\frac{\mathrm{i}\pi}{2}.\tilde{\xi}_0 \tag{D.24b}$$

These transformations imply the following substitution rules

$$c^2 = -\tilde{c}^2 \tag{D.25a}$$

$$c\sinh(\xi) = \tilde{c}\cosh(\tilde{\xi}) \tag{D.25b}$$

$$c\cosh(\xi) = \tilde{c}\sinh(\tilde{\xi}) \tag{D.25c}$$

$$\sinh^2(\xi) = -\cosh^2(\tilde{\xi}) \tag{D.25d}$$

$$\cosh^2(\xi) = -\sinh^2(\tilde{\xi}) \tag{D.25e}$$

$$\sinh(2\xi) = -\sinh(2\tilde{\xi}) \tag{D.25f}$$

$$\cosh(2\xi) = -\cosh(2\tilde{\xi}) \tag{D.25g}$$

$$\sinh(4\xi) = \sinh(4\tilde{\xi}) \tag{D.25h}$$

$$\cosh(4\xi) = \cosh(4\tilde{\xi}) \tag{D.25i}$$

D.6. Useful identities

To simplify the coefficients for the coordinate transforms, the following identities have proved to be useful (see [BMMS08, Sec. 2.7.2, p. 80ff] for the trigonometric identities and [BMMS08, Sec. 2.9.3, p. 90ff] for the hyperbolic identities)

$$1 = \sin^2(x) + \cos^2(x) \tag{D.26}$$
$$-1 = \sinh^2(x) - \cosh^2(x) \tag{D.27}$$
$$\sin^2(x) = \frac{1}{2}\left(1 - \cos(2x)\right) \tag{D.28}$$
$$\cos^2(x) = \frac{1}{2}\left(1 + \cos(2x)\right) \tag{D.29}$$
$$\sinh^2(x) = \frac{1}{2}\left(\cosh(2x) - 1\right) \tag{D.30}$$
$$\cosh^2(x) = \frac{1}{2}\left(\cosh(2x) + 1\right) \tag{D.31}$$
$$\sin(2x) = 2\sin(x)\cos(x) \tag{D.32}$$
$$\sinh(2x) = 2\sinh(x)\cosh(x) \tag{D.33}$$

which imply

$$\sinh^2(x) + \sin^2(y) = \cosh^2(x) - \cos^2(y) = \frac{1}{2}\left(\cosh(2x) - \cos(2y)\right), \tag{D.34}$$
$$\cosh^2(x) - \sin^2(y) = \frac{1}{2}\left(\cosh(2x) + \cos(2y)\right). \tag{D.35}$$

D.7. Abbreviations for the numerical solution

This section gives the abbreviations used in Section 8.2

$$\tilde{D} = \left(1 + \frac{\overline{D}}{s}\right) C^2 \tag{D.36a}$$
$$A^n_\xi(\xi,\eta) = \tilde{D}\frac{\cosh(\xi)}{\sinh(\xi)} + \mathrm{Pe}^{\mathrm{ext}} c C^2 \cos(\eta)\sinh(\xi) \tag{D.36b}$$
$$A^n_{\xi\xi}(\xi,\eta) = \tilde{D} \tag{D.36c}$$
$$A^n_\eta(\xi,\eta) = \tilde{D}\frac{\cos(\eta)}{\sin(\eta)} - \mathrm{Pe}^{\mathrm{ext}} c C^2 \sin(\eta)\cosh(\xi) \tag{D.36d}$$
$$A^n_{\eta\eta}(\xi,\eta) = \tilde{D} \tag{D.36e}$$
$$A^{m_\xi}(\xi,\eta) = -\mathrm{Pe}^{\mathrm{act}} c^2 C^3 (\sin^2(\eta) + 2\sinh^2(\xi))\frac{\cosh(\xi)}{\sinh(\xi)} \tag{D.36f}$$
$$A^{m_\xi}_\xi(\xi,\eta) = -\mathrm{Pe}^{\mathrm{act}} C \tag{D.36g}$$
$$A^{m_\eta}(\xi,\eta) = -\mathrm{Pe}^{\mathrm{act}} c^2 C^3 (2\sin^2(\eta) + \sinh^2(\xi))\frac{\cos(\eta)}{\sin(\eta)} \tag{D.36h}$$
$$A^{m_\eta}_\eta(\xi,\eta) = -\mathrm{Pe}^{\mathrm{act}} C \tag{D.36i}$$

$$B^n_\xi(\xi,\eta) = -C\frac{\mathrm{Pe}^{\mathrm{act}}}{3} \tag{D.37a}$$
$$B^{m_\xi}(\xi,\eta) = -2\frac{\mathrm{Pe}^{\mathrm{act}}}{\overline{\ell}} - \tilde{D}\left(\frac{1}{8}\frac{\cosh(4\xi) - \cos(4\eta)}{\left(\sin^2(\eta) + \sinh^2(\xi)\right)^2} + \frac{\cosh^2(\xi)}{\sinh^2(\xi)}\right) \tag{D.37b}$$
$$B^{m_\xi}_\xi(\xi,\eta) = \tilde{D}\frac{\cosh(\xi)}{\sinh(\xi)} + \mathrm{Pe}^{\mathrm{ext}} C^2 c \sinh(\xi)\cos(\eta) \tag{D.37c}$$
$$B^{m_\xi}_{\xi\xi}(\xi,\eta) = \tilde{D} \tag{D.37d}$$

$$B_{\eta}^{m_\xi}(\xi,\eta) = \tilde{D}\frac{\cos(\eta)}{\sin(\eta)} - \mathrm{Pe}^{\mathrm{ext}} C^2 c \cosh(\xi)\sin(\eta) \tag{D.37e}$$

$$B_{\eta\eta}^{m_\xi}(\xi,\eta) = \tilde{D} \tag{D.37f}$$

$$B^{m_\eta}(\xi,\eta) = -2\tilde{D}\frac{\cos(\eta)}{\sin(\eta)}\frac{\sinh(2\xi)}{\cosh(2\xi)-\cos(2\eta)} + 2\mathrm{Pe}^{\mathrm{ext}} c C^2 \sin(\eta)\sinh(\xi)\frac{\cosh^2(\xi)+\cos^2(\eta)}{\cosh(2\xi)-\cos(2\eta)} \tag{D.37g}$$

$$B_{\xi}^{m_\eta}(\xi,\eta) = 2\tilde{D}\frac{\sin(2\eta)}{\cosh(2\xi)-\cos(2\eta)} \tag{D.37h}$$

$$B_{\eta}^{m_\eta}(\xi,\eta) = -2\tilde{D}\frac{\sinh(2\xi)}{\cosh(2\xi)-\cos(2\eta)} \tag{D.37i}$$

$$C_{\eta}^{n}(\xi,\eta) = -C\frac{\mathrm{Pe}^{\mathrm{act}}}{3} \tag{D.38a}$$

$$C^{m_\xi}(\xi,\eta) = -2\tilde{D}\frac{\cosh(\xi)}{\sinh(\xi)}\frac{\sin(2\eta)}{\cosh(2\xi)-\cos(2\eta)} - 2\mathrm{Pe}^{\mathrm{ext}} c C^2 \sin(\eta)\sinh(\xi)\frac{\cosh^2(\xi)+\cos^2(\eta)}{\cosh(2\xi)-\cos(2\eta)} \tag{D.38b}$$

$$C_{\xi}^{m_\xi} = -2\tilde{D}\frac{\sin(2\eta)}{\cosh(2\xi)-\cos(2\eta)} \tag{D.38c}$$

$$C_{\eta}^{m_\xi} = 2\tilde{D}\frac{\sinh(2\xi)}{\cosh(2\xi)-\cos(2\eta)} \tag{D.38d}$$

$$C^{m_\eta} = -2\frac{\mathrm{Pe}^{\mathrm{act}}}{\bar{\ell}} - \tilde{D}\left(\frac{1}{8}\frac{\cosh(4\xi)-\cos(4\eta)}{\left(\sin^2(\eta)+\sinh^2(\xi)\right)^2} + \frac{\cos^2(\eta)}{\sin^2(\eta)}\right) \tag{D.38e}$$

$$C_{\xi}^{m_\eta} = \tilde{D}\frac{\cosh(\xi)}{\sinh(\xi)} + \mathrm{Pe}^{\mathrm{ext}} C^2 c \sinh(\xi)\cos(\eta) \tag{D.38f}$$

$$C_{\xi\xi}^{m_\eta} = \tilde{D} \tag{D.38g}$$

$$C_{\eta}^{m_\eta} = \tilde{D}\frac{\cos(\eta)}{\sin(\eta)} - \mathrm{Pe}^{\mathrm{ext}} C^2 c \cosh(\xi)\sin(\eta) \tag{D.38h}$$

$$C_{\eta\eta}^{m_\eta} = \tilde{D} \tag{D.38i}$$

$$N_n(\xi,\eta) = -\frac{\mathrm{Pe}^{\mathrm{ext}}}{\tilde{D}} c \sinh(\xi)\cos(\eta) \tag{D.39a}$$

$$N_{m_\xi}(\xi,\eta) = \frac{\mathrm{Pe}^{\mathrm{act}}}{\tilde{D}C} \tag{D.39b}$$

$$M_n^{\xi}(\xi,\eta) = \frac{\mathrm{Pe}^{\mathrm{act}}}{3\tilde{D}C} \tag{D.40a}$$

$$M_{m_\xi}^{\xi}(\xi,\eta) = -\frac{\mathrm{Pe}^{\mathrm{ext}}}{\tilde{D}} c \sinh(\xi)\cos(\eta) \tag{D.40b}$$

$$M^{\xi}_{m_\eta}(\xi,\eta) = -\frac{\sin(2\eta)}{\cosh(2\xi)-\cos(2\eta)} \tag{D.40c}$$

$$M^{\eta}_{m_\xi}(\xi,\eta) = \frac{\sin(2\eta)}{\cosh(2\xi)-\cos(2\eta)} \tag{D.41a}$$

$$M^{\eta}_{m_\eta}(\xi,\eta) = -\frac{\mathrm{Pe}^{\mathrm{ext}}}{\tilde{D}} c \sinh(\xi)\cos(\eta) \tag{D.41b}$$

E. Integral and integro-differential equations

To be able to assess the performance of the different numerical algorithms to solve the integral and integro-differential equations, we compare the numerical results to analytically known solutions. A large collection of integral equations and their solutions is given in [PM08]. The integral equations which are suitable for our testing and their solutions are presented in the this chapter.

E.1. Integral equations

Our integral equation (3.21) is a Volterra equation of the second type of the form

$$X(t) + \int_0^t A(t-t')X(t')\mathrm{d}t' = B(t). \tag{E.1}$$

In the final case $A(t)$ will be a function of $X(t)$ itself, but there are only a few analytic solutions. The easiest case is $A(t) = X(t)$ for which two particular can be solved analytically. These solutions are listed according to their corresponding memory kernel in the first section.

E.1.1. Convolution kernel $A(t) = \lambda t$

For the convolution kernel $A(t) = \lambda t$ the solutions depend on the sign of λ (cf. [PM08, p. 127, Eq. 2.1.4]). For $B(t) = 1$, we obtain

$$X(t) = \begin{cases} \cos(\sqrt{\lambda}t), & \lambda > 0, \\ \cosh(\sqrt{-\lambda}t), & \lambda < 0. \end{cases} \tag{E.2}$$

For $B(t) = \exp(-t/\tau)$ the solution is given by

$$X(t) = \left\{ \frac{1}{\tau^2}\exp(-t/\tau) - \frac{k}{\tau}\sin(kt) + \frac{k^2}{\tau^{-2}+k^2}\cos(kt), \quad \lambda > 0, \right. \tag{E.3}$$

with $k = \sqrt{|\lambda|}$.

E.1.2. Convolution kernel $A(t) = a + bt$

For the convolution kernel $A(t) = a + bt$ (cf. [PM08, p. 128, Eq. 2.1.5]) the solution for $B(t) = 1$ is given by

$$X(t) = \begin{cases} \mathrm{e}^{-\frac{at}{2}} \left(1 - \frac{at}{2}\right), & b = \frac{a^2}{4}, \\ \mathrm{e}^{-\frac{at}{2}} \left(\cos(\beta t) - \frac{a}{2\beta} \sin(\beta t)\right), & b > \frac{a^2}{4}, \\ \mathrm{e}^{-\frac{at}{2}} \left(\cosh(\beta t) - \frac{a}{2\beta} \sinh(\beta t)\right), & b < \frac{a^2}{4}, \end{cases} \tag{E.4}$$

with $\beta = \sqrt{|b - a^2/4|}$.

E.1.3. Convolution kernel $A(t) = a \exp(\lambda t)$

For the convolution kernel $A(t) = a \exp(\lambda t)$ (cf. [PM08, p. 144, Eq. 2.2.1]) and the right hand side $B(t) = 1$ we obtain

$$X(t) = \begin{cases} 1 - at, & \lambda = a, \\ 1 - \frac{a}{a-\lambda} \left(1 - \mathrm{e}^{(\lambda - a)t}\right), & \lambda \neq a. \end{cases} \tag{E.5}$$

For the right hand side $B(t) = \mathrm{e}^{-t/\tau}$ we find

$$X(t) = \begin{cases} 1 - at, & a - \lambda - \tau^{-1} = 0, \\ \mathrm{e}^{-\frac{t}{\tau}} - \frac{a}{\tau^{-1} + \lambda - a} \mathrm{e}^{-(A - \lambda + \tau^{-1})t} \left(\mathrm{e}^{\frac{t}{\tau}} - \mathrm{e}^{(A-\lambda)t}\right), & a - \lambda - \tau^{-1} \neq 0. \end{cases} \tag{E.6}$$

E.1.4. Convolution kernel $A(t) = a(\exp(\lambda t) - 1)$

For the convolution kernel $A(t) = a(\exp(\lambda t) - 1)$ (cf. [PM08, p. 144f,Eq. 2.2.3]) and the right hand side $B(t) = 1$ we obtain

$$X(t) = \begin{cases} \left(1 - \frac{\lambda t}{2}\right) \mathrm{e}^{\frac{\lambda t}{2}}, & \lambda = 4a, \\ \left(\cos\left(\frac{\sqrt{|D|}t}{2}\right) - \frac{\lambda}{\sqrt{D}} \sin\left(\frac{\sqrt{|D|}t}{2}\right)\right) \mathrm{e}^{\frac{\lambda t}{2}}, & D < 0, \\ \left(\cosh\left(\frac{\sqrt{|D|}t}{2}\right) - \frac{\lambda}{\sqrt{D}} \sinh\left(\frac{\sqrt{|D|}t}{2}\right)\right) \mathrm{e}^{\frac{\lambda t}{2}}, & D > 0. \end{cases} \tag{E.7}$$

with $D := \lambda^2 - 4a\lambda$.

E.1.5. Convolution kernel $A(t) = aX(t)$

Choosing $A(t) = aX(t)$, the integral equation becomes nonlinear, but more similar to our equation to study. However, only solutions for specific right hand sides are known. For $B(t) = ab^2t + b$ the solution is given by ([PM08, p. 406, Eq. 6.1.16])

$$X(t) = b. \tag{E.8}$$

Since the analytical solution is constant, this is a good test for the stability of the algorithms. Another solution is known for $B(t) = (ab^2t + b)e^{\lambda t}$ ([PM08, p. 406, Eq. 6.1.17]), namely

$$X(t) = b\mathrm{e}^{\lambda t}. \tag{E.9}$$

E.2. Integro-differential equations

An integro-differential equation of the form

$$\partial_t X(t) + \Gamma X(t) + \int_0^t A(t-t')\partial_{t'} X(t')\mathrm{d}t' = 0 \tag{E.10}$$

can be transformed into the following Volterra equation of the second type in $\partial_t X(t)$ using the fundamental theorem of calculus

$$\partial_t X(t) + \int_0^t (\Gamma + A(t-t'))\partial_{t'} X(t')\mathrm{d}t' = -\Gamma X(0). \tag{E.11}$$

Once this equation is solved by $\tilde{X}(t)$ for $\partial_t X(t)$, we can determine $X(t)$ via integration

$$X(t) = X_0 + \int_0^t \tilde{X}(t')\mathrm{d}t'\,. \tag{E.12}$$

E.2.1. Convolution kernel $A(t) = \lambda t$

A convolution kernel $A(t) = \lambda t$ leads to the integral equation (E.4) with $a = \Gamma$ and $b = \lambda$ for $\partial_t X(t)$. Note that $-\Gamma X_0 \tilde{X}(t)$ is a solution for the integral equation for (E.4) with $B(t) = -\Gamma X_0$ if and only if $\tilde{X}(t)$ is a solution for $B(t) = 1$ due to the linearity of the equation. Hence, we find

$$X(t) = \begin{cases} X_0\left(1 - t\Gamma \mathrm{e}^{-\frac{\Gamma t}{2}}\right) & \lambda = \frac{\Gamma^2}{4} \\ X_0 - X_0\left(\cos(\beta t) - \frac{\Gamma}{2\beta}\sin(\beta t)\right) t\mathrm{e}^{-\frac{\Gamma t}{2}} & \lambda > \frac{\Gamma^2}{4} \\ X_0 - X_0\left(\cosh(\beta t) - \frac{\Gamma}{2\beta}\sinh(\beta t)\right) t\mathrm{e}^{-\frac{\Gamma t}{2}} & \lambda < \frac{\Gamma^2}{4} \end{cases} \tag{E.13}$$

with $\beta = \sqrt{|\lambda - \Gamma^2/4|}$. The solutions are bounded for $\lambda \geq 0$ and $\Gamma > 0$.

E.2.2. Convolution kernel $A(t) = -\Gamma \exp(\lambda t)$

A convolution kernel $A(t) = -\Gamma \exp(\lambda t)$ leads to the integral equation (E.7) with $a = -\Gamma$ and $B(t) = -\Gamma X_0$. Hence, we find

$$X(t) = \begin{cases} X_0 \left(1 + \Gamma t\right) \mathrm{e}^{-2\Gamma t}, & \lambda = 4\Gamma, \\ X_0 \left(\cos\left(\frac{\sqrt{|D|}t}{2}\right) - \frac{\lambda + 2\Gamma}{\sqrt{|D|}} \sin\left(\frac{\sqrt{|D|}t}{2}\right) \right) \mathrm{e}^{\frac{\lambda t}{2}}, & D < 0, \\ X_0 \left(\cosh\left(\frac{\sqrt{|D|}t}{2}\right) - \frac{\lambda + 2\Gamma}{\sqrt{|D|}} \sinh\left(\frac{\sqrt{|D|}t}{2}\right) \right) \mathrm{e}^{\frac{\lambda t}{2}}, & D > 0, \end{cases} \tag{E.14}$$

with $D := \lambda^2 + 4\Gamma\lambda$. This solution is bounded for $\lambda < 0$ and $\Gamma > 0$.

F. Säntis — a Great Myth?

This is a bonus study for the reader who made it all the way through this thesis :-) Spending about four years in P917 I had many opportunities to enjoy the fantastic view on the Alps, in particular the Säntis massif (see Figure F.1). But — and this was the driving force for this study — there were also plenty of days, where the Alps were hiding. Of course, fog and clouds will prevent us from seeing the Alps if they already let fade away the other side of the street [Eic14]. Surprisingly, sometimes they hide even if the sky appears blue [Rei19]. An exchange coworker stayed for the whole summer without seeing the Alps, believing that the view of Säntis is a pure myth, until it unveiled itself the week before he had to leave again. Under which conditions does Säntis show up? Can we predict this? Or can we at least give some recommendation for the time of the year to see Säntis?

F.1. Methods and Materials

To answer these questions scientifically, we set up the following experiment (in my free time at weekends or after work). It consists of two parts. On one hand side, we have to evaluate whether Säntis is visible or not at certain times. On the other hand, we want to correlate this information with the weather conditions or the weather forecast.

To assess the visibility of the Alps, we set up a webcam, which takes a photo of the view from our window every hour (from 5:52 to 20:52 to be precise). In the course of the experiment two webcams were used: *AC150* from *Hama* with a resolution of 640×480 pixels and the *LiveCamHD3000* from *Microsoft* with 1280×720 pixels. To ensure proper exposure of the images, three pictures are taken with increasing exposure time. This proved to be tricky, because the support of the webcam functions by the Linux drivers is very limited and not

Figure F.1.: View from P917 in spring, summer, autumn and winter (clockwise, starting from top left panel).

documented at all. The tool `fswebcam` [Her19] finally did the trick. The images are saved to disk and their filenames are inserted into a database together with the timestamps.

Then we have to classify the visibility as described below. There are four categories:

Säntis when the silouette of Säntis can be clearly identified,

Mountains when the mountain range is visible, but the silouette of Säntis cannot be identified (mostly because of clouds),

Not visible when neither Säntis nor parts of the mountain range can be seen,

Not Analyzable when the picture cannot be analyzed (because it is dark, the blind is down, overexposure).

To prevent misclassifications, we classify each image at least three times independently. Random order is used to prevent aftervision and biases through previous images.

For the weather conditions, we could access the archive of the DWD, which is free of charge. However, this database does not include weather data from Säntis, which is in Switzerland and therefore subject to the Swiss Federal Office of Meteorology and Climatology, MeteoSwiss [MetSwi]. The following variables were kindly provided by the services of MeteoSwiss for our analysis: temperature (in °C), relative humidity (in %), pressure on sea level (in hPa), wind speed (10 minutes average in m/s), precipitation (per 10 minutes in mm), global radiation in W/m^2 on Säntis and in Kreuzlingen. Furthermore, we have analyzed the pressure difference between Zurich and Lugano, which is supposed to be an indicator for foehn weather [MetFoe], which usually comes with good visibility conditions.

We will also analyze the weather forecast, which is downloaded from weather websites three times a day, whenever it is updated. The idea is that this will allow us hopefully to predict the visibility based on the weather forecast. For each prediction time, we obtain a time series of predicted weather data, which is extracted and moved into a database. Available data are: temperature (in °C), relative humidity (in %), pressure on sea level (in hPa), wind speed (10 minutes average in m/s), sunshine (in minutes per hour), precipitation (in mm/h), and cloud coverage in low, mid and high altitudes (in %).

F.2. Results

First pictures were taken starting from January 24, 2018 with the Hama webcam. There were, however, two major issues with its pictures. First, the exposure could not be controlled properly which caused a lot of useless, because overexposed pictures. All attempts to fix this using different drivers or modules for the script failed. The second problem was the resolution of the webcam. Due to the wide angle lens, the alps cover only a few ten pixels in height. Furthermore the cheap optics induced numerous artifacts. On top of that it could not be focused to infinity. This made it very difficult to identify the alps even for perfect conditions.

The only resort was to buy a camera with better resolution and better support for Linux. This was installed and working from March 27, 2018. The pictures were indeed much better both in resolution as well as in image quality and exposure. Until the end of the data acquisition period on April 10, 2019, in total 5990 pictures have been taken. Of those, 1064 fell into the dark time of the day and could not be analyzed. Of the rest, 1204 show Säntis, which

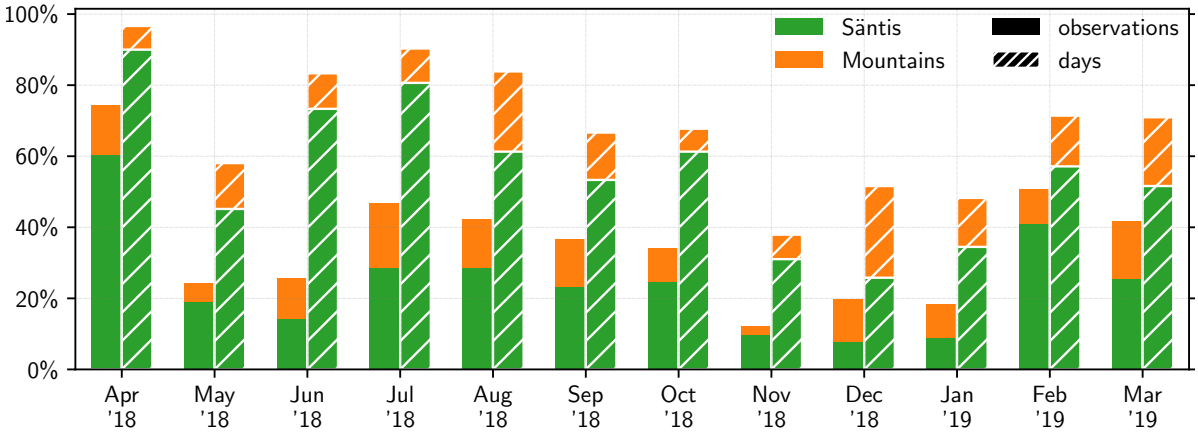

Figure F.2.: Probability to see Säntis (green) or at least some mountains (orange), split by month. The solid bars show the fraction of all observations, the hatched bars show the fraction of days with at least one sighting of Säntis or the mountains.

corresponds to about 24 % of the analyzable pictures. Another 564 pictures show parts of the mountain range, but not the silhouette of Säntis. This leaves 3158 pictures without any hint of Säntis, which corresponds to about 64 % of the analyzable pictures.

F.2.1. Statistics

In Figure F.2 we show the probability to see Säntis or at least the mountains for each month. This probability is calculated based on the total number of observations (solid bars), i.e. we count the number of images, which show Säntis and divide by the total number of analyzable images. As a comparison, we also calculate the probability for days with at least one sighting of Säntis (hatched bars). With this data, we find that April 2018 was a very fortunate month to see the Alps. More than half of the observations show them. There was barely a day, where Säntis did not show up. During the rest of the year, the chance to see Säntis is about 20 % to 30 %, with a minimum during the dark time of the year from November to January. Interestingly, the fraction of days which show Säntis at least once is about twice as large as the fraction of all observations. This indicates that the visibility changes during the day.

This hypothesis is analyzed in Figure F.3. The simplest approach is to group the observation by the hour of the day. This is shown in the left panel. We do indeed observe that the chance to see Säntis is about 40 % before eight o'clock in the morning, which then drops below 20 % around noon and increases again in the afternoon and evening. The low visibility at noon could be related to the contrast of the pictures, because Säntis is approximately south of Konstanz and therefore directly in the direction of the sun. From these statistics one could conclude that the best time of the day to see Säntis is at six or seven. This is of course not true for the whole year as it is still dark in winter at this time. Furthermore, since the days in summer are much longer, they are overweighted in this representation. Therefore, we also analyze the visibility based on the *time of the day*. For this purpose, we calculate for each day the times

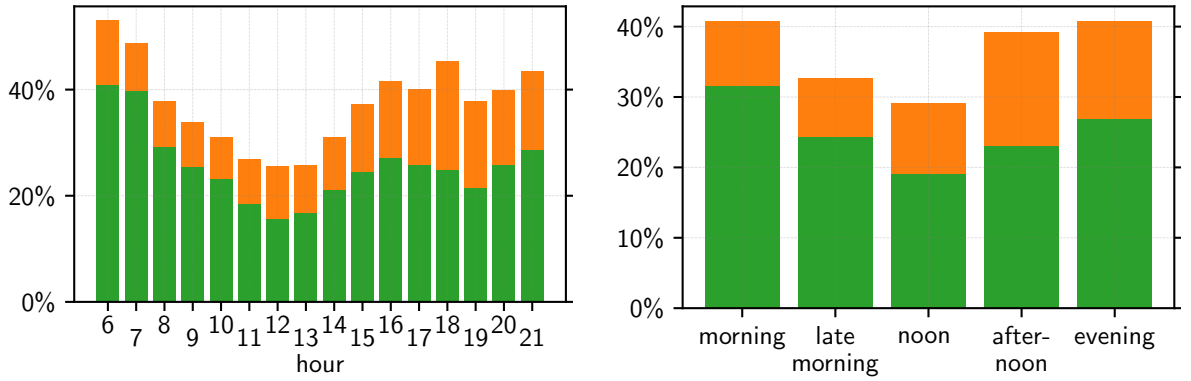

Figure F.3.: Visibility of Säntis during the day for the seasons. The fraction of observations with Säntis (green) or mountains (orange) is split by hour of the day (left) or by time of the day (right), which accounts for the different lengths of the day in summer and winter, see text for details.

for sunrise and sunset (see for example [Gre08]) and divide this time into five equal parts[1]. These five parts are labeled *morning*, *late morning*, *noon*, *afternoon* and *evening* from sunrise to sunset. On a day with sunrise at 7:00 and sunset at 17:00, this corresponds to morning from 7-9, late morning from 9-11, noon from 11-13, afternoon from 13-15 and evening from 15-17. This analysis is shown in the right panel of Figure F.3. We observe the same trend as in the analysis by hour with about 30 % visibility in the morning and 25 % in the evening and a minimum at noon. Hence, the reward for being early in the office is an increased probability for a nice view.

There is, however, a trade-off between going to work early and getting enough sleep if something was too interesting to go to bed early enough. Therefore, we may also ask if there are seasons where it is more probable to have a nice view of the mountains in the morning than others. Therefore, we evaluate the visibility by time of the day and season as shown in Figure F.4. Spring is from March to May (April and May 2018 and March 2019), summer is from June to August, autumn from September to October and winter from December to February. This reveals that it is beneficial in autumn and winter to come late and stay late as the visibility increases in the afternoon and evening. This could be related to the weather conditions at the lake, which favour fog in autumn and winter, which is often dissolved in the afternoon. In spring, the variation of the visibility during the day is comparatively small and always larger than 30 %. It seems that if Säntis is visible in the morning, it stays visible during the whole day, but it could also be that there is as many days where Säntis is only visible in the morning as days where Säntis is only visible in the afternoon and evening. The largest variation during the day is observed in summer. While the chance to see the mountains is almost 60 % in the morning, it drops below 30 % around noon and increases only slightly towards the evening. We can summarize that spring and summer are the best seasons to see Säntis (at least in the year 2018), but in summer, one should better get up early.

[1] to be precise we take the times of the nautical dusk and dawn as it is still possible to observe the horizon at those times.

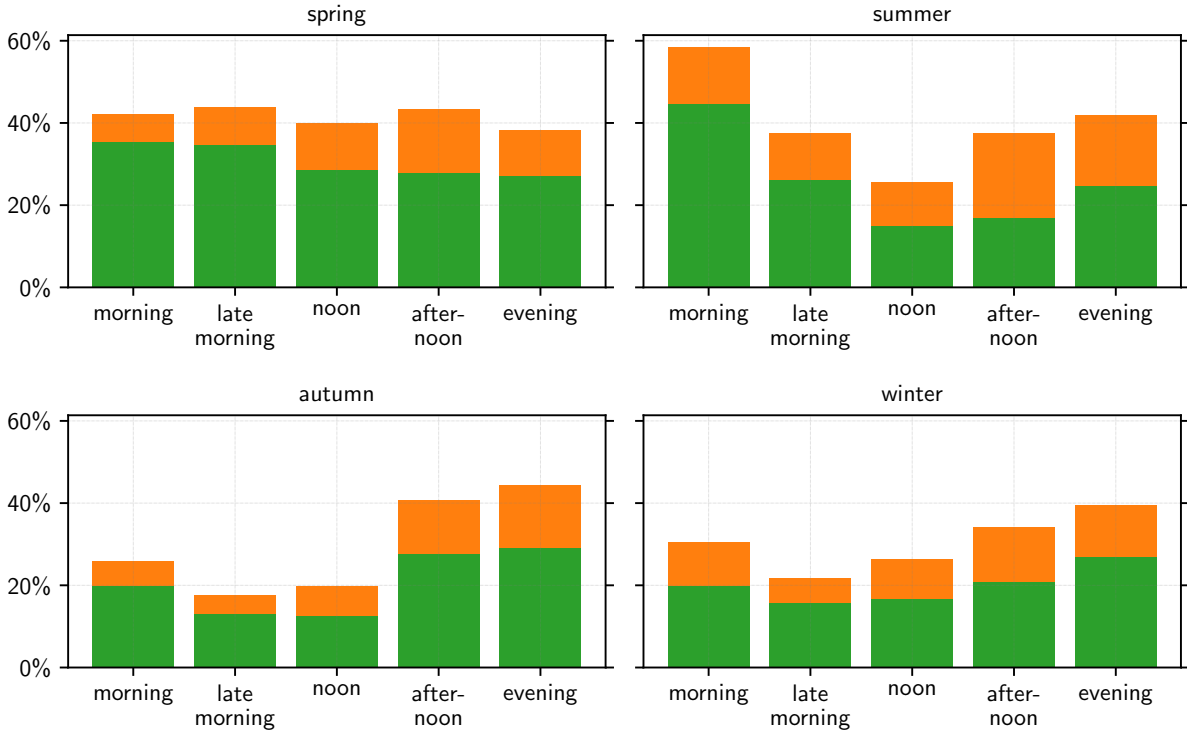

Figure F.4.: Visibility of Säntis during the day for the seasons. Spring is from March to May (April and May 2018 and March 2019), summer is from June to August, autumn from September to October and winter from December to February.

F.2.2. Conditional probabilities

In the previous section, we found from the statistics that some times and seasons have better chances for a nice view than others. For a physicist this is not yet satisfactory, because we are trained to find explanations for these patterns and are also interested in predicting phenomena. Therefore, we want to relate the visibility to the weather conditions in this section. To identify the most important indicators for or against visibility of Säntis, we use the concept of conditional probabilities. This will allow us later to predict the visibility based on Bayes' theorem [DP97]. To keep the analysis simple, we will restrict it to the cases where Säntis is either distinctly visible or distinctly not and ignore the observations where some mountains, but not the peak of Säntis were clearly visible.

In the following, we will need the concept of conditional probabilities (which we also used in the definition of the van Hove functions in (2.85)). In a nutshell, a conditional probability $P(A|B)$ describes the probability, that the event A will occur, provided the event B has occurred. It is defined via

$$P(A|B) = \frac{P(A \cap B)}{P(B)} \tag{F.1}$$

if $P(B) > 0$. In our case we will have events for the visibility: *visible* or *not visible* and events for the meteorological data (either predicted or measured), for instance, we measure

a temperature of 17 °C in Konstanz. We will collect all of these data into a vector $\boldsymbol{m}$. This allows us to determine the conditional probability for the meteorological data provided the visibility $v \in \{\text{visible}, \text{not visible}\}$ of Säntis, sloppily

$$P(\boldsymbol{m}|v) = \frac{P(\boldsymbol{m} \text{ and } v)}{P(v)}. \tag{F.2}$$

This statement will be rendered more precise below. Using the Bayes theorem [DP97, p. 104, Eq. (3)], we can invert this conditional probability to find the probability that Säntis is visible under the condition that there are given meteorological conditions

$$P(v|\boldsymbol{m}) = \frac{P(v)P(\boldsymbol{m}|v)}{P(\boldsymbol{m})} \tag{F.3}$$

The denominator is usually ignored as it a common prefactor for all categories v, which should be predicted (*visible* or *not visible* in our case). If the meteorological data $\boldsymbol{m}$ were independent, we could factorize the probabilities $P(\boldsymbol{m}|v) = P(m_1|v) \cdots P(m_N|v)$. Ignoring this condition and factorizing it anyway is the approximation for the "naive" Bayes approach [DP97, p. 104]. If has no knowledge about the probability distribution $P(v)$ one can use an equal probability for all categories v. This leads to

$$P(v|\boldsymbol{m}) \propto \prod_{i=1}^{N} P(m_i|v) \tag{F.4}$$

and the rule of the Bayes classifier is to choose the category, which has the largest value $P(v|\boldsymbol{m})$. Hence, provided we know $P(m_i|v)$, we can predict whether Säntis will be visible or not.

To apply this naive Bayes classifier, we have to give $P(m_i|v)$ a well defined meaning. Since the meteorological data are typically continuous variables, $P(m_i|v)$ is a probability density, which has to be estimated. In literature, often a Gaussian distribution is assumed for numerical values, which can be characterized by mean and variance. For our data, this is no good choice, as the distribution of the different meteorological data is often far from being Gaussian. For example, there are many days where the sky is completely free or completely covered, but only a few with values in between. We therefore resort to approximating the underlying probability distribution with a step function, by coarse-graining the continuous data into intervals. To account for the specific probability distributions, we sort our observations by value and divide this list into 20 equal bins (i.e. we calculate the α-quantiles with $\alpha = 0.05$). These bins define the categories for each observation, which have by construction all the same probability. After the bins are fixed, evaluating the corresponding conditional probabilities is a simple counting of the corresponding events.

Since we reduced the prediction to the simple decision whether Säntis is visible or not, we can rewrite the decision rule by analyzing the quotient

$$\frac{P(\text{visible}|\boldsymbol{m})}{P(\text{not visible}|\boldsymbol{m})} = \prod_{i=1}^{N} \frac{P(\text{visible}|m_i)}{P(\text{not visible}|m_i)}. \tag{F.5}$$

If it is larger than 1, it is more probable to see Säntis and if its smaller than 1, it is more probable that Säntis is hiding. This allows us to identify the categories with the largest predicting power

Table F.1.: Top five indicators of the forecasts for and against the visibility of Säntis. The ratio is given by $P(m_i|\text{visible})/(m_i|\text{not visible})$. The larger the value compared to 1, the more likely it is to see Säntis. The smaller the value compared to 1, the more unlikely it is to see Säntis. A value of 1 would indicate equal probabilities.

category m_i	ratio
precipitation in Konstanz $> 0.6\,\text{mm/h}$	$3.9 \cdot 10^{-2}$
temperature in Konstanz $< -0.7\,°\text{C}$	$6.3 \cdot 10^{-2}$
humidity in Konstanz $> 95\,\%$	$1.3 \cdot 10^{-1}$
temperature in Konstanz in $[-0.7\,°\text{C}, 0.7\,°\text{C}]$	$1.4 \cdot 10^{-1}$
precipitation in Konstanz in $[0.1\,\text{mm/h}, 0.3\,\text{mm/h}]$	$2.1 \cdot 10^{-1}$
temperature on Säntis in $[17.7\,°\text{C}, 18.9\,°\text{C}]$	2.0
low clouds on Säntis $< 1.5\,\%$	2.8
humidity on Säntis in $[43\,\%, 48\,\%]$	3.1
low clouds in Konstanz $< 1.5\,\%$	4.4
humidity on Säntis $< 43\,\%$	4.6

if the ratio is very large or very small. The top five indicators for the forecasts are listed in Table F.1 and for the measurements in Table F.2. Not surprisingly we find that precipitation in Konstanz is a strong indicator for bad visibility as well as high levels of humidity (fog). In the forecasts, we should look for small numbers of low cloud coverage in Konstanz and on Säntis as well as low humidity levels. For the measurements we again find that the humidity is an important ingredient for the visibility. If it is raining on Säntis or a relative humidity larger than 90 %, we cannot see it. On the other hand, if the relative humidity is low on Säntis and in Kreuzlingen, there is good chances that we can see Säntis. The best indicator, however, is the pressure difference between Zürich and Lugano, when it is is smaller than $-4.2\,\text{hPa}$. This is characteristic for the local weather condition foehn [MetFoe].

We can also analyze how these conditional probability ratios vary with the categories for a single observable. For example, we find that for forecasted temperatures larger than 11 °C in Konstanz or on Säntis the conditional probability to see Säntis is larger than the conditional probability not to see it. The humidity, measured or forecasted in Konstanz or on Säntis shows the opposite trend: the larger the humidity, the smaller the ratio. The turning point above which it is more likely that Säntis hides is between 65 % and 80 %. If the forecasted wind speeds in Konstanz are below 4 m/s there is also a better visibility, while the probability ratio for the wind speeds on Säntis do not exhibit any systematic variation. Using the measured wind speeds from Kreuzlingen, this threshold is even smaller: 0.5 m/s. This might be a consequence of the fact that strong wind appears in Konstanz only during storms, which also bring clouds and rain, while there is always some wind on the summits.

Good weather and naively also good visibility conditions can be associated with a lot of sunshine, i.e. many minutes of sunshine per hour. This is reflected in the conditional probabilities as well. If there is more than 25 to 30 minutes of sunshine per hour predicted, it is more likely to see Säntis. The corresponding meteorological measurement is the global radiation. If it

Table F.2.: Top five indicators of the measurements for and against the visibility of Säntis. The ratio is given by $P(m_i|\text{visible})/(m_i|\text{not visible})$. The larger the value compared to 1, the more likely it is to see Säntis. The smaller the value compared to 1, the more unlikely it is to see Säntis. A value of 1 would indicate equal probabilities.

category m_i	ratio
precipitation on Säntis $> 0.3\,\text{mm/h}$	0.0
humidity on Säntis $> 98.7\,\%$	$3.6 \cdot 10^{-2}$
humidity on Säntis in $[92.8\,\%, 96.2\,\%]$	$1.9 \cdot 10^{-1}$
humidity on Säntis in $[96.2\,\%, 98.7\,\%]$	$2.0 \cdot 10^{-1}$
humidity on Säntis in $[89.9\,\%, 92.8\,\%]$	$5.0 \cdot 10^{-1}$
humidity on Säntis in $[42.2\,\%, 52.9\,\%]$	3.2
humidity on Säntis in $[52.9\,\%, 59.4\,\%]$	3.5
pressure difference between Zürich and Lugano in $[-5.9\,\text{hPa}, -4.2\,\text{hPa}]$	3.5
humidity in Kreuzlingen $< 44.7\,\%$	7.6
pressure difference between Zürich and Lugano $< -5.9\,\text{hPa}$	8.3

exceeds $400\,\text{W/m}^2$ in Konstanz or on Säntis, we have good chances to see Säntis.

Bad weather is associated with clouds and we do indeed find that a view of Säntis is only likely if the predicted cloud coverage at low altitude is below 11 % in Konstanz and below 15 % on Säntis. For the cloud coverage at medium altitudes the threshold is between 5 % and 8 %, while at high altitudes there can be up to 80 % coverage and it is still more probable to see Säntis. Interestingly, for cloud coverages below 1 % it is more likely that Säntis is hiding. This might be related to the observation that a large fraction of the observations fall into these categories. Similarly, if there is rain in Konstanz or on Säntis (predicted or measured), it is very unlikely to see Säntis.

The simplest device to for a qualitative prediction of the weather is the barometer. However, the prediction and measurement of the atmospheric pressure is not a good indicator for the visibility of Säntis. There is no clear trend in the data and moreover it seems as if the conditional probabilities based on the measured pressures show a trend opposite to those obtained by the forecasted values. Nevertheless, we find a very strong trend when analyzing the measured pressure difference between Zurich and Lugano. If it is smaller than 0.5 hPa (i.e. when the pressure in Zurich is basically smaller than in Lugano), the chance to see Säntis is larger. The smaller this pressure difference, the larger is the probability ratio and the larger this pressure difference, the more likely it is that one cannot see Säntis.

In summary, we can confirm the naive good weather - good visibility, bad weather - bad visibility expectation, but we also find that the amount of water in the air plays an important role, either as humidity or as clouds in low and medium altitudes. A strong indicator for good visibility is also the pressure difference between Zurich and Lugano, which is representative for the local weather phenomenon of Foehn.

F.2.3. Prediction using a naive Bayes classifier

Finally, we want to test if we can predict the visibility of Säntis based on the weather forecast. To do so, we divide our observations randomly into two groups. The first one contains 80 % of our data, the second 20 %. The first group is used to calculate the conditional probabilities for each observation category, which are the temperature, the humidity, the pressure, the precipitation, the wind speed, the precipitation, the sunshine duration per hour and the cloud coverage in low, medium and high altitudes for Konstanz and Säntis. This is the training of our Bayes classifier. For the prediction, we use the naive Bayes classifier as described in (F.4).

We can then compare the results of the classifier with our classification in the second data set, which did not contribute to the conditional probabilities. We find that 71 % of the observations are properly classified. In about 7 % of the cases, our algorithms predicts that Säntis is not visible, even though it is and in the remaining 22 % of the cases, it predicts that Säntis is visible even though it is not. These probabilities also reflect the different occurrences of visible or not visible. Choosing a test sample with equal probabilities for visible and not visible, we have 74 % correct classifications, 11 % wrongly predicted that Säntis is not visible and 15 % wrongly predicted that Säntis is visible. These results suggest that we have identified some of the important variables for the prediction, but not all. Further studies could include the prediction of the pressure difference between Zurich and Lugano, which we were only able to include in the retrospective from the measurements as well as other factors such as the number of hours since the last rainfall, which washes dust out of the atmosphere. As a next step, one could also use more sophisticated neuronal networks to do the prediction.

Publications of the author

[GAPF16] M. Gruber, G. C. Abade, A. M. Puertas, and M. Fuchs, "Active microrheology in a colloidal glass", *Physical Review E*, **94**(4): 042602, (Oct. 2016). DOI: 10.1103/PhysRevE.94.042602.

[ŞGZ+19] N. Şenbil, M. Gruber, C. Zhang, M. Fuchs, and F. Scheffold, "Observation of strongly heterogeneous dynamics at the depinning transition in a colloidal glass", *Physical Review Letters*, **122**(10): 108002, (Mar. 13, 2019). DOI: 10.1103/PhysRevLett.122.108002.

Bibliography

[Aba17] G. Abade, "NOTES_MICRORHEOLOGY.PDF", (2017).

[AF14] C. P. Amann and M. Fuchs, "Transient stress evolution in repulsion and attraction dominated glasses", *Journal of Rheology*, **58**(5): 1191–1217, (Sep. 2014). DOI: 10.1122/1.4881256.

[AMY+96] F. Amblard, A. C. Maggs, B. Yurke, A. N. Pargellis, and S. Leibler, "Subdiffusion and anomalous local viscoelasticity in actin networks", *Physical Review Letters*, **77**(21): 4470–4473, (Nov. 18, 1996). DOI: 10.1103/PhysRevLett.77.4470.

[And95] P. W. Anderson, "Through the glass lightly", *Science*, **267**(5204): 1615–1616, (Mar. 17, 1995). DOI: 10.1126/science.267.5204.1615-e.

[Arn84] V. I. Arnol'd, *Catastrophe theory*. Berlin: Springer, (1984), ISBN: 978-3-540-12859-5.

[AS70] M. Abramowitz and I. A. Stegun, Eds., *Handbook of mathematical functions: with formulas, graphs, and mathematical tables*, 9th ed., Dover books on mathematics, New York, NY: Dover Publ, (1970), ISBN: 978-0-486-61272-0.

[Ash70] A. Ashkin, "Acceleration and trapping of particles by radiation pressure", *Physical Review Letters*, **24**(4): 156–159, (Jan. 26, 1970). DOI: 10.1103/PhysRevLett.24.156.

[Ban22] S. Banach, "Sur les opérations dans les ensembles abstraits et leur application aux équations intégrales", *Fundamenta Mathematicae*, **3**(1): 133–181, (1922).

[BB17] E. W. Burkholder and J. F. Brady, "Tracer diffusion in active suspensions", *Physical Review E*, **95**(5), (May 9, 2017). DOI: 10.1103/PhysRevE.95.052605.

[BB98] S. Bhattacharyya and B. Bagchi, "Decoupling of tracer diffusion from viscosity in a supercooled liquid near the glass transition", *The Journal of Chemical Physics*, **107**(15): 5852, (Aug. 31, 1998). DOI: 10.1063/1.474311.

[BDB+17] D. Bonn, M. M. Denn, L. Berthier, T. Divoux, and S. Manneville, "Yield stress materials in soft condensed matter", *Reviews of Modern Physics*, **89**(3), (Aug. 21, 2017). DOI: 10.1103/RevModPhys.89.035005.

[BFO14] N. J. Balmforth, I. A. Frigaard, and G. Ovarlez, "Yielding to stress: Recent developments in viscoplastic fluid mechanics", *Annual Review of Fluid Mechanics*, **46**(1): 121–146, (Jan. 3, 2014). DOI: 10.1146/annurev-fluid-010313-141424.

[BGK+90] J.-P. Bouchaud, A. Georges, J. Koplik, A. Provata, and S. Redner, "Superdiffusion in random velocity fields", *Physical Review Letters*, **64**(21): 2503–2506, (May 21, 1990). DOI: 10.1103/PhysRevLett.64.2503.

[BGS84] U. Bengtzelius, W. Götze, and A. Sjolander, "Dynamics of supercooled liquids and the glass transition", *Journal of Physics C: Solid State Physics*, **17**(33): 5915, (Nov. 30, 1984). DOI: 10.1088/0022-3719/17/33/005.

[BIPM18] Bureau International de Poids et Mesures. Resolution 1 of the 26th General Conference on Weights and Measures (CGPM), [Online]. Available: `https://www.bipm.org/en/CGPM/db/26/1/` (visited on 02/11/2019).

[BLJS09] T. Betz, M. Lenz, J.-F. Joanny, and C. Sykes, "ATP-dependent mechanics of red blood cells", *Proceedings of the National Academy of Sciences*, **106**(36): 15320–15325, (Sep. 8, 2009). DOI: `10.1073/pnas.0904614106`.

[BMMS08] I. N. Bronštejn, G. Musiol, H. Mühlig, and K. A. Semendjaev, *Taschenbuch der Mathematik*. Frankfurt am Main: Harri Deutsch, (2008), ISBN: 9783817120086.

[BNA09] C. Brunner, A. Niendorf, and J. A. Käs, "Passive and active single-cell biomechanics: A new perspective in cancer diagnosis", *Soft Matter*, **5**(11): 2171–2178, (2009). DOI: `10.1039/B807545J`.

[Bog00] D. Boger, "Rheology and the minerals industry", *Mineral Processing and Extractive Metallurgy Review*, **20**(1): 1–25, (Jan. 2000). DOI: `10.1080/08827509908962460`.

[Bog09] D. V. Boger, "Rheology and the resource industries", *Chemical Engineering Science*, **64**(22): 4525–4536, (Nov. 2009). DOI: `10.1016/j.ces.2009.03.007`.

[Bol68] L. Boltzmann, *Wissenschaftliche Abhandlungen*, F. Hasenöhrl, Ed., 3 vols. New York: Chelsea Pub. Co, (1968), vol. 1.

[Boo06] T. E. Booth, "Power iteration method for the several largest eigenvalues and eigenfunctions", *Nuclear Science and Engineering*, **154**(1): 48–62, (Sep. 2006). DOI: `10.13182/NSE05-05`.

[BP03] V. Breedveld and D. J. Pine, "Microrheology as a tool for high-throughput screening", *Journal of Materials Science*, **38**(22): 4461–4470, (2003).

[Bre74] H. Brenner, "Rheology of a dilute suspension of axisymmetric Brownian particles", *International Journal of Multiphase Flow*, **1**(2): 195–341, (Apr. 1974). DOI: `10.1016/0301-9322(74)90018-4`.

[Bro28] R. Brown, "A brief account of microscopical observations made in the months of June, July and August, 1827, on the particles contained in the pollen of plants; and on the general existence of active molecules in organic and inorganic bodies." *Philosophical Magazine Series 2*, **4**(21): 161–173, (Sep. 1828). DOI: `10.1080/14786442808674769`.

[BSB+10] J. M. Brader *et al.*, "Nonlinear response of dense colloidal suspensions under oscillatory shear: Mode-coupling theory and fourier transform rheology experiments", *Physical Review E*, **82**(6): 061401, (Dec. 13, 2010). DOI: `10.1103/PhysRevE.82.061401`.

[BT87] J. Bosse and J. S. Thakur, "Delocalization of small particles in a glassy matrix", *Physical Review Letters*, **59**(9): 998–1001, (Aug. 31, 1987). DOI: `10.1103/PhysRevLett.59.998`.

[But08] J. C. Butcher, *Numerical methods for ordinary differential equations*, 2nd ed. Chichester, England ; Hoboken, NJ: Wiley, (2008), ISBN: 978-0-470-72335-7.

[CH50] F. Crick and A. Hughes, "The physical properties of cytoplasm. a study by means of the magnetic particle method. part I. experimental", *Experimental Cell Research*, **1**(1): 37–80, (Jan. 1950). DOI: `10.1016/0014-4827(50)90048-6`.

[CH87] B. Cichocki and W. Hess, "On the memory function for the dynamic structure factor of interacting brownian particles", *Physica A: Statistical Mechanics and its Applications*, **141**(2–3): 475–488, (Mar. 1987). DOI: 10.1016/0378-4371(87)90176-2.

[Cri50] F. Crick, "The physical properties of cytoplasm. a study by means of the magnetic particle method. part II. theoretical treatment", *Experimental Cell Research*, **1**(4): 505–533, (Jan. 1950). DOI: 10.1016/0014-4827(50)90002-4.

[CS91] H. Clercx and P. Schram, "Quasistatic hydrodynamic interactions in suspensions", *Physica A: Statistical Mechanics and its Applications*, **174**(2): 293–324, (Jun. 1991). DOI: 10.1016/0378-4371(91)90336-B.

[CT59] M. H. Cohen and D. Turnbull, "Molecular transport in liquids and glasses", *The Journal of Chemical Physics*, **31**(5): 1164–1169, (Nov. 1959). DOI: 10.1063/1.1730566.

[Den12] R. Denk, "Skript zur Vorlesung: Mathematische Grundlagen der Quantenmechanik Wintersemester 2011/2012", Konstanz, (Feb. 23, 2012).

[dGen07] P.-G. de Gennes, *La Science des Rêves, Science et Vie Junior*, **214**, (May 18, 2007).

[DH98] B. Doliwa and A. Heuer, "Cage effect, local anisotropies, and dynamic heterogeneities at the glass transition: A computer study of hard spheres", *Physical Review Letters*, **80**(22): 4915–4918, (Jun. 1, 1998). DOI: 10.1103/PhysRevLett.80.4915.

[Dho96] J. K. G. Dhont, *An introduction to dynamics of colloids*, ser. Studies in interface science vol. 2. Amsterdam, Netherlands ; New York: Elsevier, (1996), ISBN: 978-0-444-82009-9.

[DM83] W. J. Dixon and F. J. Massey, *Introduction to statistical analysis*, 4th ed. New York: McGraw-Hill, (1983), ISBN: 978-0-07-017073-5.

[DP97] P. Domingos and M. Pazzani, "On the optimality of the simple bayesian classifier under zero-one loss", *Machine Learning*, **29**(2): 103–130, (Nov. 1, 1997). DOI: 10.1023/A:1007413511361.

[dVKvD+07] A. H. B. de Vries, B. E. Krenn, R. van Driel, V. Subramaniam, and J. S. Kanger, "Direct observation of nanomechanical properties of chromatin in living cells", *Nano Letters*, **7**(5): 1424–1427, (May 1, 2007). DOI: 10.1021/nl070603+.

[DW13] J. M. Dealy and J. Wang, *Melt Rheology and its Applications in the Plastics Industry*. Springer Science & Business Media, (May 14, 2013), ISBN: 978-94-007-6395-1.

[EG13] J. Elgeti and G. Gompper, "Wall accumulation of self-propelled spheres", *EPL (Europhysics Letters)*, **101**(4): 48003, (Feb. 1, 2013). DOI: 10.1209/0295-5075/101/48003.

[EH10] S. J. Ebbens and J. R. Howse, "In pursuit of propulsion at the nanoscale", *Soft Matter*, **6**(4): 726, (2010). DOI: 10.1039/b918598d.

[Eic14] P. Eich. Das Konstanzer Münster im Nebel, Bodenseepeter, [Online]. Available: http://www.bodenseepeter.de/2014/11/03/konstanz-nebel/ (visited on 04/16/2019).

[Ein05] A. Einstein, "Über die von der molekularkinetischen Theorie der Wärme geforderte Bewegung von in ruhenden Flüssigkeiten suspendierten Teilchen", *Annalen der Physik*, **322**(8): 549–560, (1905). DOI: 10.1002/andp.19053220806.

[Ein06] ——, "Eine neue Bestimmung der Moleküldimensionen", *Annalen der Physik*, **19**: 289–306, S1 (1906). DOI: 10.1002/andp.200590008.

[Ein36] ——, "Physics and reality", *Journal of the Franklin Institute*, **221**(3): 349–382, (Mar. 1936). DOI: 10.1016/S0016-0032(36)91047-5.

[EM14] D. J. Evans and G. P. Morriss, *Statistical mechanics of nonequilibrium liquids*, 2. ed., 1. paperb. ed. Cambridge: Cambridge Univ. Press, (2014), ISBN: 978-1-107-42453-1.

[Eve72] D. H. Everett, "Manual of symbols and terminology for physicochemical quantities and units, appendix II: Definitions, terminology and symbols in colloid and surface chemistry", *Pure and Applied Chemistry*, **31**(4): 577–638, (Jan. 1, 1972). DOI: 10.1351/pac197231040577.

[EWG15] J. Elgeti, R. G. Winkler, and G. Gompper, "Physics of microswimmers—single particle motion and collective behavior: A review", *Reports on Progress in Physics*, **78**(5): 056601, (Apr. 28, 2015). DOI: 10.1088/0034-4885/78/5/056601.

[Far90] H. Faridi, "Application of rheology in the cookie and cracker industry", *Dough Rheology and Baked Product Texture*, H. Faridi and J. M. Faubion, Eds., Boston, MA: Springer US, (1990). Pp. 363–384, ISBN: 978-1-4613-0861-4. DOI: 10.1007/978-1-4613-0861-4_8.

[FBH14] Y. Fily, A. Baskaran, and M. F. Hagan, "Dynamics of self-propelled particles under strong confinement", *Soft Matter*, **10**(30): 5609–5617, (Jul. 9, 2014). DOI: 10.1039/C4SM00975D.

[FBH15] ——, "Dynamics and density distribution of strongly confined noninteracting nonaligning self-propelled particles in a nonconvex boundary", *Physical Review E*, **91**(1), (Jan. 2015). DOI: 10.1103/PhysRevE.91.012125.

[FC02] M. Fuchs and M. E. Cates, "Theory of nonlinear rheology and yielding of dense colloidal suspensions", *Physical Review Letters*, **89**(24), (Nov. 25, 2002). DOI: 10.1103/PhysRevLett.89.248304.

[FESS17] L. S. Froufe-Pérez, M. Engel, J. J. Sáenz, and F. Scheffold, "Band gap formation and anderson localization in disordered photonic materials with structural correlations", *Proceedings of the National Academy of Sciences*, **114**(36): 9570–9574, (Sep. 5, 2017). DOI: 10.1073/pnas.1705130114.

[Fey80] R. Feynman, *The character of physical law*, 9. printing, ser. The MIT press paparback series 66. Cambridge, Mass.: The M.I.T. Press, (1980), ISBN: 978-0-262-06016-5.

[FFG+97] T. Franosch, M. Fuchs, W. Götze, M. R. Mayr, and A. P. Singh, "Asymptotic laws and preasymptotic correction formulas for the relaxation near glass-transition singularities", *Physical Review E*, **55**(6): 7153–7176, (Jun. 1997). DOI: 10.1103/PhysRevE.55.7153.

[FG94] T. Franosch and W. Götze, "A theory for a certain crossover in relaxation phenomena in glasses", *Journal of Physics: Condensed Matter*, **6**(26): 4807–4822, (Jun. 27, 1994). DOI: 10.1088/0953-8984/6/26/004.

[FGHL91] M. Fuchs, W. Götze, I. Hofacker, and A. Latz, "Comments on the alpha -peak shapes for relaxation in supercooled liquids", *Journal of Physics: Condensed Matter*, **3**(26): 5047, (1991). DOI: 10.1088/0953-8984/3/26/022.

[Fla57] C. Flammer, *Spheroidal wave functions*, ser. A Stanford Research Institute monograph. Stanford, Calif., Stanford University Press, 1957, (1957).

[Fre14] A. D. Freed, *Soft solids: a primer to the theoretical mechanics of materials*. Switzerland: Birkhäuser, (2014), ISBN: 978-3-319-03550-5.

[Fri18] S. Fritschi, "Event-driven brownian dynamics simulations of two-dimensional fluids far from equilibrium", (2018).

[FS17] E. M. Furst and T. M. Squires, *Microrheology*. Oxford University Press, (2017), ISBN: 978-0-19-965520-5.

[FS23] H. Freundlich and W. Seifriz, "Über die Elastizität von Solen und Gelen", *Zeitschrift für Physikalische Chemie*, **104U**(1), (Jan. 1, 1923). DOI: 10.1515/zpch-1923-10415.

[GAPF16] M. Gruber, G. C. Abade, A. M. Puertas, and M. Fuchs, "Active microrheology in a colloidal glass", *Physical Review E*, **94**(4): 042602, (Oct. 2016). DOI: 10.1103/PhysRevE.94.042602.

[Gaz08] I. Gazuz, "Active and passive particle transport in dense colloidal suspensions", PhD thesis, Universität Konstanz, (Aug. 25, 2008).

[GDR03] G. Gompper, J. K. G. Dhont, and D. Richter, "Komplexe Materialien auf mesoskopischer Skala: Was ist Weiche Materie?", *Physik in unserer Zeit*, **34**(1): 12–18, (Jan. 2003). DOI: 10.1002/piuz.200390002.

[GF13] I. Gazuz and M. Fuchs, "Nonlinear microrheology of dense colloidal suspensions: A mode-coupling theory", *Physical Review E*, **87**(3): 032304, (Mar. 2013). DOI: 10.1103/PhysRevE.87.032304.

[GL76] W. Götze and M. Lücke, "Dynamical structure factor $S(q, \omega)$ of liquid helium II at zero temperature", *Physical Review B*, **13**(9): 3825–3842, (May 1, 1976). DOI: 10.1103/PhysRevB.13.3825.

[Goe18] J. W. v. Goethe, *Faust: Historisch-kritische Edition*, Historisch-kritische Edition. Göttingen: Wallstein Verlag, (2018), ISBN: 978-3-8353-3334-5.

[Göt09] W. Götze, *Complex dynamics of glass-forming liquids : a mode-coupling theory*. Oxford University Press, (2009), ISBN: 978-0-19-923534-6.

[GPVF09] I. Gazuz, A. M. Puertas, T. Voigtmann, and M. Fuchs, "Active and Nonlinear Microrheology in Dense Colloidal Suspensions", *Physical Review Letters*, **102**(24): 248302, (Jun. 2009). DOI: 10.1103/PhysRevLett.102.248302.

[Gre08] R. Grena, "An algorithm for the computation of the solar position", *Solar Energy*, **82**(5): 462–470, (May 1, 2008). DOI: 10.1016/j.solener.2007.10.001.

[Gre54] M. S. Green, "Markoff random processes and the statistical mechanics of time-dependent phenomena. II. irreversible processes in fluids", *The Journal of Chemical Physics*, **22**(3): 398–413, (Mar. 1954). DOI: 10.1063/1.1740082.

[Gru14] M. Gruber, "Active microrheology considering parallel relaxation channels", Master thesis, Universität Konstanz, (Dec. 3, 2014).

[GS91] W. Götze and L. Sjögren, "β relaxation at the glass transition of hard-spherical colloids", *Physical Review A*, **43**(10): 5442–5448, (May 1, 1991). DOI: 10.1103/PhysRevA.43.5442.

[GS92] W. Götze and L. Sjögren, "Relaxation processes in supercooled liquids", *Reports on Progress in Physics*, **55**(3): 241–376, (Mar. 1992). DOI: 10.1088/0034-4885/55/3/001.

[GS95] W. Götze and L. Sjögren, "The mode coupling theory of structural relaxations", *Transport Theory and Statistical Physics*, **24**(6): 801–853, (Jul. 1, 1995). DOI: 10.1080/00411459508203936.

[GSO+97] F. Gittes, B. Schnurr, P. D. Olmsted, F. C. MacKintosh, and C. F. Schmidt, "Microscopic viscoelasticity: Shear moduli of soft materials determined from thermal fluctuations", *Physical Review Letters*, **79**(17): 3286–3289, (Oct. 27, 1997). DOI: 10.1103/PhysRevLett.79.3286.

[Har13] C. J. Harrer, "Active and nonlinear microrheology of dense colloidal suspensions", PhD thesis, Universität Konstanz, (Jul. 18, 2013).

[HB65] J. Happel and H. Brenner, *Low reynolds number hydrodynamics*, ser. Prentice-hall international series in the physical and chemical engineering sciences. Prentice-Hall, Inc., (1965).

[Hei12] A. L. Heilbronn, "Über Plasmaströmungen und deren Beziehungen zur Bewegung umlagerungsfähiger Stärke", *Berichte der Deutschen Botanischen Gesellschaft.*, **30**: 142–146, (1912).

[Hen16] S.-D. Henckell, "Length scales in active microrheology", Bachelor thesis, Universität Konstanz, Konstanz, (Sep. 2016).

[Her19] P. Heron. fswebcam. A neat and simple webcam app, Version 20140113, [Online]. Available: https://github.com/fsphil/fswebcam (visited on 01/15/2019).

[HK83] W. Hess and R. Klein, "Generalized hydrodynamics of systems of brownian particles", *Advances in Physics*, **32**(2): 173–283, (Jan. 1983). DOI: 10.1080/00018738300101551.

[HM07] J.-P. Hansen and I. R. McDonald, *Theory of simple liquids*, 3rd ed. Amsterdam; Boston: Elsevier / Academic Press, (2007), ISBN: 978-0-12-370535-8.

[Hoo78] R. Hooke, *Lectures de potentia restitutiva*. London: John Martyn, (1678).

[HPVF12] C. J. Harrer, A. M. Puertas, T. Voigtmann, and M. Fuchs, "Probability densities of a forced probe particle in glass: Results from mode coupling theory and simulations of active microrheology", *Zeitschrift für Physikalische Chemie*, **226**(7-8): 779–795, (2012). DOI: 10.1524/zpch.2012.0275.

[HR04] M. L. d. Haro and M. Robles, "The structure factor and equation of state of hard-sphere fluids", *Journal of Physics: Condensed Matter*, **16**(22): S2089–S2096, (May 2004). DOI: 10.1088/0953-8984/16/22/007.

[HSLW04] P. Habdas, D. Schaar, A. C. Levitt, and E. R. Weeks, "Forced motion of a probe particle near the colloidal glass transition", *Europhysics Letters*, **67**(3): 477, (Aug. 2004). DOI: 10.1209/epl/i2004-10075-y.

[HVCS10] Y. Hong, D. Velegol, N. Chaturvedi, and A. Sen, "Biomimetic behavior of synthetic particles: From microscopic randomness to macroscopic control", *Physical Chemistry Chemical Physics*, **12**(7): 1423–1435, (Feb. 3, 2010). DOI: 10.1039/B917741H.

[HWSF15] J. M. Häring, C. Walz, G. Szamel, and M. Fuchs, "Coarse-grained density and compressibility of nonideal crystals: General theory and an application to cluster crystals", *Physical Review B*, **92**(18): 184103, (Nov. 9, 2015). DOI: 10.1103/PhysRevB.92.184103.

[HZ16] N. J. Hoh and R. N. Zia, "Force-induced diffusion in suspensions of hydrodynamically interacting colloids", *Journal of Fluid Mechanics*, **795**: 739–783, (May 2016). DOI: 10.1017/jfm.2016.209.

[IB13] A. Ikeda and L. Berthier, "Yield stress in amorphous solids: A mode-coupling-theory analysis", *Physical Review E*, **88**(5), (Nov. 8, 2013). DOI: 10.1103/PhysRevE.88.052305.

[JF62] H. W. Jackson and E. Feenberg, "Energy spectrum of elementary excitations in helium II", *Reviews of Modern Physics*, **34**(4): 686–693, (Oct. 1, 1962). DOI: 10.1103/RevModPhys.34.686.

[Kar96] T. E. Karis, "An overview of rheology in the computer industry", *Journal of Applied Polymer Science*, **59**(9): 1405–1416, (Feb. 28, 1996). DOI: 10.1002/(SICI)1097-4628(19960228)59:9<1405::AID-APP8>3.0.CO;2-F.

[KB05] A. S. Khair and J. F. Brady, "Microviscoelasticity of colloidal dispersions", *Journal of Rheology (1978-present)*, **49**(6): 1449–1481, (Nov. 1, 2005). DOI: 10.1122/1.2085173.

[KB06] ——, "Single particle motion in colloidal dispersions: A simple model for active and nonlinear microrheology", *Journal of Fluid Mechanics*, **557**: 73–117, (Jun. 25, 2006). DOI: http://dx.doi.org/10.1017/S0022112006009608.

[KB08] ——, "Microrheology of colloidal dispersions: Shape matters", *Journal of Rheology*, **52**(1): 165, (2008). DOI: 10.1122/1.2821894.

[KEW+12] C. L. Klix, F. Ebert, F. Weysser, M. Fuchs, G. Maret, and P. Keim, "Glass elasticity from particle trajectories", *Physical Review Letters*, **109**(17), (Oct. 23, 2012). DOI: 10.1103/PhysRevLett.109.178301.

[KF17] C. Kurzthaler and T. Franosch, "Intermediate scattering function of an anisotropic Brownian circle swimmer", *Soft Matter*, **13**(37): 6396–6406, (Sep. 27, 2017). DOI: 10.1039/C7SM00873B.

[KLF16] C. Kurzthaler, S. Leitmann, and T. Franosch, "Intermediate scattering function of an anisotropic active Brownian particle", *Scientific Reports*, **6**(1), (Dec. 2016). DOI: 10.1038/srep36702.

[Kra19] D. Kraft. SciPy v1.2.1 reference guide — `scipy.optimize.fmin_slsqp`, [Online]. Available: https://docs.scipy.org/doc/scipy/reference/generated/scipy.optimize.fmin_slsqp.html (visited on 02/27/2019).

[Kub57] R. Kubo, "Statistical-Mechanical Theory of Irreversible Processes. I. General Theory and Simple Applications to Magnetic and Conduction Problems", *Journal of the Physical Society of Japan*, **12**(6): 570–586, (Jun. 15, 1957). DOI: 10.1143/JPSJ.12.570.

[Lag15] A. M. Laganapan, "Rheology and structure of ceramic suspensions under constraints : A computational study", PhD thesis, Limoges, (Nov. 26, 2015).

[Lan08] P. Langevin, "Sur la théorie du mouvement brownien", *Comptes rendus de l'Académie des sciences, Paris*, (146): 530–533, (1908).

[LBO+10] S. Lang, V. Boţan, M. Oettel, D. Hajnal, T. Franosch, and R. Schilling, "Glass transition in confined geometry", *Physical Review Letters*, **105**(12): 125701, (Sep. 2010). DOI: 10.1103/PhysRevLett.105.125701.

[LF17] S. Leitmann and T. Franosch, "Time-dependent fluctuations and superdiffusivity in the driven lattice lorentz gas", *Physical Review Letters*, **118**(1): 018001, (Jan. 3, 2017). DOI: 10.1103/PhysRevLett.118.018001.

[LL70] L. D. Landau and E. M. Lifšic, *Theory of elasticity*, 2. ed., rev. and enl, repr. 1986, ser. Course of theoretical physics. Oxford: Pergamon Press, (1970), vol. Vol. 7, ISBN: 978-0-08-006465-9.

[LLS+10] L. D. Landau, E. M. Lifšic, H.-G. Schöpf, G. Heber, and L. D. Landau, *Elastizitätstheorie*, Unveränd. Nachdr. der 7. Aufl, ser. Lehrbuch der theoretischen Physik. Frankfurt am Main: Deutsch, (2010), ISBN: 978-3-8171-1332-3.

[LMF+18] S. Leitmann, S. Mandal, M. Fuchs, A. M. Puertas, and T. Franosch, "Time-dependent active microrheology in dilute colloidal suspensions", *Physical Review Fluids*, **3**(10): 103301, (Oct. 11, 2018). DOI: 10.1103/PhysRevFluids.3.103301.

[LR15] J. L. Law and R. R. Rennie, "Glass", *A Dictionary of Physics*, J. Law and R. Rennie, Eds., Oxford University Press, (Sep. 17, 2015), ISBN: 978-0-19-871474-3.

[Max67] J. C. Maxwell, "IV. on the dynamical theory of gases", *Philosophical Transactions of the Royal Society of London*, **157**: 49–88, (Jan. 1, 1867). DOI: 10.1098/rstl.1867.0004.

[Maz02] R. M. Mazo, *Brownian motion: fluctuations, dynamics, and applications*, ser. Oxford science publications 112. Oxford : New York: Clarendon Press ; Oxford University Press, (2002), ISBN: 978-0-19-851567-8.

[MetFoe] Foehn chart, [Online]. Available: http://www.meteocentrale.ch/en/weather/foehn-and-bise/foehn.html (visited on 04/22/2019).

[MetSwi] MeteoSwiss IDAWEB, the Swiss Federal Office of Meteorology and Climatology, [Online]. Available: https://gate.meteoswiss.ch/idaweb/login.do (visited on 04/22/2019).

[MM80] G. Matheron and G. D. Marsily, "Is transport in porous media always diffusive? a counterexample", *Water Resources Research*, **16**(5): 901–917, (1980). DOI: 10.1029/WR016i005p00901.

[Mor65] H. Mori, "Transport, collective motion, and brownian motion", *Progress of Theoretical Physics*, **33**(3): 423–455, (Mar. 1, 1965). DOI: 10.1143/PTP.33.423.

[MS71] P. Moon and D. E. Spencer, *Field Theory Handbook*. Berlin, Heidelberg: Springer Berlin Heidelberg, (1971), ISBN: 978-3-540-02732-4. DOI: 10.1007/978-3-642-83243-7.

[MW12] J. Mewis and N. J. Wagner, *Colloidal suspension rheology*, ser. Cambridge series in chemical engineering. Cambridge ; New York: Cambridge University Press, (2012), ISBN: 978-0-521-51599-3.

[MW95] T. G. Mason and D. A. Weitz, "Optical measurements of frequency-dependent linear viscoelastic moduli of complex fluids", *Physical Review Letters*, **74**(7): 1250–1253, (Feb. 13, 1995). DOI: 10.1103/PhysRevLett.74.1250.

[New72] I. Newton, *Mathematische Principien der Naturlehre*. R. Oppenheim, (1872).

[New86] ——, *Philosophiae Naturalis Principia Mathematica*. London, (1686).

[Ols17] T. Olson, *Applied Fourier Analysis*. New York, NY: Springer New York, (2017), ISBN: 978-1-4939-7391-0.

[Osw09] P. Oswald, *Rheophysics: the deformation and flow of matter*. Cambridge ; New York: Cambridge University Press, (2009), ISBN: 978-0-521-88362-7.

[Pav14] G. A. Pavliotis, *Stochastic processes and applications: diffusion processes, the Fokker-Planck and Langevin equations*, ser. Texts in applied mathematics volume 60. New York: Springer, (2014), ISBN: 978-1-4939-1322-0.

[PD10] J. Perrin and J. Donau, "Die Brown'sche Bewegung und die wahre Existenz der Moleküle", *Kolloidchemische Beihefte*, **1**(6): 221–300, (Apr. 1, 1910). DOI: 10.1007/BF02552932.

[Pen55] R. Penrose, "A generalized inverse for matrices", *Mathematical Proceedings of the Cambridge Philosophical Society*, **51**(3): 406–413, (Jul. 1955). DOI: 10.1017/S0305004100030401.

[PJM12] R. E. Perez, P. W. Jansen, and J. R. R. A. Martins, "pyOpt: A python-based object-oriented framework for nonlinear constrained optimization", *Structural and Multidisciplinary Optimization*, **45**(1): 101–118, (Jan. 1, 2012). DOI: 10.1007/s00158-011-0666-3.

[PM08] A. D. Polyanin and A. V. Manzhirov, *Handbook of integral equations*, 2nd ed, ser. Handbooks of mathematical equations. Boca Raton: Chapman & Hall/CRC, (2008), ISBN: 978-1-58488-507-8.

[Pop16] G. Popkin, "The physics of life", *Nature News*, **529**(7584): 16, (Jan. 7, 2016). DOI: 10.1038/529016a.

[Pou96] A. D. Poularikas, Ed., *The transforms and applications handbook*, ser. The electrical engineering handbook series. Boca Raton Fla: CRC Press, (1996), ISBN: 978-0-8493-8342-7.

[PvM86] P. N. Pusey and W. van Megen, "Phase behaviour of concentrated suspensions of nearly hard colloidal spheres", *Nature*, **320**(6060): 340–342, (Mar. 1986). DOI: 10.1038/320340a0.

[PVP04] G. Petekidis, D. Vlassopoulos, and P. N. Pusey, "Yielding and flow of sheared colloidal glasses", *Journal of Physics: Condensed Matter*, **16**(38): S3955–S3963, (Sep. 2004). DOI: 10.1088/0953-8984/16/38/013.

[PY58] J. K. Percus and G. J. Yevick, "Analysis of classical statistical mechanics by means of collective coordinates", *Physical Review*, **110**(1): 1–13, (Apr. 1958). DOI: 10.1103/PhysRev.110.1.

[PZV+09] P. N. Pusey, E. Zaccarelli, C. Valeriani, E. Sanz, W. C. K. Poon, and M. E. Cates, "Hard spheres: Crystallization and glass formation", *Philosophical Transactions of the Royal Society of London A: Mathematical, Physical and Engineering Sciences*, **367**(1909): 4993–5011, (Dec. 28, 2009). DOI: 10.1098/rsta.2009.0181.

[Ras17] T. M. Ras, "Phonons and elasticity in disordered binary crystals", (2017).

[Rei06] M. Reichert, "Hydrodynamic interactions in colloidal and biological systems", PhD thesis, (2006).

[Rei19] L. Reinhardt. Bei welchem Wetter sehen wir von Konstanz aus das Alpenpanorama – und warum so oft nicht?, SÜDKURIER Online, [Online]. Available: https://www.suedkurier.de/region/kreis-konstanz/konstanz/Bei-welchem-Wetter-sehen-wir-von-Konstanz-aus-das-Alpenpanorama-und-warum-so-oft-auch-nicht;art372448,10026619 (visited on 01/23/2019).

[Ris96] H. Risken, *The Fokker-Planck equation: methods of solution and applications*, 2nd ed, ser. Springer series in synergetics v. 18. New York: Springer-Verlag, (1996), ISBN: 978-3-540-61530-9.

[RS05] M. G. Rasteiro and I. Salgueiros, "Rheology of particulate suspensions in ceramic industry", *Particulate Science and Technology*, **23**(2): 145–157, (Apr. 1, 2005). DOI: 10.1080/02726350590922206.

[Sai50] A. d. Saint-Exupéry, *Les oeuvres complètes d' A. de Saint-Exupéry*. Gallimard, (1950).

[SAJ+16] J. Schwarz-Linek *et al.*, "Escherichia coli as a model active colloid: A practical introduction", *Colloids and Surfaces B: Biointerfaces*, **137**: 2–16, (Jan. 2016). DOI: 10.1016/j.colsurfb.2015.07.048.

[SB05] T. M. Squires and J. F. Brady, "A simple paradigm for active and nonlinear microrheology", *Physics of Fluids (1994-present)*, **17**(7): 073101, (Jul. 1, 2005). DOI: 10.1063/1.1960607.

[Sei24] W. Seifriz, "An elastic value of protoplasm, with further observations on the viscosity of protoplasm", *Journal of Experimental Biology*, **2**(1): 1–11, (Oct. 1, 1924).

[SFK17] S. Steffenoni, G. Falasco, and K. Kroy, "Microscopic derivation of the hydrodynamics of active-Brownian-particle suspensions", en, *Physical Review E*, **95**(5), (May 2017). DOI: 10.1103/PhysRevE.95.052142.

[ŞGZ+19] N. Şenbil, M. Gruber, C. Zhang, M. Fuchs, and F. Scheffold, "Observation of strongly heterogeneous dynamics at the depinning transition in a colloidal glass", *Physical Review Letters*, **122**(10): 108002, (Mar. 13, 2019). DOI: 10.1103/PhysRevLett.122.108002.

[SH13] C. F. E. Schroer and A. Heuer, "Anomalous diffusion of driven particles in supercooled liquids", *Physical Review Letters*, **110**(6), (Feb. 8, 2013). DOI: 10.1103/PhysRevLett.110.067801.

[Sil99] H. Sillescu, "Heterogeneity at the glass transition: A review", *Journal of Non-Crystalline Solids*, **243**(2): 81–108, (Feb. 1, 1999). DOI: 10.1016/S0022-3093(98)00831-X.

[SK11] H. R. Schwarz and N. Köckler, "Numerische Integration", *Numerische Mathematik*. Wiesbaden: Vieweg+Teubner Verlag, (2011). Pp. 307–341, ISBN: 978-3-8348-1551-4. DOI: 10.1007/978-3-8348-8166-3_8.

[SK69] G. D. Scott and D. M. Kilgour, "The density of random close packing of spheres", *Journal of Physics D: Applied Physics*, **2**(6): 863–866, (Jun. 1969). DOI: 10.1088/0022-3727/2/6/311.

[SL15] F. Smallenburg and H. Löwen, "Swim pressure on walls with curves and corners", *Physical Review E*, **92**(3), (Sep. 2015). DOI: 10.1103/PhysRevE.92.032304.

[Spa15] S. E. Spagnolie, Ed., *Complex fluids in biological systems: experiment, theory, and computation*, Biological and medical physics, biomedical engineering, New York: Springer, (2015), ISBN: 978-1-4939-2064-8.

[Spe05] M. Sperl, "Nearly-logarithmic decay in the colloidal hard-sphere system", *Physical Review E*, **71**(6), (Jun. 13, 2005). DOI: 10.1103/PhysRevE.71.060401.

[SS15] D. Saintillan and M. J. Shelley, "Theory of active suspensions", *Complex Fluids in biological systems*, Springer, (2015). Pp. 319–355.

[SSV+10] L. Selvaggi *et al.*, "Multiple-particle-tracking to investigate viscoelastic properties in living cells", *Methods*, Xenopus Oocytes as an Experimental System, **51**(1): 20–26, (May 1, 2010). DOI: 10.1016/j.ymeth.2009.12.008.

[Sto51] G. G. Stokes, "On the effect of the internal friction of fluids on the motion of pendulums", *Transactions of the Cambridge Philosophical Society*, **IX**, (1851).

[Sut05] W. Sutherland, "A dynamical theory of diffusion for non-electrolytes and the molecular mass of albumin", *The London, Edinburgh, and Dublin Philosophical Magazine and Journal of Science*, **9**(54): 781–785, (Jun. 1, 1905). DOI: 10.1080/14786440509463331.

[SVF+16] J. R. Staunton, W. Vieira, K. L. Fung, R. Lake, A. Devine, and K. Tanner, "Mechanical properties of the tumor stromal microenvironment probed in vitro and ex vivo by in situ-calibrated optical trap-based active microrheology", *Cellular and Molecular Bioengineering*, **9**(3): 398–417, (Sep. 1, 2016). DOI: 10.1007/s12195-016-0460-9.

[SW04] D. Stranneby and W. Walker, *Digital Signal Processing and Applications, 2nd Edition*, 2nd ed. Newnes, (Nov. 4, 2004), ISBN: 978-0-08-047252-2.

[TB05] G. Tabilo-Munizaga and G. V. Barbosa-Cánovas, "Rheology for the food industry", *Journal of Food Engineering*, **67**(1): 147–156, (Mar. 2005). DOI: 10.1016/j.jfoodeng.2004.05.062.

[Tew73] R. P. Tewarson, *Sparse matrices*, ser. Mathematics in science and engineering 99. New York: Academic Press, (1973), ISBN: 978-0-12-685650-7.

[TKW02] Y. Tseng, T. P. Kole, and D. Wirtz, "Micromechanical mapping of live cells by multiple-particle-tracking microrheology", *Biophysical Journal*, **83**(6): 3162–3176, (Dec. 1, 2002). DOI: 10.1016/S0006-3495(02)75319-8.

[TTD00] S. Torquato, T. M. Truskett, and P. G. Debenedetti, "Is Random Close Packing of Spheres Well Defined?", en, *Physical Review Letters*, **84**(10): 2064–2067, (Mar. 2000). DOI: 10.1103/PhysRevLett.84.2064.

[TYB14] S. C. Takatori, W. Yan, and J. F. Brady, "Swim Pressure: Stress Generation in Active Matter", *Physical Review Letters*, **113**(2): 028103, (Jul. 2014). DOI: 10.1103/PhysRevLett.113.028103.

[Van54] L. Van Hove, "Correlations in space and time and born approximation scattering in systems of interacting particles", *Physical Review*, **95**(1): 249–262, (Jul. 1954). DOI: 10.1103/PhysRev.95.249.

[VBB04] F. Varnik, L. Bocquet, and J.-L. Barrat, "A study of the static yield stress in a binary lennard-jones glass", *The Journal of Chemical Physics*, **120**(6): 2788–2801, (Feb. 8, 2004). DOI: 10.1063/1.1636451.

[vMU93] W. van Megen and S. M. Underwood, "Glass transition in colloidal hard spheres: Mode-coupling theory analysis", *Physical Review Letters*, **70**(18): 2766–2769, (May 3, 1993). DOI: 10.1103/PhysRevLett.70.2766.

[Vol04] K. Vollmayr-Lee, "Single particle jumps in a binary lennard-jones system below the glass transition", *The Journal of Chemical Physics*, **121**(10): 4781, (Aug. 23, 2004). DOI: 10.1063/1.1778155.

[VPF04] T. Voigtmann, A. Puertas, and M. Fuchs, "Tagged-particle dynamics in a hard-sphere system: Mode-coupling theory analysis", *Physical Review E*, **70**(6), (Dec. 2004). DOI: 10.1103/PhysRevE.70.061506.

[vSmo06] M. von Smoluchowski, "Zur kinetischen Theorie der Brownschen Molekularbewegung und der Suspensionen", *Annalen der Physik*, **326**(14): 756–780, (Jan. 1906). DOI: 10.1002/andp.19063261405.

[VW59] V. Volterra and E. T. Whittaker, *Theory of functionals and of integral and integro-differential equations*, (1959).

[VW72] L. Verlet and J.-J. Weis, "Equilibrium theory of simple liquids", *Physical Review A*, **5**(2): 939–952, (Feb. 1, 1972). DOI: 10.1103/PhysRevA.5.939.

[VZ12] T. Vicsek and A. Zafeiris, "Collective motion", *Physics Reports*, Collective motion, **517**(3): 71–140, (Aug. 1, 2012). DOI: 10.1016/j.physrep.2012.03.004.

[WB09] N. J. Wagner and J. F. Brady, "Shear thickening in colloidal dispersions", *Physics Today*, **62**: 27–32, (Oct. 2009).

[WB51] Waterson J. J. and Beaufort Francis, "On the physics of media that are composed of free and perfectly elastic molecules in a state of motion", *Abstracts of the Papers Communicated to the Royal Society of London*, **5**: 604–604, (Jan. 1, 1851). DOI: 10.1098/rspl.1843.0077.

[WBS92] Waterson J. J., Beaufort Francis, and Strutt John William, "On the physics of media that are composed of free and perfectly elastic molecules in a state of motion", *Philosophical Transactions of the Royal Society of London. (A.)*, **183**: 1–79, (Jan. 1, 1892). DOI: 10.1098/rsta.1892.0001.

[Wee16] E. R. Weeks, "Introduction to the colloidal glass transition", *ACS Macro Letters*, **6**(1): 27–34, (Dec. 27, 2016). DOI: 10.1021/acsmacrolett.6b00826.

[WeiCom] E. W. Weisstein. Complex argument, From MathWorld – A Wolfram Web Resource, [Online]. Available: `http://mathworld.wolfram.com/ComplexArgument.html` (visited on 02/26/2019).

[WeiEll] ——, Ellipsoid, From MathWorld – A Wolfram Web Resource, [Online]. Available: `http://mathworld.wolfram.com/Ellipsoid.html` (visited on 08/15/2017).

[WeiPro] ——, Prolate spheroidal coordinates, MathWorld, [Online]. Available: `http://mathworld.wolfram.com/ProlateSpheroidalCoordinates.html` (visited on 02/05/2019).

[WH13] D. Winter and J. Horbach, "Nonlinear active micro-rheology in a glass-forming soft-sphere mixture", *The Journal of Chemical Physics*, **138**(12): 12A512, (Jan. 3, 2013). DOI: `10.1063/1.4770335`.

[WHVB12] D. Winter, J. Horbach, P. Virnau, and K. Binder, "Active nonlinear microrheology in a glass-forming yukawa fluid", *Physical Review Letters*, **108**(2): 028303, (Jan. 11, 2012). DOI: `10.1103/PhysRevLett.108.028303`.

[WMT06] D. Weihs, T. G. Mason, and M. A. Teitell, "Bio-microrheology: A frontier in microrheology", *Biophysical Journal*, **91**(11): 4296–4305, (Dec. 1, 2006). DOI: `10.1529/biophysj.106.081109`.

[WPFV10] F. Weysser, A. M. Puertas, M. Fuchs, and T. Voigtmann, "Structural relaxation of polydisperse hard spheres: Comparison of the mode-coupling theory to a langevin dynamics simulation", *Physical Review E*, **82**(1): 011504, (Jul. 27, 2010). DOI: `10.1103/PhysRevE.82.011504`.

[WWB80] P. E. Watson, I. D. Watson, and R. D. Batt, "Total body water volumes for adult males and females estimated from simple anthropometric measurements", *The American Journal of Clinical Nutrition*, **33**(1): 27–39, (Jan. 1, 1980). DOI: `10.1093/ajcn/33.1.27`.

[Wyn64] P. Wynn, "On some recent developments in the theory and application of continued fractions", *Journal of the Society for Industrial and Applied Mathematics: Series B, Numerical Analysis*, **1**(1): 177–197, (1964). DOI: `10.1137/0701015`.

[Yat74] R. C. Yates, *Curves and their properties*. National Council of Teachers of Mathematics, (1974).

[YB15a] W. Yan and J. F. Brady, "The force on a boundary in active matter", *Journal of Fluid Mechanics*, **785**, (Dec. 2015). DOI: `10.1017/jfm.2015.621`.

[YB15b] ——, "The swim force as a body force", *Soft Matter*, **11**(31): 6235–6244, (2015). DOI: `10.1039/C5SM01318F`.

[ZB10] R. N. Zia and J. F. Brady, "Single-particle motion in colloids: Force-induced diffusion", *Journal of Fluid Mechanics*, **658**: 188–210, (Sep. 2010). DOI: `10.1017/S0022112010001606`.

[ZB12] ——, "Microviscosity, microdiffusivity, and normal stresses in colloidal dispersions", *Journal of Rheology*, **56**(5): 1175, (Jun. 20, 2012). DOI: `10.1122/1.4722880`.

[ZGM+16] C. Zhang, N. Gnan, T. G. Mason, E. Zaccarelli, and F. Scheffold, "Dynamical and structural signatures of the glass transition in emulsions", *Journal of Statistical Mechanics: Theory and Experiment*, **2016**(9): 094003, (Sep. 2016). DOI: 10.1088/1742-5468/2016/09/094003.

[Zia18] R. N. Zia, "Active and passive microrheology: Theory and simulation", *Annual Review of Fluid Mechanics*, **50**(1): 371–405, (2018). DOI: 10.1146/annurev-fluid-122316-044514.

[Zwa01] R. Zwanzig, *Nonequilibrium statistical mechanics*. Oxford ; New York: Oxford University Press, (2001), ISBN: 0195140184.

[Zwa61] ——, "Memory effects in irreversible thermodynamics", *Physical Review*, **124**(4): 983–992, (Nov. 15, 1961). DOI: 10.1103/PhysRev.124.983.

[Zwa65a] R. Zwanzig, "Time-correlation functions and transport coefficients in statistical mechanics", *Annual Review of Physical Chemistry*, **16**(1): 67–102, (Oct. 1965). DOI: 10.1146/annurev.pc.16.100165.000435.

[Zwa65b] R. Zwanzig, "Frequency-dependent transport coefficients in fluid mechanics", *The Journal of Chemical Physics*, **43**(2): 714–720, (Jul. 15, 1965). DOI: 10.1063/1.1696795.

«Adieu», dit le renard. «Voici mon secret. Il est très simple:
on ne voit bien qu'avec le cœur. L'essentiel est invisible pour les yeux.»

Le pétit prince, Antoine de Saint-Exupéry [Sai50, p. 996]